Neutron Stars:
Robust Constraints on Dense Matter from Astrophysics

Thesis by
Isaac Norman Legred

In Partial Fulfillment of the Requirements for the
Degree of
Doctor of Philosophy

CALIFORNIA INSTITUTE OF TECHNOLOGY
Pasadena, California

2025
Defended May 23, 2025

Isaac Norman Legred
ORCID: 0000-0002-9523-9617

ACKNOWLEDGEMENTS

There are many people I would like to thank for their continued support in getting to the point in my life where I could write this thesis. First, *my grandfather, Norm*: who showed me on a paper tablecloth, using a crayon from a kids menu, why inertial and gravitational mass perfectly cancel in Newton's gravity. In this and in countless ways, he demonstrated the gift of meeting the world where it is, rather than where we expect it to be. I would also like to thank all of my grandparents for their support and encouragement when I was deciding what I would like to do with my life. In particular I would like to thank *my grandparents, Arlen and Mona*, for their incredible hospitality, and *my grandmother Eula*, for her demonstration of curiosity and spirit of adventure in everything she did. I would like to thank *my father, Kurt*, for teaching me how to listen before making judgements, and *my mother, Susan*, who has supported me through everything in life, while constantly reminding me to greet each new day with a hope to make the world better. I would like to thank *my brother, Spencer, and sister-in-law, Maddy*, for binding family and friends together in ways I can scarcely imagine possible. I would also like to thank all of my family for being supportive in good times and bad, and for providing a wonderful environment to grow up in. I am particularly grateful to Mahtomedi public schools, and the remarkable friends I made there. I can imagine I wouldn't have been doing physics at all without the encouragement of teachers, friends, and other mentors. I thank St. Andrew's Lutheran Church for providing a nurturing environment when I was young, and I thank the community for continued presence in my life.

I would also like to thank the friends and mentors I found at Cornell University in the course of my undergraduate studies. In particular I would like to thank the Simulating eXtreme Spacetimes group at Cornell for mentoring me. Among others, I'd like to thank Prof. Saul Teukolsky, Larry Kidder, and Prof. Nils Deppe, who spent many hours teaching me how to do computational research, and have continued to be stellar mentors over the years. I would also like to explicitly thank the many friends I found in the math and physics department at Cornell; it is easy to imagine I would not still be doing physics if it weren't for the remarkable insights shared with me by peers at sometimes unusual hours in the course of learning everything that I didn't know. In particular, I'd like to thank Linus, Misha, Jake, Kabir, Caleb, Philip, Arthur, Valerie, Jessie, Daniel, Alex, Cosmo (Ted), Murali, and others, as well as the members of Cornell's chapter of Alpha Phi Omega, including Sarah, Kei-lani, Hellen, Edison, Jia Yi, and others. Finally I'd like to thank the many other friends that supported me, including Trevor, Jesse, Michael, Jacinto, Greg, Ruojia, and many more. I'd also like to thank Rebecca for teaching me about the solution to the falling cat problem.

Finally, I would like to acknowledge all of those that have helped me in ways large and small in my time at Caltech. First, I thank all of the members of the LIGO lab, the numerical relativity group, the theoretical relativity group for providing a very stimulating environment for research. I'd first like to very emphatically thank my advisor, Prof. Katerina Chatziioannou, for providing exceptional guidance in my journey as a scientist. I do not imagine I would have been able to achieve a fraction of what I have without her expertise. I'd also like to thank Prof. Alan Weinstein for being a phenomenal catalyst of both scientific discussion, and entertaining stories. In his running of the SURF program over many years, I could not imagine a more enthusiastic and dedicated advocate for the next generation of scientists. I'd also like to thank the other members of my thesis committee for providing useful comments, questions, and insights throughout my time at Caltech. Again, I'd thank Prof. Saul Teukolsky for being both remarkably wise, but also remarkably generous in sharing wisdom with young researchers. I'd also like to thank Prof. Mansi Kasliwal who encouraged me to learn more about the remarkable nature of the universe as seen through telescopes. I'd additionally like to thank Prof. Elias Most for useful comments in preparing this thesis, along with many useful insights over the course of my Ph.D. I'd also like to thank my collaborators I have not already thanked, including Reed Essick, Philippe Landry, Sophia Han, Oscar Sy-Garcia, Francois Foucart, François Hébert, Liam Brodie, Alexander Haber, Adrian Abac, Tim Dietrich, Eliot Finch, Jacob Golomb, Yoonsoo Kim and others. Finally, I'd like to explicitly thank the postdocs of Caltech, including Derek Davis, Nils Vu, Lucy Thomas, Sophie Bini, Ryan Magee, Michael Pajkos, Jane Glanzer, Javier Roulet, Pat Myers, and many others. Finally, I'd like to thank all of the SURF students I've had the pleasure of working with, in particular Celine Wang, Oscar Sy-Garcia, Carter Anderson, and Lana Alabassi, all of whom are truly exceptional researchers.

The graduate students of Caltech have in so many ways, both academically and nonacademically made positive experiences at Caltech possible. I'd like to thank in particular, though in no particular order, the graduate students of the LIGO data group, Ethan, Simona, Rhiannon, Sophie, Taylor, and in numerical and analytical relativity, Kyle, Guido, Dongze, Himanshu, Sarah, Talya, Isabella, Yuan, Jiaxi, Vittoria, Haiyang, Brian, Colin, Andrew, Jiaxiang, and others. In addition to this, I would like to thank other graduate students in astrophysics (and former graduate students), Nicholas, Nadine, Albert, Grigory, Kiran, Saren, and others for broadening my understanding of astrophysics beyond the narrow confines of relativity. I'd also like to thank other graduate students in physics and applied physics, including Hannah, David, James, Su, Anchal, Ian(s), Radhika, and the many other members of the gravitational waves instrumentation groups, who have collectively enlightened me substantially on the nature of quantum mechanics, and in particular, the nature of lasers. I'd like to also acknowledge Steven, not the least of which because we share a Minnesotan heritage, and Sasha, for teaching me about the connection between music and oscilloscopes . Beyond this, I'd also like to thank all of the graduate student colleagues I found at Caltech, it truly is a pleasure to work with so many people who are so gifted in what they do. Among the graduate students I would like to thank, I'd especially like to mention the members of the Graduate Christian Fellowship at Caltech, who have been a remarkable source of calm in an often tumultuous student experience. I'd particularly like to thank Sami, Raymond, Tara, Grace, Maria, Nathan, Andy, and all the others who served on leadership roles in the fellowship. Finally, there are many people not associated with Caltech who I would like to mention, including members of Missio community church. I'd also thank many friends from outside Caltech, including those who have been companions in Dungeons and Dragons, and all of the members and friends of the Caltech Tango club. From the bottom of my heart, I'd like to thank Karrie for believing in me, often more than I believed in myself, as I prepared this thesis. The many kind words, thoughts, and fervent prayers of countless people have been truly invaluable to me over the years.

I would like to thank the United States government scientific funding agencies, and the American taxpayers for making this work possible. In particular, the Department of Energy, the National Science Foundation, and

In the same spirit, I'd like to thank the many people who have gone before and contributed to making the world a more wonderful place to live in and explore. This thesis is dedicated to them.

Abstract

Neutron stars are exceptional astrophysical objects, harboring likely the densest matter in the universe outside of black holes. However, uncertainty in the properties of matter at the densities achieved inside of neutron stars means that the structure of neutron stars cannot be fully understood from first principles. Modern statistical and computational tools however, along with cutting-edge observational strategies have enabled the properties of neutron stars to be constrained using astrophysical data. In this thesis, I will discuss work I have carried out examining what can be learned about neutron stars, and the dense matter inside of them, using electromagnetic and gravitational-wave observations of neutron stars. In particular, I will discuss constraints on nonparametric models of the dense-matter equation of state, and why nonparametric models are an effective strategy for faithfully representing uncertainty. I will also discuss the interplay between understanding the astrophysical channels for forming neutron stars, and the neutron-star matter equation of state, including how we can use our understanding of dense matter to classify objects. Finally, I will discuss some considerations for simulating astrophysical neutron stars, which is necessary in order to interpret the full range of astrophysical observations of merging neutron stars, such as the neutron star merger GW170817.

PUBLISHED CONTENT AND CONTRIBUTIONS

[1] Isaac Legred et al. “Nonparametric extensions of nuclear equations of state: probing the breakdown scale of relativistic mean-field theory”. In: (May 2025). I led this study which examines how nonparametric models of the equation of state can be used to extend nuclear calculations. I developed the project idea, developed software, performed analyses, and wrote the bulk of the manuscript. arXiv: 2505.07677 [nucl-th].

[2] Jacob Golomb et al. “The interplay of astrophysics and nuclear physics in determining the properties of neutron stars”. In: (Oct. 2024). I co-led this study with Jacob Golomb studying how astrophysical and dense-matter physics can be disentangled via hierarchical analysis. I performed equation of state analyses, and co-wrote the text of the manuscript. arXiv: 2410.14597 [astro-ph.HE].

[3] Jacob Golomb et al. “Using equation of state constraints to classify low-mass compact binary mergers”. In: *Phys. Rev. D* 110.6 (2024). I co-led this study with Jacob Golomb examining whether subsolar mass neutron stars could be reliably distinguished from subsolar mass black holes with current LIGO detectors. I performed the equation of state inference step, and co-wrote the manuscript, p. 063014. DOI: 10.1103/PhysRevD.110.063014. arXiv: 2403.07697 [astro-ph.HE].

[4] Isaac Legred et al. “Assessing equation of state-independent relations for neutron stars with nonparametric models”. In: *Phys. Rev. D* 109.2 (2024). I co-led this project on analyzing the goodness of fit of universal relations to nonparametric equations of state, along with Oscar Sy-Garcia who performed a substantial amount of the analyses as a SURF student. This included development of the project, writing the manuscript, and running final analyses., p. 023020. DOI: 10.1103/PhysRevD.109.023020. arXiv: 2310.10854 [astro-ph.HE].

[5] Elias R. Most et al. “Nonlinear Alfvén-wave Dynamics and Premerger Emission from Crustal Oscillations in Neutron Star Mergers”. In: *Astrophys. J. Lett.* 973.2 (2024). I contributed to this study which analyzed the prospect for electromagnetic transients to arise from resonant shattering of neutron star crusts during binary inspirals. I contributed to design of the simulation setup, and the text, p. L37. DOI: 10.3847/2041-8213/ad785c. arXiv: 2407.17026 [astro-ph.HE].

[6] Reed Essick et al. “Phase transition phenomenology with nonparametric representations of the neutron star equation of state”. In: *Phys. Rev. D* 108.4 (2023). I contributed substantially to this study which used nonparametric methods to constrain phase transitions in a nonparametric model of the equation of state. I performed the simulation analyses, developed several

diagnostic statistics, and wrote large parts of the text., p. 043013. DOI: 10.1103/PhysRevD.108.043013. arXiv: 2305.07411 [astro-ph.HE].

[7] Isaac Legred et al. "Simulating neutron stars with a flexible enthalpy-based equation of state parametrization in spectre". In: *Phys. Rev. D* 107.12 (2023). I led this project building a flexible equation of state model, implementing it in the SpECTRE code, and running relativistic simulation of neutron stars. I developed the project idea, constructed the equation of state model, implemented it, and ran analyses. I also wrote the bulk of the text in the manuscript., p. 123017. DOI: 10.1103/PhysRevD.107.123017. arXiv: 2301.13818 [astro-ph.HE].

[8] Isaac Legred et al. "Implicit correlations within phenomenological parametric models of the neutron star equation of state". In: *Phys. Rev. D* 105.4 (2022). I led this study which compared parametric to nonparametric methods of inferring the equation of state. I developed a substantial amount of software, ran the analysis, and co-wrote the manuscript., p. 043016. DOI: 10.1103/PhysRevD.105.043016. arXiv: 2201.06791 [astro-ph.HE].

[9] Isaac Legred et al. "Impact of the PSR J0740 + 6620 radius constraint on the properties of high-density matter". In: *Phys. Rev. D* 104 (6 Sept. 2021). I led this study on the impact of the the NICER mass-radius constraint on the mllisecond x-ray pulsar J0740+6620 on nonparametric equation of state constraints. I developed software, some of which was contributed by other collaborators from previous projects, ran the analysis, and co-wrote the manuscript., p. 063003. DOI: 10.1103/PhysRevD.104.063003. URL: https://link.aps.org/doi/10.1103/PhysRevD.104.063003.

CONTENTS

LIST OF FIGURES

LIST OF TABLES

Chapter 1

INTRODUCTION

Background

The earliest notion of a neutron star was introduced by Carl Baade and Fritz Zwicky in 1934 [9], almost immediately after the discovery of the neutron by James Chadwick based originally on experiments performed by Irène Joliot-Curie and Frédéric Joliot, and theoretical motivation provided by Ernest Rutherford [25]. The idea was simple: the core of a massive star could collapse to a very compact form by protons and electrons merging into neutrons. The resulting object would be stabilized by degeneracy pressure of the resulting neutrons. Such an object was quickly termed a *neutron star* or alternatively a neutron core. Calculations by J. Robert Oppenheimer and George Volkoff, however, soon showed that barring a strong repulsive force between neutrons at high densities, the maximum mass allowed for such a neutron star in general relativity would be near $0.7\ M_{\odot}$, substantially less than the maximum mass of a white dwarf (an analogous object supported by pressure from degenerate electrons). Therefore, it was unclear how a neutron star could even form, as the only plausible formation scenario for such an object would be the rapid collapse of a stellar core which would presumably be halted by electron degeneracy well before nuclear interactions were relevant. In fact, in their 1939 paper [61], Oppenheimer and Volkoff explicitly state “it seems unlikely that neutron cores can play any significant part in stellar evolution”.

Indeed, if it had turned out that the effective strong force was either not dynamically relevant, or mildly attractive in the cores of neutron stars, then very likely no neutron stars would exist. In that case we would know very little about the properties of matter above the densities of atomic nuclei. However, the discovery of pulsars by Jocelyn Bell Burnell provided nearly incontrovertible evidence of the existence of neutron-star like objects. Despite advances in nuclear physics, quantum chromodynamics is generically intractable because it is a strongly coupled quantum field theory [75], so the properties of neutron stars still are not computable from first principles. Nonetheless certain advancements such as chiral effective field theory [81] represent systematically improvable, perturbative approaches to the problem of interacting hadrons and mesons. On the other hand, phenomenological models of dense matter, which are necessary for describing neutron star cores, do not typically have well-controlled uncertainties. In this sense, neutron star observations represent the most robust strategy for constraining the property of matter at high densities, since uncertainty in our *observations* can be controlled effectively. In summary, it appears that the extent to which the properties of dense matter can be predicted robustly from theory, it can only be possible at low densities (less than two times the density of atomic nuclei) where particle energies are small compared to the fundamental energy scale of QCD [35].

Neutron stars are therefore exceptional in astrophysics. On one hand, they were predicted well before they were discovered. On the other hand, the current picture of neutron stars we hold cannot be derived theoretically from first principles. Instead, our understanding of neutron stars comes somewhat from dense-matter physics informing our understanding of astrophysics, and somewhat from astrophysical observations informing our understanding of dense matter. From the framework of modern statistics, the properties of neutron stars and the properties of the equation of state are treated as unknown variables, which are inferred from observations and experiments. This problem is technically challenging because we do not fully understand the relevant particles (or degrees of freedom) in neutron star cores.

Technical Preliminaries

I will now lay out some of the groundwork for modern neutron star physics. Though many of the derivations are elementary, I will where possible point to the key points which connect dense-matter physics to astrophysics. In this, I will point to some open problems and connect these problems to certain research directions.

Neutron stars can be viewed from essentially two different and philosophically incompatible frameworks: first, as nearly Newtonian objects, which are subject to some relativistic corrections (which are considered "small" in this approach), or as nearly black holes with some corrections due to the presence of matter (which are likewise considered "small"). The first of these approaches is widely used when considering perturbations to neutron star matter, for example nearly all deformations of neutron stars are most easily computed in an approximate Newtonian framework [59]. On the other hand, from a gravitational point of view, neutron stars most nearly resemble black holes. This can be seen in, for example, universal relations for higher multipoles which at sufficiently high compactness begin to approach black hole values [84]. However, it is also the case that the sequence of neutron stars at increasing masses is disconnected from black holes (when measured in terms of higher gravitational multipoles).

Neutron star inspirals are very interesting when viewed in this framework. Early on, when the binary separation is large compared to the neutron star radius (R) and Schwarzschild radius ($R_s = 2GM/c^2$, with c the speed of light and G Newton's gravitational constant), the system can be treated effectively as two black holes inspiraling in a nearly Keplerian orbit. However, as the orbit shrinks, the dynamics become more relativistic, while at the same time the internal structure of the neutron stars becomes more important [47]. This leads to (perhaps paradoxically) the fundamentally Newtonian effect of tidal deformation becoming important along with the details of general relativity very near the merger. Upon merger, the system is well modeled by neither a perturbed Newtonian star nor a perturbed black hole. Therefore, analyzing binary neutron star mergers holds incredible promise for understanding the physics of neutron stars and dense matter, but is also incredibly challenging because it requires fully-relativistic simulations.

Isolated neutron stars

The basic picture of neutron stars which was formulated in the 1930's and persists to this day is a self-gravitating sphere of mostly neutrons. Because of their high compactness, or alternatively because of the large interaction energy of neutrons, the relativistic stellar structure equations, the Tolman-Oppenheimer-Volkoff (TOV) [79, 61] must be used. The system that is solved is the Einstein's equations for a perfect fluid.

$$G_{\mu\nu} \equiv R_{\mu\nu} - \frac{1}{2} R g_{\mu\nu} = \frac{1}{c^4} 8\pi G T_{\mu\nu}, \tag{1.1}$$

where $G_{\mu\nu}$ is called the Einstein tensor, $R_{\mu\nu}$ is the Ricci tensor, and R is the Ricci scalar. $T_{\mu\nu}$ is the stress energy tensor, which in this case is

$$T^{\mu}_{\nu} = h\rho u^{\mu} u_{\nu} + P\delta^{\mu}_{\nu} = \begin{pmatrix} -e & 0 & 0 & 0 \\ 0 & p & 0 & 0 \\ 0 & 0 & p & 0 \\ 0 & 0 & 0 & p \end{pmatrix}, \tag{1.2}$$

where u^{μ} is the four-velocity, e is the energy density, p is the pressure, ρ is the rest-mass density of baryons, and $h = (e + p)/\rho$ is the specific enthalpy. "$-e$" is a consequence of choosing the $-, +, +, +$ metric convention. Because we seek solutions for static, spherically symmetric stars, u^{μ} can be written as $(1, 0, 0, 0)^T$

and all quantities depend only on a single radial coordinate r; the form of Eq. (1.2) reflects this choice. In the case of an isolated neutron star which has reached chemical equilibrium, the temperature is taken to be zero and the relevant conserved quantity is baryon number. Chemical equilibrium here means that all necessary reactions to reach the lowest-energy state are allowed to proceed to completion, in practice this means that these reactions are fast compared to the relevant macroscopic timescale (time for a binary to merge, for example). Generally, the slowest reaction is the emission of leptons via Urca processes; therefore the charged-lepton fraction, or where it is equivalent, the charge fraction, electron fraction, or proton fraction, is usually the most likely quantity to be away from equilibrium. This equilibrium is called $\beta-$equilbrium, and is maintained by weak interactions which control the electron (or charged lepton) fraction via neutrino emission.[1] However, if the temperature is small, and the charge fraction is close to its equilibrium value, the equation of state can be treated as one dimensional, and can be written as $p(e)$, for example. This assumption is not strictly necessary; however, if the equation of state is multidimensional, further equations will need to be supplied to close the system. A variety of possible coordinate systems are possible for solving the TOV equations, for simplicity I will use the ones originally introduced by Oppenheimer and Volkoff (OV), but will also point out that so-called isotropic coordinates are in many ways preferable [12]. In particular, in isotropic coordinates Christoffel symbols are continuously differentiable across the surface of the star, whereas in the OV coordinates they are not. Nonetheless, we take the metric to be

$$ds^2 = -e^{2\nu(r)}dt^2 + e^{2\lambda(r)}dr^2 + r^2(d\theta^2 + \sin^2\theta d\phi^2) \tag{1.3}$$

where $\nu(r)$ and $\lambda(r)$ are functions of the radial coordinate r. Generally $e^{-\lambda(r)}$ is further taken to be

$$e^{-2\lambda(r)} = 1 - \frac{2M(r)}{r}, \tag{1.4}$$

where $M(r)$ can be thought of as the enclosed gravitational mass inside a shell of coordinate radius r; it agrees with the Schwarzschild mass at the surface of the star. From here on out we will work in units where $c = 1$ and $G = 1$. The Einstein equations then furnish 3 nontrivial relations, although we only use two of them. The first is the tt component of the Einstein equations, which gives

$$\frac{dM}{dr} = 4\pi r^2 e(r). \tag{1.5}$$

[1] In proto-neutron stars formed from supernovae, both thermal and out-of-equilibrium effects may be relevant.

The second is the rr component of the Einstein equations, which gives

$$\frac{d\nu}{dr} = \frac{1}{r^2}\left(\frac{M(r) + 4\pi r^3 p}{1 - 2M(r)/r}\right). \tag{1.6}$$

Finally, we use the r component of the conservation of the stress-energy tensor (which follows from (1.1))

$$\nabla_\alpha T^{\alpha\beta} = 0, \tag{1.7}$$

which gives[2]

$$\frac{d\ln h}{dr} = -\frac{d\nu}{dr}. \tag{1.8}$$

Almost always, the equation Eq. (1.6) is solved with a matter variable on the LHS using Eq. (1.8) to eliminate the $d\nu/dr$ term. However, it is worthwhile to pause and note that Eq. (1.8) can be integrated to $\ln h + \nu = C$, where $C = \ln(1 - 2M(R)/R)$ is a constant determined by stitching the metric to the exterior Schwarzschild solution. This also makes it very clear that if $\ln h$ is not small, then ν must be substantially less than zero. The statement that $\ln h$ is not small is a criteria for matter to be relativistic (since it implies internal energy is comparable to the rest-mass density), while the statement that $\nu < 0$ is an indicator that General relativistic effects, like time dilation, are important. This is a very rudimentary, but nonetheless precise example of the following maxim: *In general relativity, the spacetime of a star is extreme if and only if the matter inside the star is extreme.*

The TOV equations are a coupled system of ordinary differential equations. While the system is solvable, there are numerical considerations that make it unappealing. In particular, the surface of the star $r = R$ is not known ahead of time. Instead it is preferable to rewrite the equations in the form of Lindblom [58]. This involves making the coordinate transformation $u \equiv r^2$, $v \equiv M(r)/r$, and treating $\ln h$ as the independent variable (which has known boundary values, $\ln h_c$, the central value, and $\ln h_0$ the boundary value, which is often taken to be zero[3]). The equations

[2] Implicit here is the identity $d\ln h = dp/(e+p)$.

[3] This is possible because the rest-mass density of baryons is defined as $\rho \equiv m_B n_B$, where m_B is the mass of a baryon and n_B is the number density of baryons. By varying the mass of a baryon, the total baryon "rest-mass" varies as well, and can be made to agree with the energy density of matter as the density goes to zero. Microphysically, matter is bound at low densities in its ground state, so the internal energy $e - \rho$ is slightly negative. Astrophysically, at least for static systems, the only observables are e and p, so changes to the overall scaling of ρ are not physically meaningful, as long as h also changes so that $h\rho = p + e$ stays fixed.

become

$$\frac{du}{d\ln h} = -(2u)\frac{1-2v}{4\pi pu + v} \tag{1.9}$$

$$\frac{dv}{d\ln h} = -(4\pi eu - v)\frac{1-2v}{4\pi pu + v}. \tag{1.10}$$

These variables are also preferable because they approach zero linearly at the center of the star, the solution goes like

$$4\pi eu(\delta \ln h) = \frac{6\delta \ln h}{1+3w} + O(\delta \ln h)^2 \tag{1.11}$$

$$v(\delta \ln h) = \frac{2\delta \ln h}{1+3w} + O(\delta \ln h)^2, \tag{1.12}$$

where w $= p/e$ and $\delta \ln h = \ln h_c - \ln h$. The system is solved from the center to the surface, but because the system is singular at the center of the star, in practice the system is solved from some finite δlnh to the surface[4]. The radius is then found by taking $R = \sqrt{u(\ln h = \ln h_0)}$ and $M = Rv(\ln h = \ln h_0)$.

For each equation of state, we can produce a family of solutions to the TOV equations parametrized by central density. This family is often represented by the mass-radius relation of the equation of state.

While the approximation that neutron stars are spherically symmetric is often good, it is violated when neutron stars are rotating. In this case, no exact solutions to the Einstein equations coupled to stress-energy conservation are known[5]. Nonetheless, strategies for constructing arbitrarily good initial data for rotating perfect-fluid neutron stars are known [31]. Before this, however, it was known how to construct approximate initial data for rotating neutron stars by expanding metric components to leading order in the rotation (angular) freqeuncy, Ω. This is the objective of the so-called Hartle-Thorne metric [44], and serves as a reasonable approximation as well as providing valuable insights about spacetimes with matter. This approach also allows for the construction of tidally perturbed neutron stars, the important point being that in both cases the leading order corrections to the matter in the star are given by $\ell = 2$ spherical harmonics. This statement is as true in Newtonian physics as it is in general relativity. However, in general relativity there is an additional

[4] An interesting application of this form of the equations is that the expansion suggested in Eq. (1.11) can be carried out to higher order. Empirically, even at just second order in $\delta \ln h$, the overall structure of the entire star is well-resolved, at least when the system is only mildly relativistic ($v, w \ll 1$).

[5] With the exception of rotating black hole solutions, no astrophysically relevant and exact solutions are known for rotating objects in general relativity.

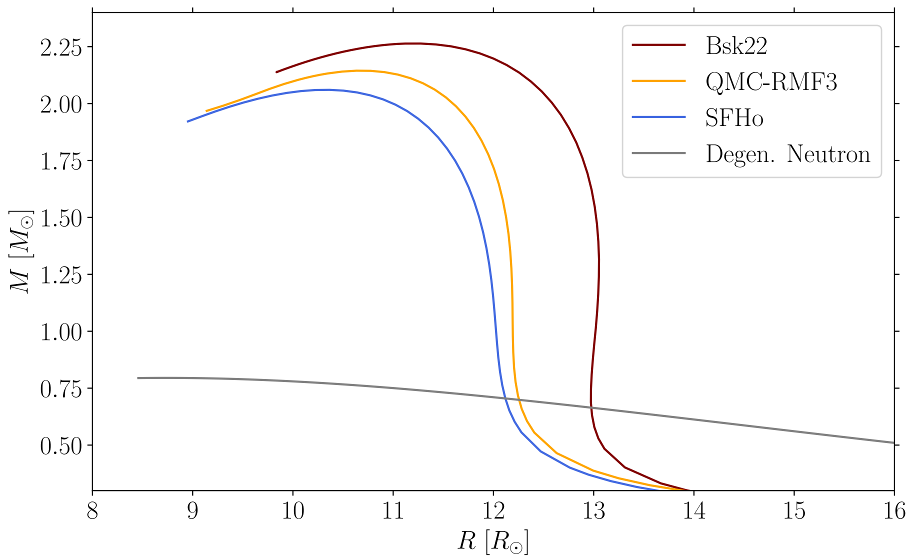

Figure 1.1: Examples of the mass radius relation for various equations of state. Shown are Bsk22 [41], QMC-RMF-3 [7], SFHo [46], and an equation of state composed purely of degenerate, non-interacting neutrons (similar to the one used by [62]). Different strategies for constructing the equation of state are discussed in Sec. 1, but for now, it is enough to recognize the extreme difference between neutron star models. Neutron star solutions with mass increasing as a function of central density (or enthalpy) are stable. There are no equilibrium solutions with masses above a certain mass (the maximum TOV mass), but this mass depends on the equation of state. Determining this mass is a key goal of nuclear astrophysics.

correction at lower order in the spin which is responsible for "frame-dragging". We can therefore write down the most generic perturbed, stationary fluid solution at leading order.

Following the approach laid out in [84], we write the metric

$$\begin{aligned} ds^2 = -e^{2\nu(r)}\left[1+2\epsilon^2 h_2(r)^2\alpha Y_{2m}(\theta,\phi)\right]dt^2 + \\ e^{2\lambda(r)}\left[1+2\frac{2\epsilon^2 m_2(r)^2\alpha Y_{2m}(\theta,\phi)}{r-2M(r)}\right]dr^2 + \\ + r^2\left[1+2\epsilon^2 K_2(r)^2\alpha Y_{2m}(\theta,\phi)\right]\times \\ \left(d\theta^2+\sin^2\theta\left[d\phi-\epsilon\left[\Omega_* - \omega_1(r)P_1'(\cos(\theta))dt\right]^2\right]\right) \end{aligned} \tag{1.13}$$

where ϵ is a bookkeeping parameter, $h_2(r)$, $m_2(r)$, and $K_2(r)$ are functions which correspond to deformations of the star, and α is a constant (which can be absorbed into the definition of the spherical harmonics, $Y_{\ell,m}$). The function $\omega_1(r)$ corresponds to the impact of the angular velocity Ω_* on the spacetime. The function $P_1'(\cos(\theta))$ is the derivative of the 1st Legendre polynomial.

Importantly, the perturbation expansion cannot be carried out in these coordinates, because the pressure perturbation is not small compared to the pressure near the boundary of the star (where the pressure may be zero in the unperturbed star). Instead, the radial coordinate is transformed to $r = r' + \epsilon^2 \xi_2(r') \alpha Y_{2m}(\theta, \phi)$, so that $\rho(r(r', \theta, \phi)) = \rho(r') = \rho^{(0)}(r)$. Put another way, this guarantees that at a fixed coordinate value r' the density is unchanged under the perturbation. The net result of this procedure is that the perturbed metric is set equal to the perturbed stress energy tensor, which is the stress-energy of a rotating perfect fluid. This gives equations for all of the unknown metric functions inside the star, which are matched to external solutions at the surface. The key insight is that in the exterior of the star, the solution for each metric component will contain an undetermined constant, which will need to be fixed by matching to the interior solution. These constants can be matched to Newtonian expressions for properties for bulk properties of the star; see Table 1.1 for a summary of the relevant properties.

Newtonian property	**metric functions at leading order**	**order of first contribution**
Mass M	$M(r)$ or $\lambda(r), \nu(r)$	ϵ^0
Moment of inertia I	$\omega_1(r)$	ϵ^1
Quadrupole moment Q,	$h_2(r), K_2(r)$	ϵ^2

Table 1.1: Bulk properties of stars in the Hartle-Thorne metric, the metric functions which are used to compute these properties, and the order at which this quantity can first be computed. Note that if the mass is defined via an analogy to Newtonian multipole moments, it receives additional corrections at second order in ϵ. Additionally, both tidal and rotational quadrupole moments are determined by the ϵ^2 term, although the calculation of the tidal Love number as presented in Ref. [84] requires $\omega_1 = 0$, so it's not immediately clear if this approach can be used for rotating, tidally deformed stars. See [53] for details.

One key result of this calculation is that the quadratic corrections to the metric have undetermined constants that cannot be determined at lower order. A Kerr black hole, on the other hand has only two relevant parameters (up to translations, boosts, and rotations), mass M, and spin angular momentum $\vec{S}$, which determine the metric at all orders in spin. Therefore, to a distant observer measuring only the gravitational field, neutron stars can be mistaken for black holes at zeroth or first order in epsilon, though at second order it is clear that stars are not black holes. Also crucially, the quadrupole moment of a neutron star depends on the internal structure of the star, and therefore also the equation of state.

Neutron Star formation

The vast majority of neutron stars are expected to be formed in core-collapse "type II, Ib, and Ic" supernovae (see [19] for a review.). The key ingredient in forming a neutron star is collecting sufficient mass in an electron-degenerate core that it surpasses the Chandrasekhar mass, destabilizes, and after sufficient electron captures, implodes. This process is in some sense generic in the lifespans of massive stars, and is expected to occur in stars with masses greater than about $8M_\odot$. Two key factors frustrate the formation of neutron stars in this case, first, some astrophysical process may prevent the collection of the necessary ingredients in the core. A prime example of this is mergers of carbon-oxygen white dwarfs, which in principle could satisfy the above criteria for neutron star formation, but in practice explode as type Ia supernovae[6]. The second factor that prevents neutron star formation is that once the baryons have arrived in a neutron star configuration, there may be no stable long-term neutron star allowed by the equation of state and general relativity. This is the case when, for example, the amount of mass deposited on a proto-neutron star after a supernova exceeds the TOV maximum mass. In this case the object will almost certainly form a black hole. From first principles, it is not obvious that both criteria should be satisfiable simultaneously, the first is generally alleviated by stronger gravity, but the second is made worse by it. If not tuned correctly, the only possible endstates of massive stars are white dwarfs, black holes, or nuclear detonations which disperse large fractions of stars matter[7].

Nevertheless, some fraction of collapsing electron-degenerate cores do form neutron stars. In fact neutron stars are abundant in galaxy, observed as radio pulsars, x-ray

[6] It's not a coincidence that these two phenomena share a common name, historically Baade and Zwicky proposed the core-collapse mechanism first, but were in practice observing degenerate explosions. The reason why the observed energies of these two explosions are comparable, even though the energy released in the core-collapse case $\sim M_{\text{Chandra}}^2/R_{\text{NS}} \sim .1M_{\text{Chandra}}$ is dozens of times larger than released in the detonation $M_{\text{Chandra}}\epsilon_{\text{bind}}$ (where M_{Chandra} is the Chandrasekhar mass (the approximate mass of the degenerate precursor), and $\epsilon_{\text{bind}} \lesssim .002$ is the binding energy per unit mass released in the nuclear reactions). This is because the vast majority of energy in a core collapse supernova is released as neutrinos, and only a few percent is transferred to the matter. More generally, this is an indication that only the strong nuclear force is capable of producing energies per particle comparable to those found highly compact objects.

[7] The white dwarf remnant of SN 1181, which is surmised to have been an underluminous type Iax supernova that exploded away some fraction of its mass, is observationally very similar to a Wolf-Rayet (i.e. high mass) star [63]. Understanding white dwarf dynamics is one key to disentangling the astrophysical origins of neutron stars.

sources, and in some cases (such as the Crab), across the entire electromagnetic spectrum [18]. Observations of pulsars in binaries imply a characteristic mass of $\sim 1.35\ M_\odot$ for typical neutron stars [8], but with a nonnegligible tail of sources at higher masses. The location of the maximum mass of the galactic pulsar distribution [8] is relevant for equation of state physics, since the equation of state must be at least stiff enough to support the most massive observed pulsar. Despite likely having very different formation properties, a similar mass distribution is observed for EM-dark compact objects identifiable with neutron stars from Gaia astrometry [10, 11]. Observed in the galaxy as well are neutron stars in binaries with other neutron stars [49, 86]. Neutron stars in these binaries seem to, more than generic galactic neutron stars, have masses closely clustered near $\sim 1.35\ M_\odot$. Interestingly, the observation of merging neutron stars in GW170817 [4] by both gravitational waves and electromagnetic sources points to the system of two neutron stars consistent with this mass. However, the second supposed binary neutron system observed by gravitational waves is not consistent with both compact objects being near $\sim 1.35\ M_\odot$ [3], though both objects are likely below the TOV maximum mass.

Untangling the exact neutron star mass distribution, and the physical processes which explain it will certainly be helped by more observations of neutron stars. However, even then, the details of how neutron stars form in supernovae is incredibly complicated, and expensive to simulate [20]. Improved understanding of the dense matter equation of state will be key here as well, as greater precision in the equation of state allows us to rule out configurations ahead of evolution. Nonetheless, results are still largely qualitative, and extensive studies of supernovae in 3D which vary the equation of state have not yet been performed.

Neutron Stars in Binaries

The problem of merging neutron stars is in many ways similar to the problem of supernovae. Physically, both involve the release of large amounts of gravitational energy to bind a compact object. Computationally, these problems are similar as well, as they both require simulating the behavior of dense matter in a changing relativistic gravitational field. Nonetheless, because of the particular details of the binary problem (in particular, the post-Newtonian expansion), to some extent the problem is easier to approach. Already, merging neutron stars have been used to constrain the equation of state [2], and more generally, merging neutron stars represent a remarkable opportunity to study dense matter and extreme gravity in a single astrophysical experiment. The overarching mechanism which allows the neutron stars to merge is gravitational radiation. Post-Newtonian calculations imply that the energy is carried away from a merging binary of two point masses [67] at a rate of

$$L_{\mathrm{GW}} = \frac{dE}{dt} = -\frac{32}{5}\frac{m_1^2 m_2^2 (m_1 + m_2)}{r^5}(1 + O(e^2)) \tag{1.14}$$

where m_1 and m_2 are the masses of the two objects, and r is the semimajor axis of the orbit, and e is the orbital eccentricity. This quantity can be compared to the gravitational energy in a Keplerian orbit, which is

$$E_{\mathrm{orb}} = -\frac{m_1 m_2}{2r} \tag{1.15}$$

$$\left|\frac{E_{\mathrm{orb}}}{L_{\mathrm{GW}}}\right| = \frac{5}{64}\frac{r^4}{m_1 m_2 (m_1 + m_2)} = \frac{5}{64} r \frac{r^3}{m_1 m_2 (m_1 + m_2)}. \tag{1.16}$$

This is an exceptionally long timescale (when compared to the orbital timescale $\sqrt{r^3/(m_1 + m_2)} = r\sqrt{r/(m_1 + m_2)}$) when $r \gg m_1, m_2$, though is not unfathomably long when $r \sim R_{\mathrm{NS}} \sim 6M$. Because of this, at merger (when $r \sim R_{\mathrm{NS}}$), the timescale for gravitational radiation is comparable to the dynamical timescale of the star. This is unlike the case of white dwarfs, which even though they are brought to merger by gravitational radiation, once the merger commences, gravitational radiation is negligible.

The characteristic quantity $(m_1 + m_2)/r$ is called the post-Newtonian parameter. This is a dimensionless number which is less than 1. For a quasi-circular orbit,

$$\frac{m_1 + m_2}{r^3} = \omega^2, \tag{1.17}$$

so the post-Newtonian parameter is $(M\omega)^{2/3}$ [8].

Despite this, it is not obvious that the calculation performed in Ref. [67] is valid, because the stars are not point masses. For neutron stars for example, the binding energy is of order $M_{NS}^2/R_{NS} \sim 1/6 M_{\mathrm{NS}}$. The linearized calculation of gravitational waves, however, assumes the gravitational binding energy is small compared to the rest mass energy. Remarkably, up to 3rd post-Newtonian order, nonrotating neutron stars are treatable as point particles with mass given by the gravitational mass of the star, at 3rd post-Newtonian order, the situation is unclear [82]. For rotating neutron stars the situation is different; since the spin-induced quadrupole moment of neutron stars is not the same as that of a BH of the same mass and spin, the dynamics of

[8] Note ω is the binary angular frequency, the gravitational wave frequency f satisfies $2\pi f = 2\omega$, the post-Newtonian parameter is often taken to be $(\pi M f)^{2/3}$.

the binary are different. This correction is relevant at leading 2nd post-Newtonian order, although the size of this correction is not exceptionally important at current sensitivity, in particular because neutron star spins are expected to be small.

Naturally, the next question to ask, given the framework above is "what is the impact of the tidally-induced quadrupole?". This quadrupole moment appears at a higher post-Newtonian order, because rather than being sourced by rotation, it is sourced by the tidal gravitational field of the companion star. This field scales like m_2/r^3, if we are interested in the primary object (object 1). In turn, object 1 will respond by deforming, which will produce a quardupolar correction to the metric component which falls off like $1/r^3$. Collectively, the net effect will scale like

$$\frac{m_2}{r^3} \times \frac{1}{r^3} \propto \frac{1}{r^6}. \tag{1.18}$$

This term enters at 5th post-Newtonian order; however, the coefficient on the term scales like $(R_1/m_1)^5$, which becomes larger at low masses and high-radii, unlike relativisitic corrections. In fact, this term is not relativistic, but is fully Newtonian in origin [9]. Therefore the high post-Newtonian order of this term is a matter of overall scaling, rather than a question of how deep exceedingly relativistic this term is. This is crucial, because the tidal deformability is measurable late in the inspiral not because the system is relativistic, but actually despite the fact that the system is highly relativistic. The tidal deformability, in gravitational-wave astronomy is typically given by a dimensionless number Λ, which appears directly in the gravitational waveform. See, for example [47, 28]. In order for the conventional picture of neutron star inspirals to be useful for precise calculations, expansions in both true "post-Newtoninan" effects and perturbations of the neutron stars away from spherical symmetry must be under control. The first could break down simply because the post-Newtonian expansion is not converging to the correct point-particle description of general relativity [83]. The second may break down because of dynamical or nonlinear tides, in particular the resonant excitation of modes; see for example [85]. However, it's also possible that while analytical expressions given by post-Newtonian theory break down, that the form of the expansion is still useful if the coefficients in the expansion are calibrated to, e.g. numerical simulations [34].

Eventually, both of these expansions must break down completely. At the very latest, when the two neutron stars contact, the system will no longer be well described by

[9]This additional quadrupole moment leads to two effects, one is a change in the binding energy at a particular frequency, which is truly Newtonian, and the other is enhanced gravitational-wave emission from the quadrupole. The second is a relativistic effect, but it is smaller than the first

a pair of nearly spherical neutron stars. Beyond this point, truly quantitative predictions are very difficult to produce, though qualitatively the postmerger dynamics are somewhat well understood; for review see [70, 30]. From the point of view of the final matter distribution at long times (compared to the characteristic time $\sim M_{\mathrm{rem}}$, the mass of the remnant) there are essentially two possible outcomes for the merger scenario. First, the object could form a stable remnant, which would be another neutron star. If the object exceeds the maximum TOV mass, but is stable because of rigid rotation, it is called a supermassive neutron star. Such a remnant may be slowed by magnetic dipole radiation, and may collapse on an arbitrary timescale. [10] It's also possible that on the timescale of the remnant it collapses to a black hole. An interesting case is the case that the remnant survives for $\sim 100 - 1,000$ dynamical times, stabilized by *differential* rotation. This object is called a hypermassive neutron star. Once the differential rotation is removed, by some combination of gravitational radiation and fluid instabilities, the star collapses. Despite appearing fine-tuned, depending on exactly the equation of state (in particular, but not exclusively the maximum mass), it may be the case that so-called "typical" mergers of two $\sim 1.35 \sim M_{\odot}$ neutron stars have a hypermassive neutron star remnant. In the case that the remnant collapses on a dynamical time, the outcome is called prompt collapse.[11]

The equation of state of dense matter in neutron stars.

Neutron stars are so extreme that the matter inside of them will, on astrophysical time scales (e.g. the inspiral timescale of a binary $\gtrsim 10^6$ years), reach the *ground state* of matter of the standard model (for reference see, e.g. Shapiro and Teukolksy [74]). This is to say that except for baryon number, there are no other nonzero conserved quantities with finite chemical potential, and the temperature will be effectively zero. This situation simplifies substantially the study of neutron stars, because the equation of state is determined by a single parameter. A corollary of this is all neutron stars with the same central density have the same macroscopic properties.

[10] The collapse of such an object may lead to electromagnetic transients, which may also allow tests of general relativity in the strong field [60].

[11] The question of to what extent gravitational-wave emission from the prompt collapse is determined by the details of the hydrodynamics of the neutron star versus the "no-hair" properties of the remnant black hole is interesting. Some authors identify excess power that is identified as a black-hole quasi-normal mode in neutron star postmerger simulations [33], while others consider it likely to be a hydrodynamic mode associated with the collapse of the star (*e.g.* [78]). Investigations by a SURF student, Lana Alabassi lead me to believe the latter explanation, but the problem is certainly not settled. This question also has interesting analogues with regards to electromagnetic transient behavior [50].

In practice, neutron stars freshly born from supernovae, or created in neutron star mergers will not satisfy these criteria, but nonetheless, understanding the equation of state of cold, equilibrated neutron stars is a crucial step in understanding neutron star physics holistically.

The general picture of neutron star interiors is somewhat analogous to Earth's interior. Each has a crust, likely an atmosphere, and various layers inside which correspond to different phases of matter. However, here is where the similarities end. While the Earth has a characteristic density of $\sim 5\,\mathrm{g/cm^3}$, neutron stars have a characteristic density of $\sim 5 \times 10^{14}\,\mathrm{g/cm^3}$, which is a bit larger than the density of atomic nuclei. Much can be learned about the matter inside of neutron stars simply from knowing their bulk properties. For example, the virial theorem indicates that the internal energy of matter in the star should be the same order of magnitude as the gravitational binding energy of the matter. In particular, the gravitational binding energy per unit mass is of order $GM/R \sim 1/6$, so the internal energy per unit mass (which we call the *specific internal energy*) should also be of order $1/6$. In contrast, the binding energy of even the most tightly bound atomic nuclei is less than 1% its rest mass. More careful accounting shows it is also at least a factor of two larger than the predicted specific internal energy of a noninteracting degenerate neutron gas. Therefore, an additional repulsive interaction must be present in neutron star interiors; this repulsion is ultimately provided by strong interactions. Fitting their name, these interactions are, in the cores of neutron stars, potentially the strongest interactions anywhere in the universe when measured by specific internal energy.

The above picture could have in principle been laid out with no reference to the standard model of particle physics, though in practice the discovery of neutron stars and the development of the standard model were nearly contemporaneous. It is clear from the current understanding of QCD that neutron stars will contain strongly interacting neutrons and protons, but also plausibly strange-quark containing hadrons (called *hyperons*), and potentially deconfined quarks, or other exotic states of matter. Nonetheless, because the theory of the strong interaction, QCD, is strongly coupled at neutron star densities it is not possible to use the theory itself to perturbatively compute the dense-matter equation of state. Lattice QCD calculations are currently infeasible for matter inside neutron star cores because of the large baryon chemical potential [**Ratti:2018ksb**]. Furthermore, it is not clear which particles will become relevant at which densities, and therefore which degrees of freedom should be included in such a calculation in the first place. Therefore, various effective theories and phenomenological models have been used to model matter inside of neutron stars.

One of the core principles of these models is that they should be able to self-consistently explain the properties of atomic nuclei, such as nuclear binding energies and scattering cross sections as well as neutron-rich matter. Historically, the earliest model of nuclear matter was the liquid-drop model [39], which treated the nucleus a liquid drop and modeled all possible contributions to the energy that could arise between nucleons within this "drop". Nonetheless, this model was classical, and obvious deficiencies such as remarkably strong binding at particular neutron and proton numbers (so-called magic numbers) required the nuclear shell model [23]. In general, each model has certain advantages and naturally makes certain correct predictions. To this day, measurements of masses [66], and collisions of heavy nuclei [21] continue to push forward the field of nuclear physics [12].

The general approach is to write down the relevant degrees of freedom for the particular model that is being used, and then include some number of relevant interactions. In nonrelativistic models, the many-body Schrödinger equation is then solved, while in relativistic models, the equations of motion are solved and the energy is computed from the stress-energy. In both cases, the state of most interest for neutron stars is homogeneous nuclear matter in the ground (minimum energy) state. The result is the energy as a function of particle density, from which all thermodynamic quantities can be computed. In general, the model written down will have parameters which are not known, and these parameters must be fit to data or guessed. Further, approximations generically must be made to render the system tractable. In relativistic calculations the *mean-field* approximation, which treats mesons as classical fields is often employed. The energy will depend on the choice of interactions, particles, and approximations, and also in most phenomenological models there is no robust way to estimate the systematic error associated with these different choices [69].

Historically, nonrelativistic models [13] were developed first, and were found to satisfactorily describe certain properties of atomic nuclei. Arguably, in the outer crust nonrelativistic calculations are sufficiently accurate that often the EoS there is considered "known". Approaches such as the Wigner-Seitz approximation ([26] and references therein) are used to compute the properties of the outer crust. Such

[12] And, increasingly, the equation of state of dense nuclear matter [77].

[13] Note that nonrelativistic here applies to hadronic degrees of freedom, electrons in neutron stars are almost everywhere highly relativistic ($E \gg m_e$, the electron mass).

approaches treat the crust as a lattice of nuclei immersed in an electron gas, for example, below neutron drip, the energy density is given by [13]

$$n_N\left(W_N(A,Z) + W_L\right) + \epsilon_e(n_e) \tag{1.19}$$

Where n_N is the number density of nuclei, $W_N(A,Z)$ is the energy of a nucleus with atomic number A and charge Z, and W_L is the lattice energy per nucleus (depends only on the charge of the nucleus and the lattice spacing), and $\epsilon_e(n_e)$ is the energy density of electrons, at electron number density n_e. The electrons are effectively noninteracting, so the energy density is that of a free Fermi gas. Beyond a certain density, it is no longer favorable for additional baryons to reside in nuclei, but rather in a continuum of states outside the lattice. Ref. [13] finds this value to be 4.3×10^{11} g/cm^3, well below the average densities of most astrophysical neutron stars. Therefore, the bulk of the crust of the neutron star is identified as the "inner crust", at densities beyond neutron drip. Here calculations are still possible, but more prone to systematic uncertainties. In general, calculations contain parameters which must be calibrated by matching to nuclear data, either experiments or *ab initio* calculations (see the discussion on chiral effective field theory below). In this region, nonrelativistic calculations are phenomenological; for example Skyrme interactions [76] build a Hamiltonian consisting of momentum dependent "contact potentials" have been used to build models such as SLy4 [24], and BSk22 [41]. Nonetheless, nonrelativistic models have drawbacks. At sufficiently high densities nucleons are relativistic, neglecting knowledge of relativity for example means EoSs need not remain causal in the sense that the sound speed $\sqrt{(dp/de)}$ remains less than the speed of light.

Relativistic models of the equation of state naturally solve certain problems, and for example automatically incorporate spin effects that would have to be explicitly added to a nonrelativistic model. One particular model, the *relativistic mean field* model is commonly used. In this case, nucleons are treated as Dirac fields, and mesons are treated "classically", see [71]. Other approaches include relativistic (or Dirac) Brueckner-Hartree-Fock methods [17] in which the Dirac equation for nucleons is solved, with the nucleons "dressed" by one-boson exchange potentials. Nonetheless, these approaches are in some sense more complicated then nonrelativistic approaches, and like nonrelativistic approaches are not fundamentally connected to QCD. Therefore, the choice of either nonrelativistic or relativistic models entails some approximation and some (potentially difficult to quantify) systematic error.

However, one approach, *chiral perturbation theory* or *chiral effective field theory* (chiral EFT) is an effective field theory approach to computing the low-energy interactions of nucleons and mesons [81] (though see [35] for a modern review). This approach involves writing down all interactions consistent with the approximate chiral symmetry of QCD. The relevant particles at low energy are neutrons, protons, and pions; significant progress has been made in computing the energy of this system up to higher and higher order in the fundamental interaction strengths. Below ~ 2 times nuclear saturation density, these calculations can be considered robust [36]. At higher densities, additional mesons, and potentially other hadrons will become relevant, however. Even without these terms, uncertainty in the the interactions lead to substantial growth in the uncertainty near $1.5 - 2$ times saturation density. Therefore, while chiral EFT is incredibly useful for constraining low-density matter, it is not capable of predicting the properties of dense matter in neutron star cores. See Fig. 1.2.

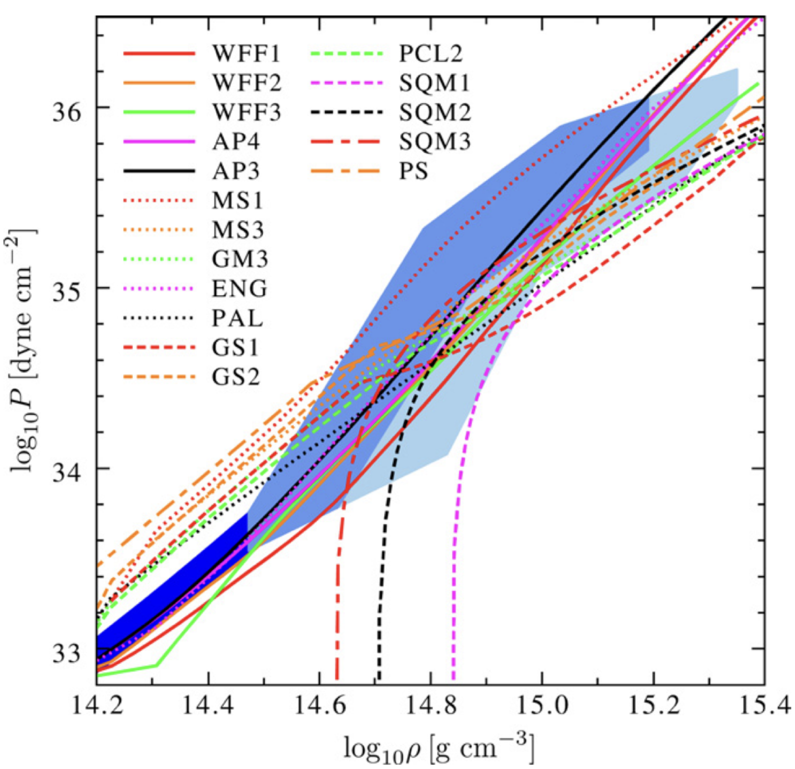

Figure 1.2: Several candidate equations of state plotted in pressure vs rest mass density. Chiral EFT uncertainities are shaded in blue; many equations of state are inconsistent with chiral EFT. Figure reproduced from Ref. [45].

Finally, the dense-matter equation of state is in fact known at sufficiently high densities around 40× nuclear saturation density [51]. In this regime the Lagrangian of QCD is perturbative, with the total energy being expandable around the energy of a noninteracting fermi gas of quarks. Therefore, the substantial uncertainty in the equation of state of matter inside neutron stars is somewhat surprising. If the density of neutron stars had been an order of magnitude larger, or smaller, then this problem would essentially be solved, up to perturbative calculations.

As it stands, however, we do not know the equation of state of matter in neutron stars, nor do we know the relevant particles or interactions for physics in neutron star cores. This is problematic, even from an astrophysical point of view (and even if we resolve only to concern ourselves with order-of-magnitude), because many real astrophysical phenomena lie at the boundary of qualitatively completely different behavior depending on the details of the equation of state. Do typical neutron stars "plunge" before merger, or is the merger interrupted by contact of the surfaces before the plunge? Do typical neutron star mergers form black holes or neutron star remnants? Can any neutron star mergers form long-lived, highly magnetized, neutron star remnants? These and many more are *astrophyical* questions related to thresholds that depend of the *nuclear* equation of state (although not all could be answered simply by knowing it). To make this problem more salient, it's important to recognize that choosing the *wrong* model for the equation of state, and proceeding without caution could lead one to make qualitatively incorrect predictions about astrophysics.

Outline of this thesis

The situation we find ourselves in is therefore both a remarkable challenge and a remarkable opportunity. On one hand, we do not know even the correct heuristic model of matter in the cores of neutron stars, much less the parameters of the model. We do not know what particles are relevant and densities greater than about twice the density of atomic nuclei, if there is a strong phase transition to additional species, or if as in quark-gluon plasma, the transition is a "crossover" (*i.e.* not associated with a discontinuity in any derivative of the thermodynamic potentials). I will discuss in this thesis how nonparametric methods provide a path toward robust inference of the dense matter equation of state. In particular I will discuss in Chapter 2 how nonparametric approaches empower us to carefully understand the distinction between modeled, and model-agnostic approaches to these problems. In connection, I will discuss in Chapter 3 constraints placed on the equation of state using the NICER observation of the very high mass pulsar J0740+6620. I will also discuss, in Chapter 4, how in particular data driven models can be used to search for phase transitions in dense matter absent any model of the underlying hadronic or quark phase.

Related to project of nonparametric EoS constraints, I will discuss what has been learned by using model-agnostic equation of state approaches in understanding the physics of neutron stars in Chapter 5. For example, some relations between neutron star properties seem to be almost independent of the given equation of state. These so-called equation of state-independent relations (also called universal relations) may, however, simply be features of the underlying nuclear physics which are built into the equation of state models against which the relation is tested. This can be discerned by comparing to a variety of nonparametric equations of state, and seeing which relations remain “independent” even under prescriptions of dense matter very far from simple parametrizations. Additionally, I will discuss how our knowledge of the equation of state can be used to inform our understanding of astrophysical phenomena. In particular, I will discuss how combining knowledge of the dense matter equation of state would very likely allow us to classify objects with less than a solar mass detected by gravitational waves in binaries in Chapter 6. This is possible because of the very strong impact of matter effects on merging binaries when the compactness is small.

Continuing, in Chapter 7, I will discuss how uncertainty in the astrophysical population of neutron stars and black holes is crucial for understanding the dense matter equation of state. Further, I will discuss how astrophysics and nuclear physics must be understood together in the context of neutron stars.

In Chapter 8, I will discuss hybridization of modeled and model-agnostic approaches to infer the properties of model breakdown, which is useful, in particular, in cases where there is no theoretical strategy known for computing a given theories breakdown scale (as is the case for most phenomenological models of dense matter). As a part of this, I will connect current models of nuclear theory to the larger problem of EoS parametrization and discuss how having modeled correlations can be extremely powerful, even if large components of the theory (such as interaction strengths), cannot be computed from first principles.

Finally in Chapters 9, and 10, I will discuss my contributions to simulations of neutron stars, in particular toward the goal of efficient and flexible representations of the dense matter equation of state. I will also discuss challenges with simulations that currently prevent certain insights in the behavior of dense matter from being easily accessible.

Chapter 2

COMPARING NONPARAMETRIC AND PARAMETRIC INFERENCE STRATEGIES FOR THE EQUATION OF STATE

[1] Isaac Legred et al. "Implicit correlations within phenomenological parametric models of the neutron star equation of state". In: *Phys. Rev. D* 105.4 (2022). I led this study which compared parametric to nonparametric methods of inferring the equation of state. I developed a substantial amount of software, ran the analysis, and co-wrote the manuscript., p. 043016. DOI: 10.1103/PhysRevD.105.043016. arXiv: 2201.06791 [astro-ph.HE].

Abstract

The rapid increase in the number and precision of astrophysical probes of neutron stars in recent years allows for the inference of their equation of state. Observations target different macroscopic properties of neutron stars which vary from star to star, such as mass and radius, but the equation of state allows for a common description of all neutron stars. To connect these observations and infer the properties of dense matter and neutron stars simultaneously, models for the equation of state are introduced. *Parametric models* rely on carefully engineered functional forms that reproduce a large array of realistic equations of state. Such models benefit from their simplicity but are limited because any finite-parameter model cannot accurately approximate all possible equations of state. *Nonparametric methods* overcome this by increasing model freedom at the cost of increased complexity. In this study, we compare common parametric and nonparametric models, quantify the limitations of the former, and study the impact of modeling on our current understanding of high-density physics. We show that parametric models impose strongly model-dependent, and sometimes opaque, correlations between density scales. Such interdensity correlations result in tighter constraints that are unsupported by data and can lead to biased inference of the equation of state and of individual neutron star properties.

2.1 Introduction

The equation of state (EoS) of the dense matter inside neutron stars (NSs) is uncertain at densities near and beyond nuclear saturation, $\rho_{\rm nuc} = 2.8 \times 10^{14} {\rm g/cm}^3$, because it cannot be precisely constrained by theoretical calculations or terrestrial experiments [47, 61, 60, 12, 55, 39, 15]. Astronomical observations [5, 21, 58, 72, 57, 73, 11, 2, 64] target the macroscopic properties of NSs, such as their mass M, radius R, and dimensionless tidal deformability Λ, which in turn can be used to constrain the EoS at densities greater than nuclear saturation [46, 51, 52].

A set of observations of different systems can be used to constrain a shared underlying property through a hierarchical inference scheme. The hierarchical formalism is derived in the context of combining data from different sources while faithfully incorporating their uncertainties and potential observational selection effects [54]; see, e.g., Refs. [15, 44]. In the context of NS structure, the main objective is to obtain a posterior for the EoS as a shared variable among many astrophysical observations. The prior corresponding to this posterior is not necessarily straightforward to define because the space of potential EoS (i.e., the space of possible functions obeying basic physical constraints) that relate the pressure p and the baryon density ρ, $p = p(\rho)$, is infinite dimensional.[1]

The simplest way to define such a prior is through a *parametrization* of the EoS, which is a functional form of $p(\rho)$ that typically depends on a few parameters. Common phenomenological models such as piecewise-polytrope [68], spectral [52, 53] and speed-of-sound [36] parametrizations have been used to effectively sample candidate EoS for use in inference. The simplicity of a closed-form parametric expression comes at the cost, though, of being unable to faithfully represent many of the possible degrees of freedom in the true EoS. While many of these models can accurately represent most EoS derived from effective nuclear interactions [52, 68], it is not always clear how to extend these parametrizations toward more general behavior in the EoS that may arise from phase transitions or new physics. This limitation of phenomenological parametric models has been recognized from the outset [68]. However, in this study we investigate another way that they may artificially restrict the inferred EoS.

Parametric models use only a few parameters, which means that the values of $p(\rho)$ at different densities are often *correlated*. These correlations represent a source of

[1] We can equivalently use $p(\varepsilon)$, with ε the internal energy density. In the zero-temperature limit, $d\varepsilon/d\rho = (p(\rho) + \varepsilon(\rho))/\rho$.

model dependence in the inference, which is undesirable insofar as it does not reflect true prior knowledge of the EoS at those densities. That is, the correlations induced by the choice of parametrization can constitute strong, unintentional prior beliefs about the EoS. This unwanted model dependence is a natural consequence of the phenomenological nature of the parametric models.

An alternative method for constructing a prior on the space of EoS, which we call *nonparametric* in what follows, targets more model flexibility by making use of Gaussian processes (GPs) [43]. This approach produces a multivariate Gaussian distribution for the function $\phi = \log\left((c/c_s)^2 - 1\right)$, where c_s is the speed of sound and c is the speed of light. By conditioning the prior only weakly on existing nuclear-theory models, we generate a *model-agnostic* prior process for EoS. The chosen correlations between $\phi(p_i)$ and $\phi(p_j)$, or equivalently between the values of the EoS at different densities, are set by a *kernel* function, which is in turn described by a few parameters. Following Ref. [26], we consider a variety of possible kernel parameters to probe a range of different correlations and thus maximize model freedom. This approach allows us, in principle, to model any function $p(\rho)$, and furthermore to probe a wide range of interdensity correlations and high-density EoS behavior.

Of course, completely unrestricted freedom in the EoS is neither desirable nor realistic, as certain physical constraints should be encoded into the EoS prior. For example, an EoS must be causal,

$$\frac{dp}{d\varepsilon} = c_s^2 < c^2, \tag{2.1}$$

and thermodynamically stable,

$$\frac{dp}{d\varepsilon} = c_s^2 > 0. \tag{2.2}$$

Imposing these constraints in the prior is desirable as it excludes unphysical models from the analysis.[2]

In this paper, we examine common parametric and nonparametric EoS models to determine the extent to which each prior's assumptions impact inference of the EoS and NS properties. We find that the three parametric models we study (spectral, piecewise polytrope, and speed of sound) build additional interdensity correlations into the EoS beyond what can be attributed to causality and stability.

[2]Some analyses allow the EoS to be slightly acausal at times; see Appendix 2.11 for more discussion.

These correlations between densities typically lead to more stringent constraints than are strictly supported by the data. On the other hand, the nonparametric model demonstrates the largest degree of model independence, restricted primarily only by causality and thermodynamic stability. We demonstrate that these strong, model-dependent interdensity correlations have already impacted inferred microscopic and macroscopic NS properties. Such effects are expected to become more severe as statistical uncertainties decrease with more data that probe different NS densities.

The remainder of the paper is organized as follows. In Sec. 2.2, we describe our inference methods and our approach to investigating model dependence. In Sec. 2.3, we examine the EoS and NS properties inferred with current data and show that they are influenced by correlations in the EoS prior. In Sec. 2.4, we illustrate the main limitations of parametric EoS inference with a toy model. In Sec. 2.5, we quantify the implicit EoS correlations and demonstrate that the nonparametric model displays the largest degree of model independence. In Sec. 2.6, we study the correlations' potential impact on upcoming EoS inference using mock astrophysical measurements. In Sec. 2.7, we demonstrate that the limitations identified in parametric models cannot be resolved by making small modifications to the prior distributions. Finally, in Sec. 3.5 we discuss our conclusions.

2.2 Methods and Models

The posterior for the EoS depends on two elements: (i) the prior EoS process, and (ii) the data. Our goal in this study is to assess the effect of the prior as generated from different parametric and nonparametric models for the EoS. We therefore always employ the same data, which we briefly describe in Sec. 2.2. The hierarchical likelihood corresponding to this data is described in Refs. [44, 48]. The EoS priors are described in detail in Sec. 2.2, where we discuss the different EoS models and parameter priors that generate each EoS prior process.

EoS prior

We wish to establish a prior process over candidate EoS. By this, we mean a probabilistic measure on the space of potential EoS. To do this, we use several *models* of the EoS. We distinguish *parametric* models, which provide a functional form for the EoS, from nonparametric models which do not impose such a functional form. We use three different phenomenological parametric models, a *piecewise-polytrope* [68] parametrization, a *spectral* parametrization [52], and a direct parametrization of the *speed of sound* [36]. The spectral and piecewise-polytrope parametrizations use a polytropic form for the EoS, so that

$$p(\rho) = K\rho^{\Gamma}.$$

In the piecewise-polytrope case, the polytropic index Γ is a piecewise-constant function of the pressure, while in the spectral case, $\log(\Gamma)$ is expanded as a polynomial in pressure. In the speed of sound parametrization, the speed of sound is expressed as a constant plus a Gaussian and a logistic curve which asymptotes to $c^2/3$. Following past practice [14], we slightly relax the causality threshold and consider EoS with $c_s^2 < 1.1c^2$ for all parametric models. See Appendix 2.11 for more details about each model and its implementation.

To establish a prior process, we must additionally supply a joint prior probability distribution on the parameters of each model from which a *draw* is a realization of the parameters and therefore a candidate EoS. For example, in the spectral model, the parameters are coefficients in the spectral expansion. In the piecewise polytrope, the parameters are the value of the polytropic index itself. For our headline results, we use standard priors for the parametric models [14, 81], except for the speed-of-sound model, which we adapt to increase access to astrophysically relevant EoS; again, see Appendix 2.11 for details.

We compare the prior processes generated by the parametric models to a prior process from a nonparametric model [43]. While our nonparametric implementation does not assume a specific functional form for the EoS, it does parametrize the correlations between the sound speed at different densities. These correlations are described by a kernel function. In practice, we choose a large set of points, p_i, and then the variable $\phi(p_i)$ is sampled from a multivariate Gaussian distribution. By changing the kernel's parameters and conditioning on different nuclear models, we can generate a range of GPs. We choose a model-agnostic prior, which is to say we average over multiple GPs with different correlations, each loosely informed by nuclear-theory models [43]. We do this to maximize the freedom of the model. See Appendix 2.10 for more details.

Due to its construction, the GP itself has parameters which control correlations. Such parameters have been termed *hyperparameters* [43], though we avoid this terminology here in order to avoid potential confusion with the term's use in hierarchical inference. In addition, the parametric models also have parameters which control the prior process; in general, such details are unique to each model. We instead focus primarily on the prior process induced by each EoS model with its chosen prior, returning to the subject of parameter distributions briefly in Sec. 2.7. For now, we simply note that our model implementations are typical of those used in the literature [69, 52, 14, 42, 36]. Lastly, we stress that our distinction between parametric and nonparametric models lies not in the existence of parameters but in the specification of a functional form for the EoS. In particular, we compare models with small, fixed numbers of parameters that are commonly used in the literature. For these models, the choice of functional form significantly impacts the range of EoS that can be represented.

Data and likelihood

Unless otherwise stated, all analyses in this paper make use of the same astronomical data as Ref. [48]. Specifically, we include two mass-tidal deformability measurements from gravitational wave (GW) detections of merging NSs [1, 3], one heavy pulsar mass measurement with radio data [10], and two x-ray observations of NS masses and radii [58, 72, 57, 73]. In the latter case, we also use the up-to-date radio mass measurement of the pulsar J0740+6620 [33]. Given these data d, the posterior probability density of a particular EoS ε is

$$P(\varepsilon|d, \mathcal{I}) = \frac{P(d|\varepsilon, \mathcal{I})}{P(d|\mathcal{I})} P(\varepsilon|\mathcal{I}), \tag{2.3}$$

where $\mathcal{I}$ is any additional information we may have about the system, e.g., knowledge that the data originate from a NS, as is the case for the pulsar observations but not for the GWs. Here $P(\varepsilon|d, \mathcal{I})$ is the *posterior* probability of the EoS given the data, $P(d|\varepsilon, \mathcal{I})$ is the *likelihood* of the astrophysical data given the EoS, $P(\varepsilon|\mathcal{I})$ is the prior probability of the EoS, and $P(d|\mathcal{I}) = \int P(d|\varepsilon, \mathcal{I}) P(\varepsilon|\mathcal{I}) \mathcal{D}\varepsilon$ is the total probability of observing this data marginalized over all EoS in the prior, often called the *evidence*. For general astrophysical data, $P(d|\varepsilon, \mathcal{I})$ must be computed by marginalizing over the astrophysical distribution of masses, spins, sky locations, and distances for individual events, which remains poorly constrained [9, 31, 17, 32, 6, 45, 30]. For the full expression, see Refs. [44, 15].

The different datasets we use primarily inform the EoS at different densities. The heaviest pulsar mass measurements serve to downweight EoS which cannot support the observed NS masses; these constraints tend to most significantly impact inference near $\sim$ (4-6)$\rho_{\rm nuc}$ and typically favor a stiffer EoS. The x-ray data provide constraints on the NS radius, and constraints so far have given information about the EoS mainly in the region $\sim$ (1-4)$\rho_{\rm nuc}$ [57, 44, 48, 66]. The GW observations provide constraints on the tidal deformabilities of the binary components, which are dominated by the

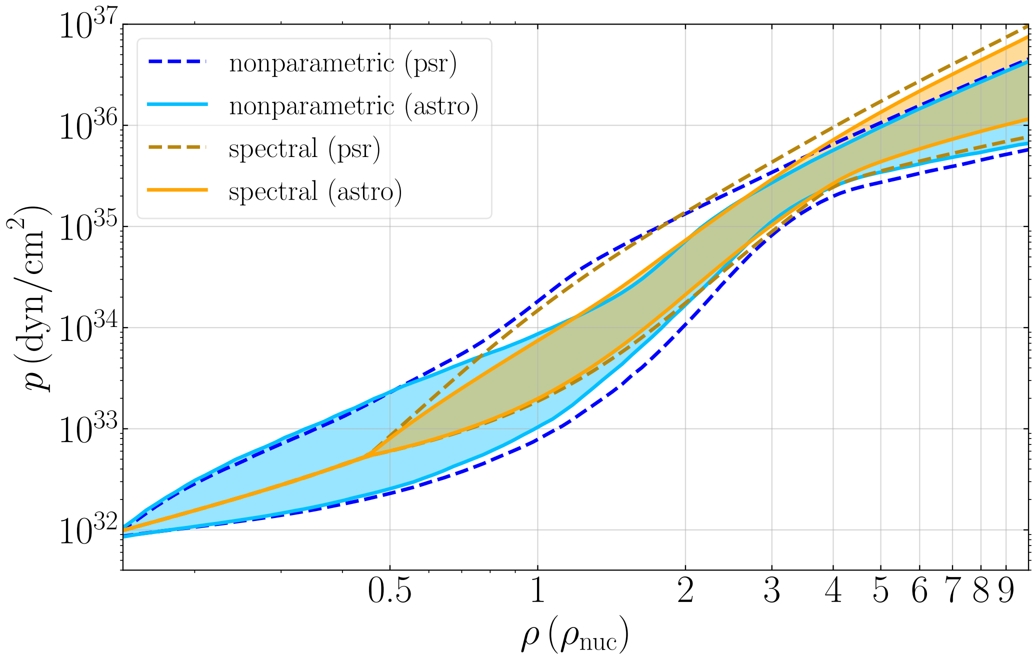

Figure 2.1: Symmetric 90% credible region for the pressure p at each density ρ in units of the nuclear saturation density using the nonparametric and spectral prior processes. We show results including all astrophysical data (labeled "astro," solid lines) and restricting to the heavy pulsars only (labeled "psr," dashed lines). The latter choice ensures that prior choices on the $M_{\rm max}$ supported by each model are irrelevant. Other parametric models are shown in Fig. 2.10. In all cases, we find that the p-ρ posterior depends on the EoS model even when identical data and inference schemes are employed.

loudest event observed so far, GW170817 [5, 44]. In terms of densities, the relevant scale constrained by this measurement is $\sim$ (1-3)$\rho_{\rm nuc}$ [44, 48]. Future constraints with GWs are likely to lie in this density range, as the fractional uncertainty in Λ will be smallest for lower-mass NSs with less dense cores and larger tidal deformabilities. In principle, nuclear experiments or calculations could also be included in such an analysis, and would mainly constrain the EoS near or below $\rho_{\rm nuc}$ [27, 28, 62, 13, 66]. However, we do not incorporate any in this work.

2.3 Impact of EoS model on current EoS constraints

Following the above prescription, we analyze the existing data using the four different EoS priors and plot the resulting marginal posteriors for $p(\rho)$ across a wide range of densities. Figure 2.1 compares the spectral and nonparametric models; similar plots for the other parametric models can be found in Appendix 2.12. The posteriors differ in their predictions for the EoS. For instance, the spectral posterior is stiffer

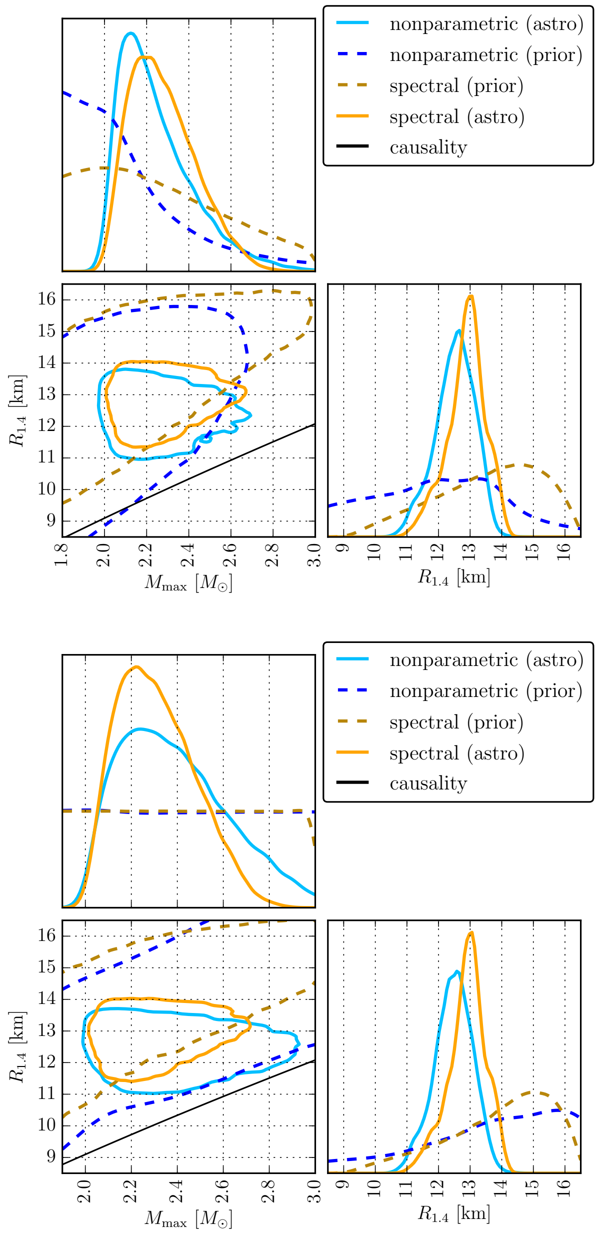

Figure 2.2: Prior (dashed) and posterior (solid) for the radius of a $1.4M_\odot$ NS, $R_{1.4}$, and maximum mass, $M_{\max}$, of a NS for two choices of the marginal $M_{\max}$ prior: default (left) and flat (right). We show results with the nonparametric and spectral EoS models, and contours denote 90% credible regions. The black line in the two-dimensional plot represents a maximally stiff M-R curve [71] stitched to a fiducial low density EoS [40]. Due to the low-density stitching, this "causality" line should be interpreted as a fuzzy boundary and not a sharp line. Both panels demonstrate that the spectral and nonparametric EoS models produce different $M_{\max}$ posteriors and that these differences cannot be attributed to the marginal priors. They are instead caused by correlations between low and high densities (equivalently, between $M_{\max}$ and $R_{1.4}$) imposed by the models. The correlations in the nonparametric case are due to causality, while the spectral case exhibits additional correlations and model dependence.

on average than the nonparametric one, especially above $4\rho_{\rm nuc}$. Similar differences have also been pointed out in Refs. [36, 57, 66], where multiple EoS models were employed under identical analysis settings. Our goal here is to understand the origin of these discrepancies.

Since it is difficult to glean information about interdensity correlations from envelope plots like Fig. 2.1, we turn our attention to two macroscopic NS properties that roughly correspond to the EoS behavior at high and low densities: the maximum mass, $M_{\rm max}$, and the radius of a $1.4 M_{\odot}$ NS, $R_{1.4}$. In Fig. 2.2 (left panel), we plot the one- and two-dimensional marginal prior and posterior for $M_{\rm max}$ and $R_{1.4}$. As expected, the marginal posteriors differ, but so do the marginal priors. Indeed, the $M_{\rm max}$ plot shows that both the spectral prior and posterior seem to have more support for $M_{\rm max}$ around $2.2 - 2.5 M_{\odot}$ than the nonparametric case. However, this trend is reversed above $2.6\,M_{\odot}$. This observation suggests that the difference between the nonparametric and spectral posteriors cannot be trivially assigned to different marginal priors. To further demonstrate this, in the right panel we plot the same variables, but now reweighted to a flat marginal $M_{\rm max}$ prior. As expected, the two posteriors differ, with the spectral model producing a narrower posterior.

To understand this discrepancy, we revisit the possible reasons $M_{\rm max}$ is constrained on the high side. Though an upper limit on $M_{\rm max}$ has been proposed based on the analysis of the counterpart of GW170817 [56], our analysis does not make use of it. Excluding an origin due to data, the upper limit on $M_{\rm max}$ must be the result of the EoS prior. The two-dimensional $M_{\rm max}$-$R_{1.4}$ panel indeed shows that the upper limit on $M_{\rm max}$ is related to the upper limit on $R_{1.4}$ [5, 1]; the $M_{\rm max}$-$R_{1.4}$ prior does not cover the entire available region for either model, with larger $M_{\rm max}$ requiring stiffer EoS and larger $R_{1.4}$.

The fact that larger $M_{\rm max}$ requires large values of $R_{1.4}$ is not unexpected from causality considerations. Indeed, the causality condition and the pressure at twice saturation, $p_{2.0}$, set an upper limit on the value of pressure at five times saturation, $p_{5.0}$. Since $p_{2.0}$ and $p_{5.0}$ correlate with $R_{1.4}$ and $M_{\rm max}$, respectively [46], any causal EoS model should limit $M_{\rm max}$ for certain low $R_{1.4}$ configurations [71]. To quantify this, we overplot the limiting $M_{\rm max}$-$R_{1.4}$ relation given by Ref. [40]: each point on the line represents a soft low-density EoS stitched to an EoS with $c_s^2 = 1$ at different densities. This curve should be interpreted approximately, as the exact causality threshold depends on the details of the low-density EoS [22].

Nonetheless, the right panel shows that in the nonparametric case the prior fills more of the physically allowable $M_{\max}$-$R_{1.4}$ parameter space compared to the spectral prior. This indicates that the nonparametric prior has non-negligible support in the entire physically allowed region even if specific marginal priors might downweight some regions (left panel). The same is not true for the spectral model which cannot access certain regions of the $M_{\max}$-$R_{1.4}$ plane.[3] This demonstrates that the correlation between $M_{\max}$-$R_{1.4}$ that appears in the spectral model is not entirely due to causality considerations, but it is also affected by the specifics of the model. The nonparametric model, however, is able to produce EoS which fall near the causality limit, indicating physics rather than modeling artifacts are the primary limitation to model freedom. Figure 2.12 presents a qualitatively similar conclusion for the piecewise-polytrope and speed-of-sound models. The piecewise polytrope exhibits behavior similar to the spectral model, while the speed-of-sound parametrization exhibits the opposite problem: its prior does not include low $M_{\max}$ for large $R_{1.4}$ values.

Crucially, the correlations we see in these corner plots are only those that are apparent from the two-dimensional marginalized posteriors. They do not reveal the many hidden correlations within the parametric EoS models that are not as easily detected. It is possible for implicit correlations within the EoS prior to bias the inference in ways that are not obvious in low-dimensional projections.

2.4 Impact of interdensity correlations: Toy Model

To better understand the effect of such implicit correlations, we first consider a simple toy model that demonstrates several of the issues with parametric models and introduce our techniques for diagnosing them.

We consider several simple linear parametrizations of the pressure as a function of energy density $p(\varepsilon)$. This allows us to examine the prior processes induced by the assumption of linearity from various perspectives. We contrast this to a GP prior process in the same context, finding particularly striking differences in the effect of a precise measurement of the pressure at one density on our uncertainty in the pressure at other densities.

We begin with the simple parametric model of a linear relationship between the pressure and the energy density

$$p(\varepsilon) = p_a + c_s^2(\varepsilon - \varepsilon_a), \tag{2.4}$$

[3] Figure 2.2 shows 90% contours. If we plotted 99% contours instead, the nonparametric model accesses even more of the allowed space, while the spectral model remains restricted.

parametrized by the pressure at $p_a = p(\varepsilon_a)$ and the slope c_s^2. Ignoring causality constraints, we choose what appear to be uninformative priors

$$p_a \sim \mathcal{N}(\mu_a, \sigma_a^2), \quad c_s^2 \sim \mathcal{N}(\mu_{c_s^2}, \sigma_{c_s^2}^2), \tag{2.5}$$

and refer to this as the point+slope process. The top panel of Fig. 2.3 shows the envelope plot for this prior process, i.e., the marginal distributions of the pressure at each energy density.

The envelope plot appears reasonable. That is, the prior process assigns approximately equal uncertainty to each pressure. However, the envelope plot only shows the marginal distributions at each density. Figure 2.4 shows the correlations between pressures at different densities. From this we see that the prior process actually imposes strong correlations between all pressures. We quantify this correlation between p_a and the pressure at some other density $p_b \equiv p(\epsilon_b)$ with the *mutual information* [20], defined as

$$I(p_a, p_b) \equiv \int dp_a dp_b \, P(p_a, p_b) \ln\left(\frac{P(p_a, p_b)}{P(p_a)P(p_b)}\right), \tag{2.6}$$

where $P(p_a) = \int dp_b \, P(p_a, p_b)$ is the marginal distribution. For the point+slope parametrization, we compute

$$I(p_a, p_b) = \frac{1}{2} \ln\left(1 + \frac{\sigma_a^2}{\sigma_{c_s^2}^2 (\varepsilon_a - \varepsilon_b)^2}\right). \tag{2.7}$$

The mutual information between p_a and p_b can be made arbitrarily small only in the limit $\sigma_a \ll \sigma_{c_s^2} |\varepsilon_b - \varepsilon_a|$; however, this limit corresponds to vanishingly small marginal uncertainty for p_a. We conclude that the assumption of a linear functional form can produce what seems to be a reasonable envelope plot in Fig. 2.3, but nevertheless induces model-dependent correlations between the pressure at different densities in Fig. 2.4.

In an attempt to remove the correlation between p_a and p_b, we consider the alternative parametrization

$$p(\varepsilon) = p_a + \frac{p_b - p_a}{\varepsilon_b - \varepsilon_a}(\varepsilon - \varepsilon_a), \tag{2.8}$$

described by the pressures at the two reference densities. We assume priors

$$p_a \sim \mathcal{N}(\mu_a, \sigma_a^2), \quad p_b \sim \mathcal{N}(\mu_b, \sigma_b^2), \tag{2.9}$$

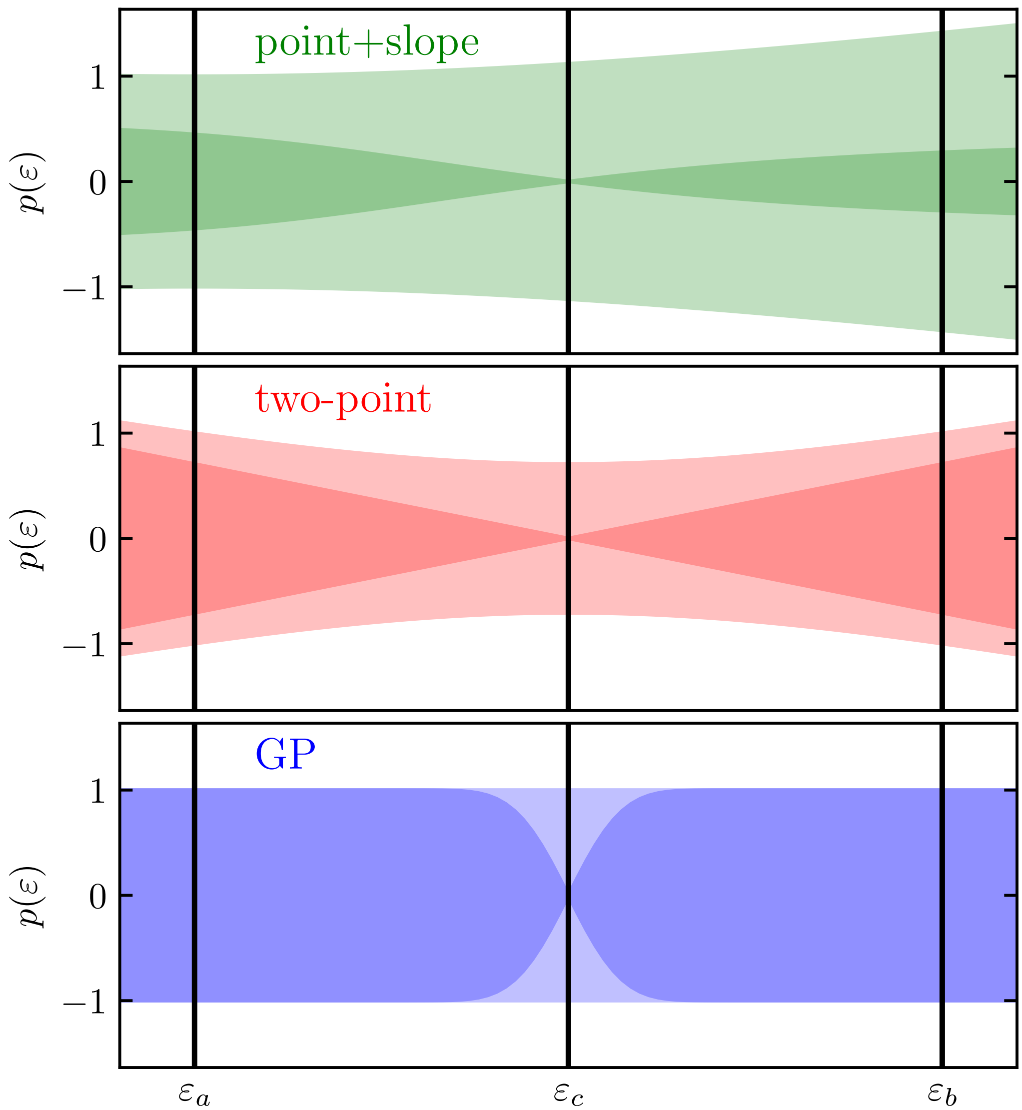

Figure 2.3: 68% (± 1-σ) marginal credible regions for the pressure at each density under the point+slope (top, green), two-point (middle, red), and GP (bottom, blue) prior processes. Shaded regions correspond to marginal distributions induced by the prior process at each energy density (light colors) and conditioned distributions for $p(\varepsilon)$ given a precise observation of p_c (dark colors). Only the GP process "fills the prior volume" rapidly as one moves away from the observation point ε_c. Compare to Fig. 2.5.

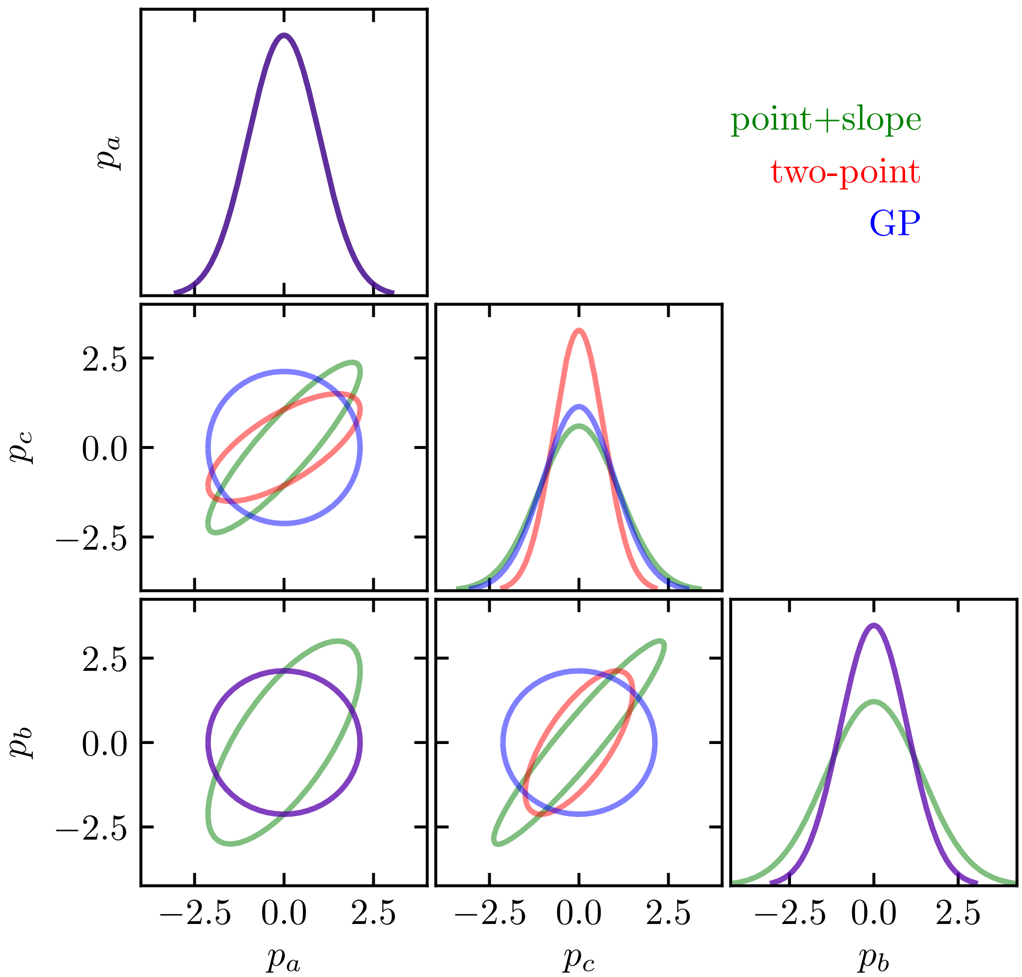

Figure 2.4: Joint and marginal distributions for the pressures at the three reference densities called out in Fig. 2.3 for the point+slope (green), two-point (red), and GP (blue) prior processes. Contours in the joint distribution represent 90% credible regions. While certain choices for the parametrization and priors can uncorrelate pairs of variables, only the GP prior process induces minimal correlations between all variables simultaneously.

and refer to this as the two-point process. Figures 2.3 and 2.4 show envelope and marginal distributions, respectively.

By construction, $I(p_a, p_b) = 0$ for the two-point prior process, as also seen in Fig. 2.4. However, the envelope plot shows that the marginal prior actually tightens for pressures between the reference densities. That is, we are able to remove the correlation between two pressures only at the expense of asserting greater prior knowledge about other pressures. Additionally, Fig. 2.4 shows that there are still correlations between $(p_a,\ p_b)$ and other pressures. This hints at the fact that, when one assumes a specific functional form, it may be possible to remove the correlations between a small number of statistics, but it is generally difficult to make all correlations vanish simultaneously or to avoid making strong assumptions about specific values of the function.

In order to consider this effect more quantitatively, we introduce a generalization of the mutual information that considers three pressures [20]

$$\begin{aligned} &I(p_a, p_b, p_c) \\ &\equiv \int dp_a dp_b dp_c\, P(p_a, p_b, p_c) \ln\left(\frac{P(p_a, p_b, p_c)}{P(p_a)P(p_b)P(p_c)}\right) \\ &= \int dp_a dp_b\, P(p_a, p_b) \int dp_c\, P(p_c|p_a, p_b) \ln\left(\frac{P(p_c|p_a, p_b)}{P(p_c)}\right) \\ &\qquad + I(p_a, p_b). \end{aligned} \tag{2.10}$$

Even if one can choose parametrizations and priors such that $I(p_a, p_b)$ vanishes, there is another term when considering mutual information for three pressures. In fact, for both the point+slope and two-point prior processes, the integral over p_c diverges as $P(p_c|p_a, p_b)$ is a delta function (determined by the closed-form parametrization), while $P(p_c)$ is a Gaussian with finite width. We conclude that the assumption of a linear relationship between the pressure and the density implies an infinite amount of information about the allowed relationships between variables. One cannot undo all these correlations at the same time by a clever choice of marginal prior distributions, although it may be possible to undo some of them. The failure of this reparametrization scheme anticipates the results of our investigation of alternative parametric priors in Sec. 2.7.

In general, the only way to undo all correlations simultaneously is to add more model freedom into the prior process. For example, one may add more reference densities to an existing model and generate a piecewise linear prior process. However, there will always be some densities between the (finite number of) reference densities, regardless of how many reference densities are chosen. In each of those regions, the piecewise-linear model is equivalent to our two-point prior process, and the strong correlations remain. One is then left with the question of how to extend the parametrization to remove all correlations in a scalable way. We show that a GP is a natural solution.

A GP, defined in terms of a mean function and a covariance kernel, describes our uncertainty in the infinitely many degrees of freedom in a function. With the assumption of Gaussianity, we can easily marginalize away uninteresting degrees of freedom, in our case retaining only the pressures on a dense grid of energy densities, and the GP reduces to a high-dimensional multivariate Gaussian distribution. Specifically, we consider the joint distribution induced over p_a, p_b, and p_c by a GP

$$\vec{p} \sim \mathcal{N}(\vec{\mu}, \Sigma), \tag{2.11}$$

with mean $\vec{\mu}$ and covariance Σ, with matrix elements defined by a covariance kernel

$$\Sigma_{ij} = \mathrm{Cov}(p_i, p_j) = K(\varepsilon_i, \varepsilon_j). \tag{2.12}$$

A common choice is the squared-exponential kernel

$$K_{\mathrm{se}}(\varepsilon_i, \varepsilon_j) = \sigma^2 \exp\left(-\frac{(\varepsilon_i - \varepsilon_j)^2}{l^2}\right), \tag{2.13}$$

although more complicated kernels are also used [26].[4]

Figures 2.3 and 2.4 show a GP assuming a squared-exponential kernel with parameters chosen to match the marginal distribution of the two-point prior process and $l \ll |\varepsilon_a - \varepsilon_b|$. We also obtain

$$\begin{aligned} I(p_a, p_b) &= -\frac{1}{2} \ln\left(1 - \frac{\sigma_{ab}^4}{\sigma_{aa}^2 \sigma_{bb}^2}\right) \\ &= -\frac{1}{2} \ln\left\{1 - \exp\left[-\frac{2(\varepsilon_a - \varepsilon_b)^2}{l^2}\right]\right\}, \end{aligned} \tag{2.14}$$

which vanishes as $\exp[-2(\varepsilon_a - \varepsilon_b)^2/l^2]$ in the limit $|\varepsilon_a - \varepsilon_b| \gg l$. Furthermore, $P(p_c|p_a, p_b)$ is a normal distribution, and the generalization of the mutual information in Eq. (2.10) no longer diverges. If $l \ll |\varepsilon_b - \varepsilon_c|, |\varepsilon_a - \varepsilon_c|$, then $\Sigma_{ij} \to \sigma^2 \delta_{ij}$

[4]It is worth noting that linear regression is a special case of a GP. That is, a GP can reproduce the linear model with an appropriate choice of covariance kernel: $K(\varepsilon_i, \varepsilon_j) \propto \varepsilon_i \varepsilon_j$.

and $P(p_c|p_a, p_b) \rightarrow P(p_c) \ \forall \ (p_a, p_b)$. Therefore, if $l \ll |\varepsilon_b - \varepsilon_a|$ as well, $I(p_a, p_b, p_c) \rightarrow 0$. We conclude, then, that the GP prior process can be made to simultaneously produce reasonable envelope plots (broad marginal distributions for all pressures) while retaining vanishingly small correlations between (reasonably separated) pressures. This is in stark contrast to the parametrized prior processes, where this is, in general, not possible.

We demonstrate one more useful diagnostic in this toy model through the conditioned distribution

$$P(p_i|p_j) = \frac{P(p_i, p_j)}{P(p_j)} \tag{2.15}$$

which shows how our knowledge of p_i depends on p_j. Figure 2.3 shows the envelope plots for the conditioned distributions corresponding to each of our prior processes when we condition on p_c. We see that a constraint at ε_c is broadcast to nearby densities in all cases, but the Gaussian process fills up the prior volume from the unconditioned marginal distributions the fastest. This is a visual manifestation of the correlations quantified by the mutual information. Indeed

$$I(a, b) = \int daP(a) \int db\, P(b|a) \ln \frac{P(b|a)}{P(b)}, \tag{2.16}$$

is just the Kullback–Leibler divergence $D_{\mathrm{KL}}\left(P(b|a)||P(b)\right)$ from the unconditioned marginal to the conditioned marginal averaged over the possible $a \sim P(a)$.

In the case of realistic EoS inference, we have to consider even higher-dimensional spaces. A natural measure of correlations, then, is a generalization of the mutual information (sometimes called the total correlation, multivariate constraint, or multi-information [20])

$$I(x_1, \cdots, x_N) \equiv -H(x_1, \cdots, x_N) + \sum_{i=1}^{N} H(x_i) \tag{2.17}$$

where $H(x) = -\int dxP(x) \ln P(x)$ is the entropy of the distribution $P(x)$. Larger H imply broader distributions. We will consider this statistic in the context of real astrophysical constraints on the EoS in Sec. 2.5. In general, one can make I small but still allow for very little model freedom (small H). We therefore seek prior processes with both large $H(x_1, \cdots, x_N)$ and small $I(x_1, \cdots, x_N)$. This is sometimes captured in the variation of information, defined as $H - I$, but we find it more useful to consider H and I separately.

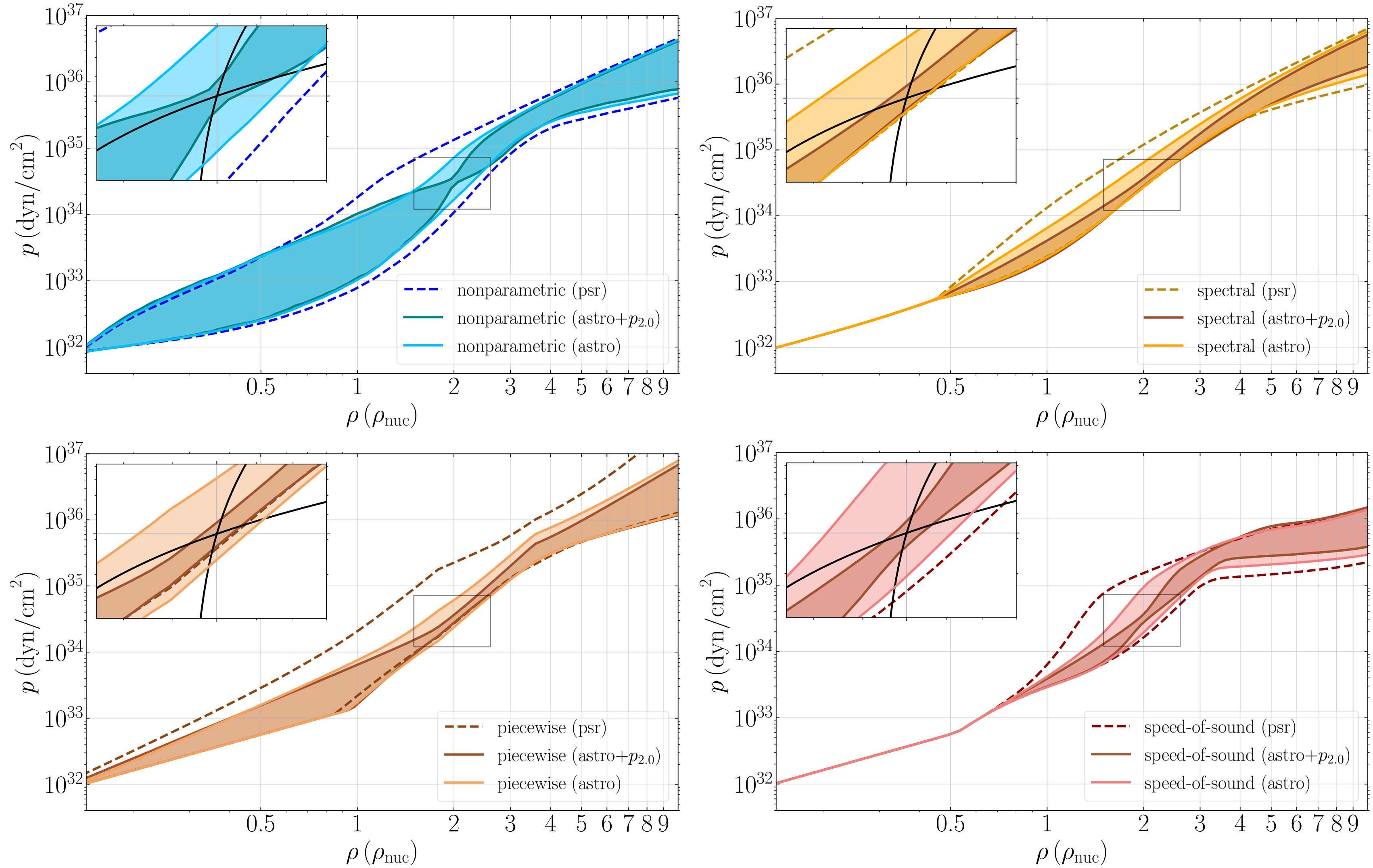

Figure 2.5: Similar to Fig. 2.1 but with a mock constraint injected directly into $p(\rho = 2\rho_{\rm nuc})$ for each EoS prior process. The posterior after the simulated constraint is included ("astro+mock") is overplotted on the posterior with all current data ("astro"), and in a darker color. The constraint at a single density affects the parametric posteriors over a much wider range of density scales than the nonparametric one. The inset focuses around $\rho = 2\rho_{\rm nuc}$. The two black straight lines provide an estimate of the constraints imposed by causality ($c_s^2 < 1$) and thermodynamic stability ($c_s^2 > 0.1$) around $\rho = 2\rho_{\rm nuc}$, subject to the heavy pulsar measurements. The nonparametric posterior quickly "fills" more of the physically available region after satisfying the mock constraint, while the parametric posteriors do not.

2.5 Impact of interdensity correlations: idealized measurement

Our toy model illustrates the potential impact of implicit correlations within EoS models on the results of EoS inference. In order to quantify the sensitivity of the parametric and nonparametric models to such model-dependent correlations between density scales, we now consider simulated NS observations. The macroscopic NS properties that astronomical observations target (masses, radii, and tides) are determined by a range of NS densities, it is therefore not straightforward to disentangle the effect of the data and the model dependence in the constraint that a single astronomical observation imposes on the EoS. Consequently, we begin with the same setup as Sec. 2.4: an idealized direct measurement of $p(\rho)$ at a single density, while keeping in mind that a realistic astronomical measurement would correspond to a combination of many such constraints correlated across many densities.[5]

We consider a tight Gaussian constraint at $p_{2.0}$ with mean of 3.20×10^{34} dyn/cm^2 based on a candidate EoS drawn from our GP prior that is consistent with all current parametric posteriors near $2\rho_{\rm nuc}$. We arbitrarily choose the standard deviation, 2.61×10^{33} dyn/cm^2 ($\sim 8\%$ relative uncertainty). We then plot the corresponding envelope for $p(\rho)$ with this mock constraint and all other real astronomical data for each model in Fig. 2.5. In the nonparametric case, imposing this constraint pinches the p-ρ envelope around $2\rho_{\rm nuc}$, but the uncertainty in the $p(\rho)$ curve is unaffected beyond $\approx \pm 0.5\rho_{\rm nuc}$. All the parametric models, though, change across several $\rho_{\rm nuc}$, indicating that the EoS at many scales is informed significantly by the EoS near $2\rho_{\rm nuc}$.

In each panel, the inset zooms in around the $\rho = 2\rho_{\rm nuc}$ region; to guide the eye the two black lines provide a rough estimate of the maximally causal ($c_s^2 = 1$) and minimally stable ($c_s^2 = 0.1$) EoS that can support the heavy pulsar observations (see Fig. 2 of Ref. [44]) around $\rho = 2\rho_{\rm nuc}$. The two lines were obtained by combining $dp/d\varepsilon = c_s^2$ and the first law of thermodynamics with the approximation that $\varepsilon_{2.0} = c^2\rho_{2.0}$. The nonparametric prior process contains EoS draws that approach this limiting behavior near the constraint. Comparing the four panels, the nonparametric model fills more of the physically available space. The parametric models, on the other hand, are clearly subject to additional correlations between pressures besides causality and stability.

To quantify these correlations, we follow Sec. 2.4 and compute the total correlation

[5] An example of how one may obtain direct constraints on the pressure from nuclear experiments is demonstrated in Refs. [27, 28].

Table 2.1: Total correlation (I) and entropy (H) of the joint distributions over $\ln p_{1.0}$, $\ln p_{1.5}$, $\ln p_{2.0}$, $\ln p_{3.0}$, and $\ln p_{4.0}$ induced by several processes as well as the entropy of the marginal distribution over only $\ln p_{2.0}$ ($H(\ln p_{2.0})$). The nonparametric processes consistently have smaller I and (much) larger H than any parametric process, implying much more model freedom. This is the case even though the entropy of the marginal distributions for $\ln p_{2.0}$ can be comparable.

	I			H			$H(\ln p_{2.0})$		
	PSR	Astro	$+p_{2.0}$	PSR	Astro	$+p_{2.0}$	PSR	Astro	$+p_{2.0}$
Nonparametric	3.7	3.1	2.9	0.7	-1.0	-2.5	1.0	0.5	-1.1
Spectral	6.6	5.5	4.7	-4.2	-5.5	-7.6	0.5	0.0	-1.1
Polytrope	5.7	4.6	3.8	-1.6	-3.6	-5.7	0.9	0.2	-1.1
Speed of sound	5.0	4.7	4.3	-2.6	-4.3	-7.1	1.0	0.6	-1.1

between the pressures at several reference densities. Table 2.1 shows the total correlation (I) and joint entropy (H) between $\ln p_{1.0}$, $\ln p_{1.5}$, $\ln p_{2.0}$, $\ln p_{3.0}$, and $\ln p_{4.0}$ induced by the posterior process conditioned on the astrophysical data as well as the astrophysical data and the mock constraint on $p_{2.0}$.[6] We consider these pressures as the central density of $M_{\rm max}$ stars may be as low as $4\rho_{\rm nuc}$ [48], and therefore we focus on pressures that are confidently relevant for NSs. Although the precise values of I and H can be difficult to interpret, we notice some trends.

Overall, the nonparametric process consistently has the largest joint entropy and smallest total correlation, as desired. The value of I is approximately equal for all of the parametric processes, which are larger than the nonparametric process by $\gtrsim 1$ nat. Additionally, the change in I when we additionally condition on a mock constraint on $p_{2.0}$ is much smaller for the nonparametric than for the parametric processes. This can be interpreted as the constraint on $p_{2.0}$ removing some correlations from the parametric processes by approximately fixing the value of $p_{2.0}$.

What is more, the parametric processes have much smaller joint entropies than the nonparametric process in all cases. This is a manifestation of the reduced model freedom in the parametric processes as the nonparametric process explores more combinations of pressures than any parametric process. Although not exact, the exponential of the difference in entropies is an estimate of the ratio of the effective number of pressure combinations supported in each distribution: the nonparametric contains between 10 and 100 times as many possible pressure combinations as the

[6] We estimate the entropies via Monte Carlo sums over kernel density estimates (KDEs) of the associated distributions. As such, the actual correlations may be smoothed by the KDE, which may act as upper limits on the estimates of the mutual information in some cases.

parametric processes.

Additionally, the constraint on $p_{2.0}$ removes more entropy from each parametric processes than from the nonparametric process. While we expect the joint entropy to be smaller in all cases after measuring $p_{2.0}$ precisely, the additional entropy lost in the parametric processes is associated with the correlations between pressures. That is, knowledge of $p_{2.0}$ decreases our uncertainty in other pressures within the parametric processes, something that does not happen as strongly in the nonparametric process. This is apparent in Fig. 2.5 as well.

As a final note, Table 2.1 also reports the entropy of the marginal distributions over $\ln p_{2.0}$. We see smaller differences between these one-dimensional (1D) distributions, reinforcing the conclusion that the differences between the nonparametric and parametric processes arise mainly from correlations between multiple pressures.

2.6 Impact of interdensity correlations: Mock astrophysical observations

Different astronomical probes provide information about different density scales, and therefore interdensity correlations are likely to matter even more for realistic EoS inference than in the idealized case considered above. Implicit correlations in EoS models could artificially give the appearance of tension between observations of NSs or nuclear matter made via different channels. This has already been shown to be relevant in comparisons of nuclear experiments with astrophysical observations [27, 28]. To investigate this possibility, we now repeat the previous sections' analysis for a simulated set of astronomical observations.

We choose a candidate EoS with $M_{\max} = 2.54\,\mathrm{M}_{\odot}$ and $R_{1.4} = 12.0\,\mathrm{km}$. This EoS is relatively soft at low densities and stiff at high densities, but is consistent with the 90% 1D marginal pressure constraints for all of our models at all densities, except the speed-of-sound parametrization above $4\rho_{\mathrm{nuc}}$. The combination of macroscopic parameters lies outside the spectral 90% credible region in Fig. 2.2, motivating its use in studying how tension appears in an analysis when such a mismatch arises.[7] We simulate three measurements of pulsar masses and radii with comparable uncertainty to the recent measurement for J0740+6620 [57, 73]. This observation incorporated radio data to constrain the pulsar mass [33] and constrained the radius with x-ray data. We also simulate 20 GW detections of binary NS mergers at A+ detector sensitivity [4]. Note, however, that we do not impose prior knowledge of the NS

[7] Due to the broad prior of the nonparametric model, finding a physically valid EoS with no support in the nonparametric macroscopic or microscopic priors is much more challenging.

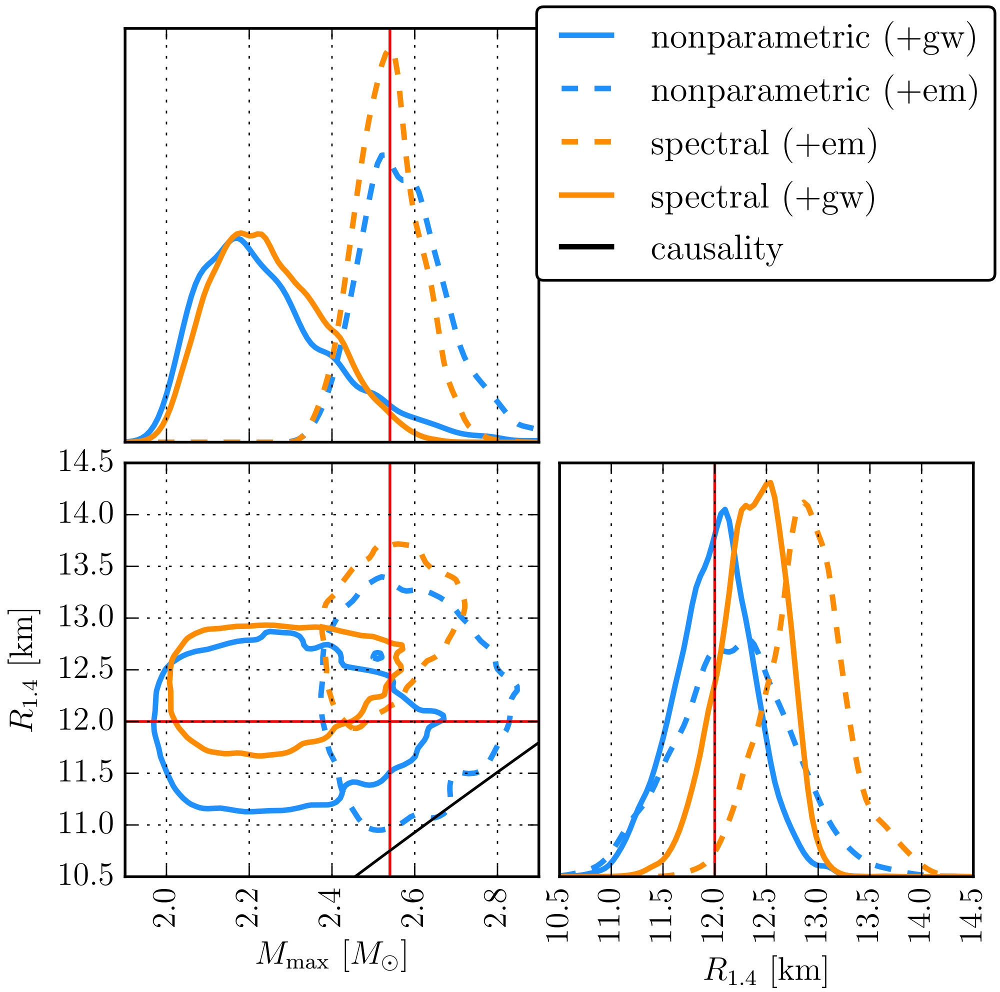

Figure 2.6: Inferred posterior for $R_{1.4}$ and $M_{\max}$ using the nonparametric model and the spectral model and mock x-ray-radio (blue and orange dashed line, respectively) and GW (blue and orange solid line, respectively) observations. All posteriors also include all current astrophysical data. The vertical and horizontal red lines show the injected value of $R_{1.4}$ and $M_{\max}$. The $M_{\max}$ posterior is only weakly informed by the GW data as they typically cannot lead to a definitive identification of a $> 2M_\odot$ object as a NS, and it is thus similar to that of Fig. 2.2.

nature of the components in our inference. The simulated pulsars are drawn from a uniform-in-central-density distribution, while the simulated binary NSs come from a uniform-in-mass distribution, under the condition that the NS masses lie below $M_{\max}$.

We analyze each dataset separately, folding the simulated measurements of each type onto all current astrophysical data. We plot the inferred posteriors in Fig. 2.6.

We find that the nonparametric posterior for $R_{1.4}$ is centered on the correct value (12 km) with either x-ray or GW data. In the spectral case, though, while the GW measurements are consistent with the correct value, the x-ray posterior is in tension at 90% credibility. Moreover, the GW and x-ray posteriors are less consistent with each other, an observation that could lead to the erroneous conclusion of tension between different EoS probes.

We can understand this as follows. We expect GW measurements of high-mass NSs ($\geq 1.7\mathrm{M}_{\odot}$) to be less informative than lower-mass NSs, as the absolute impact of tidal parameters on the signal is weaker for more compact stars. In general, high-mass NSs will most likely be indistinguishable from black holes until the advent of next-generation detectors [19, 48]. As such, high-mass systems offer little information for either $M_{\max}$ or $R_{1.4}$, and thus the GW data primarily probe only the low-mass/low-density part of the EoS. Indeed, Fig. 2.6 shows that each mock-GW $M_{\max}$ posterior is similar to the respective posterior of Fig. 2.2, indicating that additional GW observations inform $M_{\max}$ only weakly.

On the other hand, x-ray measurements have already proven capable of bounding the radius of high-mass NSs [57, 73]. Additionally, x-ray detection of pulsations in a compact object proves it is a NS, and thus its mass offers information about $M_{\max}$. Depending on the mass distribution of observed events, x-ray probes could thus probe the EoS at both low and high densities. Our mock x-ray dataset contains one such NS with mass 2.50 $M_{\odot}$. Figure 2.6, then, shows that when we use a parametric model to fit all the x-ray data, biases can arise as no EoS in the prior process can simultaneously reproduce the correct values for both $M_{\max}$ and $R_{1.4}$. The bias is smaller in the GW-based results as the data there probe a narrower density range, resulting in the appearance of mild tension between the two datasets. By extension, a newly observed GW signal for a $1.4M_{\odot}$ NS would be in tension with the x-ray-based results, despite no real astrophysical inconsistency. Recent concerns of tensions between PREX-II [70] and astrophysical predictions may be influenced by a similar mechanism, as noted in Refs. [27, 28].

2.7 Impact of parametric prior choices

These investigations show that the parametric EoS prior processes include model-dependent interdensity correlations that influence the resulting inference. Such prior processes are constructed based on two ingredients: (i) a functional form for $p(\rho)$ (or an equivalent quantity) and (ii) a prior for the parameters of the function. The former may be carefully engineered, while the latter can be changed more easily. As in Sec. 2.4, it is therefore reasonable to wonder if we can change the nature of the interdensity correlations by a trivial change in the parameter prior, or whether the correlations are inherent to the functional form. Below we argue for the latter, as also demonstrated in Sec. 2.4.

First, adding parameters does not necessarily always increase model freedom. Adding a parameter to any model we have shown so far will require choosing a distribution for that parameter, and a reasonable range will strongly depend on the functional form. For the piecewise-polytrope model, this process is somewhat easier, as additional adiabatic indices for new segments have clear physical meaning. Therefore reasonable ranges can be chosen. For the spectral model, with the addition of a new spectral component, there is no obvious mapping of parameter values to physics, and so tuning parameter ranges is much harder.

Second, of the existing parameters in the models, we typically find that only a few are meaningfully constrained. For example, the speed-of-sound model has only a single Gaussian bump, and thus current astrophysical data tightly constrain this bump to be at densities low enough to produce pulsars consistent with, e.g., Refs. [58, 72, 44]. This severely limits the flexibility of the model, as the logistic term is, by itself, not strong enough to support realistic NSs. In practice a_1 and a_2 are overconstrained in this model and a_4 and a_5 are underconstrained. As a result, the speed-of-sound model is the least flexible (and leads to the most stringent constraints) even though it has the most parameters. We find similar behavior in the spectral and piecewise-polytrope models, suggesting that the effective number of parameters in the models is fewer than what is nominally stated.

Third, due to the fine-tuning of the parametric models, attempting to redefine priors on parameters is generally not an efficient way to expand model freedom. As an example, we consider the spectral EoS where we find that EoS candidates have *a priori* strong correlations between parameters in order to satisfy causality and stability. These correlations were noted in Ref. [81] and are also shown in Fig. 2.7. We find that the γ_i are alternately strongly correlated or anticorrelated with each other. It is possible that other distributions, in particular distributions that upweight EoS further from the line of strongest correlation, reduce the strength of interdensity correlations.

We test this by upweighting more extreme γ_i values. The reweighting procedure does indeed change the posterior distribution of γ_i parameters, although the inferred

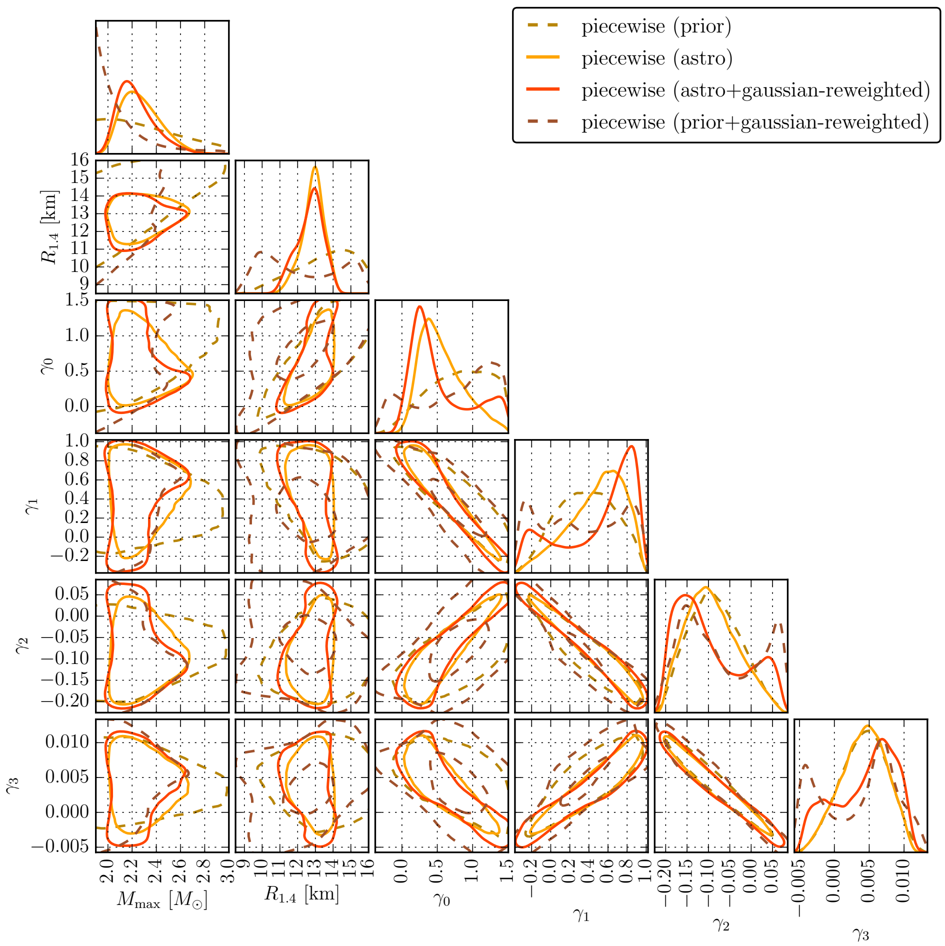

Figure 2.7: Marginal one- and two-dimensional prior and posterior distributions for the parameters of the spectral model, γ_i, as well as the maximum NS mass, $M_{\rm max}$, and the radius, $R_{1.4}$. We show the default prior as well as reweighted results that upweight more extreme values of γ_i. In both cases, $M_{\rm max}$ and $R_{1.4}$ have very similar posteriors, showing that the reweighting does not efficiently extend the coverage of the prior toward the causality threshold in the $M_{\rm max}$-$R_{1.4}$ plane. Additionally, extending the prior ranges for γ_i is unlikely to change the results as the posteriors are not limited by the prior ranges.

distribution in $M_{\max}$-$R_{1.4}$ is effectively unchanged. Moreover, the $M_{\max}$-$R_{1.4}$ prior does not significantly extend into the previously excluded region closer to the stability threshold. We find similar results with a different reweighting of γ_i that instead favors for central values. Figure 2.7 also shows that extending the prior range on γ_i will not extend the reach of the spectral model as the parameter posteriors are not significantly affected by the prior cutoffs. We reach similar conclusions with the piecewise polytrope.

Overall, while it was possible to remove correlations between only a subset of pressures within our toy models in Sec. 2.4, it is generally difficult to do even that with real parametrized EoS models.

2.8 Conclusions

All models of the dense-matter EoS should contain some correlations between density scales due to causality and thermodynamic stability requirements. However, in this study we show that phenomenological parametric models such as the spectral, piecewise-polytrope, and speed-of-sound models impose even stronger correlations *a priori*. As a result, NS properties are constrained more tightly in parametric models than in nonparametric ones in ways that are not supported by the data. Regardless of whether these tighter constraints end up being compatible with the true EoS, their emergence is attributable to what are effectively model-dependent prior assumptions dictated by the phenomenological nature of the parametrizations. Viewed in this way, they deserve the same scrutiny as other prior choices imposed by the analyst.

The concerns about implicit correlations are alleviated by GP-based nonparametric models that enjoy extensive model freedom, restricted only by causality and thermodynamic stability. They allow us to generate, with no additional modeling effort, candidate EoS with complex phenomenology that could be associated with, e.g., a transition to quark matter in the cores of NSs. For example, Refs. [77, 78] study EoS with complex speed-of-sound phenomenology, while Refs. [38, 18, 37, 23, 49, 22] consider strong first-order phase transitions that result in a discontinuity in the speed of sound and multiple stable branches. The GP prior process is able to recreate such behaviors generically.

The parametric models are relatively easier to implement. However this might come at the cost of fine-tuning which makes it harder to sample from the prior as many draws are unphysical. Extension to more complex phenomenology, such as phase transitions, is less straightforward and might need tailored parametric models [8, 7, 39] unless the parametrization supports such behavior inherently. The piecewise polytrope specifically, as implemented here, can lead to priors and posteriors with “kinks" [14, 42], while Refs. [65, 74] discuss its behavior in cases where the observed NSs do not reach high enough densities to probe all polytropic segments. More complicated parametric models exist (see Appendix 2.11), but as we argue in Sec. 2.7, improving parametric models by adding parameters or extending the priors ranges is not always straightforward or efficient. However, extreme extensions to these models (for example a $O(1000)$ parameter extension to the piecewise polytrope) could exhibit behavior that is closer to the nonparametric results than the few-parameter models they generalize.

In conclusion, commonly used parametric models of the EoS are hampered by built-in and often opaque correlations between density scales. These correlations already affect inferences based on these models, and these effects will only become more severe with additional astrophysical data. The impact of the EoS model on inference acts as an additional systematic error that must be addressed to achieve highly informative EoS constraints [24, 35, 16, 63, 41, 25]. Our work shows that the nonparametric GP-based model addresses this EoS model systematic and restores model freedom by forgoing the use of specific functional forms for the EoS itself and instead parametrizing a wide range of possible correlations directly.

2.9 Acknowledgements

We thank Les Wade for useful discussions on the implementation of the spectral model in LALsuite . R.E. thanks the Canadian Institute for Advanced Research (CIFAR) for support. Research at Perimeter Institute is supported in part by the Government of Canada through the Department of Innovation, Science and Economic Development Canada and by the Province of Ontario through the Ministry of Colleges and Universities. P.L. is supported by the Natural Sciences and Engineering Research Council of Canada (NSERC).

This research has made use of data, software and/or web tools obtained from the Gravitational Wave Open Science Center (https://www.gw-openscience.org), a service of LIGO Laboratory, the LIGO Scientific Collaboration and the Virgo Collaboration. Virgo is funded by the French Centre National de Recherche Scientifique (CNRS), the Italian Istituto Nazionale della Fisica Nucleare (INFN), and the Dutch Nikhef, with contributions by Polish and Hungarian institutes. This material is based upon work supported by NSF's LIGO Laboratory which is a major facility fully funded by the National Science Foundation. The authors are grateful for computational resources provided by the LIGO Laboratory and supported by National Science Foundation Grants No. PHY-0757058 and No. PHY-0823459.

2.10 Description of the nonparametric EoS model

Our GP is tailored to incorporate a variety of possible correlation lengths, established by the form of the kernel function. Each GP draw is a realization of a multivariate Gaussian distribution, which is loosely conditioned on nuclear models. The GP from which EoS candidates are sampled has a covariance which is governed by a kernel function through the parameters σ and ℓ that control the strength and length of the correlations respectively [26]. The EoS prior process includes EoS drawn from multiple underlying GPs with different parameters: $\log \sigma \in U(1, 10)$ and $\ell \in U(0.1, 0.9)$. However, our GPs' kernels contain additional terms as well. See Ref. [26] for more details. In total we use $\sim 2 \times 10^6$ draws, of which $\sim 3 \times 10^5$ contribute to the prior nontrivially.

In Ref. [57], a single GP is used to generate EoS realizations using the same method. This single GP is more tightly bound to the mean realization and nuclear models than corresponding piecewise-polytrope and spectral models due to the values of $\sigma = 1$ and $\ell = 1$ chosen. Such values correspond to stronger correlations and over larger length scales than any GP we employ here. This demonstrates that although the GP model is flexible, it is not necessarily agnostic. This can be useful, for example, to examine the validity of a set of related nuclear models given astrophysical data [29].

Figure 2.8 shows example draws from our prior process plotted on top of posteriors for various parameters. The candidate EoS exhibit a wide range of behavior as is perhaps most evident in the bottom panel.

2.11 Description of the parametric EoS models

Piecewise-polytrope parametrization

In the piecewise-polytrope approach, consistent with Refs. [68, 14], the polytropic exponent is a piecewise constant function, which changes value at two predetermined densities

$$p(\rho) = \begin{cases} K_1 \rho^{\Gamma_1} : \rho < \rho_1 \\ K_2 \rho^{\Gamma_2} : \rho_1 < \rho < \rho_2 \\ K_3 \rho^{\Gamma_3} : \rho_2 < \rho. \end{cases} \tag{2.18}$$

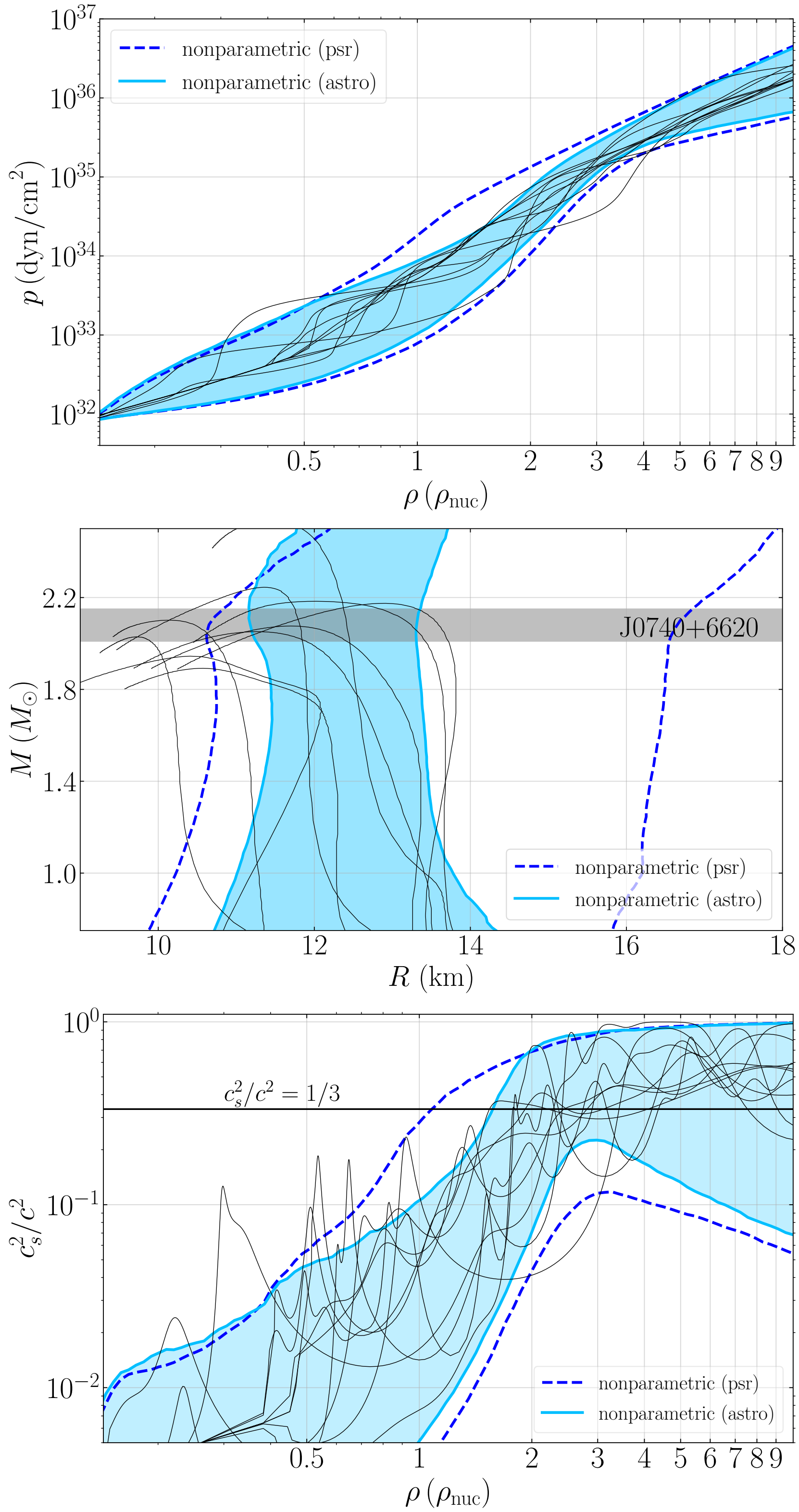

Figure 2.8: Example EoS draws from the nonparametric prior plotted in terms of the pressure p vs the density ρ (top), the mass M vs the radius R (middle), and the speed of sound c_s vs the density ρ (bottom). We only draw EoS with non-negligible contribution to the posterior. For reference, we also plot the 90% symmetric credible intervals for the posterior using only heavy pulsar observations and all astrophysical data.

EoS prior process	Parameter	Prior
Spectral	r_0	U(-4.37722, 4.91227)
	r_1	U(-1.82240, 2.06387)
	r_2	U(-0.32445, 0.36469)
	r_3	U(-0.09529, 0.11046)
Piecewise-polytrope	$\log p_1$	U(33.6, 35.4)
	Γ_1	U(1.9, 4.5)
	Γ_2	U(1.1, 4.5)
	Γ_3	U(1.1, 4.5)
Speed-of-sound	a_1	U(0.5, 1.5)
	a_2	U(1.3, 5)
	a_3	U(0.05, 3)
	a_4	U(1.5, 21)
	a_5	U(0.1, 1)

Table 2.2: List of parameters and corresponding priors on which each parametric EoS prior process depends.

Here $\rho_1 = 10^{14.7}\mathrm{g/cm}^3$ and $\rho_2 = 10^{15}\mathrm{g/cm}^3$ are fixed via an optimization for a set of candidate EoS following from nuclear models [68]. The parameter K_1 is chosen to give some value $p_1 \equiv p(\rho_1)$, and K_2 and K_3 are then fixed by continuity. Therefore $\{\Gamma_1, \Gamma_2, \Gamma_3, p_1\}$ are the parameters in this model. Their corresponding priors are given in Table 2.2. Extensions to this model with more polytropic segments or allowing the transition densities to vary are proposed in Refs. [76, 75, 67, 59].

When $\{\Gamma_1, \Gamma_2, \Gamma_3, p_1\}$ are sampled from a uniform distribution then the resulting total EoS will be neither necessarily causal or stable. Therefore, we have to enforce these constraints after the fact; specifically, we sample a set of parameters, compute the corresponding EoS, and save it only if it obeys causality and stability.[8] Overall, we retain $\sim 1.6 \times 10^5$ EoS. We verified that this number is enough to efficiently characterize the posterior by confirming that we get consistent results with half as many draws. For the computation of the $p(\rho)$, and $\varepsilon(p)$ relations, we used LALSimulation, a subsection of LALSuite [50]. For checks of NS properties such as causality, we used LALInference [50, 80]. Our priors are slightly more restrictive than those used in Ref. [42] due to computational problems that arise for candidates with the highest Γ_2, Γ_3, which tend to represent acausal EoS candidates anyway.

[8]In practice, we impose a weaker causality constraint ($c_s \leq 1.1c$) for our parametric models.

Spectral parametrization

In the spectral approach, the polytropic exponent is expanded in a series of basis functions. Following the conventions of Ref. [52] which introduced the spectral parameterization, we take $x \equiv p/p_0$ where p_0 is the smallest pressure where the spectral parametrization will be used; the parametrization is matched to some other EoS at this density which serves as the low-density crust [34]. Then we set

$$p(\rho) = \rho^{\Gamma(x)} \tag{2.19}$$

with

$$\Gamma(x) = \sum_{i=0}^{n} \gamma_i \left(\log(x)\right)^i . \tag{2.20}$$

In most of the literature, and for our purposes n is set to 3. Note that the overall scaling of $p(\rho)$ is fixed by γ_0, and again we have four total parameters $\{\gamma_0, \gamma_1, \gamma_2, \gamma_3\}$. In practice sampling individual parameters is impractical because generic combinations of parameters produce unphysical EoS, even if the parameter ranges are chosen carefully. Instead, following Ref. [81], we sample in a different parameter space $r = (r_0, r_1, r_2, r_3)$ and under an affine map construct samples in γ. The prior on r is given in Table 2.2. Our analysis uses a total of $\sim 1.9 \times 10^5$ draws from the spectral model. We again use the LALSuite components LALSimulation and LALInference [50, 80], with particular spectral components implemented by Ref. [14]. The spectral EoS is stitched to a model of the SLy EoS just below $0.5\rho_{\rm nuc}$ [14] (see Fig. 2.1).

Speed of sound parametrization

In this approach, the speed of sound is parametrized as a function of energy density. Taking $z \equiv \varepsilon/(\rho_{\rm nuc} c^2)$, we write

$$\frac{c_s^2(z)}{c^2} = a_1 e^{-\frac{1}{2}(z-a_2)^2/a_3^2} + a_6 + \frac{\frac{1}{3} - a_6}{1 + e^{-a_5(z-a_4)}} \tag{2.21}$$

with a_1, a_2, a_3, a_4, a_5 real parameters, and a_6 fixed by matching to a low-density crust. In Ref. [36], the matching is done to a chiral effective field theory at $\sim \rho_{\rm nuc}$ with limits based on Fermi liquid theory enforced up to a density of $1.5\rho_{\rm nuc}$. Since we do not wish to use more nuclear theory information for this model than others, we instead stitch to SLy at a density of $0.6\rho_{\rm nuc}$, comparable to the stitching density of the spectral model. Because of this, the parameter ranges in our implementation must be adjusted to generate realistic EoS candidates. The prior on each parameter

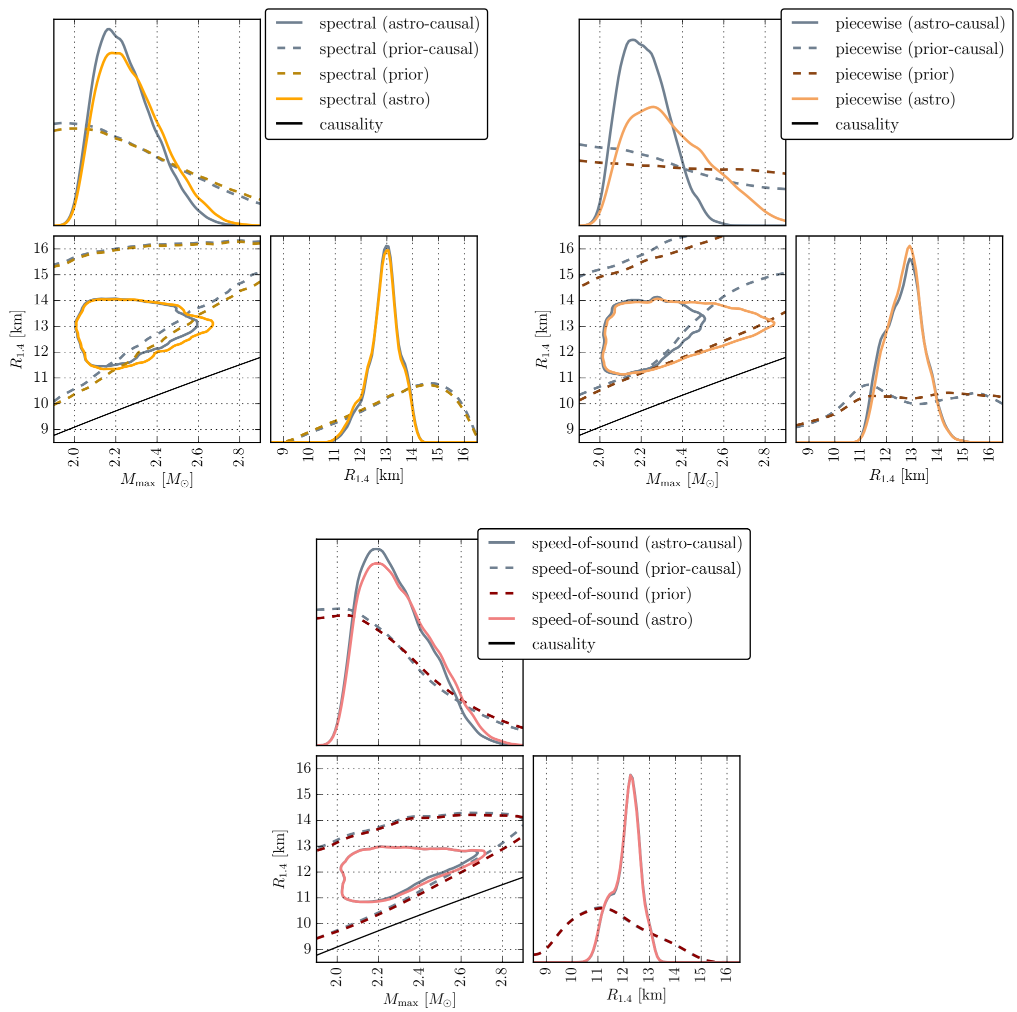

Figure 2.9: Comparison between using strictly causal ($c_s^2 < c^2$) parametric EoS with each model (gray) and the headline results allowing some violation of the causal limit ($c_s^2 < 1.1c^2$). When restricting to only causal EoS, the issues of model dependence and insufficient coverage of the physically allowed $M_{\rm max}$-$R_{1.4}$ space are more severe, especially for the piecewise-polytrope.

is given in Table 2.2. Our analysis uses a total of $\sim 1.6 \times 10^5$ draws from this model. A similar model based on the speed of sound is presented in Ref. [79].

Causality in parametric models

Because of the relatively large uncertainties, we follow Ref. [14] in not excluding parametric EoS until they have a large violation of the speed of sound $c_s > 1.1c$. This is the standard criteria used in LALINFERENCE for the piecewise-polytrope and spectral models as part of determining if an EoS is physical. For consistency we extend it to the speed-of-sound parametrization as well. The primary motivation for this is to allow a possibly acausal EoS to represent another, causal EoS which is not modeled effectively by the prior on EoS [14]. In addition, the LALInference implementation of the spectral and piecewise-polytrope models enforces this criterion only up to the central density of the maximum mass NS. In the speed-of-sound model, we require the EoS to be causal (or approximately causal) everywhere. The nonparametric model obeys exact causality ($c_s \leq c$) at all densities.

These choices were made for consistency with past work [14, 1], but we still find that this extra model freedom does not enable to spectral and piecewise-polytropic models to fill in the physically available $M_{\rm max}$-$R_{1.4}$ space up to the causality threshold. Figure 2.9 shows that excluding the acausal models minimally affects the spectral and speed-of-sound results. However, the piecewise-polytrope results are noticeably tighter, and the $M_{\rm max} - R_{1.4}$ allowed parameter space is covered significantly less. This also explains why the nominal piecewise-polytrope prior supports larger pressures than the nonparametric prior in Fig. 2.10.

2.12 Further results with the parametric models

Most results presented the main body of this paper were obtained using the spectral EoS model. In this appendix we present similar results with the piecewise-polytropic and the speed-of-sound models. Figure 2.10 shows the pressure-density and mass-radius posteriors for all EoS models. As expected, we find that the posteriors differ due to the different models. Figure 2.11 shows the posteriors for the speed of sound as a function of the density where again the nonparametric case results in the less constrained results as an outcome of larger model flexibility.

Figure 2.12 shows the equivalent of Fig. 2.2 for the piecewise-polytrope and the speed-of-sound models. We again find that both parametric models lead to tighter constraints on $M_{\rm max}$ for high values. The two-dimensional plots show that model-dependent correlations between the maximum mass and the radius (equivalently low and high densities) exclude certain regions of the $M_{\rm max}$-$R_{1.4}$ space in the parametric marginal priors. As with the spectral model, there is a gap between the piecewise-polytrope prior and the approximate causality threshold. The corresponding plots for the speed-of-sound parametrization show the opposite behavior: the prior reaches the causality threshold, but it fails to produce EoS with large $R_{1.4}$ and small $M_{\rm max}$.

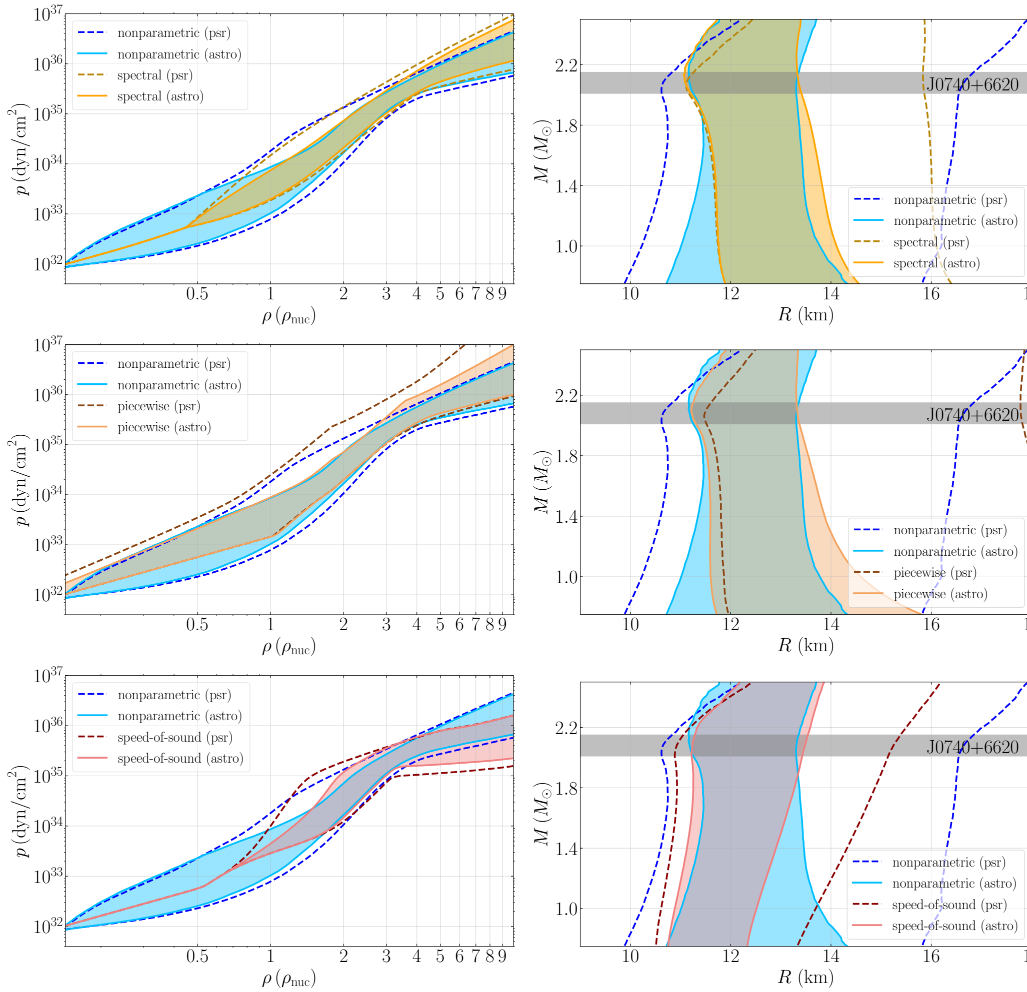

Figure 2.10: Symmetric 90% credible region for the pressure p at each density ρ in units of the nuclear saturation density (left) and the radius R as a function of the mass M. From top to bottom we show results with the spectral, piecewise-polytrope, and speed-of-sound parametric models. At each panel we overplot the corresponding nonparametric result for comparison. The spectral p-ρ panel is identical to Fig. 2.1, but we show it for completeness. As in Fig. 2.1 we show results with all astrophysical data (labeled “astro," solid lines) and restricting to the heavy pulsars only (labeled “psr," dashed lines).

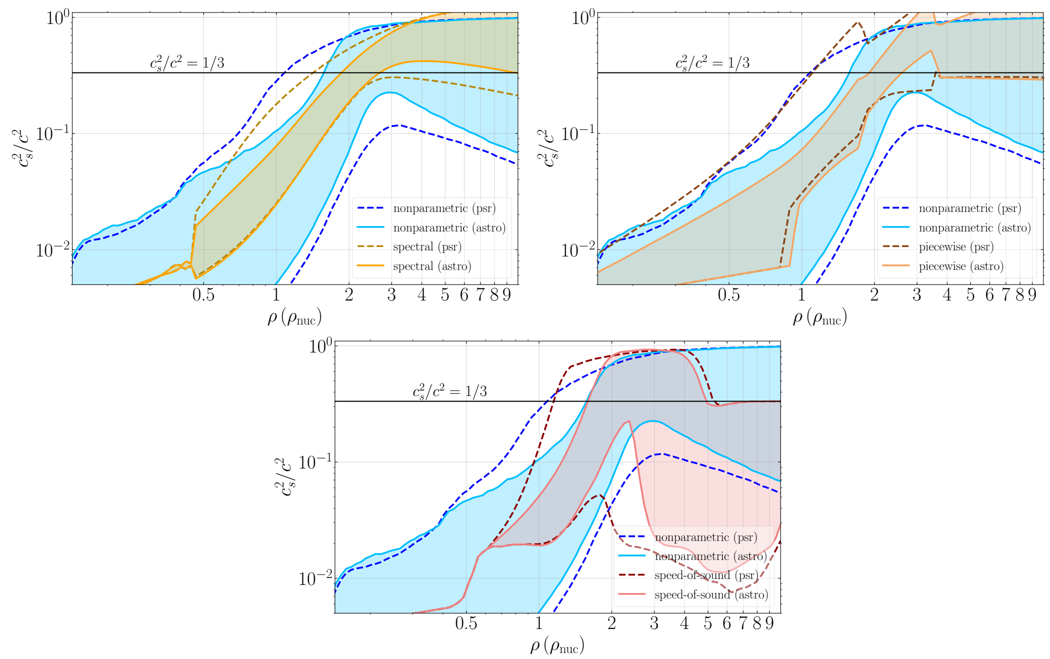

Figure 2.11: The speed of sound squared as a function of baryon density in the spectral (top), piecewise-polytrope (middle) models, and speed-of-sound (bottom) models, compared to our nonparametric model.

References

[1] B. P. Abbott et al. “GW170817: Measurements of neutron star radii and equation of state”. In: *Phys. Rev. Lett.* 121.16 (2018), p. 161101. DOI: 10.1103/PhysRevLett.121.161101. arXiv: 1805.11581 [gr-qc].

[2] B. P. Abbott et al. “GW190425: Observation of a Compact Binary Coalescence with Total Mass $\sim 3.4 M_\odot$”. In: *Astrophys. J. Lett.* 892.1 (2020), p. L3. DOI: 10.3847/2041-8213/ab75f5. arXiv: 2001.01761 [astro-ph.HE].

[3] B. P. Abbott et al. “GW190425: Observation of a Compact Binary Coalescence with Total Mass $\sim 3.4 M_\odot$”. In: *Astrophys. J. Lett.* 892.1 (2020), p. L3. DOI: 10.3847/2041-8213/ab75f5. arXiv: 2001.01761 [astro-ph.HE].

[4] B. P. Abbott et al. “Prospects for observing and localizing gravitational-wave transients with Advanced LIGO, Advanced Virgo and KAGRA”. In: *Living Reviews in Relativity* 23.1 (Sept. 2020), p. 3. ISSN: 1433-8351. DOI: 10.1007/s41114-020-00026-9. URL: https://doi.org/10.1007/s41114-020-00026-9.

[5] Benjamin P. Abbott et al. “GW170817: Observation of Gravitational Waves from a Binary Neutron Star Inspiral”. In: *Phys. Rev. Lett.* 119.16 (2017), p. 161101. DOI: 10.1103/PhysRevLett.119.161101. arXiv: 1710.05832 [gr-qc].

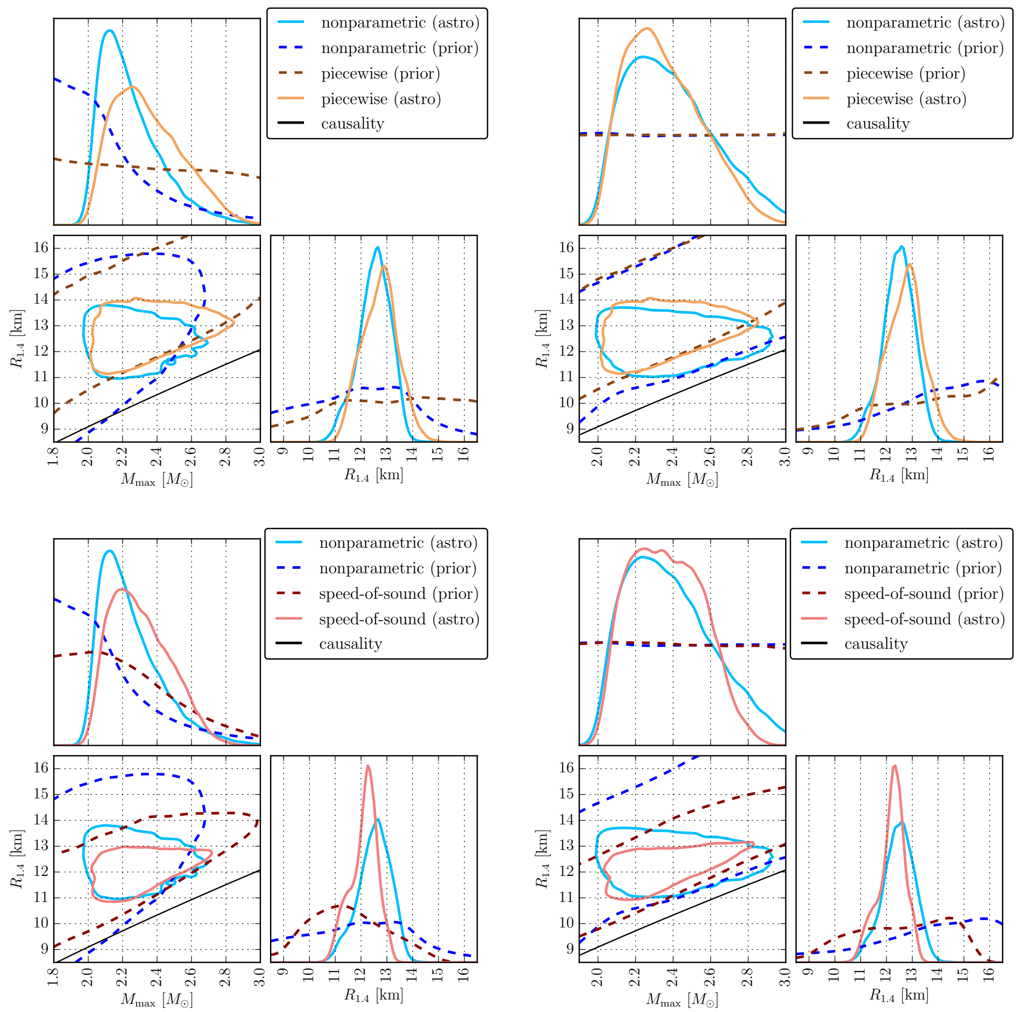

Figure 2.12: Similar to Fig. 2.2 but for the piecewise-polytrope (top panels) and the speed-of-sound (bottom panels) models. As with the spectral case, we find that the parametric model leads to tighter posteriors for $M_{\max}$ compared to the nonparametric model. The two-dimensional plots show that this is again due to model-dependent correlations in $M_{\max}$-$R_{1.4}$.

[6] R. Abbott et al. "The population of merging compact binaries inferred using gravitational waves through GWTC-3". In: (Nov. 2021). arXiv: 2111.03634 [astro-ph.HE].

[7] Mark G. Alford and Sophia Han. "Characteristics of hybrid compact stars with a sharp hadron-quark interface". In: *Eur. Phys. J. A* 52.3 (2016), p. 62. DOI: 10.1140/epja/i2016-16062-9. arXiv: 1508.01261 [nucl-th].

[8] Mark G. Alford, Sophia Han, and Madappa Prakash. "Generic conditions for stable hybrid stars". In: *Phys. Rev. D* 88.8 (2013), p. 083013. DOI: 10.1103/PhysRevD.88.083013. arXiv: 1302.4732 [astro-ph.SR].

[9] Justin Alsing, Hector O. Silva, and Emanuele Berti. "Evidence for a maximum mass cut-off in the neutron star mass distribution and constraints on the equation of state". In: *Mon. Not. Roy. Astron. Soc.* 478.1 (2018), pp. 1377–1391. DOI: 10.1093/mnras/sty1065. arXiv: 1709.07889 [astro-ph.HE].

[10] John Antoniadis et al. "A Massive Pulsar in a Compact Relativistic Binary". In: *Science* 340.6131 (2013), p. 1233232. DOI: 10.1126/science.1233232. arXiv: 1304.6875 [astro-ph.HE].

[11] John Antoniadis et al. "The millisecond pulsar mass distribution: Evidence for bimodality and constraints on the maximum neutron star mass". In: (2016). arXiv: 1605.01665 [astro-ph.HE].

[12] Gordon Baym et al. "From hadrons to quarks in neutron stars: a review". In: *Rept. Prog. Phys.* 81.5 (2018), p. 056902. DOI: 10.1088/1361-6633/aaae14. arXiv: 1707.04966 [astro-ph.HE].

[13] Bhaskar Biswas. "Impact of PREX-II, the revised mass measurement of PSRJ0740+6620, and possible NICER observation on the dense matter equation of state". In: (May 2021). arXiv: 2105.02886 [astro-ph.HE].

[14] Matthew F. Carney, Leslie E. Wade, and Burke S. Irwin. "Comparing two models for measuring the neutron star equation of state from gravitational-wave signals". In: *Phys. Rev.* D98.6 (2018), p. 063004. DOI: 10.1103/PhysRevD.98.063004. arXiv: 1805.11217 [gr-qc].

[15] Katerina Chatziioannou. "Neutron star tidal deformability and equation of state constraints". In: *Gen. Rel. Grav.* 52.11 (2020), p. 109. DOI: 10.1007/s10714-020-02754-3. arXiv: 2006.03168 [gr-qc].

[16] Katerina Chatziioannou. "Uncertainty limits on neutron star radius measurements with gravitational waves". In: (Aug. 2021). arXiv: 2108.12368 [gr-qc].

[17] Katerina Chatziioannou and Will M. Farr. "Inferring the maximum and minimum mass of merging neutron stars with gravitational waves". In: *Phys. Rev. D* 102.6 (2020), p. 064063. DOI: 10.1103/PhysRevD.102.064063. arXiv: 2005.00482 [astro-ph.HE].

[18] Katerina Chatziioannou and Sophia Han. "Studying strong phase transitions in neutron stars with gravitational waves". In: *Phys. Rev. D* 101.4 (2020), p. 044019. DOI: 10.1103/PhysRevD.101.044019. arXiv: 1911.07091 [gr-qc].

[19] An Chen et al. "Distinguishing high-mass binary neutron stars from binary black holes with second- and third-generation gravitational wave observatories". In: *Phys. Rev. D* 101.10 (2020), p. 103008. DOI: 10.1103/PhysRevD.101.103008. arXiv: 2001.11470 [astro-ph.HE].

[20] Thomas Cover and Joy Thomas. *Elements of information theory*. Wiley, 2005.

[21] H. Thankful Cromartie et al. "Relativistic Shapiro delay measurements of an extremely massive millisecond pulsar". In: *Nature Astron.* 4.1 (2019), pp. 72–76. DOI: 10.1038/s41550-019-0880-2. arXiv: 1904.06759.

[22] Christian Drischler, Sophia Han, and Sanjay Reddy. "Large and massive neutron stars: Implications for the sound speed in dense QCD". In: (Oct. 2021). arXiv: 2110.14896 [nucl-th].

[23] Christian Drischler et al. "Limiting masses and radii of neutron stars and their implications". In: *Phys. Rev. C* 103.4 (2021), p. 045808. DOI: 10.1103/PhysRevC.103.045808. arXiv: 2009.06441 [nucl-th].

[24] Reetika Dudi et al. "Relevance of tidal effects and post-merger dynamics for binary neutron star parameter estimation". In: *Phys. Rev.* D98.8 (2018), p. 084061. DOI: 10.1103/PhysRevD.98.084061. arXiv: 1808.09749 [gr-qc].

[25] Reed Essick. "Selection Effects in Periodic X-ray Data from Maximizing Detection Statistics". In: (Nov. 2021). arXiv: 2111.04244 [astro-ph.HE].

[26] Reed Essick, Philippe Landry, and Daniel E. Holz. "Nonparametric Inference of Neutron Star Composition, Equation of State, and Maximum Mass with GW170817". In: *Phys. Rev. D* 101.6 (2020), p. 063007. DOI: 10.1103/PhysRevD.101.063007. arXiv: 1910.09740 [astro-ph.HE].

[27] Reed Essick et al. "A Detailed Examination of Astrophysical Constraints on the Symmetry Energy and the Neutron Skin of ^{208}Pb with Minimal Modeling Assumptions". In: (July 2021). arXiv: 2107.05528 [nucl-th].

[28] Reed Essick et al. "Astrophysical Constraints on the Symmetry Energy and the Neutron Skin of ^{208}Pb with Minimal Modeling Assumptions". In: (Feb. 2021). arXiv: 2102.10074 [nucl-th].

[29] Reed Essick et al. "Direct Astrophysical Tests of Chiral Effective Field Theory at Supranuclear Densities". In: *Phys. Rev. C* 102.5 (2020), p. 055803. DOI: 10.1103/PhysRevC.102.055803. arXiv: 2004.07744 [astro-ph.HE].

[30] Amanda M. Farah et al. "Bridging the Gap: Categorizing Gravitational-Wave Events at the Transition Between Neutron Stars and Black Holes". In: (Nov. 2021). arXiv: 2111.03498 [astro-ph.HE].

[31] Will M. Farr and Katerina Chatziioannou. "A Population-Informed Mass Estimate for Pulsar J0740+6620". In: *Research Notes of the American Astronomical Society* 4.5, 65 (May 2020), p. 65. DOI: 10.3847/2515-5172/ab9088. arXiv: 2005.00032 [astro-ph.GA].

[32] Maya Fishbach, Reed Essick, and Daniel E. Holz. "Does Matter Matter? Using the mass distribution to distinguish neutron stars and black holes". In: *Astrophys. J. Lett.* 899 (2020), p. L8. DOI: 10.3847/2041-8213/aba7b6. arXiv: 2006.13178 [astro-ph.HE].

[33] E. Fonseca et al. "Refined Mass and Geometric Measurements of the High-mass PSR J0740+6620". In: *Astrophys. J. Lett.* 915.1 (2021), p. L12. DOI: 10.3847/2041-8213/ac03b8. arXiv: 2104.00880 [astro-ph.HE].

[34] Rossella Gamba, Jocelyn S. Read, and Leslie E. Wade. "The impact of the crust equation of state on the analysis of GW170817". In: (2019). arXiv: 1902.04616 [gr-qc].

[35] Rossella Gamba et al. "Waveform systematics in the gravitational-wave inference of tidal parameters and equation of state from binary neutron star signals". In: *Phys. Rev. D* 103.12 (2021), p. 124015. DOI: 10.1103/PhysRevD.103.124015. arXiv: 2009.08467 [gr-qc].

[36] S. K. Greif et al. "Equation of state sensitivities when inferring neutron star and dense matter properties". In: *Mon. Not. Roy. Astron. Soc.* 485.4 (2019), pp. 5363–5376. DOI: 10.1093/mnras/stz654. arXiv: 1812.08188 [astro-ph.HE].

[37] Sophia Han and Madappa Prakash. "On the Minimum Radius of Very Massive Neutron Stars". In: *Astrophys. J.* 899.2 (2020), p. 164. DOI: 10.3847/1538-4357/aba3c7. arXiv: 2006.02207 [astro-ph.HE].

[38] Sophia Han and Andrew W. Steiner. "Tidal deformability with sharp phase transitions in (binary) neutron stars". In: *Phys. Rev. D* 99.8 (2019), p. 083014. DOI: 10.1103/PhysRevD.99.083014. arXiv: 1810.10967 [nucl-th].

[39] Sophia Han et al. "Treating quarks within neutron stars". In: *Phys. Rev. D* 100.10 (2019), p. 103022. DOI: 10.1103/PhysRevD.100.103022. arXiv: 1906.04095 [astro-ph.HE].

[40] Vassiliki Kalogera and Gordon Baym. "The maximum mass of a neutron star". In: *Astrophys. J. Lett.* 470 (1996), pp. L61–L64. DOI: 10.1086/310296. arXiv: astro-ph/9608059.

[41] Nina Kunert et al. "Quantifying modelling uncertainties when combining multiple gravitational-wave detections from binary neutron star sources". In: (Oct. 2021). arXiv: 2110.11835 [astro-ph.HE].

[42] Benjamin D. Lackey and Leslie Wade. "Reconstructing the neutron-star equation of state with gravitational-wave detectors from a realistic population of inspiralling binary neutron stars". In: *Phys. Rev. D* 91.4 (2015), p. 043002. DOI: 10.1103/PhysRevD.91.043002. arXiv: 1410.8866 [gr-qc].

[43] Philippe Landry and Reed Essick. "Nonparametric inference of the neutron star equation of state from gravitational wave observations". In: *Phys. Rev. D* 99.8 (2019), p. 084049. DOI: 10.1103/PhysRevD.99.084049. arXiv: 1811.12529 [gr-qc].

[44] Philippe Landry, Reed Essick, and Katerina Chatziioannou. "Nonparametric constraints on neutron star matter with existing and upcoming gravitational wave and pulsar observations". In: *Phys. Rev. D* 101.12 (2020), p. 123007. DOI: 10.1103/PhysRevD.101.123007. arXiv: 2003.04880 [astro-ph.HE].

[45] Philippe Landry and Jocelyn S. Read. "The Mass Distribution of Neutron Stars in Gravitational-wave Binaries". In: *Astrophys. J. Lett.* 921.2 (2021), p. L25. DOI: 10.3847/2041-8213/ac2f3e. arXiv: 2107.04559 [astro-ph.HE].

[46] J. M. Lattimer and M. Prakash. "Neutron star structure and the equation of state". In: *Astrophys. J.* 550 (2001), p. 426. DOI: 10.1086/319702. arXiv: astro-ph/0002232.

[47] James M. Lattimer and Madappa Prakash. "The Equation of State of Hot, Dense Matter and Neutron Stars". In: *Phys. Rept.* 621 (2016), pp. 127–164. DOI: 10.1016/j.physrep.2015.12.005. arXiv: 1512.07820 [astro-ph.SR].

[48] Isaac Legred et al. "Impact of the PSR J0740 + 6620 radius constraint on the properties of high-density matter". In: *Phys. Rev. D* 104 (6 Sept. 2021). I led this study on the impact of the the NICER mass-radius constraint on the mllisecond x-ray pulsar J0740+6620 on nonparametric equation of state constraints. I developed software, some of which was contributed by other collaborators from previous projects, ran the analysis, and co-wrote the manuscript., p. 063003. DOI: 10.1103/PhysRevD.104.063003. URL: https://link.aps.org/doi/10.1103/PhysRevD.104.063003.

[49] Ang Li et al. "Constraints on the maximum mass of neutron stars with a quark core from GW170817 and NICER PSR J0030+0451 data". In: *Astrophys. J.* 913.1 (2021), p. 27. DOI: 10.3847/1538-4357/abf355. arXiv: 2103.15119 [astro-ph.HE].

[50] LIGO Scientific Collaboration. *LIGO Algorithm Library - LALSuite*. free software (GPL). 2018. DOI: 10.7935/GT1W-FZ16.

[51] Lee Lindblom. "Determining the Nuclear Equation of State from Neutron-Star Masses and Radii". In: *The Astrophysical Journal* 398 (Oct. 1992), p. 569. DOI: 10.1086/171882.

[52] Lee Lindblom. "Spectral Representations of Neutron-Star Equations of State". In: *Phys. Rev. D* 82 (2010), p. 103011. DOI: 10.1103/PhysRevD.82.103011. arXiv: 1009.0738 [astro-ph.HE].

[53] Lee Lindblom and Nathaniel M. Indik. "Spectral Approach to the Relativistic Inverse Stellar Structure Problem II". In: *Phys. Rev.* D89.6 (2014). [Erratum: Phys. Rev.D93,no.12,129903(2016)], p. 064003. DOI: 10.1103/PhysRevD.89.064003,10.1103/PhysRevD.93.129903. arXiv: 1310.0803 [astro-ph.HE].

[54] Thomas J. Loredo. "Accounting for source uncertainties in analyses of astronomical survey data". In: *AIP Conf. Proc.* 735.1 (2004). Ed. by Rainer Fischer, Roland Preuss, and Udo von Toussaint, pp. 195–206. DOI: 10.1063/1.1835214. arXiv: astro-ph/0409387.

[55] R. Machleidt and D. R. Entem. "Chiral effective field theory and nuclear forces". In: *Phys. Rept.* 503 (2011), pp. 1–75. DOI: 10.1016/j.physrep.2011.02.001. arXiv: 1105.2919 [nucl-th].

[56] Ben Margalit and Brian D. Metzger. "Constraining the Maximum Mass of Neutron Stars From Multi-Messenger Observations of GW170817". In: *Astrophys. J.* 850.2 (2017), p. L19. DOI: 10.3847/2041-8213/aa991c. arXiv: 1710.05938 [astro-ph.HE].

[57] M. C. Miller et al. "The Radius of PSR J0740+6620 from NICER and XMM-Newton Data". In: (May 2021). arXiv: 2105.06979 [astro-ph.HE].

[58] M. Coleman Miller, Cecilia Chirenti, and Frederick K. Lamb. "Constraining the equation of state of high-density cold matter using nuclear and astronomical measurements". In: (2019). arXiv: 1904.08907 [astro-ph.HE].

[59] Michael F. O'Boyle et al. "Parametrized equation of state for neutron star matter with continuous sound speed". In: *Phys. Rev. D* 102.8 (2020), p. 083027. DOI: 10.1103/PhysRevD.102.083027. arXiv: 2008.03342 [astro-ph.HE].

[60] M. Oertel et al. "Equations of state for supernovae and compact stars". In: *Rev. Mod. Phys.* 89.1 (2017), p. 015007. DOI: 10.1103/RevModPhys.89.015007. arXiv: 1610.03361 [astro-ph.HE].

[61] F. Özel and P. Freire. "Masses, Radii, and the Equation of State of Neutron Stars". In: *Ann. Rev. Astron. Astrophys.* 54 (2016), pp. 401–440. DOI: 10.1146/annurev-astro-081915-023322. arXiv: 1603.02698 [astro-ph.HE].

[62] Peter T. H. Pang et al. "Nuclear-Physics Multi-Messenger Astrophysics Constraints on the Neutron-Star Equation of State: Adding NICER's PSR J0740+6620 Measurement". In: (May 2021). arXiv: 2105.08688 [astro-ph.HE].

[63] Geraint Pratten, Patricia Schmidt, and Natalie Williams. "Impact of Dynamical Tides on the Reconstruction of the Neutron Star Equation of State". In: (Sept. 2021). arXiv: 2109.07566 [astro-ph.HE].

[64] G. Raaijmakers et al. "A NICER view of PSR J0030+0451: Implications for the dense matter equation of state". In: *Astrophys. J. Lett.* 887 (2019), p. L22. DOI: 10.3847/2041-8213/ab451a. arXiv: 1912.05703 [astro-ph.HE].

[65] G. Raaijmakers, T. E. Riley, and A. L. Watts. "A pitfall of piecewise-polytropic equation of state inference". In: *Mon. Not. Roy. Astron. Soc.* 478.2 (2018), pp. 2177–2192. DOI: 10.1093/mnras/sty1052. arXiv: 1804.09087 [astro-ph.HE].

[66] G. Raaijmakers et al. "Constraints on the dense matter equation of state and neutron star properties from NICER's mass-radius estimate of PSR J0740+6620 and multimessenger observations". In: (May 2021). arXiv: 2105.06981 [astro-ph.HE].

[67] Carolyn A. Raithel, Feryal Ozel, and Dimitrios Psaltis. "From Neutron Star Observables to the Equation of State: An Optimal Parametrization". In: *Astrophys. J.* 831.1 (2016), p. 44. DOI: 10.3847/0004-637X/831/1/44. arXiv: 1605.03591 [astro-ph.HE].

[68] Jocelyn S. Read et al. "Constraints on a phenomenologically parameterized neutron-star equation of state". In: *Phys. Rev. D* 79 (2009), p. 124032. DOI: 10.1103/PhysRevD.79.124032. arXiv: 0812.2163 [astro-ph].

[69] Jocelyn S. Read et al. "Measuring the neutron star equation of state with gravitational wave observations". In: *Phys. Rev. D* 79 (2009), p. 124033. DOI: 10.1103/PhysRevD.79.124033. arXiv: 0901.3258 [gr-qc].

[70] Brendan T. Reed et al. "Implications of PREX-2 on the Equation of State of Neutron-Rich Matter". In: *Phys. Rev. Lett.* 126.17 (2021), p. 172503. DOI: 10.1103/PhysRevLett.126.172503. arXiv: 2101.03193 [nucl-th].

[71] Clifford E. Rhoades Jr. and Remo Ruffini. "Maximum mass of a neutron star". In: *Phys. Rev. Lett.* 32 (1974), pp. 324–327. DOI: 10.1103/PhysRevLett.32.324.

[72] Thomas E. Riley et al. "A *NICER* View of PSR J0030+0451: Millisecond Pulsar Parameter Estimation". In: *Astrophys. J. Lett.* 887.1 (2019), p. L21. DOI: 10.3847/2041-8213/ab481c. arXiv: 1912.05702 [astro-ph.HE].

[73] Thomas E. Riley et al. "A NICER View of the Massive Pulsar PSR J0740+6620 Informed by Radio Timing and XMM-Newton Spectroscopy". In: (May 2021). arXiv: 2105.06980 [astro-ph.HE].

[74] Thomas E. Riley, Geert Raaijmakers, and Anna L. Watts. “On parametrized cold dense matter equation-of-state inference”. In: *Mon. Not. Roy. Astron. Soc.* 478.1 (2018), pp. 1093–1131. DOI: 10.1093/mnras/sty1051. arXiv: 1804.09085 [astro-ph.HE].

[75] A. W. Steiner, J. M. Lattimer, and E. F. Brown. “Neutron Star Radii, Universal Relations, and the Role of Prior Distributions”. In: *Eur. Phys. J. A* 52.2 (2016), p. 18. DOI: 10.1140/epja/i2016-16018-1. arXiv: 1510.07515 [astro-ph.HE].

[76] Andrew W. Steiner, James M. Lattimer, and Edward F. Brown. “The Equation of State from Observed Masses and Radii of Neutron Stars”. In: *Astrophys. J.* 722 (2010), pp. 33–54. DOI: 10.1088/0004-637X/722/1/33. arXiv: 1005.0811 [astro-ph.HE].

[77] Hung Tan, Jacquelyn Noronha-Hostler, and Nico Yunes. “Neutron Star Equation of State in light of GW190814”. In: *Phys. Rev. Lett.* 125.26 (2020), p. 261104. DOI: 10.1103/PhysRevLett.125.261104. arXiv: 2006.16296 [astro-ph.HE].

[78] Hung Tan et al. “Extreme Matter meets Extreme Gravity: Ultra-heavy neutron stars with crossovers and first-order phase transitions”. In: (June 2021). arXiv: 2106.03890 [astro-ph.HE].

[79] Ingo Tews et al. “Constraining the speed of sound inside neutron stars with chiral effective field theory interactions and observations”. In: *Astrophys. J.* 860.2 (2018), p. 149. DOI: 10.3847/1538-4357/aac267. arXiv: 1801.01923 [nucl-th].

[80] J. Veitch et al. “Parameter estimation for compact binaries with ground-based gravitational-wave observations using the LALInference software library”. In: *Phys. Rev. D* 91.4 (2015), p. 042003. DOI: 10.1103/PhysRevD.91.042003. arXiv: 1409.7215 [gr-qc].

[81] Daniel Wysocki et al. “Inferring the neutron star equation of state simultaneously with the population of merging neutron stars”. In: (2020). arXiv: 2001.01747 [gr-qc].

Chapter 3

CONSTRAINTS ON THE EQUATION OF STATE USING THE X-RAY MILLISECOND PULSAR J0740+6620

[1] Isaac Legred et al. "Impact of the PSR J0740 + 6620 radius constraint on the properties of high-density matter". In: *Phys. Rev. D* 104 (6 Sept. 2021). I led this study on the impact of the the NICER mass-radius constraint on the mllisecond x-ray pulsar J0740+6620 on nonparametric equation of state constraints. I developed software, some of which was contributed by other collaborators from previous projects, ran the analysis, and co-wrote the manuscript., p. 063003. DOI: 10.1103/PhysRevD.104.063003. URL: https://link.aps.org/doi/10.1103/PhysRevD.104.063003.

Abstract

X-ray pulse profile modeling of PSR J0740+6620, the most massive known pulsar, with data from the NICER and XMM-Newton observatories recently led to a measurement of its radius. We investigate this measurement's implications for the neutron star equation of state (EoS), employing a nonparametric EoS model based on Gaussian processes and combining information from other x-ray, radio, and gravitational-wave observations of neutron stars. Our analysis mildly disfavors EoSs that support a disconnected hybrid star branch in the mass-radius relation, a proxy for strong phase transitions, with a Bayes factor of 6.9. For such EoSs, the transition mass from the hadronic to the hybrid branch is constrained to lie outside $(1, 2)$ $M_\odot$. We also find that the conformal sound-speed bound is violated inside neutron star cores, which implies that the core matter is strongly interacting. The squared sound speed reaches a maximum of $0.75^{+0.25}_{-0.24}\, c^2$ at $3.60^{+2.25}_{-1.89}$ times nuclear saturation density at 90% credibility. Since all but the gravitational-wave observations prefer a relatively stiff EoS, PSR J0740+6620's central density is only $3.57^{+1.3}_{-1.3}$ times nuclear saturation, limiting the density range probed by observations of cold, nonrotating neutron stars in β-equilibrium.

3.1 Introduction

The properties and composition of matter at the highest densities achieved in neutron star (NS) cores remain uncertain [80, 98, 95, 18]. The main observational constraints on the equation of state (EoS) of NS matter at densities $\gtrsim 3\,\rho_{\rm nuc}$, where $\rho_{\rm nuc} = 2.8 \times 10^{14}\mathrm{g/cm^3}$ is the nuclear saturation density, come from radio measurements of the masses of the heaviest known pulsars [37, 59, 15, 36, 58]. These observations place the maximum nonspinning NS mass above $2\,\mathrm{M}_\odot$, which limits the softness of the high-density EoS and tends to decrease the probability of exotic degrees of freedom that reduce the pressure within NS matter.

Other probes of NS matter are typically less informative about these high densities. Nuclear calculations and experiments constrain the EoS respectively around [41, 125, 40, 42, 49] and below [54, 107, 10, 48, 21] $\rho_{\rm nuc}$. Recent measurements of the neutron skin thickness of ^{208}Pb suggest a stiff EoS for densities $\lesssim \rho_{\rm nuc}$ [107, 10], though uncertainties are still large and there is potential tension with other laboratory probes [116, 107, 48]. Gravitational wave (GW) observations by LIGO [1] and Virgo [9] provide information about the tidal properties of merging NSs [57, 67, 28], and have thus far set an upper limit on the stiffness at $\sim 2\,\rho_{\rm nuc}$. However, they are intrinsically less informative for larger NS masses. Tidal effects are quantified through the dimensionless tidal deformability Λ, which scales roughly as $(R/m)^6$ [132] for a NS of mass m and radius R, implying that the most massive—and thus most compact—NSs exhibit inherently weaker tidal interactions. As a result, the very nature of some $\sim$ 2–3 $\mathrm{M}_\odot$ compact objects observed with GWs, such as the primary in GW190425 [3] and the secondary in GW190814 [8], cannot be determined beyond a reasonable doubt [124, 45, 38, 126, 55, 22]. In the same density regime as the GWs, the electromagnetic counterpart to GW170817 may bound the EoS stiffness from below [104, 34, 103, 35], though it is subject to significant systematic modeling uncertainty [71, 16].

Another means of probing dense matter is x-ray emission from hotspots on the surface of rotating NSs. Identifying and modeling modulations in the hotspot lightcurve can be used to measure NS radii. Initial results obtained by NICER [25, 26, 24] for PSR J0030+0451 [89, 111] complement the tidal measurements from GW170817 [7, 4, 2], as they constrain the EoS at 1-2 $\rho_{\rm nuc}$ [79], disfavoring the softest EoSs [77]. This ensemble of theory, experiment and observation has helped to establish an overall picture of NS matter in the last few years [68, 101, 39, 77, 23], which is nonetheless still unresolved at high densities.

Recently, a measurement of the radius of the 2.08 $M_\odot$ pulsar PSR J0740+6620 [36, 58] using x-ray data from NICER and XMM-Newton was reported by two independent analyses [90, 112]. This radius constraint presents a rare glimpse of the properties of the most massive NSs, and a golden opportunity to obtain observational information about the maximum NS mass, $M_{\rm max}$, as well as potential phase transitions in NS cores. In the context of the preferred hotspot model in each analysis, [90] finds $13.7^{+2.6}_{-1.5}$ km and [112] obtains $12.4^{+1.3}_{-1.0}$ km for J0740+6620's radius (medians and symmetric 68% credible intervals). For context, the inference reported in [77] predicts the radius of 2.08 $M_\odot$ NSs to be $12.08^{+0.79}_{-0.98}$ km at the 68% confidence level.

Observations of the most massive NSs, such as J0740+6620, have important implications beyond the EoS. They inform the NS mass distribution [99, 72, 14, 53, 51, 129, 29, 56], the classification of the heaviest NS candidates observed with GWs [45], our understanding of the proposed mass gap between NSs and black holes [73, 52], and the characteristics of NS merger remnants [20] that influence electromagnetic counterpart emission [87, 17]. The properties of the high-density EoS are also connected to the properties at other density scales through correlations shaped by causality considerations [110, 69].

To determine the implications of J0740+6620's radius measurement for NS matter, we employ a nonparametric model for the NS EoS based on Gaussian processes (GPs), which offers us the flexibility of an analysis that (i) is not tightly linked to specific nuclear models, (ii) can account for phase transitions, including strong first-order phase transitions that result in disconnected stable branches in the mass-radius relation, and (iii) is not subject to the systematic errors that arise with parametrized EoS families described by a finite set of parameters. Additionally, the nonparametric EoS model allows us to probe a wider range of intra-density correlations in the EoS than parametric models, something especially relevant for the current data set, which targets a wide range of NS densities [81].

We find that the new J0740+6620 observation pushes the inferred radii and maximum mass for NSs to larger values: we obtain $R_{1.4} = 12.56^{+1.00}_{-1.07}$ km for the radius of a 1.4 $M_\odot$ NS and $M_{\rm max} = 2.21^{+0.31}_{-0.21}\,M_\odot$ for the maximum nonrotating NS mass (we quote medians and 90% highest-probability-density credible regions unless otherwise noted). Despite significant statistical uncertainties, the inferred NS radii are consistent with being equal over a broad mass range, with a radius difference of $\Delta R \equiv R_{2.0} - R_{1.4} = -0.12^{+0.83}_{-0.85}$ km between 2.0 $M_\odot$ and 1.4 $M_\odot$ NSs. This conclusion rules out a large reduction in the radius for massive NSs, a feature that is sometimes characteristic of strong phase transitions in the mass regime of typical NSs. Further, we find that EoSs with at least one disconnected hybrid star branch in their mass-radius relation are disfavored compared to those with a single stable branch by a factor of approximately 6.9. This supports the current consensus that all dense-matter observations can be accommodated by a standard hadronic EoS, although the possibility of a phase transition remains viable; only the strongest first-order phase transitions produce more than one stable sequence of compact stars. If, on the other hand, the mass-radius relation has multiple stable branches, the heaviest star on the first stable branch is either $\lesssim 1\,\mathrm{M}_\odot$ or $\sim 2\,\mathrm{M}_\odot$. Our results disfavor a transition mass in the intermediate mass regime, suggesting that either all NSs observed to date contain exotic cores, or virtually all are purely hadronic.

We also find support for a violation of the conjectured conformal bound on the sound speed c_s in NS matter, $c_s^2 \leq c^2/3$ [75, 32, 19], where c is the speed of light. Such a violation indicates that the sound speed does not rise monotonically to the perturbative QCD limit ($c_s^2 \to c^2/3$) at asymptotically high densities [125] and signals the presence of strongly interacting matter in NS cores [77]. The stiff high-density EoS required by the massive pulsar observations already put the conformal bound in jeopardy [19, 125, 88, 14, 106], but the softer low-density behavior favored by GWs and the NICER radius measurements help reach a Bayes factor of 1000 ± 340 (mean and standard deviation from Monte Carlo uncertainty), securely in favor of a violation. We infer that c_s^2 reaches a maximum of $0.75^{+0.25}_{-0.24}$ at a density of $1.01^{+6.3}_{-5.3} \times 10^{14}\,\mathrm{g/cm^3}$ ($3.60^{+2.25}_{-1.89}\,\rho_{\mathrm{nuc}}$) in NS matter.

Our results are comparable to other analyses of the new J0740+6620 radius measurement. Reference [90] examined the pressure-density relation, the NS radius, and M_{max} using the same set of observational data as we do but did not comment on the possibility of phase transitions in the EoS. They adopted three different models for the EoS(including a simple, more restricted implementation of a GP) which each yielded different but overlapping constraints on the EoS. EoS models informed by chiral effective field theory (χEFT) at low densities and GW170817's electromagnetic counterpart were considered in Refs. [102, 100]; the latter analysis also disfavors EoSs with strong first-order phase transitions, while the former compared two parametric EoS models, finding some model-dependence in their results. A hybrid nuclear parameterization and piecewise polytrope EoS model was employed in [21], which also accounted for the recent PREX-II measurement of the neutron skin of ^{208}Pb [10]. Compared to these studies, our less restrictive treatment of the EoS model broadly results in both qualitative and quantitative agreement. Nonetheless, it allows us more freedom to investigate the consequences of the J0740+6620 radius measurement for NS matter microphysics, including phase transitions, the conformal sound-speed bound, and the inferred stiffness of the EoS.

The remainder of the paper describes the details and results of our analysis. In Sec. 3.2 we briefly describe the methodology we employ as well as the relevant data sets. In Sec. 3.3 we present the results of our inference for macroscopic NS properties. In Sec. 3.4 we discuss the constraints that can be placed on microscopic EoS properties in terms of the sound speed in NS matter and phase transitions. We conclude and discuss other studies of J0740+6620's EoS implications in the literature in more detail in Sec. 3.5.

3.2 Equation of state inference

Our analysis methodology closely follows that of [77]; here we briefly summarize the main features and discuss the updated treatment of J0740+6620.

Hierarchical inference

In order to combine information from multiple data sets that include statistical uncertainties, we use hierarchical inference [85]. The relevant formalism and equations are described in detail in Sec. III B of [77]. The marginal likelihood of each observation (for example, a GW tidal measurement) for a given EoS model is obtained by marginalizing over the relevant parameters for individual events (in the GW case, the binary masses and tidal parameters) assuming some prior distribution (i.e., population model) for the nuisance parameters (in the GW case, the binary masses). Similar to [77], we assume a fixed population for all observations given the relatively low number of observations to date. This simplification also makes the EoS likelihood independent of selection effects [86]. However, as the size of each data set increases (for example through the observation of additional GW signals), we will need to simultaneously fit the population in order to avoid biases in the EoS inference [11, 129].

In the absence of knowledge of the true compact object mass distribution, we choose a uniform population model that extends beyond the maximum mass of all EoSs we consider. For a given EoS model, we further assume that all objects with $m \leq M_{\rm max}$ are NSs. In other words, we assume that it is the EoS, and not the astrophysical formation mechanism, that limits the maximum NS mass. Then, for observations of objects known *a priori* to be NSs (such as J0740+6620, but unlike the components of the GW events), the normalization of the mass prior mildly penalizes EoSs that predict a maximum mass larger than all observed NS masses. This is an Occam penalty that favors EoSs that occupy a smaller prior volume and do not predict unobserved data in the form of very massive NSs, all else being equal. If, instead, we truncated the NS mass distribution below $M_{\max}$—e.g., because we had knowledge of an astrophysical process that limits the maximum NS mass—all EoSs with $M_{\max}$ greater than the largest population mass would be assigned equal marginal likelihood. However, such a choice would have to be accompanied by an arbitrary choice of the truncation mass, given our lack of prior knowledge about the upper limit of the astrophysical NS mass distribution.

The distinction between these scenarios is important for any analysis of J0740+6620, given its high mass. We employ a uniform mass distribution with a lower limit of $0.5\,\mathrm{M}_\odot$; hence, an EoS with $M_{\max} = 3\,\mathrm{M}_\odot$ is disfavored in our inference compared to an EoS with $M_{\max} = 2.5\,\mathrm{M}_\odot$ by a factor of $(3 - 0.5)/(2.5 - 0.5) = 1.25$. In the results presented in later sections, for example Fig. 3.2, this contributes to the fact that the tail of our $M_{\max}$ posterior is slightly tighter than the prior. More details and a quantitative assessment of the effect of the mass prior are given in the appendix.

Nonparametric EoS model

The procedure outlined above requires a model that describes the NS EoS and can be used to compute all relevant macroscopic NS properties, such as masses, radii, and tidal deformabilities [96, 127, 66]. Following [77], we use a nonparametric EoS model constructed through GPs conditioned on existing dense-matter EoS models available in the literature; see [76, 46, 77] for more details. While the GP never assumes a specific functional form for the EoS, unlike parametric analyses, it does assume probabilistic knowledge about correlations within the EoS. Each GP is constructed with different hyperparameters that specify a covariance kernel, which in turn controls the scale and strength of correlations between the sound speed at different pressures. The specific model employed here is described in detail in [46]. It is constructed as a mixture of ~ 150 individual GPs with a broad set of hyperparameters, allowing us to probe a wide range of EoS models with different intra-density correlations.

The nuclear models on which the process is conditioned contain EoSs with different degrees of freedom, including purely hadronic, hyperonic, and quark models. We intentionally condition only loosely on these models, resulting in the process termed *model-agnostic* in [46].[1] As a result, our EoS prior contains a large variety of EoS behavior, including phase transitions at different density scales and of different strengths; see for example Fig. 1 of [46]. This nonparametric approach offers two further advantages over more traditional parametric models [105, 84, 61]: it avoids (i) systematic errors and (ii) strong (and perhaps opaque) intra-density correlations [81] that arise from restricting the EoS to a specific functional form with finite parameters, which will inevitably not match the correct EoS.

To that end, Ref. [90] also employed a GP EoS model, citing the same benefits we point out here. However, [90] used a single GP with a single set of hyperparameters (compared to $\sim$ 150 GPs we consider) and chose those hyperparameters to approximate the variability observed within tabulated EoSs from the CompOSE database [33]. Therefore, the GP prior explored in [90] is more reminiscent of the *model-informed* prior considered in [76, 46] than the *model-agnostic* prior considered here and in [76, 46, 77, 49, 48]. In fact, the hyperparameters used in [90] assume less variance (smaller σ) and stronger correlations between pressures (larger l) than any of the allowed hyperparameters within our hyperprior (see [46] for more details). Our results, therefore, intentionally explore broader ranges of possible EoS behavior and intra-density correlations than [90], particularly at high densities where the GP model in [90] forces the sound speed to approach the speed of light *a priori*. Their more closely tailored GP design may explain why Fig. 10 of [90] shows that their GP analysis leads to more stringent EoS constraints than parametric EoS inferences.

Data

The data we use are similar to [77, 78], with the addition of the new constraints on the mass and radius of J0740+6620. Specifically, we make use of different combinations of (i) the radio mass measurements for J0348+0432 [15] and J0740+6620 [36, 58], (ii) the GW mass and tidal deformability measurements from GW170817 [7, 4, 83] and GW190425 [3, 82], and (iii) the x-ray mass and radius constraints from J0030+0451 [89, 111] and J0740+6620 [90, 112]. For J0030+0451, we follow [77] and select the 3-spot model from [89, 91], though one can obtain very similar bounds with the J0030+0451 results from [111, 113] instead (see [77]). As before, we do not assume that any of the binary components of GW170817 and GW190425 were NSs *a priori*.

[1] We emphasize that model-agnostic does not mean model-independent.

One notable difference compared to [77] is that J0740+6620 now appears in the list of both radio and x-ray observations. As described in [90, 112], the measured mass of J0740+6620 is still dominated by the radio observations [58]. The most recent mass estimate of $2.08^{+0.07}_{-0.07}\,\mathrm{M}_\odot$ is slightly lower than the originally reported value of $2.14^{+0.10}_{-0.09}\,\mathrm{M}_\odot$ [36] (68% confidence level), making it more consistent with other Galactic NS mass measurements [51]. To avoid double-counting, we include J0740+6620 either through its updated mass estimate in the radio list *or* through its mass and radius estimate in the x-ray list. The difference gives an estimate of the impact of the radius constraint alone on the NS EoS.

When treating J0740+6620 as either a radio or an x-ray observation, we explicitly account for the normalization of the mass prior in Eqs. (9) and (11) of [77], in accordance with our choice of fixed population model.[2] For the J0740+6620 x-ray data, we use either the NICER+XMM samples from [90, 92] or the ST-U samples from [112, 114]. Both sets of samples already incorporate the updated mass estimate from [58], though [90] inflates the uncertainty in this measurement by $\pm 0.02\,\mathrm{M}_\odot$ out of concern for systematic uncertainties. For our analysis, we choose to revert back to the published result from [58] and remove the additional uncertainty of $0.04\,\mathrm{M}_\odot$. In practice, we use the posterior samples from [90, 92] but weight each sample by $\mathcal{N}(2.08\,\mathrm{M}_\odot, 0.07\,\mathrm{M}_\odot)/\mathcal{N}(2.08\,\mathrm{M}_\odot, 0.09\,\mathrm{M}_\odot)$, the ratio of the inferred mass estimate from [58] to the inflated mass estimate used in [90]. This allows for a more direct comparison between the results of [90] and [112]. We find a negligible effect on our results when we repeat our analysis with the increased mass uncertainty. Table 3.1 summarizes the mass and radius data we use for J0740+6620.

Measurement	m [$\mathrm{M}_\odot$]	R [km]
Radio [58]	$2.08^{+0.11}_{-0.11}$	-
x-ray NICER+XMM [90]	$2.07^{+0.11}_{-0.12}$	$14.30^{+4.33}_{-2.97}$
x-ray NICER+XMM [112]	$2.07^{+0.11}_{-0.11}$	$12.34^{+1.89}_{-1.67}$

Table 3.1: Measurements of PSR J0740+6620's mass and radius used in our inference. Medians and 90% highest-probability credible intervals are given. For the Miller et al. [90] measurement we remove the inflated mass uncertainty and convert to a flat-in-radius prior.

[2]Unlike in [77], where we assumed the population of NICER targets ended at masses well below $M_{\max}$, we assume the population of NICER targets extends well beyond $M_{\max}$ and include the proper normalization for the mass prior for both J0030+0451 and J0740+6620.

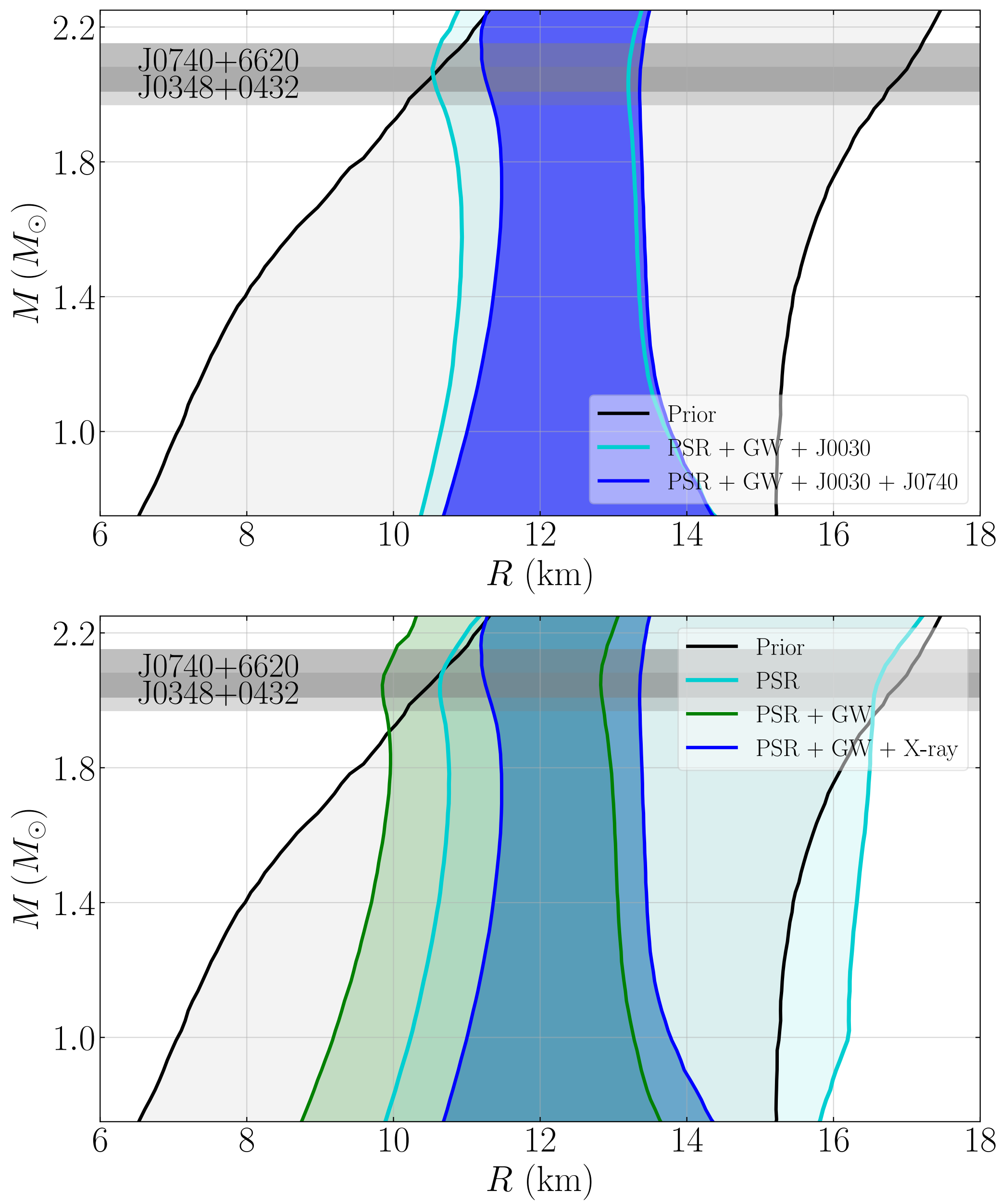

Figure 3.1: Constraints on the NS mass-radius relation. Shaded regions enclose the 90% symmetric credible intervals for the radius for each value of the mass. The top panel shows the effect of the J0740+6620 radius constraint by comparing the prior (black), and results with (without) the J0740+6620 radius in blue (turquoise). The bottom panel presents cumulative constraints on the mass-radius relation as each type of data set is analyzed. In black we again show the prior. The turquoise region shows the posterior after including the mass measurement of the two heavy pulsars (including the updated J0740+6620 mass estimate). The green region correspond to constraints obtained after adding the GW data. Finally, the blue region correspond to constraints after further adding the J0030+0451 and J0740+6620 mass and radius constraints from NICER. In the last case we remove the J0740+6620 mass constraint from the list of radio constraints so as to avoid double-counting.

Unlike J0030+0451, the two independent analyses of J0740+6620 arrive at slightly different values for its radius, even if one accounts for their different priors (flat in mass-radius [112] vs. flat in mass-compactness [90]) and their different treatments of the uncertainty in the mass estimate from [58]. Accounting for the prior differences *increases* the discrepancy between the two results, as the flat-in-compactness prior disfavors large radii. Miller *et al.* [90] use the nominal XMM-Newton calibration uncertainty, while Riley *et al.* [112] use a larger uncertainty. The main effect of the XMM-Newton data is to provide an estimate of the pulsar count rate, which aids in the determination of the relative modulation depth of the x-ray pulse profile, which is essential for placing an upper limit on J0740+6620's compactness. Consequently, the larger calibration uncertainty of [112] results in a less stringent lower bound on the radius. We focus on results based on the analysis in [90], since it uses the nominal calibration uncertainty, although we provide select comparisons to the results of [112].

Nonetheless, we stress that hierarchical EoS constraints are unaffected by the choice of prior for the J0740+6620 radius measurement; any discrepancies are solely due to systematic differences between the two analyses, such as the choice of XMM-Newton calibration uncertainty or issues of convergence within sampling algorithms (see the discussion in Sec. 4.6 of [90]).

3.3 Neutron star mass and radius

We apply our analysis to the combined radio, GW, and x-ray data and present the resulting constraints for macroscopic NS properties, notably masses, radii, and tidal deformabilities. In what follows, whenever we refer to results without the J0740+6620 radius measurement, we still use its updated mass estimate from [58] within the inference. Unless otherwise stated, all results make use of the Miller et al. [90] mass and radius constraints without the inflated mass uncertainty.

We infer the NS mass-radius relation shown in Fig. 3.1, which plots the 90% symmetric credible region for R as a function of m.[3] The top panel focuses on the effect of the new J0740+6620 radius measurement: it tightens the 90% credible constraint on the radius from the low side by 0.57 km at $1.4\,\mathrm{M}_\odot$ and 0.71 km at $2.0\,\mathrm{M}_\odot$. The bottom panel shows cumulative constraints on the mass-radius relation as the different data sets (radio, GW, x-ray) are added one at a time. As discussed in [77], the radio and x-ray observations tend to drive the lower bound on the NS

[3]Fig. 3.1 shows credible regions for $R(m)$ restricted to those EoSs with $M_{\max} \geq m$. That is, we show the bounds for stable NSs only.

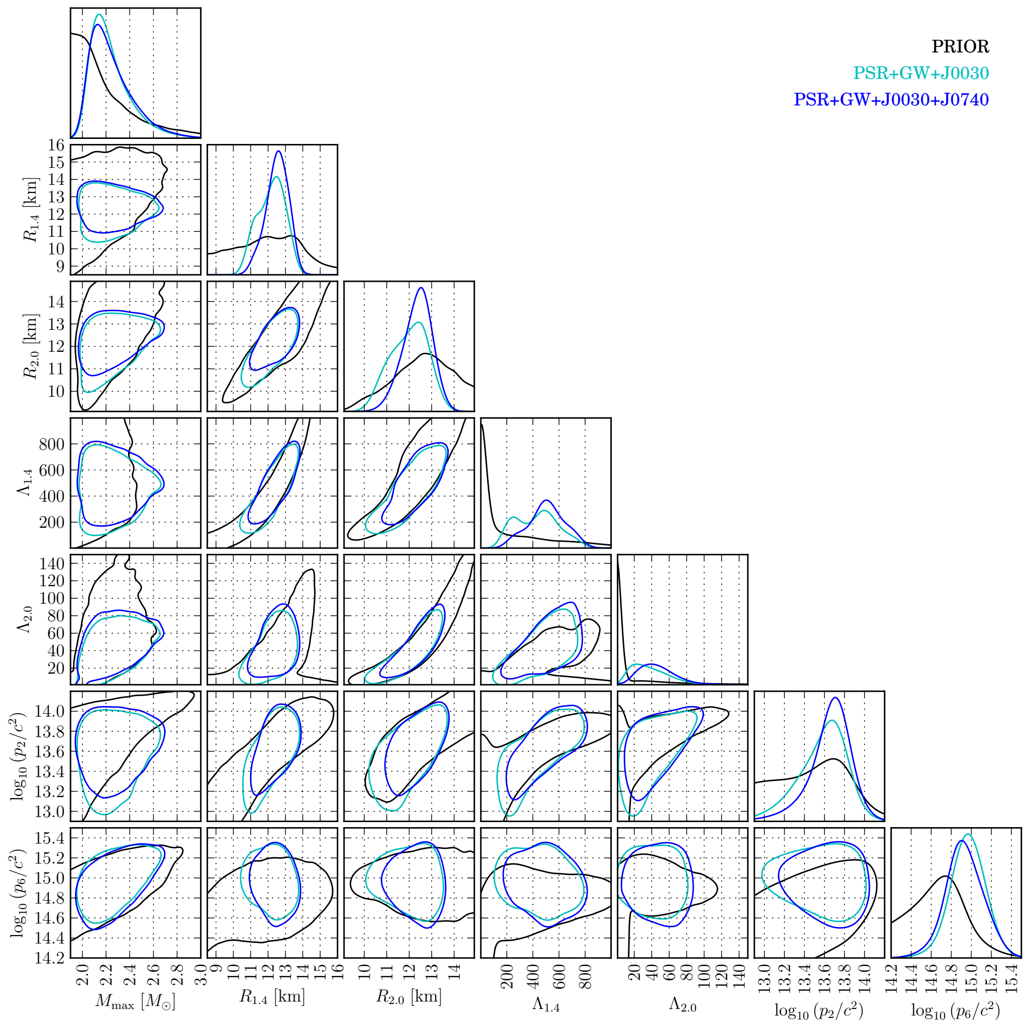

Figure 3.2: Prior and posterior distributions of the radius at $1.4\,\mathrm{M}_\odot$ ($R_{1.4}$) and $2.0\,\mathrm{M}_\odot$ ($R_{2.0}$), the maximum mass (M_{max}), the dimensionless tidal deformability at $1.4\,\mathrm{M}_\odot$ ($\Lambda_{1.4}$) and $2.0\,\mathrm{M}_\odot$ ($\Lambda_{2.0}$), and the pressure at twice (p_2) and six times (p_6) the saturation density, such that p_2/c^2, and p_6/c^2 have units $\mathrm{g/cm^3}$. Contours in the 2D distributions correspond to the 90% level. Black lines denote the prior, while blue (turquoise) lines correspond to results with (without) the J0740+6620 radius constraint. The prior includes numerous EoSs that do not support massive NSs, in which case we report quantities assuming black holes, corresponding to the sharp peak at $\Lambda = 0$ in the prior.

radius, while the GW data and causality set the upper bound. This is because the GW measurements mainly constrain $\Lambda \sim (R/m)^6$ from above, while the x-ray measurements primarily set an upper bound on the compactness m/R and therefore a lower bound on R. The J0740+6620 radius measurement reinforces this picture of complementary constraints.

One- and two-dimensional marginalized priors and posteriors for various macroscopic and microscopic parameters are given in Fig. 3.2, while Table 3.2 presents medians and 90% highest-probability-density credible regions for these and other quantities of interest. Like the left panel of Fig. 3.1, we compare the prior and posterior with and without the J0740+6620 radius constraint. However, we no longer restrict the prior to EoSs that support stable NSs at a given mass scale: it includes EoSs with $M_{\max}$ significantly smaller than $1\,\mathrm{M}_{\odot}$, such that, for example, the prior on $\Lambda_{1.4}$ peaks at the black hole value of zero. This distinction is less relevant for the posterior, as the data significantly disfavor EoSs that do not support $M_{\max} \gtrsim 2\,\mathrm{M}_{\odot}$. Nonetheless, it explains the shape of some priors in Fig. 3.2.

On the whole, we find that the J0740+6620 radius constraint increases support for stiffer EoSs with larger radii and tidal deformabilities. Our inferred $M_{\max}$ is also slightly increased. This is because J0740+6620's radius is no smaller than that of a lower-mass NS, indicating that the turning point in the mass-radius relation occurs above the pulsar's mass. As discussed above, the tail of the $M_{\max}$ posterior is slightly lower than its prior. This is driven by two factors: first the bound on $R_{1.4}$ provided by GW170817 that limits $M_{\max}$ via causality considerations, and second, our assumption that the maximum NS possible is determined by the EoS and not NS formation mechanisms, resulting in EoSs that predict very heavy (and unobserved) NSs being disfavored. An upper limit on $M_{\max} \lesssim 2.2-2.6\,\mathrm{M}_{\odot}$ has been proposed by assuming that the electromagnetic counterpart to GW170817 suggests that the merger remnant collapsed to a BH shortly after merger [87, 121, 117, 109, 120, 6]. We do not employ this upper limit here (nor any other information from the GW170817 counterpart), and thus our inferred $M_{\max}$ extends to higher values. Indeed the data sets we use can only stringently constrain $M_{\max}$ from below. The effect of folding in such an upper limit is demonstrated in [100].

Based on Fig. 3.2, we also see that $R_{2.0}$ is more strongly correlated with the pressure at $2\,\rho_{\mathrm{nuc}}$ than at $6\,\rho_{\mathrm{nuc}}$ [79, 43]. Additionally, J0740+6620's radius measurement from [90] eliminates the bimodality in the posterior on $\Lambda_{1.4}$ [4], now favoring the (initially subdominant) upper mode at ~ 500 rather than the dominant one at

~ 200. This suggests that the EoS lies on the stiff side of the constraints established by GW170817 at intermediate densities. We expand on this and quantify the implications for NS central densities in Sec. 3.4.

The general trend in favor of stiffer EoSs also increases the lower bound of the 90% highest-probability-density credible region for $\Lambda_{1.4}$ (respectively, $\Lambda_{2.0}$) from 168 (7) to 265 (14). Setting the tidal deformability equal to this lower limit, we can obtain a conservative estimate of the signal-to-noise ratio (SNR) required for a GW observation to confidently detect tidal effects, i.e., bound Λ away from zero. The measurement uncertainty in Λ was ~ 700 at an SNR of ~ 33 for GW170817 [4]. Assuming that this measurement is typical and that uncertainties scale inversely with the SNR [128], a back-of-the-envelope estimate suggests that tidal effects can be measured to within 265 (14) for a binary with masses of 1.4 $M_\odot$ (2.0 $M_\odot$) with SNR of 44 (770). The threshold SNR for $\Lambda_{1.4}$ is within reach of current advanced detectors [5], although the SNR for $\Lambda_{2.0}$ will require next-generation detectors, consistent with the findings of [31].

The full EoS inference also allows us to obtain an updated radius estimate for J0740+6620 informed by all the data, as plotted in Fig. 3.3. We find $12.41^{+0.93}_{-1.16}$ km at the 90% level, compared to $13.24^{+2.25}_{-1.93}$ km when using only the J0740+6620 x-ray data conditioned on our nonparametric EoS model. For reference, the J0740+6620 measurement from [90] is $14.30^{+4.33}_{-2.97}$ km at 90% credibility when adjusted to remove the 0.04 $M_\odot$ systematic error estimate and intrinsic flat-in-compactness prior. The radius uncertainty for J0740+6620 at the 90% level is reduced by 3.12 km by conditioning on our EoS prior and further by 2.09 km when additionally including all our astrophysical data. Most of this improvement comes from the exclusion of large radii due to two reasons: (i) the EoS prior model favors realistic EoSs and a radius below ~ 17 km, see prior in Fig. 3.1, and (ii) the GW data are inconsistent with large radii above $\sim 13-14$ km. The updated radius estimate is consistent with the constraint of $12.28^{+0.60}_{-0.68}$ km from [90] (68% level) after conditioning on other data and their EoS prior.

We also investigate how our results change if we use the J0740+6620 data from [112] in place of the data from [90]. The two sets of inferred NS properties are compared in Table 3.2. Because of their more conservative treatment of calibration error, the Riley et al. [112] data place a less constraining lower bound on J0740+6620's radius and therefore result in a more modest shift towards stiff EoSs. Out of the ~ 0.8 km difference between the lower bounds of the 68% credible intervals on

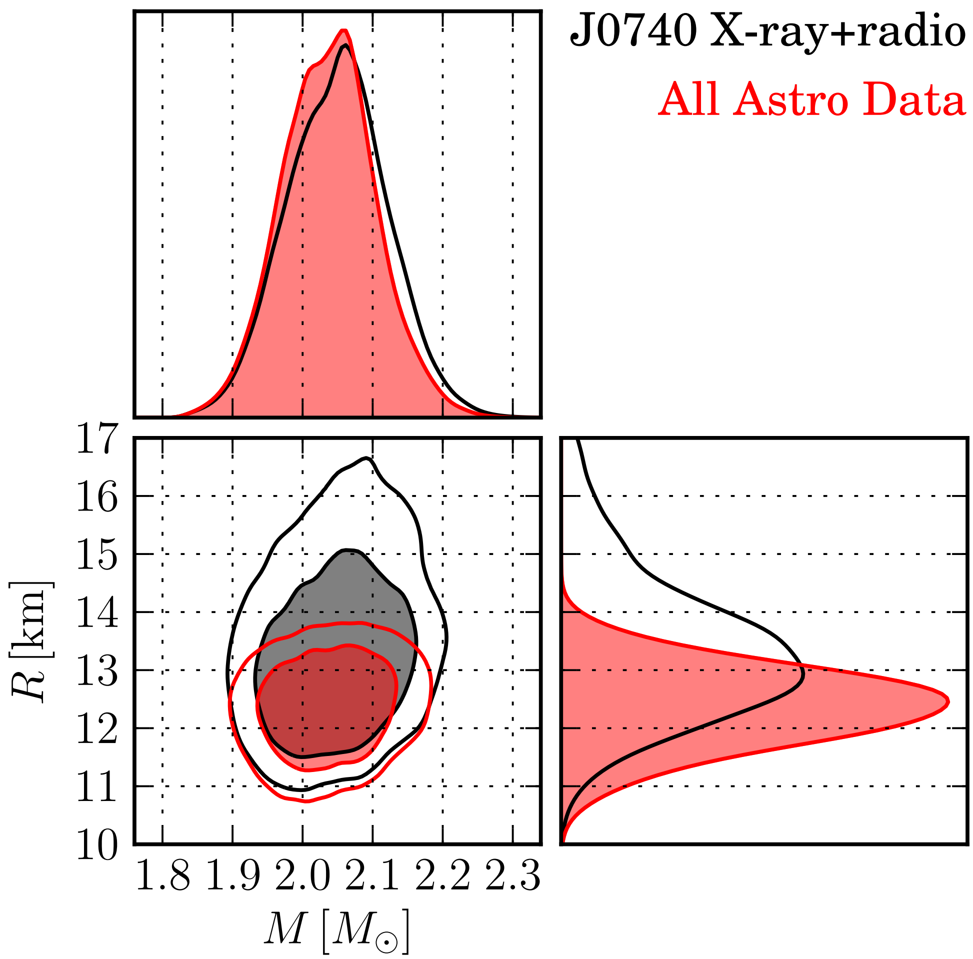

Figure 3.3: Estimates for the radius of J0740+6620 using only NICER+XMM observations (black) and all astrophysical observations (red), both conditioned on our nonparametric EoS representation. Contours correspond to the 68% and 90% credible levels. The primary impact of other astrophysical observations is to lower the inferred radius of J0740+6620 from $13.24^{+2.25}_{-1.93}$ km to $12.41^{+0.93}_{-1.16}$ km at 90% credibility.

	Observable	Prior	w/ PSRs	w/o J0740+6620	w/J0740+6620 Miller+	w/J0740+6620 Riley+
Properties of the EoS	$M_{\max}$ [$\mathrm{M}_\odot$]	$1.47^{+0.71}_{-1.37}$	$2.24^{+0.48}_{-0.24}$	$2.20^{+0.30}_{-0.19}$	$2.21^{+0.31}_{-0.21}$	$2.19^{+0.27}_{-0.19}$
	$p(\rho_{\rm nuc})$ [$10^{33}dyn/cm^2$]	$2.25^{+5.81}_{-2.15}$	$6.07^{+7.53}_{-5.93}$	$4.05^{+3.59}_{-3.74}$	$4.30^{+3.37}_{-3.80}$	$4.15^{+3.50}_{-3.76}$
	$p(2\rho_{\rm nuc})$ [$10^{34}dyn/cm^2$]	$1.22^{+4.86}_{-1.21}$	$6.00^{+4.79}_{-5.99}$	$3.75^{+2.36}_{-2.98}$	$4.38^{+2.46}_{-2.96}$	$3.90^{+2.11}_{-2.88}$
	$p(6\rho_{\rm nuc})$ [$10^{35}dyn/cm^2$]	$2.43^{+4.70}_{-2.43}$	$7.51^{+6.77}_{-5.15}$	$8.33^{+5.22}_{-4.14}$	$7.41^{+5.87}_{-4.18}$	$7.82^{+5.47}_{-3.53}$
	$\max\left\{c_s^2/c^2\right\} \mid \rho \leq \rho_c(M_{\max})$	$0.76^{+0.24}_{-0.37}$	$0.72^{+0.28}_{-0.26}$	$0.84^{+0.16}_{-0.28}$	$0.75^{+0.25}_{-0.24}$	$0.80^{+0.20}_{-0.26}$
	$\rho\left(\max\left\{c_s^2/c^2\right\}\right)$ [$10^{15}\mathrm{g/cm^3}$]	$1.38^{+1.65}_{-1.34}$	$0.97^{+0.64}_{-0.70}$	$1.13^{+0.64}_{-0.63}$	$1.01^{+0.63}_{-0.53}$	$1.10^{+0.63}_{-0.58}$
	$p\left(\max\left\{c_s^2/c^2\right\}\right)$ [$10^{35}\mathrm{dyn/cm^2}$]	$1.65^{+8.16}_{-1.65}$	$2.68^{+5.18}_{-2.68}$	$3.52^{+6.90}_{-3.48}$	$2.77^{+5.81}_{-2.70}$	$3.26^{+6.51}_{-3.15}$
Properties defined for both NSs and BHs	$R_{1.4}$ [km]	$8.09^{+5.68}_{-3.96}$	$13.54^{+2.61}_{-3.13}$	$12.25^{+1.13}_{-1.33}$	$12.56^{+1.00}_{-1.07}$	$12.34^{+1.01}_{-1.25}$
	$R_{2.0}$ [km]	$5.90^{+6.97}_{-0.00}$	$13.18^{+3.02}_{-2.90}$	$12.05^{+1.18}_{-1.45}$	$12.41^{+1.00}_{-1.10}$	$12.09^{+1.07}_{-1.17}$
	$\Delta R \equiv R_{2.0} - R_{1.4}$ [km]	$0.48^{+1.28}_{-6.67}$	$-0.07^{+1.00}_{-1.04}$	$-0.17^{+0.85}_{-0.83}$	$-0.12^{+0.83}_{-0.85}$	$-0.20^{+0.82}_{-0.88}$
	$\Lambda_{1.4}$	24^{+841}_{-24}	795^{+1262}_{-708}	442^{+235}_{-274}	507^{+234}_{-242}	457^{+219}_{-256}
	$\Lambda_{2.0}$	0^{+54}_{-0}	66^{+184}_{-66}	34^{+35}_{-27}	44^{+34}_{-30}	35^{+32}_{-24}
Properties defined only for NSs	$\rho_{\rm c}(1.4\,\mathrm{M}_\odot)$ [$10^{14}\mathrm{g/cm^3}$]	$8.4^{+12.5}_{-6.0}$	$5.7^{+3.2}_{-3.1}$	$7.2^{+2.6}_{-1.7}$	$6.7^{+1.7}_{-1.3}$	$7.1^{+2.1}_{-1.5}$
	$\rho_{\rm c}(2.0\,\mathrm{M}_\odot)$ [$10^{14}\mathrm{g/cm^3}$]	$9.0^{+5.7}_{-6.3}$	$8.5^{+4.8}_{-5.3}$	$10.5^{+4.1}_{-3.8}$	$9.7^{+3.6}_{-3.1}$	$10.4^{+3.6}_{-3.5}$
	$\rho_{\rm c}(M_{\max})$ [$10^{15}\mathrm{g/cm^3}$]	$2.4^{+0.9}_{-2.0}$	$1.4^{+0.5}_{-0.6}$	$1.6^{+0.3}_{-0.4}$	$1.5^{+0.3}_{-0.4}$	$1.6^{+0.3}_{-0.3}$

Table 3.2: Constraints on selected parameters of interest. We present the median and 90% highest-probability-density credible regions of the marginalized 1D distribution for the maximum mass, the radius, tidal deformability, and central density of a $1.4\,\mathrm{M}_\odot$ and a $2.0\,\mathrm{M}_\odot$ compact object, the corresponding radius difference, the central density of the maximum-mass NS, the pressure at various densities, the maximum speed of sound, and the pressure and density where the maximum speed of sound is reached. For macroscopic observables that are defined for both NSs and BHs, we present credible regions that span both, assuming the Schwarzschild radius ($2GM/c^2$) and $\Lambda = 0$ if $m > M_{\max}$. For properties defined only for NSs, we additionally condition all our distributions on the requirement that $M_{\max} \geq m$ so that we only consider EoSs that support stable NSs at m. Note that this defines slightly different prior distributions for $1.4\,\mathrm{M}_\odot$ and $2.0\,\mathrm{M}_\odot$ stars, although the point is less relevant for the posteriors. The speed of sound is maximized over densities corresponding to stable NSs (below the central density of the $M_{\max}$ stellar configuration: $\rho \leq \rho_{\rm c}(M_{\max})$), and therefore the exact density range over which we maximize depends on the EoS. Columns correspond to the prior, the posterior with only the two heavy pulsars, and the posterior with and without the radius constraint from J0740+6620. Results with only the two heavy pulsars and without the radius constraint include the updated mass measurement of J0740+6620. The column with the pulsar-only posterior is similar to the second column of Table IV in [77]. We include it as it roughly corresponds to the assumption that all objects up to $\sim 2\,\mathrm{M}_\odot$ are NSs (as opposed to our prior in some cases). We also present results based on both the Miller et al. [90] and the Riley et al. [112] analyses.

the pulsar's radius obtained by the two analyses, [90] attributes 0.55 km to the calibration difference and choices of prior boundaries. Our hierarchical analysis is immune to the prior difference, and after conditioning on all the observational data we find an overall difference of 0.4 km (respectively, 0.29 km) in the lower bound of the 90% credible interval on $R_{1.4}$ ($R_{2.0}$) due to other systematic differences between [90] and [112].[4]

3.4 Properties of dense matter

We now turn our attention to the properties of dense matter and examine the implications of the J0740+6620 radius constraint. We begin in Fig. 3.4 with the inferred pressure-density relation. In the left panel, we show the effect of the new J0740+6620 radius constraint: it restricts the low-pressure side of the EoS at densities of 2-3 $\rho_{\rm nuc}$. This is comparable, but a bit lower, than the central density of J0740+6620, denoted by the magenta contours. In the right panel, we show the cumulative constraints that result from adding the different data sets sequentially. Red contours here denote the central pressure-density posterior for the maximum-mass NS.

The central density of J0740+6620 is $10.0^{+3.5}_{-3.6} \times 10^{14}\mathrm{g/cm^3} \sim 3.57^{+1.3}_{-1.3}\,\rho_{\rm nuc}$, as inferred from all available data under our EoS model. The relatively low inferred central density for a $\sim 2\,\mathrm{M}_\odot$ NS is indicative of a relatively stiff EoS at densities $\sim$ 1-2 $\rho_{\rm nuc}$; see, e.g., Table III of [63] for a comparison between two representative hadronic models. However, our analysis intentionally does not closely follow specific nuclear theoretic predictions. At low densities (up to $\sim 2\,\rho_{\rm nuc}$), theoretical predictions from χEFT may place an upper limit on the pressure, which would tend to increase the central density of J0740+6620, although the most recent measurement of the neutron skin thickness of ^{208}Pb [10] may suggest a relatively stiff EoS below and around $\rho_{\rm nuc}$; see [48] for more discussion.[5]

We further investigate the NS central densities in Fig. 3.5, which shows the mass-central density posterior inferred using all the data. The central density of the maximum-mass NS is $1.5^{+0.3}_{-0.4} \times 10^{15}\mathrm{g/cm^3} \sim 5.4^{+1.1}_{-1.4}\,\rho_{\rm nuc}$, corresponding to the

[4]The overall difference we find is smaller than the one quoted in [90] as we report 90% and not 68% levels. The radius distribution for J0740+6620 is fairly asymmetric, so quoting a smaller credible level tends to inflate discrepancies.

[5]Fig. 2 of [60] depicts the central densities obtained by extrapolating the realistic two- and three-nucleon interactions predicted by microscopic theory to higher densities. The central values of pressure at around $2\,\rho_{\rm nuc}$ inferred from our analysis (see Table 3.2) point to the stiffest EoS compatible with low-density chiral effective-field-theory (χEFT) [40, 42, 43, 102, 100].

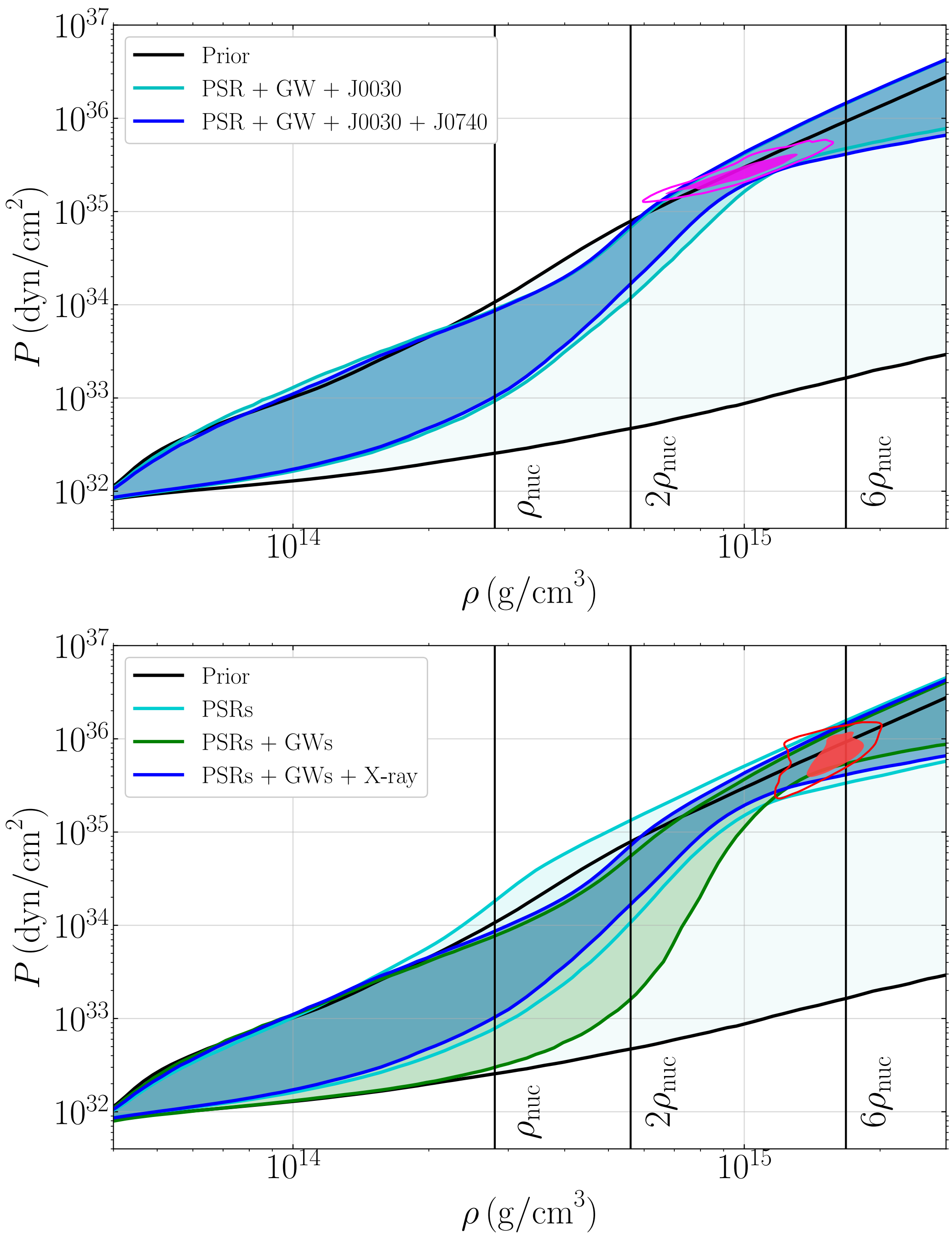

Figure 3.4: Same as Fig. 3.1 but for the pressure-density relation. In the left panel, magenta contours give the 50% and 90% level of the central pressure-density posterior for J0740+6620 inferred from all available data. In the right panel, red contours give the 50% and 90% level of the central pressure-density posterior for the maximum-mass NS.

maximum matter density that can be probed with observations of cold, nonspinning NSs. Table 3.2 also gives the central densities for NSs of $1.4\,\mathrm{M}_\odot$ and $2.0\,\mathrm{M}_\odot$. In general, we can understand the trends in the central densities within the same context as Figs. 3.1 and 3.4. Typically, the central density remains low (stiff EoS) until masses are $\gtrsim 2\,\mathrm{M}_\odot$. Beyond this limit, set primarily by J0740+6620, the EoS can soften appreciably and the central density can increase considerably. Indeed, the density range explored by NSs above $2\,\mathrm{M}_\odot$ could be a factor of two times larger than what is explored by canonical $1.4\,\mathrm{M}_\odot$ stars. High-mass NSs may yet have surprises in store for future measurements.

Speed of sound

We examine the speed of sound inside NSs in Figs. 3.6 and 3.7. Figure 3.6 shows the speed of sound squared (c_s^2) as a function of density with and without the J0740+6620 radius measurement. Already in [77], we concluded that the conformal limit of $c_s^2/c^2 = 1/3$ is likely violated inside NSs, primarily due to the combination of a soft low-density and a stiff high-density EoS and in agreement with [19, 125, 88, 14, 106]. We here find that the lower limit on the J0740+6620 radius agrees with this picture and pushes the maximum of the marginal 90% lower limit for c_s^2 to lower densities. In other words, the pressure needs to increase more rapidly at even lower densities in order to accommodate the relatively large radius of J0740+6620. The red contours corresponds to the central speed of sound and central density of the maximum-mass NS, again bounding the densities that can be probed observationally. The central speed of sound is essentially unconstrained, which means that, for some EoSs, the speed of sound sharply decreases after it reaches its maximum value.

Figure 3.7 shows the maximum c_s^2 inside NSs and the density at which it is reached. For each EoS, we maximize c_s^2 over all densities smaller than the central density of the maximum-mass stellar configuration (i.e., a different range for each EoS). Comparing the posterior to the conformal limit, we again find that the latter is violated inside NSs with a maximum c_s^2/c^2 of $0.75^{+0.25}_{-0.24}$ achieved at a density of $1.01^{+6.3}_{-5.3} \times 10^{14}\mathrm{g/cm}^3$ ($3.60^{+2.25}_{-1.89}\,\rho_{\mathrm{nuc}}$). Compared to results without J0740+6620, the maximum speed of sound is slightly lower and occurs at slightly lower densities, as also seen in Fig. 3.6. This behavior was also observed for J0030+0451 [77]. Since both J0030+0451 and J0740+6620 data place a lower limit on the NS radius we interpret the reduced value for the maximum speed of sound as follows: the preference for a stiffer EoS at $\sim 2\rho_{\mathrm{nuc}}$ means that the stiff EoS at $\sim 5\rho_{\mathrm{nuc}}$ can be achieved with a milder pressure-density slope and thus a smaller speed of sound.

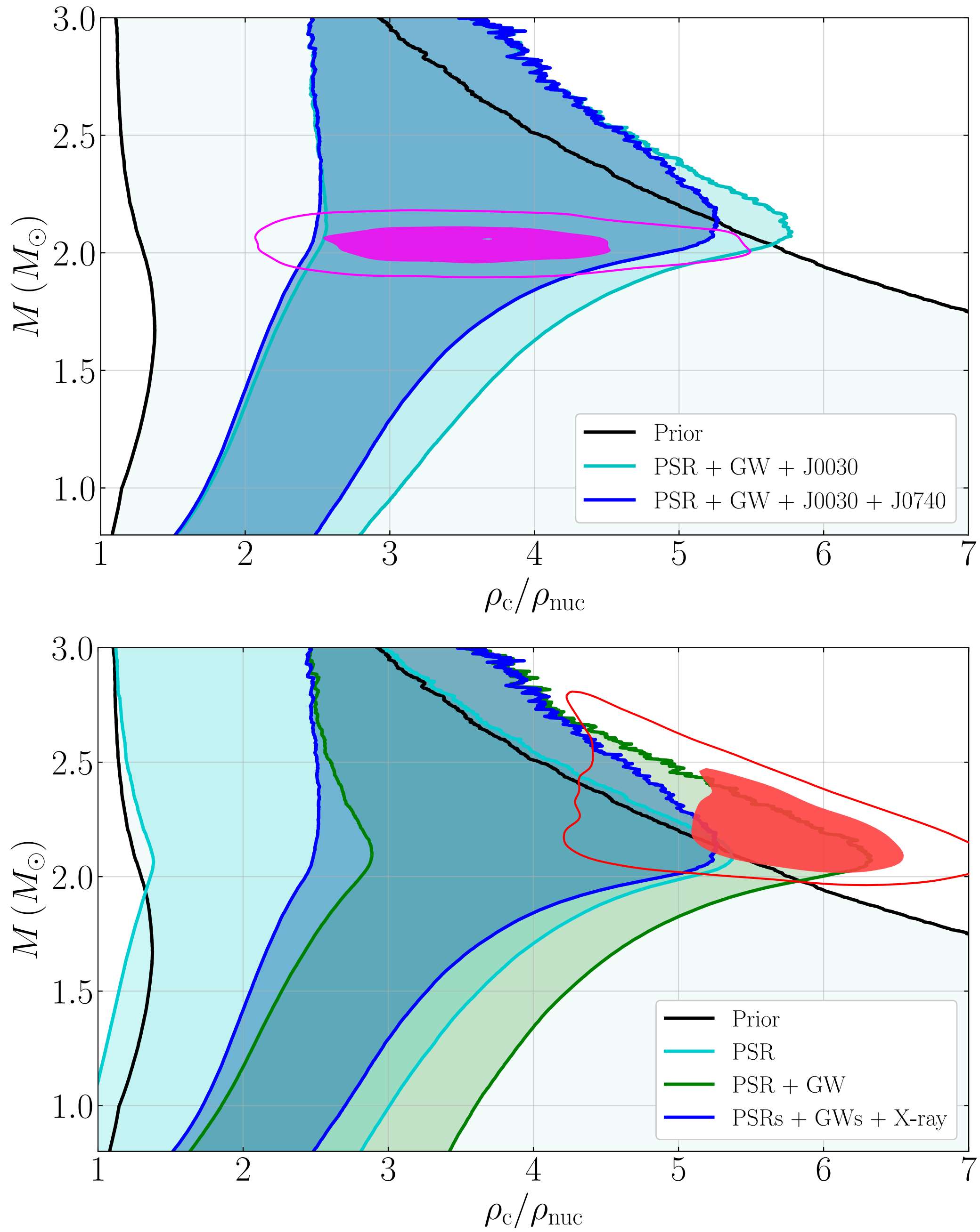

Figure 3.5: Same as Figs. 3.1 and 3.4 but for the central baryon density (in units of saturation density) as a function of NS mass. Magenta (red) contours in the left (right) panel show the 50% and 90% credible level for the mass-central density posterior for J0740+6620 (maximum-mass NS).

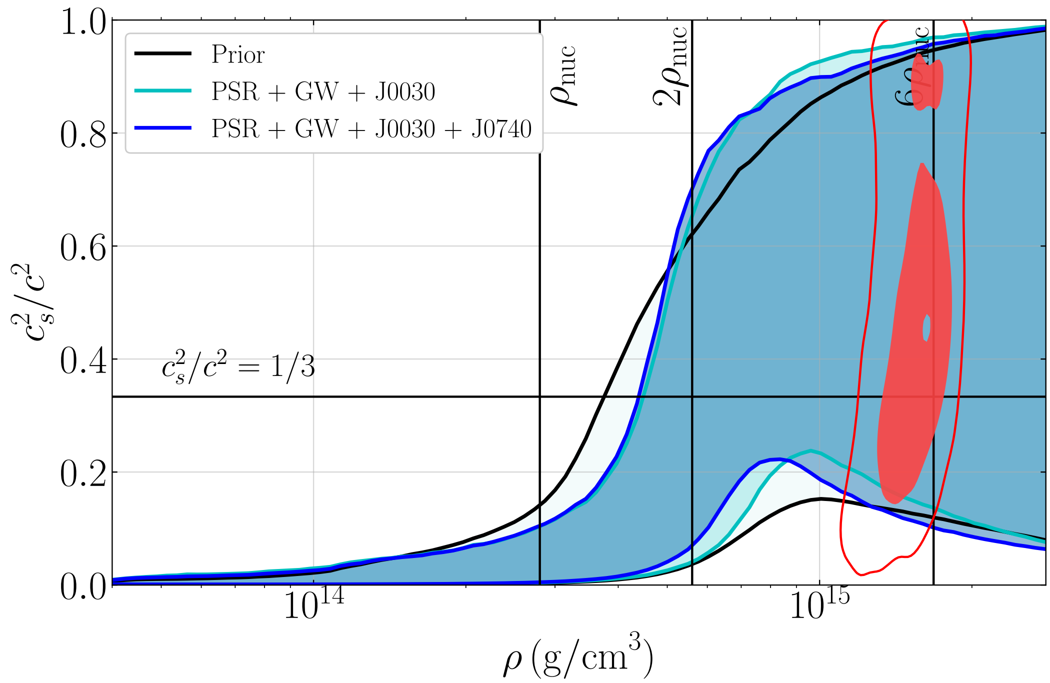

Figure 3.6: Similar to the left panels of Figs. 3.1, 3.4, and 3.5 but for the speed of sound inside NSs. The horizontal black line denotes the conformal limit $c_s^2/c^2 = 1/3$ and the red contour corresponds to the 50% and 90% inferred speed of sound and central density for the maximum-mass NS.

The strongest support for a large speed of sound comes from the combination of GW and heavy pulsar data that point to a soft low-density and stiff high-density EoS respectively, thus necessitating a steep slope in between. Figure 3.7 also shows our prior on the maximum c_s^2 and, even though it is consistent with the conformal limit, it certainly disfavors it.

To further assess the impact of data on the conformal limit in relation to the prior, Table 3.3 compares the evidence for EoSs that violate the conformal limit (max $c_s^2 > c^2/3$) with those that obey the conformal limit within nonrotating NSs through the corresponding Bayes factor:

$$\mathcal{B}^{c_s^2 > c^2/3}_{c_s^2 \leq c^2/3} \equiv \frac{p(\text{data}|\max c_s^2 > c^2/3)}{p(\text{data}|\max c_s^2 \leq c^2/3)}\,. \tag{3.1}$$

We find strong support that the conformal limit is violated: $\mathcal{B}^{c_s^2 > c^2/3}_{c_s^2 \leq c^2/3} \gtrsim 10^3$. Although our prior is consistent with EoSs that obey the conformal limit, it includes relatively few realizations that do so. As such, our Bayes factors are subject to sizeable sampling uncertainty from the finite number of Monte Carlo samples we

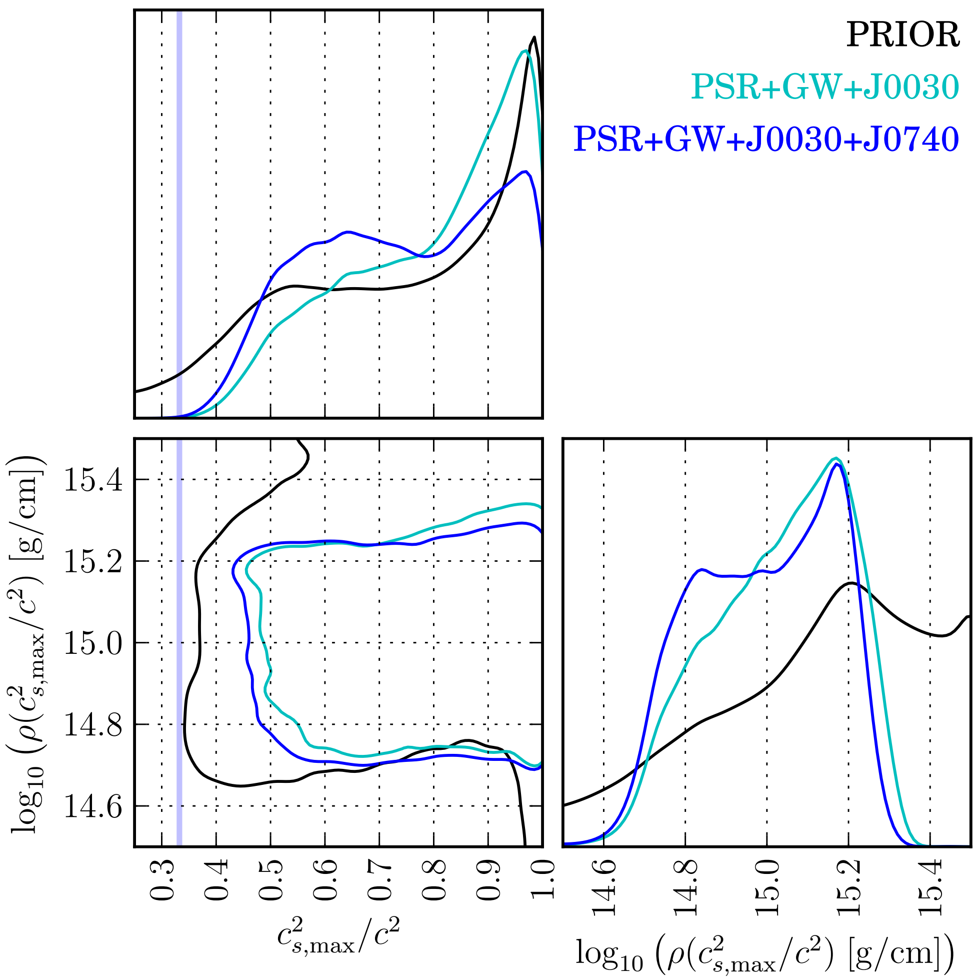

Figure 3.7: One- and two-dimensional marginalized prior and posterior of the maximum c_s^2/c^2 encountered inside the NS and the density at which this happens. We show the prior in black and the posterior with (without) the J0740+6620 radius measurement in blue (turquoise). The vertical line denotes the conformal limit of $c_s^2/c^2 = 1/3$.

Data		$\max \mathcal{L}^{n>1}_{n=1}$	$\mathcal{B}^{n>1}_{n=1}$	$\max \mathcal{L}^{c_s^2>c^2/3}_{c_s^2\leq c^2/3}$	$\mathcal{B}^{c_s^2>c^2/3}_{c_s^2\leq c^2/3}$
w/PSRs		1.00	0.120 ± 0.002	1.0	10.2 ± 0.5
w/o J0740+6620		0.97	0.220 ± 0.007	50.8	2220 ± 790
w/J0740+6620	Miller+	0.60	0.146 ± 0.005	26.7	1000 ± 340
	Riley+	0.94	0.185 ± 0.006	72.7	2450 ± 1820

Table 3.3: Ratios of the maximum likelihoods and marginal likelihoods (Bayes factors) comparing EoSs for which the sound speed violates the conformal limit vs. those for which it is satisfied [$\max \mathcal{L}^{c_s^2>c^2/3}_{c_s^2\leq c^2/3}$and $\mathcal{B}^{c_s^2>c^2/3}_{c_s^2\leq c^2/3}$, Eqs. (3.1) and (3.2)], and comparing EoSs with multiple stable branches vs. a single stable branch in their mass-radius relation [$\mathcal{B}^{n>1}_{n=1}$ and $\max \mathcal{L}^{n>1}_{n=1}$, Eqs. (3.3) and (3.4)]. We report point estimates and standard deviation from Monte Carlo sampling uncertainty. Data sets are labeled in the same way as in Table 3.2.

employ, making it hard to conclude whether support for the violation of the conformal limit increases or decreases due to J0740+6620. Nonetheless, we recover large Bayes factors, even considering this sampling uncertainty, and typically find that $\mathcal{B}^{c_s^2>c^2/3}_{c_s^2\leq c^2/3} > 1$ at the 3σ level.

Similarly, we report the ratio of the maximum likelihood observed for each type of EoS:

$$\max \mathcal{L}^{c_s^2>c^2/3}_{c_s^2\leq c^2/3} = \frac{\max\limits_{\max c_s^2>c^2/3} p(\mathrm{data}|\mathrm{EoS})}{\max\limits_{\max c_s^2\leq c^2/3} p(\mathrm{data}|\mathrm{EoS})}. \tag{3.2}$$

This measures how well each type of EoS is able to fit the observed data, and Table 3.3 shows that EoSs that violate the conformal limit are typically favored over those that obey it by between a factor of 40–110.

Strong first-order phase transitions

We now turn our attention to the implications of J0740+6620 for strong phase transitions. Figure 3.8 compares the pressure-density posterior inferred with EoSs that support different numbers of stable branches in the mass-radius relation, used here as a proxy for strong phase transitions. While strong first-order phase transitions can lead to EoSs with multiple stable branches and possibly even "twin stars", i.e., stars with roughly the same mass but very different radii [119], the converse is not necessarily true. Only the strongest phase transitions lead to disconnected branches, and so what follows concerns only the most extreme phase transitions. Typically, strong phase transitions and multiple branches result in a large decrease in the

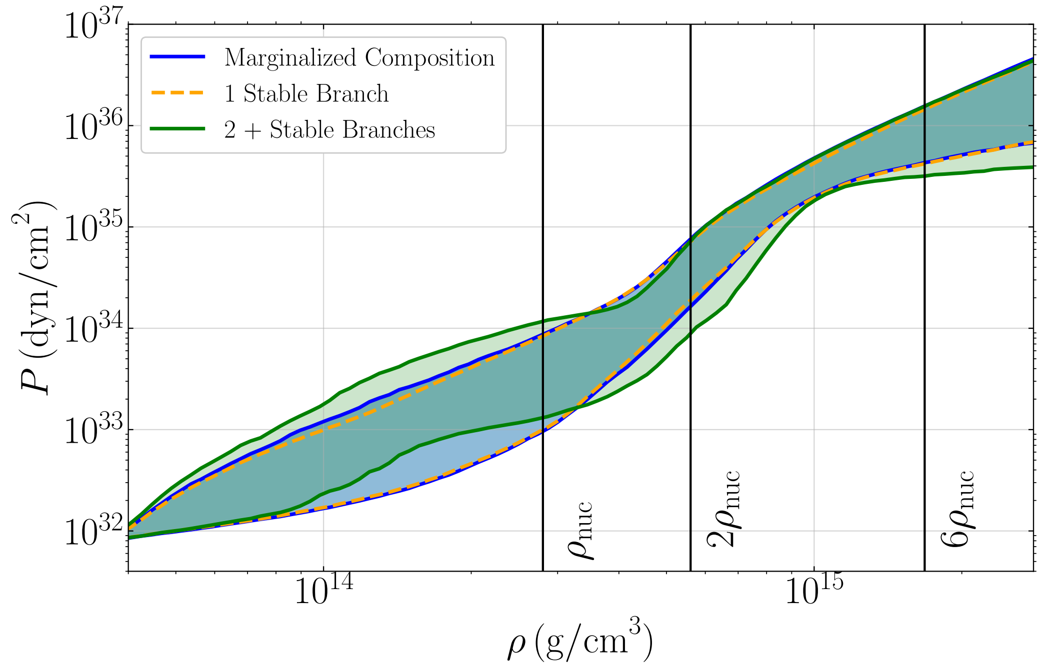

Figure 3.8: Dependence of the pressure-density posterior on the number of stable branches in the EoS. The blue region shows the full posterior, the green shaded regions show the posterior when restricting to EoSs with multiple stable branches, and the gold dashed lines denote the posterior region when restricting to a single stable branch.

radius between subsequent branches [13, 12, 64, 30]. The lower limit on the radius of J0740+6620 constrains such a sudden decrease.

Indeed, we find that the full posterior is similar (though not identical) to the one obtained from restricting to EoSs with only a single stable branch. This suggests that the full posterior marginalized over the number of branches is dominated by EoSs with a single stable branch, though this is also true of the prior. Table 3.3 reports the evidence ratios for EoSs with different numbers of stable branches:

$$\mathcal{B}^{n>1}_{n=1} \equiv \frac{p(\text{data}|\text{num branches} > 1)}{p(\text{data}|\text{num branches} = 1)}\,. \tag{3.3}$$

We find a Bayes factor of 6.9 in favor of a single stable branch, compared to < 5 without the J0740+6620 radius measurement. Astrophysical data generally disfavor the existence of multiple stable branches, driven primarily by the requirement that the EoS supports $\sim 2\,\mathrm{M}_\odot$ stars. As expected, the lower limit on the J0740+6620 further reduces the evidence for multiple stable branches. However, even the most extreme preference for a single stable branch only suggest a Bayes factor of $\simeq 8$.

Just as with the EoSs that obey vs. violate the conformal limit, we also report ratios in the maximum likelihood observed with EoSs that have a single stable branch vs. those with multiple stable branches:

$$\max \mathcal{L}_{n=1}^{n>1} = \frac{\max\limits_{n>1}\ p(\text{data}|\text{EoS})}{\max\limits_{n=1}\ p(\text{data}|\text{EoS})}. \tag{3.4}$$

Similar to $\mathcal{B}_{n=1}^{n>1}$, we find a preference for EoSs with a single stable branch, but it is small (at most a factor of $\lesssim 2$).

Previous work reported $\mathcal{B}_{n=1}^{n>1}$ additionally conditioned on the existence of massive pulsars *a priori* [77], equivalent to dividing any $\mathcal{B}_{n=1}^{n>1}$ by the result using only the massive pulsar observations. This amounts to examining whether the GW and x-ray data are consistent with multiple stable branches, after we have already assumed the existence of $\sim 2\,\mathrm{M}_{\odot}$ stars. If we follow suit, we obtain $\mathcal{B}_{n=1}^{n>1} \sim 1.2$ conditioning on the existence of massive PSRs *a priori* and including the x-ray observations of J0740+6620, compared to ~ 1.8 reported in [77]. As such, we again find that x-ray observations of J0740+6620 lower the evidence in favor of multiple stable branches. Our conclusions are generally consistent with those reported in [100] ($\mathcal{B}_{n=1}^{n>1} \sim 0.2$), although our results disfavor multiple stable branches slightly more strongly. A direct comparison is difficult as [100] do not quote uncertainties in their estimates. However, the observed differences could easily be due to priors (e.g., our priors allow for more model freedom and therefore contain more EoSs with multiple stable branches that are not forced *a priori* to support massive stars) or by how exactly phase transitions are defined (here we define them in terms of stable branches).

Several caveats should be kept in mind when interpreting our Bayes factors. Most importantly, it is well documented that Bayes factors are affected by the prior coverage of each model under consideration, particularly if they span regions of parameter space without any support *a posteriori*. That is to say, the marginal likelihoods that appear in, e.g., Eqs. (3.1) and (3.3) are averages of the likelihood over each prior; if priors span large regions of parameter space with small likelihood values, their marginal evidence will be smaller even if they achieve the same maximum likelihood (match the data just as well) as other, more compact priors.[6] Indeed, this is why we additionally report $\max \mathcal{L}_{c_s^2 \leq c^2/3}^{c_s^2 > c^2/3}$ and $\max \mathcal{L}_{n=1}^{n>1}$. In particular, differences in the prior support are thought to be a driving factor behind the Bayes factors' apparent preference for EoSs with a single stable branch (multiple-branch EoSs span

[6]For more discussion in a related context, see [45] for a discussion of why posterior odds can be more useful than Bayes factors.

a broader range of behavior, comparing max $\mathcal{L}^{n>1}_{n=1}$ and $\mathcal{B}^{n>1}_{n=1}$ in Table 3.3) as well as the preference for χEFT models over more agnostic EoS priors [49, 47]. While this type of Occam factor is desirable in many cases (see, e.g., discussion in Sec. 3.2), one needs to take care when drawing conclusions based on such effects. Although not guaranteed, we generally find that prior choices of this kind shift our Bayes factor by only a factor of a few, typically much smaller than the variability due to different realizations of experimental noise [118], which can be as large as factors of $O(10)$. It is therefore always prudent to check both the priors and posteriors for the behavior in question, for example checking both Fig. 3.7 and Table 3.3 when considering the conformal limit.

In the case of an EoS with multiple stable branches, we find a pressure-density envelope that is morphologically similar to the one in Fig. 4 of [77] (obtained without the J0740+6620 radius data). These plots show that, if the EoS has multiple stable branches, then the pressure is higher below nuclear saturation and lower at 2-3 $\rho_{\rm nuc}$, hinting towards a phase transition in this density regime and suggesting that all observed NSs may already contain an exotic core. Besides such a low-density phase transition, another possibility is a phase transition at higher densities. Such an effect is expected to lead to a reduction in the radius of no more than ~ 3 km [64, 30, 63, 43] for the most massive NSs compared to $R_{1.4}$, which would have been undetectable before the J0740+6620 radius lower limit.

To further explore the implications of a sudden decrease in the radius, in Fig. 3.9 we plot the posterior for the radius difference $\Delta R \equiv R_{2.0} - R_{1.4}$ and the maximum c_s^2, broken down again by the number of stable branches. A large negative value for ΔR suggests a strong phase transition at low densities, a scenario tightly constrained by the lower limit on the J0740+6620 radius. We find $\Delta R = -0.12^{+0.83}_{-0.85}$ km, consistent with zero although with large uncertainties, as also demonstrated in [90, 112]. This effectively rules only out the most extreme case of phase transitions that lead to a $\gtrsim 2$ km decrease in radii [30] but still remains consistent with milder or smooth phase transitions [63, 122]. In the case of multiple stable branches, we find that the maximum c_s^2 is higher than the single-branch case, though this does not seem to affect ΔR.

The larger speed of sound is consistent with previous work that suggests that, in the case of sharp phase transitions, the post-transition speed of sound in general needs to be larger in order to compensate for the intrinsic softening induced by the phase transition [64]. Indeed, as previously studied in [43], the absolute bounds on NS

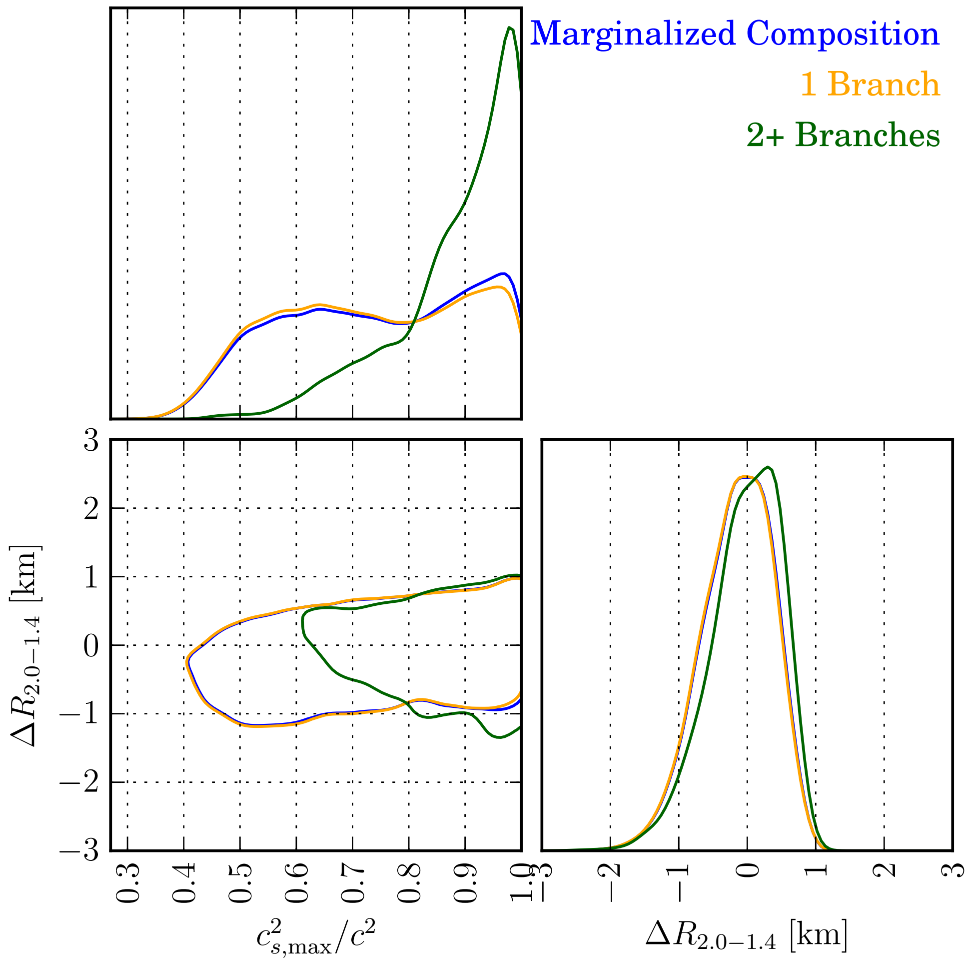

Figure 3.9: Two-dimensional posterior for the radius difference $\Delta R \equiv R_{2.0} - R_{1.4}$ against the maximum speed of sound squared reached in the NS. We show results with all EoSs (blue) as well as only EoSs with one (gold) and multiple (green) stable branches.

radii assuming an EoS with a constant sound speed at high densities is very sensitive to the assumed value of max $\{c_s^2/c^2\}$. The lower (upper) radius bound decreases (increases) as max $\{c_s^2/c^2\}$ increases. This is in agreement with Fig. 3.9. The absolute lower bound on NS radii derived in [43] corresponds to the most negative value of ΔR induced by the strongest possible phase transition (limited by $c_s^2 \leq c^2$ at high densities) compatible with M_{max}. On the other hand, a positive ΔR suggests weaker phase transitions, progressing towards the absolute upper bound on NS radii. We also note that for various physical models of hadronic matter (with or without a smooth crossover to exotic matter), $\Delta R \gtrsim -1.5$ km is typical, although a few exhibit an increase from $R_{1.4}$ to $R_{2.0}$ [65, 63, 131].

To further explore this, in Fig. 3.10 we plot the posterior for the transition mass M_{t}, defined as the largest mass of the first stable EoS branch, and the transition density ρ_{t}, defined as the central density at the transition mass, and select macroscopic quantities. Fig. 3.10 also considers *only* EoSs with multiple stable branches. We plot $R_{1.4}$, $R_{2.0}$, and M_{max}, which roughly represent the main observables from GWs, the two NICER pulsars, and the radio mass observations. We find that, if the EoS has multiple stable branches, the transition from the first branch probably happens for masses $\lesssim 1\,\text{M}_\odot$ or $\sim 2\,\text{M}_\odot$. The corresponding transition density is $\lesssim 2.2\,\rho_{\text{nuc}}$ or $\sim 4.5\,\rho_{\text{nuc}}$. High-density phase transitions would be the most challenging to detect, as they could result in small changes in the radius and thus be indistinguishable from EoSs without a phase transition [13].

The posteriors also indicate that transition mass M_{t} and the radius difference ΔR are anticorrelated. If the transition mass is very low, then the entire star is mostly composed of exotic matter. As expected for quark stars, we find that ΔR is closer to zero and can even be positive, i.e., the most massive star is bigger (as expected for self-bound configurations). This is similar to the behavior of the two brown curves in Fig. 1 of [30]. As the transition mass increases, ΔR becomes more negative. This is similar to the purple and red curves from Fig. 1 of [30] that result in stars that are hadronic in the outer layers but possess a large quark core. If future GW detections place further upper limits on $R_{1.4}$, then large negative values for ΔR will be further constrained, thus pushing M_{t} even lower.

The current data disfavor phase transitions that lead to multiple stable branches occurring in the mass range $\sim$ (1-2) $\text{M}_\odot$, suggesting that the majority of NSs we observe belong in a single branch: if the true EoS has multiple stable branches, either all sub-2 $\text{M}_\odot$ contain exotic material or none do. The two-dimensional M_{t}-

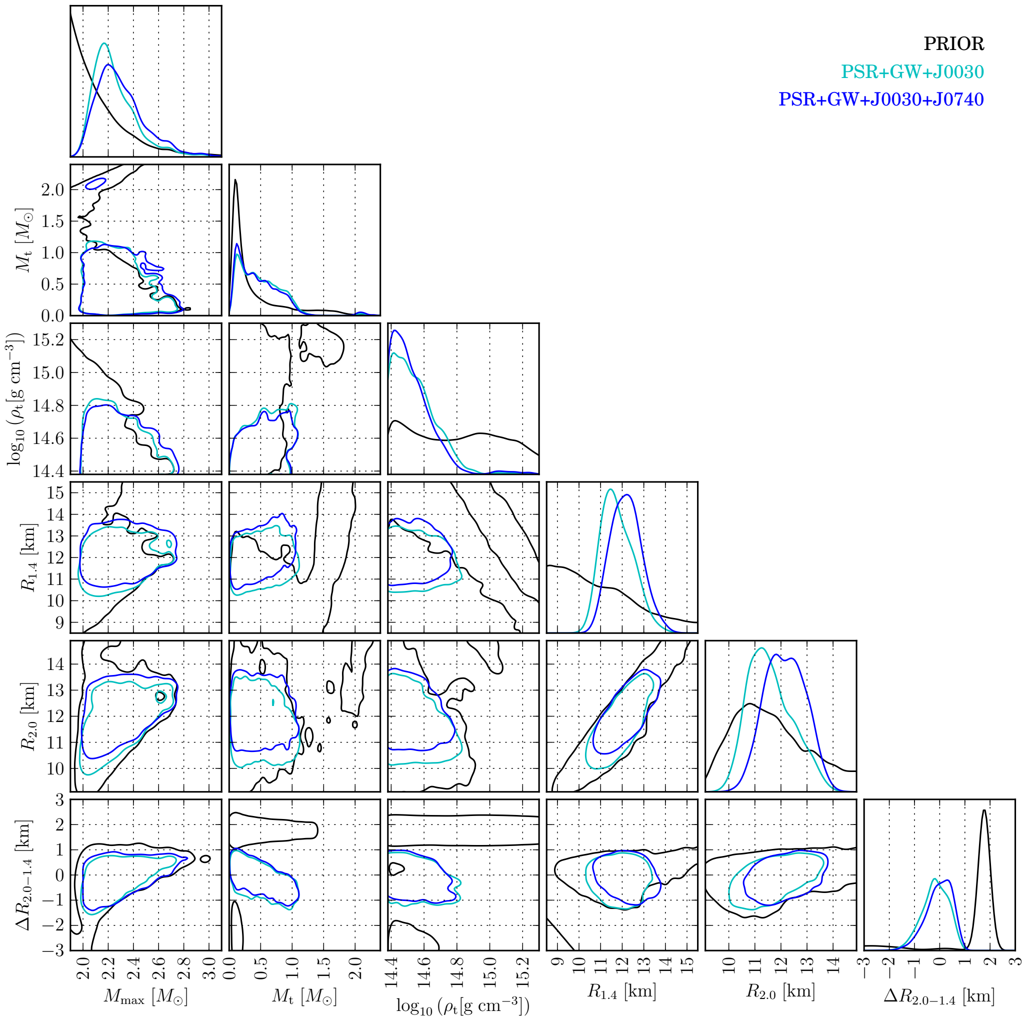

Figure 3.10: Corner plot for the transition mass $M_{\rm t}$ corresponding to the most massive hadronic NS in EoSs with multiple stable branches, the transition density $\rho_{\rm t}$ corresponding to the central density of a star with mass $M_{\rm t}$, $R_{1.4}$, $R_{2.0}$, $M_{\rm max}$, and $\Delta R \equiv R_{2.0} - R_{1.4}$. Contours in the 2D distributions denote the 90% credible level. Black lines denote the prior, while blue (turquoise) lines correspond to results with (without) the J0740+6620 radius constraint.

$M_{\rm max}$ plot reveals that this is due to the requirement that $M_{\rm max} \gtrsim 2\,{\rm M}_\odot$, which disfavors $M_{\rm t} \sim 1.5\,{\rm M}_\odot$ *a priori* and "splits" the $M_{\rm t}$ posterior into two modes [12]. This behavior is expected, for example, from Fig. 3 of [64] which shows that an $M_{\rm max}$ measurement constrains the intermediate values of the transition pressure. We leave extraction of further characteristics of the phase transition (such as the transition strength) and EoSs with phase transitions that do not lead to multiple stable branches to future work [44].

Finally, Fig. 3.11 shows distributions of the same variates as Fig. 3.2, but separates the EoSs with one and multiple stable branches. We find that all posteriors are consistent with each other, though EoSs with multiple stable branches are on average consistent with a softer EoS at low densities around 1-2 $\rho_{\rm nuc}$ and a stiffer high-density EoS than single-branch EoSs. This is expressed through a slightly higher maximum mass and pressure at $6\,\rho_{\rm nuc}$, but slightly lower radii, tidal parameters, and pressure at $2\,\rho_{\rm nuc}$. The trend towards a stiffer high-density EoS agrees with the maximum speed of sound of Fig. 3.9. Similarly, the softer low-density EoS agrees with the pressure-density curves of Fig. 3.8.

Overall, we find that the data mildly disfavor multiple stable branches, though they do not rule out their presence. However, if the true EoS indeed has multiple branches, then this would suggest that some extra softening in the EoS, ostensibly due to a phase transition, has already taken place at densities below $\sim 2.2\,\rho_{\rm nuc}$. Currently, of all the available astronomical data sets, the GW data dominate the upper limits on the stiffness or pressure of EoS around $2\,\rho_{\rm nuc}$. Should further GW observations continue to push in the same direction, then the evidence for the presence of a strong phase transition in the relevant density region could be strengthened. To this end, astrophysical observations have limited constraining power at very low densities [49, 48], and improved theoretical calculations or terrestrial experiments will likely determine whether the pressure is small or large near $\rho_{\rm nuc}$ (see, e.g., [10, 116]).

3.5 Discussion

In summary, the new radius measurement for J0740+6620 refines our inference of the EoS by tightening the constraint on the pressure at densities $\sim$ 2–3 $\rho_{\rm nuc}$. Like NICER's previous observation of J0030+0451, this constraint comes mainly from the soft side, as the x-ray pulse-profiling available to date primarily bounds NS radii, tides, and pressures from below. We infer that all observed NSs have the same radius to within $\sim$ 2 km. This picture is consistent with other recent studies of J0740+6620 [90, 102, 100]. Our analysis draws three further principal conclusions: (i) the sound speed in NS cores very likely exceeds the conformal bound; (ii) the lack of a large radius difference between high- and low-mass NSs renders the existence of a separate stable branch in the mass-radius relation less likely; and (iii) the stiff EoS around $2\,\rho_{\rm nuc}$ implied by the ensemble of observations results in a relatively low central density of $3.57^{+1.3}_{-1.3}\,\rho_{\rm nuc}$ for J0740+6620, capping the density range that

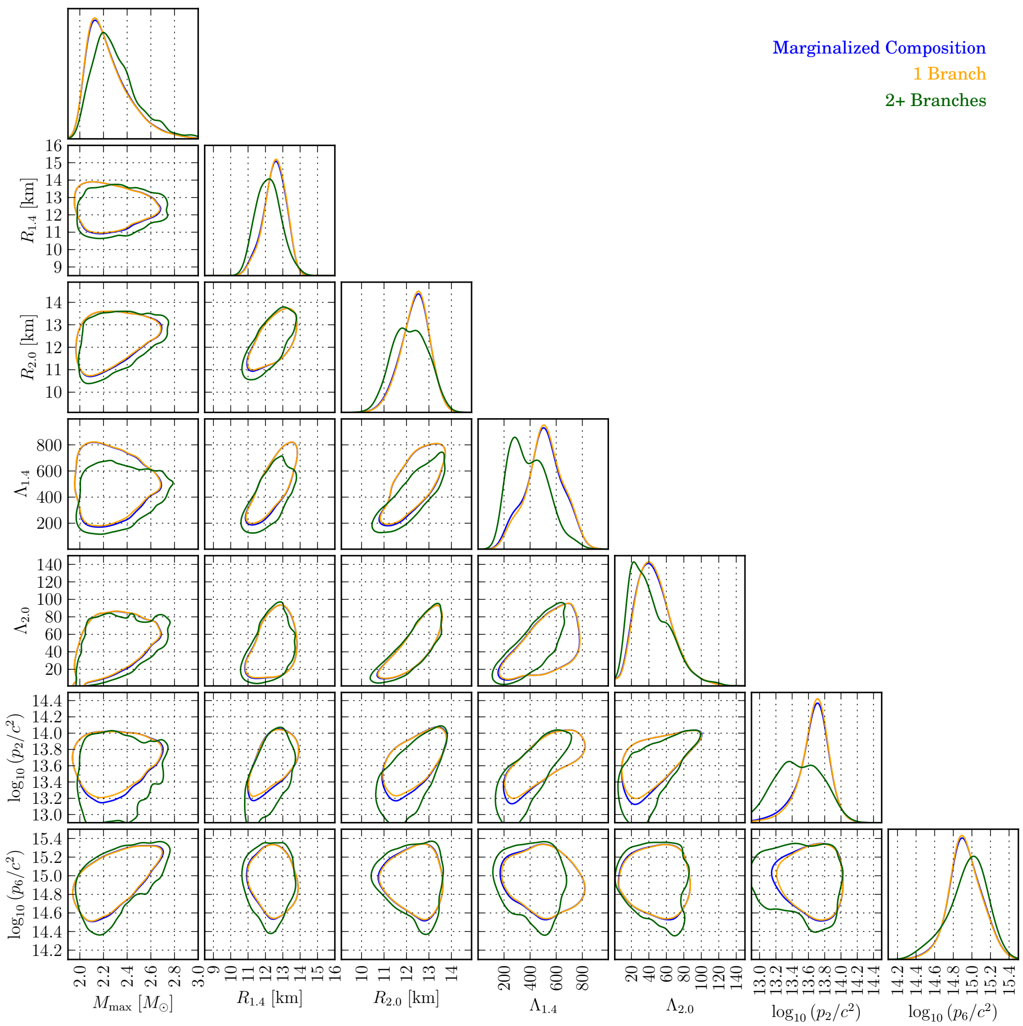

Figure 3.11: Corner plot for various macroscopic and microscopic parameters of interest broken down by number of stable branches. Contours in the 2D distributions denote the 90% level and we plot the same quantities as in Fig. 3.2. Blue lines denote the full posterior, while gold (green) lines correspond to results with EoSs with one (multiple) stable branches.

astronomical observations of nonrotating NSs can probe to date. However, the fact that the radius of J0740+6620 is comparable to $R_{1.4}$ suggests that J0740+6620 at $\sim 2.08\,\mathrm{M}_\odot$ might not be at the turning-point of the mass-radius curve and more massive NSs are possible; the inferred central density of the maximum-mass NS is $5.4^{+1.1}_{-1.4}\,\rho_{\mathrm{nuc}}$.

Our main results are based on the J0740+6620 mass-radius constraint from [90], mainly due to the fact that this analysis uses the nominal relative NICER/XMM-Newton calibration uncertainty. Nonetheless, we find broadly consistent results when using the data from [112] instead. The larger calibration uncertainty assumed by [112] results in a weaker lower bound on the radius of J0740+6620, and after conditioning on all the observational data this translates to a 0.4 km difference in the lower limit of the 90% credible interval we extract for $R_{1.4}$. Our conclusions about strong phase transitions and the violation of the conformal sound-speed bound are unaltered when the data from [112] is used. Prior differences in the two analyses (flat-in-compactness [90] vs. flat-in-radius [112]) do not affect results within the hierarchical inference formalism.

A direct numerical comparison between our results and [90, 102, 100, 21] must be done with care due to the different data sets used and other assumptions. For example, [102, 100] include GW170817 counterpart models, which we omit here due to concerns about systematic errors, and they assume *a priori* that GW190425 was a binary neutron star merger, which informs the M_{max} inference because of its large primary mass. Nonetheless, with those caveats in mind, we can compare posterior constraints on the radius of a $1.4\,\mathrm{M}_\odot$ NS and the maximum NS mass. Ref. [90] finds $R_{1.4} = 12.63^{+0.48}_{-0.46}$ km and $M_{\mathrm{max}} = 2.23^{+0.24}_{-0.15}\,\mathrm{M}_\odot$ at the 68% credible level for their GP model, in very close agreement with our results. Ref. [100] finds $R_{1.4} = 12.03^{+0.77}_{-0.87}$ km and $M_{\mathrm{max}} = 2.18^{+0.15}_{-0.15}\,\mathrm{M}_\odot$ at the 90% credible level, which are smaller and more tightly constrained than our corresponding estimates, using a χEFT-informed parametric EoS model. Besides the aforementioned caveats, this difference can be partly attributed to the fact that Ref. [100] reports the radius with respect to a flat prior, whereas we report it, like all our constraints, with respect to the prior informed by our nonparametric EoS model. Both of these results refer to the J0740+6620 data from [90] and can therefore be compared to the second-last column in Table 3.2. Meanwhile, Ref. [102] reports $R_{1.4} = 12.33^{+0.76}_{-0.81}$ km and $M_{\mathrm{max}} = 2.23^{+0.14}_{-0.23}\,\mathrm{M}_\odot$ at the 95% credible level based on piecewise polytropes informed by χEFT at low densities, and Ref. [21] obtains $R_{1.4} = 12.61^{+0.36}_{-0.41}$ km at the 68% credible level and a maximum mass of $\sim 2.2\,\mathrm{M}_{\odot}$ using a nuclear parameterization for the EoS with a piecewise polytrope extension. These numbers can be compared to the last column in Table 3.2 as they are based on the J0740+6620 data from [112]. The results from [102] in particular match our inferred values very closely, though our uncertainties are broader, which we attribute to the larger model freedom inherent in our GP prior. All these results are further broadly consistent with radius estimates from x-ray observations of NSs in low-mass x-ray binaries during quiescent or bursts phases [123, 94, 93, 97, 74], though these are subject to considerable modeling uncertainties.

This comparison of our results with the existing literature [90, 112, 102, 100] brings forward the issue of model dependence in EoS constraints obtained from observations, experiments, and calculations that span many orders of magnitude in density. By design, the GP EoS prior used in [90] does not allow for as much model freedom as our *model-agnostic* process due to the strong intra-density correlations it assumes *a priori*. This is especially true at high densities. Another approach to nonparametric inference is to use neural networks, as in [62], though the model constructed in that study deliberately seeks to closely reproduce the behavior of a handful of tabulated EoSs from the literature. In this sense, the nonparametric models used in [62] and [90] are more analogous to the *model-informed* GP prior from [46] that makes relatively strong prior assumptions about correlations within the EoS. Parametric EoS models, such as piecewise polytropes [105], the spectral decomposition [84], and the speed-of-sound parameterization [61, 125], impose even more restrictive assumptions on EoS morphology by virtue of specifying the functional form of the EoS with a finite number of parameters to describe an infinite-dimensional function space. Examples of such model dependence are given in Fig. 10 of [90] and the variation between the two models presented in [102].

These considerations pose the problem of the degree to which EoS constraints are driven by the data, rather than by correlations between different densities imposed by the EoS model. Under that light, it is interesting to consider the effect of folding nuclear theoretic calculations into the inference of the EoS. Figure 3.4 shows that the J0740+6620 radius measurement does not inform the EoS below ρ_{nuc}, something also confirmed by [90]. References [49, 48] further show that our GP EoS prior is designed with no strong correlations between low-density information and high-density physics by explicitly showing that the same results are obtained at high densities regardless of whether the EoS is conditioned on χEFT at low densities or not. As such, we do not expect the J0740+6620 radius data to offer new insights about χEFT predictions within its regime of applicability, i.e. $\lesssim 1 - 2\rho_{nuc}$, nor do we expect χEFT predictions to influence our conclusions about NS matter at high densities. In contrast, the parametric EoS inference in [102] is sensitive to the χEFT calculations they condition on up to $1.1\,\rho_{\mathrm{nuc}}$ even at the highest densities probed. Figure 7 of [102] shows that the NS radii and pressures they infer with both of their parametric EoS models have some dependence on which χEFT calculation is assumed. This suggests that statements both about the validity of nuclear calculations based on astrophysical data and the inference of NS properties after assuming a specific low-density calculation must take care to avoid introducing unwanted systematic modeling assumptions through the choice of high-density EoS representation.

In addition to χEFT and other theoretical models, several terrestrial experiments probe the EoS at densities up to ρ_{nuc}. In particular, the PREX collaboration recently measured the neutron skin thickness of lead $R_{\mathrm{skin}}^{208\mathrm{Pb}}$ [10], which is tightly correlated with the density dependence of the nuclear symmetry energy (the difference in the energy per particle for matter that contains only neutrons and matter that contains an equal number of neutrons and protons) and therefore the pressure at ρ_{nuc} [27, 115, 107]. Using a *model-agnostic* nonparametric analysis similar to ours, Ref. [48] found no strong correlation between the results of several low-density experiments and high-density NS observables. Claims to the contrary [107, 21], therefore, are driven by specific modeling assumptions, which may not be justified. Nevertheless, the large $R_{\mathrm{skin}}^{208\mathrm{Pb}}$ reported in [10] suggests a relatively stiff EoS at low densities, although there are other low-energy experiments (e.g., [116, 50, 130]) and alternative interpretations of the data [108] that favor softer EoSs.[7] A stiff EoS at low densities may increase the evidence in favor of multiple stable branches, but we expect the effect to be small with current experimental uncertainties. Given the slight tension between nuclear experiments and the fact that additional constraints at low densities will not strongly influence our conclusions from J0740+6620's radius measurement, we omit nuclear experimental data from our current analysis and leave such investigations to future work.

Nevertheless, the growing number of constraints on the NS EoS is progressively sharpening our picture of dense matter. The radius measurement for J0740+6620 is a reminder of how different observations, experiments, and theoretical calculations

[7] All current bounds on the symmetry energy agree to within 2-σ.

complement each other by targeting different density scales inside NSs. Joint analyses of this ensemble of data require models for the EoS that span many orders of magnitude in pressure and density. As a result, it is important to understand how different EoS models, both parametric and nonparametric, correlate different densities to distinguish data-driven features from those driven by the prior. The nonparametric model we use is deliberately constructed to emphasize flexibility in EoS morphology and impose few correlations between high and low densities besides those dictated by the physical requirements of causality and thermodynamic stability. The intra-density correlations introduced by different parametric and nonparametric EoS models will be investigated in quantitative detail in upcoming work [81].

3.6 Acknowledgements

Research at Perimeter Institute is supported in part by the Government of Canada through the Department of Innovation, Science and Economic Development Canada, and by the Province of Ontario through the Ministry of Colleges and Universities. S.H. is supported by the National Science Foundation, Grant PHY-1630782, and the Heising-Simons Foundation, Grant 2017-228. P.L. is supported by National Science Foundation award PHY-1836734 and by a gift from the Dan Black Family Foundation to the Nicholas & Lee Begovich Center for Gravitational-Wave Physics & Astronomy. This research has made use of data, software and/or web tools obtained from the Gravitational Wave Open Science Center (https://www.gw-openscience.org), a service of LIGO Laboratory, the LIGO Scientific Collaboration and the Virgo Collaboration. Virgo is funded by the French Centre National de Recherche Scientifique (CNRS), the Italian Istituto Nazionale della Fisica Nucleare (INFN) and the Dutch Nikhef, with contributions by Polish and Hungarian institutes. This material is based upon work supported by NSF's LIGO Laboratory which is a major facility fully funded by the National Science Foundation. The authors are grateful for computational resources provided by the LIGO Laboratory and supported by National Science Foundation Grants PHY-0757058 and PHY-0823459.

3.7 Appendix: Choosing a Mass Prior

Substantial uncertainty persists in the distribution of compact-object masses, including the question of whether the NS and BH mass distributions overlap. However, any hierarchical analysis of the EoS needs to assume a compact-object mass distribution to specify the mass prior for a given EoS.[8] The full framework was laid out in Sec. III B of [77] where the likelihood for an EoS model ε was written in terms of the compact-object mass distribution $P(m|\varepsilon)$. In the current study and [77], we assume a uniform mass distribution, such that the mass prior takes the general form

$$P\left(m|\varepsilon\right) = \frac{\Theta(M_{\rm lower} \leq m)\Theta(m \leq M_{\rm upper})}{M_{\rm upper} - M_{\rm lower}} \,. \tag{3.5}$$

However, a choice still needs to be made for the lower and upper limits, $M_{\rm lower}$ and $M_{\rm upper}$. We set $M_{\rm lower} = 0.5\,\mathrm{M}_\odot$, but $M_{\rm upper}$ is subject to three possible assumptions.

Assumption 1: The compact object might not be a NS

The first option accounts for the possibility that the compact object in question is a BH, rather than a NS. If we do not have definite prior knowledge that it is a NS, our mass prior does not require its mass to be below the maximum NS mass. In this case, $M_{\rm upper}$ is the maximum formation mass for the relevant type of compact object. If $m > M_{\rm max}(\varepsilon)$, with $M_{\rm max}(\varepsilon)$ the TOV mass of EoS ε, the radius and tidal deformability of the compact object are set to their Schwarzschild BH values, $2Gm/c^2$ and 0, respectively. If $m \leq M_{\rm max}(\varepsilon)$, the compact object is a NS, and its properties are set by the EoS ε. The mass prior itself is independent of the EoS ε in this scenario. This is the assumption we employ for both GW170817 and GW190425. While it is the most agnostic assumption possible, it is clearly erroneous for compact objects detected as pulsars, such as J0740+6620.

Assumption 2: The astrophysical formation mechanism limits the maximum possible mass

In the second scenario, the compact object under consideration is assumed to be a NS, but astrophysical formation mechanisms (for example, supernovae) are known *a priori* not to produce NSs above a certain mass, $M_{\rm pop}$. This upper limit might be comparable to $M_{\rm max}(\varepsilon)$ for some EoSs. In this case,

$$M_{\rm upper} = \min\left(M_{\rm pop}, M_{\rm max}(\varepsilon)\right) \,. \tag{3.6}$$

While it is plausible that there may be an astrophysical limit to the mass of NSs, in practice this assumption comes at the expense of a completely arbitrary choice for

[8] Another common equivalent choice is to work with a prior on the central density of NSs instead of the mass, see for example [102]. Given an EoS, there is a one-to-one mapping between the NS mass and central density; this appendix's discussion consequently applies to these works as long as the central density distribution includes an upper and/or lower limit.

$M_{\rm pop}$, given the current state of compact-object population knowledge. As such, we do not employ it for any of the compact objects analyzed in the main body of the paper. Nonetheless, Fig. 3.12 compares the impact of one possible choice of $M_{\rm pop}$ against the other two assumptions.

Assumption 3: The EoS limits the maximum possible mass

Under the third assumption, the compact object under consideration is known to be a NS, and astrophysical formation mechanisms can produce NSs as heavy as the EoS can support. Thus, $M_{\rm upper} = M_{\rm max}(\varepsilon)$. In this case, the prior depends on the EoS both through the upper limit (which rejects any masses above $M_{\rm max}$) and the normalization (which constitutes an Occam penalty against EoSs that predict masses larger than have been observed). Stated differently, an EoS with $M_{\rm max}(\varepsilon)$ slightly above the most massive known pulsar will be favored compared to an EoS that predicts the existence of much more massive NSs that have not been observed. We employ this assumption for all pulsars in our main study, including both radio and x-ray observations. To the best of our understanding, the same assumption is employed in [102, 21, 90].

The advantage of this assumption is that it does not rely on an explicit choice of $M_{\rm pop}$. The disadvantage is that the lack of observations of more massive NSs is attributed to (and therefore informs) the EoS, while other factors (astrophysical conditions and selection effects) are ignored, even as potential higher-mass NS candidates have been identified [70]. A simultaneous inference of the compact-object population and the EoS would obviate the need for choosing between Assumptions 2 and 3; instead, it would select the appropriate case as a function of the population model realization within the inference. This is possible because Assumption 3 is really just a special case of Assumption 2 in which $M_{\rm pop} \geq M_{\rm max}(\varepsilon)$ for all viable EoSs.

In order to quantitatively assess the impact of assumptions about the mass prior on J0740+6620, we repeat the main analysis with the alternative assumptions. In Assumption 1, we effectively assume that J0740+6620 could be a BH. In Assumption 2, we arbitrarily select $M_{\rm pop} = 2.3\,{\rm M}_\odot$, motivated by the approximate upper limit of the inferred J0740+6620 mass posterior [58]. In Assumption 3 (same as the main body of the text), we assume $M_{\rm pop} = 3.0\,{\rm M}_\odot$, which is larger than $M_{\rm max}$ for the vast majority of EoSs in our prior. In Fig. 3.12, we plot the 2-dimensional and 1-dimensional $M_{\rm max} - R_{1.4}$ marginalized prior and posterior under these three assumptions. We find that the different mass prior choices only affect the inferred

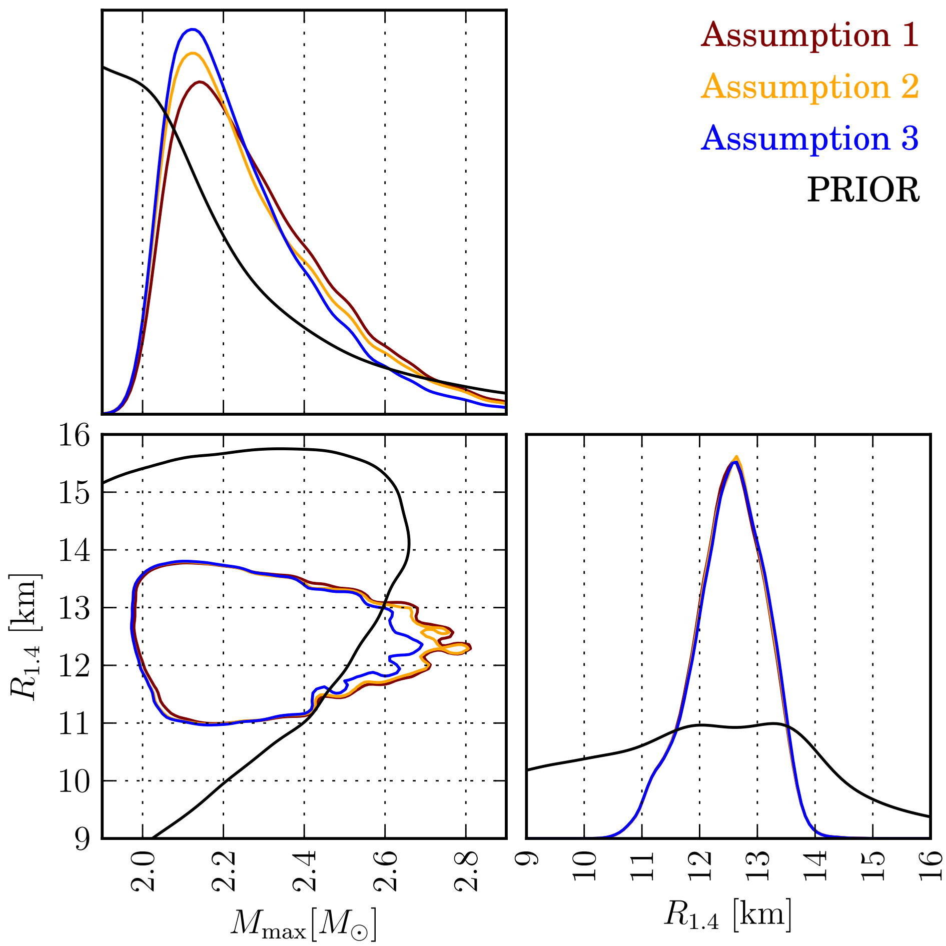

Figure 3.12: Corner plots of $M_{\max}$ versus $R_{1.4}$ for the three assumptions about the J0740+6620 mass prior illustrated above. (*black*) our EoS prior. (*brown*) Assumption 1: J0740+6620 could be either a NS or a BH. (*orange*) Assumption 2: a hypothetical formation channel does not produce NSs with $m > 2.3\,M_\odot$, which limits the effects of the Occam penalty. (*blue*) Assumption 3: only the EoS limits M_{upper}, and EoS that support the largest masses incur the full Occam penalty. We see the expected ordering in the tail of the $M_{\max}$ distribution; assumptions that introduce larger Occam penalties result in suppressed tails.

value of the maximum mass. Even then, the effect is small compared to current statistical uncertainties. Quantities determined at lower density scales, such as $R_{1.4}$, are essentially unaffected.

References

[1] J. Aasi et al. "Advanced LIGO". In: *Class. Quant. Grav.* 32 (2015), p. 074001. DOI: 10.1088/0264-9381/32/7/074001. arXiv: 1411.4547 [gr-qc].

[2] B. P. Abbott et al. "GW170817: Measurements of neutron star radii and equation of state". In: *Phys. Rev. Lett.* 121.16 (2018), p. 161101. DOI: 10.1103/PhysRevLett.121.161101. arXiv: 1805.11581 [gr-qc].

[3] B. P. Abbott et al. "GW190425: Observation of a Compact Binary Coalescence with Total Mass $\sim 3.4 M_\odot$". In: *Astrophys. J. Lett.* 892.1 (2020), p. L3. DOI: 10.3847/2041-8213/ab75f5. arXiv: 2001.01761 [astro-ph.HE].

[4] B. P. Abbott et al. "Properties of the binary neutron star merger GW170817". In: *Phys. Rev. X* 9.1 (2019), p. 011001. DOI: 10.1103/PhysRevX.9.011001. arXiv: 1805.11579 [gr-qc].

[5] B. P. Abbott et al. "Prospects for observing and localizing gravitational-wave transients with Advanced LIGO, Advanced Virgo and KAGRA". In: *Living Reviews in Relativity* 23.1 (Sept. 2020), p. 3. ISSN: 1433-8351. DOI: 10.1007/s41114-020-00026-9. URL: https://doi.org/10.1007/s41114-020-00026-9.

[6] Benjamin P Abbott et al. "Model comparison from LIGO–Virgo data on GW170817's binary components and consequences for the merger remnant". In: *Class. Quant. Grav.* 37.4 (2020), p. 045006. DOI: 10.1088/1361-6382/ab5f7c. arXiv: 1908.01012 [gr-qc].

[7] Benjamin P. Abbott et al. "GW170817: Observation of Gravitational Waves from a Binary Neutron Star Inspiral". In: *Phys. Rev. Lett.* 119.16 (2017), p. 161101. DOI: 10.1103/PhysRevLett.119.161101. arXiv: 1710.05832 [gr-qc].

[8] R. Abbott et al. "GW190814: Gravitational Waves from the Coalescence of a 23 Solar Mass Black Hole with a 2.6 Solar Mass Compact Object". In: *Astrophys. J. Lett.* 896.2 (2020), p. L44. DOI: 10.3847/2041-8213/ab960f. arXiv: 2006.12611 [astro-ph.HE].

[9] F. Acernese et al. "Advanced Virgo: a second-generation interferometric gravitational wave detector". In: *Class. Quant. Grav.* 32.2 (2015), p. 024001. DOI: 10.1088/0264-9381/32/2/024001. arXiv: 1408.3978 [gr-qc].

[10] D. Adhikari et al. "Accurate Determination of the Neutron Skin Thickness of ^{208}Pb through Parity-Violation in Electron Scattering". In: *Phys. Rev. Lett.* 126.17 (2021), p. 172502. DOI: 10.1103/PhysRevLett.126.172502. arXiv: 2102.10767 [nucl-ex].

[11] Michalis Agathos et al. "Constraining the neutron star equation of state with gravitational wave signals from coalescing binary neutron stars". In: *Phys. Rev. D* 92.2 (2015), p. 023012. DOI: 10.1103/PhysRevD.92.023012. arXiv: 1503.05405 [gr-qc].

[12] Mark G. Alford and Sophia Han. "Characteristics of hybrid compact stars with a sharp hadron-quark interface". In: *Eur. Phys. J. A* 52.3 (2016), p. 62. DOI: 10.1140/epja/i2016-16062-9. arXiv: 1508.01261 [nucl-th].

[13] Mark G. Alford, Sophia Han, and Madappa Prakash. "Generic conditions for stable hybrid stars". In: *Phys. Rev. D* 88.8 (2013), p. 083013. DOI: 10.1103/PhysRevD.88.083013. arXiv: 1302.4732 [astro-ph.SR].

[14] Justin Alsing, Hector O. Silva, and Emanuele Berti. "Evidence for a maximum mass cut-off in the neutron star mass distribution and constraints on the equation of state". In: *Mon. Not. Roy. Astron. Soc.* 478.1 (2018), pp. 1377–1391. DOI: 10.1093/mnras/sty1065. arXiv: 1709.07889 [astro-ph.HE].

[15] John Antoniadis et al. "A Massive Pulsar in a Compact Relativistic Binary". In: *Science* 340.6131 (2013), p. 1233232. DOI: 10.1126/science.1233232. arXiv: 1304.6875 [astro-ph.HE].

[16] Andreas Bauswein et al. "Equation of state constraints from the threshold binary mass for prompt collapse of neutron star mergers". In: *Phys. Rev. Lett.* 125.14 (2020), p. 141103. DOI: 10.1103/PhysRevLett.125.141103. arXiv: 2004.00846 [astro-ph.HE].

[17] Andreas Bauswein et al. "Neutron-star radius constraints from GW170817 and future detections". In: *Astrophys. J.* 850.2 (2017), p. L34. DOI: 10.3847/2041-8213/aa9994. arXiv: 1710.06843 [astro-ph.HE].

[18] Gordon Baym et al. "From hadrons to quarks in neutron stars: a review". In: *Rept. Prog. Phys.* 81.5 (2018), p. 056902. DOI: 10.1088/1361-6633/aaae14. arXiv: 1707.04966 [astro-ph.HE].

[19] Paulo Bedaque and Andrew W. Steiner. "Sound velocity bound and neutron stars". In: *Phys. Rev. Lett.* 114.3 (2015), p. 031103. DOI: 10.1103/PhysRevLett.114.031103. arXiv: 1408.5116 [nucl-th].

[20] Sebastiano Bernuzzi. "Neutron Star Merger Remnants". In: *Gen. Rel. Grav.* 52.11 (2020), p. 108. DOI: 10.1007/s10714-020-02752-5. arXiv: 2004.06419 [astro-ph.HE].

[21] Bhaskar Biswas. "Impact of PREX-II, the revised mass measurement of PSRJ0740+6620, and possible NICER observation on the dense matter equation of state". In: (May 2021). arXiv: 2105.02886 [astro-ph.HE].

[22] Bhaskar Biswas et al. "GW190814: on the properties of the secondary component of the binary". In: *Mon. Not. Roy. Astron. Soc.* 505.2 (2021), pp. 1600–1606. DOI: 10.1093/mnras/stab1383. arXiv: 2010.02090 [astro-ph.HE].

[23] Bhaskar Biswas et al. "Towards mitigation of apparent tension between nuclear physics and astrophysical observations by improved modeling of neutron star matter". In: *Phys. Rev. D* 103.10 (2021), p. 103015. DOI: 10.1103/PhysRevD.103.103015. arXiv: 2008.01582 [astro-ph.HE].

[24] Slavko Bogdanov et al. "Constraining the Neutron Star Mass–Radius Relation and Dense Matter Equation of State with NICER. III. Model Description and Verification of Parameter Estimation Codes". In: (Apr. 2021). arXiv: 2104.06928 [astro-ph.HE].

[25] Slavko Bogdanov et al. "Constraining the Neutron Star Mass–Radius Relation and Dense Matter Equation of State with *NICER*. I. The Millisecond Pulsar X-Ray Data Set". In: *Astrophys. J. Lett.* 887.1 (2019), p. L25. DOI: 10.3847/2041-8213/ab53eb. arXiv: 1912.05706 [astro-ph.HE].

[26] Slavko Bogdanov et al. "Constraining the Neutron Star Mass–Radius Relation and Dense Matter Equation of State with *NICER*. II. Emission from Hot Spots on a Rapidly Rotating Neutron Star". In: *Astrophys. J. Lett.* 887.1 (2019), p. L26. DOI: 10.3847/2041-8213/ab5968. arXiv: 1912.05707 [astro-ph.HE].

[27] B. Alex Brown. "Neutron radii in nuclei and the neutron equation of state". In: *Phys. Rev. Lett.* 85 (2000), pp. 5296–5299. DOI: 10.1103/PhysRevLett.85.5296.

[28] Katerina Chatziioannou. "Neutron star tidal deformability and equation of state constraints". In: *Gen. Rel. Grav.* 52.11 (2020), p. 109. DOI: 10.1007/s10714-020-02754-3. arXiv: 2006.03168 [gr-qc].

[29] Katerina Chatziioannou and Will M. Farr. "Inferring the maximum and minimum mass of merging neutron stars with gravitational waves". In: *Phys. Rev. D* 102.6 (2020), p. 064063. DOI: 10.1103/PhysRevD.102.064063. arXiv: 2005.00482 [astro-ph.HE].

[30] Katerina Chatziioannou and Sophia Han. "Studying strong phase transitions in neutron stars with gravitational waves". In: *Phys. Rev. D* 101.4 (2020), p. 044019. DOI: 10.1103/PhysRevD.101.044019. arXiv: 1911.07091 [gr-qc].

[31] An Chen et al. "Distinguishing high-mass binary neutron stars from binary black holes with second- and third-generation gravitational wave observatories". In: *Phys. Rev. D* 101.10 (2020), p. 103008. DOI: 10.1103/PhysRevD.101.103008. arXiv: 2001.11470 [astro-ph.HE].

[32] Aleksey Cherman, Thomas D. Cohen, and Abhinav Nellore. "A Bound on the speed of sound from holography". In: *Phys. Rev. D* 80 (2009), p. 066003. DOI: 10.1103/PhysRevD.80.066003. arXiv: 0905.0903 [hep-th].

[33] CompStar Online Supernovae Equations of State (CompOSE). In: https://compose.obspm.fr. 2013. URL: %5Cmbox%7Bhttps://compose.obspm.fr%7D.

[34] Michael W. Coughlin et al. "Constraints on the neutron star equation of state from AT2017gfo using radiative transfer simulations". In: *Mon. Not. Roy. Astron. Soc.* 480.3 (2018), pp. 3871–3878. DOI: 10.1093/mnras/sty2174. arXiv: 1805.09371 [astro-ph.HE].

[35] Michael W. Coughlin et al. "Multimessenger Bayesian parameter inference of a binary neutron star merger". In: *Mon. Not. Roy. Astron. Soc.* 489.1 (2019), pp. L91–L96. DOI: 10.1093/mnrasl/slz133. arXiv: 1812.04803 [astro-ph.HE].

[36] H. Thankful Cromartie et al. "Relativistic Shapiro delay measurements of an extremely massive millisecond pulsar". In: *Nature Astron.* 4.1 (2019), pp. 72–76. DOI: 10.1038/s41550-019-0880-2. arXiv: 1904.06759.

[37] Paul Demorest et al. "Shapiro Delay Measurement of A Two Solar Mass Neutron Star". In: *Nature* 467 (2010), pp. 1081–1083. DOI: 10.1038/nature09466. arXiv: 1010.5788 [astro-ph.HE].

[38] V. Dexheimer et al. "GW190814 as a massive rapidly rotating neutron star with exotic degrees of freedom". In: *Phys. Rev. C* 103.2 (2021), p. 025808. DOI: 10.1103/PhysRevC.103.025808. arXiv: 2007.08493 [astro-ph.HE].

[39] Tim Dietrich et al. "Multimessenger constraints on the neutron-star equation of state and the Hubble constant". In: *Science* 370.6523 (2020), pp. 1450–1453. DOI: 10.1126/science.abb4317. arXiv: 2002.11355 [astro-ph.HE].

[40] C. Drischler et al. "How Well Do We Know the Neutron-Matter Equation of State at the Densities Inside Neutron Stars? A Bayesian Approach with Correlated Uncertainties". In: *Phys. Rev. Lett.* 125.20 (2020), p. 202702. DOI: 10.1103/PhysRevLett.125.202702. arXiv: 2004.07232 [nucl-th].

[41] C. Drischler et al. "Neutron matter from chiral two- and three-nucleon calculations up to N^3LO". In: *Phys. Rev. C* 94.5 (2016), p. 054307. DOI: 10.1103/PhysRevC.94.054307. arXiv: 1608.05615 [nucl-th].

[42] C. Drischler et al. "Quantifying uncertainties and correlations in the nuclear-matter equation of state". In: *Phys. Rev. C* 102.5 (2020), p. 054315. DOI: 10.1103/PhysRevC.102.054315. arXiv: 2004.07805 [nucl-th].

[43] Christian Drischler et al. "Limiting masses and radii of neutron stars and their implications". In: *Phys. Rev. C* 103.4 (2021), p. 045808. DOI: 10.1103/PhysRevC.103.045808. arXiv: 2009.06441 [nucl-th].

[44] R. Essick et al. In: (in preparation).

[45] Reed Essick and Philippe Landry. "Discriminating between Neutron Stars and Black Holes with Imperfect Knowledge of the Maximum Neutron Star Mass". In: *Astrophys. J.* 904.1 (2020), p. 80. DOI: 10.3847/1538-4357/abbd3b. arXiv: 2007.01372 [astro-ph.HE].

[46] Reed Essick, Philippe Landry, and Daniel E. Holz. "Nonparametric Inference of Neutron Star Composition, Equation of State, and Maximum Mass with GW170817". In: *Phys. Rev. D* 101.6 (2020), p. 063007. DOI: 10.1103/PhysRevD.101.063007. arXiv: 1910.09740 [astro-ph.HE].

[47] Reed Essick et al. "A Detailed Examination of Astrophysical Constraints on the Symmetry Energy and the Neutron Skin of ^{208}Pb with Minimal Modeling Assumptions". In: (July 2021). arXiv: 2107.05528 [nucl-th].

[48] Reed Essick et al. "Astrophysical Constraints on the Symmetry Energy and the Neutron Skin of ^{208}Pb with Minimal Modeling Assumptions". In: (Feb. 2021). arXiv: 2102.10074 [nucl-th].

[49] Reed Essick et al. "Direct Astrophysical Tests of Chiral Effective Field Theory at Supranuclear Densities". In: *Phys. Rev. C* 102.5 (2020), p. 055803. DOI: 10.1103/PhysRevC.102.055803. arXiv: 2004.07744 [astro-ph.HE].

[50] J. Estee et al. "Probing the Symmetry Energy with the Spectral Pion Ratio". In: *Phys. Rev. Lett.* 126.16 (2021), p. 162701. DOI: 10.1103/PhysRevLett.126.162701. arXiv: 2103.06861.

[51] Will M. Farr and Katerina Chatziioannou. "A Population-Informed Mass Estimate for Pulsar J0740+6620". In: *Research Notes of the American Astronomical Society* 4.5, 65 (May 2020), p. 65. DOI: 10.3847/2515-5172/ab9088. arXiv: 2005.00032 [astro-ph.GA].

[52] Will M. Farr et al. "The Mass Distribution of Stellar-Mass Black Holes". In: *Astrophys. J.* 741 (2011), p. 103. DOI: 10.1088/0004-637X/741/2/103. arXiv: 1011.1459 [astro-ph.GA].

[53] Nicholas Farrow, Xing-Jiang Zhu, and Eric Thrane. "The mass distribution of Galactic double neutron stars". In: *Astrophys. J.* 876.1 (2019), p. 18. DOI: 10.3847/1538-4357/ab12e3. arXiv: 1902.03300 [astro-ph.HE].

[54] F. J. Fattoyev, J. Piekarewicz, and C. J. Horowitz. "Neutron Skins and Neutron Stars in the Multimessenger Era". In: *Phys. Rev. Lett.* 120.17 (2018), p. 172702. DOI: 10.1103/PhysRevLett.120.172702. arXiv: 1711.06615 [nucl-th].

[55] F. J. Fattoyev et al. "GW190814: Impact of a 2.6 solar mass neutron star on the nucleonic equations of state". In: *Phys. Rev. C* 102.6 (2020), p. 065805. DOI: 10.1103/PhysRevC.102.065805. arXiv: 2007.03799 [nucl-th].

[56] Maya Fishbach, Reed Essick, and Daniel E. Holz. "Does Matter Matter? Using the mass distribution to distinguish neutron stars and black holes". In: *Astrophys. J. Lett.* 899 (2020), p. L8. DOI: 10.3847/2041-8213/aba7b6. arXiv: 2006.13178 [astro-ph.HE].

[57] Eanna E. Flanagan and Tanja Hinderer. "Constraining neutron star tidal Love numbers with gravitational wave detectors". In: *Phys. Rev. D* 77 (2008), p. 021502. DOI: 10.1103/PhysRevD.77.021502. arXiv: 0709.1915 [astro-ph].

[58] E. Fonseca et al. "Refined Mass and Geometric Measurements of the High-mass PSR J0740+6620". In: *Astrophys. J. Lett.* 915.1 (2021), p. L12. DOI: 10.3847/2041-8213/ac03b8. arXiv: 2104.00880 [astro-ph.HE].

[59] Emmanuel Fonseca et al. "The NANOGrav Nine-year Data Set: Mass and Geometric Measurements of Binary Millisecond Pulsars". In: *Astrophys. J.* 832.2 (2016), p. 167. DOI: 10.3847/0004-637X/832/2/167. arXiv: 1603.00545 [astro-ph.HE].

[60] S. Gandolfi, J. Carlson, and Sanjay Reddy. "The maximum mass and radius of neutron stars and the nuclear symmetry energy". In: *Phys. Rev. C* 85 (2012), 032801(R). DOI: 10.1103/PhysRevC.85.032801. arXiv: 1101.1921.

[61] S. K. Greif et al. "Equation of state sensitivities when inferring neutron star and dense matter properties". In: *Mon. Not. Roy. Astron. Soc.* 485.4 (2019), pp. 5363–5376. DOI: 10.1093/mnras/stz654. arXiv: 1812.08188 [astro-ph.HE].

[62] Ming-Zhe Han et al. "Bayesian nonparametric inference of neutron star equation of state via neural network". In: (Mar. 2021). arXiv: 2103.05408 [hep-ph].

[63] Sophia Han and Madappa Prakash. "On the Minimum Radius of Very Massive Neutron Stars". In: *Astrophys. J.* 899.2 (2020), p. 164. DOI: 10.3847/1538-4357/aba3c7. arXiv: 2006.02207 [astro-ph.HE].

[64] Sophia Han and Andrew W. Steiner. "Tidal deformability with sharp phase transitions in (binary) neutron stars". In: *Phys. Rev. D* 99.8 (2019), p. 083014. DOI: 10.1103/PhysRevD.99.083014. arXiv: 1810.10967 [nucl-th].

[65] Sophia Han et al. "Treating quarks within neutron stars". In: *Phys. Rev. D* 100.10 (2019), p. 103022. DOI: 10.1103/PhysRevD.100.103022. arXiv: 1906.04095 [astro-ph.HE].

[66] Tanja Hinderer. "Tidal Love numbers of neutron stars". In: *Astrophys. J.* 677 (2008), pp. 1216–1220. DOI: 10.1086/533487. arXiv: 0711.2420 [astro-ph].

[67] Tanja Hinderer et al. "Tidal deformability of neutron stars with realistic equations of state and their gravitational wave signatures in binary inspiral". In: *Phys. Rev. D* 81 (2010), p. 123016. DOI: 10.1103/PhysRevD.81.123016. arXiv: 0911.3535 [astro-ph.HE].

[68] Jin-Liang Jiang et al. "PSR J0030+0451, GW170817 and the nuclear data: joint constraints on equation of state and bulk properties of neutron stars". In: *Astrophys. J.* 892 (2020), p. 1. DOI: 10.3847/1538-4357/ab77cf. arXiv: 1912.07467 [astro-ph.HE].

[69] Vassiliki Kalogera and Gordon Baym. "The maximum mass of a neutron star". In: *Astrophys. J. Lett.* 470 (1996), pp. L61–L64. DOI: 10.1086/310296. arXiv: astro-ph/9608059.

[70] M. H. van Kerkwijk, R. Breton, and S. R. Kulkarni. "Evidence for a Massive Neutron Star from a Radial-Velocity Study of the Companion to the Black Widow Pulsar PSR B1957+20". In: *Astrophys. J.* 728 (2011), p. 95. DOI: 10.1088/0004-637X/728/2/95. arXiv: 1009.5427 [astro-ph.HE].

[71] Kenta Kiuchi et al. "Revisiting the lower bound on tidal deformability derived by AT 2017gfo". In: *Astrophys. J. Lett.* 876.2 (2019), p. L31. DOI: 10.3847/2041-8213/ab1e45. arXiv: 1903.01466 [astro-ph.HE].

[72] Bülent Kiziltan et al. "The Neutron Star Mass Distribution". In: *Astrophys. J.* 778 (2013), p. 66. DOI: 10.1088/0004-637X/778/1/66. arXiv: 1309.6635 [astro-ph.SR].

[73] Laura Kreidberg et al. "Mass Measurements of Black Holes in X-Ray Transients: Is There a Mass Gap?" In: *Astrophys. J.* 757 (2012), p. 36. DOI: 10.1088/0004-637X/757/1/36. arXiv: 1205.1805 [astro-ph.HE].

[74] Bharat Kumar and Philippe Landry. "Inferring neutron star properties from GW170817 with universal relations". In: *Phys. Rev. D* 99.12 (2019), p. 123026. DOI: 10.1103/PhysRevD.99.123026. arXiv: 1902.04557 [gr-qc].

[75] Aleksi Kurkela, Paul Romatschke, and Aleksi Vuorinen. "Cold Quark Matter". In: *Phys. Rev. D* 81 (2010), p. 105021. DOI: 10.1103/PhysRevD.81.105021. arXiv: 0912.1856 [hep-ph].

[76] Philippe Landry and Reed Essick. "Nonparametric inference of the neutron star equation of state from gravitational wave observations". In: *Phys. Rev. D* 99.8 (2019), p. 084049. DOI: 10.1103/PhysRevD.99.084049. arXiv: 1811.12529 [gr-qc].

[77] Philippe Landry, Reed Essick, and Katerina Chatziioannou. "Nonparametric constraints on neutron star matter with existing and upcoming gravitational wave and pulsar observations". In: *Phys. Rev. D* 101.12 (2020), p. 123007. DOI: 10.1103/PhysRevD.101.123007. arXiv: 2003.04880 [astro-ph.HE].

[78] Philippe Landry, Reed Essick, and Katerina Chatziioannou. *Nonparametric constraints on neutron star matter with existing and upcoming gravitational wave and pulsar observations: Weighted Monte Carlo samples for neutron star observables*. Version v1.0.0. Zenodo, Apr. 2021. DOI: 10.5281/zenodo.4678703. URL: https://doi.org/10.5281/zenodo.4678703.

[79] J. M. Lattimer and M. Prakash. "Neutron star structure and the equation of state". In: *Astrophys. J.* 550 (2001), p. 426. DOI: 10.1086/319702. arXiv: astro-ph/0002232.

[80] James M. Lattimer and Madappa Prakash. "The Equation of State of Hot, Dense Matter and Neutron Stars". In: *Phys. Rept.* 621 (2016), pp. 127–164. DOI: 10.1016/j.physrep.2015.12.005. arXiv: 1512.07820 [astro-ph.SR].

[81] I. Legred et al. In: (in preparation).

[82] LIGO Scientific Collaboration. "Parameter estimation sample release for GW190425". In: *https://dcc.ligo.org/LIGO-P2000026/public* (2020). URL: https://dcc.ligo.org/LIGO-P2000026/public.

[83] LIGO Scientific Collaboration. "Properties of the binary neutron star merger GW170817". In: *https://dcc.ligo.org/LIGO-P1800061/public* (2018). URL: https://dcc.ligo.org/LIGO-P1800061/public.

[84] Lee Lindblom. "Spectral Representations of Neutron-Star Equations of State". In: *Phys. Rev. D* 82 (2010), p. 103011. DOI: 10.1103/PhysRevD.82.103011. arXiv: 1009.0738 [astro-ph.HE].

[85] Thomas J. Loredo. "Accounting for source uncertainties in analyses of astronomical survey data". In: *AIP Conf. Proc.* 735.1 (2004). Ed. by Rainer Fischer, Roland Preuss, and Udo von Toussaint, pp. 195–206. DOI: 10.1063/1.1835214. arXiv: astro-ph/0409387.

[86] Ilya Mandel, Will M. Farr, and Jonathan R. Gair. "Extracting distribution parameters from multiple uncertain observations with selection biases". In: *Mon. Not. Roy. Astron. Soc.* 486.1 (2019), pp. 1086–1093. DOI: 10.1093/mnras/stz896. arXiv: 1809.02063 [physics.data-an].

[87] Ben Margalit and Brian D. Metzger. "Constraining the Maximum Mass of Neutron Stars From Multi-Messenger Observations of GW170817". In: *Astrophys. J.* 850.2 (2017), p. L19. DOI: 10.3847/2041-8213/aa991c. arXiv: 1710.05938 [astro-ph.HE].

[88] Larry McLerran and Sanjay Reddy. "Quarkyonic Matter and Neutron Stars". In: *Phys. Rev. Lett.* 122.12 (2019), p. 122701. DOI: 10.1103/PhysRevLett.122.122701. arXiv: 1811.12503 [nucl-th].

[89] M. C. Miller et al. "PSR J0030+0451 Mass and Radius from *NICER* Data and Implications for the Properties of Neutron Star Matter". In: *Astrophys. J. Lett.* 887.1 (2019), p. L24. DOI: 10.3847/2041-8213/ab50c5. arXiv: 1912.05705 [astro-ph.HE].

[90] M. C. Miller et al. "The Radius of PSR J0740+6620 from NICER and XMM-Newton Data". In: (May 2021). arXiv: 2105.06979 [astro-ph.HE].

[91] M. C. Miller et al. *NICER PSR J0030+0451 Illinois-Maryland MCMC Samples*. Version 1.0.0. Zenodo, Dec. 2019. DOI: 10.5281/zenodo.3473466. URL: https://doi.org/10.5281/zenodo.3473466.

[92] M.C. Miller et al. *NICER PSR J0740+6620 Illinois-Maryland MCMC Samples*. Zenodo, Apr. 2021. DOI: 10.5281/zenodo.4670689. URL: https://doi.org/10.5281/zenodo.4670689.

[93] J. Nättilä et al. "Equation of state constraints for the cold dense matter inside neutron stars using the cooling tail method". In: *Astron. Astrophys.* 591 (2016), A25. DOI: 10.1051/0004-6361/201527416. arXiv: 1509.06561 [astro-ph.HE].

[94] J. Nättilä et al. "Neutron star mass and radius measurements from atmospheric model fits to X-ray burst cooling tail spectra". In: *Astron. Astrophys.* 608 (2017), A31. DOI: 10.1051/0004-6361/201731082. arXiv: 1709.09120 [astro-ph.HE].

[95] M. Oertel et al. "Equations of state for supernovae and compact stars". In: *Rev. Mod. Phys.* 89.1 (2017), p. 015007. DOI: 10.1103/RevModPhys.89.015007. arXiv: 1610.03361 [astro-ph.HE].

[96] J.R. Oppenheimer and G.M. Volkoff. "On Massive neutron cores". In: *Phys. Rev.* 55 (1939), pp. 374–381. DOI: 10.1103/PhysRev.55.374.

[97] Feryal Ozel et al. "The Dense Matter Equation of State from Neutron Star Radius and Mass Measurements". In: *Astrophys. J.* 820.1 (2016), p. 28. DOI: 10.3847/0004-637X/820/1/28. arXiv: 1505.05155 [astro-ph.HE].

[98] F. Özel and P. Freire. "Masses, Radii, and the Equation of State of Neutron Stars". In: *Ann. Rev. Astron. Astrophys.* 54 (2016), pp. 401–440. DOI: 10.1146/annurev-astro-081915-023322. arXiv: 1603.02698 [astro-ph.HE].

[99] Feryal Özel et al. "On the Mass Distribution and Birth Masses of Neutron Stars". In: *The Astrophysical Journal* 757.1, 55 (Sept. 2012), p. 55. DOI: 10.1088/0004-637X/757/1/55. arXiv: 1201.1006 [astro-ph.HE].

[100] Peter T. H. Pang et al. "Nuclear-Physics Multi-Messenger Astrophysics Constraints on the Neutron-Star Equation of State: Adding NICER's PSR J0740+6620 Measurement". In: (May 2021). arXiv: 2105.08688 [astro-ph.HE].

[101] G. Raaijmakers et al. “Constraining the dense matter equation of state with joint analysis of NICER and LIGO/Virgo measurements”. In: *Astrophys. J. Lett.* 893.1 (2020), p. L21. DOI: 10.3847/2041-8213/ab822f. arXiv: 1912.11031 [astro-ph.HE].

[102] G. Raaijmakers et al. “Constraints on the dense matter equation of state and neutron star properties from NICER’s mass-radius estimate of PSR J0740+6620 and multimessenger observations”. In: (May 2021). arXiv: 2105.06981 [astro-ph.HE].

[103] David Radice and Liang Dai. “Multimessenger Parameter Estimation of GW170817”. In: *Eur. Phys. J. A* 55.4 (2019), p. 50. DOI: 10.1140/epja/i2019-12716-4. arXiv: 1810.12917 [astro-ph.HE].

[104] David Radice et al. “GW170817: Joint Constraint on the Neutron Star Equation of State from Multimessenger Observations”. In: *Astrophys. J.* 852.2 (2018), p. L29. DOI: 10.3847/2041-8213/aaa402. arXiv: 1711.03647 [astro-ph.HE].

[105] Jocelyn S. Read et al. “Constraints on a phenomenologically parameterized neutron-star equation of state”. In: *Phys. Rev. D* 79 (2009), p. 124032. DOI: 10.1103/PhysRevD.79.124032. arXiv: 0812.2163 [astro-ph].

[106] Brendan Reed and C. J. Horowitz. “Large sound speed in dense matter and the deformability of neutron stars”. In: *Phys. Rev. C* 101.4 (2020), p. 045803. DOI: 10.1103/PhysRevC.101.045803. arXiv: 1910.05463 [astro-ph.HE].

[107] Brendan T. Reed et al. “Implications of PREX-2 on the Equation of State of Neutron-Rich Matter”. In: *Phys. Rev. Lett.* 126.17 (2021), p. 172503. DOI: 10.1103/PhysRevLett.126.172503. arXiv: 2101.03193 [nucl-th].

[108] Paul-Gerhard Reinhard, Xavier Roca-Maza, and Witold Nazarewicz. “Information content of the parity-violating asymmetry in ^{208}Pb”. In: (May 2021). arXiv: 2105.15050 [nucl-th].

[109] Luciano Rezzolla, Elias R. Most, and Lukas R. Weih. “Using gravitational-wave observations and quasi-universal relations to constrain the maximum mass of neutron stars”. In: *Astrophys. J. Lett.* 852.2 (2018), p. L25. DOI: 10.3847/2041-8213/aaa401. arXiv: 1711.00314 [astro-ph.HE].

[110] Clifford E. Rhoades Jr. and Remo Ruffini. “Maximum mass of a neutron star”. In: *Phys. Rev. Lett.* 32 (1974), pp. 324–327. DOI: 10.1103/PhysRevLett.32.324.

[111] Thomas E. Riley et al. “A *NICER* View of PSR J0030+0451: Millisecond Pulsar Parameter Estimation”. In: *Astrophys. J. Lett.* 887.1 (2019), p. L21. DOI: 10.3847/2041-8213/ab481c. arXiv: 1912.05702 [astro-ph.HE].

[112] Thomas E. Riley et al. "A NICER View of the Massive Pulsar PSR J0740+6620 Informed by Radio Timing and XMM-Newton Spectroscopy". In: (May 2021). arXiv: 2105.06980 [astro-ph.HE].

[113] Thomas E. Riley et al. *A NICER View of PSR J0030+0451: Nested Samples for Millisecond Pulsar Parameter Estimation*. Version v1.0.0. Zenodo, Dec. 2019. DOI: 10.5281/zenodo.3386449. URL: https://doi.org/10.5281/zenodo.3386449.

[114] Thomas E. Riley et al. *A NICER View of the Massive Pulsar PSR J0740+6620 Informed by Radio Timing and XMM-Newton Spectroscopy: Nested Samples for Millisecond Pulsar Parameter Estimation*. Version v1.0.0. Zenodo, Apr. 2021. DOI: 10.5281/zenodo.4697625. URL: https://doi.org/10.5281/zenodo.4697625.

[115] X. Roca-Maza et al. "Neutron skin of ^{208}Pb, nuclear symmetry energy, and the parity radius experiment". In: *Phys. Rev. Lett.* 106 (2011), p. 252501. DOI: 10.1103/PhysRevLett.106.252501. arXiv: 1103.1762 [nucl-th].

[116] X. Roca-Maza et al. "The neutron skin thickness from the measured electric dipole polarizability in ^{68}Ni, ^{120}Sn, and ^{208}Pb". In: *Phys. Rev. C* 92 (2015), p. 064304. DOI: 10.1103/PhysRevC.92.064304. arXiv: 1510.01874 [nucl-th].

[117] Milton Ruiz, Stuart L. Shapiro, and Antonios Tsokaros. "GW170817, General Relativistic Magnetohydrodynamic Simulations, and the Neutron Star Maximum Mass". In: *Phys. Rev. D* 97.2 (2018), p. 021501. DOI: 10.1103/PhysRevD.97.021501. arXiv: 1711.00473 [astro-ph.HE].

[118] Daniel J. Schad et al. "Workflow Techniques for the Robust Use of Bayes Factors". In: (Mar. 2021). arXiv: 2103.08744 [stat.ME].

[119] K. Schertler et al. "Quark phases in neutron stars and a 'third family' of compact stars as a signature for phase transitions". In: *Nucl. Phys. A* 677 (2000), pp. 463–490. DOI: 10.1016/S0375-9474(00)00305-5. arXiv: astro-ph/0001467 [astro-ph].

[120] Masaru Shibata et al. "Constraint on the maximum mass of neutron stars using GW170817 event". In: *Phys. Rev. D* 100.2 (2019), p. 023015. DOI: 10.1103/PhysRevD.100.023015. arXiv: 1905.03656 [astro-ph.HE].

[121] Masaru Shibata et al. "Modeling GW170817 based on numerical relativity and its implications". In: *Phys. Rev. D* 96.12 (2017), p. 123012. DOI: 10.1103/PhysRevD.96.123012. arXiv: 1710.07579 [astro-ph.HE].

[122] Rahul Somasundaram and Jérôme Margueron. "Impact of massive neutron star radii on the nature of phase transitions in dense matter". In: (Apr. 2021). arXiv: 2104.13612 [astro-ph.HE].

[123] A. W. Steiner et al. “Constraining the Mass and Radius of Neutron Stars in Globular Clusters”. In: *Mon. Not. Roy. Astron. Soc.* 476.1 (2018), pp. 421–435. DOI: 10.1093/mnras/sty215. arXiv: 1709.05013 [astro-ph.HE].

[124] Hung Tan, Jacquelyn Noronha-Hostler, and Nico Yunes. “Neutron Star Equation of State in light of GW190814”. In: *Phys. Rev. Lett.* 125.26 (2020), p. 261104. DOI: 10.1103/PhysRevLett.125.261104. arXiv: 2006.16296 [astro-ph.HE].

[125] Ingo Tews et al. “Constraining the speed of sound inside neutron stars with chiral effective field theory interactions and observations”. In: *Astrophys. J.* 860.2 (2018), p. 149. DOI: 10.3847/1538-4357/aac267. arXiv: 1801.01923 [nucl-th].

[126] Ingo Tews et al. “On the Nature of GW190814 and Its Impact on the Understanding of Supranuclear Matter”. In: *Astrophys. J. Lett.* 908.1 (2021), p. L1. DOI: 10.3847/2041-8213/abdaae. arXiv: 2007.06057 [astro-ph.HE].

[127] Richard C. Tolman. “Static solutions of Einstein’s field equations for spheres of fluid”. In: *Phys. Rev.* 55 (1939), pp. 364–373. DOI: 10.1103/PhysRev.55.364.

[128] Leslie Wade et al. “Systematic and statistical errors in a bayesian approach to the estimation of the neutron-star equation of state using advanced gravitational wave detectors”. In: *Phys. Rev. D* 89.10 (2014), p. 103012. DOI: 10.1103/PhysRevD.89.103012. arXiv: 1402.5156 [gr-qc].

[129] Daniel Wysocki et al. “Inferring the neutron star equation of state simultaneously with the population of merging neutron stars”. In: (2020). arXiv: 2001.01747 [gr-qc].

[130] Tong-Gang Yue et al. “Constraints on the Symmetry Energy from PREX-II in the Multimessenger Era”. In: (Feb. 2021). arXiv: 2102.05267.

[131] Tianqi Zhao and James M. Lattimer. “Quarkyonic Matter Equation of State in Beta-Equilibrium”. In: *Phys. Rev. D* 102.2 (2020), p. 023021. DOI: 10.1103/PhysRevD.102.023021. arXiv: 2004.08293 [astro-ph.HE].

[132] Tianqi Zhao and James M. Lattimer. “Tidal Deformabilities and Neutron Star Mergers”. In: *Phys. Rev. D* 98.6 (2018), p. 063020. DOI: 10.1103/PhysRevD.98.063020. arXiv: 1808.02858 [astro-ph.HE].

Chapter 4

SEARCHING FOR PHASE TRANSITIONS IN THE EQUATION OF STATE USING NONPARAMETRIC MODELS

[1] Reed Essick et al. "Phase transition phenomenology with nonparametric representations of the neutron star equation of state". In: *Phys. Rev. D* 108.4 (2023). I contributed substantially to this study which used nonparametric methods to constrain phase transitions in a nonparametric model of the equation of state. I performed the simulation analyses, developed several diagnostic statistics, and wrote large parts of the text., p. 043013. DOI: 10.1103/PhysRevD.108.043013. arXiv: 2305.07411 [astro-ph.HE].

Abstract

Astrophysical observations of neutron stars probe the structure of dense nuclear matter and have the potential to reveal phase transitions at high densities. Most recent analyses are based on parametrized models of the equation of state with a finite number of parameters and occasionally include extra parameters intended to capture phase transition phenomenology. However, such models restrict the types of behavior allowed and may not match the true equation of state. We introduce a complementary approach that extracts phase transitions directly from the equation of state without relying on, and thus being restricted by, an underlying parametrization. We then constrain the presence of phase transitions in neutron stars with astrophysical data. Current pulsar mass, tidal deformability, and mass-radius measurements disfavor only the strongest of possible phase transitions (latent energy per particle $\gtrsim 100\,\mathrm{MeV}$). Weaker phase transitions are consistent with observations. We further investigate the prospects for measuring phase transitions with future gravitational-wave observations and find that catalogs of $O(100)$ events will (at best) yield Bayes factors of $\sim 10:1$ in favor of phase transitions even when the true equation of state contains very strong phase transitions. Our results reinforce the idea that neutron star observations will primarily constrain trends in macroscopic properties rather than detailed microscopic behavior. Fine-tuned equation of state models will likely remain unconstrained in the near future.

4.1 Introduction

Recent astronomical data, such as gravitational waves (GWs) from coalescing neutron star (NS) binaries [6, 3] observed by LIGO [1] and Virgo [9], X-ray pulse profiles from hotspots on rotating NSs observed by NICER [77, 90, 78, 91], and mass measurements for heavy radio pulsars [20, 34, 44], have advanced our understanding of matter at supranuclear densities [2, 68, 84, 87, 88, 24, 62, 36, 69]. Nonetheless, there is still considerable uncertainty in the equation of state (EoS) of cold, dense matter, which relates the pressure p to the energy density ε, or rest-mass density ρ. The data favor a sound speed $c_s = \sqrt{dp/d\varepsilon}$ that exceeds the conjectured conformal bound of $\sqrt{1/3}$ expected for weakly interacting ultra-relativistic particles [23, 76, 68, 69]. The potential violation of this bound at high densities may point to a state of matter with strongly coupled interactions.

Such strong couplings call into question the accuracy of perturbative expansions of interactions between neutrons, protons, and pions at high densities, and raise the possibility that other degrees of freedom may be a more natural description. Theoretical studies have investigated whether the smooth crossover from hadron resonance gas to quark-gluon plasma observed with lattice quantum chromodynamics (QCD) at low baryon chemical potential and high temperature implies the existence of a critical endpoint in the QCD phase diagram [22] and how EoS calculations at low density and temperature connect to perturbative QCD (pQCD) calculations at high densities ($\sim$ 40 times nuclear saturation $\rho_{\rm nuc}$) [64, 52, 99]. Other work predicts a variety of phase transitions stemming from a range of microphysical descriptions for dense matter [96, 50, 95, 13, 106, 61, 49, 22, 76, 15].

Many theorized phase transitions in NS matter are characterized by a softening of the EoS, i.e., a decrease in c_s. This occurs because the NS is supported by degeneracy pressure, and additional degrees of freedom (e.g., hyperons or quarks) initially do not contribute significantly to the pressure due to their low number density n. This manifests as an interval of nearly constant pressure (small c_s) over a density range in which the new degrees of freedom first appear. A decrease in pressure support relative to an EoS without a phase transition leads to more compact NSs. Such compactification can lead to bends or kinks in the relation between macroscopic observables, such as the gravitational mass M, radius R, tidal deformability Λ, and moment of inertia I. The strongest phase transitions can even give rise to disconnected sequences of stable NSs separated by a range of central densities for which no stable NSs exist. This manifests as, e.g., two or more disconnected branches in the M-R relation and twin stars with the same mass but different radii [72, 94, 97, 96, 14, 16, 59, 80]. Moreover, the relative loss of pressure support from the phase transition often reduces the maximum mass (M_{TOV}) for cold, non-rotating NSs.

Current observational evidence for a sudden softening in the EoS is inconclusive. Both the PREX neutron skin measurement [10] and the existence of $2\,\mathrm{M}_{\odot}$ pulsars [44] suggest a relatively stiff EoS (near ρ_{nuc} and above $\sim 3\rho_{\mathrm{nuc}}$, respectively). In contrast, the relatively small tidal deformability of GW170817 points to a moderately soft EoS around $\sim 2\rho_{\mathrm{nuc}}$ [2, 69]. While this stiff–soft–stiff sequence resembles the morphology of a phase transition, the actual statistical evidence for or against this scenario remains inconclusive [69, 84, 54]. Furthermore, while observations favor a violation of the conformal bound around $\sim 3\rho_{\mathrm{nuc}}$, they do not strictly rule out EoSs with $c_s \leq \sqrt{1/3}$ at higher densities [69]. Additionally, the CREX collaboration's neutron skin measurement favors lower pressures near ρ_{nuc} than PREX [11]. At present, consistency between *ab initio* theoretical models, laboratory experiments, and astrophysical data within statistical uncertainties does not require a phase transition [40, 39].

Several features of NSs' macroscopic properties have been proposed as a way to identify a phase transition in NS matter with forthcoming GW observations. During a compact binary's inspiral (before the objects touch), the relevant observable is the (adiabatic or static) tidal deformability [43, 104, 28], which is strongly correlated with the radius. Both are expected to be smaller for NSs with exotic cores than their nucleonic counterparts. Chen, Chesler, and Loeb [31] leveraged this fact to search for phase transitions via a change in the slope of the inferred M–R relation, parametrized as a piecewise linear function. Chatziioannou and Han [29] pursued a related method, modeling the detected binary merger population hierarchically and searching for a subpopulation with smaller radii. Parametrizing the M–Λ relation itself, Landry and Chakravarti [66] sought to identify twin stars in the binary NS population based on gaps in the joint distribution of masses and binary tidal deformabilities. Proposals for identifying phase transitions based on the presence of disconnected stable branches in the M–R or M–Λ relation, independently of a parametrization, have also been investigated [38, 84, 69]. However, approaches that directly model macroscopic observables cannot easily enforce physical precepts like causality and thermodynamic stability, nor do they offer an obvious pathway to microscopic EoS properties. At best, one can constrain proxies for microphysical phase transitions, such as the difference between radii at different masses, e.g., $\Delta R \equiv R_{1.4} - R_{2.0}$ [37, 84, 88, 69]. Moreover, macroscopic signatures test a sufficient, but not necessary, condition for exotic phases. A phase transition may not be strong enough to leave a measurable imprint on NS observables. This ambiguity is known as the masquerade problem [13].

An alternative approach is to directly model the EoS and connect it to macroscopic NS observables by solving the Tolman-Oppenheimer-Volkoff (TOV) equations [103, 83]. A plethora of phenomenological EoS parametrizations adapted to phase transitions have been proposed [14, 54, 101]. For example, Pang et al. [85] modeled the EoS as a piecewise polytrope, including a segment with vanishing adiabatic index ($c_s = 0$) to represent the phase transition. They performed model selection on a catalog of simulated GW observations to test whether they favored the presence of a phase transition. Tan et al. [101] performed a similar analysis with a more complex parametric EoS model, which nonetheless retained the characteristic morphology of regions of large c_s bracketing a range of densities with small c_s. We discuss these and other approaches at length in Sec. 9.5.

However, it is also possible to model the EoS directly without introducing a parametrization. Flexible nonparametric models, such as the Gaussian process (GP) representation introduced in Refs. [67, 38, 68], avoid the *ad hoc* correlations across density scales that are inevitable in parametric representations with a finite number of parameters [70]. While some interdensity correlations are desirable (e.g., those dictated by causality, thermodynamic stability, or predictions from nuclear theory), phenomenological parametric models implicitly impose much stronger prior assumptions by virtue of their chosen functional form. Nonparametric models need not impose such correlations. They can also provide a faithful representation of theoretical uncertainty at low densities without sacrificing model flexibility at high densities [41, 40, 39]. However, the lack of phenomenological parameters can make it difficult to map features in the EoS to underlying microphysics. In order to address this, a generic mapping from the EoS to a set of physically interpretable microscopic parameters is needed.

We develop such a mapping: a phenomenological approach to identifying physically meaningful properties of phase transitions via softening in the EoS. We show that a nonparametric model's lack of obvious physically interpretable parameters does not fundamentally limit its utility for inferences about phase transitions in NSs. We propose and test model-independent features that characterize a broad range of phase

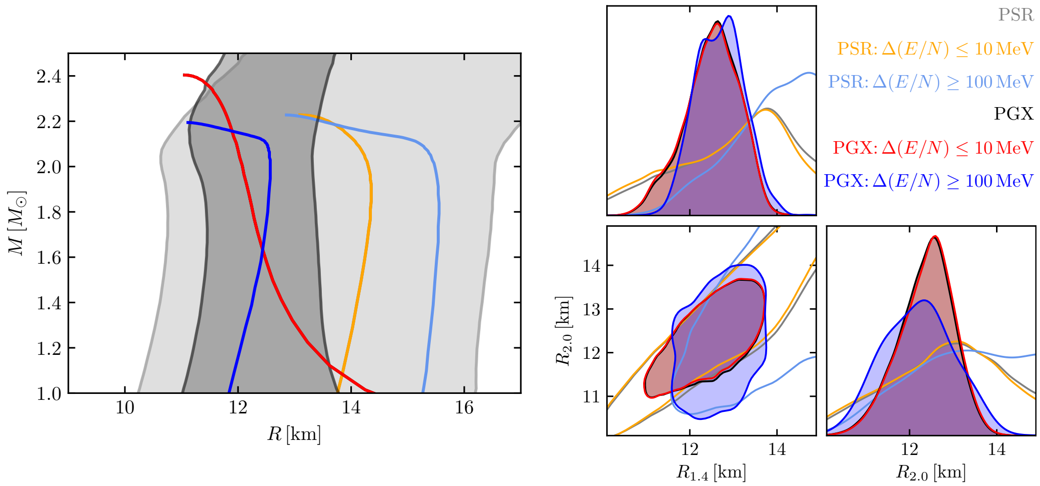

Figure 4.1: (*left*) one-dimensional 90% symmetric marginal posterior credible regions for the radius as a function of mass conditioned on current data. We show results with only pulsar masses (denoted PSR) and pulsar masses, GW observations, and NICER X-ray pulse profiling (denoted PGX). We additionally show maximum-likelihood EoSs from subsets of the prior conditioned on the size of the latent energy per particle $\Delta(E/N)$ of phase transitions that overlap with the central densities of NSs between 1.1–2.3 $\mathrm{M}_\odot$ (*small*: $\Delta(E/N) \leq 10\,\mathrm{MeV}$ and *large*: $\Delta(E/N) \geq 100\,\mathrm{MeV}$). (*right*) Correlations between the radius at two reference masses: $M = 1.4$ and $2.0\,\mathrm{M}_\odot$. While the one-dimensional marginal distributions are similar, EoSs with small $\Delta(E/N)$ show stronger correlations between $R_{1.4}$ and $R_{2.0}$ than EoSs with large $\Delta(E/N)$. This is because the radius can change rapidly when $\Delta(E/N)$ is large, as is evident in the maximum-likelihood EoS.

transition phenomenology. Our procedure goes beyond existing nonparametric tests based on the number of distinct stable NS sequences in the M–R (or M–Λ) relation [38, 68, 69] and enables us to directly extract information about the onset and strength of both large and weak phase transitions that respectively do and do not create multiple stable branches. As such, it provides an alternative to parametric phase transition inferences, whose inflexible parametrizations may introduce systematic biases if they do not closely match the true EoS [73, 55, 27, 70].

We introduce our methodology in Sec. 4.2. Section 4.2 reviews the basic phenomenology of phase transitions and, motivated by these considerations, Sec. 4.2 proposes novel features that can be used to identify the presence of a phase transition and extract physically relevant properties without the need for a direct parametrization. Our new features are based on the mass dependence of the moment of inertia (I) and the density dependence of the speed of sound, although similar features can also be derived from other macroscopic observables. We apply our methodology to current astrophysical data in Sec. 4.3. Current astrophysical data (Fig. 4.1) disfavor the strongest of possible phase transitions, but only when those transitions occur within NSs between $\sim$ 1–2 $M_\odot$. Even the presence of multiple stable branches cannot be unambiguously ruled out, although they are disfavored compared to EoS with a single branch and smaller phase transitions. Section 4.4 examines the prospects for detecting and characterizing phase transitions with large catalogs of simulated GW detections. We obtain Bayes factors of $\sim 10:1$ in favor of phase transitions with $O(10^2)$ events, a larger catalog than is likely [5] within the lifetime of advanced LIGO [1] and Virgo [9]. We discuss our conclusions in the context of previous studies in the literature as well as possible future research in Sec. 9.5.

4.2 Phenomenological identification of phase transitions

We begin by reviewing the basic phenomenology of phase transitions from microscopic and macroscopic perspectives in Sec. 4.2 and then introduce our novel model-independent features in Sec. 4.2. We discuss our ability to identify phase transitions in the context of the masquerade problem in Sec. 4.2.

Phase Transition Morphology

The basic phenomenology associated with the phase transitions we consider is a softening of the EoS over some density range. The following microscopic picture is often invoked. Consider two species of degenerate, noninteracting fermions with light (m_l) and heavy ($m_h > m_l$) rest masses, respectively. At zero temperature, the system will fill all states up to the Fermi energy (E_F) choosing between light and heavy fermions to balance their chemical potentials. The partial pressure contributed by each fermion will be determined by their respective number densities. The relation between E_F and the fermion rest masses then determines the system's composition.

If $E_F < m_h$, only light fermions exist. As the density increases, the pressure must increase as additional light fermions are added to high-momentum states. However, if $E_F \geq m_h$, heavy fermions in low-momentum states can become energetically favorable. These heavy fermions contribute to the rest-mass (and energy) density but have a much lower partial pressure due to their relatively low number density. The total pressure, then, remains nearly constant at the pressure set by the light fermions at E_F. This will continue until enough heavy fermions appear that a significant fraction of additional particles are light fermions (to balance the chemical potential

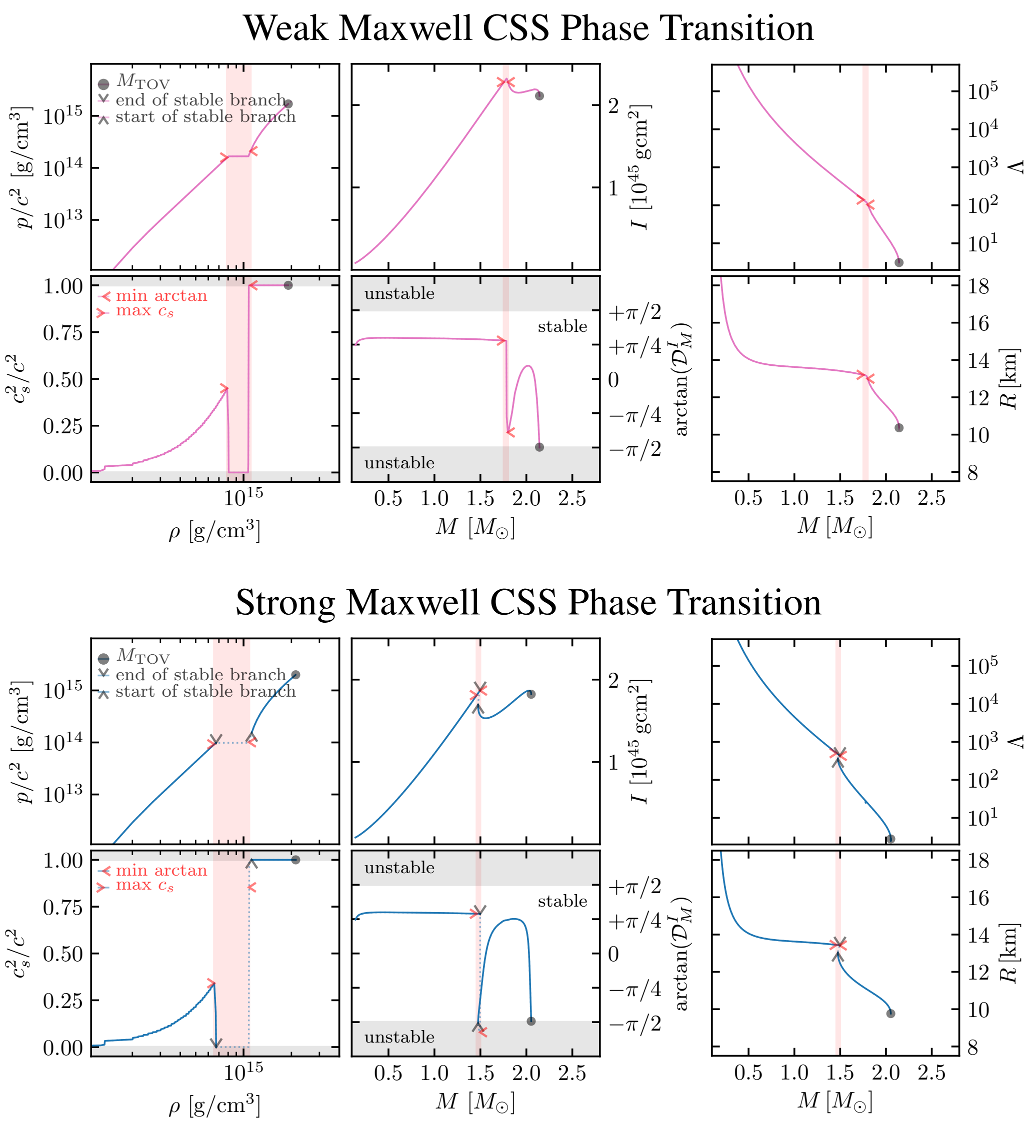

Figure 4.2: Examples of CSS EoSs based on DBHF [56] with a causal extension ($c_s = c$) beyond the end of the phase transition. We show examples with (*top*) weak and (*bottom*) strong phase transitions, defined by whether there are multiple stable branches. For each EoS, we show (*top left*) the pressure and (*bottom left*) the sound-speed as a function of baryon density, (*top center*) the moment of inertia and (*bottom center*) the novel feature introduced in Sec. 4.2 (Eq. (4.2)) as a function of gravitational mass, and (*top right*) the M–Λ and the (*bottom right*) M–R relations. Stable (unstable) branches are shown with dark solid (light dashed) lines. Each curve is labeled with connections between macroscopic phenomenology and microphysical features. (*black annotations*) The maximum mass of cold, non-rotating stars ($M_{\rm TOV}$) and, where relevant, the beginning and end of stable branches. (*red annotations*) The beginning and end of features as identified by the procedure in Sec. 4.2. (*red shading*) The extent of the identified features.

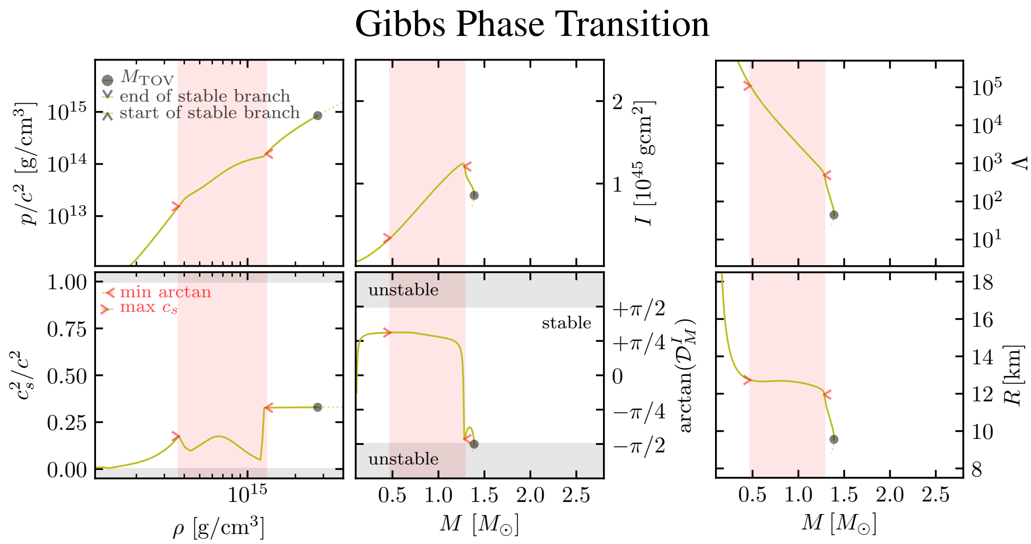

Figure 4.3: Analogous to Fig. 4.2 but for more complicated phase transition phenomenology associated with mixed phases (Gibbs construction) from Han et al. [60], obtained by implementing specific hadronic and quark models.. Again, the features introduced in Sec. 4.2 correctly identify the beginning and end of the phase transition even though there is no discontinuity in c_s at the onset and the phase transition corresponds to a wide range of masses. The broad extent of the phase transition is not readily apparent from the macroscopic properties alone, which show a sharp feature only at the end of the phase transition.

of heavy fermions) or the partial pressure of the heavy fermions becomes comparable to that of the light fermions. At that point, the pressure will once again increase with density.

The actual microphysics in a NS is complicated by interactions between particles, but the expected softening based on this heuristic picture is often present in more complicated models. Fig. 4.2 shows the typical behavior of a first-order phase transition with examples constructed from a hadronic model (DBHF [56]) at low densities and a constant sound-speed (CSS) extension [14] to higher densities. These EoSs have a sharp boundary separating the two different phases (Maxwell construction); ε is discontinuous across the boundary and c_s vanishes within the transition. The EoS in Fig. 4.3 employs a mixed phase (Gibbs) construction that exhibits more complicated sound-speed behavior [60], taking into account global charge neutrality (valid for small surface tension between the two phases [51]) when hadronic and quark matter coexist. The sound-speed decreases across the phase transition, but does not necessarily drop all the way to zero. The EoS also shows an approximately density-independent sound speed towards high densities (due to the specific vMIT model for the pure quark phase), which can be well represented by the generic CSS parametrization. In both figures, c_s initially increases at low densities, then suddenly decreases across the density range corresponding to the phase transition before recovering and plateauing at a value set by the CSS extension (Maxwell case) or by the microscopic model describing the high-density pure phase (Gibbs case).

While the microscopic details of the phases and their interface may vary, the phase transitions can be characterized phenomenologically by a few parameters, such as the onset density (or pressure) at which the phase transition begins, the density at which it ends, and the latent energy of the transition. We consider the difference in energy per particle across the phase transition

$$\Delta(E/N) \equiv \left(\frac{\varepsilon}{n}\right)_{\text{end}} - \left(\frac{\varepsilon}{n}\right)_{\text{onset}} . \tag{4.1}$$

We compute the energy per particle from the energy density ε and rest-mass density ρ assuming a typical nucleonic mass of $m_n = 938.5\,\text{MeV}$ via $E/N = m_n(\varepsilon/\rho)$.

We wish to associate these microscopic properties of the phase transition with the behavior of macroscopic observables (such as the masses and radii of NSs) that can be probed astronomically. Strong phase transitions can produce sharp features, such as bends or kinks, in the M–R relation. Figs. 4.1 and 4.2 show examples. However, EoSs with less abrupt phase transitions, such as the example in Fig. 4.3, may not have a perceptible impact on NS properties. Moreover, even if a bend or kink is readily apparent in, e.g., the M–R relation, it is not immediately clear how to best extract the relevant microphysical parameters of the phase transition.

Phase Transition Feature Extraction

We now introduce a set of statistics to identify phase-transition-like behavior in nonparametric EoS realizations. These statistics are motivated by common features observed in EoSs with phase transitions, such as the ones in Figs. 4.2 and 4.3, and nonparametric EoS realizations with multiple stable branches. Our statistics comprise both macroscopic and microscopic features of the EoS and are not tied to an underlying parametrization. A key macroscopic feature associated with phase transitions is the presence of bends or kinks in the M-R, M-Λ, and M-I relations.[1] We consider the M–I relation, but our procedure also works with other NS observables.

We now describe the algorithm for identifying moment of inertia features.

[1]A feature in one of these relations is accompanied by a similar feature in the others.

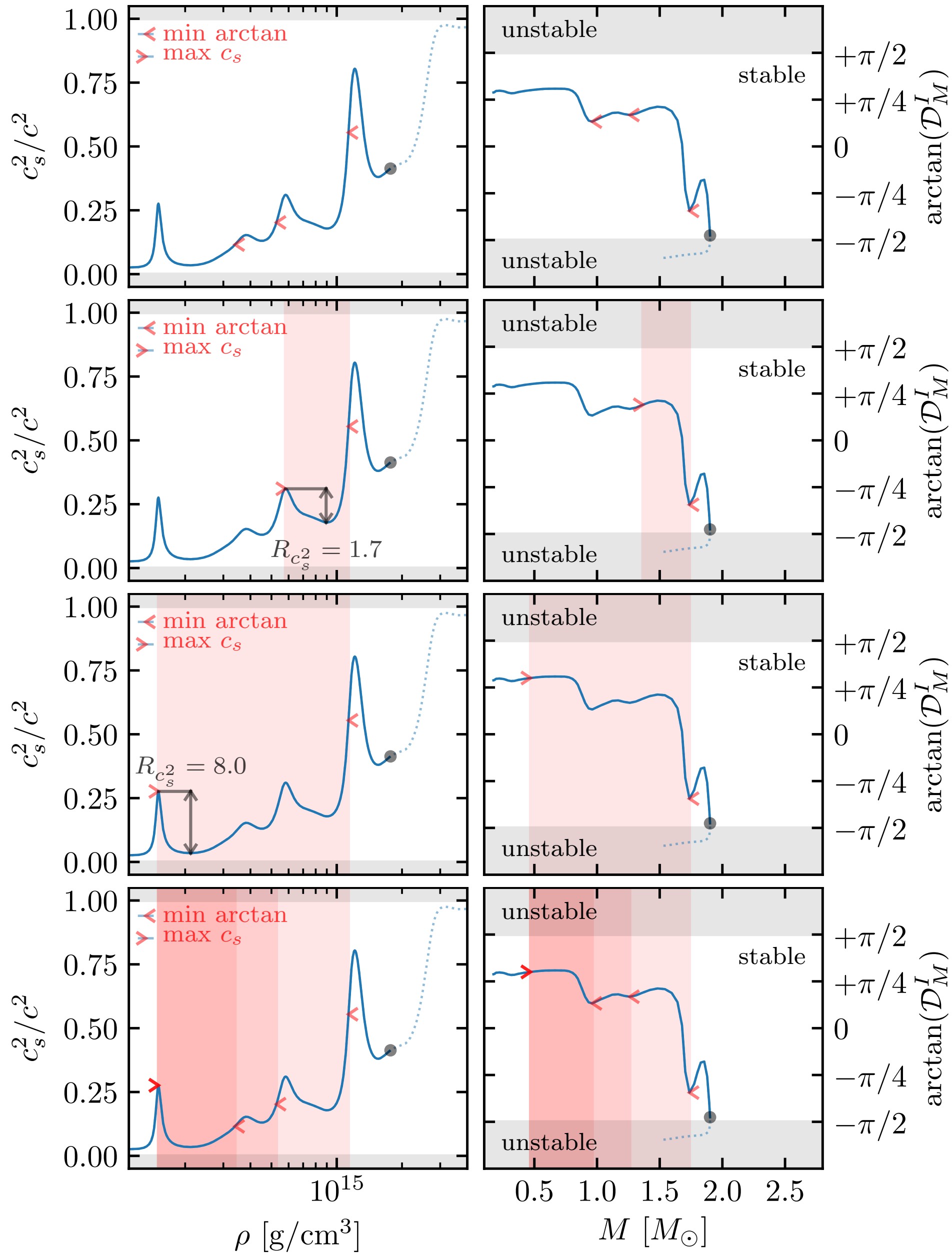

Figure 4.4: The feature extraction algorithm: (*left*) the sound-speed as a function of baryon density and (*right*) $\arctan(\mathcal{D}_M^I)$ (Eq. 4.2) as a function of the gravitational mass. The algorithm progresses from top to bottom, first with the identification of local minima in $\arctan(\mathcal{D}_M^I)$ and then pairing each with a corresponding running local maximum in c_s. The *number of features* reported corresponds to the number of unique running local maxima in c_s selected; in this case 1. The *multiplicity of each feature* corresponds to the number of local minima in $\arctan(\mathcal{D}_M^I)$ that are paired with the same running local max in c_s, in this case 3. For demonstration purposes, we show how the algorithm would progress if we had $R_{c_s^2} > 1.7$. If the threshold on the drop in the sound-speed $R_{c_s^2}$ was ≤ 1.7, the algorithm would accept the first pairing (second row) and instead report two features: one at lower densities with multiplicity two and one at higher densities with multiplicity one. This would be the case for the main results presented in Secs. 4.3 and 4.4, which use a threshold $R_{c_s^2} > 1.1$.

1. Identify all local minima in $\arctan(\mathcal{D}_M^I)$. In this example there are three with $M \gtrsim 1\mathrm{M}_\odot$. Each local minimum is associated with the end of a candidate phase transition.

2. For each local minimum, find the preceding running local maximum in c_s. This is the start of the candidate phase transition. Compute the fraction by which c_s^2 decreases from the running local maximum to the smallest c_s^2 observed within the candidate phase transition ($R_{c_s^2}$).

3. If $R_{c_s^2}$ is sufficiently large, accept the candidate onset density. Proceed to the next local minimum in $\arctan(\mathcal{D}_M^I)$.

4. Otherwise, reject the candidate's running local maximum c_s and proceed to the next largest running local maximum. Compute the new $R_{c_s^2}$ and compare to the threshold. Repeat until $R_{c_s^2}$ is large enough or there are no remaining running local maxima in c_s. If $R_{c_s^2}$ never passes the threshold, reject this local minimum in $\arctan(\mathcal{D}_M^I)$ entirely.

5. Repeat for remaining local minima. This EoS has three local minima that pair with the same running local maximum to produce $R_{c_s^2} \geq 2$ (larger than the threshold used in our main results).

We identify phase transitions by looking for characteristic behavior in the derivative of the moment of inertia along a NS sequence. Specifically, we examine the logarithmic derivative

$$\mathcal{D}_M^I \equiv \frac{d\log I/d\log p_c}{d\log M/d\log p_c}\,, \tag{4.2}$$

where p_c is the central pressure. To aid in categorization, we map the logarithmic derivative to a finite interval by considering its arctangent.[2] For example, if $|\arctan(\mathcal{D}_M^I)| > \pi/2$, then $dM/dp_c < 0$ and the NS is unstable. If $|\arctan(\mathcal{D}_M^I)| < \pi/2$, then $dM/dp_c > 0$ and the NS is stable. Importantly, the logarithmic derivative is typically constant for EoSs not undergoing a phase transition, but it varies rapidly across the density interval associated with rapid changes in compactness. Sudden changes in compactness can be caused by a phase transition or the final collapse to a black hole (BH) near M_{TOV}. Appendix 4.7 provides a simple example of this behavior with an incompressible Newtonian star.

[2]Technically, we consider $\texttt{arctan2}(d\log I/d\log p_c,\ d\log M/d\log p_c)$ which preserves information about the relative signs of the numerator and denominator within Eq. (4.2).

A phase transition is identified by a sharp decrease in $\arctan(\mathcal{D}_M^I)$. The change can be discontinuous, but need not be. Similarly, $\arctan(\mathcal{D}_M^I)$ may decrease enough that the star loses stability, but it does not have to. One can often identify a feature in $\arctan(\mathcal{D}_M^I)$ regardless of the exact behavior of c_s or whether there are multiple stable branches. Thus, it can identify both weak or strong phase transitions, including those with mixed phases.

More concretely, Fig. 4.4 demonstrates our algorithm for one EoS drawn from our nonparametric prior process. We implement the following scheme for identifying phase transitions in arbitrary EoS realizations:

(1) Identify candidate ends of phase transitions as local minima in $\arctan(\mathcal{D}_M^I)$. We first search for local minima in $\arctan(\mathcal{D}_M^I)$ bracketed by stable NSs. This excludes the sudden decrease in $\arctan(\mathcal{D}_M^I)$ associated with the collapse to a BH above M_{TOV}. Each such feature is associated with a phase transition, and the density at which this $\mathcal{D}_M^I$ feature occurs is taken to be the end of the phase transition (ε_e). In the absence of a suitable local minimum, we deem the EoS to have no phase transition.

(2) Identify a candidate onset density for an end point. We then associate each local minimum in $\arctan(\mathcal{D}_M^I)$ with the largest local maximum in c_s that precedes it (i.e., occurs at lower densities). Specifically, we select a running maximum in c_s, defined as the local maximum that is larger than all preceding local maxima. The density at which this c_s feature occurs becomes the candidate for the onset density ε_t. If there is no preceding local maximum in c_s, then we deem the EoS to have no phase transition.

(3) Repeat step (2) until an acceptable onset density is found. We require the minimum c_s^2 between the candidate onset and end densities to be at least 10% smaller than c_s^2 at the onset. If this threshold on the fractional change ($R_{c_s^2}$) is not met, the candidate onset density is rejected, and the preceding running local maximum is considered in its place. This procedure is repeated until $R_{c_s^2}$ is large enough (candidate is accepted) or there are no more local maxima in c_s^2 (candidate phase transition is rejected). See Appendix 4.8 for more discussion of thresholds within the feature selection process.

(4) Repeat steps (2-3) for remaining local minima in $\arctan(\mathcal{D}_M^I)$. We identify exactly one onset density for each end density.

If there is more than one local minimum in $\arctan(\mathcal{D}_M^I)$, several of them may be associated with the same onset density. In that case, we define the *multiplicity* of the phase transition as the number of local minima in $\arctan(\mathcal{D}_M^I)$ associated with the same running local maximum in c_s. We use the multiplicity of the phase transition as a proxy for the complexity of the phase transition morphology. For example, the complexity of the sound speed's behavior within the phase transition could indicate the (dis)appearance of (new) species of particles within the system or be related to inflection points in the particle fractions. See, e.g., examples of the equilibrium sound speed profiles in Constantinou et al. [33, 32] exploring various conditions. Complementarily, the number of selected running local maxima in c_s^2 defines the number of $\mathcal{D}_M^I$ features within the EoS. These basic counting exercises provide a classification scheme for simple (multiplicity 1) and complex (multiplicity > 1) c_s structure within the phase transition along with the number of transitions.

After this procedure, each phase transition is characterized by an onset density (or pressure or stellar mass) and an end density (largest density of all local minima in $\arctan(\mathcal{D}_M^I)$ associated with the onset). Based on these points, we define various properties of the phase transition. We focus on $\Delta(E/N)$ in Secs. 4.3 and 4.4.

Of course, the points identified by the above procedure are only proxies for the true onset and end of the phase transition. While the correspondence is excellent for Maxwell constructions (Fig. 4.2), it may not be perfect for more complicated models. See, e.g., Fig. 4.15. Moreover, because the feature identification hinges on the presence of local minima in $\arctan(\mathcal{D}_M^I)$, we sometimes cannot identify phase transitions that occur near M_{TOV}, i.e., that terminate in collapse to a BH. As such, it may be difficult to determine whether NSs collapse to BHs because of a sudden decrease in c_s at high densities or whether c_s remains large and the NS's self-gravity wins without assistance. Empirically, we find a correlation between the sharpness of the bend in $\arctan(\mathcal{D}_M^I)$ near the collapse to a BH and the existence of a phase transition at those densities, but we leave further investigations of this to future work.

Additionally, the specific onset, end, and latent energy values we extract for the phase transition are sensitive to the threshold on $R_{c_s^2}$. A lower threshold would favor the identification of a greater number of weaker phase transitions at the risk of selecting small upward fluctuations in c_s (unconstrained by current data) as the onset even if more plausible features in c_s exist at lower densities. A higher threshold would retain only the strongest phase transitions. In what follows, we choose to ignore phase-transition-like features with $R_{c_s^2} < 1.1$ as an attempt to balance these extremes, but the exact choice is *ad hoc*. See Appendix 4.8 for more discussion.

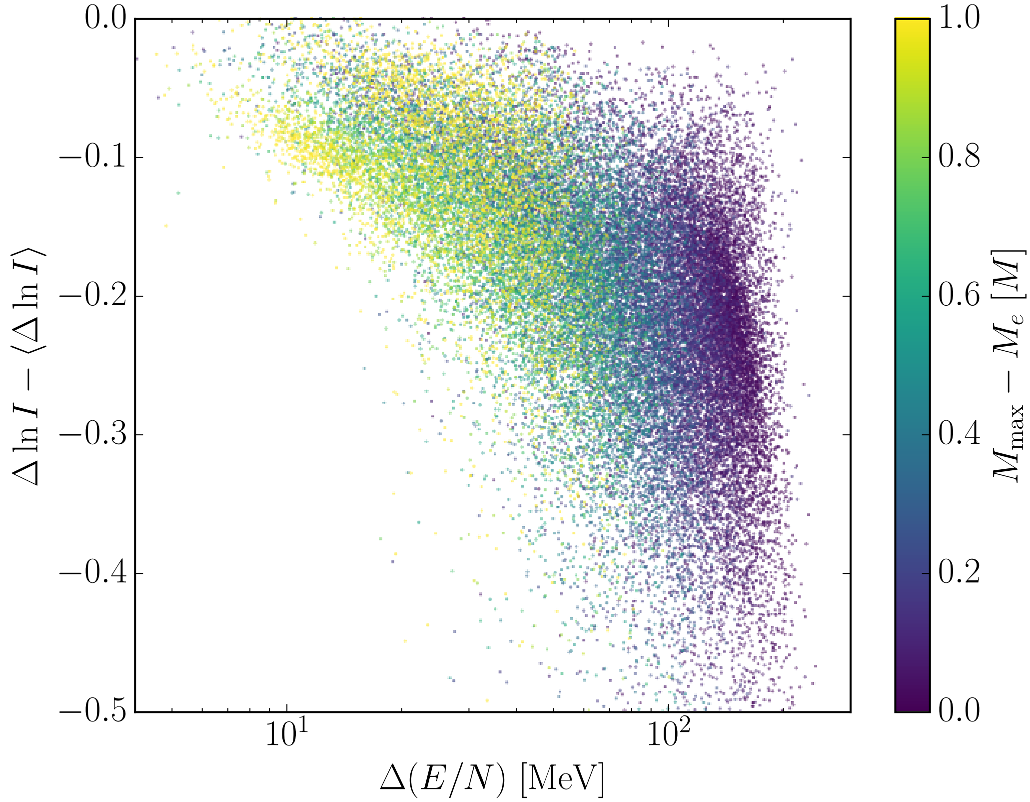

Figure 4.5: Correlations between the divergence between macroscopic properties caused by a phase transition $\Delta \ln I - \langle \Delta \ln I \rangle$ and the latent energy per particle of the associated phase transition $\Delta(E/N)$ for all transitions that begin at masses greater than $0.7\,\mathrm{M}_\odot$. Color indicates the proximity of the phase transition's end to M_{TOV}. Large divergences in macroscopic properties can only be caused by phase transitions with large $\Delta(E/N)$, but not all phase transitions with large $\Delta(E/N)$ cause large divergences in macroscopic properties.

Connections between Macroscopic and Microphysical Behavior: the Masquerade Problem

We expect $\Delta(E/N)$ to be related to phase transition's impact on macroscopic properties. However, this mapping is complicated because the same $\Delta(E/N)$ can lead to very different changes in NS properties depending on the onset density and pressure. In order to explore this relation, we consider how much the phase transition causes the macroscopic properties to diverge from what they would have been without it. This provides a natural interpretation to the masquerade problem, as it will be difficult to distinguish between two nearby M–I curves that never diverge from each other without extremely precise observations.

While it is not trivial to construct such a divergence without an underlying parametrization (one cannot just "turn off" the phase transition), Fig. 4.5 shows an example: the difference between the change in the (logarithm of the) moment of inertia across the phase transition and what it would have been if the transition was not present. We measure the actual $\Delta \ln I$ directly from the identified onset and end of a transition, and approximate what it would have been without a phase transition via the following observation. In the absence of phase-transition-like behavior, $\mathcal{D}^I_M$ is roughly constant: $\left\langle \mathcal{D}^I_M \right\rangle$. Appendix 4.7 shows that $\left\langle \mathcal{D}^I_M \right\rangle = 5/3$ for incompressible Newtonian stars, and we empirically find values near $\left\langle \mathcal{D}^I_M \right\rangle \sim 1.7$ for general EoSs in full General Relativity. Therefore, we approximate the change in the moment of inertia that would have occurred without the phase transition as $\langle \Delta \ln I \rangle = \left\langle \mathcal{D}^I_M \right\rangle \Delta \ln M$, where $\Delta \ln M$ is again defined by the onset and end of the transition.

Figure 4.5 shows $\Delta \ln I - \langle \Delta \ln I \rangle$ as a function of the phase transition's latent energy per particle. We see that large $|\Delta \ln I - \langle \Delta \ln I \rangle\,|$ are only possible with large $\Delta(E/N)$, but large $\Delta(E/N)$ do not always lead to large divergences. Again, this demonstrates the masquerade problem: large microphysical changes may not always manifest as observable features within macroscopic NS observables. Additionally, large $\Delta(E/N)$ tend to produce end masses (NS mass with central density at the end of the phase transition) close to M_{TOV}. This is because large phase transitions imply very compact stellar cores (due to relatively low pressures at high densities), which are likely to collapse to BHs if even a small amount of additional matter is added. Similarly, transitions with very large $\Delta(E/N)$ may lead to direct collapse to a BH. Because our identification algorithm (Sec. 4.2) struggles to detect features that cause the stellar sequence to collapse to a BH, this may cause a selection in the maximum $\Delta(E/N)$ for which we can identify $\mathcal{D}^I_M$ features in Fig. 4.5. Empirically, we only identify $\Delta(E/N) \lesssim 300\,\mathrm{MeV}$.

4.3 Constraints with Current Astrophysical Observations

Equipped with the procedure defined in Sec. 4.2, we now turn to current astrophysical observations. Following Legred et al. [69], we consider GW observations (GW170817 [6, 4] and GW190425 [3]) assuming that all objects below (above) M_{TOV} are NSs (BHs), NICER observations of pulsar hotspots (J0030+0451 [77] and J0740+6620[3]. [78]), and radio-based mass measurements of pulsars (J0348+0432 [20] and J0740+6620 [34, 44]).

We use a model-agnostic nonparametric EoS prior, which by construction includes

[3]We use the headline results from Miller et al. [78] rather than Riley et al. [91] because the former implements the measured cross-calibration between NICER and XMM. See also [93]

little information from either nuclear theory or experiment at any density beyond the requirements of thermodynamic stability and causality. See e.g., Essick, Landry, and Holz [38]. This prior allows us to isolate the impact of astrophysical observations on the high-density EoS ($\gtrsim \rho_{\rm nuc}$) without introducing modeling artifacts, as are common in phenomenological parametric models [70]. Compared to other nonparametric efforts [57, 78, 52], our nonparametric prior was constructed with the goal of maximizing model freedom. It therefore already contains many EoS realizations that exhibit characteristics of phase transition phenomenology, including EoSs with multiple stable branches. While additional theoretical and/or experimental low-density information could be considered (see, e.g. Refs. [41, 40, 39]) we leave those to future work and focus on astrophysical observations. Similarly, we do not incorporate pQCD calculations at high densities [64, 52] as initial explorations indicated that these constraints are model-dependent.[4]

Current observations span masses roughly between 1.2-2.1 $M_\odot$.[5] What is more, the answer to questions such as, "how many phase transitions does the EoS have?" depends on the mass or density range considered, and we do not wish to confound our inference with the presence of $\mathcal{D}^I_M$ features that occur at masses below the smallest observed NS. As such, we divide the prior into multiple sets defined by whether or not the EoS has a $\mathcal{D}^I_M$ feature that overlaps with a specific mass range. That is, whether the range of densities spanning the feature overlaps with the range of central densities for stellar models within a specified mass interval. We consider three mass ranges:

- $M \in [0.8, 1.1)\,M_\odot$: features that occur below the current observed set of NSs.
- $M \in [1.1, 1.6)\,M_\odot$: features that could influence observed NSs, particularly in the peak of the distribution of known galactic pulsars [17, 42].
- $M \in [1.6, 2.3)\,M_\odot$: features that may influence observed NSs, but at high enough masses that individual GW systems are unlikely to confidently bound the tidal deformability away from zero.

[4] Specifically, when evaluating the pQCD likelihood at $10\rho_{\rm nuc}$ we find that pQCD results influence NS near $M_{\rm TOV}$ in agreement with [52]. However, those constraints are weaker when we use the central density of stars with $M = M_{\rm TOV}$, in agreement with [99]. The robustness of the procedure to connect pQCD calculations to lower densities is therefore still an open question.

[5] The smallest observed mass we consider is likely the secondary in GW190425 [3], although there is considerable uncertainty in the event's mass ratio. The largest observed mass is J0740+6620 [44].

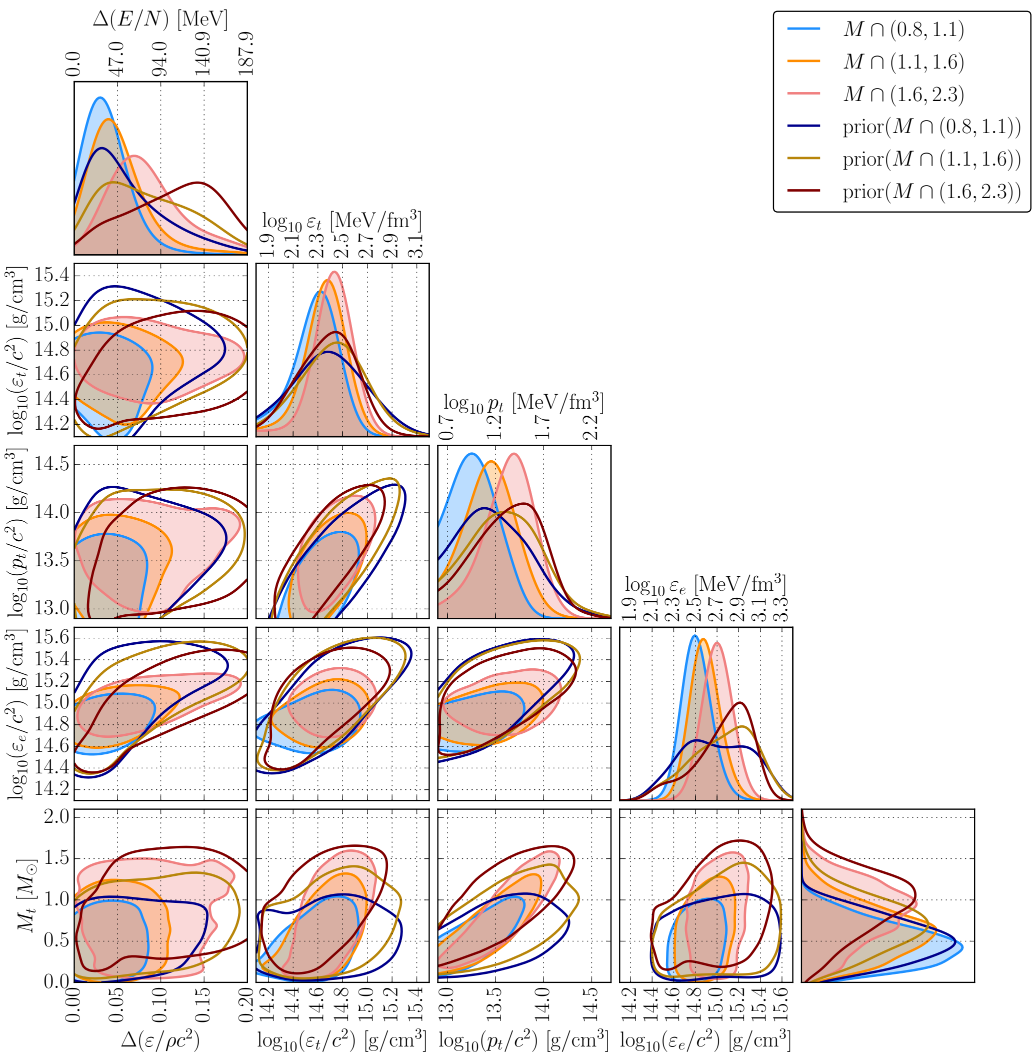

Figure 4.6: Marginalized (*unshaded*) priors and (*shaded*) posteriors for parameters that characterize phase transitions based on current astrophysical data from pulsar masses, GWs, and X-ray mass-radius measurements. For each EoS we report the properties of the transition with the largest $\Delta(E/N)$ that overlaps with each mass interval. We report (*left to right*), the latent energy ($\Delta(E/N)$), the onset energy density (ε_t), the onset pressure (p_t), the energy density at the end of the transition (ε_e), and the onset mass scale (M_t) for three mass-overlap regions: 0.8–1.1 $M_\odot$, 1.1–1.6 $M_\odot$, and 1.6–2.3 $M_\odot$.

Table 4.1: Ratios of maximized and marginalized likelihoods for different types of features based on current astrophysical observations: (P) pulsar masses, (G) GW observations from LIGO/Virgo, and (X) X-ray timing from NICER. See Eqs. (4.3) and (4.4) for an explicit definition of this notation. We consider multiple mass ranges (features must span stellar masses that overlap with the specified range) and latent energies (where appropriate, there must be at least one feature with latent energy larger than the threshold). We show the statistics for both the number of stable branches and $\mathcal{D}_M^I$ features. Error estimates for Bayes factors ($\mathcal{B}$) approximate 1-σ uncertainty from the finite Monte Carlo sample size. See Tables in Appendix 4.10 for additional combinations of subsets of astrophysical data.

M	Stable Branches			$\min \Delta(E/N)$	$\mathcal{D}_M^I$ Features		
$[M_\odot]$	$\max \mathcal{L}_{n=1}^{n>1}$(PGX)	$\mathcal{B}_{n=1}^{n>1}$(PGX)	$\mathcal{B}_{n=1}^{n>1}$(GX|P)	[MeV]	$\max \mathcal{L}_{n=0}^{n>0}$(PGX)	$\mathcal{B}_{n=0}^{n>0}$(PGX)	$\mathcal{B}_{n=0}^{n>0}$(GX|P)
0.8–1.1	0.47	0.362 ± 0.036	2.219 ± 0.162	10	0.57	1.222 ± 0.020	0.684 ± 0.011
				50	0.49	0.366 ± 0.011	0.588 ± 0.016
				100	0.26	0.117 ± 0.008	0.292 ± 0.021
1.1–1.6	0.14	0.030 ± 0.006	0.291 ± 0.055	10	0.57	1.043 ± 0.020	0.552 ± 0.010
				50	0.49	0.463 ± 0.013	0.552 ± 0.010
				100	0.26	0.152 ± 0.009	0.267 ± 0.017
1.6–2.3	0.20	0.147 ± 0.028	0.120 ± 0.026	10	0.52	1.012 ± 0.035	0.385 ± 0.013
				50	0.49	0.898 ± 0.034	0.385 ± 0.013
				100	0.29	0.383 ± 0.023	0.256 ± 0.016

Individual EoSs may belong to multiple sets if they have multiple or large $\mathcal{D}_M^I$ features or just happen to straddle a boundary.

Table 4.1 presents ratios of maximized and marginal likelihoods conditioned on different datasets. The ratio of maximized likelihoods for all astrophysical data (pulsars (P), GWs (G), and X-ray observations (X)) for different subsets of our prior (A and B) is

$$\max \mathcal{L}_B^A(\mathrm{PGX}) = \frac{\max\limits_{\varepsilon\in A}\ p(\mathrm{PGX}|\varepsilon)}{\max\limits_{\varepsilon\in B}\ p(\mathrm{PGX}|\varepsilon)}\,, \tag{4.3}$$

where the maximization is over different EoSs ε. The Bayes factor is the ratio of marginal likelihoods

$$\mathcal{B}_B^A(\mathrm{GX}|\mathrm{P}) = \frac{p(\mathrm{GX}|\mathrm{P};A)}{p(\mathrm{GX}|\mathrm{P};B)}\,, \tag{4.4}$$

where, for example,

$$p(\mathrm{GX}|\mathrm{P};A) = \int \mathcal{D}\varepsilon\, p(\mathrm{GX}|\varepsilon)p(\varepsilon|\mathrm{P},A)\,, \tag{4.5}$$

and

$$p(\varepsilon|\mathrm{P},A) = \frac{p(\mathrm{P}|\varepsilon)p(\varepsilon|A)}{\int \mathcal{D}\varepsilon\, p(\mathrm{P}|\varepsilon)p(\varepsilon|A)}\,. \tag{4.6}$$

We report these statistics for both the number of stable branches and the number of $\mathcal{D}_M^I$ features, conditioned on several minimum $\Delta(E/N)$ thresholds. We present both statistics because each has its relative strengths and weaknesses. While Occam factors may be important for Bayes factors, they do not affect the ratio of maximized likelihoods. At the same time, the maximized likelihoods may correspond to an extremely rare EoS, whereas the Bayes factors provide an average over typical EoS behavior. We therefore should trust statements about which both statistics broadly agree.

Overall, we expect stronger constraints on features that overlap with the observed mass range. In Figs. 4.6, 4.7, and Table 4.1, we indeed find the strongest constraints on phase transitions that occur in NSs less massive than $1.6\,\mathrm{M}_\odot$, although constraints for $M \in [0.8, 1.1)\,\mathrm{M}_\odot$ and $M \in [1.1, 1.6)\,\mathrm{M}_\odot$ are comparable. Indeed, in Fig. 4.6 the posterior for the latent energy is more constrained with respect to the prior for masses below $1.6\,\mathrm{M}_\odot$. Furthermore, Table 4.1 shows that the Bayes factor using all astrophysical data disfavors the presence of large $\mathcal{D}_M^I$ features ($\Delta(E/N) \geq 100\,\mathrm{MeV}$) at low and medium masses (0.8–1.1 and 1.1–$1.6\,\mathrm{M}_\odot$) approximately three times as strongly as at high masses (1.6–$2.3\,\mathrm{M}_\odot$).

As shown in Legred et al. [69], all NS observations are consistent with a single radius near ~ 12.5 km. We therefore expect the data to disfavor the existence of strong phase transitions and place an upper limit on $\Delta(E/N)$. Fig. 4.6 bears this out. It shows posterior distributions on the properties of the $\mathcal{D}^I_M$ feature with the largest $\Delta(E/N)$ that overlaps with the specified mass range (i.e., features with larger $\Delta(E/N)$ may exist in the EoS, but they do not overlap with the mass range). Astrophysical data place an upper limit on the largest phase transition within an EoS, but are less informative about weaker phase transitions.

Figure 4.6 shows the onset energy density and pressure as well as the energy density at the end of the phase transition. Beyond limiting the possible size of $\mathcal{D}^I_M$ features, astrophysical data also disfavor phase transitions with large onset densities and pressures. This likely corresponds to the observation that the sound-speed must increase rapidly around $3\rho_{\mathrm{nuc}}$ in order to support $\sim 2\,\mathrm{M}_\odot$ pulsars against gravitational collapse while remaining compatible with observations at lower densities, primarily from GW170817 [69]. The peak in the posteriors for the onset parameters is likely due to a combination of the (peaked) prior and these upper limits. This trend is also encountered in the behavior of the p–ε bounds for EoSs with multiple stable branches. That is, Fig. 8 in Legred et al. [69] suggests it is more likely for phase transitions to begin below ρ_{nuc} than above it when the EoS supports multiple stable branches.

Figure 4.1 provides an additional perspective on current constraints by showing one-dimensional symmetric credible regions for the radius as a function of the gravitational mass. While current astrophysical data generally disfavor EoSs with large $\Delta(E/N)$, Fig. 4.1 nevertheless shows that there are EoSs with large $\Delta(E/N)$ that are consistent with observations. In particular, the maximum-likelihood draw from the full PGX posterior conditioned on $\Delta(E/N) \geq 100\,\mathrm{MeV}$ places a sharp feature in the M–R curve at high masses, just above J0740+6620's observed mass. Such behavior maximizes the likelihood from the PSR masses due to the assumption that the EoS itself is what limits the largest observed NS mass. See discussions in [68, 79]. Furthermore, the maximum-likelihood EoS favors smaller radii at low masses (in line with GW170817) and larger radii at high masses (in line with J0740+6620). Notably, the model-agnostic nonparametric prior was not designed to favor this specific behavior, which instead emerges from the data without direct supervision or fine-tuning.

We quantify the degree to which data prefer EoSs with different numbers and types

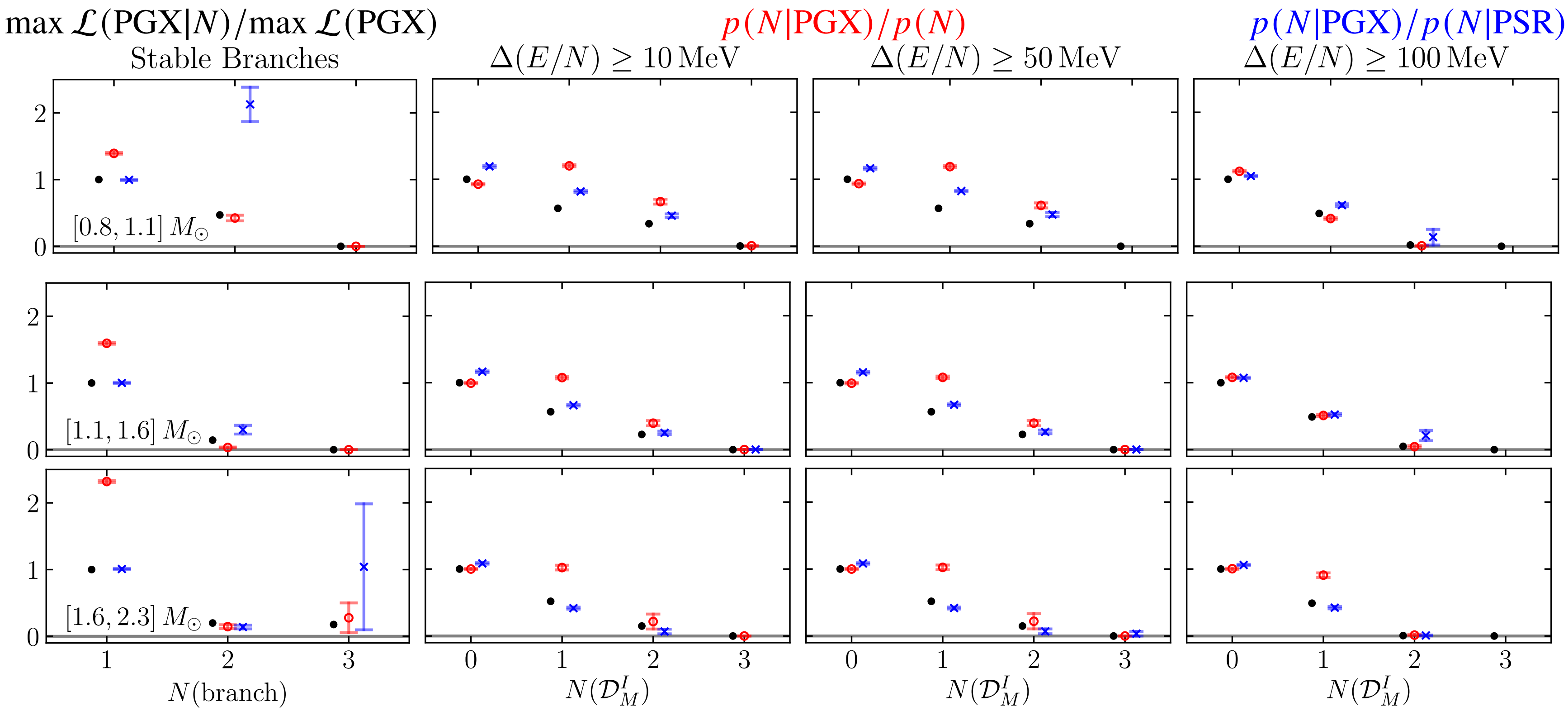

Figure 4.7: Ratios of probabilities conditioned on different numbers of features. Compare to Table 4.1; see Eqs. (4.3) and (4.4) for an explicit definitions of our notation. (*left*) Distributions over the number of stable branches and (*right*) distributions over the number of $\mathcal{D}_M^I$ features for EoSs with $\Delta(E/N) \geq 10$, 50, and 100 MeV, respectively for different mass-overlap regions: (*top*) 0.8–1.1 $\mathrm{M}_\odot$, (*middle*) 1.1–1.6 $\mathrm{M}_\odot$, and (*bottom*) 1.6–2.3 $\mathrm{M}_\odot$. We show the ratio of maximum likelihoods (*black dots*) and the posterior divided by the prior (*circles and x's*). As in Table 4.1, we consider (PGX, *red circles*) the ratio of the posterior conditioned on PSR masses, GW coalescences, and X-ray timing and compare it to our nonparametric prior as well as (*blue x's*) the posterior conditioned on only PSR masses. Error bars approximate 1-σ uncertainties from the finite size of our prior sample. In general, a single stable branch without strong $\mathcal{D}_M^I$ features is preferred.

of features in Table 4.1 and Fig. 4.7. Table 4.1 shows the ratio of maximized likelihoods as well as the ratio of marginal likelihoods for EoSs with different numbers of features. We compare EoSs with a single stable branch against EoSs with multiple stable branches, as well as EoSs with and without at least one $\mathcal{D}_M^I$ feature above a certain $\Delta(E/N)$. Generally, these statistics are consistent with Fig. 4.6: the astrophysical data disfavor large phase transitions (multiple stable branches or large $\Delta(E/N)$) more strongly than weaker ones. However, the statistical evidence is still weak, and further observations are required to definitively rule out even the presence of multiple stable branches.

Figure 4.7 expands on Table 4.1 by examining the preference for different numbers of features, rather than just their absence or presence. That is, Table 4.1 in effect provides a summary of Fig. 4.7 by marginalizing over all EoS with more than one stable branch or at least one $\mathcal{D}_M^I$ feature. Overall, although current astrophysical observations cannot rule out the presence of a phase transition, they more strongly disfavor the presence of multiple features. The astrophysical posterior strongly disfavors EoSs with more than two stable branches and less strongly disfavor EoSs with more than one large $\mathcal{D}_M^I$ feature. This suggests that one may not need to consider arbitrarily complicated EoS in order to model the observed population of NSs, or at least that there is a limit to how exotic astrophysical NSs are.

Finally, current astrophysical data carries little information about the multiplicity of any phase transitions, should they exist. Conditioning on the presence of a phase transition, we find Bayes factors between ~0.8–1.5 in favor of multiplicity > 1 compared to multiplicity 1 for the feature with the largest $\Delta(E/N)$ within each EoS, even for the strongest phase transitions. This should be expected. We cannot yet confidently determine whether a phase transition exists, and it would therefore be surprising if we could already identify even basic features of the phase transition.

4.4 Future Prospects with Gravitational Wave Observations

Building upon current data, we now consider future prospects from GW observations of inspiraling compact binaries. Section 4.4 explores the prospects for detecting the presence of phase transitions, and Sec. 4.4 considers our ability to characterize them. In brief, we find that we will not be able to confidently detect the presence of even relatively extreme phase transitions with catalogs of 100 events. Rather, we will need at least 200 events or more. However, we will be able to rule out the presence of multiple stable branches at low mass scales with 100 GW events.

Nevertheless, we will be able to infer the correct $\Lambda(M)$ for all M simultaneously regardless of what the true EoS is, and obtain $\sim 6\%$ (50%) relative uncertainty in $\Lambda_{1.2}$ ($\Lambda_{2.0}$) after 100 GW detections.

To explore a range of potential behavior, we simulate catalogs of GW events assuming a few representative CSS EoSs based on DBHF [56]. We consider

- DBHF [56]: a hadronic EoS without phase transitions.
- DBHF_3504: a modification to DBHF with a weak phase transition at $\sim 1.9\,\mathrm{M}_\odot$ and a causal CSS extension at higher densities.
- DBHF_2507: a modification to DBHF with a strong phase transition at $\sim 1.5\,\mathrm{M}_\odot$ and a causal CSS extension at higher densities. This is the Strong Maxwell CSS example in Fig. 4.2.

These EoSs are not drawn from our nonparametric prior, and in fact their sharp features are relatively extreme examples of possible EoS behavior. As such, we expect them to be rigorous tests of the inference framework.

The simulated catalogs assume a network signal-to-noise ratio ($\mathcal{S}/\mathcal{N}$) detection threshold of 12, and they approximate measurement uncertainty in the masses and tidal parameters according to the procedure described in Landry, Essick, and Chatziioannou [68]. We inject a population of non-spinning NSs uniform in component masses between 1.0 $\mathrm{M}_\odot$ and M_{TOV}. Injections are drawn assuming $p(\mathcal{S}/\mathcal{N}) \sim (\mathcal{S}/\mathcal{N})^{-4}$, consistent with a uniform rate per comoving volume at low redshift. We assume the mass, spin, and redshift distributions are known exactly and therefore ignore selection effects. For more details, see Refs. [68, 69].

For computational expediency, we consider the ability of GW observations alone to constrain phase transition phenomenology. That is, we do not impose lower bounds on M_{TOV} from pulsar masses in order to retain a large effective sample size within the Monte Carlo integrals. We do assume, however, that all objects below M_{TOV} are NSs, and, therefore, placing a lower limit on $\Lambda(M)$ from GW observations will *de facto* place a lower limit on M_{TOV}. See Appendix 4.9 for more discussion.

Prospects for Detecting Phase Transitions

We first consider detection of a phase transition with a catalog of GW events. Fig. 4.8 shows the statistics from Table 4.1 for various simulated catalog sizes for injected

EoSs both with and without a phase transition. Generally speaking, we recover the expected behavior: confidence in the presence (or absence) of a phase transition grows as the catalog increases. Moreover, when a phase transition is present, evidence grows the most in the mass range where the phase transition occurs.

The Number of Stable Branches

We begin by considering the number of stable branches, with the left panels of Fig. 4.8 showing Bayes factors for multiple stable branches ($n > 1$) vs. a single stable branch ($n = 1$). As none of the injected EoSs have a phase transition at low masses and GW observations should be able to confidently bound $\Lambda \gg 0$ at low masses, we quickly obtain relatively high confidence that there is only a single stable branch within 0.8–1.1 $\mathrm{M}_{\odot}$. We find Bayes factors as large as $\sim 100 : 1$ in favor of a single branch after 100 events.

For moderate masses (1.1–1.6 $\mathrm{M}_{\odot}$), we again see the expected evidence in favor of a single stable branch for both DBHF (no phase transition) and DBHF_3504 (phase transition at $\sim 1.9\,\mathrm{M}_{\odot}$). The Bayes factors are only $\sim 10 : 1$ after 100 events, but nonetheless the trend is clear. In contrast, DBHF_2507 (phase transition at $\sim 1.5\,\mathrm{M}_{\odot}$ and multiple stable branches) exhibits a notably different pattern. Although a strong preference is not developed either way, Bayes factors begin to (correctly) favor multiple stable branches after 100 events.

Finally, we are not able to confidently distinguish between EoSs with a single stable branch or multiple stable branches in the mass range 1.6–2.3 $\mathrm{M}_{\odot}$. This is because the individual events' uncertainties on Λ are much larger than the true Λ in this mass range.[6] It will therefore take the combination of many GW events to be able to precisely resolve the true value of Λ at high masses.

The Number and Properties of $\mathcal{D}^I_M$ Features

The remaining panels of Fig. 4.8 show similar trends for $\mathcal{D}^I_M$ features. We show Bayes factors for at least one $\mathcal{D}^I_M$ feature ($n > 0$) vs. no $\mathcal{D}^I_M$ features ($n = 0$). In general, the strongest preference for a $\mathcal{D}^I_M$ feature is for DBHF_2507, which has the largest phase transition among the three EoSs we consider. The evidence in favor of at least one $\mathcal{D}^I_M$ feature is nevertheless smaller for the largest $\Delta(E/N)$ ($\geq 100\,\mathrm{MeV}$) compared to more moderate values ($\geq 50\,\mathrm{MeV}$). This is true for all mass ranges,

[6] Λ typically scales as $\Lambda \propto M^{-5}$ and rapidly decreases at high masses.

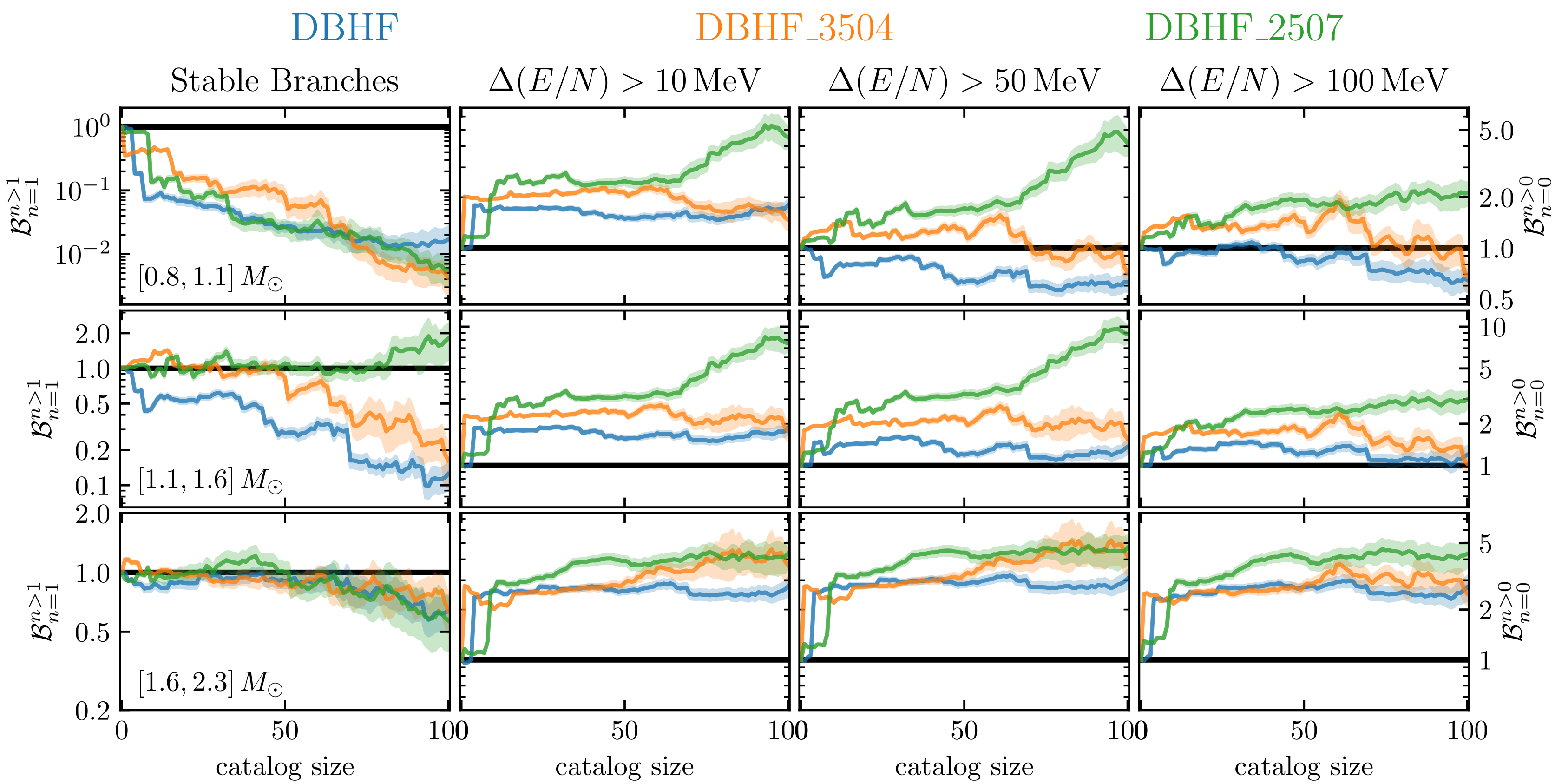

Figure 4.8: Bayes factors vs. catalog size comparing (*left-most column*) multiple stable branches vs. a single stable branch and (*right three columns*) at least one $\mathcal{D}^I_M$ feature vs. no $\mathcal{D}^I_M$ features. We consider features that overlap with three mass ranges: (*top row*) 0.8–1.1 $\mathrm{M}_\odot$, (*middle row*) 1.1–1.6 $\mathrm{M}_\odot$, and (*bottom row*) 1.6–2.3 $\mathrm{M}_\odot$. We also show three different injected EoSs: (*blue*, no phase transition) DBHF, (*orange*, weak phase transition at ~ 1.9 $\mathrm{M}_\odot$) DBHF_3504, and (*green*, strong phase transition at ~ 1.5 $\mathrm{M}_\odot$) DBHF_2507. Shaded regions denote 1-σ uncertainties from the finite size of our Monte Carlo sample sets. Different realizations of catalogs will also produce different trajectories; these should only be taken as representative.

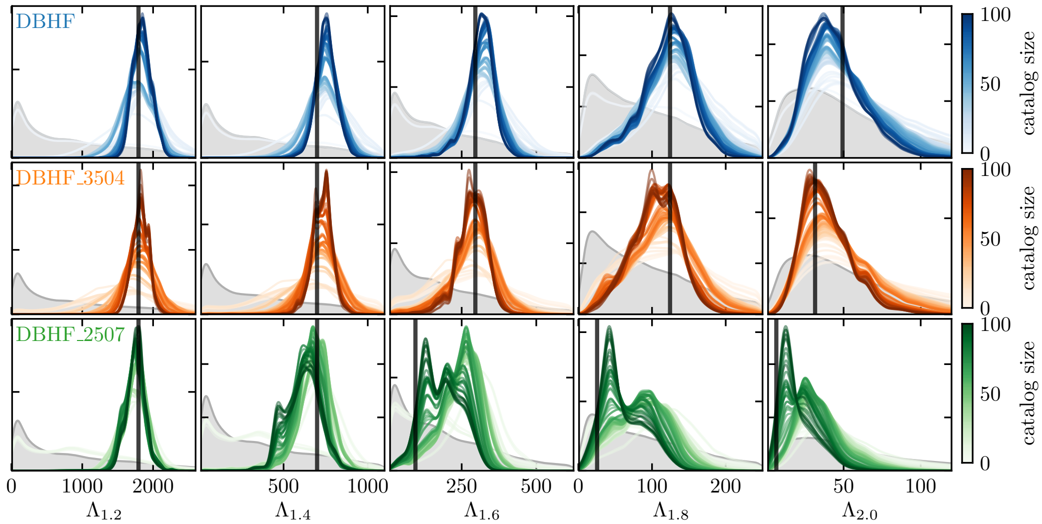

Figure 4.9: Sequences of one-dimensional marginal posteriors for $\Lambda(M)$ at (*left to right*) 1.2, 1.4, 1.6, 1.8, and 2.0 $M_\odot$ for different simulated EoSs: (*top, blue*) DBHF, (*middle, orange*) DBHF_3504 (phase transition at $\sim 1.9\,M_\odot$) and (*bottom, green*) DBHF_2507 (phase transition at $\sim 1.5\,M_\odot$). These posteriors show the distributions of $\Lambda(M) > 0$ (i.e., they only consider EoSs with $M_{\rm TOV} \geq M$). These posteriors are conditioned only on simulated GW events (no real observations), and a line's color denotes the number of simulated GW events within the catalog (*light to dark : fewer to more events*) along with the true injected values (*vertical black lines*). The prior is shown for reference (*grey shaded distributions*). For very small Λ, primarily associated with DBHF_2507 at high masses, the true value falls near the lower bound in the prior. The primary effect of additional observations is to reduce support for larger values of Λ. While significant uncertainty in $\Lambda(M)$ remains after 100 events, the nonparametric prior is able to correctly infer $\Lambda(M)$ at all M simultaneously, including sharp changes in $\Lambda(M)$ over relatively small mass ranges.

suggesting that we will be able to constrain a feature's $\Delta(E/N)$ more easily than we may be able to constrain the mass range over which it occurs. Additionally, we will need very large catalogs to confidently detect the presence of a $\mathcal{D}^I_M$ feature. At best, we find Bayes factors of $\sim 10:1$ after 100 events. This matches previous estimates, which place the required number of events between 200-400 [29, 85, 66]. See Sec. 9.5 for more discussion. Furthermore, while there will not be unambiguous statistical evidence in favor of a $\mathcal{D}^I_M$ feature at high masses (1.6–2.3 $M_\odot$), we do see an upward trend for DBHF_3504. This suggests that, even though our individual-event uncertainties on tidal parameters are large at these masses, we will nevertheless eventually be able to detect small phase transitions at high masses given enough events.

Occam factors are readily apparent in these results, causing systematic shifts of comparable magnitude for all three injected EoSs. These tend to favor the presence of $\mathcal{D}_M^I$ features, as it is likely that very stiff EoSs at intermediate densities (unlikely to have $\mathcal{D}_M^I$ features) are quickly ruled out by GW observations. As such, some fraction of the prior is ruled out after only a few detections reducing the evidence even though there are still many EoSs without $\mathcal{D}_M^I$ features that match the data well. Furthermore, selecting EoSs with at least one feature at high masses requires M_{TOV} to be at least as high as the lower-edge of this mass range because of how our $\mathcal{D}_M^I$ feature extraction algorithm works. Such EoSs are better matches to the data for all the true EoSs considered. Even a few detections can quickly rule out $M_{\mathrm{TOV}} \ll 1.6\,\mathrm{M}_\odot$, which penalizes EoSs for which our algorithm did not detect a $\mathcal{D}_M^I$ feature above $1.6\,\mathrm{M}_\odot$ because the EoS's M_{TOV} was below $1.6\,\mathrm{M}_\odot$. Nevertheless, these Ocaam factors are typically $\lesssim 2$, implying that large Bayes factors can still be interpreted at face value.

Finally, it may be difficult to completely rule out the presence of $\mathcal{D}_M^I$ features even if the true EoS does not have any phase transitions. Fig. 4.8 shows a possible exception at the lowest masses considered, but even there the Bayes factors are only ~ 0.5 after 100 events. This is yet another manifestation of the masquerade problem: EoSs with and without $\mathcal{D}_M^I$ features can produce similar M–I relations, even for relatively large $\Delta(E/N)$.

Prospects for Characterizing Phase Transitions

In addition to detecting the presence of a phase transition, we wish to determine its properties should it exist. Fundamental to this is the ability to infer the correct M–Λ relation. That is, to infer the correct $\Lambda(M)$ for all M simultaneously. Fig. 4.9 demonstrates that our nonparametric inference is capable of this, regardless of the true EoS used to generate injections. This is often not the case for parametric models of the EoS (see [85, 66] and discussion in Sec. 9.5). Fig. 4.9 shows one-dimensional marginal posteriors for $\Lambda(M)$ at $M = 1.2$, 1.4, 1.6, 1.8, and $2.0\,\mathrm{M}_\odot$ for different catalog sizes and each of the three injected EoSs. We find that the low-density (low-mass) EoS is relatively well measured. $\Lambda_{1.2}$ will have a relative uncertainty (standard deviation divided by the mean) between 6% (DBHF_3504) and 7% (DBHF_2507) at $M = 1.2\,\mathrm{M}_\odot$ after 100 detections. However, it will generally take more events before we can confidently resolve features at higher masses, even without the presence of a phase transition. With catalogs of 100 events, we are only able to constrain $\Lambda_{2.0}$ to between 40% (DBHF_3504) and 55% (DBHF_2507). In agreement with Fig. 4.8,

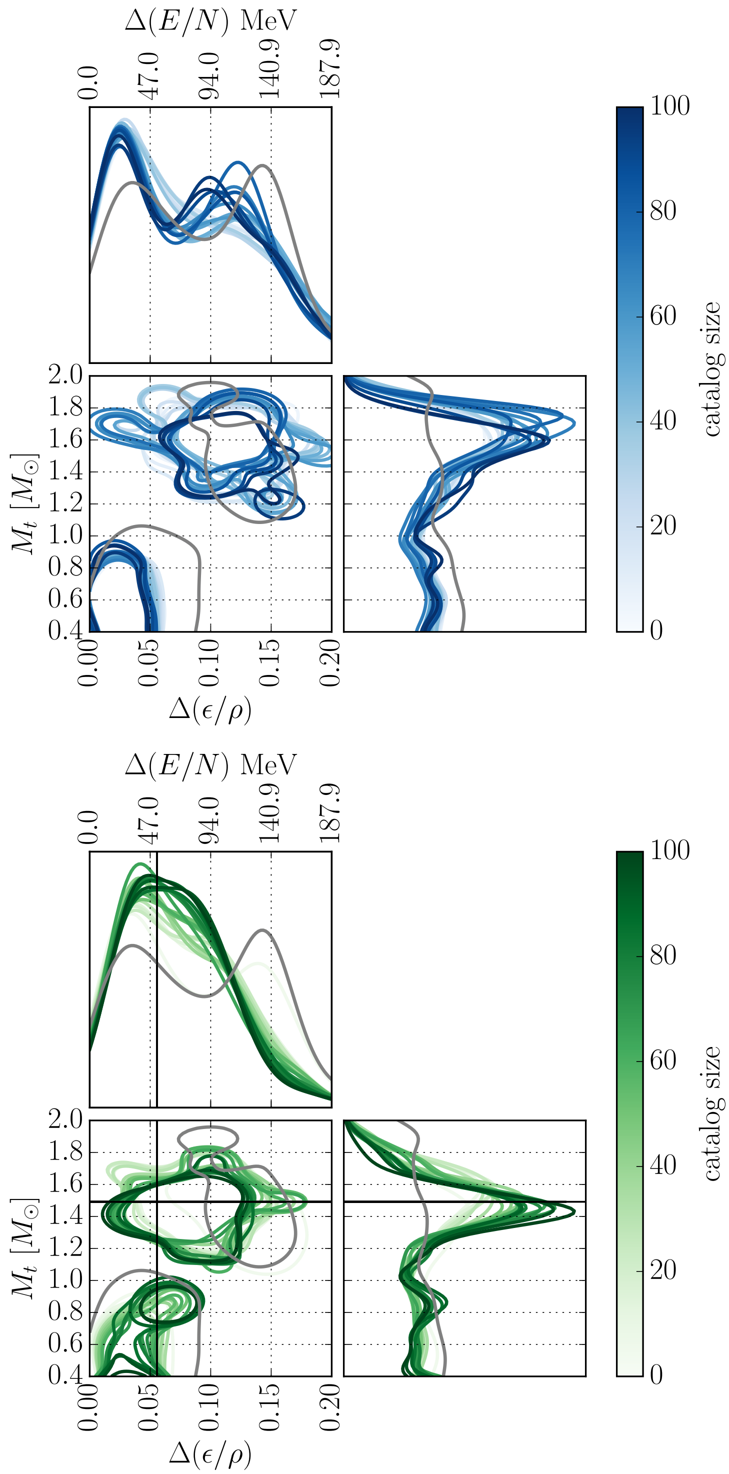

Figure 4.10: Joint posteriors for $\Delta(E/N)$ and transition onset mass (M_t) inferred from simulated GW catalogs for (*top, blue*) DBHF and (*bottom, green*) DBHF_2507. Grey curves denote the (reweighed) prior, color denotes the size of the catalog, and contours in the joint distribution are 50% highest-probability-density credible regions. Solid lines denote the true parameters for DBHF_2507; there are no such lines for DBHF because it does not contain a phase transition. As in Fig. 4.6, extracted parameters correspond to the feature with the largest $\Delta(E/N)$, but here we only require features to overlap the broad range 0.8–2.3 $\mathrm{M}_\odot$.

it is likely to take more than 100 events to unambiguously distinguish between EoSs with and without phase transitions. For example, the $\Lambda_{2.0}$ posterior for DBHF_2507 still has nontrivial support at the location of the DBHF's $\Lambda_{2.0}$, and vice versa, even with the full catalog of 100 events.

Even though we identify phase transition features from macroscopic relations, we expect the inferred microscopic properties to be robust given the one-to-one mapping between p–ε and, e.g., M–R [71]. Fig. 4.10 shows how constraints on the onset mass (M_t) and $\Delta(E/N)$ evolve with the catalog size for DBHF (no phase transition) and DBHF_2507 (strong phase transition). In order to highlight constraints on the transition mass, Fig. 4.10 additionally reweighs the posterior so that it corresponds to a (as much as possible) uniform prior in the transition mass. It only shows EoSs that have at least one identified $\mathcal{D}_M^I$ feature that overlaps with 0.8–2.3 $\mathrm{M}_\odot$.

Characterizing onset properties is challenging because of the wide variability in softening behavior during the course of the phase transition. That is, the onset density as identified by a running local maximum in c_s may not correspond to any immediately obvious features in macroscopic relations, as is the case in Fig. 4.3. Therefore, we may expect a long tail towards low onset masses even if the end of the transition is well determined.

Additionally, we sometimes observe unintuitive behavior when we condition on the presence of features that do not exist (left panel). For example, the marginal posterior for M_t (conditioned on the existence of at least one feature) peaks at $M_t \gtrsim 1.6\,\mathrm{M}_\odot$ for DBHF. Transitions that begin at these masses are difficult to detect with GW observations alone; see Figs. 4.8 and 4.9. Therefore, these EoSs are not strongly constrained by observations, particularly compared to EoSs that have transitions that begin at lower masses. This explains why the posterior tends to disfavor low M_t, and the peak at higher masses should be interpreted primarily as a lower limit.

However, transitions that begin at very high masses ($M_t \gtrsim 1.8\,\mathrm{M}_\odot$) are also disfavored by the data. This is unintuitive, as we expect very weaker tidal constraints for high mass systems. However, by conditioning on the presence of at least one identified $\mathcal{D}_M^I$ feature, which in turn are only identified by our algorithm if the EoS does not collapse to a BH as part of the transition, we *de facto* require EoSs with large onset masses to be rather stiff. That is, only the stiffest EoS can have an $\mathcal{D}_M^I$ feature begin at high mass and not collapse directly to a BH. At the same time, these EoSs are ruled out by observations at smaller masses, which favor more compact stars and soft EoSs. Therefore, a high M_t is disfavored by low-mass observations and the correlation induced within the prior by requiring at least one identified $\mathcal{D}_M^I$ feature at high mass.

We contrast this with DBHF_2507, in which there is a phase transition near $1.5\,\mathrm{M}_\odot$ (right panel). Here, we find a similar peak in the one-dimensional marginal posterior for M_t, but there is additional information in the joint posterior for M_t and $\Delta(E/N)$. The joint posterior for DBHF mostly follows the prior, particularly for $M_t \sim 1.6\,\mathrm{M}_\odot$, whereas for DBHF_2507 it is shifted relative to the prior towards the injected values and disfavors large $\Delta(E/N)$. These considerations highlight the fact that low-dimensional marginal posteriors conditioned on specific, sometimes *ad hoc*, features will require care to interpret correctly. It may be better, then, to consider sets of marginal distributions for macroscopic observables, such as Fig. 4.9, at the same time. At the very least, the latter can provide context for inferred constraints on proxies for microphysical properties.

4.5 Discussion

We summarize our main conclusions in Sec. 4.5 before comparing them to existing work in the literature in Sec. 4.5. We conclude by discussing possible extensions to our study in Sec. 4.5.

Summary

We introduced a new algorithm to identify phase transitions within the EoS of dense matter based on NS properties and the underlying c_s behavior. This algorithm does not rely on a parametrization, and as such works for both parametric and nonparametric representation of the EoS. Our approach improves upon previous studies by demonstrating that physically meaningful density scales can be extracted directly from NS observables. We further demonstrated that nonparametric EoS inference can recover the correct macroscopic properties, such as $\Lambda(M)$, at all masses simultaneously. As such, we suggest that extracting physical quantities from nonparametric EoS draws is preferable to directly modeling of the p–ε relation with *ad hoc* parametric functional forms, as different choices for the parametrization can introduce strong model-dependence on the conclusions [70].

This approach is similar in spirit to efforts to constrain the nuclear symmetry energy and its derivatives (slope parameter: L) with nonparametric EoSs [40, 39]. Studies based on parametric EoS models described in terms of L have suggested tension between terrestrial experiments and astrophysical observations [89, 25, 24]. Refs. [40, 39] instead extracted L from nonparametric EoS realizations by imposing

β-equilibrium at ρ_{nuc} without relying on an explicit parametrization far from ρ_{nuc}. They demonstrated that any apparent tension was due to model assumptions rather than the data, as nonparametric models were able to accommodate both terrestrial constraints on L and astrophysical observations of NSs.

Returning to this work, we showed that current astrophysical data disfavor only the strongest phase transitions and the presence of multiple phase transitions. However, the data are still consistent with two stable branches and/or one moderate phase transition. We also showed that we will not be able to confidently detect the presence of a phase transition with catalogs of ≤ 100 GW events. Although we do not directly estimate how many events will be needed for computational reasons, extrapolating Fig. 4.8 suggests that we may need several hundred events to reach Bayes factors $\gtrsim 100$, often taken as a rule-of-thumb for confident detections [63]. We can, however, expect to confidently rule out the presence of multiple stable branches at low masses after 100 events. While the exact rates of NS coalescences and future GW-detector sensitivities are still uncertain, it is unlikely that we will obtain a catalog of this size within the lifetime of the advanced LIGO and Virgo detectors [5].

Comparison to other work

As discussed briefly in Sec. 5.1, several authors have proposed tests based on features in the distribution of macroscopic observables. Chen, Chesler, and Loeb [31] investigated a piecewise linear fit of the M–R relation with two segments that captures phase transitions through a change in the slope. However, beyond possible systematics associated with the simplicity of the piecewise linear model, quantitative conclusions hinge on the assumption that the measurement uncertainty on R from GW events is roughly the same for all masses. This is unrealistic for massive systems in which the relative uncertainty in the tidal deformability grows quickly. Chatziioannou and Han [29] pursued a related method that models the population of detections hierarchically and searches for a second population with significantly different radii at high masses.[7] They found that phase transitions could be identified with $O(100)$ events if hybrid stars emerge at $\sim 1.4\,\mathrm{M}_{\odot}$. Landry and Chakravarti [66] introduced a method for identifying the presence of twin stars, which can arise due to strong first-order phase transitions, in the population of

[7] Chen and Chatziioannou [30] proposed a similar technique to distinguish between binary NS and NS-BH systems. In this case, a reduced inferred radius is attributed to the presence of a BH in the binary (which does not exhibit tidal effects) rather than a softening in the EoS.

merging binary NSs based on gaps in the joint distribution of masses and binary tidal deformabilities. However, these and related approaches that directly model the M-Λ relation [35, 12] offer no obvious pathway to microscopic EoS properties nor the ability to enforce physical precepts such as causality and thermodynamic stability. What is more, not all microscopic models that contain phase transitions produce macroscopic observables with this phenomenology (the masquerade problem), and this phenomenology might be caused by other effects, such as a mix of binary NS and NS-BH binaries at the same masses [30] or even dark matter [92].

Alternative approaches involve modeling the p–ε relation directly. Several authors have attempted this with parametric models of varying complexity. Pang et al. [85] introduced a piecewise-polytropic model for first-order phase transitions and carried out model selection between models that do and do not support phase transitions, respectively. They concluded that a strong phase transition could be identified with 12 GW events, each with signal-to-noise ratio $\mathcal{S}/\mathcal{N} > 30$.[8] However, in addition to technical issues associated with their Bayes factor calculation, their results appear to be affected by model systematics within their EoS parametrization. They arrive at counterintuitive conclusions: weaker phase transitions are detected more easily than stronger ones (their Fig. 5), and the inference precision is largely unaffected by the observation of more events (their Fig. 9).[9] We speculate that the cause is the fact that their parametric EoS model does not closely reproduce either of their injected EoSs, leading to model systematics [70]. If systematic issues are less severe for the injected EoS with a weak phase transition than the one with a strong transition, the former could be more easily distinguished from EoSs without phase transitions.

Two other recent studies have looked at the astrophysical evidence for or against the presence of phase transitions. Both Tan et al. [101] and Mroczek et al. [82] constructed EoS models by adding features to the speed of sound such as spikes, dips, and plateaus. As explained in Tan et al. [101], these features are motivated by specific theoretical expectations of phase transition phenomenology. Mroczek et al. [82] employs underlying EoS realizations drawn from a few simple GP priors, resulting in what they call a modified Gaussian Process. In comparison, our nonparametric prior inherently generates broad ranges of phase transition morphology without the

[8] Assuming merging binaries are uniformly distributed in volume within a Euclidean universe, the $\mathcal{S}/\mathcal{N}$ is distributed as $p(\mathcal{S}/\mathcal{N}) \propto (\mathcal{S}/\mathcal{N})^{-4}$. This means that to observe 12 events with $\mathcal{S}/\mathcal{N} > 30$ requires a total of > 187 events above the detection threshold used in Sec. 4.4 ($\mathcal{S}/\mathcal{N} = 12$) and 324 events above the more realistic detection threshold $\mathcal{S}/\mathcal{N} = 10$ [8, 7].

[9] For most parameters, statistical uncertainty roughly scales as $N^{-1/2}$, where N is the number of detections. Systematic uncertainty is independent of N.

need to modify realizations *post hoc*. Mroczek et al. [82] must add features by hand because their original GP was constructed with long correlation lengths and small variances. As such, it only produces smooth EoSs without phase-transition-like features by itself. Additionally, Mroczek et al. [82] report a Bayes factor for models with or without such features, finding no strong evidence either way. Though this generally agrees with our conclusions, the quantitative comparison might be affected by the fact that their prior is first "pruned" by rejecting EoSs that do not fall within broad boundaries that represent realistic EoS. Inevitably, these boundaries carry information about current astrophysical observations. Therefore, it may not be surprising that subsets of different priors (each chosen to resemble current astrophysical data) predict the current observed data with comparable frequency, which is what is implied by a Bayes factor ~ 1.

Several other authors have investigated models intended to test specifically for the presence of deconfined quarks in NS cores, e.g. [100, 18, 19]. Many of these studies base the evidence for the presence of quark matter on the behavior of the polytropic index ($\gamma = d\log p/d\log\varepsilon$) in addition to using various parametric and nonparametric representations of the EoS and approximations to astrophysical likelihoods. For example, Annala et al. [19] present approximate ranges for γ, c_s, and other statistics and propose that massive NS cores likely contain matter displaying approximate conformal symmetry, which may be indicative of a transition to deconfined quarks. These studies typically focus on the composition of matter at the highest densities possible within NSs (near M_{TOV}). Some studies have even claimed evidence for the presence of deconfined quark matter based on γ at high densities. Our $\mathcal{D}_M^I$ features are more agnostic about the composition of new matter and are sensitive over a broad range of masses. They should therefore provide a complementary approach to direct modeling based on assumptions about NS composition and microphysical interactions.

Finally, several other authors have introduced EoS models with many parameters and increased model freedom, some of which are implemented as neural networks of varying complexity [47, 46, 45, 57, 58]. Our conclusions based on current observations are broadly consistent with these other approaches, and therefore we only remark that our $\mathcal{D}_M^I$ feature could be extracted from any EoS, regardless of the underlying model (or lack thereof). It should be straightforward to investigate phase transition phenomenology with realizations from any EoS prior in the literature, although this is beyond the scope of our current study.

Future work

Finally, we discuss possible extensions and the impact that additional assumptions may have on our analysis.

As mentioned in Sec. 4.3, we intentionally condition our nonparametric prior on very little information from nuclear theory or experiment beyond causality and thermodynamic stability. It would be of interest to better understand how terrestrial experiments or *ab initio* theoretical calculations such as chiral EFT at low densities may impact our conclusions. For example, Fig. 3 from Essick et al. [41] shows that improved constraints at very low densities ($\lesssim \rho_{\rm nuc}/2$) can improve uncertainty in the pressure at higher densities ($\sim 3\rho_{\rm nuc}$) when combined with astrophysical data. Furthermore, theoretical calculations suggest a moderate value of L, which would remove even the hint that a phase transition may occur at low densities found in Essick et al. [39] when they assumed L was large.

At the other extreme, it is worth clarifying the impact of pQCD calculations. Several conflicting reports exist in the literature, suggesting that the pressures at very high densities ($\sim 40\rho_{\rm nuc}$) limit the pressures achieved in the highest-mass NS [52, 53], while other studies point out that these conclusions depend on the details of how the densities relevant for NSs are extrapolated to the pQCD regime [99]. Indeed, the current proposal for mapping pQCD calculations to lower densities [64] maximizes the likelihood over the extrapolation rather than marginalizing over the EoS within the extrapolation region, although Gorda et al. [53] marginalize over a nonparametric extrapolation based on GPs for at least part of the extrapolation region (up to $\sim 10\rho_{\rm nuc}$ but not all the way to $\sim 40\rho_{\rm nuc}$). The fact that the conclusions depend on the choice of where the extrapolation begins suggests that they could depend strongly on the prior assumptions for EoS behavior within the (unobserved and unobservable) extrapolation region between the central density of $M_{\rm TOV}$ stars and the pQCD regime.

Additional information about the EoS will be imprinted in post-merger signals from coalescing NS systems. An extensive literature exists (e.g., Refs. [81, 21]) mostly focusing on the ability to resolve the dominant frequency of the post-merger emission thought to be associated with the fundamental 2-2 mode of the massive remnant. Additional work will be needed to connect our nonparametric inference based on tides observed during the GW inspiral to the complicated physics at work during the post-merger. See, e.g., Wijngaarden et al. [105] for a way to model the full GW signal. This may include extending our nonparametric EoS representation to include finite-temperature effects [26].

In addition to incorporating more information within the inference, we may be able to dig deeper into features of the current data. As mentioned in Sec. 4.2, our procedure does not identify phase transitions that results in the direct collapse to a BH, although we do find that the sharpness of the final decrease in $\arctan(\mathcal{D}_M^I)$ may correlate with whether the collapse was due to only self-gravity or assisted by a sudden decrease in c_s. Future work may develop additional features targeting this phenomenology, as it could have implications for the behavior of merger remnants that may or may not power electromagnetic counterparts depending on how long the remnant survives [75, 98, 65].

Assuming a phase transition is identified, an open challenge is to extend the inference to determine the order of the phase transition (e.g., first- vs. second-order). A smooth crossover from hadronic to quark matter may, for example, be mimicked by either a weak first-order phase transition or a second-order one [48]. Condensation of pions or kaons may also give rise to a second-order phase transition [86]. Our feature is able to detect a variety of possible morphologies, but additional statistics will need to be developed to further categorize the c_s behavior within the phase transition's extent.

Finally, we would also be remiss if we did not remind the reader that our feature specifically targets phenomenology associated with decreases in c_s and associated increase of compactness. If, instead, a smooth crossover as realized in, e.g., quarkyonic matter [49, 22, 76] only manifests as a sudden increase in the speed of sound, the features introduced here will not detect it. Additional features targeting such behavior would need to be developed. To that end, it may be of general interest to more carefully study the types of correlations between c_s at different densities that are preferred by astrophysical data. In the future, we will interrogate our nonparametric posteriors to not only constrain c_s but also how quickly c_s can vary. For example, we do not expect periodic, extremely rapid oscillations in c_s to have a significant impact on NS properties, and therefore they may only be very weakly constrained by the data. See, e.g., Tan et al. [101] for more discussion. However, this will likely require more advanced sampling techniques to efficiently draw representative sets from our nonparametric processes. See Appendix 4.9.

4.6 Acknowledgements

The authors thank Aditya Vijaykumar for reviewing this manuscript within the LIGO Scientific Collaboration.

R.E. and P.L. are supported by the Natural Sciences & Engineering Research Council of Canada (NSERC).

Research at Perimeter Institute is supported in part by the Government of Canada through the Department of Innovation, Science and Economic Development Canada and by the Province of Ontario through the Ministry of Colleges and Universities. R.E. also thanks the Canadian Institute for Advanced Research (CIFAR) for support.

The work of S.H. was supported by Startup Funds from the T.D. Lee Institute and Shanghai Jiao Tong University. S.H. also acknowledges support from the Network for Neutrinos, Nuclear Astrophysics, and Symmetries (N3AS) during the early stages of this project, funded by the National Science Foundation under cooperative agreements 2020275 and 1630782 and by the Heising-Simons Foundation under award 00F1C7.

IL and KC acknowledge support from the Department of Energy under award number DE-SC0023101 and the Sloan Foundation.

The authors gratefully acknowledge the program "Neutron Rich Matter on Heaven and Earth" (INT-22-2a) held at the Institute for Nuclear Theory, University of Washington for useful discussion. They also thank the LIGO laboratory for providing computational resources supported by National Science Foundation Grants PHY-0757058 and PHY-0823459. This material is based upon work supported by NSF's LIGO Laboratory which is a major facility fully funded by the National Science Foundation.

4.7 Incompressible Newtonian Stars with Two Phases

We examine the feature extraction procedure laid out in Sec. 4.2 within a simpler context: incompressible stars with two phases in Newtonian gravity. Despite its simplicity, this demonstrates the main features of more realistic stars while greatly simplifying the mathematics.

We consider incompressible stars with a piecewise constant density ρ as a function of the pressure p separated by a transition pressure p_T

$$\rho(p) = \begin{cases} \rho_L & \text{if} \quad p \leq p_T \\ \rho_H & \text{if} \quad p > p_T \end{cases} . \tag{4.7}$$

We combine this EoS with the Newtonian equations of stellar structure

$$\frac{dm}{dr} = 4\pi r^2 \rho \,, \tag{4.8}$$

$$\frac{dp}{dr} = -\frac{Gm\rho}{r^2} \,, \tag{4.9}$$

and a central pressure p_c, where m is the enclosed mass up to radius r.

For $p_c \leq p_T$, the solution is trivial as the star is described by a single fluid:

$$R = \sqrt{\frac{3p_c}{2\pi G \rho_L^2}} \,, \tag{4.10}$$

$$M = \frac{4\pi}{3} \rho_L R^3 \,, \tag{4.11}$$

$$I = \frac{2}{5} M R^2 \,, \tag{4.12}$$

for the radius R, mass M, and moment of inertia I. In this case, the star is always stable as $dM/dp_c > 0$ and $\mathcal{D}_M^I = d \log I / d \log M = 5/3$ is constant.

For $p_c > p_T$, the star contains a core of high-density matter with radius

$$R_c = \sqrt{\frac{3(p_c - p_T)}{2\pi G \rho_H^2}} \,. \tag{4.13}$$

The entire star's macroscopic properties are then implicitly determined by

$$\begin{aligned} p_T = {} & \frac{4\pi G \rho_L (\rho_H - \rho_L) R_c^3}{3} \left(\frac{1}{R_c} - \frac{1}{R} \right) \\ & + \frac{2\pi G \rho_L^2}{3} \left(R^2 - R_c^2 \right) \,, \end{aligned} \tag{4.14}$$

$$M = \frac{4\pi}{3} \left[(\rho_H - \rho_L) R_c^3 + \rho_L R^3 \right] \,, \tag{4.15}$$

$$I = \frac{8\pi}{15} \left[(\rho_H - \rho_L) R_c^5 + \rho_L R^5 \right] \,, \tag{4.16}$$

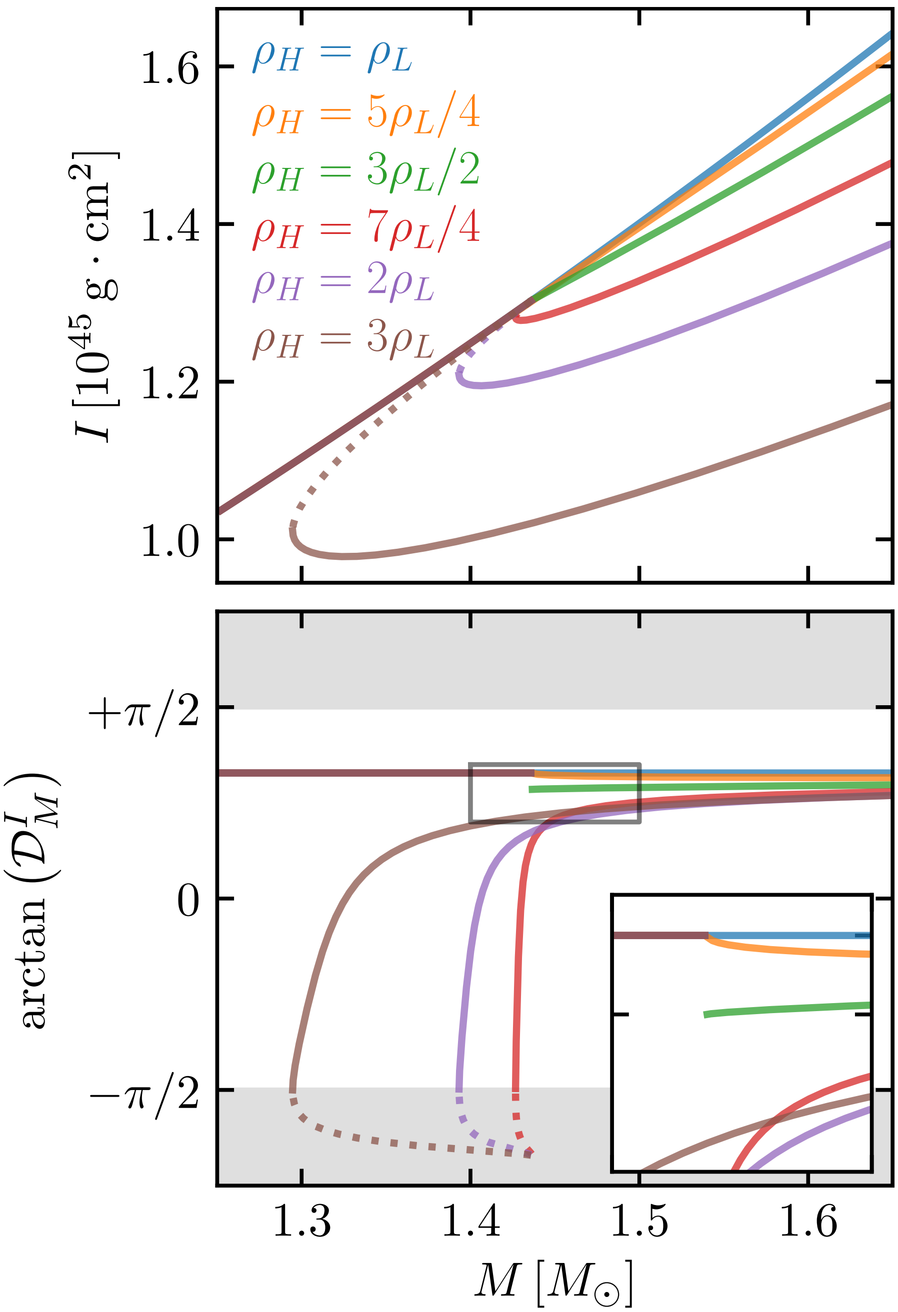

Figure 4.11: Stellar sequences for incompressible two-phase Newtonian stars with $\rho_L = 2\rho_{\rm nuc} = 5.6\times10^{14}\mathrm{g/cm^3}$, $p_T = 5\times10^{34}\mathrm{dyne/cm^2}$, and various values of ρ_H. We plot (*top*) the M-I relation and (*bottom*) $\arctan(\mathcal{D}_M^I)$ as a function of the stellar mass. Stable branches are shown with solid lines, and unstable branches are shown with dotted lines. The bottom panel inset focuses near the discontinuity for curves with; ticks on the y-axis correspond to the values in Eq. 4.17.

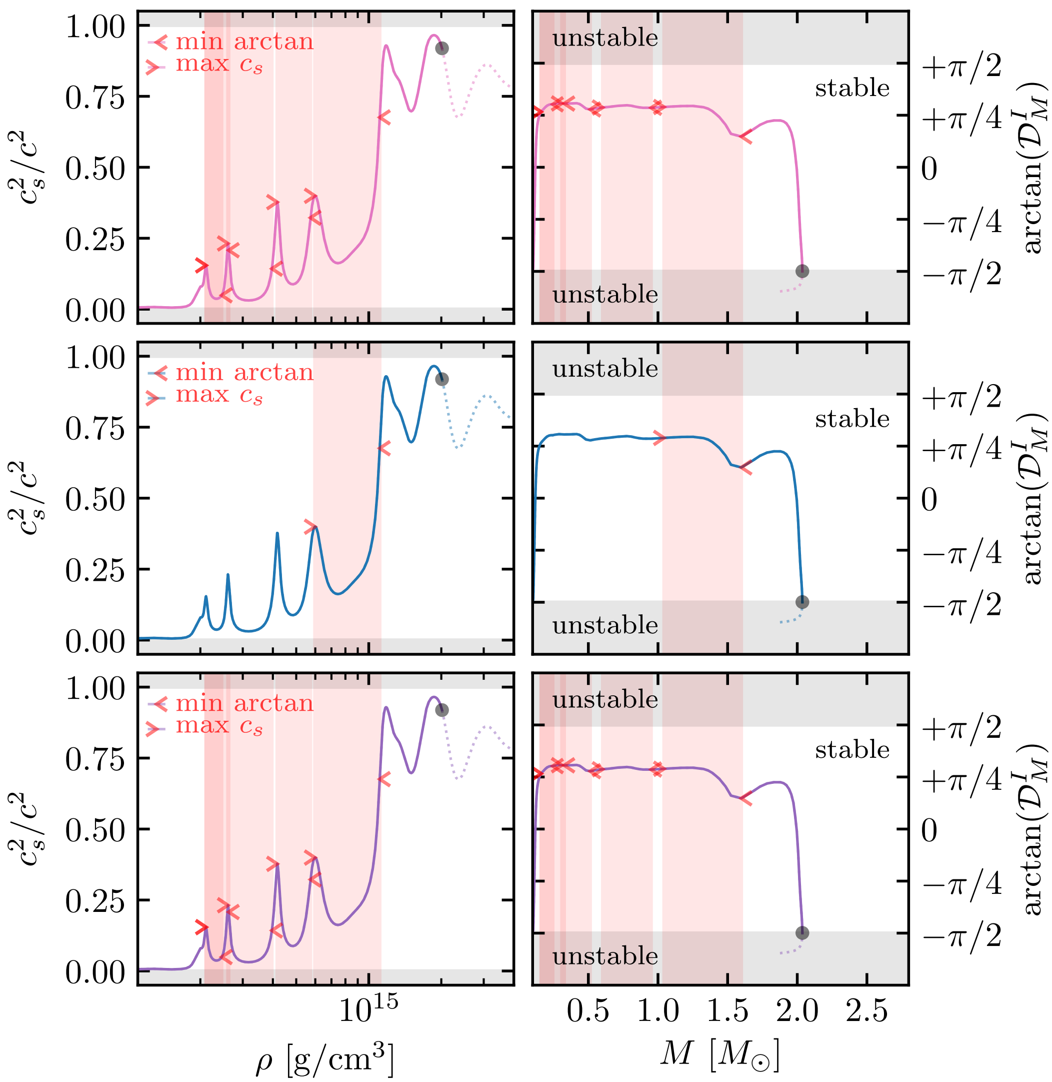

Figure 4.12: An additional example of the impact of thresholds within the feature extraction algorithm with an EoS realization with a relatively short correlation length. (*top*) trivial thresholds $\Delta\arctan(\mathcal{D}_M^I) = 0.0$, $\mathcal{R}_{c_s^2} = 1.0$; (*middle*) threshold on the size of $\Delta\arctan(\mathcal{D}_M^I)$, $\Delta\arctan(\mathcal{D}_M^I) = 0.15$, $\mathcal{R}_{c_s^2} = 1.0$; (*bottom*) threshold on the amount c_s^2 must decrease, $\Delta\arctan(\mathcal{D}_M^I) = 0.0$ $\mathcal{R}_{c_s^2} = 1.5$ (analogous to Fig. 4.4). The rapid oscillations in c_s^2 are identified when selecting based on $\mathcal{R}_{c_s^2}$ but they are rejected when selecting based on $\Delta\arctan(\mathcal{D}_M^I)$; their relatively small $\Delta(E/N)$ do not produce significant changes in the M-I relation.

In this case, the star can become unstable ($dM/dp_c < 0$) if ρ_H is much larger than ρ_L. Regardless of stability, $\mathcal{D}^I_M$ is discontinuous whenever $\rho_H \geq \rho_{\text{thr}} \equiv 3\rho_L/2$. Fig. 4.11 shows that

$$\lim_{p_c \to p_T^+} \frac{d \log I}{d \log M} = \begin{cases} +5/3 & \text{if } \rho_H < \rho_{\text{thr}} \\ +5/4 & \text{if } \rho_H = \rho_{\text{thr}} \\ -5/3 & \text{if } \rho_H > \rho_{\text{thr}} \end{cases} . \tag{4.17}$$

Similar threshold behavior is encountered in other parameters combinations, for example the mass, radius or tidal deformability, as also shown for relativistic polytropic NSs with 1$^{\text{st}}$-order phase transitions [72].

4.8 The role of thresholds within feature extraction

As part of the feature identification algorithm introduced in Sec. 4.2, we included a threshold on the amount the sound-speed must decrease within a candidate $\mathcal{D}^I_M$ feature. We now discuss the motivation for and impact of this and other thresholds in more detail.

We represent our uncertainty in the EoS as a random process for c_s as a function of pressure with support for every possible causal and thermodynamically stable EoS. We can therefore think of the behavior of our feature extraction algorithm in terms "fluctuations" in c_s under different realizations of this random process. Specifically, by selecting the running local maximum, we *de facto* set a threshold on c_s that subsequent local maxima must pass if they are to be associated with the start of a phase transition. This means that small fluctuations in the height of subsequent local maxima, either above or below the previous running local maximum, can change the features extracted. These changes can sometimes be dramatic, as the proxy for the onset density selected may jump to a much lower density. By imposing a threshold on $R_{c_s^2}$, we make this type of selection explicit within the algorithm. Although this does not remove the issue of small fluctuations qualitatively changing the estimated onset density, it at least provides a more concrete way to control the types of features selected. Fig. 4.4 demonstrates the impact of a large threshold on $R_{c_s^2}$ for one EoS realization.

Although not used within our main analysis, we implement an additional threshold on the change in $\arctan(\mathcal{D}^I_M)$ observed within the candidate phase transition. That is, we define $\Delta \arctan(\mathcal{D}^I_M)$ as the difference between the maximum $\arctan(\mathcal{D}^I_M)$ for any density between the onset and end points and the local minimum in $\arctan(\mathcal{D}^I_M)$ that defines the end point. If this value is small, it will likely be difficult to detect

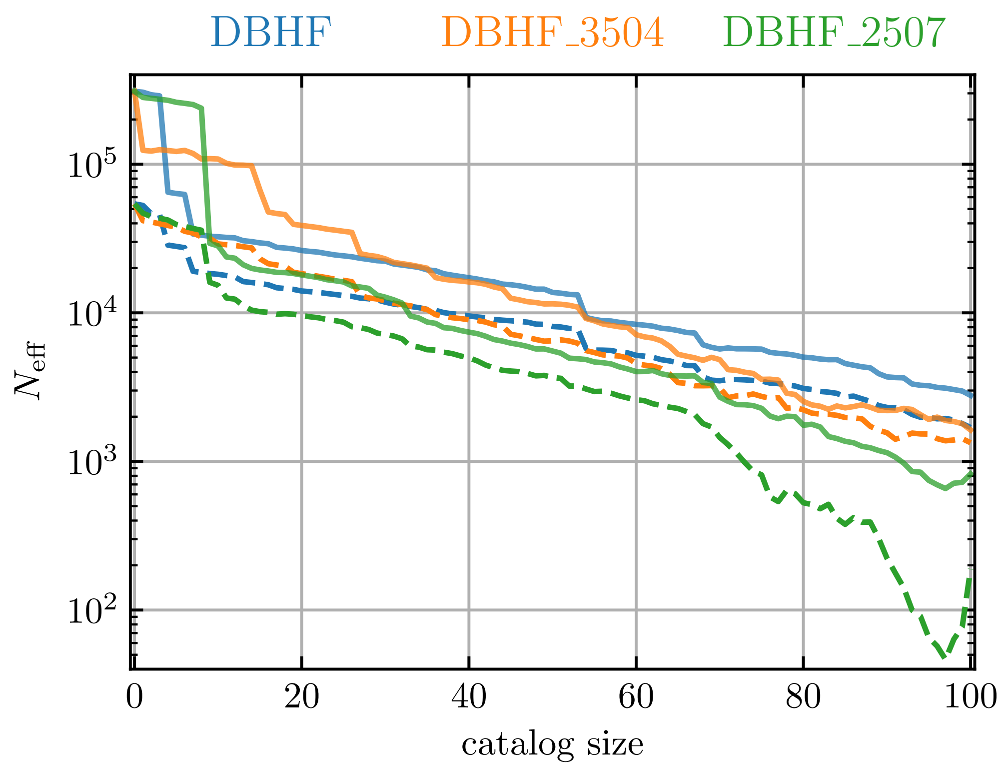

Figure 4.13: The effective number of EoS samples from the posterior process as a function of catalog size for (*solid*) catalogs comprised of only mock GW observations and (*dashed*) catalogs that include real pulsar mass measurements in addition to mock GW observations. For each of the three true EoS considered in Sec. 4.4, we find an approximately exponential decrease of the number of effective samples with the catalog size.

such a feature from macroscopic properties of NSs. One may wish to remove them at the time of extracting features. In practice, though, we choose to record all features, regardless of how small $\Delta\,\arctan(\mathcal{D}^I_M)$ is, and then filter them *post hoc* by selecting subsets of features with different $\Delta(E/N)$.

Fig. 4.12 shows the impacts of threshold on both $R_{c_s^2}$ and $\Delta\,\arctan(\mathcal{D}^I_M)$ for an EoS realization with rapid oscillations in c_s. Our main results require $\Delta\,\arctan(\mathcal{D}^I_M) \geq 0$ (satisfied axiomatically) and $R_{c_s^2} \geq 1.1$.

4.9 Computational Challenges

As discussed in Sec. 4.4, our current nonparametric sampling methods (i.e., direct Monte Carlo sampling) may not scale to catalogs of $\gtrsim$ 100 detections. This is perhaps not surprising. That is, the total likelihood becomes increasingly peaked with more detections, and the majority of realizations from the nonparametric prior will have vanishingly small likelihoods. As such, they do not contribute to the posterior. With our current set of $\sim 310,000$ prior samples, we retain $\sim 19,300$ effective samples in the posterior conditioned on real astrophysical data. Heavy pulsar mass measurements alone rule out the largest portion of our prior, about 80%. See, e.g., Fig. 4 of Essick et al. [41].

The number of effective samples is substantially higher in our simulation campaigns if we do not include massive pulsars (Fig. 4.13). Since our main goal is to explore how well GWs can constrain phase transitions, we only consider catalogs of simulated GW events in Sec. 4.4 and do not include the heavy pulsars.

Although the existing set of EoS realizations from the nonparametric prior process will be sufficient for the catalog sizes expected over the next few years (current data and an additional $O(10)$ GW detections [68]), analyzing larger simulated catalogs might be challenging. Fig. 4.13 shows the number of effective EoS samples in the posterior as a function of the simulated GW catalog size and for different simulated EoS. Solid lines only include simulated GW events; dashed lines include both heavy pulsars and simulated GW events. Although there are differences between the injected EoS, we observe an approximately exponential decay in the number of effective posterior samples with the size of the catalog. This implies we will need exponentially more draws from the current prior in order to analyze larger catalogs, which is computationally untenable in the long run.

However, given the expected rate of detections over the next few years, brute force may still be sufficient in the short run. That is, given the low computational cost of producing additional EoS realizations, we may be able to draw more samples from the existing prior processes, solve the TOV equations, and compute the corresponding astrophysical weights fast enough to keep up. With the current implementation, this takes $O(10)$ sec/EoS, which is tractable compared to the expected rate of GW detections of $O(\text{few})/\text{year}$.

However, this approach will not work indefinitely. We would be much better off spending (finite) computational resources in regions of the (infinite dimensional) vector-space of EoS with significant posterior support. This is one motivation for sampling from the posterior using a Monte Carlo Markov Chain (MCMC) rather than direct Monte Carlo sampling. Some authors in the broader GP literature have investigated implementations of GPs within MCMC schemes. These typically involve evolving a handful of reference points used to model the GP's mean function along with the hyperparameters of the covariance kernel (see, for example, Titsias, Rattray, and Lawrence [102]). This *de facto* parametrizes the EoS prior with a handful of hyperparameters, at which point standard techniques for sampling from parametric distributions in hierarchical inference can be employed. Other authors have suggested neural networks as a computationally efficient way to generate EoS proposal, but many (if not all) of these proposal are also *de facto* parametric representations of the EoS itself or uncertainty in the EoS, which are then sampled with standard techniques [47, 46, 45, 57, 58].

An alternative method to focus computational efforts in high-likelihood region is to use the posterior from initial analyses with small catalogs to draw additional EoS proposals for future (larger) catalogs, similar to simulated annealing [74]. The rate of detection is likely to be slow enough that new posteriors could be periodically developed (along with emulators to efficiently draw more samples) without the need for extensive automation. As long as the noise at the time of each event is independent, this may be a computationally efficient path forward. However, we leave exploration of such methods for future work.

4.10 Additional Representations of Current Astrophysical constraints

Here we present additional representations of the constraints on phase transition phenomenology with current astrophysical data. Similar to Fig. 4.1, Fig. 4.14 shows posteriors for macroscopic observables conditioned on EoSs with either small ($\Delta(E/N) \leq 10\,\mathrm{MeV}$) or large ($\Delta(E/N) \geq 100\,\mathrm{MeV}$) phase transitions for masses between 1.1–2.3 $\mathrm{M}_\odot$. In general, we see that there are weaker correlations between macroscopic properties at low masses (1.4 $\mathrm{M}_\odot$) and high masses (2.0 $\mathrm{M}_\odot$) for EoSs with large phase transitions than for EoSs with small phase transitions, even though the marginal uncertainty for each is approximately the same. Notable exceptions are that EoS with small $\Delta(E/N)$ can support smaller $R_{1.4}$ and larger M_{TOV} than EoS with large $\Delta(E/N)$.

Tables 4.2–4.5 show additional detection statistics for different types of features conditioned on different subsets of the data, analogous to Table 4.1. We report different combinations of (P) pulsar mass measurements, (G) GW tidal measurements, and (X) X-ray pulse profiling with NICER. Tables 4.2 and 4.3 report the evidence for multiple stable branches. Tables 4.4 and 4.5 report the evidence for $\mathcal{D}_M^I$ features. Note that one can compute additional Bayes factors for different combinations of

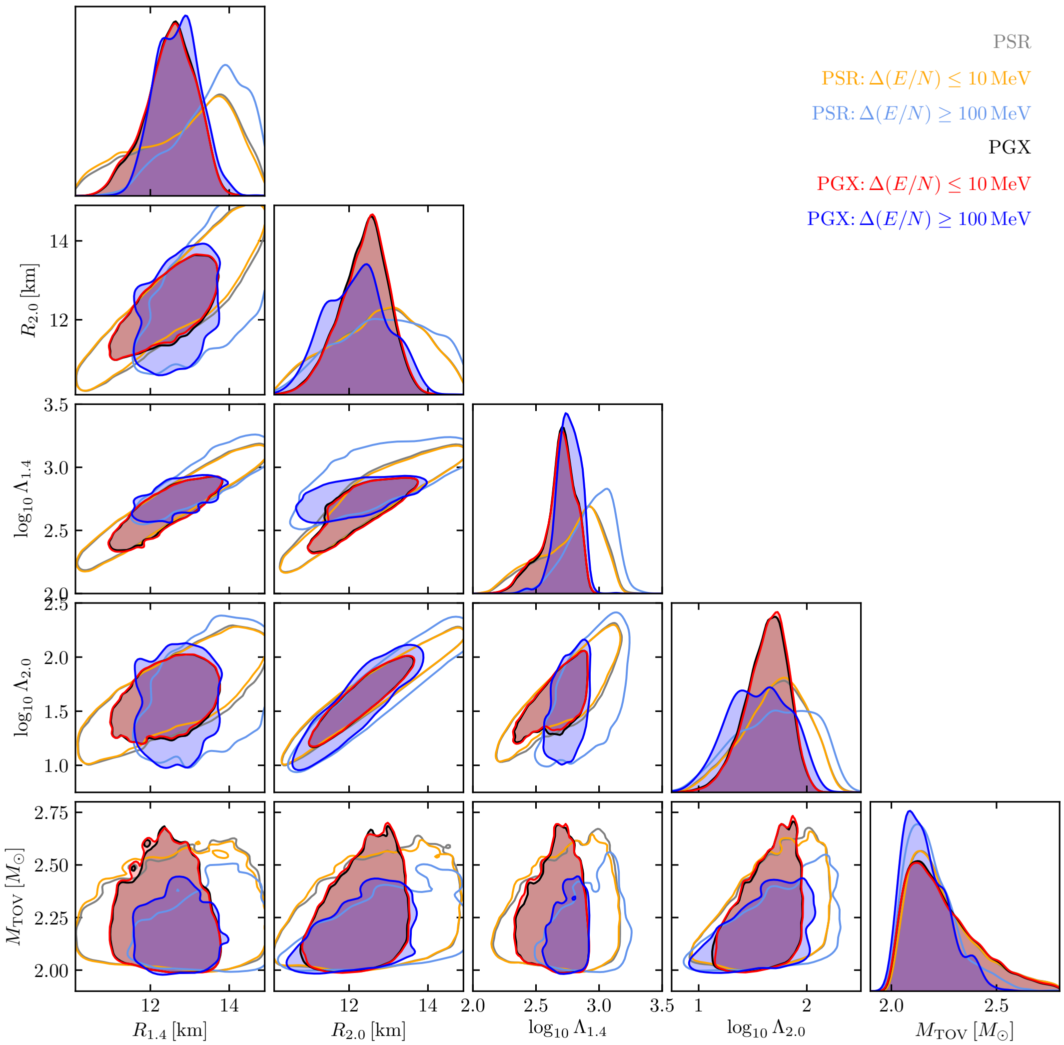

Figure 4.14: Distributions of radii and tidal deformabilities at reference masses as well as M_{TOV} conditioned on current data. These distributions *de facto* exclude EoSs with $M_{\text{TOV}} < 2\,\mathrm{M}_\odot$ by requiring $\Lambda_{2.0} > 0$ (enforced through the logarithmic scale). As in Fig. 4.1, there are much weaker correlations between low-mass and high-mass observables.

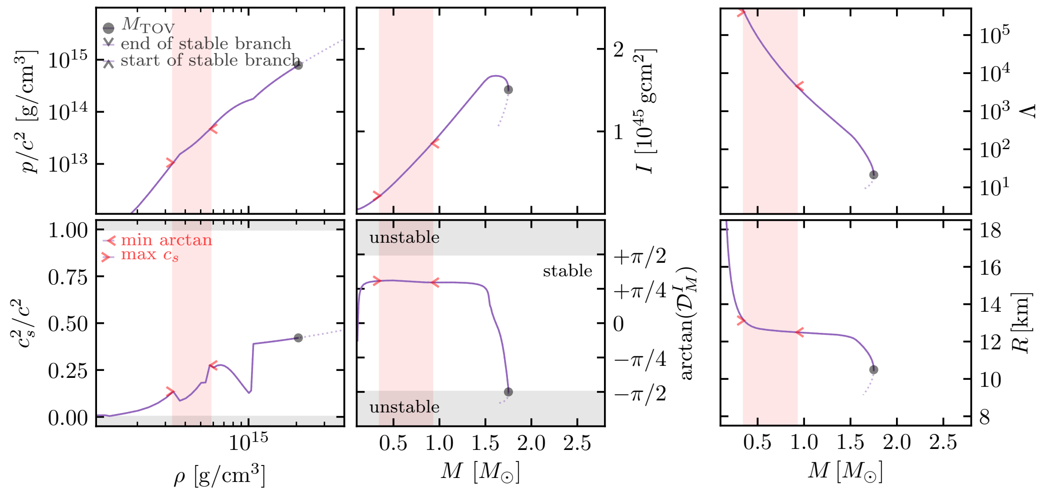

Figure 4.15: An additional example of an EoS with mixed phases (Gibbs construction) from Han et al. [60], analogous to Fig. 4.3.

the data based on these numbers. For example,

$$\mathcal{B}(GX|P) = \frac{\mathcal{B}(GXP)}{\mathcal{B}(P)}. \tag{4.18}$$

4.11 Additional Examples of Phase Transition Phenomenology

This appendix includes additional examples of phase transition phenomenology using both EoSs with known microphysical descriptions (Fig. 4.15) as well as realizations from our nonparametric prior (Figs. 4.16 and 4.17).

Fig. 4.15 shows an EoS with mixed phases, analogous to Fig. 4.3. The more complicated structure in c_s demonstrates two shortcomings of the new feature introduced in Sec. 4.2. The feature does not always identify the correct beginning and end of the phase transition; the microphysical model used to construct this transition has the mixed phase extend beyond the end of the identified region. The true end of the phase transition occurs near $\rho \sim 10^{15}$ g/cm^3 and $M \sim 1.5\,\mathrm{M}_\odot$. Also, some features may be difficult to identify as they are overwhelmed by the final collapse to a BH, which often means there is no local minimum in arctan($\mathcal{D}_M^I$). This is the case for the true end of this transition.

Figs. 4.16 and 4.17 show a few realizations from our nonparametric prior with particularly complex behavior, such as multiple strong phase transitions leading to three disconnected stable branches. These demonstrate that our $\mathcal{D}_M^I$ feature identifies and classifies a broad range of behavior, some of which may not have been anticipated

Table 4.2: Additional ratios of maximized likelihoods for the number of stable branches based on current astrophysical observations: (P) pulsar masses, (G) GW observations from LIGO/Virgo, and (X) X-ray timing from NICER.

$M\ [M_\odot]$	Stable Branches				
	max $\mathcal{L}_{n=1}^{n\geq2}$(P)	max $\mathcal{L}_{n=1}^{n\geq2}$(G)	max $\mathcal{L}_{n=1}^{n\geq2}$(X)	max $\mathcal{L}_{n=1}^{n\geq2}$(PG)	max $\mathcal{L}_{n=1}^{n\geq2}$(PGX)
0.8-1.1	1.00	0.84	0.45	0.79	0.47
1.1-1.6	1.00	0.81	0.33	0.23	0.14
1.6-2.3	1.00	0.75	0.68	0.69	0.20

Table 4.3: Additional ratios of marginal likelihoods for the number of stable branches based on current observations.

M	Stable Branches						
$[M_\odot]$	$\mathcal{B}_{n=1}^{n\geq2}$(P)	$\mathcal{B}_{n=1}^{n\geq2}$(G)	$\mathcal{B}_{n=1}^{n\geq2}$(X)	$\mathcal{B}_{n=1}^{n\geq2}$(PG)	$\mathcal{B}_{n=1}^{n\geq2}$(PGX)	$\mathcal{B}_{n=1}^{n\geq2}$(G|P)	$\mathcal{B}_{n=1}^{n\geq2}$(GX|P)
0.8-1.1	0.169 ± 0.012	0.872 ± 0.010	0.115 ± 0.010	0.421 ± 0.043	0.362 ± 0.036	2.485 ± 0.181	2.219 ± 0.162
1.1-1.6	0.102 ± 0.009	1.369 ± 0.014	0.042 ± 0.005	0.029 ± 0.005	0.030 ± 0.006	0.282 ± 0.064	0.291 ± 0.055
1.6-2.3	1.007 ± 0.043	0.586 ± 0.017	0.384 ± 0.028	0.088 ± 0.027	0.147 ± 0.028	0.088 ± 0.026	0.120 ± 0.026

Table 4.4: Additional ratios of maximized likelihoods for the number of $\mathcal{D}_M^I$ features based on current observations.

M $[M_\odot]$	$\min \Delta(E/N)$ [MeV]	$\mathcal{D}_M^I$ Features				
		$\max \mathcal{L}_{n=0}^{n\geq1}$(P)	$\max \mathcal{L}_{n=0}^{n\geq1}$(G)	$\max \mathcal{L}_{n=0}^{n\geq1}$(X)	$\max \mathcal{L}_{n=0}^{n\geq1}$(PG)	$\max \mathcal{L}_{n=0}^{n\geq1}$(PGX)
0.8-1.1	10	1.00	1.01	0.95	0.88	0.57
	50	1.00	1.01	0.73	0.86	0.49
	100	1.00	1.01	0.68	0.31	0.26
1.1-1.6	10	1.00	1.01	0.83	0.85	0.57
	50	1.00	1.01	0.73	0.78	0.49
	100	1.00	1.01	0.68	0.31	0.26
1.6-2.3	10	1.00	0.91	0.83	0.78	0.52
	50	1.00	0.91	0.73	0.78	0.49
	100	1.00	0.83	0.68	0.31	0.29

Table 4.5: Additional ratios of marginal likelihoods for the number of $\mathcal{D}_M^I$ features based on current astrophysical observations.

M $[M_\odot]$	$\min\Delta(E/N)$ [MeV]	$\mathcal{D}_M^I$ Features						
		$\mathcal{B}_{n=0}^{n\geq1}$(P)	$\mathcal{B}_{n=0}^{n\geq1}$(G)	$\mathcal{B}_{n=0}^{n\geq1}$(X)	$\mathcal{B}_{n=0}^{n\geq1}$(PG)	$\mathcal{B}_{n=0}^{n\geq1}$(PGX)	$\mathcal{B}_{n=0}^{n\geq1}$(G|P)	$\mathcal{B}_{n=0}^{n\geq1}$(GX|P)
0.8-1.1	10	1.781 ± 0.014	1.244 ± 0.005	1.519 ± 0.016	0.897 ± 0.017	1.222 ± 0.020	0.504 ± 0.009	0.684 ± 0.011
	50	0.624 ± 0.008	1.379 ± 0.007	0.451 ± 0.008	0.355 ± 0.011	0.366 ± 0.011	0.570 ± 0.017	0.588 ± 0.016
	100	0.373 ± 0.010	1.393 ± 0.010	0.254 ± 0.009	0.067 ± 0.005	0.117 ± 0.008	0.180 ± 0.013	0.292 ± 0.021
1.1-1.6	10	1.865 ± 0.016	1.250 ± 0.006	1.420 ± 0.016	0.778 ± 0.018	1.043 ± 0.020	0.417 ± 0.009	0.563 ± 0.010
	50	0.950 ± 0.012	1.426 ± 0.008	0.682 ± 0.011	0.368 ± 0.011	0.463 ± 0.013	0.388 ± 0.012	0.481 ± 0.013
	100	0.516 ± 0.011	1.377 ± 0.009	0.350 ± 0.011	0.073 ± 0.004	0.152 ± 0.009	0.142 ± 0.009	0.267 ± 0.017
1.6-2.3	10	2.671 ± 0.028	0.457 ± 0.006	1.761 ± 0.030	0.512 ± 0.020	1.012 ± 0.035	0.192 ± 0.007	0.387 ± 0.013
	50	2.265 ± 0.029	0.512 ± 0.007	1.596 ± 0.030	0.469 ± 0.020	0.898 ± 0.034	0.207 ± 0.009	0.399 ± 0.015
	100	1.366 ± 0.027	0.604 ± 0.009	0.914 ± 0.026	0.170 ± 0.010	0.383 ± 0.023	0.124 ± 0.008	0.256 ± 0.016

with parametric descriptions. For example, Tan et al. [101] and Mroczek et al. [82] introduced a variety of parametric features in the sound-speed and attempted to classify which types of features led to observable effects within macroscopic relations. Our procedure can identify relevant density scales associated with these behaviors and others *without* access to the underlying parametric construction.

This flexibility is due to the fact that our nonparametric prior contains support for multiple different correlation length scales and marginal variances in the speed of sound, particularly compared to some others in the literature, e.g., Refs. [82, 53, 78]. This is achieved by marginalizing over covariance-kernel hyperparameters as described in Essick, Landry, and Holz [38] so that the overall prior process contains $O(150)$ different GPs, each of which generates different types of correlation behavior.

References

[1] J. Aasi et al. "Advanced LIGO". In: *Class. Quant. Grav.* 32 (2015), p. 074001. DOI: 10.1088/0264-9381/32/7/074001. arXiv: 1411.4547 [gr-qc].

[2] B. P. Abbott et al. "GW170817: Measurements of neutron star radii and equation of state". In: *Phys. Rev. Lett.* 121.16 (2018), p. 161101. DOI: 10.1103/PhysRevLett.121.161101. arXiv: 1805.11581 [gr-qc].

[3] B. P. Abbott et al. "GW190425: Observation of a Compact Binary Coalescence with Total Mass $\sim 3.4 M_\odot$". In: *Astrophys. J. Lett.* 892.1 (2020), p. L3. DOI: 10.3847/2041-8213/ab75f5. arXiv: 2001.01761 [astro-ph.HE].

[4] B. P. Abbott et al. "Properties of the binary neutron star merger GW170817". In: *Phys. Rev. X* 9.1 (2019), p. 011001. DOI: 10.1103/PhysRevX.9.011001. arXiv: 1805.11579 [gr-qc].

[5] B. P. Abbott et al. "Prospects for observing and localizing gravitational-wave transients with Advanced LIGO, Advanced Virgo and KAGRA". In: *Living Reviews in Relativity* 23.1 (Sept. 2020), p. 3. ISSN: 1433-8351. DOI: 10.1007/s41114-020-00026-9. URL: https://doi.org/10.1007/s41114-020-00026-9.

[6] Benjamin P. Abbott et al. "GW170817: Observation of Gravitational Waves from a Binary Neutron Star Inspiral". In: *Phys. Rev. Lett.* 119.16 (2017), p. 161101. DOI: 10.1103/PhysRevLett.119.161101. arXiv: 1710.05832 [gr-qc].

[7] R. Abbott et al. *GWTC-3: Compact Binary Coalescences Observed by LIGO and Virgo During the Second Part of the Third Observing Run — O1+O2+O3 Search Sensitivity Estimates*. Zenodo, Nov. 2021. DOI: 10.

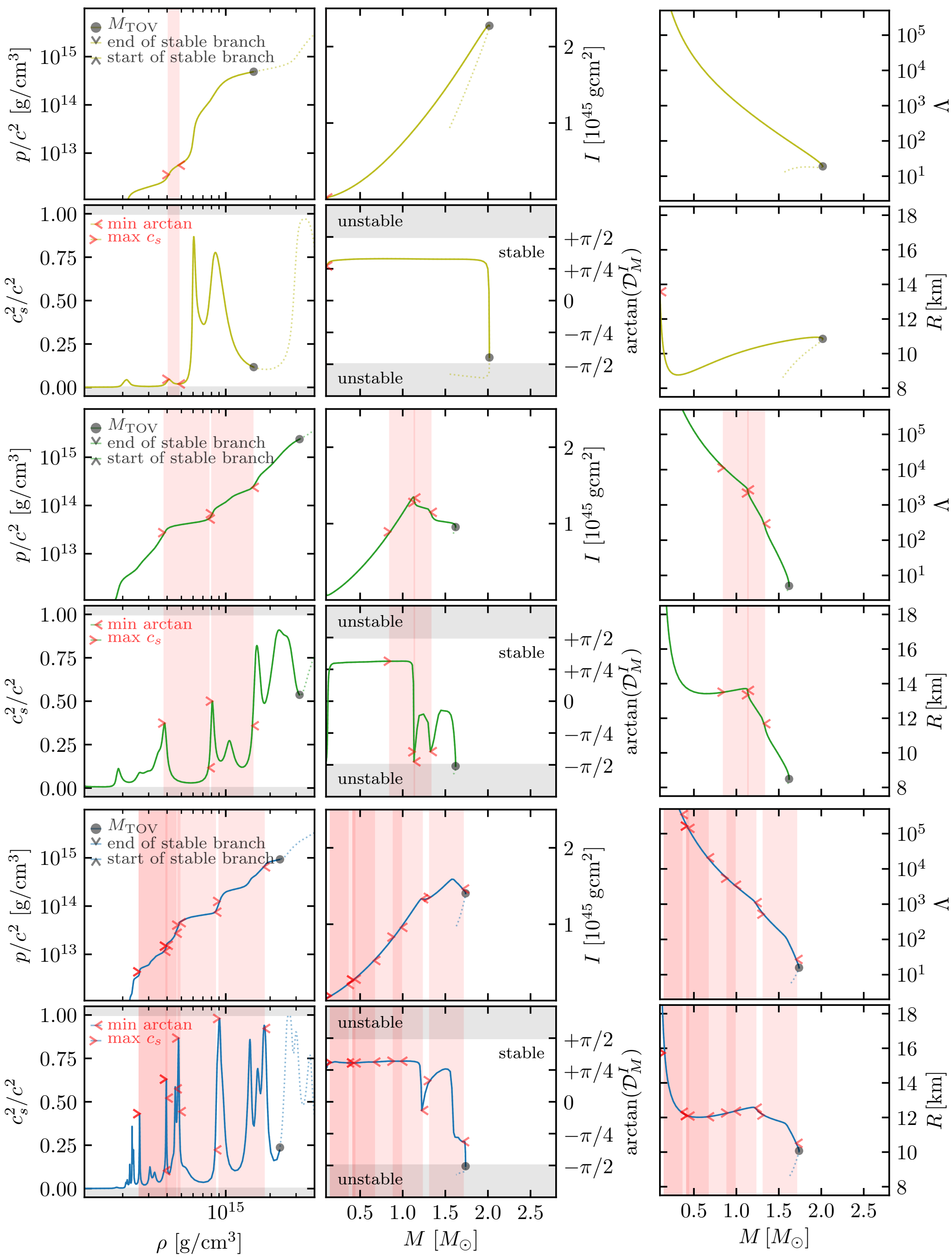

Figure 4.16: Several realizations from our nonparametric prior, each with a single stable branch but with different numbers of phase transitions.

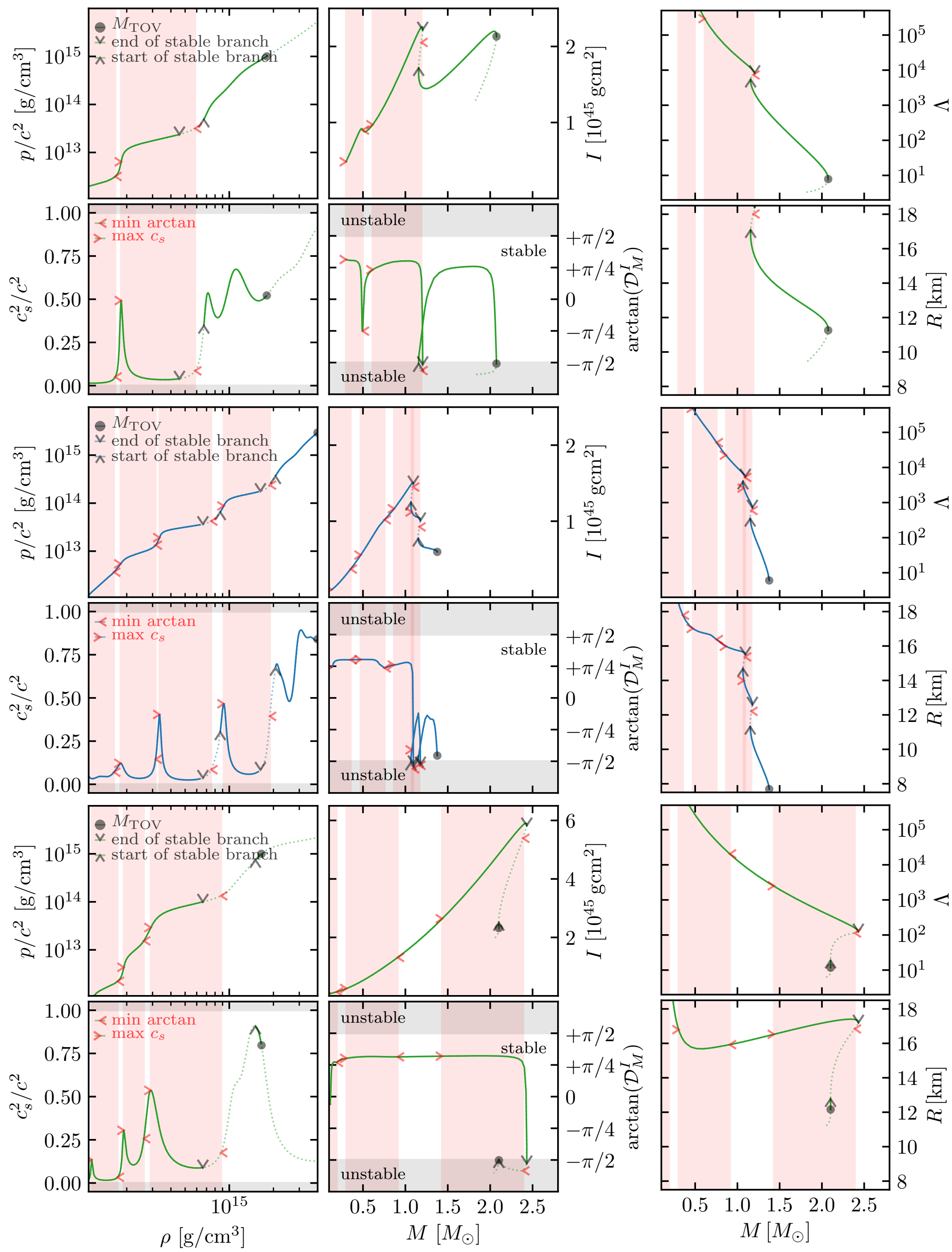

Figure 4.17: Additional realizations from our nonparametric prior, each with multiple stable branches. Typically, we always identify a phase transition associated with the loss of stability between stable branches, even if the stable branches are small (*bottom row*).

5281/zenodo.5636816. URL: https://doi.org/10.5281/zenodo.5636816.

[8] R. Abbott et al. *GWTC-3: Compact Binary Coalescences Observed by LIGO and Virgo During the Second Part of the Third Observing Run — O3 search sensitivity estimates*. Zenodo, Nov. 2021. DOI: 10.5281/zenodo.5546676. URL: https://doi.org/10.5281/zenodo.5546676.

[9] F. Acernese et al. "Advanced Virgo: a second-generation interferometric gravitational wave detector". In: *Class. Quant. Grav.* 32.2 (2015), p. 024001. DOI: 10.1088/0264-9381/32/2/024001. arXiv: 1408.3978 [gr-qc].

[10] D. Adhikari et al. "Accurate Determination of the Neutron Skin Thickness of ^{208}Pb through Parity-Violation in Electron Scattering". In: *Phys. Rev. Lett.* 126.17 (2021), p. 172502. DOI: 10.1103/PhysRevLett.126.172502. arXiv: 2102.10767 [nucl-ex].

[11] D. Adhikari et al. "Precision Determination of the Neutral Weak Form Factor of ^{48}Ca". In: (May 2022). arXiv: 2205.11593 [nucl-ex].

[12] Michalis Agathos et al. "Constraining the neutron star equation of state with gravitational wave signals from coalescing binary neutron stars". In: *Phys. Rev. D* 92.2 (2015), p. 023012. DOI: 10.1103/PhysRevD.92.023012. arXiv: 1503.05405 [gr-qc].

[13] Mark Alford et al. "Hybrid stars that masquerade as neutron stars". In: *Astrophys. J.* 629 (2005), pp. 969–978. DOI: 10.1086/430902. arXiv: nucl-th/0411016.

[14] Mark G. Alford, Sophia Han, and Madappa Prakash. "Generic conditions for stable hybrid stars". In: *Phys. Rev. D* 88.8 (2013), p. 083013. DOI: 10.1103/PhysRevD.88.083013. arXiv: 1302.4732 [astro-ph.SR].

[15] Mark G. Alford, Sophia Han, and Kai Schwenzer. "Signatures for quark matter from multi-messenger observations". In: *J. Phys. G* 46.11 (2019), p. 114001. DOI: 10.1088/1361-6471/ab337a. arXiv: 1904.05471 [nucl-th].

[16] Mark G. Alford and Armen Sedrakian. "Compact stars with sequential QCD phase transitions". In: *Phys. Rev. Lett.* 119.16 (2017), p. 161104. DOI: 10.1103/PhysRevLett.119.161104. arXiv: 1706.01592 [astro-ph.HE].

[17] Justin Alsing, Hector O. Silva, and Emanuele Berti. "Evidence for a maximum mass cut-off in the neutron star mass distribution and constraints on the equation of state". In: *Mon. Not. Roy. Astron. Soc.* 478.1 (2018), pp. 1377–1391. DOI: 10.1093/mnras/sty1065. arXiv: 1709.07889 [astro-ph.HE].

[18] Eemeli Annala et al. "Quark-matter cores in neutron stars". In: (2019). arXiv: 1903.09121 [astro-ph.HE].

[19] Eemeli Annala et al. "Strongly interacting matter exhibits deconfined behavior in massive neutron stars". In: (Mar. 2023). arXiv: 2303.11356 [astro-ph.HE].

[20] John Antoniadis et al. "A Massive Pulsar in a Compact Relativistic Binary". In: *Science* 340.6131 (2013), p. 1233232. DOI: 10.1126/science.1233232. arXiv: 1304.6875 [astro-ph.HE].

[21] Andreas Bauswein et al. "Identifying a first-order phase transition in neutron star mergers through gravitational waves". In: *Phys. Rev. Lett.* 122.6 (2019), p. 061102. DOI: 10.1103/PhysRevLett.122.061102. arXiv: 1809.01116 [astro-ph.HE].

[22] Gordon Baym et al. "From hadrons to quarks in neutron stars: a review". In: *Rept. Prog. Phys.* 81.5 (2018), p. 056902. DOI: 10.1088/1361-6633/aaae14. arXiv: 1707.04966 [astro-ph.HE].

[23] Paulo Bedaque and Andrew W. Steiner. "Sound velocity bound and neutron stars". In: *Phys. Rev. Lett.* 114.3 (2015), p. 031103. DOI: 10.1103/PhysRevLett.114.031103. arXiv: 1408.5116 [nucl-th].

[24] Bhaskar Biswas. "Impact of PREX-II, the revised mass measurement of PSRJ0740+6620, and possible NICER observation on the dense matter equation of state". In: (May 2021). arXiv: 2105.02886 [astro-ph.HE].

[25] Bhaskar Biswas et al. "Towards mitigation of apparent tension between nuclear physics and astrophysical observations by improved modeling of neutron star matter". In: *Phys. Rev. D* 103 (10 May 2021), p. 103015. DOI: 10.1103/PhysRevD.103.103015. URL: https://link.aps.org/doi/10.1103/PhysRevD.103.103015.

[26] Sebastian Blacker, Andreas Bauswein, and Stefan Typel. "Exploring thermal effects of the hadron-quark matter transition in neutron star mergers". In: (Apr. 2023). arXiv: 2304.01971 [astro-ph.HE].

[27] Matthew F. Carney, Leslie E. Wade, and Burke S. Irwin. "Comparing two models for measuring the neutron star equation of state from gravitational-wave signals". In: *Phys. Rev.* D98.6 (2018), p. 063004. DOI: 10.1103/PhysRevD.98.063004. arXiv: 1805.11217 [gr-qc].

[28] Katerina Chatziioannou. "Neutron star tidal deformability and equation of state constraints". In: *Gen. Rel. Grav.* 52.11 (2020), p. 109. DOI: 10.1007/s10714-020-02754-3. arXiv: 2006.03168 [gr-qc].

[29] Katerina Chatziioannou and Sophia Han. "Studying strong phase transitions in neutron stars with gravitational waves". In: *Phys. Rev. D* 101.4 (2020), p. 044019. DOI: 10.1103/PhysRevD.101.044019. arXiv: 1911.07091 [gr-qc].

[30] Hsin-Yu Chen and Katerina Chatziioannou. "Distinguishing Binary Neutron Star from Neutron Star–Black Hole Mergers with Gravitational Waves". In: *Astrophys. J. Lett.* 893.2 (2020), p. L41. DOI: 10.3847/2041-8213/ab86bc. arXiv: 1903.11197 [astro-ph.HE].

[31] Hsin-Yu Chen, Paul M. Chesler, and Abraham Loeb. "Searching for exotic cores with binary neutron star inspirals". In: *Astrophys. J. Lett.* 893.1 (2020), p. L4. DOI: 10.3847/2041-8213/ab830f. arXiv: 1909.04096 [astro-ph.HE].

[32] Constantinos Constantinou et al. "A framework for phase transitions between the Maxwell and Gibbs constructions". In: (Feb. 2023). arXiv: 2302.04289 [nucl-th].

[33] Constantinos Constantinou et al. "g modes of neutron stars with hadron-to-quark crossover transitions". In: *Phys. Rev. D* 104.12 (2021), p. 123032. DOI: 10.1103/PhysRevD.104.123032. arXiv: 2109.14091 [astro-ph.HE].

[34] H. Thankful Cromartie et al. "Relativistic Shapiro delay measurements of an extremely massive millisecond pulsar". In: *Nature Astron.* 4.1 (2019), pp. 72–76. DOI: 10.1038/s41550-019-0880-2. arXiv: 1904.06759.

[35] Walter Del Pozzo et al. "Demonstrating the feasibility of probing the neutron star equation of state with second-generation gravitational wave detectors". In: *Phys. Rev. Lett.* 111.7 (2013), p. 071101. DOI: 10.1103/PhysRevLett.111.071101. arXiv: 1307.8338 [gr-qc].

[36] Tim Dietrich et al. "Multimessenger constraints on the neutron-star equation of state and the Hubble constant". In: *Science* 370.6523 (2020), pp. 1450–1453. DOI: 10.1126/science.abb4317. arXiv: 2002.11355 [astro-ph.HE].

[37] Christian Drischler et al. "Limiting masses and radii of neutron stars and their implications". In: *Phys. Rev. C* 103.4 (2021), p. 045808. DOI: 10.1103/PhysRevC.103.045808. arXiv: 2009.06441 [nucl-th].

[38] Reed Essick, Philippe Landry, and Daniel E. Holz. "Nonparametric Inference of Neutron Star Composition, Equation of State, and Maximum Mass with GW170817". In: *Phys. Rev. D* 101.6 (2020), p. 063007. DOI: 10.1103/PhysRevD.101.063007. arXiv: 1910.09740 [astro-ph.HE].

[39] Reed Essick et al. "A Detailed Examination of Astrophysical Constraints on the Symmetry Energy and the Neutron Skin of ^{208}Pb with Minimal Modeling Assumptions". In: (July 2021). arXiv: 2107.05528 [nucl-th].

[40] Reed Essick et al. "Astrophysical Constraints on the Symmetry Energy and the Neutron Skin of ^{208}Pb with Minimal Modeling Assumptions". In: (Feb. 2021). arXiv: 2102.10074 [nucl-th].

[41] Reed Essick et al. “Direct astrophysical tests of chiral effective field theory at supranuclear densities”. In: *Phys. Rev. C* 102 (5 Nov. 2020), p. 055803. DOI: 10.1103/PhysRevC.102.055803. URL: https://link.aps.org/doi/10.1103/PhysRevC.102.055803.

[42] Will M. Farr and Katerina Chatziioannou. “A Population-Informed Mass Estimate for Pulsar J0740+6620”. In: *Research Notes of the American Astronomical Society* 4.5, 65 (May 2020), p. 65. DOI: 10.3847/2515-5172/ab9088. arXiv: 2005.00032 [astro-ph.GA].

[43] Eanna E. Flanagan and Tanja Hinderer. “Constraining neutron star tidal Love numbers with gravitational wave detectors”. In: *Phys. Rev. D* 77 (2008), p. 021502. DOI: 10.1103/PhysRevD.77.021502. arXiv: 0709.1915 [astro-ph].

[44] E. Fonseca et al. “Refined Mass and Geometric Measurements of the High-mass PSR J0740+6620”. In: *Astrophys. J. Lett.* 915.1 (2021), p. L12. DOI: 10.3847/2041-8213/ac03b8. arXiv: 2104.00880 [astro-ph.HE].

[45] Yuki Fujimoto, Kenji Fukushima, and Koichi Murase. “Extensive Studies of the Neutron Star Equation of State from the Deep Learning Inference with the Observational Data Augmentation”. In: *JHEP* 03 (2021), p. 273. DOI: 10.1007/JHEP03(2021)273. arXiv: 2101.08156 [nucl-th].

[46] Yuki Fujimoto, Kenji Fukushima, and Koichi Murase. “Mapping neutron star data to the equation of state using the deep neural network”. In: *Phys. Rev. D* 101 (5 Mar. 2020), p. 054016. DOI: 10.1103/PhysRevD.101.054016. URL: https://link.aps.org/doi/10.1103/PhysRevD.101.054016.

[47] Yuki Fujimoto, Kenji Fukushima, and Koichi Murase. “Methodology study of machine learning for the neutron star equation of state”. In: *Phys. Rev. D* 98 (2 July 2018), p. 023019. DOI: 10.1103/PhysRevD.98.023019. URL: https://link.aps.org/doi/10.1103/PhysRevD.98.023019.

[48] Yuki Fujimoto et al. “Gravitational Wave Signal for Quark Matter with Realistic Phase Transition”. In: *PhRvL* 130.9, 091404 (Mar. 2023), p. 091404. DOI: 10.1103/PhysRevLett.130.091404. arXiv: 2205.03882 [astro-ph.HE].

[49] Kenji Fukushima and Toru Kojo. “The Quarkyonic Star”. In: *Astrophys. J.* 817.2 (2016), p. 180. DOI: 10.3847/0004-637X/817/2/180. arXiv: 1509.00356 [nucl-th].

[50] N. K. Glendenning. “Phase transitions and crystalline structures in neutron star cores”. In: *Phys. Rept.* 342 (2001), pp. 393–447. DOI: 10.1016/S0370-1573(00)00080-6.

[51] Norman K. Glendenning. “First order phase transitions with more than one conserved charge: Consequences for neutron stars”. In: *Phys. Rev. D* 46 (1992), pp. 1274–1287. DOI: 10.1103/PhysRevD.46.1274.

[52] Tyler Gorda, Oleg Komoltsev, and Aleksi Kurkela. “Ab-initio QCD calculations impact the inference of the neutron-star-matter equation of state”. In: (Apr. 2022). arXiv: 2204.11877 [nucl-th].

[53] Tyler Gorda et al. “Bayesian uncertainty quantification of perturbative QCD input to the neutron-star equation of state”. In: (Mar. 2023). arXiv: 2303.02175 [hep-ph].

[54] Tyler Gorda et al. “Constraints on strong phase transitions in neutron stars”. In: (Dec. 2022). arXiv: 2212.10576 [astro-ph.HE].

[55] S. K. Greif et al. “Equation of state sensitivities when inferring neutron star and dense matter properties”. In: *Mon. Not. Roy. Astron. Soc.* 485.4 (2019), pp. 5363–5376. DOI: 10.1093/mnras/stz654. arXiv: 1812.08188 [astro-ph.HE].

[56] T. Gross-Boelting, C. Fuchs, and Amand Faessler. “Covariant representations of the relativistic Bruckner T matrix and the nuclear matter problem”. In: *Nucl. Phys. A* 648 (1999), pp. 105–137. DOI: 10.1016/S0375-9474(99)00022-6. arXiv: nucl-th/9810071.

[57] Ming-Zhe Han et al. “Bayesian nonparametric inference of neutron star equation of state via neural network”. In: (Mar. 2021). arXiv: 2103.05408 [hep-ph].

[58] Ming-Zhe Han et al. “Plausible presence of new state in neutron stars with masses above $0.98M_{\mathrm{TOV}}$”. In: (July 2022). DOI: 10.1016/j.scib.2023.04.007. arXiv: 2207.13613 [astro-ph.HE].

[59] Sophia Han and Andrew W. Steiner. “Tidal deformability with sharp phase transitions in (binary) neutron stars”. In: *Phys. Rev. D* 99.8 (2019), p. 083014. DOI: 10.1103/PhysRevD.99.083014. arXiv: 1810.10967 [nucl-th].

[60] Sophia Han et al. “Treating quarks within neutron stars”. In: *Phys. Rev. D* 100 (10 Nov. 2019), p. 103022. DOI: 10.1103/PhysRevD.100.103022. URL: https://link.aps.org/doi/10.1103/PhysRevD.100.103022.

[61] Matthias Hempel et al. “Noncongruence of the nuclear liquid-gas and deconfinement phase transitions”. In: *Phys. Rev. C* 88.1 (2013), p. 014906. DOI: 10.1103/PhysRevC.88.014906. arXiv: 1302.2835 [nucl-th].

[62] Jin-Liang Jiang et al. “PSR J0030+0451, GW170817 and the nuclear data: joint constraints on equation of state and bulk properties of neutron stars”. In: *Astrophys. J.* 892 (2020), p. 1. DOI: 10.3847/1538-4357/ab77cf. arXiv: 1912.07467 [astro-ph.HE].

[63] Robert E. Kass and Adrian E. Raftery. “Bayes Factors”. In: *Journal of the American Statistical Association* 90.430 (1995), pp. 773–795. DOI: 10.1080/01621459.1995.10476572. URL: https://www.tandfonline.com/doi/abs/10.1080/01621459.1995.10476572.

[64] Oleg Komoltsev and Aleksi Kurkela. "How Perturbative QCD Constrains the Equation of State at Neutron-Star Densities". In: *Phys. Rev. Lett.* 128.20 (2022), p. 202701. DOI: 10.1103/PhysRevLett.128.202701. arXiv: 2111.05350 [nucl-th].

[65] Sven Köppel, Luke Bovard, and Luciano Rezzolla. "A General-relativistic Determination of the Threshold Mass to Prompt Collapse in Binary Neutron Star Mergers". In: *Astrophys. J. Lett.* 872.1 (2019), p. L16. DOI: 10.3847/2041-8213/ab0210. arXiv: 1901.09977 [gr-qc].

[66] Philippe Landry and Kabir Chakravarti. "Prospects for constraining twin stars with next-generation gravitational-wave detectors". In: *arXiv*, arXiv:2212.09733 (Dec. 2022), arXiv:2212.09733. DOI: 10.48550/arXiv.2212.09733. arXiv: 2212.09733 [astro-ph.HE].

[67] Philippe Landry and Reed Essick. "Nonparametric inference of the neutron star equation of state from gravitational wave observations". In: *Phys. Rev. D* 99 (8 Apr. 2019), p. 084049. DOI: 10.1103/PhysRevD.99.084049. URL: https://link.aps.org/doi/10.1103/PhysRevD.99.084049.

[68] Philippe Landry, Reed Essick, and Katerina Chatziioannou. "Nonparametric constraints on neutron star matter with existing and upcoming gravitational wave and pulsar observations". In: *Phys. Rev. D* 101.12 (2020), p. 123007. DOI: 10.1103/PhysRevD.101.123007. arXiv: 2003.04880 [astro-ph.HE].

[69] Isaac Legred et al. "Impact of the PSR J0740+6620 radius constraint on the properties of high-density matter". In: *Phys. Rev. D* 104.6 (2021), p. 063003. DOI: 10.1103/PhysRevD.104.063003. arXiv: 2106.05313 [astro-ph.HE].

[70] Isaac Legred et al. "Implicit correlations within phenomenological parametric models of the neutron star equation of state". In: *Phys. Rev. D* 105.4 (2022). I led this study which compared parametric to nonparametric methods of inferring the equation of state. I developed a substantial amount of software, ran the analysis, and co-wrote the manuscript., p. 043016. DOI: 10.1103/PhysRevD.105.043016. arXiv: 2201.06791 [astro-ph.HE].

[71] Lee Lindblom. "Determining the Nuclear Equation of State from Neutron-Star Masses and Radii". In: *The Astrophysical Journal* 398 (Oct. 1992), p. 569. DOI: 10.1086/171882.

[72] Lee Lindblom. "Phase transitions and the mass radius curves of relativistic stars". In: *Phys. Rev. D* 58 (1998), p. 024008. DOI: 10.1103/PhysRevD.58.024008. arXiv: gr-qc/9802072.

[73] Lee Lindblom. "Spectral representations of neutron-star equations of state". In: *Phys. Rev. D* 82 (10 Nov. 2010), p. 103011. DOI: 10.1103/PhysRevD.82.103011. URL: https://link.aps.org/doi/10.1103/PhysRevD.82.103011.

[74] Tyson B. Littenberg and Neil J. Cornish. "Prototype global analysis of LISA data with multiple source types". In: *Phys. Rev. D* 107.6 (2023), p. 063004. DOI: 10.1103/PhysRevD.107.063004. arXiv: 2301.03673 [gr-qc].

[75] Ben Margalit and Brian D. Metzger. "Constraining the Maximum Mass of Neutron Stars From Multi-Messenger Observations of GW170817". In: *Astrophys. J.* 850.2 (2017), p. L19. DOI: 10.3847/2041-8213/aa991c. arXiv: 1710.05938 [astro-ph.HE].

[76] Larry McLerran and Sanjay Reddy. "Quarkyonic Matter and Neutron Stars". In: *Phys. Rev. Lett.* 122.12 (2019), p. 122701. DOI: 10.1103/PhysRevLett.122.122701. arXiv: 1811.12503 [nucl-th].

[77] M. C. Miller et al. "PSR J0030+0451 Mass and Radius from *NICER* Data and Implications for the Properties of Neutron Star Matter". In: *Astrophys. J. Lett.* 887.1 (2019), p. L24. DOI: 10.3847/2041-8213/ab50c5. arXiv: 1912.05705 [astro-ph.HE].

[78] M. C. Miller et al. "The Radius of PSR J0740+6620 from NICER and XMM-Newton Data". In: *Astrophys. J. Lett.* 918.2 (2021), p. L28. DOI: 10.3847/2041-8213/ac089b. arXiv: 2105.06979 [astro-ph.HE].

[79] M. Coleman Miller, Cecilia Chirenti, and Frederick K. Lamb. "Constraining the equation of state of high-density cold matter using nuclear and astronomical measurements". In: (2019). arXiv: 1904.08907 [astro-ph.HE].

[80] Gloria Montana et al. "Constraining twin stars with GW170817". In: *Phys. Rev. D* 99.10 (2019), p. 103009. DOI: 10.1103/PhysRevD.99.103009. arXiv: 1811.10929 [astro-ph.HE].

[81] Elias R. Most et al. "Signatures of quark-hadron phase transitions in general-relativistic neutron-star mergers". In: *Phys. Rev. Lett.* 122.6 (2019), p. 061101. DOI: 10.1103/PhysRevLett.122.061101. arXiv: 1807.03684 [astro-ph.HE].

[82] Debora Mroczek et al. "Searching for phase transitions in neutron stars with modified Gaussian processes". In: *Compact Stars in the QCD Phase Diagram: From RHIC to Astrophysics, probing the quark-gluon plasma*. Feb. 2023. arXiv: 2302.07978 [astro-ph.HE].

[83] J. R. Oppenheimer and G. M. Volkoff. "On Massive Neutron Cores". In: *Phys. Rev.* 55 (4 Feb. 1939), pp. 374–381. DOI: 10.1103/PhysRev.55.374. URL: https://link.aps.org/doi/10.1103/PhysRev.55.374.

[84] Peter T. H. Pang et al. "Nuclear-Physics Multi-Messenger Astrophysics Constraints on the Neutron-Star Equation of State: Adding NICER's PSR J0740+6620 Measurement". In: (May 2021). arXiv: 2105.08688 [astro-ph.HE].

[85] Peter T. H. Pang et al. "Parameter estimation for strong phase transitions in supranuclear matter using gravitational-wave astronomy". In: *Phys. Rev. Res.* 2.3 (2020), p. 033514. DOI: 10.1103/PhysRevResearch.2.033514. arXiv: 2006.14936 [astro-ph.HE].

[86] Jonas P. Pereira et al. "Differentiating between sharp and smoother phase transitions in neutron stars". In: *PhRvD* 105.12, 123015 (June 2022), p. 123015. DOI: 10.1103/PhysRevD.105.123015. arXiv: 2201.01217 [astro-ph.HE].

[87] G. Raaijmakers et al. "A NICER view of PSR J0030+0451: Implications for the dense matter equation of state". In: *Astrophys. J. Lett.* 887 (2019), p. L22. DOI: 10.3847/2041-8213/ab451a. arXiv: 1912.05703 [astro-ph.HE].

[88] G. Raaijmakers et al. "Constraints on the dense matter equation of state and neutron star properties from NICER's mass-radius estimate of PSR J0740+6620 and multimessenger observations". In: (May 2021). arXiv: 2105.06981 [astro-ph.HE].

[89] Brendan T. Reed et al. "Implications of PREX-2 on the Equation of State of Neutron-Rich Matter". In: *Phys. Rev. Lett.* 126 (17 Apr. 2021), p. 172503. DOI: 10.1103/PhysRevLett.126.172503. URL: https://link.aps.org/doi/10.1103/PhysRevLett.126.172503.

[90] Thomas E. Riley et al. "A *NICER* View of PSR J0030+0451: Millisecond Pulsar Parameter Estimation". In: *Astrophys. J. Lett.* 887.1 (2019), p. L21. DOI: 10.3847/2041-8213/ab481c. arXiv: 1912.05702 [astro-ph.HE].

[91] Thomas E. Riley et al. "A NICER View of the Massive Pulsar PSR J0740+6620 Informed by Radio Timing and XMM-Newton Spectroscopy". In: *Astrophys. J. Lett.* 918.2 (2021), p. L27. DOI: 10.3847/2041-8213/ac0a81. arXiv: 2105.06980 [astro-ph.HE].

[92] Nathan Rutherford et al. "Constraining bosonic asymmetric dark matter with neutron star mass-radius measurements". In: (Aug. 2022). arXiv: 2208.03282 [astro-ph.HE].

[93] Tuomo Salmi et al. "The Radius of PSR J0740+6620 from NICER with NICER Background Estimates". In: *Astrophys. J.* 941.2 (2022), p. 150. DOI: 10.3847/1538-4357/ac983d. arXiv: 2209.12840 [astro-ph.HE].

[94] R Schaeffer, L Zdunik, and P Haensel. "Phase transitions in stellar cores. I-Equilibrium configurations". In: *Astron. Astrophys.* 126 (1983), pp. 121–145.

[95] Jurgen Schaffner-Bielich et al. "Phase transition to hyperon matter in neutron stars". In: *Phys. Rev. Lett.* 89 (2002), p. 171101. DOI: 10.1103/PhysRevLett.89.171101. arXiv: astro-ph/0005490.

[96] K. Schertler et al. "Quark phases in neutron stars and a 'third family' of compact stars as a signature for phase transitions". In: *Nucl. Phys. A* 677 (2000), pp. 463–490. DOI: 10.1016/S0375-9474(00)00305-5. arXiv: astro-ph/0001467 [astro-ph].

[97] Z. F. Seidov. "The Stability of a Star with a Phase Change in General Relativity Theory". In: *Sov. Astron.* 15 (Oct. 1971), p. 347.

[98] Masaru Shibata et al. “Constraint on the maximum mass of neutron stars using GW170817 event”. In: *Phys. Rev. D* 100.2 (2019), p. 023015. DOI: 10.1103/PhysRevD.100.023015. arXiv: 1905.03656 [astro-ph.HE].

[99] Rahul Somasundaram, Ingo Tews, and Jérôme Margueron. “Perturbative QCD and the Neutron Star Equation of State”. In: (Apr. 2022). arXiv: 2204.14039 [nucl-th].

[100] Janos Takatsy et al. “What neutron stars tell about the hadron-quark phase transition: a Bayesian study”. In: (Feb. 2023). arXiv: 2303.00013 [astro-ph.HE].

[101] Hung Tan et al. “Extreme Matter meets Extreme Gravity: Ultra-heavy neutron stars with crossovers and first-order phase transitions”. In: (June 2021). arXiv: 2106.03890 [astro-ph.HE].

[102] Michalis K. Titsias, Magnus Rattray, and Neil D. Lawrence. “Markov chain Monte Carlo algorithms for Gaussian processes”. In: *Bayesian Time Series Models*. Ed. by David Barber, A. Taylan Cemgil, and SilviaEditors Chiappa. Cambridge University Press, 2011, pp. 295–316. DOI: 10.1017/CBO9780511984679.015.

[103] Richard C. Tolman. “Static Solutions of Einstein’s Field Equations for Spheres of Fluid”. In: *Phys. Rev.* 55 (4 Feb. 1939), pp. 364–373. DOI: 10.1103/PhysRev.55.364. URL: https://link.aps.org/doi/10.1103/PhysRev.55.364.

[104] Leslie Wade et al. “Systematic and statistical errors in a bayesian approach to the estimation of the neutron-star equation of state using advanced gravitational wave detectors”. In: *Phys. Rev. D* 89.10 (2014), p. 103012. DOI: 10.1103/PhysRevD.89.103012. arXiv: 1402.5156 [gr-qc].

[105] Marcella Wijngaarden et al. “Probing neutron stars with the full premerger and postmerger gravitational wave signal from binary coalescences”. In: *Phys. Rev. D* 105.10 (2022), p. 104019. DOI: 10.1103/PhysRevD.105.104019. arXiv: 2202.09382 [gr-qc].

[106] J. L. Zdunik and P. Haensel. “Maximum mass of neutron stars and strange neutron-star cores”. In: *Astron. Astrophys.* 551 (2013), A61. DOI: 10.1051/0004-6361/201220697. arXiv: 1211.1231 [astro-ph.SR].

Chapter 5

UNIVERSAL RELATIONS IN LIGHT OF MODEL-AGNOSTIC EOS DESCRIPTIONS.

[1] Isaac Legred et al. "Assessing equation of state-independent relations for neutron stars with nonparametric models". In: *Phys. Rev. D* 109.2 (2024). I co-led this project on analyzing the goodness of fit of universal relations to nonparametric equations of state, along with Oscar Sy-Garcia who performed a substantial amount of the analyses as a SURF student. This included development of the project, writing the manuscript, and running final analyses., p. 023020. DOI: 10.1103/PhysRevD.109.023020. arXiv: 2310.10854 [astro-ph.HE].

Abstract

Relations between neutron star properties that do not depend on the nuclear equation of state offer insights on neutron star physics and have practical applications in data analysis. Such relations are obtained by fitting to a range of phenomenological or nuclear physics equation of state models, each of which may have varying degrees of accuracy. In this study we revisit commonly-used relations and re-assess them with a very flexible set of phenomenological nonparametric equation of state models that are based on Gaussian Processes. Our models correspond to two sets: equations of state which mimic hadronic models, and equations of state with rapidly changing behavior that resemble phase transitions. We quantify the accuracy of relations under both sets and discuss their applicability with respect to expected upcoming statistical uncertainties of astrophysical observations. We further propose a goodness-of-fit metric which provides an estimate for the systematic error introduced by using the relation to model a certain equation-of-state set. Overall, the nonparametric distribution is more poorly fit with existing relations, with the I–Love–Q relations retaining the highest degree of universality. Fits degrade for relations involving the tidal deformability, such as the Binary-Love and compactness-Love relations, and when introducing phase transition phenomenology. For most relations, systematic errors are comparable to current statistical uncertainties under the nonparametric equation of state distributions.

5.1 Introduction

While most neutron star (NS) properties depend sensitively on the unknown equation of state (EoS) of dense nuclear matter, some properties are interrelated in an approximate EoS-independent way [87]. The impact of EoS-independent relations ranges from enhancing our understanding of NS physics [45, 92, 91, 10, 71] to practical applications in analyses of data. For example, relations between the NS multiple moments [61, 91, 74, 23] have led to a generalization of the no-hair theorem for black holes to the three-hair relations for Newtonian NSs [74], while the so-called "I–Love–Q" relations [89, 90] have been attributed to the self-similarity of isodensity contours [92]. On the data analysis side, EoS-independent relations reduce the number of degrees of freedom [86, 22, 93, 19, 84] and enable consistency tests [90, 72, 73, 82, 16].

EoS-independent relations may include static or dynamic and macroscopic or microscopic quantities. One of the earliest proposed such relation is the one between the (complex) NS modes and their mass and radius, which can be used to translate gravitational wave (GW) observations from isolated NSs to constraints on the radius [7, 6, 79, 12, 46]. Additionally, relations including the NS tidal parameters can simplify analysis of GW data. In general, the signal emitted during the coalescence of two NSs depends on a list of tidal deformability parameters and the rotational quadrupole moment of each star. Relations between the different tidal parameters and the quadrupole moment [85, 86, 89, 90] reduce the number of free parameters to one per star, typically the so-called dimensionless tidal deformability Λ_i, $i \in \{1, 2\}$. A relation between Λ_1 and Λ_2 (and the binary mass ratio) further reduces the number of free parameters to just one [88, 22, 1, 63, 27, 13].

EoS-independent relations are typically constructed empirically by fitting a large number of EoS models, obtained either through phenomenological or theoretical nuclear models. Their applicability is therefore limited to the nuclear physics represented in the set of EoSs, while deviations from the relations may be a sign of new (relevant) physics. For example, an observed deviation from the relation between the frequency content of the post-merger GW signal from a NS coalescence and the tidal properties of the pre-merger signal that hold for hadronic matter [9, 76, 10, 14, 33, 49] can signal the presence of quark matter in the merger remnant [11, 56, 82, 16]. The breakdown of universal behavior in a catalog of observations can further be used to identify outliers that can be attributed to quark matter [21] or NS-black hole binaries [25].

Beyond relations breaking down outside their regime of validity, EoS-independent relations display different degrees of independence even within it, which furthermore varies across the NS parameter space. The set of EoSs the relation is fitted to sensitively impacts the degree of EoS-independence. A potential choice of such a set is EoS candidates from nuclear theory, and corresponds to evaluating the degree of independence present in existing nuclear models [89, 88, 60]. Nonetheless, the extent to which current nuclear models cover the entire range of possible behaviors of matter at high densities is unclear.

More extended sets of EoSs can be obtained by considering phenomenological models, designed to mimic nuclear theory while maintaining some degree of flexibility at high densities. Examples of such phenomenological models include piecewise polytropes [68, 58] and spectral representations [50, 51, 52]. This approach leads to large sets of EoSs and statistical distributions on the EoS which can further be conditioned on astrophysical observations. Such studies directly quantify the impact of astrophysical constraints on the degree of EoS-independence compared to fully agnostic nuclear behavior. For example, Carson et al. [18] considered spectral EoSs that have been conditioned on GW170817 [4, 3] and found that the degree of EoS-independence can be improved by more than 50% compared to an agnostic EoS set. Similar improvements have been reported in [35, 36, 57].

Though more generic than a set of selected nuclear models, parametric EoS representations are still limited in flexibility by the functional form of the EoS, which is usually not determined from first principles. This can lead to strong correlations between the EoS at different densities that are not an outcome of nuclear insight, but of the arbitrary functional form of the representation [48]. These correlations effectively cause many EoSs in the fitting set to share similar macroscopic and microscopic features, mimicking or strengthening true EoS-independence [48]. Figure 5.1 shows an example of such emerging EoS-independence in the radius $R_{1.4}$ and dimensionless tidal deformability $\Lambda_{1.4}$ of a $1.4M_\odot$ NS, and the pressure at twice saturation[1] $p_{2.0}$. The $R_{1.4}$–$\Lambda_{1.4}$ relation is an outcome of the so called C–Love relation [53, 87] (discussed more later), while a correlation with $p_{2.0}$ has been observed in several theoretical models [45], is analogous to the C–α_c relation described later. Using the spectral parameterization, perfect knowledge of $\Lambda_{1.4}$ would give a $R_{1.4}$ uncertainty of $\sim 1\,\mathrm{km}$, consistent with the error in the C–Love relation computed in [18].[2]

[1] We define the saturation density as $2.8 \times 10^{14}\ \mathrm{g/cm}^3$.

[2] When computing the compactness (and throughout unless otherwise stated), we use units with

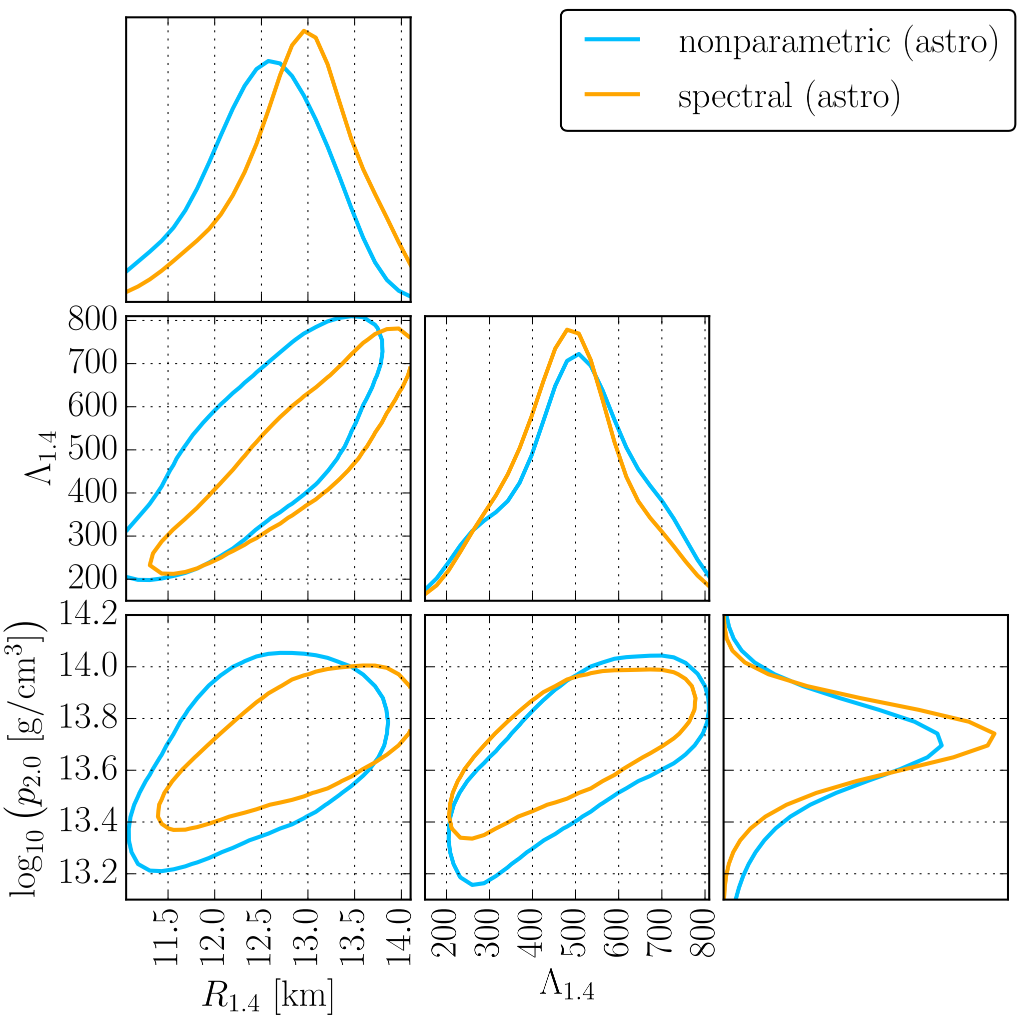

Figure 5.1: The astrophysically-informed posterior distributions for $R_{1.4}$, $\Lambda_{1.4}$, and $p_{2.0}$ when using nonparametric (blue) and spectral (orange) EoSs. Astrophysical distributions are conditioned on pulsar mass, mass-radius, and mass-tidal deformability measurements; see Sec. 5.2. The spectral EoS result shows less variability in $R_{1.4}$ at a fixed value of $\Lambda_{1.4}$ than the nonparametric one. This suggests that the degree of EoS-independence in $R_{1.4}$–$\Lambda_{1.4}$ is linked to the flexibility of the EoS model. Similar conclusions hold for $p_{2.0}$.

Figure 5.1 also shows the same relations obtained with a more flexible set of nonparametric EoSs based on Gaussian Processes [41, 29] that is only minimally informed by nuclear physics. The nonparametric EoSs are drawn from a collection of Gaussian Processes and explore a wide rage of intra-density correlations lengths and strengths. As shown in Legred et al. [48], this EoS set is extremely agnostic and intra-density correlations are only imposed by physical considerations such as causality and thermodynamic stability. Due to its flexibility, the set also inherently includes EoSs with phase-transition-like behavior, including nonmonotonic behavior in the speed of sound and multiple stable branches [30]. As expected, under the nonparametric EoSs, perfect knowledge of $\Lambda_{1.4}$ yields an increased uncertainty in $R_{1.4}$ of $\sim 2\,\mathrm{km}$, larger than the nominal error of the C-Love relation.

In this work and motivated by Fig. 5.1, we revisit common EoS-independent relations and assess them under nonparametric EoSs. Following Ref. [18], we evaluate EoS-independent relations separately against hadronic EoS sets as well as mixed hadronic and hybrid EoSs. Because of the difficulty in fitting the relation over an unstable branch of the M–R relation, we only study EoSs with a single stable branch, thus restricting to weak phase transitions. We also consider EoSs that are only required to be consistent with the existence of massive pulsar measurements, contrasted with a set required to be consistent with additional GW and X-ray measurements [47].

With a focus on the applicability of EoS-independent relations, we further revisit the issue of EoS-independence across the parameter space. In general, relations are most useful in the regions of parameter space where data are most informative, since tight constraints on some parameters can be interpreted as constraints on other parameters. A higher degree of EoS-independence in these regions will therefore expand their applicability. For example, the relations that link the dimensional tidal deformabilities of two NSs in a binary to each other are most useful for NS with masses $\lesssim 1.7M_{\odot}$ as GW observations are largely uninformative about the tidal properties of more massive NSs [2, 24]. In Sec. 5.2, we propose a statistic to measure the goodness-of-fit of an EoS-independent relation, by comparing to a *tolerance factor* which is chosen based on the application. Fitting via optimization of this metric allows more control over the precision of the EoS-independent relation as a function of NS mass.

With the extended EoS set and goodness-of-fit metric in hand, we revisit the following relations in Sec. 7.4 :

$G = c = 1$.

- *I–Love–Q* [89, 90], Sec. 5.3: a relation between the (normalized) moment of inertia I, the tidal deformability Λ, and the rotational quadrupole moment Q of a NS. The I–Love–Q relations remain highly universal, likely useful even with sensitivies more than ten times current GW detectors.

- *C–Love* [53, 87], Sec. 5.3: a relation between the compactness $C = m/R$ and the tidal deformability Λ of a NS. Its main applicability is in translating GW tidal constraints to radii, given the NS mass m. The C–Love relation is relatively non-universal; for nonparametric EoS distributions, it leads to systematic errors of $\sim 30\%$ compared to statistical uncertainties at current sensitivity. This holds true for EoSs both with and without strong phase transitions.

- *Binary-Love* [88], Sec. 5.3: a relation between the dimensionless tidal deformabilities of two NSs in a binary Λ_1 and Λ_2 given the mass ratio q. Its main applicability is in reducing the number of parameters in GW analyses on NS binaries, though its EoS-independence breaks down for EoSs with phase transitions [78, 18]. The binary-Love relation is similarly non-universal under the nonparametric EoS distribution with systematic errors $\sim 50\%$ of current statistical uncertainties. The Binary-Love relation universality is further degraded for EoSs with phase transitions.

- $R_{1.4}$-*Love* [63, 27, 93], Sec. 5.3: a relation between the NS radius and the chirp mass and chirp tidal deformability of a NS binary, essentially combining the C–Love and Binary-Love relations above. $R_{1.4}$-Love likely would introduce bias before the advent of next-generation detectors, with systematic errors becoming comparable to statistical uncertainties for a GW170817-like but $O(3-5)$ times louder.

- α_c-*C* [71], Sec. 5.3: a relation between the EoS stiffness measure $\alpha_c \equiv p_c/\epsilon_c$ where p_c and ϵ_c are the central pressure and energy density respectively, and the compactness. The $\alpha_c - C$ relation is a very poor fit to the nonparametric mixed distribution with systematic errors greater than or equal to current statistical uncertainties. The relation is somewhat better fit by the parametric and hadronic nonparametric distributions.

5.2 Goodness-Of-Fit and Quantifying EoS-independence

In this section we formalize the discussion of EoS-independent relations by quantifying EoS-independence through a goodness-of-fit metric in Sec. 5.2, introducing a tolerance factor for the fit in Sec. 5.2, and describing the EoS sets we use in Sec. 5.2.

In general, an individual NS is characterized by an EoS ϵ and the NS central density ρ_c. Given two NS properties $F(\epsilon, \rho_c)$ and $G(\epsilon, \rho_c)$ which are each one-to-one[3] with ρ_c, we define their relation $G(\epsilon, F(\epsilon, \rho_c))$. Remarkably, for a number of property pairs the induced function $G(\epsilon, F(\epsilon, \rho_c))$ is nearly independent of ϵ. These are so-called universal, or EoS-independent relations.

Defining a goodness-of-fit metric

Following [90], we fit an analytic phenomenological approximant to the EoS-independent relation

$$\tilde{G}(F; \boldsymbol{\theta}) \approx G(\bullet, F(\bullet, \rho_c)), \tag{5.1}$$

where $\bullet$ in place of the EoS ϵ indicates this should hold regardless of the EoS and $\boldsymbol{\theta}$ are fitting parameters. Given a functional form for $\tilde{G}(F; \boldsymbol{\theta})$ (typically in terms of simple functions such as polynomials and logarithms) and a particular EoS ϵ, we select $\boldsymbol{\theta}$ such that a goodness-of-fit metric is minimized. A least-squares metric is[4]

$$\chi^2_\epsilon(\boldsymbol{\theta}) \equiv \sum_i^N \frac{\left[\tilde{G}(F_i; \boldsymbol{\theta}) - G(\epsilon, F_i(\epsilon, \rho_{c,i}))\right]^2}{\sigma_i^2}, \tag{5.2}$$

where i iterates over individual stellar solutions (i.e., central densities), σ_i is a tolerance factor for the goodness-of-fit of data point i, and N represents the number of central densities the relations are evaluated at. In what follows we use $N = 200$ which ensures smooth relations and that $\chi^2/(N - N_p)$, the χ^2 per number of degrees of freedom (with N_p the number of parameters of the fit), is independent of N.

Unless otherwise stated, we fit each relation on a grid of NS central densities. We build a linear grid for each EoS in the central rest-mass density, ρ_c, for $1.0 M_\odot$ to $M_{\rm max}$, the maximum TOV mass. We use only EoSs with a single stable branch in the $M - R$ relation. Both the choice of grid used, and the truncation are inputs and

[3] If F is not one-to-one with ρ_c (for example the mass $m(\epsilon, \rho_c)$ for EoSs with multiple stable branches and twin stars), then this construction works on each monotonic branch.

[4] Though this metric is not strictly a χ^2 statistic, as there is no statistical interpretation of the scatter which induces the χ^2, we use familiar notation since many conventional intuitions hold. For instance, $\chi^2/N_{\rm dof} = 1$ is a threshold for a good fit, and any value significantly smaller than 1 would be regarded as overfitting [62]. In our case, we expect the EoS-independent relations to overfit the "data", $\chi^2/N_{\rm dof} \ll 1$. A large value would be considered a poor fit.

represent a *de facto* choice of relative significance weighting between mass scales, which may or may not be realistic depending on the true distribution of NS masses (equivalently, given an EoS, the distribution of central densities). For most EoSs, the spacing of central density favors higher masses; given the uncertainty in populations of NSs, we do not attempt to modify this distribution substantially. Implications of this choice are discussed further in Sec. 9.5.

The tolerance factor σ_i can be freely chosen and, as its name suggests, quantifies the degree of deviation from EoS-independence we tolerate. Different choices for σ_i will result in different best-fit $\boldsymbol{\theta}$ parameters and goodness-of-fit estimates. We discuss the tolerance factor extensively in the next section.

Beyond a single EoS ϵ, we consider a (normalized) distribution on EoSs $P(\epsilon)$, potentially conditioned on observations. The distribution-dependent goodness-of-fit is then defined as the distribution average of χ^2_ϵ over $P(\epsilon)$,

$$\chi^2(\boldsymbol{\theta}) \equiv \int \chi^2_\epsilon(\boldsymbol{\theta}) P(\epsilon) d\epsilon = \sum_\epsilon P_\epsilon \chi^2_\epsilon(\boldsymbol{\theta}) \,, \tag{5.3}$$

where P_ϵ is the weight of each EoS in the distribution $P(\epsilon)$. EoSs are sampled for the Monte Carlo sum by directly sampling an EoS prior set for each distribution; we use the same prior distributions as [48]. In Eq. (5.3) the fitting parameters $\boldsymbol{\theta}$ are shared among and fitted with all $\chi^2_\epsilon(\boldsymbol{\theta})$ –this is equivalent to seeking a set of parameters which are EoS-independent over $P(\epsilon)$. In practice, we sample EoSs uniformly from the approximate support of P_ϵ, i.e. $\{\epsilon | P_\epsilon > P_{th}\}$ for some threshold P_{th}, and weigh each EoS draw by P_ϵ. This allows us to better resolve the "tails" of the EoS distribution where χ^2_ϵ may be large. W sample 1000 draws from the given EoS set in order to approximate the integral, as we found reasonable convergence of the total χ^2 was achieved by this point for all EoS distributions (see Sec. 5.2).

Role of the tolerance factor

Setting $\sigma_i = 1$ would be sufficient to uniquely specify a fitting problem for $\boldsymbol{\theta}$ if the goal is simply to obtain a fit. However, in this case, no information about goodness-of-fit is contained in Eq. (5.3), because rescaling $\sigma_i \to \alpha\sigma_i$ changes $\chi^2 \to \chi^2/\alpha^2$; any level of goodness-of-fit could be achieved by rescaling. In fact, no specific fit corresponds in any sense to the "best fit" possible as a different (non-constant) σ_i would produce a different fit. This is analogous to a nonlinear change of variables producing a different fit. We instead select σ_i by considering the tolerance we have for error in the EoS-independent relation. This results in a $\chi^2(\boldsymbol{\theta})$

that is simultaneously used during the fitting procedure and whose (dimensionless) numerical value can be interpreted as a goodness-of-fit.

To clarify, we dig further into a common application of EoS-independent relations in inference, namely the computation of certain NS properties from others without knowledge of the EoS. The Binary-Love relations [88, 87] facilitate the computation of the tidal deformability of one NS Λ_1 from that of another Λ_2 given their mass ratio q [22]. The systematic error in the estimation of Λ_1 due to the relation's error is $\delta\Lambda_{sys}$. Whether this systematic error is tolerable in a GW analysis depends on the statistical measurement uncertainty $\delta\Lambda_{stat}$. If $\delta\Lambda_{sys} \gtrsim \delta\Lambda_{stat}$, then the application of the relation introduces an uncertainty comparable to the statistical uncertainty, which is undesirable. If, however, $\delta\Lambda_{sys} \ll \delta\Lambda_{stat}$, then the relation may be useful as the statistical uncertainty dominates. This consideration motivates choosing the tolerance factor σ_i to be the approximate measurability of the quantity of interest. In doing do, the goodness-of-fit $\chi^2(\boldsymbol{\theta})$ is a direct check of the relation between $\delta\Lambda_{sys}$ and $\delta\Lambda_{stat}$. Unless otherwise stated, throughout this work we use a fiducial estimate of $\delta\Lambda_{stat} = 210$, a constant motivated by the tidal measurement of GW170817 and rescaling the symmetric 90% region to 1-σ [1]. Improvements in detector sensitivity mean that a GW170817-like event observed today would have a lower statistical uncertainty; per Eq. (5.2), halving the statistical uncertainty in Λ would increase the χ^2 (i.e., decrease the goodness-of-fit) by a factor of 4.

In certain cases the measurability of NS tidal deformability is a very poor estimate for the measurability of other NS properties. For example, for higher-mass NSs, the compactness will likely be better measured by non-GW techniques, such as X-ray pulse-profile modeling. In such cases, we approximate statistical uncertainty by assuming that the compactness, $C(M)$, can be measured to within $\delta C = 0.02$, a constant representing the uncertainty from X-ray observations [15, 69, 70, 54, 55]. See Secs. 5.3 and 5.3 for more details of how we simultaneously incorporate separate estimates of NS measurability.

Generically, the χ^2 value represents how poorly fit the relation is to the EoS distribution. Per Eq. (5.2), χ^2_ϵ represents the square error in the quantity predicted by the relation relative to the tolerance factor. Given a value for χ^2, the typical error in the underlying variable is

$$\Delta G \sim \sigma(F)\sqrt{\chi^2/N_{\rm dof}}\,. \tag{5.4}$$

Here, $\sigma(F)$ represents the tolerance factor on the quantity F used in evaluating the fit. This is to be taken as an order of magnitude estimate, and is useful for quickly diagnosing the error expected from applying an EoS-independent relation. For example, if $\sigma(F)$ represents statistical measurement uncertainty, then a χ^2 value of 10^{-4} indicates that systematic errors in parameters are of order $0.01 = 1\%$ statistical uncertainties.

An alternative choice for the tolerance factor would be

$$\sigma(F) = G(F)\,. \tag{5.5}$$

This corresponds to constant tolerance for the *fractional* error in the fit. This tolerance factor is independent of measurement uncertainty, and so the best fit bears a different interpretation. In many cases a constant relative tolerance may be preferred, especially when an observable varies over orders of magnitude. We give an example of a fit where a constant fractional error tolerance gives a seemingly better fit in Sec. 5.3. The χ^2 in this case is a measure of the total fractional deviation in the relation.

Nonetheless, there are subtleties to interpretation of the χ^2 value within the fractional uncertainty approach. For example, assume we decided to try to identify EoS-independent relations for $R(M)$ or $\Lambda(M)$. Since $R(M)$ is approximately constant for a large class of EoSs, we adopt a constant fit:

$$\chi^2 = \sum_i \frac{(R(M_i) - \hat{R})^2}{\hat{R}_0^2}\,, \tag{5.6}$$

with $\hat{R}$ the universal predictor and $\hat{R}_0 = 12$km a crude estimate of $\hat{R}$. Since $R(M) \in [10, 14]$ km for the majority of astrophysical EoSs, we would find $\chi^2/N_{\rm dof} \sim (2/10)^2 = 0.04$. On the other hand, $\Lambda(M)$ varies over orders of magnitude, and $\Lambda_{1.4} \in [200, 800]$, see Fig. 5.1. Then the goodness-of-fit will average to $\chi^2/N_{\rm dof} \sim (300/500)^2 \sim 0.36$. The radius is relatively EoS-independent by this metric under a fractional uncertainty approach; this contrasts with the use of measurement uncertainty as the tolerance factor, where both relations would be comparably poor. Therefore, the choice of tolerance factor sensitively impacts what the resulting goodness-of-fit represents. This is true even when only the fit parameters are of interest, as those will also depend on the tolerance.

The tolerance factors we use are coarse heuristics for potentially better-motivated choices. For example, a complete GW simulation study would allow a precise estimate of σ_Λ for a range of binary parameters and detector sensitivities. There are additional choices for the tolerance factor that we do not investigate, such as

$\sigma_\Lambda = \alpha\delta\Lambda_{stat}^{\beta}$, for some (potentially dimensionful) constant α and exponent β. Additionally, the tolerance factor may be designed to be agnostic to errors of the fit in certain mass ranges; if for example, sub-solar mass NSs cannot be formed astrophysically, then it is not necessary that the relation is well fit below $M_\odot$. This choice is degenerate, however, with a choice of which NSs the χ^2 is marginalized over; see the discussion in Sec. 9.5.

EoS set

The final ingredient of the EoS-independent relation fits is the EoS set and its distribution $P(\epsilon)$. Since our goal is to assess EoS-independence for flexible EoS sets, we use the model-agnostic prior of Ref. [29], constructed to minimize the impact of nuclear theory input[5]. EoSs are drawn from multiple Gaussian Processes sampling a range of covariance kernels (correlation scale and strength) between different densities. Each EoS is stitched to a low-density representation of the SLy4 EoS [28] at low densities. The final EoS prior predicts NSs with a very wide range of $R \in (8, 16)$ km. We condition this set against radio data [8, 26, 32] for the maximum NS mass, and refer to this as the *pulsar-informed set*. We also consider an *astrophysically-informed set*, obtained in [47] by further conditioning on X-ray [54, 55, 69, 70] and GW [4, 2] data[6].

Due to its flexible construction, both the pulsar-informed and the astrophysically-informed sets contain EoSs with phase transitions, both strong and weak. We therefore further split each set in EoSs without (referred to as the *hadronic set*) and with (referred to as the *mixed-composition set*) phase transitions. In order to identify EoSs with phase transitions, we use the moment-of-inertia-based feature extraction procedure from [30]. This procedure can identify both strong and weak phase transitions, including phase transitions that do not result in multiple stable branches or have a large impact on the macroscopic observables. We set a high threshold for phase transitions, requiring a change in internal energy per particle of $\Delta(E/N) \geq 30$MeV; see Ref. [30]. As before, we also only use EoSs with a single stable branch in the M–R relation. Including EoSs with multiple stable branches would require choices in the construction of the χ^2 to weight each branch and exclude unstable branches, but would likely decrease the goodness-of-fit of the

[5] Though certain EoS models are used to condition the process, the final EoS distribution depends only weakly on those EoSs which are used for conditioning; see [41, 29].

[6] The astrophysical data we use are independent of any choice of the EoS and do not use any EoS-independent relations. Therefore the inclusion of additional data will only improve the quality of fits if the data explicitly favor a set of EoSs which are well fit by the relations.

relations to the mixed composition EoS set.

Finally, for comparison, we repeat the same fits with piecewise-polytropic and spectral EoSs, using the pulsar-informed and astrophysically-informed distributions from Ref. [48]. We use a 4-parameter piecewise-polytrope parametrization [68], with 2 fixed stitching densities, 3 sampled polytropic indices, and one sampled overall pressure scaling. For the spectral EoS, we use a 4 parameter EoS (i.e. 4 basis functions in the spectral exponent) [50], and the parameter distribution given by Ref. [83], which reduces the range of parameter space sampled while significantly improving the fraction of EoS samples which are physically viable. In both cases, we stitch to a low-parameter representation of the Sly4 EoS, as described in Ref. [17]. We follow Ref. [17] in allowing the EoS prior to extend up to $c_s \leq 1.1$, in order to allow an acausal model to represent a potential causal model which is not representable by the parametrization. In Legred et al. [48], this choice was found to affect the distribution on the piecewise-polytrope EoS; it may additionally affect EoS-independence by allowing additional (unphysical) variation in the EoS.

5.3 EoS-independent relations

We fit a set of proposed EoS-independent relations to different EoS distributions and evaluate their universality. Throughout, unless otherwise stated, we use a fixed tolerance factor value of $\sigma_\Lambda = 210$.[7] When Λ is not predicted by the fit but it is the independent variable of the relation, we propagate the uncertainty through the relation to the dependent quantity. For example

$$\sigma_I(\Lambda) = \frac{d\tilde{I}(\Lambda, \boldsymbol{\theta}_f)}{d\Lambda}\bigg|_\Lambda \sigma_\Lambda\,, \tag{5.7}$$

where $\boldsymbol{\theta}_f$ are fiducial parameters of the fit, and $\tilde{I}$ is the EoS-independent predictor of I from Λ which depends on Λ via the derivative of the predictor. When neither the independent or dependent variable are Λ, we use a different strategy; see Secs. 5.3 and 5.3. For relations where Λ is indeed the dependent quantity and the tolerance factor is constant, this strategy results in optimization problems which are mathematically identical to previous work, e.g. [18]. Crucially though, now the goodness-of-fit statistic can be interpreted as a measure of EoS-independence relative to observations.

In this section we show plots for the nonparametric-mixed and spectral astrophysically-informed EoS distributions. We display additional plots for the piecewise-polytrope

[7]Simulations suggest that measurement uncertainty in Λ is approximately independent of the value of Λ (equivalently, the NS mass) and inversely proportional to the signal strength [81].

and hadronic-nonparametric EoS distributions as well as fit parameters in Appendix 5.6.

I–Love–Q

We begin with the I–Love–Q relations [90] for the dimensionless quadrupole moment Q, moment of inertia I, and tidal deformability Λ of a NS. The existence of such relations, at least approximately, may not be surprising. In Newtonian gravity, for example, the quadrupole moment can be computed from the moment of inertia exactly. In GR, however, the definitions of these quantites do not coincide, which is to say the relationship of angular momentum, angular velocity, and the second multipole of the gravitational field is nontrivial for slowly-spinning compact objects [37].

We use a slightly modified form for the I–Love–Q relations compared to Ref. [90], which was shown by Ref. [18] to produce better behavior in the Newtonian limit:

$$\hat{I}(\Lambda; a, b, K_{yx}) = K_{yx}\Lambda^{\alpha}\frac{1+\sum_{i=1}^{3} a_i\Lambda^{-i/5}}{1+\sum_{i=1}^{3} b_i\Lambda^{-i/5}}\,, \tag{5.8}$$

$$\hat{Q}(\Lambda; a, b, K_{yx}) = K_{yx}\Lambda^{\alpha}\frac{1+\sum_{i=1}^{3} a_i\Lambda^{-i/5}}{1+\sum_{i=1}^{3} b_i\Lambda^{-i/5}}\,, \tag{5.9}$$

$$\hat{I}(Q; a, b, K_{yx}) = K_{yx}Q^{\alpha}\frac{1+\sum_{i=1}^{3} a_iQ^{-i/5}}{1+\sum_{i=1}^{3} b_iQ^{-i/5}}\,. \tag{5.10}$$

Here, a_i, b_i, and K_{yx} are free parameters which are fit. These forms ensure that when a_i and b_i are zero, these relations limit to the Newtonian form. We display best-fit parameters in Table 5.6.

We solve the TOV equations in the slow-rotation limit up to second order [37] to compute the dimensionless moment of inertia, quadrupole moment, and tidal deformability[8]. We then fit the parameters of each relation using a nonlinear least squares algorithm. We display the *loss*, i.e., best fit χ^2/N_{dof} value, of each fit for each EoS distribution in Table 5.1. In this context N_{dof} represents the number of degrees of freedom in the data, which is the number of points fit (200) minus the number of fitted parameters. The loss measures the residuals in the fit relative to $\sigma_\Lambda = 210$, as described in Sec. 5.2.

The I–Love–Q relations hold independent of EoS distribution to very high precision, with loss values less than 3×10^{-3} for almost all relations. In particular $I(Q)$, with

[8]We thank Victor Guedes for the use of code to solve the TOV equations in the slow-rotation limit up to second order.

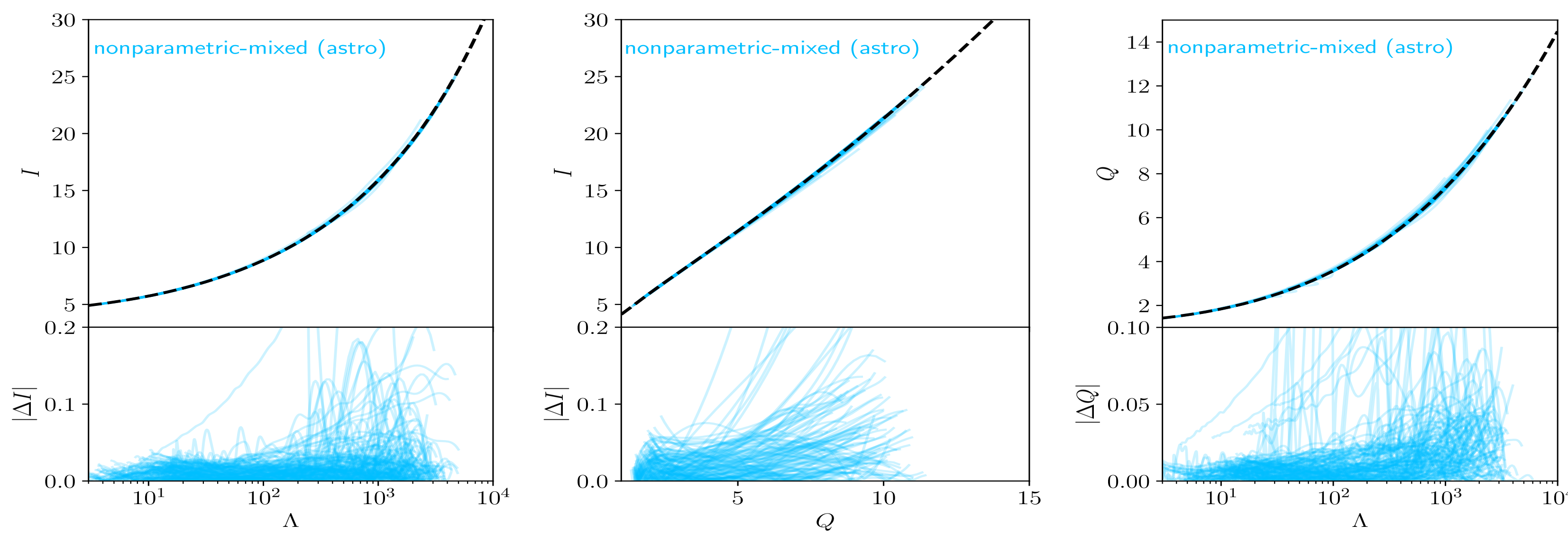

Figure 5.2: *Top, each panel*: EoSs drawn from nonparametric mixed-composition EoS distribution conditioned on all astrophysical data (in blue), along with the best-fits (black dashed). From left to right we display the I-Love, I-Q, and Q-Love relations. *Bottom, each panel*: Residuals of the fit relative to each of the sampled EoSs. This represents a measure of the "error" of using the particular relation with the given EoS set.

$\chi^2/N_{\rm dof}$

Relation / EoS Dist.	$I(\Lambda)$	$I(Q)$	$Q(\Lambda)$
GP-hadronic (astro)	4.6×10^{-5}	2.9×10^{-7}	6.9×10^{-4}
GP-hadronic (psr)	5.3×10^{-4}	6.2×10^{-7}	8.9×10^{-3}
GP-mixed (astro)	1.5×10^{-4}	5.0×10^{-7}	2.0×10^{-3}
GP-mixed (psr)	2.6×10^{-3}	7.9×10^{-7}	3.9×10^{-2}
SP (astro)	5.9×10^{-7}	8.4×10^{-8}	3.3×10^{-5}
SP (psr)	3.1×10^{-6}	1.2×10^{-7}	1.0×10^{-4}
PP (astro)	4.2×10^{-6}	2.7×10^{-7}	2.1×10^{-4}
PP (psr)	4.1×10^{-5}	1.3×10^{-6}	4.2×10^{-3}

Table 5.1: Table $\chi^2/N_{\rm dof}$ for the I–Love–Q relations for several EoS distributions. Here GP represents the nonparametric (Gaussian Process) distributions, SP represents the spectral distributions, and PP represents the piecewise-polytrope distributions. We show results for each of the pulsar-informed distributions (psr), and fully astrophysically-informed distributions (astro).

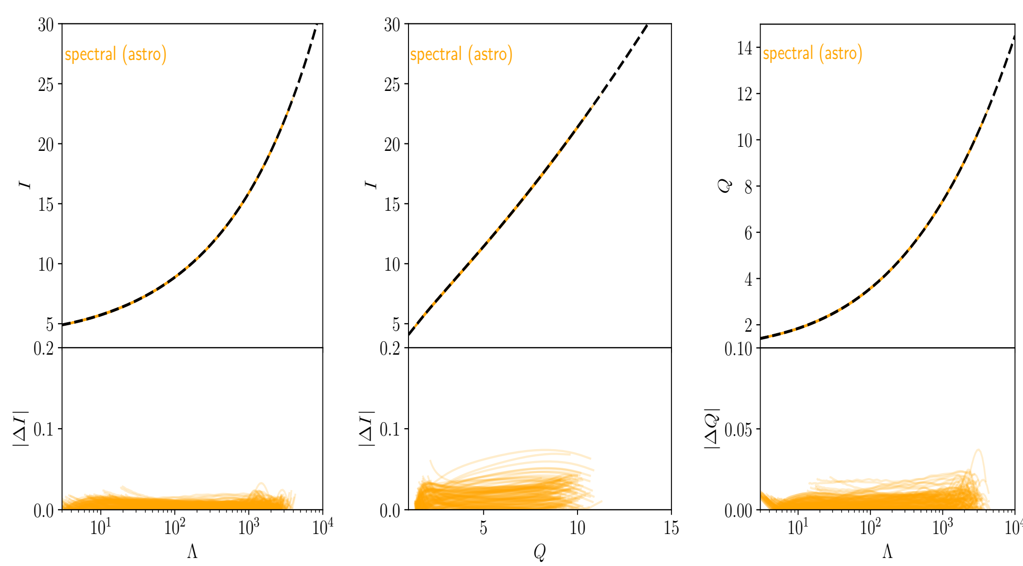

Figure 5.3: The same as Fig. 5.2 but with the spectral EoS distribution conditioned on all astrophysical data. We use identical axes ranges between the two figures. Worst-case residuals are of order 10 times smaller than the nonparametric mixed-composition distribution seen in Fig. 5.2.

losses of $\lesssim 10^{-5}$ indicates that even with $O(10)$ improvement in GW detector sensitivity, the systematic error of the relation will still be at sub-percent level compared to statistical uncertainties. Nonetheless, the parametric EoS distributions display moderately better EoS-independence than the corresponding nonparametric distributions, typically by a factor of 3-10. Similarly, the hadronic nonparametric distribution is typically a factor of 2-3 better than the corresponding mixed-composition distributions. In all cases, the fits to pulsar-informed distributions show higher losses than the ones conditioned on all astrophysical data. For the spectral distributions, the difference is marginal, about a factor of 2, whereas for the nonparametric mixed distribution the difference is almost a factor of 20 for the relations involving Λ.

We display the fits for the nonparametric mixed-composition, and spectral EoS distributions in Figs. 5.2 and 5.3 respectively; again each distribution conditioned on all astrophysical data. For other distributions, see Appendix 5.6. The higher degree of EoS-independence in the spectral fit is apparent in the residuals, which are several times smaller than the nonparametric residuals.

The I–Q relation shows the smallest loss in EoS-independence (by a factor of 10) when moving from the spectral pulsar-informed distribution to the equivalent nonparametric distribution. This indicates that the I–Q relation is fundamentally more EoS-independent than relations involving Λ. This is potentially related to the discussion of emergent symmetries in Ref. [92], which demonstrated that the I–Q relation is indeed EoS-independent under the elliptical isodensity approximation, which is nearly true in astrophysically relevant NSs [92].

Binary-Love

The *Binary-Love* relation allows us to estimate the tidal deformability of one NS in a binary given its NS companion's deformability. The expression is given in terms of the symmetric deformability $\Lambda_s \equiv (\Lambda_1 + \Lambda_2)/2$ and the antisymmetric deformability, $\Lambda_a = (\Lambda_2 - \Lambda_1)/2$ where Λ_1 and Λ_2 are the deformabilities of two NSs [88]:

$$\Lambda_a(\Lambda_s, q; b, c) = F_n(q)\Lambda_s \frac{1 + \sum_{i=1}^{3}\sum_{j=1}^{2} q^j b_{ij} \Lambda_s^{-1/5}}{1 + \sum_{i=1}^{3}\sum_{j=1}^{2} q^j c_{ij} \Lambda_s^{-1/5}} \,. \tag{5.11}$$

Here b_{ij}, and c_{ij} are parameters which are fit. For the Binary-Love relation, we use a NS distribution truncated at $0.8 M_\odot$ rather than $1.0 M_\odot$, this is necessary to allow the relationship to be evaluated over a wider range of mass ratios q. Fit coefficients for the astrophysically-informed EoS sets are given in Table 5.7. Here, and in the rest of the paper, we solve the TOV equations only to first order in the small spin parameter using the approach from [42]. We display the fit losses in Table 5.2, and additionally plot them in Fig. 5.4.

The losses are noticeably higher than any of the I–Love–Q relations for corresponding EoS sets, indicating the relation is less EoS-independent. The use of lower mass cutoff inevitably leads to an increase in loss for the relation, as low-mass NSs have larger tidal deformabilities; however, raising the mass cutoff to $M_{\min} = 0.9$ lowers losses by only a factor of $\sim 2-3$. This indicates that the fits are indeed worse than the I–Love–Q relations.

Nonetheless, the spectral EoS distribution fits are ~50 times better than the non-parametric and piecewise-polytrope distributions. The better fit to the spectral distribution might be due to large correlations between density scales. Such correlations may reduce the variation in Λ across mass scales, making the relation between $\Lambda(m_1)$ and $\Lambda(m_2)$ more EoS-independent. The astrophysically-informed fits show improvement over pulsar-informed fits, with typical loss values 3-5 times better. The piecewise polytrope is by far the most improved distribution upon inclusion of more data, with losses decreasing by factors of more than 10. In all cases the hadronic distributions give improved fits relative to the mixed composition distributions, typically by a factor of 10 in loss. For the worst-fit case, the nonparametric pulsar-informed mixed distribution, the fit quality ($\chi^2/N_{\rm dof} = 2.6 \times 10^{-1}$) may be poor enough to pose challenges for current-generation GW detectors, as it indicates systematic errors of order 60% in the predicted value of Λ_a relative to statistical uncertainties. Figure 5.5 shows nonparametric mixed and spectral fits relative to sampled EoSs. The larger variation of the nonparametric EoS set relative to the spectral set is apparent.

The large differences in fit quality for nonparametric distribution with mixed composition and hadronic composition are consistent with observations of the Binary-Love relation (as presented here) failing to describe effectively EoSs with phase transitions [18, 78]. This could potentially lead to analyses using Binary-Love relations artificially downranking EoSs which support hybrid stars. This effect will likely be smaller than an e-fold in likelihood for any individual event, but such effects may multiply in a hierarchical analysis, leading to large errors after many events.

Changing fit quality with the tolerance factor

The deteriorating quality of the fit at low values of Λ_s is apparent in Fig. 5.5, left panel. This is because assuming a constant tolerance factor for Λ upweights

χ^2/N_{dof}

Relation / EoS Dist.	$q = 0.55$	$q = 0.75$	$q = 0.9$
GP-hadronic (astro)	6.6×10^{-3}	1.8×10^{-2}	9.1×10^{-3}
GP-hadronic (psr)	2.7×10^{-2}	1.0×10^{-1}	8.5×10^{-2}
GP-mixed (astro)	1.0×10^{-2}	5.2×10^{-2}	4.9×10^{-2}
GP-mixed (psr)	5.5×10^{-2}	2.6×10^{-1}	2.2×10^{-1}
SP (astro)	3.3×10^{-3}	6.5×10^{-3}	2.0×10^{-3}
SP (psr)	6.7×10^{-3}	1.0×10^{-2}	2.9×10^{-3}
PP (astro)	3.5×10^{-3}	1.6×10^{-2}	1.1×10^{-2}
PP (psr)	6.2×10^{-2}	2.2×10^{-1}	9.6×10^{-2}

Table 5.2: Table χ^2/N_{dof} for the Binary-Love relations for several distributions on the EoS and binary mass ratios.

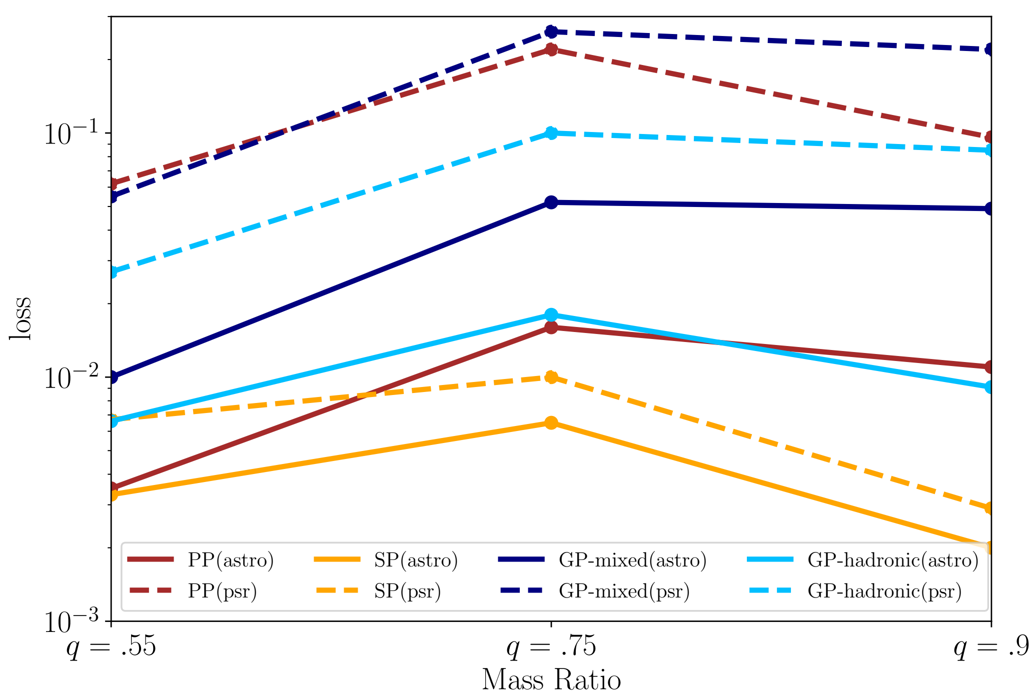

Figure 5.4: The costs shown in Table 5.2. The spectral costs are in general the lowest, especially for more equal-mass binaries.

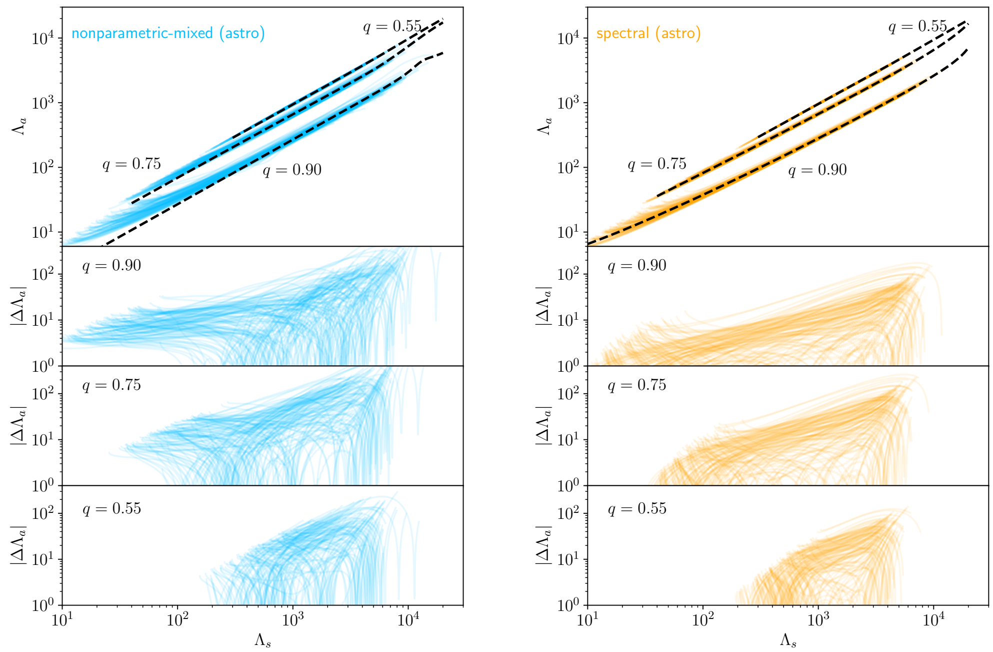

Figure 5.5: Similar to Fig. 5.2. *Left*: The Binary-Love relation fitted, along with all EoSs for the nonparametric EoS distribution with mixed composition when conditioning on all astrophysical data. We plot each fit for three different mass ratios, $q = 0.55, q = 0.75$, and $q = 0.9$. *Right*: The same for the spectral EoS distribution.

relative errors where Λ is large, i.e. the regime where small relative differences lead to very large χ^2 values. It is possible to use the tolerance factor to improve the fit quality at low Λ. Instead of choosing an observational value for the tolerance factor $\sigma(\Lambda_s)$, we set $\sigma(\Lambda_s) = \Lambda_a(\Lambda_s)$. Such a fit may be useful for tidal analyses of binaries containing a massive NS, as it gives constant relative uncertainty and therefore tolerates only small errors in Λ_a when Λ_a itself is small. We plot the fit achieved in Fig. 5.6, scaling the uncertainty by a factor of 0.5 for display purposes. We additionally plot the region encompassed by $\pm\sigma(\Lambda_s)$ and shade the region in between for the $q = 0.9$ fit. This demonstrates the role of tolerance factors and the flexibility they offer.

C–Love

Another established EoS-independent relation relates compactness to tidal deformability [53, 90]. This relation is useful for determining the radii of NS with measured

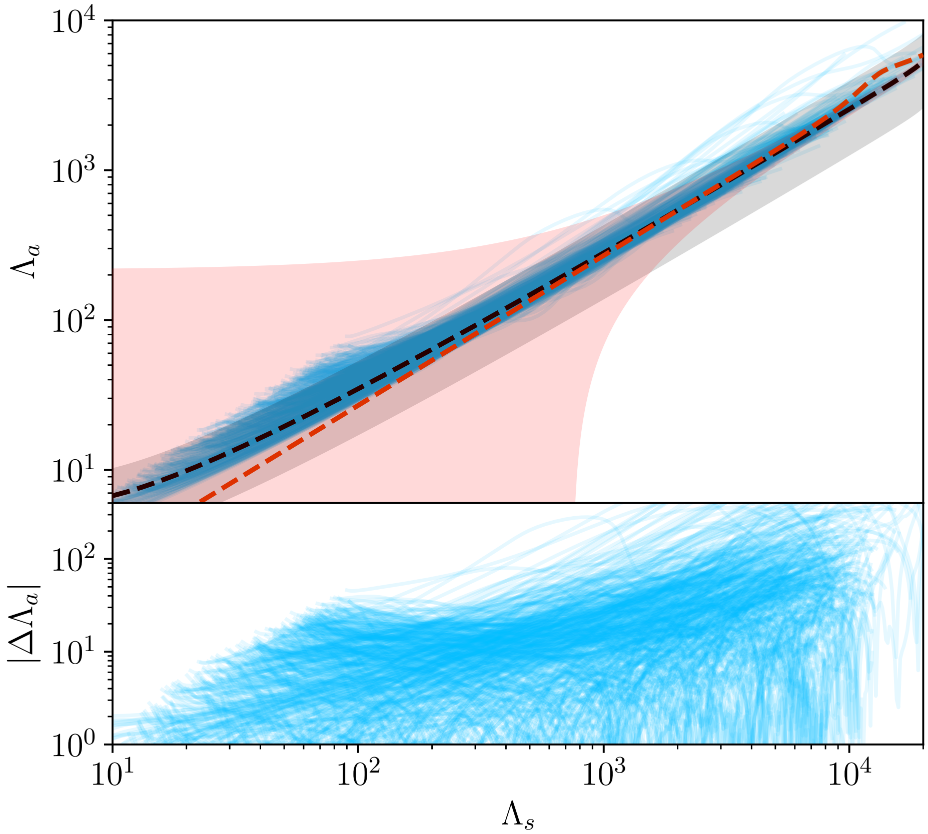

Figure 5.6: The Binary-Love fit to the mixed nonparametric, astrophysically-informed EoS distribution when applying a modified tolerance factor that favors better fits at low-Λ values. The best fit line is in dashed black, plotted over draws from the nonparametric distribution in blue. For comparison, we plot in dashed red the best-fit line for the uniform tolerance factor fit to the same distribution, the same as Fig. 5.5. We shade the $\sigma(\Lambda_s)/2$ area away from best fit $q = 0.9$ curve in pink for the uniform tolerance factor, and in gray for the modified, constant relative tolerance factor. The fit requires better agreement at low Λ_a in order to achieve low cost, and therefore it appears better by eye than the fit in Fig. 5.5, especially on a log-log plot.

tidal deformabilities and masses from GW observations. Such a relation is plausible: radius and tidal deformability are linked by definition

$$\Lambda = \frac{2}{3}k_2(m)\,(R/m)^5 = \frac{2}{3}k_2 C^{-5}\,, \tag{5.12}$$

though a truly EoS-independent description would require k_2, the tidal Love number, to be either independent of the EoS or expressible only as a function of C.

The relation is given as follows, again using a fitting form from Ref. [18]

$$C = K_{C\Lambda}\frac{1 + \sum_{i=1}^{3} a_i \Lambda^{-i/5}}{1 + \sum_{i=1}^{3} b_i \Lambda^{-i/5}}\,. \tag{5.13}$$

Similar to the I-Love-Q case, a_i, b_i, and $K_{C\Lambda}$ are parameters to be fit. As before, we propagate a constant Λ uncertainty to a C uncertainty. However, for high-compactness stars, GWs are expected to be weakly informative probe, leading to poor fits for the high-compactness part of the relation. Moreover, X-ray probes of compactness can provide complementary constraints [69, 54]. We therefore hybridize two tolerance factors:

$$\sigma_C^{-2} = \sigma_{C,\text{x-ray}}^{-2} + \sigma_{C,\text{GW}}^{-2}\,. \tag{5.14}$$

The X-ray uncertainty $\sigma_{C,\text{x-ray}}^{-2}$ is negligible for $C \lesssim 0.16$, while the GW uncertainty $\sigma_{C,\text{GW}}$ is negligible for $C \gtrsim 0.2$. This corresponds to a transition from X-ray to GW data dominating constraints near $\Lambda = 200 - 500$. The total tolerance factor is not representative of any particular measurement, but rather provides a holistic picture of the statistical uncertainty.

Results are shown in Table 5.3. We find the fit qualities to be ~ 100 times poorer than for the I–Love–Q relations, even for the parametric distributions. Contrary to the Binary-Love case, the C–Love goodness-of-fit is relatively independent of conditioning on additional data, with the loss changing by $\lesssim 2$ in all cases when additional astrophysical data are included. Also, for the nonparametric EoSs, the C–Love relation is not appreciably better fit to the hadronic distribution than to the mixed distribution. Similarly to the Binary-Love relations, the mixed-composition nonparametric distribution conditioned only on heavy pulsar mass measurements shows a loss of 3.6×10^{-1}, indicating systematic errors are already comparable to statistical uncertainties. The same holds true for the piecewise-polytrope distribution, though the piecewise-polytrope loss decreases by almost a factor of 10 upon the introduction of additional astrophysical data, while the nonparametric distribution

$\chi^2/N_{\rm dof}$

Relation / EoS Dist.	$C(\Lambda)$
GP-hadronic (astro)	7.2×10^{-2}
GP-hadronic (psr)	2.2×10^{-1}
GP-mixed (astro)	1.2×10^{-1}
GP-mixed (psr)	3.6×10^{-1}
SP (astro)	1.6×10^{-2}
SP (psr)	2.6×10^{-2}
PP (astro)	6.4×10^{-2}
PP (psr)	4.7×10^{-1}

Table 5.3: Table $\chi^2/N_{\rm dof}$ for the C–Love relations for several distributions on the EoS.

decreases by only a factor of 3. This is consistent with the discussion in Sec. 5.3, and indicates that the large variance in the piecewise-polytrope distribution that leads to large losses is not consistent with current astrophsyical data from x-ray pulsars and gravitational waves.

Finally, we also display the fits to the nonparametric mixed-composition and spectral EoS distributions conditioned on all astrophysical data in Fig. 5.7. The nonparametric EoSs have residuals larger by about a factor of 2, as in the previous examples. Fit parameters are given in Table 5.8.

The relatively large losses in the C–Love relation are consistent with the existence of doppelgangers [64, 65]: EoSs with similar Λ across the parameter space, $\Delta\Lambda < 30$, but different R, ΔR up to 0.5 km. This phenomenon is due to variability in the EoS at densities below $2\rho_{\rm nuc}$; the nonparametric EoS prior contains a wide range of low-density behaviors and thus produces EoSs with similar features. Approximating the nonparametric EoS distribution with this relation may result in errors in compactness $\Delta C \sim 0.02$, although typical errors are $\Delta C \lesssim 0.01$. Choosing a fiducial NS radius of 10.5 km, and a fiducial mass of $1.4\,M_\odot$, this error can be translated to maximal radius uncertainty of $\sim$ 1km, with typical errors half that, in line with Refs. [64, 65]. The presence of these features is additionally consistent with Fig. 5.1; the nonparametric EoS distribution shows a less EoS-independent relations between R and Λ. This indicates that independent radius and tidal deformability measurements will be required in order to effectively constrain the EoS at intermediate ($\sim 1 - 2\rho_{\rm nuc}$) densities.

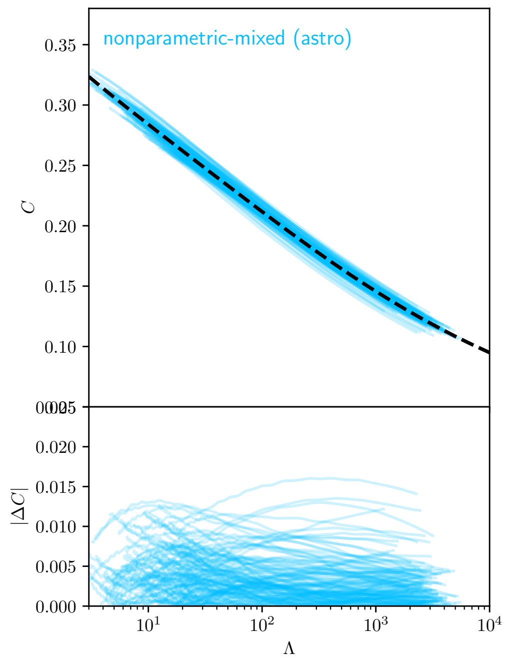

Figure 5.7: *Left:* The C–Love relation fitted along sampled EoSs for the nonparametric EoS distribution with mixed composition when conditioning on all astrophysical data. *Right:* The same for the spectral parametrization. Relative errors are larger for the C–Love relation than for the I–Love–Q relation, and the nonparametric mixed distribution shows greater variability than the spectral distribution.

$R_{1.4}$–$\tilde{\Lambda}$

An additional relation between NS tidal properties and the radius has been proposed by Refs. [27, 63, 93]. The relation leverages the relative insensitivity of $\tilde{\Lambda}$, the leading order tidal parameter in the post-Newtonian expansion of the GW phase [31, 81] as a function of q, and the relation given in Eq. (5.12): $\tilde{\Lambda}(R_{1.4}, \mathcal{M}_c)$. That is, we write the tidal deformability as a EoS-independent function of typical star radius and the chirp mass, $\mathcal{M}_c \equiv (m_1 m_2)^{3/5}/(m_1+m_2)^{1/5}$, of the binary.

The relation is given, following Ref. [93], by

$$\frac{a}{\tilde{\Lambda}}\left(\frac{R_{1.4}}{\mathcal{M}_c}\right)^6 = 1\,. \tag{5.15}$$

For it to be useful, it should hold for some (perhaps narrow) range of mass ratios, chirp masses, and for a wide range of EoSs for some constant a. In practice, the relation is used to infer $R_{1.4}$ so we use this to define the uncertainty in this case (unlike all other examples), we can no longer only propagate uncertainty from Λ measurements because the chirp mass is also uncertain. We assume a fiducial uncertainty of $\Delta R_{1.4} = 1.0\,\mathrm{km}$, which represents a $\sim \pm 8\%$ measurement of the radius of a NS and use a typical $R_{1.4}$ value of 12 km; we select a fiducial grid of $\mathcal{M}_c$ for each EoS, induced by requiring both components to be below $M_{\max}$ and above $1.05 M_\odot$. We find that additionally by fixing the chirp mass, the loss of the fit may decrease by a factor of 5 for the spectral distribution, but by only a factor of 2 for the nonparametric distribution, and a factor of 1.5 for the piecewise-polytropic distribution. The χ^2 in this case is then

$$\chi^2(a) = \sum_i \sum_j P(\epsilon_i) \frac{\left(\frac{1}{a} \tilde{\Lambda}_{(i)}^{1/6} \mathcal{M}_c^{(j)} - R_{1.4}^{(i)}\right)^2}{\Delta R_{1.4}^2}; \tag{5.16}$$

where $R_{1.4}^{(i)}$ depends on the EoS(ϵ_i), and $\tilde{\Lambda}_{(i,j)}$ depends on the EoS and the binary parameters, but $R_{1.4}$, the fiducial radius value, is independent of both EoS and binary parameters. In this case the optimal solution can be obtained analytically by differentiating the cost with respect to $1/a$. The loss is then given by $\chi^2(a_*)$, with a_* the optimal solution, as shown in Table 5.4. Fit parameters are given in Table 5.9.

χ^2/N_{dof}

Relation / EoS Dist.	$R_{1.4}$–$\tilde{\Lambda}$
GP-hadronic (astro)	1.2×10^{-1}
GP-hadronic (psr)	1.3×10^{-1}
GP-mixed (astro)	1.4×10^{-1}
GP-mixed (psr)	1.7×10^{-1}
SP (astro)	2.5×10^{-2}
SP (psr)	1.8×10^{-2}
PP (astro)	7.7×10^{-2}
PP (psr)	1.4×10^{-1}

Table 5.4: Table χ^2/N_{dof} for the $R_{1.4} - \tilde{\Lambda}$ relations for several distributions on the EoS.

The spectral EoS distributions again show greater levels of EoS-independence than the nonparametric distribution, indicating a tighter relationship between $R_{1.4}$ and Λ in the spectral model, consistent with Fig. 5.1. However, fits are typically poorer relative to the I–Love–Q relations and more consistent with the Binary-Love relations. Similar to the Binary-Love case, the nonparametric and piecewise-polytrope, pulsar-informed distributions show nearly identical loss, $\sim 1.3 - 1.7 \times 10^{-1}$. The mixed composition distribution shows marginally worse fits, with losses about 1.3 times worse for the pulsar-informed distributions. When conditioning on additional astrophysical data, the piecewise-polytrope distribution is better fit with the relation, improving by a factor of 2, while the nonparametric distributions improve by less than 25%. This distinction is likely due to relatively strong correlations between $\sim \rho_{\rm nuc}$ and higher densities in the piecewise-polytrope distribution, which are absent in the nonparametric EoS distribution. See, e.g., Fig. 5 of [48]. These correlations cause astrophysical measurements to be highly informative at and below nuclear densities in the piecewise-polytrope case, and therefore likely rule out many of the configurations which lead to "doppleganger"-like behavior [64, 65]. This leads to less variation in the relation between R and Λ and therefore improves the quality of the fit. By contrast, there is still a range of low-density behavior within the nonparametric posterior [48], which likely increases the range of behaviors seen in the $\Lambda - R$ relations of nonparametric EoSs. This variability would be associated with a lower degree of EoS-independence in the $R_{1.4}$–$\tilde{\Lambda}$ relation.

α_c–C

A EoS-independent relation between $\alpha_c \equiv p_c/\epsilon_c$ and compactness C was proposed by Ref. [71]. The quantity α_c is most sensitive to the EoS only at the highest densities in a star, while the compactness depends on the all densities in the star. Therefore we would expect EoS parametrizations which impose strong inter-density correlations to be most consistent with the relation. The expression to be fit is [71]

$$\ln(\alpha_c) = \sum_{j=0}^{5} a_j \ln(C)^5 \,. \tag{5.17}$$

The parameters to be fit are a_j. We define a tolerance factor for this relation by propagating the uncertainty in Λ through the C–Love relation, and then through the α_c–C relation, using fiducial parameters for the C–Love relation given by [18] and for the α_c–C relation given by [71]. In Fig. 5.8 we display the fit and residuals of this relation to our nonparametric, mixed composition, astrophysically-informed EoS distribution, and to the corresponding astrophysically-informed spectral EoS distribution. Fit coefficients are given in Table 5.10.

We show in Table 5.5 the losses for this relation for all of the distributions studied. This relation, like all others studied, shows higher losses than the I–Love–Q relations. Also similar to other relations, the nonparametric distributions show higher losses than the parametric distributions, typically by orders of magnitude. Likewise the hadronic nonparametric distributions show improvements in loss compared to the mixed distributions, though effects are less than an order of magnitude.

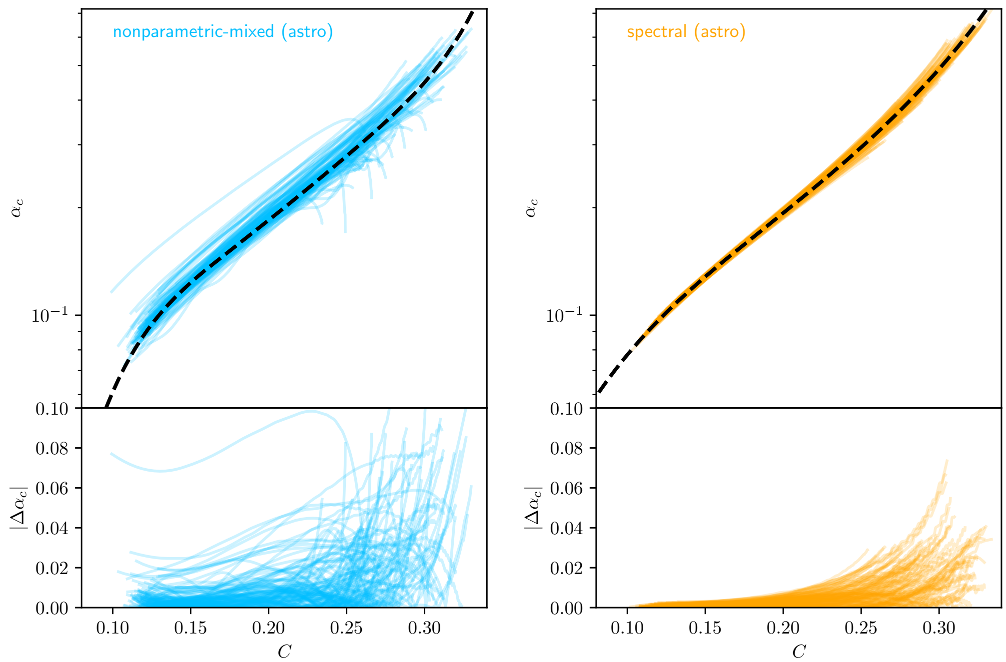

Figure 5.8: Similar to Fig. 5.2 but for the α_c–C relation. Left: the relations between α_c and C for the nonparametric EoS model with mixed composition conditioned on all astrophysical data. Right: the same for the spectral parametrization, conditioned on all astrophysical data.

$\chi^2/N_{\rm dof}$

EoS Dist. \ Relation	$\alpha_c(C)$
GP-hadronic (astro)	2.7×10^{-1}
GP-hadronic (psr)	1.8×10^{0}
GP-mixed (astro)	1.4×10^{0}
GP-mixed (psr)	5.8×10^{0}
SP (astro)	2.9×10^{-2}
SP (psr)	7.2×10^{-2}
PP (astro)	1.5×10^{-1}
PP (psr)	2.9×10^{-1}

Table 5.5: Table $\chi^2/N_{\rm dof}$ for the $\alpha_c - C$ relations for several distributions on the EoS. The quality of the fit decreases for all distributions except the piecewise-polytrope upon incorporating more astrophysical data, unlike the bulk of all the relations we study.

In contrast to the other relations, however, the α_c–C relations show losses greater than one for the nonparametric EoS distributions. This indicates that systematic errors are likely greater than statistical uncertainties for this relation. Additionally the large errors for the piecewise-polytrope and spectral distributions relative to other relations demonstrate that, even for these distributions, the EoS independence is questionable. The tolerance factor we use is conservative, though removing the component which models X-ray mass-radius measurability still gives loss values greater than one, which indicates this relation very poorly models the nonparametric EoS distributions even for just the purposes of GW observations.

The appearance of EoS independence in, e.g., the spectral model, even though it is weak, is likely due to model-dependent correlations. Under the spectral distribution, strong correlations appear between density scales which can lead to, e.g., the compactness (a function of the entire matter profile of the star) being correlated with the central pressure-energy density. These correlations are not present for the nonparametric EoS distributions, and are present to a weaker extent in the piecewise-polytropic EoS distributions.

5.4 Discussion

In this paper, we tested the EoS-independence of relations between NS properties under multiple EoS models, including parametric and nonparametric distributions. In particular, we used a nonparametric EoS distribution, and evaluated the goodness-of-fit of the relations both to subsets mimicking hadronic EoSs or mixed-composition EoSs. We found that effectively all relations are better fit by parametric models. Additionally within the nonparametric distributions, relations are better satisfied by EoSs which do not show signs of phase transitions.

The I–Love–Q relation is qualitatively better than other proposed relations, with typical loss values of 10^{-3} or below. In particular, the I–Q relation is very well fit by all EoS distributions. This could be expected based on Ref. [92], which indicated that the I–Q relation should indeed be mostly EoS independent due to the near self-similarity of isodensity contours and near EoS independence of the elliptcity profile of NSs. In fact, the best-fit relations we studied are I–Q relations under the spectral distributions, with prediction errors of $|\Delta I|/I \sim |\Delta Q|/Q \sim 0.001$, in line with Refs. [18, 90]. The piecewise-polytrope and nonparametric distributions are worse fit, especially for relations involving Λ. Nonetheless even the worst-fit relation, $Q(\Lambda)$, still has prediction errors at percent level ($\Delta Q/Q \lesssim 0.1$). For the piecewise-polytrope model, this is qualitatively similar to the findings of Ref. [13]. Systematic errors of $\sim 1 - 10\%$ are comparable to systematic errors from many other factors, such as detector calibration [75] and waveform modeling [40, 34, 38, 20, 67].

At a comparable precision to the errors presented here, the quality of numerical solutions to the TOV equations may become important for stars containing sharp phase transitions [77]. Because the speed of sound of Gaussian process draws is analytically greater than zero, we are not subject to this concern, we do not have truly sharp transitions, and therefore standard techniques for computing the tidal Love numbers is sufficient. Nonetheless, improved accuracy in TOV solutions will likely be important in future analyses with much improved detector sensitivities.

In contrast, the other relations involving tidal deformability show worse fits, especially among nonparametric EoSs not informed by all astrophysical measurements. All of the C–Love, Binary-Love, and $R_{1.4}$–$\tilde{\Lambda}$ relations show losses of order 10^{-1} or more for the mixed-composition nonparametric EoS distribution. This indicates systematic errors from these relations are already of order the statistical uncertainties. All relations, though, do improve with the inclusion of additional astrophysical data, which indicates that data have ruled out some EoS candidates inconsistent with the relations posed.

In fitting the Binary-Love relation, the inclusion of phase transition EoSs appreciably worsens the fit to the nonparametric EoS distribution, increasing losses by a factor of 10 in the astrophysically-informed case. This is consistent with Ref. [18] which found that hybrid EoSs are poorly modeled with a Binary-Love relation. In particular, Carson et al. [18] found that hybrid EoSs would likely have residuals of order $\Lambda_a \sim 50$ at $\Lambda_s \sim 100$, which is consistent with the worst-case residuals we find in Fig. 5.5. However, the mixed-composition distributions are not universally worse-fit among relations, the C–Love fit sees comparable losses among the two distributions, indicating this relation is essentially insensitive to the presence of a phase transition.

On the other hand, the α_c–C relation is the only relation we studied with loss values greater than 1 for the nonparametric EoS distribution. A similar near total-loss of universality was observed for modes in hybrid stars [66], which could be a useful target for future work. The loss values for the nonparametric distribution are almost 100 times worse for the nonparametric distributions than for the spectral distributions, indicating that modeling systematics are likely responsible for the appearance of EoS independence in this relation. Nonetheless, the improvement of EoS independence in the hadronic nonparametric case, especially upon the inclusion of additional astrophysical data, may indicate that this relation does hold universally for certain classes of EoSs (e.g. hadronic EoSs), under certain assumptions (such as astrophysically reasonable compactness-mass-radii) relations. For this reason, even relations which are not truly EoS independent may still be useful, depending on the use cases intended.

The goodness-of-fit improvement seen when using parametric models rather than nonparametric models is not surprising. The parametric models have fixed functional forms which forces consistency across EoS samples within each of these sets. Contrarily, the nonparametric EoS distribution produces EoSs with no fixed functional form and therefore no guarantee of displaying any particular phenomenology. Therefore, we expect a much larger variety of EoS behaviors from the nonparametric distribution compared to the parametric distributions.

These results are all dependent on the choice of tolerance factor; it is difficult to chose a completely realistic representation when many different potential sources of NS measurements exist. Nonetheless, certain conclusions, such as the relatively poor fits to the nonparametric mixed distribution relative to the spectral distribution, are independent of choice of tolerance factor. Additionally the distribution of points (NSs) that the relations are evaluated with cannot be prescribed universally. A potentially more physical choice that uniform-in-central-density would be a distribution which is consistent with the known population of NS sources:

$$\chi^2 = \int P(\epsilon)\pi(m)\chi^2(G; F, \epsilon)dmd\epsilon, \tag{5.18}$$

where $\pi(m)$ is the distribution of NS masses, and F is a generic NS property which serves as the independent variable for a relation and G is the dependent variable of the relation. A mapping from $F(m)$, $G(m)$ must be chosen in the case that EoSs with multiple stable branches in the M–R relation are used. Then the loss would be equal to the expected failure of the EoS-independent relation to correctly model the next NS source detected. However, the population of NSs observable via GWs is still poorly known [5, 43]. Mathematically, such modifications to the analysis are equivalent to changes to the tolerance factor, though they have different physical interpretation.

It is important to recognize the sensitivity of the loss to choices such as the distribution of NSs used in evaluating each EoS χ^2 and in the tolerance factor chosen for each NS. As seen in, e.g., Fig. 5.5, the highest χ^2 contributions appear at high Λ values for relations involving Λ, equivalent to larger residuals there (under the constant uncertainty model). There may not exist merging BNSs with symmetric tidal deformabilities as high as 10^4, or they may be exceedingly rare. However,

Fig. 5.5 also demonstrates that at $\Lambda \sim 10^3$, deviations from the EoS-independent relation of order 100 or larger are still possible within the nonparametric model. Therefore, we expect variation in the loss based on choices in the truncation of the population, though we do not expect the relationship between losses for the various models to change appreciably under different assumptions. Additionally, assessing the EoS independence of relations when matter is not in cold β-equilibrium, or when NSs are not isolated and nonspinning [44], may be challenging. In particular, NS merger remnants may be highly spinning, hot, and dynamically perturbed, so the cold relations explored here, and the strategy used to evaluate them, will likely have to be extended. Longer-term EoS independence tests will likely have to carefully examine all of these factors in order to determine, with higher fidelity, the usefulness of EoS-independent relations to our understanding of NSs and the nuclear EoS.

5.5 Acknowledgments

We thank Victor Guedes for code to compute the quadrupole moment for NSs. We thank Lami Suleiman for comments on the manuscript. This work is supported by National Science Foundation grant No. PHY-2150027 as part of the LIGO Caltech REU Program. I.L. and K.C. acknowledge support from the Department of Energy under award number DE-SC0023101. K.C. acknowledges support from the Sloan Foundation. R.E. is supported by the Natural Sciences & Engineering Research Council of Canada (NSERC). The authors are grateful for computational resources provided by the LIGO Laboratory and supported by National Science Foundation Grants PHY-0757058 and PHY-0823459. Software: This work makes use of `scipy` [80], `numpy` [59], and `matplotlib` [39]. This material is based upon work supported by NSF's LIGO Laboratory which is a major facility fully funded by the National Science Foundation. The authors gratefully acknowledge the Italian Instituto Nazionale de Fisica Nucleare (INFN), the French Centre National de la Recherche Scientifique (CNRS), and the Netherlands Organization for Scientific Research for the construction and operation of the Virgo detector and the creation and support of the EGO consortium.

5.6 Additional Figures and Tables

In this appendix we display results for the piecewise-polytrope and nonparametric hadronic EoS distributions, in similar form as the main text results for the spectral and nonparametric mixed distributions. The χ^2 values for each fit are given in the main text tables. We use the astrophysically-informed EoS distributions, again

Coefficient	GP-mixed (astro)			SP (astro)			PP (astro)		
	$I(\Lambda)$	$Q(\Lambda)$	$I(Q)$	$I(\Lambda)$	$Q(\Lambda)$	$I(Q)$	$I(\Lambda)$	$Q(\Lambda)$	$I(Q)$
α	2/5	1/5	2	2/5	1/5	2	2/5	1/5	2
K_{yx}	0.5356	0.0072	0.0072	0.5139	0.0052	0.0052	0.4192	0.0007	0.0007
a_1	1.7583	11.1589	11.1589	2.0486	12.1774	12.1774	2.2881	30.3545	30.3545
a_2	1.3883	-37.6926	-37.6926	0.8249	-37.0504	-37.0504	-3.7192	-16.5079	-16.5079
a_3	-5.6089	42.7718	42.7718	6.7629	43.0395	43.0395	72.9633	48.3485	48.3485
b_1	-0.7071	-2.5557	-2.5557	-1.0615	-2.6161	-2.6161	-3.5874	-2.7902	-2.7902
b_2	-0.9748	2.3251	2.3251	2.2034	2.4074	2.4074	16.8924	2.6775	2.6775
b_3	0.5105	-7.3937	-7.3937	-0.9326	-7.6697	-7.6697	-7.6431	-8.7651	-8.7651

Table 5.6: Table of coefficients for the I–Love–Q relations for the nonparametric mixed-composition, spectral, and piecewise-polytrope astrophysical posterior EoS distributions. See Eqs. (5.8), (5.9), and (5.10) respectively.

because we do not find significant differences modulo improvements of order no more than 10 to the fit quality upon conditioning.

For the I–Love–Q relation, we display the fits for the hadronic nonparametric distribution in Fig. 5.9, and for the piecewise-polytrope EoS distribution in Fig. 5.10. I–Q is still the best fit EoS-independent relation. We also give fitting coefficients in Table 5.6.

We display the fits for the Binary-Love relation for the hadronic nonparametric distribution and piecewise-polytrope distribution in Fig. 5.11. We display the best-fit coefficients in Table 5.7.

We display the fits for the C–Love relation for the hadronic nonparametric distribution and piecewise-polytrope distribution in Fig. 5.12. We display the best-fit coefficients in Table 5.8.

For the $\tilde{\Lambda}$–$R_{1.4}$ relation we display the value for the coefficient a for all of the EoS sets in Table 5.9.

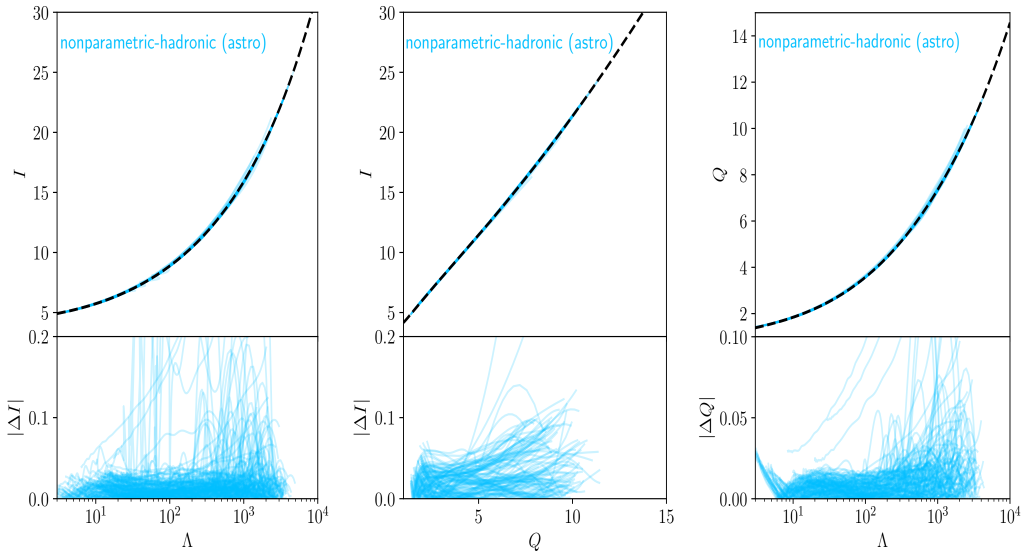

Figure 5.9: The same as Fig. 5.2, but with the hadronic nonparametric distribution conditioned on all astrophysical data.

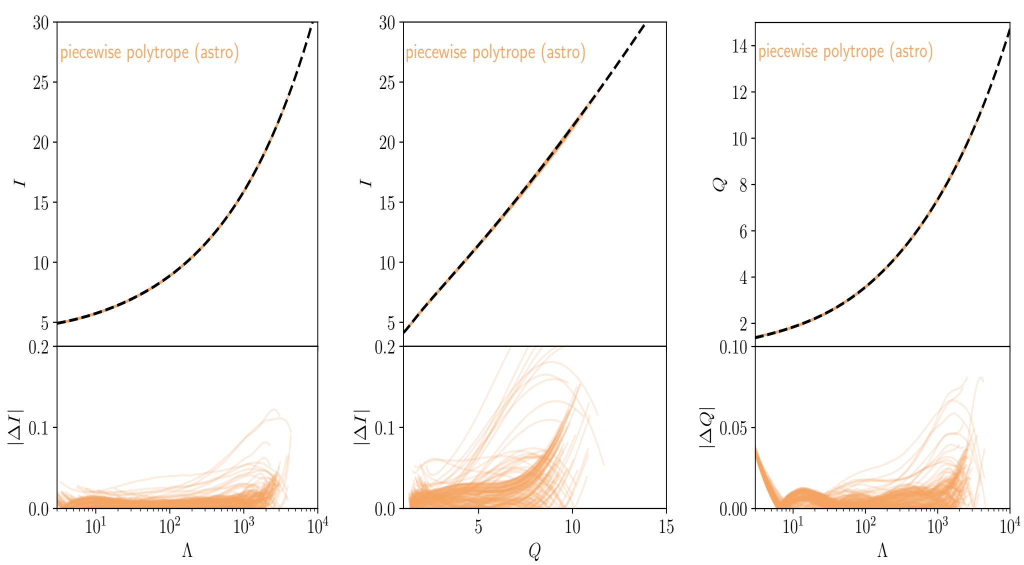

Figure 5.10: The same as Fig. 5.2 but with the piecewise-polytrope EoS distribution conditioned on all astrophysical data.

Coefficient	GP-mixed (astro)			SP (astro)			PP (astro)		
	q = .55	q = .75	q = .9	q = .55	q = .75	q = .9	q = .55	q = .75	q = .9
b_{11}	-13.6363	-13.0286	-35.8727	89.3902	-114.1202	-13.7126	-13.318	-16.0181	-14.2241
b_{12}	16.6082	11.9352	38.1073	-199.4862	153.6543	14.5353	14.5180	13.5785	14.6087
b_{21}	60.9451	49.595	17.3353	137.5437	65.0962	30.3579	60.5649	60.5607	29.9721
b_{22}	-22.4131	-15.7433	-10.7606	-97.1215	-86.1626	-36.4909	-17.0596	-9.8172	-33.4993
b_{31}	-132.7392	-95.409	-85.2499	-227.1308	-150.6500	-21.6415	-125.4819	-117.0661	-22.0825
b_{32}	-35.1957	-33.9646	66.3908	-12.4604	-37.6394	20.1071	-31.7949	-50.6147	20.6718
c_{11}	-36.1830	-121.3958	20.9222	-34.3331	-17.6402	-1.2833	-27.6276	-79.3091	-14.3035
c_{12}	62.3338	157.5113	-24.9027	49.3492	30.3484	0.9211	43.9329	99.8593	15.0504
c_{21}	60.2142	57.6574	44.7671	69.5378	-46.8838	34.3594	63.5022	62.0146	35.7453
c_{22}	-27.5988	-38.6213	-42.4961	24.7469	2.4981	-43.3557	-30.8961	-31.4480	-43.0991
c_{31}	-132.3099	-89.4668	-25.8278	-193.2270	-145.6506	-29.3931	-125.3372	-101.7505	-28.5082
c_{32}	-18.1968	-6.9804	4.5299	-43.5078	142.7302	36.7860	-11.8738	-18.4297	35.8010

Table 5.7: Table of coefficients for the Binary-Love relations for the nonparametric mixed-composition, spectral, and piecewise-polytrope posterior EoS distributions. See Eq. (5.11).

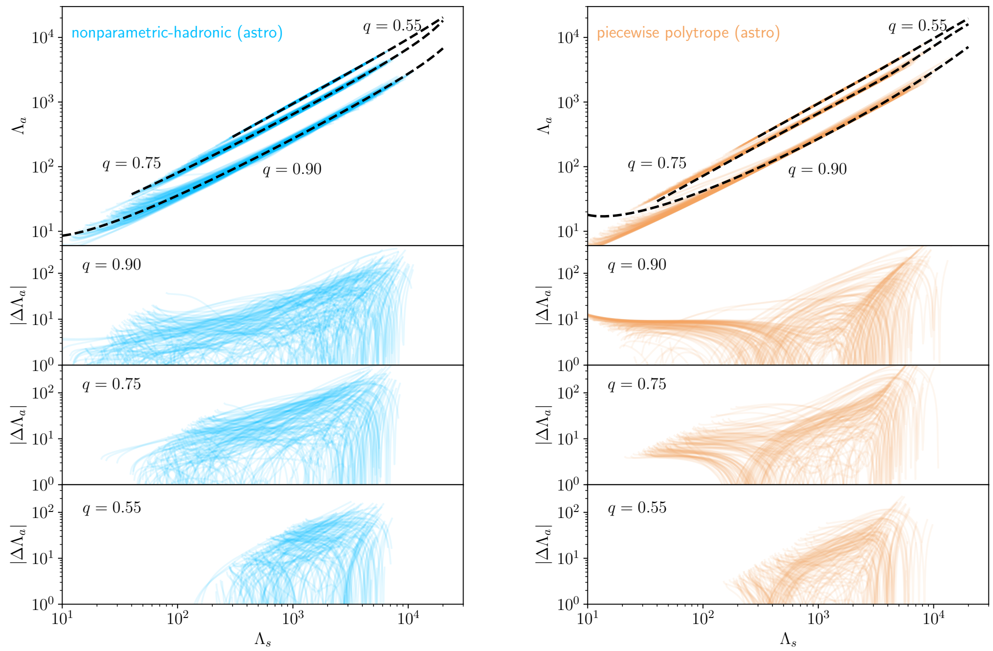

Figure 5.11: The same as Fig. 5.5, but with the hadronic nonparametric EoS distribution on the left, and the piecewise-polytrope distribution on the right.

Coefficient	GP-mixed (astro)	SP (astro)	PP (astro)
	$C(\Lambda)$	$C(\Lambda)$	$C(\Lambda)$
K_{yx}	0.0833	1.9392	3.5446
a_1	-529.6368	-96.4366	-28.1750
a_2	666.1701	-69.8059	-127.7955
a_3	-1119.5632	-191.0251	-43.2623
b_1	-84.2438	-360.1569	-191.1053
b_2	144.0589	152.5207	-433.2343
b_3	-2.7723	-1702.2789	-1318.6131

Table 5.8: Table of coefficients for the C–Love relations for the nonparametric mixed-composition, spectral, and piecewise-polytrope astrophysical posterior EoS distributions. See Eq. (5.13).

Coefficient	GP-mixed (astro)	SP (astro)	PP (astro)
a	3.6387	3.7867	3.8086

Table 5.9: Table of coefficients for the $R_{1.4}$–$\tilde{\Lambda}$ relation. See Eq. (5.15).

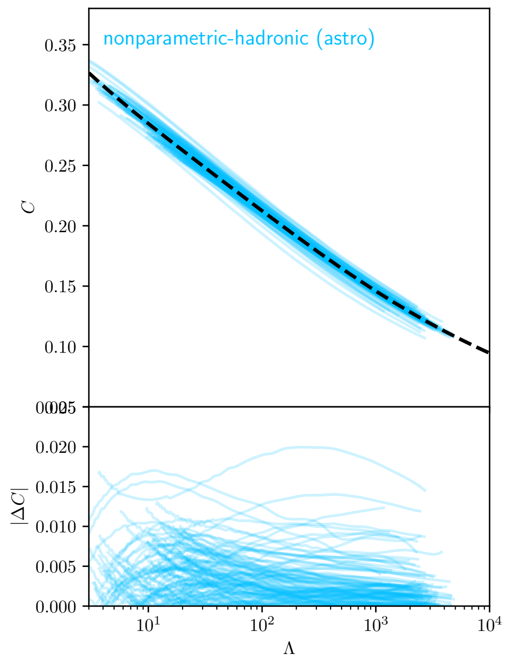

Figure 5.12: The same as Fig. 5.7, but with the hadronic nonparametric EoS distribution on the left, and the piecewise-polytrope EoS distribution on the right. Both distributions are conditioned on all astrophysical data.

Coefficient	GP-mixed (astro)	SP (astro)	PP (astro)
	$\alpha_c(C)$	$\alpha_c(C)$	$\alpha_c(C)$
a_0	-7.3477	-5.1067	-4.7738
a_1	88.5223	49.9461	45.8993
a_2	-591.4298	-379.9054	-389.7208
a_3	1960.4713	1729.6551	2051.4967
a_4	-2799.1485	-3988.1116	-5396.4668
a_5	1215.7415	3783.0214	5.6082

Table 5.10: Table of coefficients for the α_c–C relation for the nonparametric mixed-composition and Spectral posterior EoS distributions. See Eq.(5.17).

We display the fits to the α_c–C EoS-independent relation for the nonparametric hadronic, and piecewise-polytrope distribution both conditioned only on mass measurements of heavy pulsars, and conditioned on all astrophysical data in Fig. 5.13. The piecewise-polytropic distribution is the only one which is better fit by the α_c–C relation after the inclusion of GW mass-tidal deformability and X-ray mass-radius measurements. This can be attributed to *a priori* large values of α_c in the cores of the most massive neutron stars under the piecewise-polytrope models.

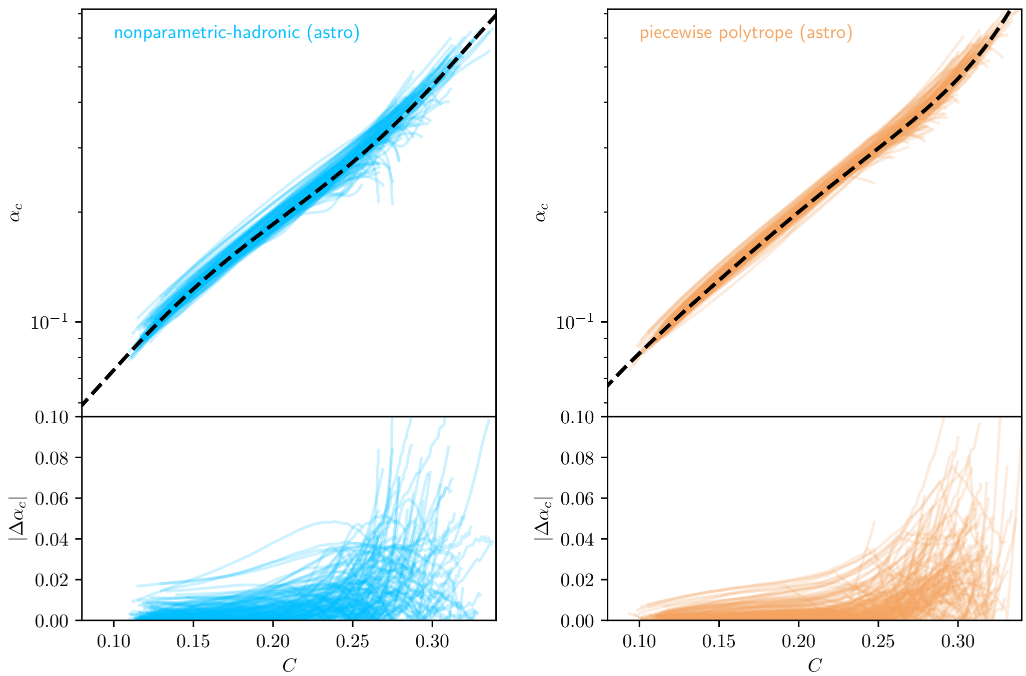

Figure 5.13: Left: The same for the nonparametric EoS distribution, conditioned on all astrophysical data. Right : The same for the piecewise-polytrope parametrization, conditioned on all astrophysical data. Same as Fig. 5.8.

References

[1] B. P. Abbott et al. "GW170817: Measurements of neutron star radii and equation of state". In: *Phys. Rev. Lett.* 121.16 (2018), p. 161101. DOI: 10.1103/PhysRevLett.121.161101. arXiv: 1805.11581 [gr-qc].

[2] B. P. Abbott et al. "GW190425: Observation of a Compact Binary Coalescence with Total Mass $\sim 3.4 M_{\odot}$". In: *Astrophys. J. Lett.* 892.1 (2020), p. L3. DOI: 10.3847/2041-8213/ab75f5. arXiv: 2001.01761 [astro-ph.HE].

[3] B. P. Abbott et al. "Properties of the binary neutron star merger GW170817". In: *Phys. Rev. X* 9.1 (2019), p. 011001. DOI: 10.1103/PhysRevX.9.011001. arXiv: 1805.11579 [gr-qc].

[4] Benjamin P. Abbott et al. "GW170817: Observation of Gravitational Waves from a Binary Neutron Star Inspiral". In: *Phys. Rev. Lett.* 119.16 (2017), p. 161101. DOI: 10.1103/PhysRevLett.119.161101. arXiv: 1710.05832 [gr-qc].

[5] R. Abbott et al. "Population of Merging Compact Binaries Inferred Using Gravitational Waves through GWTC-3". In: *Phys. Rev. X* 13.1 (2023), p. 011048. DOI: 10.1103/PhysRevX.13.011048. arXiv: 2111.03634 [astro-ph.HE].

[6] Nils Andersson and Kostas D. Kokkotas. "Gravitational waves and pulsating stars: What can we learn from future observations?" In: *Phys. Rev. Lett.* 77 (1996), pp. 4134–4137. DOI: 10.1103/PhysRevLett.77.4134. arXiv: gr-qc/9610035.

[7] Nils Andersson and Kostas D. Kokkotas. "Towards gravitational wave asteroseismology". In: *Mon. Not. Roy. Astron. Soc.* 299 (1998), pp. 1059–1068. DOI: 10.1046/j.1365-8711.1998.01840.x. arXiv: gr-qc/9711088.

[8] John Antoniadis et al. "A Massive Pulsar in a Compact Relativistic Binary". In: *Science* 340.6131 (2013), p. 1233232. DOI: 10.1126/science.1233232. arXiv: 1304.6875 [astro-ph.HE].

[9] A. Bauswein and H. -Th. Janka. "Measuring neutron-star properties via gravitational waves from binary mergers". In: *Phys. Rev. Lett.* 108 (2012), p. 011101. DOI: 10.1103/PhysRevLett.108.011101. arXiv: 1106.1616 [astro-ph.SR].

[10] A. Bauswein and N. Stergioulas. "Unified picture of the post-merger dynamics and gravitational wave emission in neutron star mergers". In: *Phys. Rev. D* 91.12 (2015), p. 124056. DOI: 10.1103/PhysRevD.91.124056. arXiv: 1502.03176 [astro-ph.SR].

[11] Andreas Bauswein et al. "Identifying a first-order phase transition in neutron star mergers through gravitational waves". In: *Phys. Rev. Lett.* 122.6 (2019), p. 061102. DOI: 10.1103/PhysRevLett.122.061102. arXiv: 1809.01116 [astro-ph.HE].

[12] Omar Benhar, Valeria Ferrari, and Leonardo Gualtieri. "Gravitational wave asteroseismology revisited". In: *Phys. Rev. D* 70 (2004), p. 124015. DOI: 10.1103/PhysRevD.70.124015. arXiv: astro-ph/0407529.

[13] Ernesto Benitez et al. "Investigating the I-Love-Q and w-mode Universal Relations Using Piecewise Polytropes". In: *Phys. Rev. D* 103.2 (2021), p. 023007. DOI: 10.1103/PhysRevD.103.023007. arXiv: 2010.02619 [astro-ph.HE].

[14] Sebastiano Bernuzzi, Tim Dietrich, and Alessandro Nagar. "Modeling the complete gravitational wave spectrum of neutron star mergers". In: *Phys. Rev. Lett.* 115.9 (2015), p. 091101. DOI: 10.1103/PhysRevLett.115.091101. arXiv: 1504.01764 [gr-qc].

[15] Slavko Bogdanov et al. "Constraining the Neutron Star Mass–Radius Relation and Dense Matter Equation of State with NICER. III. Model Description and Verification of Parameter Estimation Codes". In: (Apr. 2021). arXiv: 2104.06928 [astro-ph.HE].

[16] Matteo Breschi, Gregorio Carullo, and Sebastiano Bernuzzi. "Pre/post-merger consistency test for gravitational signals from binary neutron star mergers". In: (Jan. 2023). arXiv: 2301.09672 [gr-qc].

[17] Matthew F. Carney, Leslie E. Wade, and Burke S. Irwin. "Comparing two models for measuring the neutron star equation of state from gravitational-wave signals". In: *Phys. Rev.* D98.6 (2018), p. 063004. DOI: 10.1103/PhysRevD.98.063004. arXiv: 1805.11217 [gr-qc].

[18] Zack Carson et al. "Equation-of-state insensitive relations after GW170817". In: *Phys. Rev.* D99.8 (2019), p. 083016. DOI: 10.1103/PhysRevD.99.083016. arXiv: 1903.03909 [gr-qc].

[19] Katerina Chatziioannou. "Neutron star tidal deformability and equation of state constraints". In: *Gen. Rel. Grav.* 52.11 (2020), p. 109. DOI: 10.1007/s10714-020-02754-3. arXiv: 2006.03168 [gr-qc].

[20] Katerina Chatziioannou. "Uncertainty limits on neutron star radius measurements with gravitational waves". In: (Aug. 2021). arXiv: 2108.12368 [gr-qc].

[21] Katerina Chatziioannou and Sophia Han. "Studying strong phase transitions in neutron stars with gravitational waves". In: *Phys. Rev. D* 101.4 (2020), p. 044019. DOI: 10.1103/PhysRevD.101.044019. arXiv: 1911.07091 [gr-qc].

[22] Katerina Chatziioannou, Carl-Johan Haster, and Aaron Zimmerman. "Measuring the neutron star tidal deformability with equation-of-state-independent relations and gravitational waves". In: *Phys. Rev. D* 97 (10 May 2018), p. 104036. DOI: 10.1103/PhysRevD.97.104036. arXiv: 1804.03221 [gr-qc]. URL: https://link.aps.org/doi/10.1103/PhysRevD.97.104036.

[23] Katerina Chatziioannou, Kent Yagi, and Nicolás Yunes. "Toward realistic and practical no-hair relations for neutron stars in the nonrelativistic limit". In: *Phys. Rev. D* 90.6 (2014), p. 064030. DOI: 10.1103/PhysRevD.90.064030. arXiv: 1406.7135 [gr-qc].

[24] An Chen et al. "Distinguishing high-mass binary neutron stars from binary black holes with second- and third-generation gravitational wave observatories". In: *Phys. Rev. D* 101.10 (2020), p. 103008. DOI: 10.1103/PhysRevD.101.103008. arXiv: 2001.11470 [astro-ph.HE].

[25] Hsin-Yu Chen and Katerina Chatziioannou. "Distinguishing Binary Neutron Star from Neutron Star–Black Hole Mergers with Gravitational Waves". In: *Astrophys. J. Lett.* 893.2 (2020), p. L41. DOI: 10.3847/2041-8213/ab86bc. arXiv: 1903.11197 [astro-ph.HE].

[26] H. Thankful Cromartie et al. "Relativistic Shapiro delay measurements of an extremely massive millisecond pulsar". In: *Nature Astron.* 4.1 (2019), pp. 72–76. DOI: 10.1038/s41550-019-0880-2. arXiv: 1904.06759.

[27] Soumi De et al. “Tidal Deformabilities and Radii of Neutron Stars from the Observation of GW170817”. In: *Phys. Rev. Lett.* 121.9 (2018). [Erratum: Phys. Rev. Lett.121,no.25,259902(2018)], p. 091102. DOI: 10.1103/PhysRevLett.121.259902, 10.1103/PhysRevLett.121.091102. arXiv: 1804.08583 [astro-ph.HE].

[28] F. Douchin and P. Haensel. “A unified equation of state of dense matter and neutron star structure”. In: *Astron. Astrophys.* 380 (2001), p. 151. DOI: 10.1051/0004-6361:20011402. arXiv: astro-ph/0111092.

[29] Reed Essick, Philippe Landry, and Daniel E. Holz. “Nonparametric Inference of Neutron Star Composition, Equation of State, and Maximum Mass with GW170817”. In: *Phys. Rev. D* 101.6 (2020), p. 063007. DOI: 10.1103/PhysRevD.101.063007. arXiv: 1910.09740 [astro-ph.HE].

[30] Reed Essick et al. “Phase transition phenomenology with nonparametric representations of the neutron star equation of state”. In: *Phys. Rev. D* 108.4 (2023). I contributed substantially to this study which used nonparametric methods to constrain phase transitions in a nonparametric model of the equation of state. I performed the simulation analyses, developed several diagnostic statistics, and wrote large parts of the text., p. 043013. DOI: 10.1103/PhysRevD.108.043013. arXiv: 2305.07411 [astro-ph.HE].

[31] Eanna E. Flanagan and Tanja Hinderer. “Constraining neutron star tidal Love numbers with gravitational wave detectors”. In: *Phys. Rev. D* 77 (2008), p. 021502. DOI: 10.1103/PhysRevD.77.021502. arXiv: 0709.1915 [astro-ph].

[32] E. Fonseca et al. “Refined Mass and Geometric Measurements of the High-mass PSR J0740+6620”. In: *Astrophys. J. Lett.* 915.1 (2021), p. L12. DOI: 10.3847/2041-8213/ac03b8. arXiv: 2104.00880 [astro-ph.HE].

[33] Francois Foucart et al. “Low mass binary neutron star mergers : gravitational waves and neutrino emission”. In: *Phys. Rev. D* 93.4 (2016), p. 044019. DOI: 10.1103/PhysRevD.93.044019. arXiv: 1510.06398 [astro-ph.HE].

[34] Rossella Gamba et al. “Waveform systematics in the gravitational-wave inference of tidal parameters and equation of state from binary neutron star signals”. In: *Phys. Rev. D* 103.12 (2021), p. 124015. DOI: 10.1103/PhysRevD.103.124015. arXiv: 2009.08467 [gr-qc].

[35] Daniel A. Godzieba and David Radice. “High-Order Multipole and Binary Love Number Universal Relations”. In: *Universe* 7.10 (2021), p. 368. DOI: 10.3390/universe7100368. arXiv: 2109.01159 [astro-ph.HE].

[36] Daniel A. Godzieba et al. “Updated universal relations for tidal deformabilities of neutron stars from phenomenological equations of state”. In: *Phys. Rev. D* 103.6 (2021), p. 063036. DOI: 10.1103/PhysRevD.103.063036. arXiv: 2012.12151 [astro-ph.HE].

[37] James B. Hartle. "Slowly Rotating Relativistic Stars. I. Equations of Structure". In: *The Astrophysical Journal* 150 (Dec. 1967), p. 1005. DOI: 10.1086/149400.

[38] Yiwen Huang et al. "Statistical and systematic uncertainties in extracting the source properties of neutron star - black hole binaries with gravitational waves". In: *Phys. Rev. D* 103.8 (2021), p. 083001. DOI: 10.1103/PhysRevD.103.083001. arXiv: 2005.11850 [gr-qc].

[39] J. D. Hunter. "Matplotlib: A 2D graphics environment". In: *Computing In Science & Engineering* 9.3 (2007), pp. 90–95. DOI: 10.1109/MCSE.2007.55.

[40] Nina Kunert et al. "Quantifying modelling uncertainties when combining multiple gravitational-wave detections from binary neutron star sources". In: (Oct. 2021). arXiv: 2110.11835 [astro-ph.HE].

[41] Philippe Landry and Reed Essick. "Nonparametric inference of the neutron star equation of state from gravitational wave observations". In: *Phys. Rev. D* 99.8 (2019), p. 084049. DOI: 10.1103/PhysRevD.99.084049. arXiv: 1811.12529 [gr-qc].

[42] Philippe Landry and Eric Poisson. "Relativistic theory of surficial Love numbers". In: *Phys. Rev. D* 89.12 (2014), p. 124011. DOI: 10.1103/PhysRevD.89.124011. arXiv: 1404.6798 [gr-qc].

[43] Philippe Landry and Jocelyn S. Read. "The Mass Distribution of Neutron Stars in Gravitational-wave Binaries". In: *Astrophys. J. Lett.* 921.2 (2021), p. L25. DOI: 10.3847/2041-8213/ac2f3e. arXiv: 2107.04559 [astro-ph.HE].

[44] Noshad Khosravi Largani et al. "Universal relations for rapidly rotating cold and hot hybrid stars". In: *Mon. Not. Roy. Astron. Soc.* 515.3 (2022), pp. 3539–3554. DOI: 10.1093/mnras/stac1916. arXiv: 2112.10439 [astro-ph.HE].

[45] J. M. Lattimer and M. Prakash. "Neutron star structure and the equation of state". In: *Astrophys. J.* 550 (2001), p. 426. DOI: 10.1086/319702. arXiv: astro-ph/0002232.

[46] H. K. Lau, P. T. Leung, and L. M. Lin. "Inferring physical parameters of compact stars from their f-mode gravitational wave signals". In: *Astrophys. J.* 714 (2010), pp. 1234–1238. DOI: 10.1088/0004-637X/714/2/1234. arXiv: 0911.0131 [gr-qc].

[47] Isaac Legred et al. "Impact of the PSR J0740+6620 radius constraint on the properties of high-density matter". In: *Phys. Rev. D* 104.6 (2021), p. 063003. DOI: 10.1103/PhysRevD.104.063003. arXiv: 2106.05313 [astro-ph.HE].

[48] Isaac Legred et al. "Implicit correlations within phenomenological parametric models of the neutron star equation of state". In: *Phys. Rev. D* 105.4 (2022). I led this study which compared parametric to nonparametric methods of inferring the equation of state. I developed a substantial amount of software, ran the analysis, and co-wrote the manuscript., p. 043016. DOI: 10.1103/PhysRevD.105.043016. arXiv: 2201.06791 [astro-ph.HE].

[49] Luis Lehner et al. "Unequal mass binary neutron star mergers and multimessenger signals". In: *Class. Quant. Grav.* 33.18 (2016), p. 184002. DOI: 10.1088/0264-9381/33/18/184002. arXiv: 1603.00501 [gr-qc].

[50] Lee Lindblom. "Spectral Representations of Neutron-Star Equations of State". In: *Phys. Rev. D* 82 (2010), p. 103011. DOI: 10.1103/PhysRevD.82.103011. arXiv: 1009.0738 [astro-ph.HE].

[51] Lee Lindblom and Nathaniel M. Indik. "Spectral approach to the relativistic inverse stellar structure problem". In: *Phys.Rev.D* 86.8, 084003 (Oct. 2012), p. 084003. DOI: 10.1103/PhysRevD.86.084003. arXiv: 1207.3744 [astro-ph.HE].

[52] Lee Lindblom and Nathaniel M. Indik. "Spectral Approach to the Relativistic Inverse Stellar Structure Problem II". In: *Phys. Rev.* D89.6 (2014). [Erratum: Phys. Rev.D93,no.12,129903(2016)], p. 064003. DOI: 10.1103/PhysRevD.89.064003,10.1103/PhysRevD.93.129903. arXiv: 1310.0803 [astro-ph.HE].

[53] Andrea Maselli et al. "Equation-of-state-independent relations in neutron stars". In: *Phys. Rev. D* 88.2 (2013), p. 023007. DOI: 10.1103/PhysRevD.88.023007. arXiv: 1304.2052 [gr-qc].

[54] M. C. Miller et al. "PSR J0030+0451 Mass and Radius from *NICER* Data and Implications for the Properties of Neutron Star Matter". In: *Astrophys. J. Lett.* 887.1 (2019), p. L24. DOI: 10.3847/2041-8213/ab50c5. arXiv: 1912.05705 [astro-ph.HE].

[55] M. C. Miller et al. "The Radius of PSR J0740+6620 from NICER and XMM-Newton Data". In: (May 2021). arXiv: 2105.06979 [astro-ph.HE].

[56] Elias R. Most et al. "Signatures of quark-hadron phase transitions in general-relativistic neutron-star mergers". In: *Phys. Rev. Lett.* 122.6 (2019), p. 061101. DOI: 10.1103/PhysRevLett.122.061101. arXiv: 1807.03684 [astro-ph.HE].

[57] KamalKrishna Nath, Ritam Mallick, and Sagnik Chatterjee. "Universal Relations For Generic Family Of Neutron Star Equations Of State". In: (Feb. 2023). arXiv: 2302.05088 [gr-qc].

[58] Michael F. O'Boyle et al. "Parametrized equation of state for neutron star matter with continuous sound speed". In: *Phys. Rev. D* 102.8 (2020), p. 083027. DOI: 10.1103/PhysRevD.102.083027. arXiv: 2008.03342 [astro-ph.HE].

[59] Travis Oliphant. *NumPy: A guide to NumPy*. USA: Trelgol Publishing. [Online; accessed <today>]. 2006–. URL: http://www.numpy.org/.

[60] Grigorios Papigkiotis and George Pappas. "Universal Relations for rapidly rotating neutron stars using supervised machine-learning techniques". In: (Mar. 2023). arXiv: 2303.04273 [astro-ph.HE].

[61] George Pappas and Theocharis A. Apostolatos. "Effectively universal behavior of rotating neutron stars in general relativity makes them even simpler than their Newtonian counterparts". In: *Phys. Rev. Lett.* 112 (2014), p. 121101. DOI: 10.1103/PhysRevLett.112.121101. arXiv: 1311.5508 [gr-qc].

[62] William H. Press et al. *Numerical Recipes 3rd Edition: The Art of Scientific Computing*. 3rd ed. USA: Cambridge University Press, 2007. ISBN: 0521880688.

[63] Carolyn Raithel, Feryal Özel, and Dimitrios Psaltis. "Tidal deformability from GW170817 as a direct probe of the neutron star radius". In: *Astrophys. J.* 857.2 (2018), p. L23. DOI: 10.3847/2041-8213/aabcbf. arXiv: 1803.07687 [astro-ph.HE].

[64] Carolyn A. Raithel and Elias R. Most. "Tidal Deformability Doppelgangers: I. Differentiability of gravitational waveforms for neutron stars with a low-density phase transition". In: (Aug. 2022). arXiv: 2208.04294 [astro-ph.HE].

[65] Carolyn A. Raithel and Elias R. Most. "Tidal Deformability Doppelgangers: II. Implications of a low-density phase transition in the neutron star equation of state". In: (Aug. 2022). arXiv: 2208.04295 [astro-ph.HE].

[66] Ignacio F. Ranea-Sandoval et al. "Asteroseismology using quadrupolar f-modes revisited: Breaking of universal relationships in the slow hadron-quark conversion scenario". In: *Phys. Rev. D* 107.12 (2023), p. 123028. DOI: 10.1103/PhysRevD.107.123028. arXiv: 2306.02823 [astro-ph.HE].

[67] Jocelyn S. Read. "Waveform uncertainty quantification and interpretation for gravitational-wave astronomy". In: *Class. Quant. Grav.* 40.13 (2023), p. 135002. DOI: 10.1088/1361-6382/acd29b. arXiv: 2301.06630 [gr-qc].

[68] Jocelyn S. Read et al. "Constraints on a phenomenologically parameterized neutron-star equation of state". In: *Phys. Rev. D* 79 (2009), p. 124032. DOI: 10.1103/PhysRevD.79.124032. arXiv: 0812.2163 [astro-ph].

[69] Thomas E. Riley et al. "A *NICER* View of PSR J0030+0451: Millisecond Pulsar Parameter Estimation". In: *Astrophys. J. Lett.* 887.1 (2019), p. L21. DOI: 10.3847/2041-8213/ab481c. arXiv: 1912.05702 [astro-ph.HE].

[70] Thomas E. Riley et al. "A NICER View of the Massive Pulsar PSR J0740+6620 Informed by Radio Timing and XMM-Newton Spectroscopy". In: (May 2021). arXiv: 2105.06980 [astro-ph.HE].

[71] Jayana A. Saes and Raissa F. P. Mendes. “Equation-of-state-insensitive measure of neutron star stiffness”. In: *Phys. Rev. D* 106.4 (2022), p. 043027. DOI: 10.1103/PhysRevD.106.043027. arXiv: 2109.11571 [gr-qc].

[72] Anuradha Samajdar and Tim Dietrich. “Constructing Love-Q-Relations with Gravitational Wave Detections”. In: *Phys. Rev. D* 101.12 (2020), p. 124014. DOI: 10.1103/PhysRevD.101.124014. arXiv: 2002.07918 [gr-qc].

[73] Hector O. Silva et al. “Astrophysical and theoretical physics implications from multimessenger neutron star observations”. In: *Phys. Rev. Lett.* 126.18 (2021), p. 181101. DOI: 10.1103/PhysRevLett.126.181101. arXiv: 2004.01253 [gr-qc].

[74] Leo C. Stein, Kent Yagi, and Nicolás Yunes. “Three-Hair Relations for Rotating Stars: Nonrelativistic Limit”. In: *Astrophys. J.* 788 (2014), p. 15. DOI: 10.1088/0004-637X/788/1/15. arXiv: 1312.4532 [gr-qc].

[75] Ling Sun et al. “Characterization of systematic error in Advanced LIGO calibration”. In: *Class. Quant. Grav.* 37.22 (2020), p. 225008. DOI: 10.1088/1361-6382/abb14e. arXiv: 2005.02531 [astro-ph.IM].

[76] Kentaro Takami, Luciano Rezzolla, and Luca Baiotti. “Constraining the Equation of State of Neutron Stars from Binary Mergers”. In: *Phys. Rev. Lett.* 113.9 (2014), p. 091104. DOI: 10.1103/PhysRevLett.113.091104. arXiv: 1403.5672 [gr-qc].

[77] János Takátsy and Péter Kovács. “Comment on ”Tidal Love numbers of neutron and self-bound quark stars””. In: *Phys. Rev. D* 102.2 (2020), p. 028501. DOI: 10.1103/PhysRevD.102.028501. arXiv: 2007.01139 [astro-ph.HE].

[78] Hung Tan et al. “Finding Structure in the Speed of Sound of Supranuclear Matter from Binary Love Relations”. In: *Phys. Rev. Lett.* 128.16 (2022), p. 161101. DOI: 10.1103/PhysRevLett.128.161101. arXiv: 2111.10260 [astro-ph.HE].

[79] L. K. Tsui and P. T. Leung. “Universality in quasi-normal modes of neutron stars”. In: *Mon. Not. Roy. Astron. Soc.* 357 (2005), pp. 1029–1037. DOI: 10.1111/j.1365-2966.2005.08710.x. arXiv: gr-qc/0412024.

[80] Pauli Virtanen et al. “SciPy 1.0: Fundamental Algorithms for Scientific Computing in Python”. In: *Nature Methods* 17 (2020), pp. 261–272. DOI: 10.1038/s41592-019-0686-2.

[81] Leslie Wade et al. “Systematic and statistical errors in a bayesian approach to the estimation of the neutron-star equation of state using advanced gravitational wave detectors”. In: *Phys. Rev. D* 89.10 (2014), p. 103012. DOI: 10.1103/PhysRevD.89.103012. arXiv: 1402.5156 [gr-qc].

[82] Marcella Wijngaarden et al. "Probing neutron stars with the full premerger and postmerger gravitational wave signal from binary coalescences". In: *Phys. Rev. D* 105.10 (2022), p. 104019. DOI: 10.1103/PhysRevD.105.104019. arXiv: 2202.09382 [gr-qc].

[83] Daniel Wysocki et al. "Inferring the neutron star equation of state simultaneously with the population of merging neutron stars". In: (2020). arXiv: 2001.01747 [gr-qc].

[84] Yiqi Xie et al. "Breaking bad degeneracies with Love relations: Improving gravitational-wave measurements through universal relations". In: *Phys. Rev. D* 107.4 (2023), p. 043010. DOI: 10.1103/PhysRevD.107.043010. arXiv: 2210.09386 [gr-qc].

[85] Kent Yagi. "Multipole Love Relations". In: *Phys. Rev. D* 89.4 (2014). [Erratum: Phys.Rev.D 96, 129904 (2017), Erratum: Phys.Rev.D 97, 129901 (2018)], p. 043011. DOI: 10.1103/PhysRevD.89.043011. arXiv: 1311.0872 [gr-qc].

[86] Kent Yagi and Nicolas Yunes. "Approximate Universal Relations among Tidal Parameters for Neutron Star Binaries". In: *Class. Quant. Grav.* 34.1 (2017), p. 015006. DOI: 10.1088/1361-6382/34/1/015006. arXiv: 1608.06187 [gr-qc].

[87] Kent Yagi and Nicolas Yunes. "Approximate Universal Relations for Neutron Stars and Quark Stars". In: *Phys. Rept.* 681 (2017), pp. 1–72. DOI: 10.1016/j.physrep.2017.03.002. arXiv: 1608.02582 [gr-qc].

[88] Kent Yagi and Nicolas Yunes. "Binary Love Relations". In: *Class. Quant. Grav.* 33.13 (2016), 13LT01. DOI: 10.1088/0264-9381/33/13/13LT01. arXiv: 1512.02639 [gr-qc].

[89] Kent Yagi and Nicolas Yunes. "I-Love-Q". In: *Science* 341 (2013), pp. 365–368. DOI: 10.1126/science.1236462. arXiv: 1302.4499 [gr-qc].

[90] Kent Yagi and Nicolas Yunes. "I-Love-Q Relations in Neutron Stars and their Applications to Astrophysics, Gravitational Waves and Fundamental Physics". In: *Phys. Rev. D* 88.2 (2013), p. 023009. DOI: 10.1103/PhysRevD.88.023009. arXiv: 1303.1528 [gr-qc].

[91] Kent Yagi et al. "Effective No-Hair Relations for Neutron Stars and Quark Stars: Relativistic Results". In: *Phys. Rev. D* 89.12 (2014), p. 124013. DOI: 10.1103/PhysRevD.89.124013. arXiv: 1403.6243 [gr-qc].

[92] Kent Yagi et al. "Why I-Love-Q: Explaining why universality emerges in compact objects". In: *Phys. Rev. D* 90.6 (2014), p. 063010. DOI: 10.1103/PhysRevD.90.063010. arXiv: 1406.7587 [gr-qc].

[93] Tianqi Zhao and James M. Lattimer. "Tidal Deformabilities and Neutron Star Mergers". In: *Phys. Rev. D* 98.6 (2018), p. 063020. DOI: 10.1103/PhysRevD.98.063020. arXiv: 1808.02858 [astro-ph.HE].

Chapter 6

DISTINGUISHING LOW-MASS COMPACT BINARIES SEEN IN GRAVITATIONAL WAVES USING KNOWLEDGE OF THE EQUATION OF STATE

[1] Jacob Golomb et al. "Using equation of state constraints to classify low-mass compact binary mergers". In: *Phys. Rev. D* 110.6 (2024). I co-led this study with Jacob Golomb examining whether subsolar mass neutron stars could be reliably distinguished from subsolar mass black holes with current LIGO detectors. I performed the equation of state inference step, and co-wrote the manuscript, p. 063014. DOI: 10.1103/PhysRevD.110.063014. arXiv: 2403.07697 [astro-ph.HE].

Abstract

Compact objects observed via gravitational waves are classified as black holes or neutron stars primarily based on their inferred mass with respect to stellar evolution expectations. However, astrophysical expectations for the lowest mass range, $\lesssim 1.2\,M_\odot$, are uncertain. If such low-mass compact objects exist, ground-based gravitational wave detectors may observe them in binary mergers. Lacking astrophysical expectations for classifying such observations, we go beyond the mass and explore the role of tidal effects. We evaluate how combined mass and tidal inference can inform whether each binary component is a black hole or a neutron star based on consistency with the supranuclear-density equation of state. Low-mass neutron stars experience a large tidal deformation; its observational identification (or lack thereof) can therefore aid in determining the nature of the binary components. Using simulated data, we find that the presence of a sub-solar mass neutron star (black hole) can be established with odds $\sim 100:1$ when two neutron stars (black holes) merge and emit gravitational waves at signal-to-noise ratio ~ 20. For the same systems, the absence of a black hole (neutron star) can be established with odds $\sim 10:1$. For mixed neutron star-black hole binaries, we can establish that the system contains a neutron star with odds $\gtrsim 5:1$. Establishing the presence of a black hole in mixed neutron star-black hole binaries is more challenging, except for the case of a $\lesssim 1\,M_\odot$ black hole with a $\gtrsim 1\,M_\odot$ neutron star companion. On the other hand, classifying each individual binary component suffers from an inherent

labeling ambiguity.

6.1 Introduction

Astronomical observations have revealed a diversity in compact objects with masses $\lesssim 3\,M_\odot$. Classifying these observations as black holes (BHs), neutron stars (NSs), or white dwarfs (WDs), requires identifying observational signatures that are unique to each type. For example, pulsars are identified as NSs [56], while unique electromagnetic spectrum or emission signatures can distinguish between NSs and BHs even if the mass is unknown, as is the case for accreting X-ray binaries [95, 42, 110]. On the gravitational-wave (GW) side, classification is simplified by the fact that ground-based GW detectors are only sensitive to objects that do not disrupt or collide before reaching the detector sensitive band $\gtrsim 10$ Hz. For example, a pair of maximum compactness WDs each with mass $1.3\,M_\odot$ and radius 1700 km collide at a GW frequency of ≈ 1 Hz, see App. 6.8 for calculation details. However, even after excluding WDs, distinguishing between NSs and BHs is challenging because, unlike electromagnetic emission, their GW emission is more similar, as it is primarily determined by the object's mass.

GW mass measurements in conjunction with astrophysical and nuclear physics can lead to preliminary classification indications. Causality limits NS masses $\lesssim 3\,M_\odot$ [97, 69]; more massive objects observed in GWs must be BHs. Astronomical and nuclear constraints suggest that NSs do not reach this theoretical maximum, however. Estimates of the maximum mass of stable nonrotating NSs [111, 88] range $2.0-2.5\,M_\odot$ [76, 96, 38, 90, 94, 54]; rigidly rotating NS can be $\sim 20\%$ more massive [32]. Based on these constraints, Refs. [3, 43, 10] argued that the GW190425 [3] primary was likely a NS, while the GW190814 [10] secondary was a BH. However, it is unclear if stellar evolution creates NSs up to the maximum mass allowed by nuclear physics; little evidence for or against this scenario is observationally available [11].

Switching to the full mass distribution, Galactic observations indicate that the observed NS population is strongly peaked at $\sim 1.4\,M_\odot$, with a lower (upper) truncation near $1.1(2.0)\,M_\odot$ [16, 49]. The Galactic BNS population is narrower and peaked at $1.4\,M_\odot$ [16, 101], though the impact of selection effects on these results is unclear. Neither result is consistent with the GW-observed NS mass distribution that displays no prominent peak at $1.4\,M_\odot$ [27, 73, 11]. Electromagnetic observations suggest a scarcity or even absence of sub-$5\,M_\odot$ BHs [89, 70, 50, 102], though candidates, subject to debate [62, 109, 19], exist [108, 68]. The $2.6\,M_\odot$ secondary in GW190814 [10] as well as galactic observations [20, 29] indicate that if a mass gap between NSs and BHs does exist, it is not empty [11]. In the absence of unambiguous classification for $\sim 2-3\,M_\odot$ objects, Refs. [52, 11, 48] modeled the mass distribution of all sub-10 $M_\odot$ objects and identified a feature at $\sim 2.4\,M_\odot$. Under the assumption of nonoverlapping NS and BH distributions, such a feature could signal the transition from the NS to the BH population.

In contrast to these astrophysics- and nuclear physics-informed considerations about the high end of the NS mass range, the low end remains uncharted. No widely-accepted *astrophysical* process results in stellar remnants of either type with masses $\lesssim 1.2\,M_\odot$ [106, 74, 75], although *physically* cold NSs remain stable down to $O(10^{-1})\,M_\odot$ [74, 75].[1] Radio and X-ray observations have led to NS candidates with masses $\sim 1.17\,M_\odot$ [79] and $\sim 0.8\,M_\odot$ [39]. Additionally, masses and eccentricities of *Gaia* binaries suggest the existence of $\sim 1\,M_\odot$ NSs [101]. As for BHs, while sub-1 $M_\odot$ BHs do not form through stellar collapse, early-universe density fluctuations and sufficiently dissipative dark matter could collapse into primordial BHs with masses in this range [25, 86]. Searches for subsolar mass compact objects with GWs have as of yet yielded no detections [12, 13, 85]. If such BHs do exist, they may be detectable by current and future GW detectors, and properties such as their masses and spins may be measurable [116, 83].

Given these uncertainties, classification of potential sub-1.2 $M_\odot$ GW candidates requires an additional unique signature: matter effects.[2] GWs from mergers involving NSs carry the imprint of tidal interactions in the signal phase evolution [26, 65, 53]. To leading order[3], the effect is quantified by the dimensionless tidal deformability which depends on the nuclear equation of state (EoS) ($c = G = 1$):

$$\Lambda \equiv \frac{2}{3} k_2 C^{-5} , \tag{6.1}$$

where k_2 is the quadrupole tidal love number, and $C = m/R$ is the compactness, the ratio of the NS mass m to its radius R. Tidal interactions enter the GW phase to leading $5th$ Post-Newtonian (PN) order [53, 51] through $\tilde{\Lambda}$, a mass-weighted combination of the component tidal deformabilities. BHs in General Relativity

[1] The minimum mass of a hot proto-NS is however likely larger than that of a cold NS [103, 75, 105].

[2] On the electromagnetic side, matter effects manifest as counterparts, such as with GW170817 [4], proving the presence of at least one NS and a 10:4 preference for two [63, 33, 34]. Absence of a counterpart does not necessarily rule out NSs, as detectability may be limited by beaming or prompt collapse [3].

[3] Higher-order effects, such as dynamical tides [64, 92, 55], also affect the waveform and can aid in distinguishing NSs and BHs.

have vanishing k_2, making Λ a unique signature of the compact object nature [21, 31] [4]. Tidal information has previously suggested the presence of at least one NS in GW170817 based on disfavoring zero tides [5], EoS-independent relations [9], and consistency of the tidal measurement with EoS inference [44]. Furthermore, Ref. [30] showed that lack of tidal signature can be used to identify $\sim 1-2\,M_\odot$ BHs if they exist, though distinguishing between NSBHs and BBHs is more challenging if the BH has a higher mass [23].

Tidal deformability becomes an increasingly better discriminator between BHs and NSs as the object's mass decreases. For $m \gtrsim 1\,M_\odot$, k_2 scales as $k_2 \sim m^{-1}$ [119], resulting in $\Lambda(m) \sim m^{-6}$ (see Fig. 6.1) assuming an approximately constant radius.[5] The lowest-mass NSs therefore exhibit the strongest tidal signatures and differ the most from BHs [36], with $\Lambda \sim O(10^4)$ for $m \sim 1\,M_\odot$, compared to $\Lambda \sim O(10)$ for $m \gtrapprox 2\,M_\odot$.

In this work, we leverage the expected large tidal deformabilities of low-mass NSs, combined with astrophysically-informed EoS constraints to classify compact objects as either NSs or BHs. Our classification is based on the fact that a compact object's tidal deformability must be consistent with the EoS prediction if it is a NS (see the $m-\Lambda$ relation in Fig. 6.1) or zero if it is a BH. While the true EoS is unknown, astronomical observations have placed constraints, giving independent predictions for the tidal deformability of a NS of a given mass, e.g., [38, 72, 76, 90, 94]. This method expands upon efforts to identify NSs through a $\tilde{\Lambda} > 0$ condition [5], as we additionally require Λ to be consistent with predictions from the dense-matter EoS, similar to the GW170817 classification of [44]. In other words, our analysis combines the discriminatory power of two conditions: BHs are consistent with $\Lambda = 0$ and NSs are consistent with $\Lambda = \Lambda(m)$ as predicted by the EoS.

We test our classification approach with simulated data from low-mass sources with signal-to-noise ratios (SNRs) of 20 and 12 at advanced detector sensitivity. Lower (upper) limits on Λ allow us to rule out a BH-BH (NS-NS) origin when at least one of the binary components is a NS (BH). Figure 6.1 shows a demonstration of this idea in the BH-BH case. Though this plot is restricted to two dimensions and does not capture the strong correlations between Λ_1 and Λ_2, c.f., Fig. 6.3, the full-dimensional posterior structure is leveraged in the classification scheme laid out in Sec. 6.2. In systems with sufficiently unequal masses, $m_2/m_1 \lesssim 0.8$, it might be

[4]Beyond static tides and Λ, Kerr BHs have nonvanishing dynamical tides [91].

[5]This is a good approximation excluding EoSs with phase transitions [59, 74].

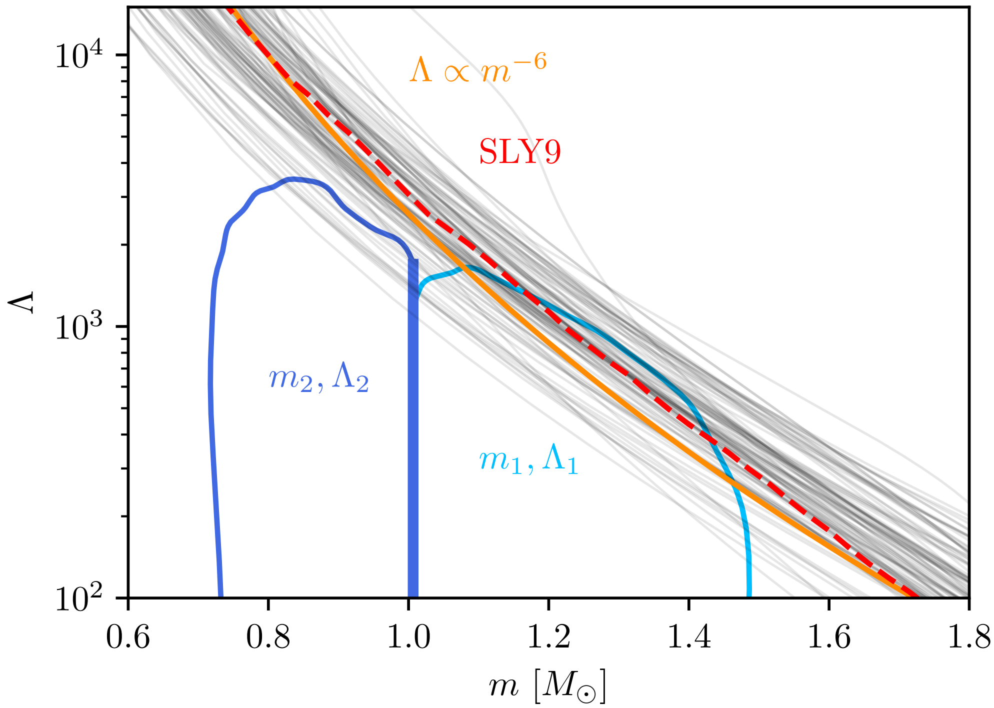

Figure 6.1: The $m - \Lambda$ relation for draws from the EoS posterior from [76] (gray lines). A red dashed line denotes the SLY9 EoS. An orange solid line indicates the $\Lambda \propto m^{-6}$ trend. The posteriors of the masses and tidal deformabilties of the primary and secondary component of a BBH simulated signal are shown in light blue and dark blue, respectively. Despite poorer tidal constraints, the secondary is less consistent with the EoSs, suggestive of a BH. While this demonstration does not capture the full four-dimensional mass-Λ correlations, it sketches the main classification idea.

possible to conclude that there is only a single NS. We also discuss an ambiguity in labeling individual objects that makes it difficult to identify the NS in a single-NS system.

The rest of the paper is organized as follows. In Sec. 6.2, we overview the parameter estimation methodology and source classification procedure. We present parameter estimation results on simulated signals in Sec. 6.3. Using these results, we quantify the evidence of BHs and NSs in Secs. 6.4 and 6.5, respectively. We conclude in Sec. 7.5.

6.2 Methods

In this section, we describe the classification procedure and the methods for demonstrating its effectiveness. In Sec. 6.2, we describe the simulated low-mass signals and parameter estimation. In Sec. 6.2, we fold in EoS information to quantify the probability of each source type.

Classification-agnostic Parameter Estimation

We simulate data for binaries with all unique configurations of source-frame masses $(m_1, m_2) \in \{0.8, 0.9, 1.0, 1.1, 1.2\}\, M_\odot$ with $m_1 \geq m_2$ and source type NS-NS, BH-NS, NS-BH, and BH-BH, where the first (second) initial corresponds to the primary (secondary). The lower mass is selected both for computational reasons and because distinguishability is easier for even lower-mass systems. This results in 55 total configurations.[6] For brevity, we refer to BH-BH as BBH and NS-NS as BNS. We simulate sources with no spins and two network SNRs, one high-SNR set with $\rho_{\rm net} \approx 20$ and another lower-SNR set with $\rho_{\rm net} \approx 12$. The former corresponds to an optimistic detection scenario, although still quieter than GW170817 [8], while the latter is representative of the bulk of detections. Further details are provided in App. 6.9. BHs are simulated with vanishing Λ. For NSs, we assign $\Lambda(m)$ according to their mass m and the EoS SLY9 [60], chosen as a representative EoS that is consistent with current astronomical data [76]; see Fig. 6.1. We adopt standard priors for all parameters, detailed in App. 6.9. We remain agnostic on source type and adopt a uniform prior between 0 and 20×10^3 for the tidal deformabilities for all simulated signals.

We simulate data observed by the LIGO-Virgo detector network [6, 1, 14] with a zero noise realization, corresponding to a geometric mean of many noise realizations [84]. For the noise Power Spectral Densities (PSDs), we use the LIGO O4 low-sensitivity and O3 Virgo noise curves [6, 24, 15]. Signals are simulated and modeled with IMRPhenomXAS_NRTidalv3 [2], a phenomenological, frequency-domain waveform model for the dominant GW emission from the coalescence of BNS mergers with aligned spin components. The model is based on a BBH GW model [93], which is then augmented with a closed-form tidal expression [37, 2]. The model incorporates dynamical tidal effects [64] and is calibrated to a suite of numerical-relativity simulations. Two of these simulations are unequal-mass systems with a subsolar mass secondary (0.98 $M_\odot$ and 0.90 $M_\odot$, with tidal deformabilities ~ 2600 and ~ 4600, respectively). The model has also been compared against an unequal-mass system with a subsolar mass component $\sim 0.94\, M_\odot$ and a tidal deformability of ~ 9300 [112]. Its reliability has been checked within $m_{1,2} \in [0.5, 3.0]\, M_\odot$ and

[6] The total number of possible systems is 100. Enforcing $m_1 > m_2$ and taking into account that equal-mass NS-BH and BH-NS systems are identical reduces this to 55.

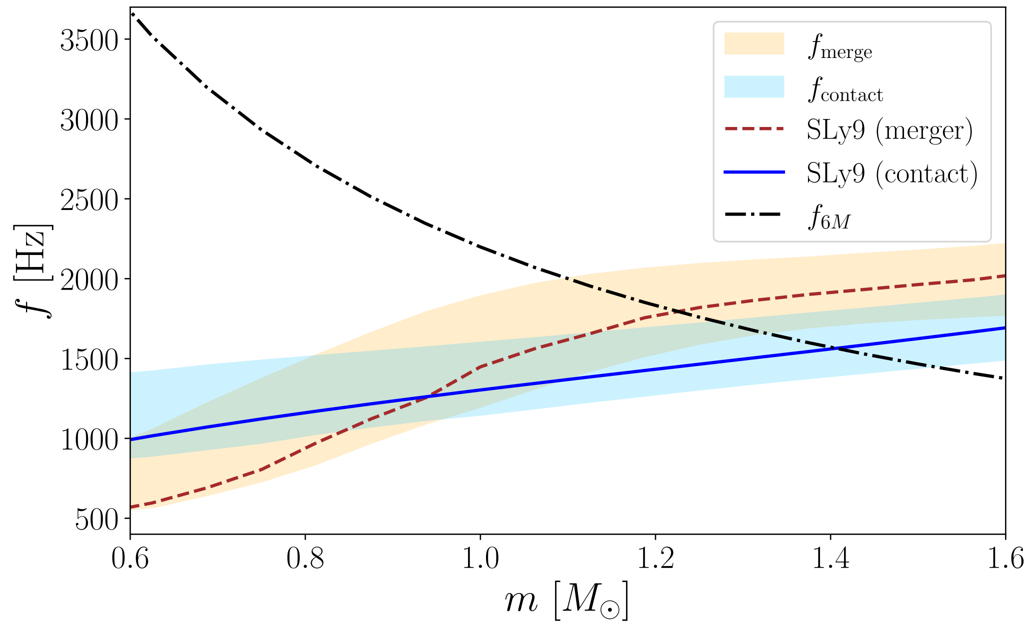

Figure 6.2: Relevant frequencies for late-inspiral signals: merger (peak strain, tan) and contact (orbital separation corresponding to objects touching, light blue) of NSs in equal-mass systems as a function of component mass. Shaded regions correspond to marginalization over the EoS posterior from [76]. Colored lines correspond to the SLy9 EoS [40, 60], which we use to simulate data. Lastly, we display an approximation for the plunge frequency of a comparable mass BBH f_{6M} with a black dash-dot line.

$\Lambda_{1,2} \in [0, 20000]$, a range well-suited for our study.

For illustrative purposes, we show relevant frequencies around the binary merger as a function of mass in Fig. 6.2, see App. 6.8 for a detailed definition. We include the merger frequency, defined as the frequency of peak strain [58], the contact frequency, defined from a binary separation equal to the sum of the components' radii, and $f_{6M} \equiv (6^{3/2}(m_1+m_2))^{-1}/(2\pi)$, an approximation for the plunge frequency of BBHs. In the mass range of interest, all frequencies are between $\sim 1-3\,\mathrm{kHz}$.

Classifying Compact Binaries using EoS Information

The possible source classes for each detected binary are (T_1, T_2) one of $\{(\mathrm{BH}, \mathrm{BH}), (\mathrm{NS}, \mathrm{BH}), (\mathrm{BH}, \mathrm{NS}), (\mathrm{NS}, \mathrm{NS})\}$, where T_1 and T_2 refer to the source type (BH or NS) of the primary (more massive) or secondary (less massive) object, respectively. For each event, the likelihood given an EoS ϵ and source type T_1, T_2 is obtained by marginalizing over the binary masses and tidal deformabilities:

$$\begin{aligned}\mathcal{L}(d|\epsilon, T_1, T_2) = \int & dm_1\, dm_2\, d\Lambda_1\, d\Lambda_2\, \mathcal{L}(d|m_1, m_2, \Lambda_1, \Lambda_2) \\ & \times \pi(m_1, m_2)\pi(\Lambda_1, \Lambda_2|\epsilon, m_1, m_2, T_1, T_2)\,,\end{aligned} \tag{6.2}$$

where $\mathcal{L}(d|m_1, m_2, \Lambda_1, \Lambda_2)$ is the GW likelihood over the masses and tidal deformabilities, $\pi(m_1, m_2)$ is the prior on masses, and $\pi(\Lambda_1, \Lambda_2|\epsilon, m_1, m_2, T_1, T_2)$ is the prescription for computing the tidal deformabilities. For EoSs with a single stable branch[7]

$$\pi(\Lambda_i|\epsilon, m_i, T_i) = \begin{cases} \delta(\Lambda_i - \Lambda(m_i|\epsilon))\,, & \text{if } T_i = \text{NS} \\ \delta(\Lambda_i)\,, & \text{if } T_i = \text{BH} \end{cases}. \tag{6.3}$$

Equation (6.3) corresponds to the following prior on Λ_i: under the T_i = NS hypothesis, Λ_i is determined by the EoS ϵ and m_i, whereas under the T_i = BH hypothesis, the object has a vanishing tidal deformability. Equation (6.2) is independent of the prior on Λ_i and m_i used in the original single-event analysis of Sec. 6.2 as it only depends on the single-event likelihood. The Λ_i prior in Eq. (6.2) is instead the EoS-informed prior of Eq. (6.3).

The mass prior is encoded in $\pi(m_1, m_2)$, which is selected to be uniform in the joint source-frame component mass space, with $m_1, m_2 \in [0.5, 1.8]\, M_\odot$. This uniform prior is chosen for simplicity, as no constraints exist on the mass distribution of $\leq 1.2\, M_\odot$ NSs and BHs. It is nonetheless consistent with constraints on the $\sim 1 - 2\, M_\odot$ mass distribution [73, 11]. If a population of low-mass binaries were discovered, the mass prior would also be inferred via an extension of Eq. (6.2), e.g, [57, 117].

Whereas Eq. (6.2) is conditioned on a single EoS ϵ, the true EoS is unknown. We instead marginalize over the EoS and compute the likelihood for each classification:

$$P(d|T_1, T_2) = \int \mathcal{L}(d|\epsilon, T_1, T_2)\pi(\epsilon|d_{\text{aux}})d\epsilon\,, \tag{6.4}$$

where $\pi(\epsilon|d_{\text{aux}})$ is a distribution over EoSs informed by auxiliary data d_{aux}. We adopt the posterior from Ref. [76] computed using a model-agnostic prior on the EoS based on a Gaussian process [71, 44, 77] and informed by radio-pulsar measurements [54, 17], X-ray pulse-profile [80, 98, 81, 99], and GW observations [8,

[7] If there are multiple stable branches we use a prior $\pi(\Lambda_i) = \sum_{j=0}^{N} \frac{1}{N}\delta(\Lambda_i - \Lambda(m_i|\epsilon, j))$, where j indexes stable branches and $\Lambda(m_i|\epsilon, j)$ is the tidal deformability on the $j-$th branch. A NS of a given mass is equally likely to be formed on any stable branch.

5, 3]. The EoS posterior is consistent with chiral effective field theory calculations at densities $\lesssim 1.5\,\rho_{\rm nuc}$ (where $\rho_{\rm nuc}$ is nuclear saturation density) [115, 61, 107, 41], comparable to the central densities of $\sim$ 1–1.5 $M_\odot$ NSs, though it does not explicitly incorporate this information [45]. It is also consistent with the existence of strong phase transitions [47].

The main physically relevant questions are

1. whether a source contains at least one BH,
2. whether a source contains at least one NS,
3. and, if so, whether it contains two NSs.

Due to the lack of constraints on the merger rates of different source types in the relevant mass range we assign equal prior probability on three hypotheses $\mathcal{H}$: (i) the system has two NSs (BNS), (ii) the system has exactly one NS (OneNS), and (iii) the system has no NSs (BBH).

The marginal likelihood[8] of $\mathcal{H}$ is obtained by integrating over the relevant constituent source types:

$$\mathcal{Z}_{\mathcal{H}} \equiv \int p(d|T_1, T_2)\pi(T_1, T_2|\mathcal{H})\, dT_1\, dT_2\,, \tag{6.5}$$

where $p(d|T_1, T_2)$ is given in Eq. (6.4), and $\pi(T_1, T_2|H)$ is the normalized prior on the source types. The hypotheses $\mathcal{H}$ = BNS and $\mathcal{H}$ = BBH contain a single source type each, with the trivial priors $\pi(\mathrm{NS}, \mathrm{NS}\,|\mathrm{BNS}) = 1$, and $\pi(\mathrm{BH}, \mathrm{BH}\,|\mathrm{BBH}) = 1$ respectively. The hypothesis $\mathcal{H}$ = OneNS encompasses two source types, NSBH and BHNS, which we take to be equally likely *a priori*, $\pi(\mathrm{NS}, \mathrm{BH}\,|\mathrm{OneNS}) = \pi(\mathrm{BH}, \mathrm{NS}\,|\mathrm{OneNS}) = 1/2$.

The marginal likelihood for whether the system contains at least one NS ("HasNS") is then

$$\begin{aligned}\mathcal{Z}_{\rm HasNS} = \mathcal{Z}_{\rm OneNS}\, &\pi(\mathrm{OneNS}|\mathrm{HasNS}) \\ &+ \mathcal{Z}_{\rm BNS}\, \pi(\mathrm{BNS}|\mathrm{HasNS})\,,\end{aligned} \tag{6.6}$$

where $\pi(\mathrm{OneNS}|\mathrm{HasNS}) = \pi(\mathrm{BNS}|\mathrm{HasNS}) = 1/2$, meaning under the assumption the system has at least one NS, we assign an equal prior probability that it has one

[8] The marginal likelihood is also commonly referred to as the "evidence", though we use this term in its colloquial meaning.

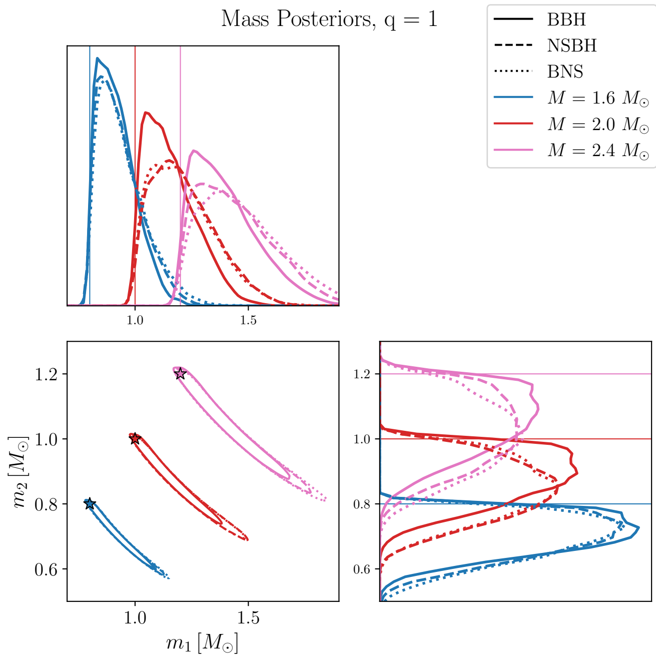

Figure 6.3: One- and two-dimensional marginalized source-frame mass posteriors for the $q \equiv m_2/m_1 = 1$ signals. Same-color lines denote systems with varying total mass M with true values marked. For a given mass, varying line styles denote BBH, NSBH, and BNS systems. Contours represent two-dimensional 2-σ regions. Given a simulated mass, similar posteriors across source types shows the subdominant effect of tides on the inferred masses.

or two NSs. The marginal likelihood for whether the system contains at least on BH ("HasBH") is Eq. (6.6), with BNS → BBH.

In what follows, we present odds ratios between two hypotheses $\mathcal{H}_1$ and $\mathcal{H}_2$:

$$O^{\mathcal{H}_1}_{\mathcal{H}_2} = \frac{\mathcal{Z}_{\mathcal{H}_1}}{\mathcal{Z}_{\mathcal{H}_2}} \frac{\pi(\mathcal{H}_1)}{\pi(\mathcal{H}_2)}\,, \tag{6.7}$$

where $\pi(\mathcal{H})$ is the prior on the hypothesis $\mathcal{H}$, with $\pi(\text{HasNS}) = \pi(\text{HasBH}) = 2\pi(\text{BNS}) = 2/3$.

6.3 Measuring the Masses and Tides of Low-mass Compact Binaries

In this section, we present posteriors from simulated signals. We do not assume we know whether each component is a NS or BH *a priori*. Throughout, we present results from simulations with $\rho = 20$.

The dominant intrinsic feature of a GW signal is the mass. In Fig. 6.3, we present marginal posteriors for the source-frame masses for select equal-mass systems. Measurement uncertainties are consistent with those of Ref. [116], c.f., their Figs. 1

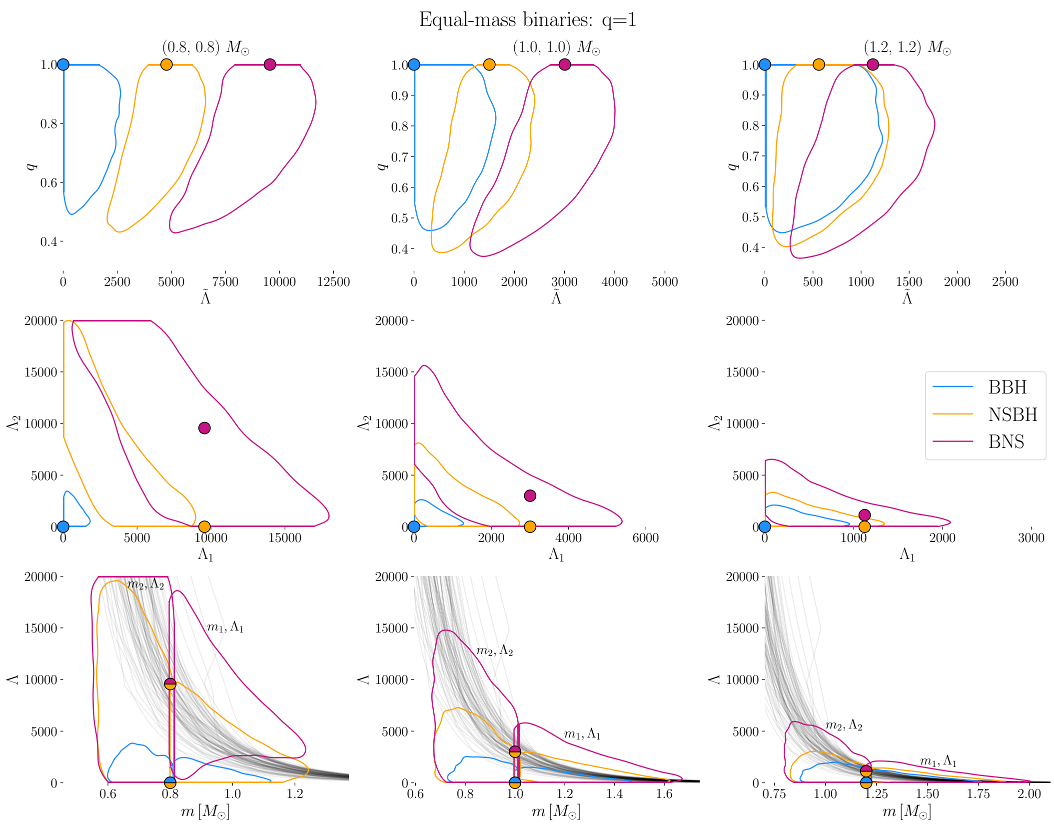

Figure 6.4: Two-dimensional marginal posteriors for select parameters for systems with $q = 1$, with each column referring to a different simulated total mass. Blue, yellow, and magenta lines outline the 2-σ contours of the posterior for the BBH, NSBH, and BNS systems, respectively. We omit the BHNS configuration as it is identical to NSBH for equal-mass simulations. The left (right) halves of the third row plots are the posterior of the primary (secondary), and include draws from the EoS distribution [76] for reference. A decreasing total mass increases the tidal signature and correspondingly affects all posteriors.

and 2, at the same SNR. Same-color lines denote systems with the same total mass, while varying line styles denote simulated source types. Same-mass signals result in similar mass posteriors, regardless of the source type, with a minor trend for longer tails as the tidal effects increase. This is due to the fact that the mass is primarily measured by the long inspiral phase (thousands of cycles), while tidal effect are relevant for the last ~ 20 cycles. We obtain qualitatively similar posteriors for non-equal mass signals.

Having established that the presence of tides does not strongly impact mass inference, we now turn to tidal inference. Figures 6.3 and 6.5 show marginal posteriors for systems with fixed q and M, respectively, with colors denoting the source type. The

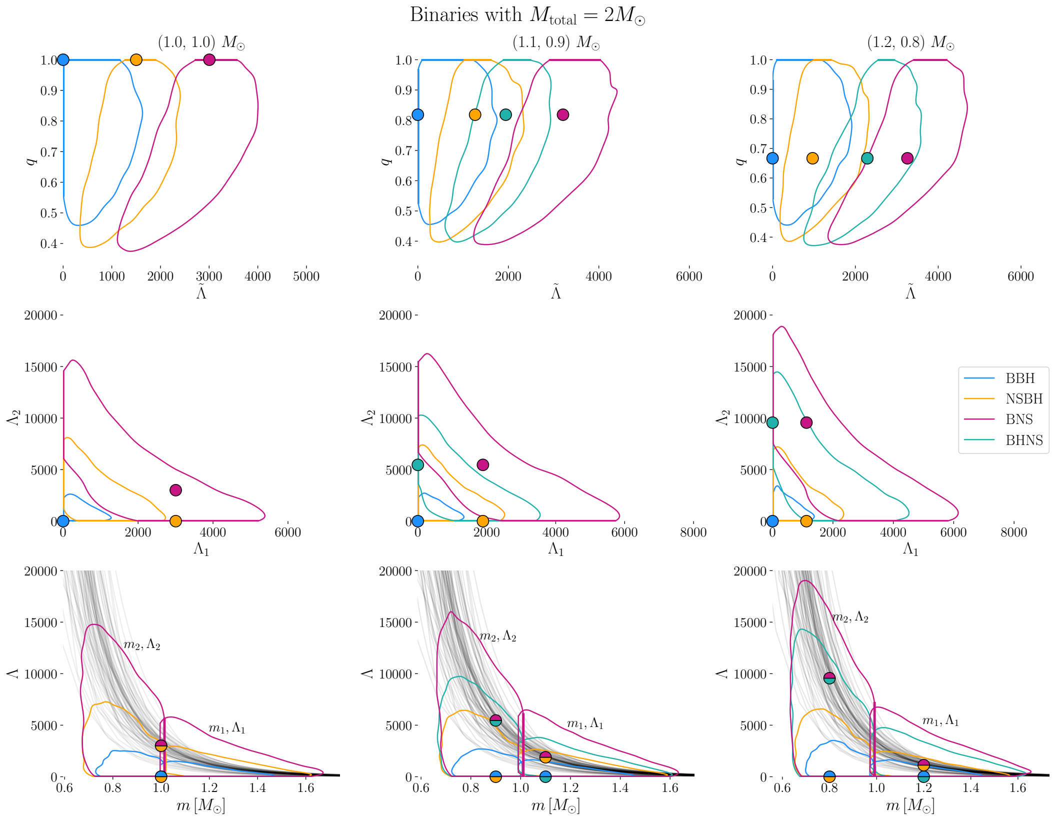

Figure 6.5: Similar to Fig. 6.3 but for systems with the same simulated total mass $M = 2\,M_\odot$, with each column referring to a different simulated the mass ratio. When relevant, we also include BHNS configurations in green. The posteriors of all parameters are, weakly sensitive to the true mass ratio, with the exception of the BHNS cases.

top rows show the marginal $q - \tilde{\Lambda}$ posteriors. All posteriors are consistent with the true (simulated) values. Within each panel, i.e., for configurations of the same mass, the posterior moves to higher values as the system contains more NSs and tidal effects become stronger. The posteriors further show a positive correlation between q and $\tilde{\Lambda}$ which becomes stronger as $\tilde{\Lambda}$ increases in value, consistent with [5]. An outcome of the increasing correlation strength is that the uncertainty also increases as the posterior is more extended both in the q; see also Fig. 6.3, and $\tilde{\Lambda}$ directions.

The $q - \tilde{\Lambda}$ posterior offers the first evidence about the presence/absence of tides and thus source classification. For all mass configurations, the BBH signals are consistent with the true value $\tilde{\Lambda} = 0$, and the posteriors are similar for different masses, c.f., blue contours in Figs. 6.3 and 6.5, left to right. For NS-containing systems, the posteriors move away from $\tilde{\Lambda} = 0$, signaling the presence of tides. As expected, signals from lower-M systems can rule out $\tilde{\Lambda} = 0$ with higher credibility due to their higher true $\tilde{\Lambda}$ value, c.f., yellow and magenta contours in Fig. 6.3, left to right. At a fixed M, the dependence of $\tilde{\Lambda}$ on the mass ratio is less pronounced, resulting in similar posteriors and thus ability to detect tides, c.f., yellow, green, and magenta contours in Fig. 6.5, left to right.

Going beyond $\tilde{\Lambda}$, we turn to the tidal deformability of the individual binary components. The second row of Figs. 6.3 and 6.5 shows posteriors for $\Lambda_1 - \Lambda_2$. The posteriors span much of the prior and show a strong anticorrelation consistent with [28, 5, 7]. The direction of the anticorrelation is approximately a constant $\tilde{\Lambda}$ suggesting that almost all tidal information comes from measuring $\tilde{\Lambda}$, with limited higher-order information [114, 51]. This is further demonstrated in App. 6.10. Consequently, $\Lambda_1 - \Lambda_2$ (second row) does not offer much additional information about the source type beyond $q - \tilde{\Lambda}$ (first row): exclusion of $\tilde{\Lambda} = 0$ amounts to exclusion of $\Lambda_1 = \Lambda_2 = 0$. Crucially for source classification, all component tidal deformabilities are individually consistent with $\Lambda_i = 0$.[9] Effectively, a $\tilde{\Lambda}$ measurement is "spread" between Λ_1 and Λ_2 and the posterior for *both* parameters is consistent with high values when *either parameter* has a high true value.

In the final row of Figs. 6.3 and 6.5, we show the component $\Lambda_i - m_i$ posteriors, where gray lines are draws from the EoS posterior. As expected from the second row, even in cases where $\tilde{\Lambda} = 0$ is confidently ruled out, the posteriors are consistent with $\Lambda_i = 0$. More information can however be obtained by comparing the *upper limit* on Λ_i to EoS expectations at the relevant mass. As expected, all BNS posteriors (magenta) are consistent with the EoS draws in both (m_1, Λ_1) and (m_2, Λ_2). Switching to the NSBH signals (yellow), the primary is always consistent with being a NS: for all masses nearly all the EoS draws fall within the yellow posteriors. In contrast and again for all mass configurations, about half the EoS draws fall within the posterior for the secondary binary component, indicating decreasing support for a NS interpretation. Interestingly, this is despite the fact that the upper limit on Λ_1 is lower than that of Λ_2. The expected tidal deformability increases so rapidly for lower masses that Λ_1 is more consistent with the EoSs than Λ_2. The BHNS posteriors (green contours in Fig. 6.5) fully overlap with the EoS draws for all masses. This is because BHNSs have a larger $\tilde{\Lambda}$ than NSBHs for the same mass, pushing all upper limits to high enough values that are consistent with EoS predictions.

Finally, for BBH signals the posteriors for both components show some tension with

[9] The only seeming exception is the lowest-mass BNS in Fig. 6.3 but this is due to a posterior railing against the prior upper bound.

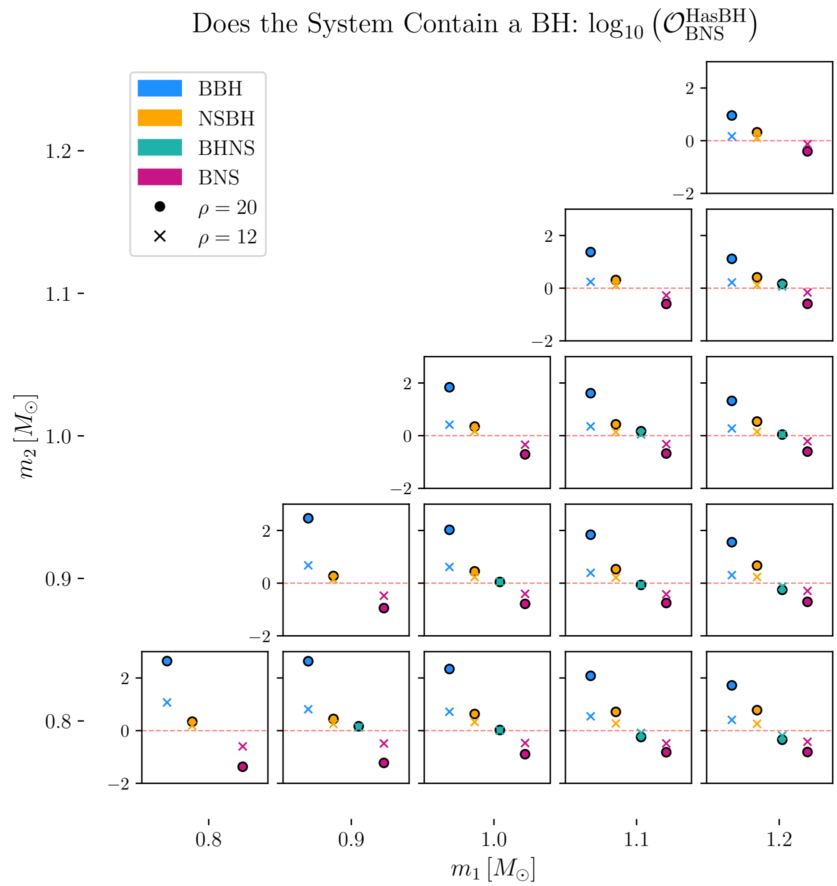

Figure 6.6: Base-10 logarithm of the odds ratio for each system containing at least one BH. Monte-Carlo errors for the odds ratios are too small to be visible in the scale of the figure. Panels correspond to the system source-frame masses and colors correspond to source type. The equal-mass panels do not contain BHNS systems as they are identical to the NSBH ones. Dots (crosses) denote signals with SNR 20(12). Points above $\log_{10}(O^{\mathrm{HasBH}}_{\mathrm{BNS}}) = 0$ (red dashed line) denote support for the presence of at least one BH in the binary.

EoS draws, which decreases with the total mass, c.f., blue contours of Fig. 6.3, left to right. For the lowest mass configuration, c.f., left-most panel of Fig. 6.3, neither binary component overlaps with hardly any EoS draw. In these cases, the GW data can constrain the tides to values that are too low compared to viable EoSs. The binary mass ratio, on the other hand, does not strongly impact the overlap between the posterior and the EoSs, c.f., blue contours in Fig. 6.5, left to right. This is because the Λ_i posterior does not strongly depend on the system mass; what changes is the EoS prediction, which is a strong function of the total mass.

6.4 Determining if a System Contains a Black Hole

Astronomical observations and nuclear physics considerations cannot directly motivate the nature of potential $\lesssim 1.2\,M_\odot$ GW detections such as the ones studied in Sec. 6.3. We undertake signal classification with the fundamental question: does the signal provide evidence for the *presence* of a BH, thus establishing the existence of BHs below the expected astrophysical minimum mass?

We quantify this with the odds ratio $O^{\rm HasBH}_{\rm BNS}$, where the "HasBH" hypothesis consists of the BBH, NSBH, and BHNS source types with equal prior probabilities. The alternative hypothesis is that the system is a BNS and thus the inferred masses and tides of both objects must be consistent with the EoS. In practice, the test comes down to whether the upper bound on the tidal effects is constraining enough to be in tension with the EoS prediction. We present the base-10 logarithm of the odds ratio, $\log_{10} O^{\rm HasBH}_{\rm BNS}$ in Fig. 6.6 for the $\rho = 20$ (solid dots) and the $\rho = 12$ signals (crosses). Below we focus on the $\rho = 20$ results; we obtain qualitatively similar though weaker constraints when $\rho = 12$.

The BBH signals (blue) show evidence for the presence of a BH, with odds $\gtrsim$10:1 for all masses. The evidence is stronger for lower-mass systems, with the odds ratio increasing from 10:1 to 100:1 between masses $1.2 - 1.2\,M_\odot$ and $0.8 - 0.8\,M_\odot$. This can be understood in the context of the EoS predictions; even though the Λ posteriors are similar for all masses, c.f., blue contours in Fig. 6.3, bottom row, right to left, the EoS predicts that less massive NSs have much higher Λ values. As the mass decreases, the EoS predictions move away from the (m, Λ) posterior support; this brings the data from less massive systems into more tension with the BNS hypothesis.

NSBH signals (yellow) result in odds ranging between a few to $\sim 10 : 1$. For a given m_2, as m_1 increases (left to right), the odds ratio increases and we can more confidently infer the presence of a BH. This happens because both the true and inferred value of $\tilde{\Lambda}$ are smaller as m_1 increases. Both Λ_1 and Λ_2 are thus inferred to be smaller, but the estimate for m_2 is essentially unchanged; therefore, the secondary becomes more consistent with being a BH as the primary mass increases. This contrasts with the case of increasing the total mass at constant mass ratio (bottom left to top right) where the inferred value of Λ_2 decreases and the inferred value of m_2 increases, so consistency with EoS predictions remains unchanged.

Turning to the BHNS signals (green), we obtain near-equal odds for the presence of a BH for all masses. This is likely due to the larger tidal effects compared to the

NSBH case (since now the secondary is a NS) and the corresponding higher upper limits on tidal parameters, *c.f.*, Fig. 6.5, allowing both objects to agree with the EoS predictions. The odds for the presence of a BH decrease as the primary (BH) mass increases (left to right), as BHs and NSs become less distinguishable.

Finally, BNSs (magenta) always yield evidence against the presence of a BH, which decreases with the mass.

6.5 Determining the Neutron Star Content of a System

The complementary question is whether a system contains at least one NS and if yes, whether it contains two. Here, the evidence comes from both consistency of each object with EoS predictions and the exclusion of $\tilde{\Lambda} = 0$.

Does the System Contain a Neutron Star?

The evidence for whether there is at least one NS in a system is quantified with the odds ratio $O^{\mathrm{HasNS}}_{\mathrm{BBH}}$, Eq. (6.7). This is not equivalent to solely determining if the binary contains any matter; we further require the inferred tidal deformabilities to be consistent with the EoS.

In Fig. 6.7, we show $\log_{10} O^{\mathrm{HasNS}}_{\mathrm{BBH}}$. We again focus on the $\rho = 20$ results as $\rho = 12$ gives qualitatively similar, though less constraining, conclusions. The log odds ratios for BBHs are negative, indicating that the data favor the absence of any NSs. As the mass decreases, so does the odds ratio from $O^{\mathrm{HasNS}}_{\mathrm{BBH}} \approx 1/50$ for 1.2–1.2 $M_\odot$ to $\approx 2/3$ for 0.8–0.8 $M_\odot$. It becomes less plausible for the lowest-mass BBH systems to contain a NS as the signals lack the strong tidal signature that the EoSs predict for these masses (c.f., blue contours in Fig. 6.3 bottom left compared to bottom right panel). All NS-containing systems yield $\log_{10} O^{\mathrm{HasNS}}_{\mathrm{BBH}} > 0$ though again the evidence decreases as the NS mass increases. For example, the odds ratio for $m_1 = 1.2\,M_\odot$, $m_2 = 0.8\,M_\odot$ is $O^{\mathrm{HasNS}}_{\mathrm{BBH}} \approx 4$, much lower than the $m_1 = m_2 = 0.8\,M_\odot$ case which has $O^{\mathrm{HasNS}}_{\mathrm{BBH}} > 100$. At all masses, there is more evidence for a NS in BHNSs than NSBHs. This is because the predicted tidal deformability of the primary is smaller than for the secondary, and thus a NS primary is more indistinguishable from a BH than a NS secondary. For systems containing exactly one $\lesssim 1\,M_\odot$ NS, we obtain $O^{\mathrm{HasNS}}_{\mathrm{BBH}} \gtrapprox 10$. The strongest evidence is obtained for the presence of a NS in the BNS systems, all of which have $\log_{10} O^{\mathrm{HasNS}}_{\mathrm{BBH}} \gtrapprox 2$. This is consistent with the BNS posteriors of Fig. 6.3 and 6.5 that always rule out $\tilde{\Lambda} = 0$.

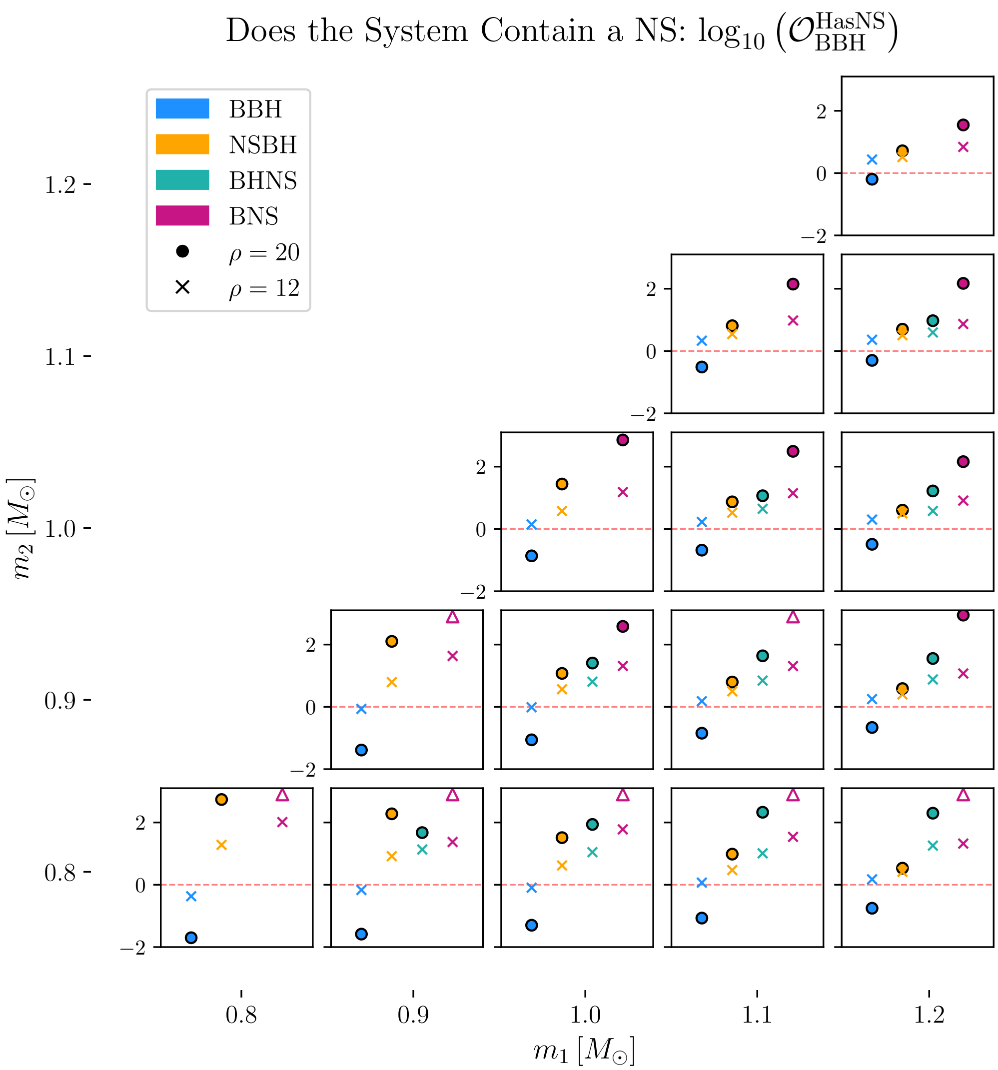

Figure 6.7: Similar to Fig. 6.6 but for the odds ratio for each system containing at least one NS. Points above $\log_{10}(\mathcal{O}^{\mathrm{HasNS}}_{\mathrm{BBH}}) = 0$ (red dashed line) denote support for the presence of at least one NS in the binary. Triangular markers indicate that the odds ratio lies somewhere above the y-axis limit.

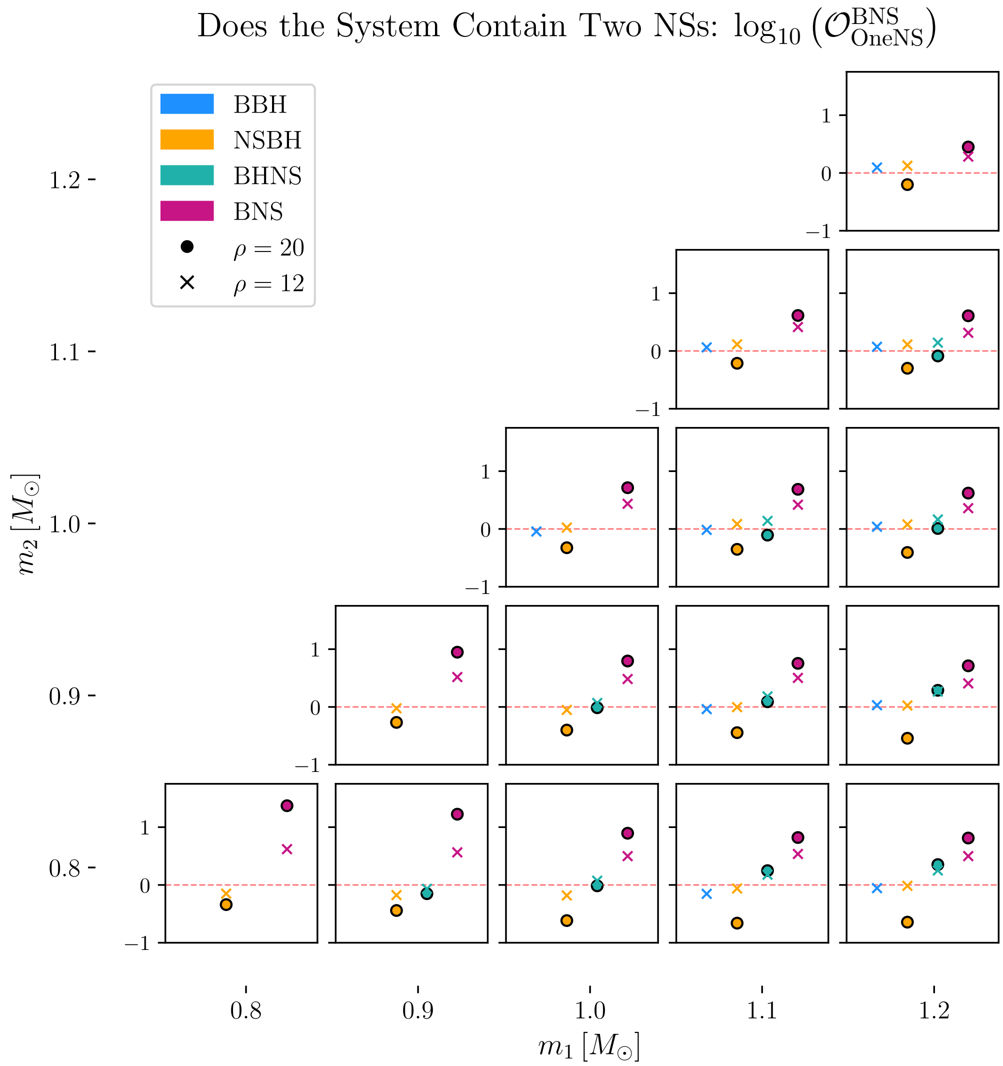

Figure 6.8: Similar to Fig. 6.6 but for the odds ratio for each system containing exactly two NSs versus one NS. We only present results for systems with evidence of at least one NS in Fig. 6.7 which includes all NS-containing systems. Points above $\log_{10}(\mathcal{O}^{\mathrm{BNS}}_{\mathrm{OneNS}}) = 0$ (red dashed line) correspond to systems that are more likely to have two NSs than one.

Does the System Contain Two Neutron Stars?

Having established the presence of a NS, the next question is whether the source is a BNS or it contains only one NS. We compare these two hypotheses with the odds ratio $O^{\text{BNS}}_{\text{OneNS}}$.

We show results in Fig. 6.8, restricting to systems with evidence for at least one NS in Fig. 6.7 which in practice is all the NS-containing systems and a few BBHs with marginal evidence. We again focus on the $\rho = 20$ results. BNS signals (pink) favor the presence of two NSs for all masses. As before, this evidence is stronger for less massive systems with odds $\gtrapprox 10:1$ when both components are $\lesssim 1\,M_{\odot}$. NSBHs (yellow) provide stronger evidence against the presence of two NSs than BHNSs. This is again because determining the nature of the secondary (least massive) is easier than primary (most massive) component.

However, neither BHNS nor NSBH signals result in odds greater than 10:1 against the BNS hypothesis; the strongest evidence is obtained for the 1.2–0.8 $M_{\odot}$ NSBH binary with $O^{\text{BNS}}_{\text{OneNS}} \sim 1/8$. The reason refers back to the posteriors in Figs. 6.3 and 6.5. The BNS hypothesis requires that the EoS draws overlap with both the (m_1, Λ_1) and (m_2, Λ_2) posteriors. The bottom row of Figs. 6.3 and 6.5 show that the EoS draws completely overlap the primary posterior for all NSBH (yellow) and BHNS (green) signals. What is more, the posterior for the secondary is also fully (BHNS; green) or partially (NSBH; yellow) consistent with the EoS draws.

If the System Contains One Neutron Star, is it the primary or the secondary?

Though establishing the presence of exactly one NS is challenging at current sensitivity, we look forward to higher-SNR signals and consider how to identify which binary component it is. Most analyses label objects based on relative mass, e.g., primary and secondary, hence the most straightforward approach is to examine whether the primary is a NS or a BH:

$$O^{\text{NSBH}}_{\text{BHNS}} = \frac{\mathcal{Z}_{\text{NSBH}}}{\mathcal{Z}_{\text{BHNS}}}\,. \tag{6.8}$$

However, this suffers from a labeling ambiguity. For example, an equal-mass NSBH system is equally-well described by assigning the tides on either component. This is due to the ambiguity in distinguishing binary components based on a property that is symmetric, i.e., the mass, and also plagues the component spins [22].

This ambiguity can be resolved by instead labeling the binary components with a unique property of each object that breaks this symmetry. For example, labeling binary components based on their tidal deformability would allow us to explore the properties of the stiffer and softer objects that reflect the NS and BH, respectively. Such an approach is of course only applicable for systems with *measurable* tidal asymmetry. For example, for BNSs, this approach would identify a "stiff" and a "soft" component, even if the tidal deformabilities are similar. More generally, there is no guarantee that objects are in fact distinguishable, e.g., an equal-mass and nonspinning BBH; there is thus no generic strategy for extracting individual component properties.

6.6 Conclusions

We have explored source classification for low-mass, $\leq 1.2\, M_\odot$ compact binary mergers based on the GW signal they emit and external information about the dense-matter EoS. The classification is based on the fact that the inferred component mass and tidal deformability must be consistent with EoS expectations if the object is a NS. A tidal measurement that is inconsistent with EoS predictions provides evidence that the object is not a NS, while $\Lambda = 0$ provides evidence for the object being a BH. The method's distinguishing power increases with decreasing mass, due to the fact that EoS predictions are a steep function of the mass, $\Lambda \sim m^{-6}$, and NSs become indistinguishable to BHs as the mass increases. Similarly, distinguishability is easier if the true EoS is stiffer as it would predict larger NS tidal deformabilities for all masses; here we have considered SLy9 that is consistent with the astrophysical data we employ.

We generally find it is easier to confirm the presence of a BH or NS than to refute it. For systems with subsolar-mass BHs, their presence can be identified at SNR $\rho = 20$. In contrast, BNSs strongly disfavor the presence of a BH, with the evidence growing with decreasing masses. Complimentarily, signals from $\lesssim 1\, M_\odot$ NS-containing binaries can reveal the NS presence based on compatibility of the mass-tidal measurement with EoS predictions. In contrast, if the binary *does not* contain a NS, its presence is disfavored with the evidence again growing as the mass decreases. Finally, identifying which object in a binary is a NS (or a BH) is subject to a labeling ambiguity that could be mitigated by labeling components based on relative tides rather than mass. Higher-SNR signals due to detector upgrades [6] or tighter EoS predictions thanks to future data will further strengthen distinguishability.

If subsolar-mass binaries exist and merge, combined mass and tidal information can aid in identifying the component nature and lead to constraints on primordial BH and NS physics. This prospect further motivates numerical simulations [78] and developing waveform models that can faithfully capture the large tidal effects of low-mass NSs. It further motivates studies of alternative possibilities to BHs and standard NSs such as dark matter admixed NSs with lower tidal deformability [66]. Tidal-based classification, as previously explored for higher-mass objects such as GW170817 [5, 44, 9], is especially promising for sub-solar mass objects whose nature is not otherwise astrophysically informed.

As this study was nearing completion, a preprint [35] that reached similar conclusions about the distinguishability of sub-solar mass BNS systems from BBHs appeared. Our methods differ in a few ways. The authors of [35] use Fisher matrix estimates (complemented with select full parameter estimation) and a modified TaylorF2 approximant to account for NS disruption, as compared to our use of full parameter estimation (with priors that keep Λ_1 and Λ_2 positive) with the NRTidalv3 waveform that includes appropriate termination conditions. Classification also differs: while Ref. [35] compares the upper limits on tidal inference to a fixed NS EoS, we form relevant hypotheses and marginalize over current uncertainty in the EoS to compute odds ratios. Additionally, we consider mixed NS-BH binaries, as opposed to only BNS and BBH systems. On the other hand, Ref. [35] also considers exotic compact objects. Regardless, both studies find that we can tell apart a sub-solar mass BBH from a BNS at SNR $\gtrsim 12$.

6.7 Acknowledgements

We thank Kareem El-Badry for helpful discussions about astronomical observations of compact objects. We also thank Jocelyn Read for useful comments on the manuscript. I.L. and K.C. acknowledge support from the Department of Energy under award number DE-SC0023101 and the Sloan Foundation. J.G. acknowledges funding from NSF Grant PHY-2207758. The project was supported by the European Union (ERC, SMArt, 101076369). Views and opinions expressed are those of the authors only and do not necessarily reflect those of the European Union or the European Research Council. Neither the European Union nor the granting authority can be held responsible for them. The authors are grateful for computational resources provided by the LIGO Laboratory and supported by National Science Foundation Grants PHY-0757058 and PHY-0823459.

Software: `bilby` [18, 100], `dynesty` [104], `scipy` [113], `numpy` [87], `matplotlib` [67], `lwp` [46].

6.8 Limiting Frequencies

Compact binary inspirals terminate when the objects merge, disrupt each other, or their surfaces contact. In this appendix, we quantify how compact binary components need to be in order to avoid disruption and contact and thus emit GWs in the sensitive band of ground-based detectors; see, e.g., [118] for a similar calculation.

The onset of merger is not precisely defined, but a separation of $r = 6M = 6(m_1+m_2)$ gives an order-of-magnitude estimate and a Keplerian frequency

$$f_{6M} = \frac{1}{\pi}\sqrt{\frac{M}{(6M)^3}}\,, \tag{6.9}$$

plotted in Fig. 6.2; for $m_1 = m_2 = 1\,M_\odot$, $f_{6M} \sim 2\,\mathrm{kHz}$. Solar-mass compact objects therefore enter the LIGO-Virgo sensitive band before merger.

However, finite sizes might terminate the inspiral earlier if the objects contact each other before reaching $r = 6M$. For objects with radii R_1 and R_2, contact $r = R_1 + R_2$ occurs at a Keplerian frequency

$$f_{\rm cont} = \sqrt{\frac{G(m_1+m_2)}{4\pi^2(R_1+R_2)^3}}\,, \tag{6.10}$$

also plotted in Fig. 6.2. For a BNS with $m_1 = m_2 = 1\,M_\odot$ and $R_1 = R_2 = 12\,\mathrm{km}$, $f_{\rm cont} \sim 1.5\,\mathrm{kHz}$. But for a NS-WD binary with an Earth-sized WD, $f_{\rm cont} \sim 0.2\,\mathrm{Hz}$, two orders of magnitude below the relevant frequency band.

Another possibility that prematurely ends an inspiral is disruption. The Newtonian tidal force felt by the secondary binary component due to the primary is

$$F_{21} = \frac{Gm_1m_2(r_{\rm out}-r_{\rm in})(r_{\rm out}+r_{\rm in})}{(r_{\rm out}r_{\rm in})^2}\,, \tag{6.11}$$

where $r_{\rm in} = r - R_2/2$ and $r_{\rm out} = r + R_2/2$ correspond to the distance between the primary and the outer and inner edge of the secondary, respectively. In the limit of wide orbital separation, $r \gg R_2$, Eq. (6.11) simplifies to

$$F_{21} \approx \frac{2Gm_1m_2R_2}{r^3}\,. \tag{6.12}$$

The secondary disrupts when F_{21} is comparable to its gravitational binding (self-) force

$$F_{21} \approx \frac{Gm_2^2}{R_2^2}\,, \tag{6.13}$$

which occurs at

$$r \approx \left(2\frac{m_1 R_2^3}{m_2}\right)^{1/3}, \tag{6.14}$$

corresponding to a Keplerian orbital frequency of

$$f_{\rm dis} \approx \sqrt{\frac{G m_2 (m_1 + m_2)}{8\pi^2 m_1 R_2^3}}\,. \tag{6.15}$$

Therefore,

$$\left(\frac{f_{\rm dis}}{f_{\rm cont}}\right)^2 = \frac{m_2 (R_1 + R_2)^3}{2 m_1 R_2^3}\,. \tag{6.16}$$

For compact objects with comparable radii and masses, $f_{\rm dis} \approx 2 f_{\rm cont}$ and thus the binary contacts before disruption. For a highly compact primary, for example a NS-WD binary with $R_1 \ll R_2$, $f_{\rm dis} < f_{\rm cont}$ and thus the binary disrupts before contact. In any case, for binaries involving WDs, both of these frequencies are well below the LIGO sensitive band.

6.9 Injection Properties

In this appendix we provide more details for the parameter estimation analysis of Sec. 6.2. In Table 6.9 we list the extrinsic parameters of the simulated signals. We select the luminosity distance unique to each system by scaling it to reach a target SNR, either 20 or 12.

For the single-event analyses, we sample the parameter posterior using Dynesty [104] as implemented in Bilby [18, 100], with a prior that is uniform in component detector-frame masses and aligned spin components. We adopt standard isotropic priors for position and inclination parameters, and a luminosity distance prior that is uniform in comoving volume [100]. The prior on the component tidal deformabilities is uniform and ranges from $\Lambda = 0$ to $\Lambda = 20000$, the maximum value the waveform was validated on [2]. In some cases, the Λ posterior distribution rails against this upper limit, but the simulated values for Λ are always within in the prior bounds.

We use a multibanding likelihood [82] and analyze 512 or 256 s of data (depending on the mass) at 8 kHz with lower and upper frequency cutoffs of 20 Hz and 3.5 kHz, respectively. The upper cutoff is above the inherent waveform termination [2, 58].

Parameter	Label	Value
Phase at 20 Hz	ϕ	0.24 rad
Right Ascension	α	0.18 rad
Declination	δ	0.62 rad
Inclination	ι	2.7 rad
Polarization Angle	ψ	0.58 rad
Merger time at geocenter	t_c	0 sec (GPS)

Table 6.1: Values for extrinsic parameters used for simulating the data.

6.10 Impact of measurements of $\delta\tilde{\Lambda}$

In order to constrain the component tidal deformabilities, measurement of an additional parameter beyond $\tilde{\Lambda}$, such as $\delta\tilde{\Lambda}$, is required. The parameter $\delta\tilde{\Lambda}$ represents the tidal contributions to the frequency-domain phase which appear at 6PN and are not proportional to $\tilde{\Lambda}$; intuitively it is a measure of the asymmetry in the tidal contributions from the two components [114]. We examine the impact of the constraints on $\delta\tilde{\Lambda}$ in the tidal parameters from the $(m_1, m_2) = (1.1, 0.9)\ M_\odot$ BNS signal in Fig. 6.9. In the left panel, we present the induced prior, see Sec. 6.2, and the recovered marginal posterior for $\tilde{\Lambda}$ and $\delta\tilde{\Lambda}$. We obtain a symmetric 90% credible interval for $\tilde{\Lambda} \in (1804, 4131)$ with respect to a prior that covers $0 < \tilde{\Lambda} \lesssim 26000$. In order to break the degeneracy between Λ_1 and Λ_2, we must measure additional parameters. However, $\delta\tilde{\Lambda}$ is relatively poorly measured at current sensitivity. The left panel of Fig. 6.9 shows that, even though the 1-d marginal posterior for $\delta\tilde{\Lambda}$ (red) appears to be well constrained relative to the prior (gray), this is primarily driven by $\tilde{\Lambda}$, c.f., the $2-d$ marginal posterior.

In order to investigate how information about $\delta\tilde{\Lambda}$ impacts the component tidal deformabilities, we approximate an inference where no information about $\delta\tilde{\Lambda}$ exists. We draw $(q, \tilde{\Lambda})$ samples from the full posterior and combine them with samples of $\delta\tilde{\Lambda}$ from its effective prior implied by the given $(q, \tilde{\Lambda})$, subject to the condition $\Lambda_i(q, \tilde{\Lambda}, \delta\tilde{\Lambda}) > 0$. We display the marginal distribution in the left panel panel of Fig. 6.9 (teal). We compare this to the full marginal posterior on $\Lambda_1 - \Lambda_2$ (red). We find that while knowledge of $\delta\tilde{\Lambda}$ does change the distribution on Λ_1–Λ_2, this information does not substantially change the correlation structure. As expected for a well-measured parameter, this procedure leaves the $\tilde{\Lambda}$ posterior unaffected (left). The measurement of $\delta\tilde{\Lambda}$ itself favors higher values of $\delta\tilde{\Lambda}$ (left), which correspond to higher values of Λ_2 and lower values for Λ_1 (right).

References

[1] J. Aasi et al. “Advanced LIGO”. In: *Class. Quant. Grav.* 32 (2015), p. 074001. DOI: 10.1088/0264-9381/32/7/074001. arXiv: 1411.4547 [gr-qc].

[2] Adrian Abac et al. “New and robust gravitational-waveform model for high-mass-ratio binary neutron star systems with dynamical tidal effects”. In: *Phys. Rev. D* 109 (2 Jan. 2024), p. 024062. DOI: 10.1103/PhysRevD.109.024062. URL: https://link.aps.org/doi/10.1103/PhysRevD.109.024062.

[3] B. P. Abbott et al. “GW190425: Observation of a Compact Binary Coalescence with Total Mass $\sim 3.4 M_{\odot}$”. In: *Astrophys. J. Lett.* 892.1 (2020), p. L3. DOI: 10.3847/2041-8213/ab75f5. arXiv: 2001.01761 [astro-ph.HE].

[4] B. P. Abbott et al. “Multi-messenger Observations of a Binary Neutron Star Merger”. In: *Astrophys. J. Lett.* 848.2 (2017), p. L12. DOI: 10.3847/2041-8213/aa91c9. arXiv: 1710.05833 [astro-ph.HE].

[5] B. P. Abbott et al. “Properties of the binary neutron star merger GW170817”. In: *Phys. Rev. X* 9.1 (2019), p. 011001. DOI: 10.1103/PhysRevX.9.011001. arXiv: 1805.11579 [gr-qc].

[6] B. P. Abbott et al. “Prospects for observing and localizing gravitational-wave transients with Advanced LIGO, Advanced Virgo and KAGRA”. In: *Living Rev. Rel.* 21.1 (2018), p. 3. DOI: 10.1007/s41114-020-00026-9. arXiv: 1304.0670 [gr-qc].

[7] B. P. Abbott, R. Abbott, et al. “GW170817: Measurements of Neutron Star Radii and Equation of State”. In: *Phys. Rev. Lett.* 121 (16 Oct. 2018), p. 161101. DOI: 10.1103/PhysRevLett.121.161101. URL: https://link.aps.org/doi/10.1103/PhysRevLett.121.161101.

[8] B.P. Abbott et al. “GW170817: Observation of Gravitational Waves from a Binary Neutron Star Inspiral”. In: *Physical Review Letters* 119.16 (Oct. 2017). ISSN: 1079-7114. DOI: 10.1103/physrevlett.119.161101. URL: http://dx.doi.org/10.1103/PhysRevLett.119.161101.

[9] Benjamin P Abbott et al. “Model comparison from LIGO–Virgo data on GW170817’s binary components and consequences for the merger remnant”. In: *Class. Quant. Grav.* 37.4 (2020), p. 045006. DOI: 10.1088/1361-6382/ab5f7c. arXiv: 1908.01012 [gr-qc].

[10] R. Abbott et al. “GW190814: Gravitational Waves from the Coalescence of a 23 Solar Mass Black Hole with a 2.6 Solar Mass Compact Object”. In: *The Astrophysical Journal Letters* 896.2 (June 2020), p. L44. ISSN: 2041-8213. DOI: 10.3847/2041-8213/ab960f. URL: http://dx.doi.org/10.3847/2041-8213/ab960f.

[11] R. Abbott et al. “Population of Merging Compact Binaries Inferred Using Gravitational Waves through GWTC-3”. In: *Phys. Rev. X* 13 (1 Mar. 2023), p. 011048. DOI: 10.1103/PhysRevX.13.011048. URL: https://link.aps.org/doi/10.1103/PhysRevX.13.011048.

[12] R. Abbott et al. “Search for Subsolar-Mass Binaries in the First Half of Advanced LIGO’s and Advanced Virgo’s Third Observing Run”. In: *Phys. Rev. Lett.* 129.6 (2022), p. 061104. DOI: 10.1103/PhysRevLett.129.061104. arXiv: 2109.12197 [astro-ph.CO].

[13] R. Abbott et al. “Search for subsolar-mass black hole binaries in the second part of Advanced LIGO’s and Advanced Virgo’s third observing run”. In: (Dec. 2022). arXiv: 2212.01477 [astro-ph.HE].

[14] F. Acernese et al. “Advanced Virgo: a second-generation interferometric gravitational wave detector”. In: *Class. Quant. Grav.* 32.2 (2015), p. 024001. DOI: 10.1088/0264-9381/32/2/024001. arXiv: 1408.3978 [gr-qc].

[15] F. Acernese et al. “Increasing the Astrophysical Reach of the Advanced Virgo Detector via the Application of Squeezed Vacuum States of Light”. In: *Phys. Rev. Lett.* 123 (23 Dec. 2019), p. 231108. DOI: 10.1103/PhysRevLett.123.231108. URL: https://link.aps.org/doi/10.1103/PhysRevLett.123.231108.

[16] Justin Alsing, Hector O. Silva, and Emanuele Berti. “Evidence for a maximum mass cut-off in the neutron star mass distribution and constraints on the equation of state”. In: *Mon. Not. Roy. Astron. Soc.* 478.1 (2018), pp. 1377–1391. DOI: 10.1093/mnras/sty1065. arXiv: 1709.07889 [astro-ph.HE].

[17] John Antoniadis et al. “A Massive Pulsar in a Compact Relativistic Binary”. In: *Science* 340.6131 (2013), p. 1233232. DOI: 10.1126/science.1233232. arXiv: 1304.6875 [astro-ph.HE].

[18] Gregory Ashton et al. “BILBY: A User-friendly Bayesian Inference Library for Gravitational-wave Astronomy”. In: *Astrophysical Journal, Supplement* 241.2, 27 (Apr. 2019), p. 27. DOI: 10.3847/1538-4365/ab06fc. arXiv: 1811.02042 [astro-ph.IM].

[19] Kareem El-Badry et al. “Unicorns and giraffes in the binary zoo: stripped giants with subgiant companions”. In: *Monthly Notices of the Royal Astronomical Society* 512.4 (June 2022), pp. 5620–5641. DOI: 10.1093/mnras/stac815. arXiv: 2203.06348 [astro-ph.SR].

[20] Ewan D. Barr et al. “A pulsar in a binary with a compact object in the mass gap between neutron stars and black holes”. In: (Jan. 2024). DOI: 10.1126/science.adg3005. arXiv: 2401.09872 [astro-ph.HE].

[21] Taylor Binnington and Eric Poisson. "Relativistic theory of tidal Love numbers". In: *Phys. Rev. D* 80 (8 Oct. 2009), p. 084018. DOI: 10.1103/PhysRevD.80.084018. URL: https://link.aps.org/doi/10.1103/PhysRevD.80.084018.

[22] Sylvia Biscoveanu et al. "New Spin on LIGO-Virgo Binary Black Holes". In: *Physical Review Letters* 126.17 (Apr. 2021). ISSN: 1079-7114. DOI: 10.1103/physrevlett.126.171103. URL: http://dx.doi.org/10.1103/PhysRevLett.126.171103.

[23] Stephanie M. Brown, Collin D. Capano, and Badri Krishnan. "Using Gravitational Waves to Distinguish between Neutron Stars and Black Holes in Compact Binary Mergers". In: *The Astrophysical Journal* 941.1 (Dec. 2022), p. 98. ISSN: 1538-4357. DOI: 10.3847/1538-4357/ac98fe. URL: http://dx.doi.org/10.3847/1538-4357/ac98fe.

[24] A. Buikema et al. "Sensitivity and performance of the Advanced LIGO detectors in the third observing run". In: *Phys.Rev.D* 102.6, 062003 (Sept. 2020), p. 062003. DOI: 10.1103/PhysRevD.102.062003. arXiv: 2008.01301 [astro-ph.IM].

[25] B. J. Carr and S. W. Hawking. "Black holes in the early Universe". In: *Monthly Notices of the Royal Astronomical Society* 168 (Aug. 1974), pp. 399–416. DOI: 10.1093/mnras/168.2.399.

[26] Katerina Chatziioannou. "Neutron-star tidal deformability and equation-of-state constraints". In: *General Relativity and Gravitation* 52.11 (Nov. 2020). ISSN: 1572-9532. DOI: 10.1007/s10714-020-02754-3. URL: http://dx.doi.org/10.1007/s10714-020-02754-3.

[27] Katerina Chatziioannou and Will M. Farr. "Inferring the maximum and minimum mass of merging neutron stars with gravitational waves". In: *Phys. Rev. D* 102.6 (2020), p. 064063. DOI: 10.1103/PhysRevD.102.064063. arXiv: 2005.00482 [astro-ph.HE].

[28] Katerina Chatziioannou, Carl-Johan Haster, and Aaron Zimmerman. "Measuring the neutron star tidal deformability with equation-of-state-independent relations and gravitational waves". In: *Phys. Rev. D* 97 (10 May 2018), p. 104036. DOI: 10.1103/PhysRevD.97.104036. arXiv: 1804.03221 [gr-qc]. URL: https://link.aps.org/doi/10.1103/PhysRevD.97.104036.

[29] Zu-Cheng Chen and Lang Liu. "Is PSR J0514–4002E in a PBH-NS binary?" In: (Jan. 2024). arXiv: 2401.12889 [astro-ph.HE].

[30] Hsin-Yu Chen and Katerina Chatziioannou. "Distinguishing Binary Neutron Star from Neutron Star–Black Hole Mergers with Gravitational Waves". In: *The Astrophysical Journal* 893.2 (Apr. 2020), p. L41. ISSN: 2041-8213. DOI: 10.3847/2041-8213/ab86bc. URL: http://dx.doi.org/10.3847/2041-8213/ab86bc.

[31] Horng Sheng Chia. "Tidal deformation and dissipation of rotating black holes". In: *Physical Review D* 104.2 (July 2021). ISSN: 2470-0029. DOI: 10.1103/physrevd.104.024013. URL: http://dx.doi.org/10.1103/PhysRevD.104.024013.

[32] Gregory B. Cook, Stuart L. Shapiro, and Saul A. Teukolsky. "Rapidly rotating polytropes in general relativity". In: *Astrophys. J.* 422 (1994), pp. 227–242.

[33] Michael W. Coughlin and Tim Dietrich. "Can a black hole-neutron star merger explain GW170817, AT2017gfo, GRB170817A?" In: (2019). arXiv: 1901.06052 [astro-ph.HE].

[34] Michael W. Coughlin et al. "Multimessenger Bayesian parameter inference of a binary neutron star merger". In: *Mon. Not. Roy. Astron. Soc.* 489.1 (2019), pp. L91–L96. DOI: 10.1093/mnrasl/slz133. arXiv: 1812.04803 [astro-ph.HE].

[35] F. Crescimbeni et al. "Primordial black holes or else? Tidal tests on subsolar mass gravitational-wave observations". In: (Feb. 2024). arXiv: 2402.18656 [astro-ph.HE].

[36] Torrey Cullen et al. "Matter Effects on LIGO/Virgo Searches for Gravitational Waves from Merging Neutron Stars". In: *Class. Quant. Grav.* 34.24 (2017), p. 245003. DOI: 10.1088/1361-6382/aa9424. arXiv: 1708.04359 [gr-qc].

[37] Tim Dietrich, Sebastiano Bernuzzi, and Wolfgang Tichy. "Closed-form tidal approximants for binary neutron star gravitational waveforms constructed from high-resolution numerical relativity simulations". In: *Phys. Rev.* D96.12 (2017), p. 121501. DOI: 10.1103/PhysRevD.96.121501. arXiv: 1706.02969 [gr-qc].

[38] Tim Dietrich et al. "Multimessenger constraints on the neutron-star equation of state and the Hubble constant". In: *Science* 370.6523 (Dec. 2020), pp. 1450–1453. ISSN: 1095-9203. DOI: 10.1126/science.abb4317. URL: http://dx.doi.org/10.1126/science.abb4317.

[39] Victor Doroshenko et al. "A strangely light neutron star within a supernova remnant". In: *Nature Astronomy* 6 (Dec. 2022), pp. 1444–1451. DOI: 10.1038/s41550-022-01800-1.

[40] F. Douchin and P. Haensel. "A unified equation of state of dense matter and neutron star structure". In: *Astron. Astrophys.* 380 (2001), p. 151. DOI: 10.1051/0004-6361:20011402. arXiv: astro-ph/0111092.

[41] C. Drischler, J. W. Holt, and C. Wellenhofer. "Chiral Effective Field Theory and the High-Density Nuclear Equation of State". In: *Ann. Rev. Nucl. Part. Sci.* 71 (2021), pp. 403–432. DOI: 10.1146/annurev-nucl-102419-041903. arXiv: 2101.01709 [nucl-th].

[42] J. van den Eijnden et al. “A new radio census of neutron star X-ray binaries”. In: *Mon. Not. Roy. Astron. Soc.* 507.3 (2021), pp. 3899–3922. DOI: 10.1093/mnras/stab1995. arXiv: 2107.05286 [astro-ph.HE].

[43] Reed Essick and Philippe Landry. “Discriminating between Neutron Stars and Black Holes with Imperfect Knowledge of the Maximum Neutron Star Mass”. In: *Astrophys. J.* 904.1 (2020), p. 80. DOI: 10.3847/1538-4357/abbd3b. arXiv: 2007.01372 [astro-ph.HE].

[44] Reed Essick, Philippe Landry, and Daniel E. Holz. “Nonparametric Inference of Neutron Star Composition, Equation of State, and Maximum Mass with GW170817”. In: *Phys. Rev. D* 101.6 (2020), p. 063007. DOI: 10.1103/PhysRevD.101.063007. arXiv: 1910.09740 [astro-ph.HE].

[45] Reed Essick et al. “Direct Astrophysical Tests of Chiral Effective Field Theory at Supranuclear Densities”. In: *Phys. Rev. C* 102.5 (2020), p. 055803. DOI: 10.1103/PhysRevC.102.055803. arXiv: 2004.07744 [astro-ph.HE].

[46] Reed Essick et al. *lwp*. URL: https://git.ligo.org/reed.essick/lwp.

[47] Reed Essick et al. “Phase transition phenomenology with nonparametric representations of the neutron star equation of state”. In: *Phys. Rev. D* 108.4 (2023). I contributed substantially to this study which used nonparametric methods to constrain phase transitions in a nonparametric model of the equation of state. I performed the simulation analyses, developed several diagnostic statistics, and wrote large parts of the text., p. 043013. DOI: 10.1103/PhysRevD.108.043013. arXiv: 2305.07411 [astro-ph.HE].

[48] Amanda Farah et al. “Bridging the Gap: Categorizing Gravitational-wave Events at the Transition between Neutron Stars and Black Holes”. In: *The Astrophysical Journal* 931.2 (May 2022), p. 108. ISSN: 1538-4357. DOI: 10.3847/1538-4357/ac5f03. URL: http://dx.doi.org/10.3847/1538-4357/ac5f03.

[49] Will M. Farr and Katerina Chatziioannou. “A Population-Informed Mass Estimate for Pulsar J0740+6620”. In: *Research Notes of the American Astronomical Society* 4.5, 65 (May 2020), p. 65. DOI: 10.3847/2515-5172/ab9088. arXiv: 2005.00032 [astro-ph.GA].

[50] Will M. Farr et al. “THE MASS DISTRIBUTION OF STELLAR-MASS BLACK HOLES”. In: *The Astrophysical Journal* 741.2 (Oct. 2011), p. 103. ISSN: 1538-4357. DOI: 10.1088/0004-637x/741/2/103. URL: http://dx.doi.org/10.1088/0004-637X/741/2/103.

[51] Marc Favata. “Systematic Parameter Errors in Inspiraling Neutron Star Binaries”. In: *Physical Review Letters* 112.10 (Mar. 2014). ISSN: 1079-7114. DOI: 10.1103/physrevlett.112.101101. URL: http://dx.doi.org/10.1103/PhysRevLett.112.101101.

[52] Maya Fishbach, Reed Essick, and Daniel E. Holz. "Does Matter Matter? Using the Mass Distribution to Distinguish Neutron Stars and Black Holes". In: *The Astrophysical Journal* 899.1 (Aug. 2020), p. L8. ISSN: 2041-8213. DOI: 10.3847/2041-8213/aba7b6. URL: http://dx.doi.org/10.3847/2041-8213/aba7b6.

[53] Eanna E. Flanagan and Tanja Hinderer. "Constraining neutron star tidal Love numbers with gravitational wave detectors". In: *Phys. Rev. D* 77 (2008), p. 021502. DOI: 10.1103/PhysRevD.77.021502. arXiv: 0709.1915 [astro-ph].

[54] E. Fonseca et al. "Refined Mass and Geometric Measurements of the High-mass PSR J0740+6620". In: *Astrophys. J. Lett.* 915.1 (2021), p. L12. DOI: 10.3847/2041-8213/ac03b8. arXiv: 2104.00880 [astro-ph.HE].

[55] Rossella Gamba and Sebastiano Bernuzzi. "Resonant tides in binary neutron star mergers: Analytical-numerical relativity study". In: *Phys. Rev. D* 107.4 (2023), p. 044014. DOI: 10.1103/PhysRevD.107.044014. arXiv: 2207.13106 [gr-qc].

[56] Thomas Gold. "Rotating neutron stars and the nature of pulsars". In: *Nature* 221 (1969), pp. 25–27. DOI: 10.1038/221025a0.

[57] Jacob Golomb and Colm Talbot. "Hierarchical Inference of Binary Neutron Star Mass Distribution and Equation of State with Gravitational Waves". In: *The Astrophysical Journal* 926.1, 79 (Feb. 2022), p. 79. DOI: 10.3847/1538-4357/ac43bc. arXiv: 2106.15745 [astro-ph.HE].

[58] Alejandra Gonzalez et al. "Second release of the CoRe database of binary neutron star merger waveforms". In: *Class. Quant. Grav.* 40.8 (2023), p. 085011. DOI: 10.1088/1361-6382/acc231. arXiv: 2210.16366 [gr-qc].

[59] Sebastien Guillot et al. "Measurement of the Radius of Neutron Stars with High Signal-to-noise Quiescent Low-mass X-Ray Binaries in Globular Clusters". In: *The Astrophysical Journal* 772.1, 7 (July 2013), p. 7. DOI: 10.1088/0004-637X/772/1/7. arXiv: 1302.0023 [astro-ph.HE].

[60] F. Gulminelli and Ad. R. Raduta. "Unified treatment of subsaturation stellar matter at zero and finite temperature". In: *Phys. Rev. C* 92 (5 Nov. 2015), p. 055803. DOI: 10.1103/PhysRevC.92.055803. URL: https://link.aps.org/doi/10.1103/PhysRevC.92.055803.

[61] K. Hebeler et al. "Constraints on neutron star radii based on chiral effective field theory interactions". In: *Phys. Rev. Lett.* 105 (2010), p. 161102. DOI: 10.1103/PhysRevLett.105.161102. arXiv: 1007.1746 [nucl-th].

[62] P. J. van den Heuvel and Thomas M. Tauris. "Comment on "A non-interacting low-mass black hole – giant star binary system"". In: (May 2020). DOI: 10.1126/science.aba3282. arXiv: 2005.04896 [astro-ph.SR].

[63] Tanja Hinderer et al. "Discerning the binary neutron star or neutron star-black hole nature of GW170817 with Gravitational Wave and Electromagnetic Measurements". In: (2018). arXiv: 1808.03836 [astro-ph.HE].

[64] Tanja Hinderer et al. "Effects of neutron-star dynamic tides on gravitational waveforms within the effective-one-body approach". In: *Phys. Rev. Lett.* 116.18 (2016), p. 181101. DOI: 10.1103/PhysRevLett.116.181101. arXiv: 1602.00599 [gr-qc].

[65] Tanja Hinderer. "Tidal Love numbers of neutron stars". In: *Astrophys. J.* 677 (2008), pp. 1216–1220. DOI: 10.1086/533487. arXiv: 0711.2420 [astro-ph].

[66] Maurício Hippert et al. "Dark matter or regular matter in neutron stars? How to tell the difference from the coalescence of compact objects". In: *Phys. Rev. D* 107.11 (2023), p. 115028. DOI: 10.1103/PhysRevD.107.115028. arXiv: 2211.08590 [astro-ph.HE].

[67] J. D. Hunter. "Matplotlib: A 2D graphics environment". In: *Computing in Science & Engineering* 9.3 (2007), pp. 90–95. DOI: 10.1109/MCSE.2007.55.

[68] T. Jayasinghe et al. "A unicorn in monoceros: the 3 $M_\odot$ dark companion to the bright, nearby red giant V723 Mon is a non-interacting, mass-gap black hole candidate". In: *Monthly Notices of the Royal Astronomical Society* 504.2 (June 2021), pp. 2577–2602. DOI: 10.1093/mnras/stab907. arXiv: 2101.02212 [astro-ph.SR].

[69] Vassiliki Kalogera and Gordon Baym. "The maximum mass of a neutron star". In: *Astrophys. J. Lett.* 470 (1996), pp. L61–L64. DOI: 10.1086/310296. arXiv: astro-ph/9608059.

[70] Laura Kreidberg et al. "Mass Measurements of Black Holes in X-Ray Transients: Is There a Mass Gap?" In: *The Astrophysical Journal* 757.1, 36 (Sept. 2012), p. 36. DOI: 10.1088/0004-637X/757/1/36. arXiv: 1205.1805 [astro-ph.HE].

[71] Philippe Landry and Reed Essick. "Nonparametric inference of the neutron star equation of state from gravitational wave observations". In: *Phys. Rev. D* 99.8 (2019), p. 084049. DOI: 10.1103/PhysRevD.99.084049. arXiv: 1811.12529 [gr-qc].

[72] Philippe Landry, Reed Essick, and Katerina Chatziioannou. "Nonparametric constraints on neutron star matter with existing and upcoming gravitational wave and pulsar observations". In: *Phys. Rev. D* 101.12 (2020), p. 123007. DOI: 10.1103/PhysRevD.101.123007. arXiv: 2003.04880 [astro-ph.HE].

[73] Philippe Landry and Jocelyn S. Read. "The Mass Distribution of Neutron Stars in Gravitational-wave Binaries". In: *Astrophys. J. Lett.* 921.2 (2021), p. L25. DOI: 10.3847/2041-8213/ac2f3e. arXiv: 2107.04559 [astro-ph.HE].

[74] J. M. Lattimer and M. Prakash. "Neutron Star Structure and the Equation of State". In: *The Astrophysical Journal* 550.1 (Mar. 2001), pp. 426–442. ISSN: 1538-4357. DOI: 10.1086/319702. URL: http://dx.doi.org/10.1086/319702.

[75] James M. Lattimer and Madappa Prakash. "Neutron star observations: Prognosis for equation of state constraints". In: *Physics Reports* 442.1-6 (Apr. 2007), pp. 109–165. DOI: 10.1016/j.physrep.2007.02.003. arXiv: astro-ph/0612440 [astro-ph].

[76] Isaac Legred et al. "Impact of the PSR J0740 + 6620 radius constraint on the properties of high-density matter". In: *Phys. Rev. D* 104 (6 Sept. 2021), p. 063003. DOI: 10.1103/PhysRevD.104.063003. URL: https://link.aps.org/doi/10.1103/PhysRevD.104.063003.

[77] Isaac Legred et al. "Implicit correlations within phenomenological parametric models of the neutron star equation of state". In: *Phys. Rev. D* 105 (4 Feb. 2022), p. 043016. DOI: 10.1103/PhysRevD.105.043016. URL: https://link.aps.org/doi/10.1103/PhysRevD.105.043016.

[78] Ivan Markin et al. "General-relativistic hydrodynamics simulation of a neutron star–sub-solar-mass black hole merger". In: *Phys. Rev. D* 108.6 (2023), p. 064025. DOI: 10.1103/PhysRevD.108.064025. arXiv: 2304.11642 [gr-qc].

[79] J. G. Martinez et al. "PULSAR J0453+1559: A DOUBLE NEUTRON STAR SYSTEM WITH A LARGE MASS ASYMMETRY". In: *The Astrophysical Journal* 812.2 (Oct. 2015), p. 143. ISSN: 1538-4357. DOI: 10.1088/0004-637x/812/2/143. URL: http://dx.doi.org/10.1088/0004-637X/812/2/143.

[80] M. C. Miller et al. "PSR J0030+0451 Mass and Radius from *NICER* Data and Implications for the Properties of Neutron Star Matter". In: *Astrophys. J. Lett.* 887.1 (2019), p. L24. DOI: 10.3847/2041-8213/ab50c5. arXiv: 1912.05705 [astro-ph.HE].

[81] M. C. Miller et al. "The Radius of PSR J0740+6620 from NICER and XMM-Newton Data". In: *Astrophys. J. Lett.* 918.2 (2021), p. L28. DOI: 10.3847/2041-8213/ac089b. arXiv: 2105.06979 [astro-ph.HE].

[82] Soichiro Morisaki. "Accelerating parameter estimation of gravitational waves from compact binary coalescence using adaptive frequency resolutions". In: *Phys.Rev.D* 104.4, 044062 (Aug. 2021), p. 044062. DOI: 10.1103/PhysRevD.104.044062. arXiv: 2104.07813 [gr-qc].

[83] Gonzalo Morrás et al. "Analysis of a subsolar-mass compact binary candidate from the second observing run of Advanced LIGO". In: *Physics of the Dark Universe* 42 (Dec. 2023), p. 101285. ISSN: 2212-6864. DOI: 10.1016/j.dark.2023.101285. URL: http://dx.doi.org/10.1016/j.dark.2023.101285.

[84] Samaya Nissanke et al. "Exploring short gamma-ray bursts as gravitational-wave standard sirens". In: *Astrophys. J.* 725 (2010), pp. 496–514. DOI: 10.1088/0004-637X/725/1/496. arXiv: 0904.1017 [astro-ph.CO].

[85] Alexander H. Nitz and Yi-Fan Wang. "Broad search for gravitational waves from subsolar-mass binaries through LIGO and Virgo's third observing run". In: *Phys. Rev. D* 106.2 (2022), p. 023024. DOI: 10.1103/PhysRevD.106.023024. arXiv: 2202.11024 [astro-ph.HE].

[86] I. D. Novikov et al. "Primordial black holes". In: *Astronomy and Astrophysics* 80.1 (Nov. 1979), pp. 104–109.

[87] Travis Oliphant. *NumPy: A guide to NumPy*. USA: Trelgol Publishing. [Online; accessed <today>]. 2006–. URL: http://www.numpy.org/.

[88] J. R. Oppenheimer and G. M. Volkoff. "On Massive Neutron Cores". In: *Phys. Rev.* 55 (4 Feb. 1939), pp. 374–381. DOI: 10.1103/PhysRev.55.374. URL: https://link.aps.org/doi/10.1103/PhysRev.55.374.

[89] Feryal Özel et al. "The Black Hole Mass Distribution in the Galaxy". In: *The Astrophysical Journal* 725.2 (Dec. 2010), pp. 1918–1927. DOI: 10.1088/0004-637X/725/2/1918. arXiv: 1006.2834 [astro-ph.GA].

[90] Peter T. H. Pang et al. "Nuclear-Physics Multi-Messenger Astrophysics Constraints on the Neutron-Star Equation of State: Adding NICER's PSR J0740+6620 Measurement". In: (May 2021). arXiv: 2105.08688 [astro-ph.HE].

[91] Malcolm Perry and Maria J. Rodriguez. "Dynamical Love Numbers for Kerr Black Holes". In: *arXiv e-prints*, arXiv:2310.03660 (Oct. 2023), arXiv:2310.03660. DOI: 10.48550/arXiv.2310.03660. arXiv: 2310.03660 [gr-qc].

[92] Geraint Pratten, Patricia Schmidt, and Natalie Williams. "Impact of Dynamical Tides on the Reconstruction of the Neutron Star Equation of State". In: (Sept. 2021). arXiv: 2109.07566 [astro-ph.HE].

[93] Geraint Pratten et al. "Setting the cornerstone for a family of models for gravitational waves from compact binaries: The dominant harmonic for nonprecessing quasicircular black holes". In: *Phys. Rev. D* 102.6 (2020), p. 064001. DOI: 10.1103/PhysRevD.102.064001. arXiv: 2001.11412 [gr-qc].

[94] G. Raaijmakers et al. "Constraints on the dense matter equation of state and neutron star properties from NICER's mass-radius estimate of PSR J0740+6620 and multimessenger observations". In: (May 2021). arXiv: 2105.06981 [astro-ph.HE].

[95] Ronald A. Remillard and Jeffrey E. McClintock. “X-ray Properties of Black-Hole Binaries”. In: *Ann. Rev. Astron. Astrophys.* 44 (2006), pp. 49–92. DOI: 10.1146/annurev.astro.44.051905.092532. arXiv: astro-ph/0606352.

[96] Luciano Rezzolla, Elias R. Most, and Lukas R. Weih. “Using Gravitational-wave Observations and Quasi-universal Relations to Constrain the Maximum Mass of Neutron Stars”. In: *The Astrophysical Journal Letters* 852.2 (Jan. 2018), p. L25. ISSN: 2041-8213. DOI: 10.3847/2041-8213/aaa401. URL: http://dx.doi.org/10.3847/2041-8213/aaa401.

[97] Clifford E. Rhoades Jr. and Remo Ruffini. “Maximum mass of a neutron star”. In: *Phys. Rev. Lett.* 32 (1974), pp. 324–327. DOI: 10.1103/PhysRevLett.32.324.

[98] Thomas E. Riley et al. “A *NICER* View of PSR J0030+0451: Millisecond Pulsar Parameter Estimation”. In: *Astrophys. J. Lett.* 887.1 (2019), p. L21. DOI: 10.3847/2041-8213/ab481c. arXiv: 1912.05702 [astro-ph.HE].

[99] Thomas E. Riley et al. “A NICER View of the Massive Pulsar PSR J0740+6620 Informed by Radio Timing and XMM-Newton Spectroscopy”. In: *Astrophys. J. Lett.* 918.2 (2021), p. L27. DOI: 10.3847/2041-8213/ac0a81. arXiv: 2105.06980 [astro-ph.HE].

[100] I. M. Romero-Shaw et al. “Bayesian inference for compact binary coalescences with BILBY: validation and application to the first LIGO-Virgo gravitational-wave transient catalogue”. In: *Monthly Notices of the Royal Astronomical Society* 499.3 (Dec. 2020), pp. 3295–3319. DOI: 10.1093/mnras/staa2850. arXiv: 2006.00714 [astro-ph.IM].

[101] S. Shahaf et al. “Triage of the Gaia DR3 astrometric orbits - I. A sample of binaries with probable compact companions”. In: *Monthly Notices of the Royal Astronomical Society* 518.2 (Jan. 2023), pp. 2991–3003. DOI: 10.1093/mnras/stac3290. arXiv: 2209.00828 [astro-ph.SR].

[102] Yong Shao. “On the Neutron Star/Black Hole Mass Gap and Black Hole Searches”. In: *Res. Astron. Astrophys.* 22.12 (2022), p. 122002. DOI: 10.1088/1674-4527/ac995e. arXiv: 2210.00425 [astro-ph.HE].

[103] Hector O. Silva, Hajime Sotani, and Emanuele Berti. “Low-mass neutron stars: universal relations, the nuclear symmetry energy and gravitational radiation”. In: *Monthly Notices of the Royal Astronomical Society* 459.4 (Apr. 2016), pp. 4378–4388. ISSN: 1365-2966. DOI: 10.1093/mnras/stw969. URL: http://dx.doi.org/10.1093/mnras/stw969.

[104] Joshua S Speagle. “dynesty: a dynamic nested sampling package for estimating Bayesian posteriors and evidences”. In: *Monthly Notices of the Royal Astronomical Society* 493.3 (Feb. 2020), pp. 3132–3158. ISSN: 1365-2966. DOI: 10.1093/mnras/staa278. URL: http://dx.doi.org/10.1093/mnras/staa278.

[105] K. Strobel and M. K. Weigel. "On the minimum and maximum mass of neutron stars and the delayed collapse". In: *Astronomy &; Astrophysics* 367.2 (Feb. 2001), pp. 582–587. ISSN: 1432-0746. DOI: 10.1051/0004-6361:20000428. URL: http://dx.doi.org/10.1051/0004-6361:20000428.

[106] Yudai Suwa et al. "On the minimum mass of neutron stars". In: *Monthly Notices of the Royal Astronomical Society* 481.3 (Sept. 2018), pp. 3305–3312. ISSN: 1365-2966. DOI: 10.1093/mnras/sty2460. URL: http://dx.doi.org/10.1093/mnras/sty2460.

[107] Ingo Tews et al. "Constraining the speed of sound inside neutron stars with chiral effective field theory interactions and observations". In: *Astrophys. J.* 860.2 (2018), p. 149. DOI: 10.3847/1538-4357/aac267. arXiv: 1801.01923 [nucl-th].

[108] Todd A. Thompson et al. "Discovery of a Candidate Black Hole - Giant Star Binary System in the Galactic Field". In: (June 2018). DOI: 10.1126/science.aau4005. arXiv: 1806.02751 [astro-ph.HE].

[109] Todd A. Thompson et al. "Response to Comment on "A Non-Interacting Low-Mass Black Hole – Giant Star Binary System""". In: (May 2020). DOI: 10.1126/science.aba4356. arXiv: 2005.07653 [astro-ph.HE].

[110] Lev Titarchuk and Elena Seifina. "How to distinguish white dwarf and neutron star X-ray binaries during their X-ray outbursts?" In: (Nov. 2023). arXiv: 2311.12982 [astro-ph.HE].

[111] Richard C. Tolman. "Static Solutions of Einstein's Field Equations for Spheres of Fluid". In: *Phys. Rev.* 55 (4 Feb. 1939), pp. 364–373. DOI: 10.1103/PhysRev.55.364. URL: https://link.aps.org/doi/10.1103/PhysRev.55.364.

[112] Maximiliano Ujevic et al. "High-accuracy high-mass-ratio simulations for binary neutron stars and their comparison to existing waveform models". In: *Phys. Rev. D* 106.2 (2022), p. 023029. DOI: 10.1103/PhysRevD.106.023029. arXiv: 2202.09343 [gr-qc].

[113] Pauli Virtanen et al. "SciPy 1.0: Fundamental Algorithms for Scientific Computing in Python". In: *Nature Methods* 17 (2020), pp. 261–272. DOI: 10.1038/s41592-019-0686-2.

[114] Leslie Wade et al. "Systematic and statistical errors in a bayesian approach to the estimation of the neutron-star equation of state using advanced gravitational wave detectors". In: *Phys. Rev. D* 89.10 (2014), p. 103012. DOI: 10.1103/PhysRevD.89.103012. arXiv: 1402.5156 [gr-qc].

[115] Steven Weinberg. "Phenomenological Lagrangians". In: *Physica A* 96.1-2 (1979). Ed. by S. Deser, pp. 327–340. DOI: 10.1016/0378-4371(79)90223-1.

[116] Noah E. Wolfe, Salvatore Vitale, and Colm Talbot. "Too small to fail: characterizing sub-solar mass black hole mergers with gravitational waves". In: *Journal of Cosmology and Astroparticle Physics* 2023.11, 039 (Nov. 2023), p. 039. DOI: 10.1088/1475-7516/2023/11/039. arXiv: 2305.19907 [astro-ph.HE].

[117] Daniel Wysocki et al. "Inferring the neutron star equation of state simultaneously with the population of merging neutron stars". In: *arXiv e-prints*, arXiv:2001.01747 (Jan. 2020), arXiv:2001.01747. DOI: 10.48550/arXiv.2001.01747. arXiv: 2001.01747 [gr-qc].

[118] Takahiro S. Yamamoto et al. "Prospects of detection of subsolar mass primordial black hole and white dwarf binary mergers". In: *arXiv e-prints*, arXiv:2401.00044 (Dec. 2023), arXiv:2401.00044. DOI: 10.48550/arXiv.2401.00044. arXiv: 2401.00044 [gr-qc].

[119] Tianqi Zhao and James M. Lattimer. "Tidal deformabilities and neutron star mergers". In: *Phys. Rev. D* 98 (6 Sept. 2018), p. 063020. DOI: 10.1103/PhysRevD.98.063020. URL: https://link.aps.org/doi/10.1103/PhysRevD.98.063020.

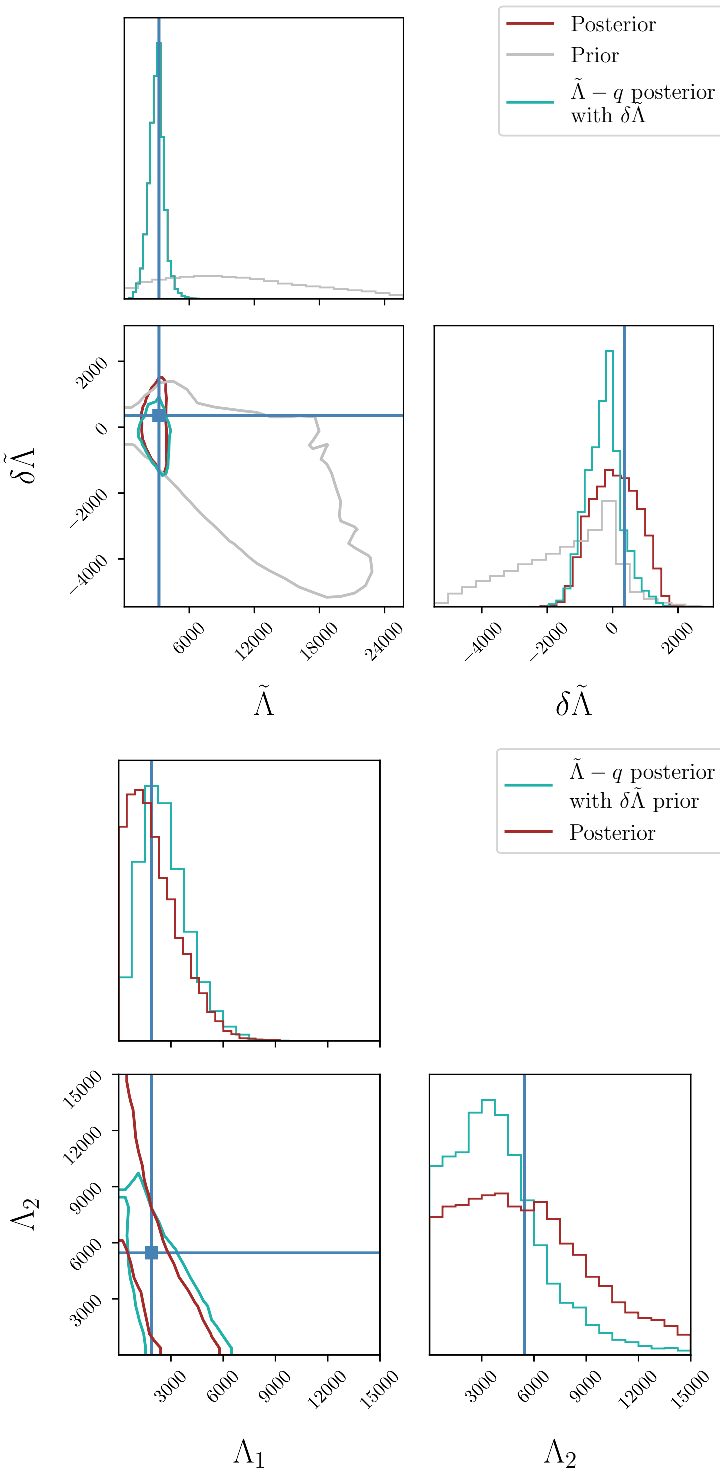

Figure 6.9: Marginal posterior (in brown) for tidal parameters from the BNS signal with $(m_1, m_2) = (1.1, 0.9)\, M_\odot$. (Left) Tidal parameters $\tilde{\Lambda}$ and $\delta\tilde{\Lambda}$, with the prior plotted in grey. (Right) Component tidal deformabilties Λ_1 and Λ_2. In both panels, the turquoise distribution corresponds to the posterior assuming that there is no information about $\delta\tilde{\Lambda}$. We find that information about $\delta\tilde{\Lambda}$ is nonnegligible, though insufficient to break the degeneracy between Λ_1 and Λ_2.

Chapter 7

THE CONNECTION BETWEEN THE DENSE MATTER EQUATION OF STATE AND THE ASTROPHYSICAL POPULATION OF COMPACT OBJECTS

[1] Jacob Golomb et al. "The interplay of astrophysics and nuclear physics in determining the properties of neutron stars". In: (Oct. 2024). I co-led this study with Jacob Golomb studying how astrophysical and dense-matter physics can be disentangled via hierarchical analysis. I performed equation of state analyses, and co-wrote the text of the manuscript. arXiv: 2410.14597 [astro-ph.HE].

Abstract

Neutron star properties depend on both nuclear physics and astrophysical processes, and thus observations of neutron stars offer constraints on both large-scale astrophysics and the behavior of cold, dense matter. In this study, we use astronomical data to jointly infer the universal equation of state of dense matter along with two distinct astrophysical populations: galactic neutron stars observed electromagnetically and merging neutron stars in binaries observed with gravitational waves. We place constraints on neutron star properties and quantify the extent to which they are attributable to macrophysics or microphysics. We confirm previous results indicating that the galactic and merging neutron stars have distinct mass distributions. The inferred maximum mass of both galactic neutron stars, $M_{\mathrm{pop,EM}} = 2.05^{+0.11}_{-0.06}\,M_\odot$ (median and 90% symmetric credible interval), and merging neutron star binaries, $M_{\mathrm{pop,GW}} = 1.85^{+0.39}_{-0.16}\,M_\odot$, are consistent with the maximum mass of nonrotating neutron stars set by nuclear physics, $M_{\mathrm{TOV}} = 2.28^{+0.41}_{-0.21}\,M_\odot$. The radius of a $1.4\,M_\odot$ neutron star is $12.2^{+0.8}_{-0.9}$ km, consistent with, though $\sim 20\%$ tighter than, previous results using an identical equation of state model. Even though observed galactic and merging neutron stars originate from populations with distinct properties, there is currently no evidence that astrophysical processes cannot produce neutron stars up to the maximum value imposed by nuclear physics.

7.1 Introduction

The properties of neutron stars (NSs) depend on both the dense-matter physics that governs their interiors and the astrophysical context in which they form, evolve, and are observed [69, 82, 29, 31]. This interplay is driven by an apparent coincidence: the mass scale of maximally-compact matter in its ground state is comparable to the Chandrasekhar mass. The NS characteristic compactness (defined as M/R with M the mass and R its radius) is just below the black-hole (BH) limit of 1/2[1]. This implies $2M/R \sim c_s^2 \sim 1$ [96], where c_s^2 is the characteristic speed of sound squared in the body. In the standard model, cold matter can only achieve such sound-speeds at densities greater than an atomic nucleus, $\rho_{\rm nuc} \sim 2.8 \times 10^{14}\,{\rm g/cm}^3$ at high neutron-to-proton ratio. This requirement fixes both the compactness *and* density of such a near-maximally compact object, and therefore its mass and radius scales to $M \sim 1\,M_\odot$ and $R \sim 10\,$km respectively. The former is remarkably close to the Chandrasekhar mass, $\sim$1.4 $M_\odot$, the maximum mass that can be supported by electron degeneracy. As NSs form from cores that are too massive to be supported by electron degeneracy, this sets another characteristic mass scale for NSs [33].

Substantial uncertainties in the details of NS formation and dense-matter physics mean it is not immediately clear which of the two drives the distribution of NS masses. For example, general relativity and the dense-matter equation of state (EoS) set a maximum mass for nonrotating NSs, the Tolman-Oppenheimer-Volkoff (TOV) limit $M_{\rm TOV}$ [103, 81]. Originally speculated to be near 0.7 $M_\odot$, $M_{\rm TOV}$ is now understood to be $\sim$2–3 $M_\odot$ [89, 62, 68, 84, 86, 70, 77], but it is unknown whether astrophysical formation mechanisms can produce NSs up to this mass. Moreover, NSs form in a variety of ways, including in core-collapse supernovae and binary mergers, each of which likely results in different natal mass and spin distributions. Even after formation, NSs are modified via binary interactions: for instance, "spider" pulsars [92] may achieve large masses and spins via accretion.

galactic observations have constrained the masses of dozens of NSs in binaries via pulsar timing [25]. The mass distribution of galactic NSs with a mass measurement includes a primary peak at $\sim$1.35 $M_\odot$ preferred at 3:1 over a secondary peak at $\sim$1.8 $M_\odot$ [17, 15, 49]. The observed cutoff in the distribution above $\sim$2 $M_\odot$ [15, 49] may correspond to the TOV mass, or to a different maximum mass imposed by astrophysical processes; the most general interpretation of the cutoff identifies it as an astrophysical maximum mass that may differ from $M_{\rm TOV}$. The galactic NS

[1] In units where $G = c = 1$, which we use unless otherwise stated.

population is broadly consistent with the masses of NS-like compact objects in wide-period binaries revealed by Gaia astrometry [19, 20]. However, this inferred mass distribution does not account for selection effects in the various surveys, and lumps together NSs in different astrophysical systems, e.g., NS–NS binaries (BNS) and NS–WD binaries, that may have different inherent distributions. Indeed, the known galactic BNSs are all contained within the $\sim 1.35\,M_\odot$ component of the bimodal distribution [51].

A subset of galactic millisecond pulsars [74] show persistent pulsed X-ray emission originating from surface hotspots. Detailed modeling of the hotspot emission has placed constraints on the mass and radius of three pulsars using NICER and XMM-Newton [76, 90, 77, 91, 32], two of which are in binaries and thus have radio-based mass constraints. Since two of the NICER targets are known radio pulsars, they are commonly treated as part of the galactic NS population. For example, the properties of PSR J0740+6620, one of the most massive known pulsars [36, 55], have been inferred simultaneously with the galactic population [50]. Requiring PSR J0740+6620 to hail from the bimodal galactic NS mass distribution revises its mass downward to $2.03^{+0.14}_{-0.11}\,M_\odot$ [50].

A different population consists of NSs in merging compact binaries with NSs or black holes (BHs) observed with gravitational waves (GWs) [10]. Among BNSs, GW170817 [5] is consistent with the galactic BNS population with a total mass of $\sim 2.7\,M_\odot$. GW190425, at a total mass of $\sim 3.4\,M_\odot$ [6], is however an outlier. Attempts to explain this discrepancy include selection effects [94, 97] and non-BNS interpretations [59, 54]. Regardless, this discrepancy suggests that the galactic and merging BNS distributions should be treated separately. The distribution of all NSs observed in merging binaries to date, including both BNSs and likely NSBH systems [9, 2], is relatively flat with no prominent peak at $\sim 1.35\,M_\odot$ [67, 10]. The population of NSs in BNSs and NSBHs might, however, be different owing to different formation and evolutionary histories [10, 22]. NS spins are ignored from these constraints due to large measurement uncertainties [23]; it is therefore unknown how merging NS spins relate to the well-measured spins of galactic NSs. GW-based NS observations (primarily GW170817) also drive constraints on the EoS through mass and tidal deformability constraints [5, 3, 4].

The picture is much simpler when it comes to the nuclear physics and the EoS of NSs. Even when originating from different formation mechanisms, cold NSs are expected to be described by the same universal EoS. This expectation has been widely utilized to combine mass, radius, and tidal deformability measurements from various observations to place constraints on the EoS, e.g. [3, 78, 85, 40, 66, 58, 77, 86, 84, 70, 48, 24]. Even then, assumptions about NS masses have to be made.

Such assumptions typically include a uniform mass distribution, and whether astrophysical mechanisms create NSs up to the TOV mass or up to a different predetermined value [66, 70].

In this paper, we study the properties of NSs in binaries with a focus on separating the impact of nuclear physics and astrophysics. We use radio, X-ray, and GW data to jointly infer the dense-matter EoS and the NS mass distribution, each with their own maximum mass. We go beyond considering a single mass distribution for all NSs that terminates at the TOV mass [24, 48] and separately infer the populations of galactic NSs and merging BNSs. Moreover, rather than the TOV mass, we allow the possibility of the astrophysical mass distribution terminating at a different "astrophysical maximum mass" that is lower than the TOV mass. Our model and inference set up allow us to begin to answer whether the maximum mass of NSs in various subpopulations is limited by the EoS or by astrophysical processes. Beyond access to such questions, simultaneous inference mitigates biases that can arise with as few as $O(10)$ GW detections when inferring either the EoS or the mass distribution alone while making improper assumptions about the other [108, 57]. We also account for GW selection effects, which cause the detected population to be biased towards higher masses; as the selection effects in the electromagnetic surveys are unknown, we do not consider them.

The subpopulations, datasets, and models are described in Sec. 7.2. The EoS is modeled with a mixture of Gaussian processes (GPs) [65, 44], which allows for a wide range of EoS morphologies including phase transitions [47] and imposes minimal intra-density correlations that hamper the flexibility of parametric models [71]. We consider two subpopulations:

1. The galactic NS population is modeled with a bimodal distribution with a maximum mass cutoff [15, 17]. The relevant datasets include radio, optical, and X-ray observations of pulsars in binaries [15] and X-ray pulse-profile observations of pulsars J0030+0451 [76, 90], J0740+6620 [77, 91], and J0437-4715 [32].

2. The merging BNS population observed with GWs is modeled with a power-law with a maximum mass cutoff. The dataset consists of GW170817 [5] and

GW190425 [6], both assumed to be BNSs.

Joint inference on the EoS and mass subpopulations is performed with a reweighting scheme that is described in Sec. 7.3 and Appendix 7.7.

Our results are presented in Sec. 7.4. We find no evidence that the maximum mass of the two subpopulations is different than the TOV mass. The difference between the maximum galactic NS (merging BNS) mass and the TOV mass is less than $0.53\,M_\odot$ ($0.73\,M_\odot$) at 90% credibility, with zero difference consistent with the posteriors. Even though the maximum masses are consistent, we confirm previous results that the mass distributions of galactic NSs and merging BNSs are different. The latter possesses no prominent peak at $1.35\,M_\odot$, indicating that the two distributions should be modeled separately in an inference framework and have the freedom to differ from one another.

For the NS EoS, we infer a sound-speed profile that exceeds the conformal bound of $1/\sqrt{3}$ for weakly interacting nucleonic matter [21], in line with a previous study using the same EoS model [70]: the 90% lower bound on the maximum speed of sound squared anywhere inside the NS is 0.59. We constrain the radius of a canonical NS, a proxy for the stiffness of the EoS, to $R_{1.4} = 12.2^{+0.8}_{-0.9}$ km, and the TOV mass to $M_{\rm TOV} = 2.28^{+0.41}_{-0.21}\,M_\odot$. Uncertainties are lower than Legred et al. [70] due to the recent NICER observation of PSR J0437-4715 and the impact of the ensemble of galactic NS mass measurements via the updated treatment of the maximum mass.

We conclude in Sec. 7.5.

7.2 Modeling the Equation of State and the mass distribution

In this section we describe the data, as well as the EoS and astrophysical populations we model them with.

Data

The observations that inform the joint inference of the NS EoS and astrophysical population come from three sources: radio/optical pulsar mass measurements (PSR), X-ray pulse profile modeling for pulsar masses and radii (NICER), and GW constraints on BNS masses and tidal deformabilities (GW).

The PSR dataset includes the 74 galactic pulsars with a mass measurement from

Ref. [15], minus PSR J0437–4715, which is counted as part of the NICER dataset.[2] The PSR observations are heterogeneous, including NSs in various types of binaries and several different mass determination methods.

The NICER dataset consists of the observations of PSR J0030+0451 [78, 90], PSR J0740+6620 [77, 91], and PSR J0437–4715 [32]. The constraints on the masses and radii of these pulsars are sensitive to the details of the X-ray pulse profile modeling, such as the assumed hotspot geometry and the stochastic sampling of the multidimensional parameter posterior; thus different interpretations of the NICER data exist. Here we use results from the three-hotspot model of Ref. [78] for J0030+0451, the combined NICER-XMM Newton analysis with the two-hotspot model from Ref. [77] for J0740+6620, and the `CST+PDT` model from Ref. [32] for J0437–4715. As the NICER analyses for J0740+6620 and J0437–4715 incorporate pre-existing radio-based mass estimates, we exclude them from the PSR dataset to avoid double-counting. In Appendix 7.10 we quantify the sensitivity of our inference to alternative data selection choices for the NICER observations.

For the GW dataset, we consider compact binary coalescences from the third Gravitational Wave Transient Catalog [8] of the LIGO-Virgo-KAGRA network [1, 11, 14] with source-frame chirp mass $\mathcal{M} \lesssim 2.176\, M_{\odot}$, corresponding to equal-mass component masses below $2.5\, M_{\odot}$. This leaves us with GW170817 [5] and GW190425 [6] as the only events consistent with BNS mergers. We do not consider the recent observation of GW230529_181500 [2], which is potentially a BNS merger according to this criterion, as sensitivity estimates for the fourth observing run do not exist. For GW170817, we generate new posterior samples with the waveform approximant `IMRPhenomPv2_NRTidal`, which includes spin-precession and tidal effects [39], using the parameter estimation package `bilby` [18, 93] and the nested sampler `dynesty` [99]. We fix the source location to the host galaxy NGC4993 and adopt spin priors that are isotropic in orientation and uniform in dimensionless magnitude up to 0.05, motivated by the spin distribution of pulsars in binary systems expected to merge within a Hubble time [112]. For GW190425, we use the publicly released parameter estimation samples [72] for the `IMRPhenomPv2_NRTidal` waveform. Since GW190425's total mass is inconsistent with those of galactic BNSs, we allow for dimensionless spin magnitudes up to 0.4, roughly corresponding to a 1 ms spin period [60]. Appendix 7.12 investigates the impact of a spin-magnitude upper limit of 0.05 for both GW170817 and GW190425.

[2]While J0437–4715 is in the NICER dataset, we use its radio mass measurement to inform the mass distribution.

EoS model

The dense-matter EoS, i.e., the pressure-density relation, is described with a model-agnostic Gaussian process [65, 44], which builds a prior EoS process via a mixture of GP hyperparameters probing a large range of correlation scales and strengths. This procedure produces an EoS distribution that is relatively insensitive to the nuclear models it is conditioned on [44] and imposes minimal model-dependent correlations between the low- and high-density EoS [71]. The GP flexibility is particularly important for our goal of disentangling the maximum TOV mass $M_{\rm TOV}$ and the maximum astrophysical mass. Less flexible parametric EoS models implicitly correlate the radius or tidal deformability and $M_{\rm TOV}$ [71] which in turn translate to model-dependent correlations between $M_{\rm TOV}$ and the astrophysical parameters. All NSs are assumed to be described by the same EoS. For efficiency, we restrict the prior to EoSs with $M_{\rm TOV} > 1.8\,M_\odot$.

Astrophysical population models

For the astrophysical mass distribution we use parametric distributions with hyperparameters η. We consider two classes of observations modeled with separate distributions: galactic NSs observed via electromagnetic (EM) radiation as part of the PSR and NICER datasets, and NSs in merging BNSs observed via GWs constituting the GW dataset.

We restrict to the NS masses while ignoring spins and assume that all objects are NSs.

Galactic neutron stars with radio and X-rays

Motivated by Refs. [17, 15, 50], we model the galactic NS masses m as a mixture of two Gaussians:

$$\pi(m|\eta_{\rm EM}) = f\mathcal{N}(\mu_1, \sigma_1) + (1-f)\mathcal{N}(\mu_2, \sigma_2)\,, \tag{7.1}$$

for $m \in [M_{\rm min}, M_{\rm pop,EM}]$, and where $\mathcal{N}(\mu, \sigma)$ is a truncated normal distribution with mean μ and standard deviation σ, and f is the mixture weight. Following Ref. [15], we fix $M_{\rm min} = 1\,M_\odot$ and infer the hyperparameters $\eta_{\rm EM} = \{\mu_1, \mu_2, \sigma_1, \sigma_2, f, M_{\rm pop,EM}\}$ with flat priors: $M_{\rm pop,EM} \in (1.8, 3.0)\,M_\odot$, $\mu_1 \in (1, 2)\,M_\odot$, $\mu_2 \in (\mu_1, 2.5)\,M_\odot$, $f \in (0, 1)$, and $\sigma_{1,2} \in (0.05, 1)\,M_\odot$. Since all analyzed objects are NSs, we impose $M_{\rm pop,EM} < M_{\rm TOV}$.[3] This prior restriction leads to a marginal pri-

[3]We ignore the impact of pulsar spin on the maximum mass. Using approximate relations to fourth order in spin magnitude [79, 27], we estimate that the maximum allowed mass will differ from

ors on $M_{\rm pop,EM}$ and the EoSs that are not uniform, although the full multidimensional prior is flat within its domain of support.

Although the PSR and NICER datasets include NSs in different astrophysical settings, i.e. in binaries with various companions, or in isolation in the case of J0030+0451, and could in principle hail from different subpopulations, we model these NSs as a single population for consistency with previous results and due to the lack of selection effect estimates. (We are not aware of any established methods to account for selection effects in radio surveys or for NICER's target selection procedure [26].) Given the lack of selection effect estimates for the PSR and NICER datasets, we simply assume the observed mass distribution to be equivalent to the astrophysical distribution.[4] We quantify the impact of this assumption in Appendix 7.11, where we present results with a fixed uniform mass distribution in place of Eq. (7.1).

Merging neutron stars with gravitational waves

We model BNS masses with a truncated power-law for both binary components m_1 and m_2:

$$\pi(m_1, m_2|\eta_{\rm GW}) \propto m_1^\alpha m_2^\alpha \,, \tag{7.2}$$

for $m \in [m_{\rm min}, M_{\rm pop,GW}]$ and random pairing between m_1 and m_2 in the two-dimensional space. We again fix $m_{\rm min} = 1\,M_\odot$ and infer the hyperparameters $\eta_{\rm GW} = \{\alpha, M_{\rm pop,GW}\}$ with flat priors $\alpha \in (-5, 5)$, $M_{\rm pop,GW} \in (1.6, 2.5)\,M_\odot$. Since we assume that both GW170817 and GW190425 are BNSs, we again impose $M_{\rm pop,GW} < M_{\rm TOV}$.

GW selection effects are well understood, and we incorporate them in our inference. Because the GW data selection procedure involves identifying events as BNSs based on a component mass cut at $2.5\,M_\odot$, our analysis only places constraints on the mass distribution below $2.5\,M_\odot$. The GW selection modeling is described in Sec. 7.3.

7.3 Joint inference via reweighting

The joint mass-EoS model is a combination of EoS draws from the GP prior process and the parametric mass models of Eqs. (7.1) and (7.2). While the joint posterior could be sampled with standard stochastic sampling methods with pre-computed

$M_{\rm TOV}$ by $\lesssim 1\%$ compared to statistical uncertainties $\sim 20-30\%$ for the range of pulsar periods in our dataset, $P \gtrsim 2\,$ms.

[4] This procedure can result in a bias even for the detected population [42]. Such a bias however is expected to be small. For example, Fig. 4 of [42] shows the bias for ~800 simulated GW observations.

GP draws, we instead use a multi-stage reweighting scheme and the GP draws from Ref. [70].

The reweighting scheme includes the following steps, with technical details relegated to the Appendices:

1. Use standard stochastic sampling to infer the mass population and the EoS using Eqs. (7.1) and (7.2) for the mass distribution and a simplified, low-dimensional EoS model. Details about the EoS model are given in Appendix 7.8. The EoS model is included here to mitigate potential biases of a mass-only inference [57].

2. Treat the inferred mass distribution as a proposal distribution. For each sample from the distribution of $\eta = \{\eta_{\rm EM}, \eta_{\rm GW}\}$, calculate the likelihood for each pre-computed GP draw. The likelihood form depends on the dataset considered [67] and is described in Secs. 7.3 and 7.3 for the GW and EM data respectively.

3. With these likelihoods, calculate weights from the proposal mass distribution to the target joint mass-GP EoS distribution as described in Appendix 7.7.

4. Combine the new posterior distributions for each dataset. This procedure allows us to obtain weighted samples from the joint posterior of the mass distribution and the GP EoS. We validate the reweighting scheme in Appendix 7.9 with simulated GW observations.

Each of the datasets considered (GW, NICER, and PSR) results in unique constraints and thus requires a unique formulation of the likelihood [67, 29]. Below we discuss each dataset likelihood noting that the full likelihood is the product over the individual datasets.

GW likelihood

Given $N_{\rm GW}$ independent events, the likelihood for the EoS ε and population hyperparameters $\eta_{\rm GW}$ is[5] [107, 101, 75]

$$\begin{aligned}\mathcal{L}_{\rm GW}(d|\varepsilon, \eta_{\rm GW}) \propto\ & p_{\rm det}(\eta_{\rm GW})^{-N_{\rm GW}} \times \\ & \prod_i^{N_{\rm GW}} \int \mathcal{L}(d_i|m_1, m_2, \varepsilon)\pi(m_1, m_2|\eta_{\rm GW}) dm_1 dm_2 \,,\end{aligned} \tag{7.3}$$

[5] This expression assumes a $1/R$ prior on the event rate R and marginalizes over it [75, 53].

where $\pi(m_1, m_2|\eta_{\rm GW})$ is the model of Eq. (7.2) and

$$\mathcal{L}(d_i|m_1, m_2, \varepsilon) = \mathcal{L}(d_i|m_1, m_2, \Lambda(m_1, \varepsilon)\Lambda(m_2, \varepsilon))\,, \tag{7.4}$$

is the ith individual-event GW likelihood (e.g., [52, 104]) marginalized over all binary parameters other than the component masses m_1, m_2 and tidal deformabilities Λ_1, Λ_2. Consistency with the EoS is ensured by calculating the likelihood for $\Lambda_1 = \Lambda(m_1, \varepsilon), \Lambda_2 = \Lambda(m_2, \varepsilon)$, i.e., the EoS prediction for the tidal deformability given the mass. We estimate the individual-event likelihood from the posterior samples for the source-frame masses and tidal deformabilities using a Gaussian mixture model [57], and the integral in Eq. (7.3) is computed as a Monte Carlo sum.

The term $p_{\rm det}(\eta_{\rm GW})$ encodes the selection effect which characterizes how parts of the parameter space are over-represented in a catalog of GW events, as determined by the sensitivity of the detectors. Defining $p_{\rm det}(d)$ as the probability that search algorithms detect a significant signal in data d results in

$$\begin{aligned} p_{\rm det}(\eta_{\rm GW}) &\equiv \int \mathcal{D}d \int d\theta\, p(d|\theta)\pi(\theta|\eta_{\rm GW})p_{\rm det}(d) \\ &= \int d\theta\, \pi(\theta|\eta_{\rm GW})p_{\rm det}(\theta)\,, \end{aligned} \tag{7.5}$$

where we identify $p_{\rm det}(\theta) \equiv \int \mathcal{D}d\, p(d|\theta)p_{\rm det}(d)$ as the probability of detecting an event with parameters θ, marginalized over possible realizations of data d. For example, neglecting the specifics of the noise-generating process, the sensitivity to an event increases with its chirp mass $\sim\mathcal{M}_c^{5/6}$ and decreases inversely with its distance. We then further marginalize over possible realizations from the population $\theta \sim \pi(\theta|\eta_{\rm GW})$. The presence of $p_{\rm det}(\eta_{\rm GW})$ in Eq. (7.3) ensures that the final result reflects the true astrophysical population rather than the observed population. In practice, $p_{\rm det}(\eta_{\rm GW})$ might also depend on the EoS, but Ref. [37] showed that the effect is negligible except for very stiff EoSs and low-mass NSs: there is a $\lesssim 2\%$ change in the match between a template that sets $\Lambda = 0$ and the true waveform.

We compute $p_{\rm det}(\eta_{\rm GW})$ by reweighting recovered simulated signals in data from the first three observing runs, using standard techniques [10, 49, 102].

NICER likelihood

Given $N_{\rm NICER}$ observations, the likelihood for the EoS ε and population hyperparameters $\eta_{\rm EM}$ is obtained by marginalizing over the pulsar mass

$$p_{\rm NICER}(d|\varepsilon, \eta_{\rm EM}) = \prod_i^{N_{\rm NICER}} \int \mathcal{L}(d_i|m, \varepsilon)\pi(m|\eta_{\rm EM})dm\,, \tag{7.6}$$

where i indexes the NICER observations, $\pi(m|\eta_{\rm EM})$ is the mass distribution of Eq. (7.1), and

$$\mathcal{L}(d_i|m,\varepsilon) = \mathcal{L}(d_i|m, C(m,\varepsilon))\,, \tag{7.7}$$

is the individual-pulsar likelihood marginalized over all NICER parameters other than the mass m and compactness C, which is again evaluated on the EoS prediction. The likelihoods are described in the publications associated with each observation [32, 76, 77]. We use a Gaussian mixture model [57] to evaluate Eq. (7.7), and a Monte Carlo sum for the integral in Eq. (7.6).

The NICER analysis of PSR J0437-4715 in Ref. [32] uses a prior that is flat in radius, rather than flat in compactness (or inverse compactness) like the analyses of PSR J0030-0451- [76] and PSR J0770+6620 [77]. We correct for this with the appropriate Jacobian term to obtain a likelihood function in mass and compactness. Unlike Eq. (7.3) for the GW observations, the NICER likelihood ignores selection effects per the discussion in Sec. 7.2.

PSR likelihood

Finally, the likelihood for $N_{\rm PSR}$ pulsar mass measurements is

$$p_{\rm PSR}(d|\varepsilon,\eta_{\rm EM}) = \prod_{i}^{N_{\rm PSR}} \int \mathcal{L}(d_i|m)\pi(m|\eta_{\rm EM})dm\,, \tag{7.8}$$

where i indexes the pulsars and $\pi(m|\eta_{\rm EM})$ is the mass distribution of Eq. (7.1). The form of $\mathcal{L}(d_i|m)$ for each observation is prescribed analytically in Refs. [15, 50], depending on whether the measurement constrains the pulsar mass, the binary mass function and the total mass, or the binary mass function and the mass ratio. Like the NICER likelihoods, the PSR likelihoods do not account for selection effects, and we evaluate the integral in Eq. (7.8) via Monte Carlo.

7.4 Implications of joint mass-EoS inference

In this section, we present results from the joint inference over the EoS and the mass distribution of two NS populations. We begin with mass-specific and EoS-specific results in Secs. 7.4 and 7.4 respectively, before contrasting their impact on NS properties in Sec. 7.4.

Constraints on astrophysical populations

Figure 7.1 shows the inferred mass distribution of merging BNSs observed with GWs (modeled with a truncated power-law) and the observed distribution of galactic

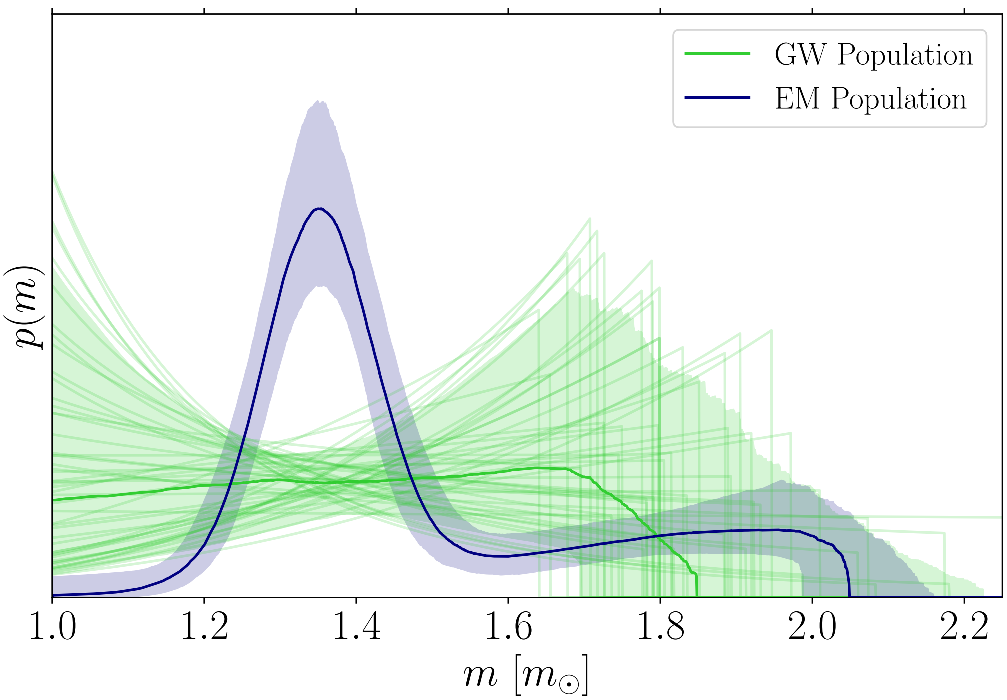

Figure 7.1: Posterior on the mass distribution of the GW BNS (orange) and the galactic NS (blue) population. We plot the median and 90% highest-probability credible regions. The EM population is constrained to much better precision than the GW one due to the low number of GW BNS detections. With the caveat that they correspond to the astrophysical BNS and observed galactic NS distributions respectively, we find that the two distribution are inconsistent, in agreement with Ref. [10]. Faint lines are random draws from the GW mass distribution, illustrating the bimodal uncertainties in the mass distribution.

NSs observed with EM (modeled with a truncated Gaussian mixture). The BNS population is consistent with being flat and has large uncertainties due to the now number of events (a total of 4 NSs). The smallest uncertainty is at $\sim 1.4\, M_\odot$, corresponding to the relatively well-measured masses on GW170817, while there is vanishing support for masses above $\sim 2.2\, M_\odot$ with $M_{\rm pop,GW} = 1.85^{+0.39}_{-0.16}\, M_\odot$. This shape is broadly consistent with the results of Refs. [10, 67] that additionally considered the two NSs in the NSBH binaries GW200105 and GW200115 and did not model the EoS. The seemingly "bimodal" shape with peaks at high and low masses at the 90% level is model-dependent: it is an outcome of the fact that the distribution is well-measured at $\sim 1.4\, M_\odot$ and we model it with a truncated power-law. Figure 7.2 indeed shows that the power-law index α and the maximum mass, $M_{\rm pop,GW}$, are correlated and the upper limit on $M_{\rm pop,GW}$ depends on the α prior. In particular, while the one-dimensional posterior peaks at $\alpha \approx 0$, $\alpha \gtrsim 4$ cannot be

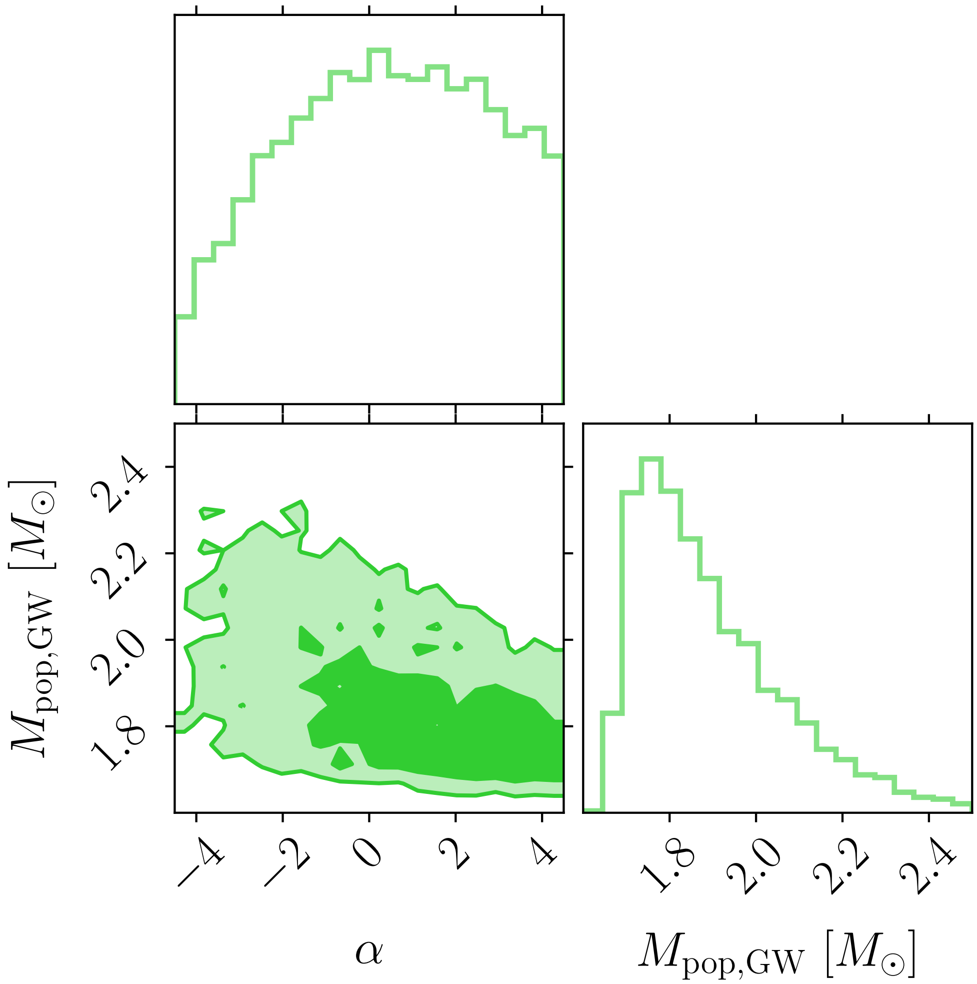

Figure 7.2: Marginalized posterior for the power-law slope α and maximum mass $M_{\mathrm{pop,GW}}$ of the GW population. The slope α is poorly constrained and thus its posterior rails against the upper prior bound, in turn affecting the $M_{\mathrm{pop,GW}}$ posterior.

ruled out but is only consistent with $M_{\mathrm{pop,GW}} \lesssim 2.0 M_\odot$.

The observed EM population is comparatively better constrained as it is based on a total of 74 pulsar mass measurements. We find consistent results with Refs. [15, 50] that used the same pulsar mass data but did not infer the EoS with $\mu_1 = 1.35^{+0.02}_{-0.02}\, M_\odot$ and $\mu_2 = 2.01^{+0.43}_{-0.27}\, M_\odot$, $f = 0.65^{+0.11}_{-0.13}$, and $\sigma_1 = 0.07^{+0.02}_{-0.02}\, M_\odot$ and $\sigma_2 = 0.39^{+0.37}_{-0.22}\, M_\odot$. The maximum mass is $M_{\mathrm{pop,EM}} = 2.05^{+0.11}_{-0.06}\, M_\odot$, compared to $2.12^{+0.12}_{-0.17}\, M_\odot$ in [15] and $2.25^{+0.82}_{-0.26}\, M_\odot$ in [50]. Our estimate is lower due to the fact that we simultaneously infer the EoS and impose $M_{\mathrm{pop,EM}} < M_{\mathrm{TOV}}$.

Assuming that the three NICER pulsars are part of the general galactic NS population leads to updated mass inference. The original mass estimates quoted in

Refs. [76, 77, 32] refer to flat mass priors, while our analysis effectively updates the prior to be the population distribution [50].[6] The mass for each NICER target under a population-informed (flat) prior is $1.37^{+0.22}_{-0.11}$ ($1.44^{+0.25}_{-0.23}$) $M_\odot$ for J0030+0451, $1.39^{+0.08}_{-0.05}$ ($1.42^{+0.06}_{-0.06}$) $M_\odot$ for J0437-4715, and $2.01^{+0.08}_{-0.09}$ ($2.07^{+0.11}_{-0.12}$) $M_\odot$ for J0740+6620. The J0740+6620 result is somewhat larger than the value in Farr and Chatziioannou [50], $2.03^{+0.17}_{-0.14}\,M_\odot$. The effect is most stark for J0030+0451 whose mass is poorly measured from the X-ray data alone, but now resides in the dominant peak of the mass distribution.

Constraints on EoS quantities

Figure 7.3 shows the prior and posterior for various macroscopic and microscopic EoS properties: the TOV mass, $M_{\rm TOV}$, the radius and tidal deformability of a canonical $1.4\,M_\odot$ NS, $R_{1.4}$ and $\Lambda_{1.4}$ respectively, the radius of a $1.8\,M_\odot$ NS, $\Lambda_{1.8}$, and the pressure at twice and 6 times nuclear saturation, $p_{2.0}$ and $p_{6.0}$ respectively. We infer $\Lambda_{1.4} = 438^{+224}_{-166}$ and $R_{1.4} = 12.2^{+0.8}_{-0.9}$ km. For comparison, we also plot the corresponding analysis from Legred et al. [70] that fixes all mass distributions to uniform. To isolate the effect of the mass distribution inference, we repeat the analysis of Ref. [70] while adding the X-ray mass-radius measurement of J0437-4715 such that the two analyses use the same NICER and GW data. We obtain largely consistent results: mass-marginalization leads to mild changes in $R_{1.4}$ and $\Lambda_{1.4}$, while including spider pulsars in the analysis and introducing an EoS-limited astrophysical maximum mass leads to a mild increase in the inferred value of $M_{\rm TOV}$.

These results are consistent with previous estimates. Legred et al. [70] used the GP EoS model with the same GW dataset, the first two NICER objects, J0030+0451 and J0740+6620, and the mass of J0348+0432 (all with a fixed flat mass prior) to find $R_{1.4} = 12.6^{+1.0}_{-1.1}$ km and $M_{\rm TOV} = 2.21^{+0.31}_{-0.21}\,M_\odot$. Our updated radius estimate has a ∼0.4 km lower median due to the new J0437-4715 data that favor softer EoSs and a ∼20% smaller uncertainty due to the fact that we use more NICER and massive pulsar data. Our updated $M_{\rm TOV}$ estimate of $2.28^{+0.41}_{-0.21}\,M_\odot$ is marginally larger than the value found in Legred et al. [70], which can be attributed to the spider pulsars, and the removal of the EoS Occam penalty for massive pulsar measurements; see the Appendix of Ref. [70].

The full mass-radius inferred relation is shown in Fig. 7.4 which plots the 90% symmetric credible region for the radius at each mass. We include the prior and the

[6] The same is true for the two GW events, but the effect is minimal as the mass distribution uncertainty is wide and consistent with flat which was the inference prior to begin with.

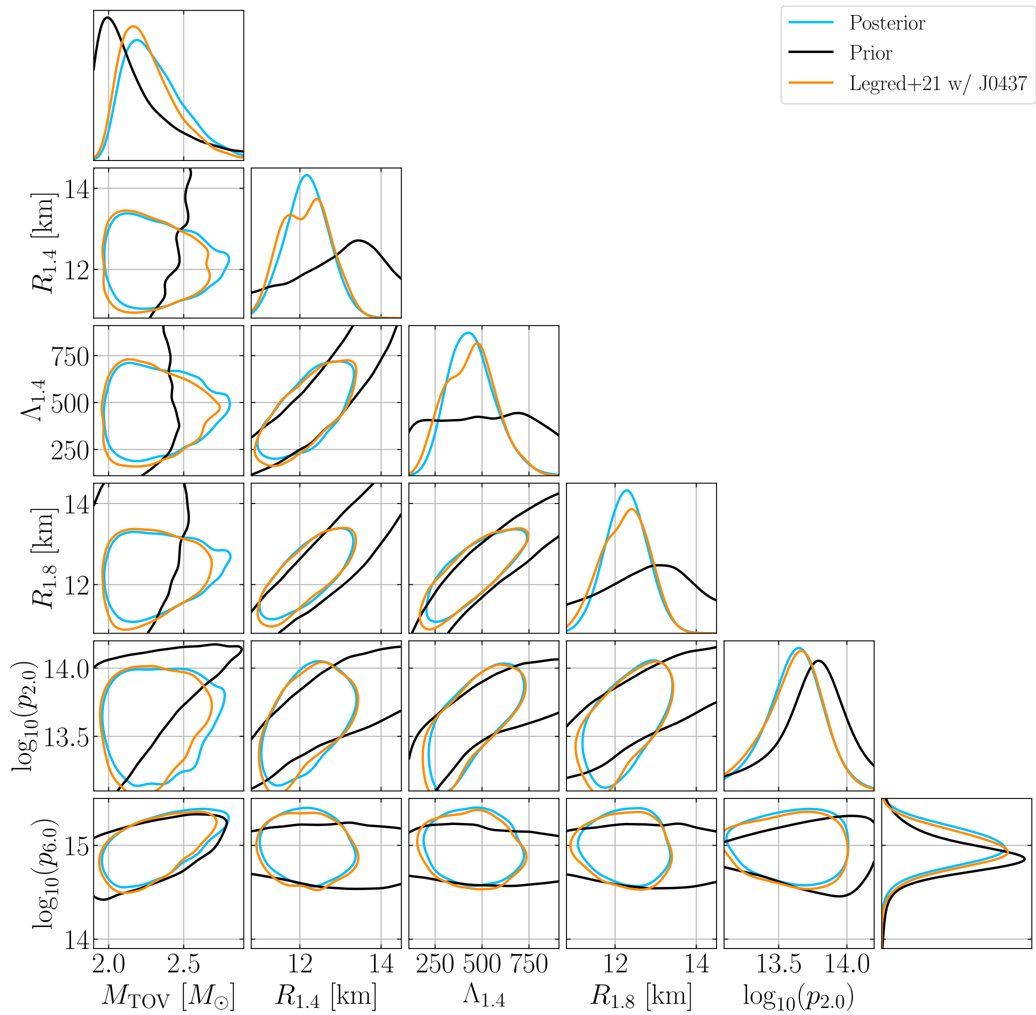

Figure 7.3: One- and two-dimensional posteriors for select EoS macroscopic and microscopic parameters: the TOV mass, M_{TOV}, the radius and tidal deformability of a canonical 1.4 $M_\odot$ NS, $R_{1.4}$ and $\Lambda_{1.4}$ respectively, the radius of a 1.8 $M_\odot$ NS, $R_{1.8}$, and the log-base-10 pressure (divided by the speed of light squared) at twice and six times nuclear saturation, $p_{2.0}$ and $p_{6.0}$ respectively, when measured in g/cm^3. Two-dimensional contours denote the boundaries of the 90% credible regions. We show the prior (black), the posterior from the main analysis that marginalizes over the mass distribution (blue), and the analogous posterior that arises from additionally including the mass-radius measurement of J0437-4715 in the analysis of Ref. [70].

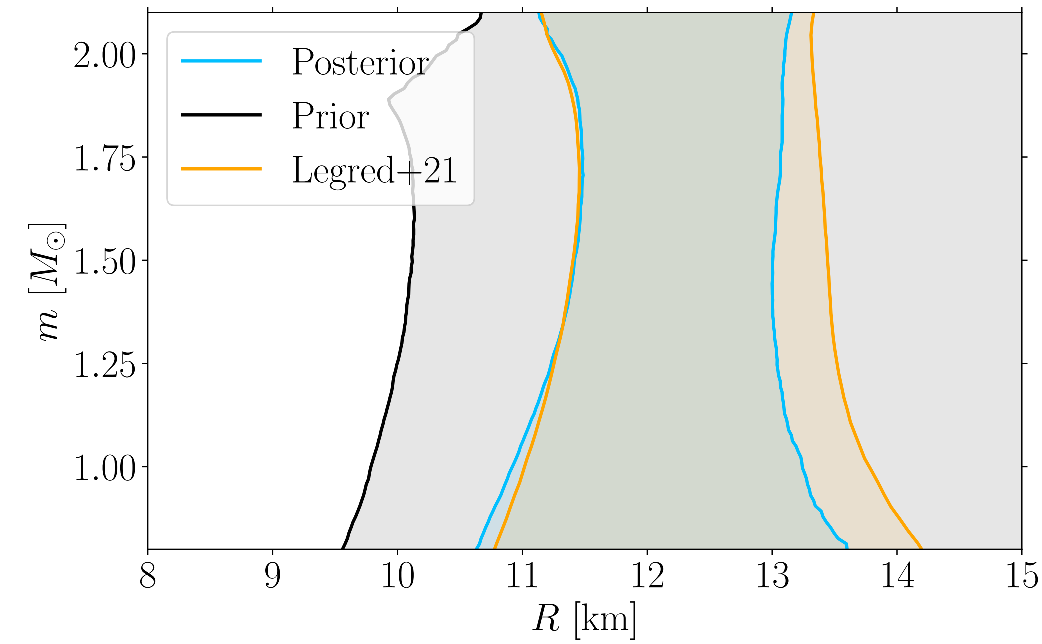

Figure 7.4: Mass-radius inference, we show the 90% symmetric credible region for the radius at each mass. We plot the prior (black), posterior from the main analysis that marginalizes over the mass distribution (blue), and posterior from Ref. [70] that fixes the mass distribution to flat and does not include J0437-4715. The upper limit on the radius decreases by ~ 0.5 km for all masses.

posterior from our analysis, and compare against the posterior from Legred et al. [70], i.e., without J0437-4715. While the radius lower limit is broadly consistent with Ref. [70], we obtain a lower radius upper limit for all masses by ~500 m, which we attribute to the new data for the J0437-4715 radius. We additionally plot credible regions for the relation between the NS mass m and its central density ρ_c in Fig. 7.5. The upper limit on the mass of a NS with central density 4 times the nuclear saturation density ($\rho_{\rm nuc}$) increases from ~$2.55\,M_\odot$ to ~$2.69\,M_\odot$, primarily due to the removal of the Occam penalty and the inclusion of spider pulsars. The central density of the maximum mass star is inferred to be $5.53^{+1.07}_{-1.24}\,\rho_{\rm nuc}$ (red contours).

We examine the EoS microscopic properties and specifically the speed of sound as a function of density in Fig. 7.6 and the maximum speed of sound inside NSs in Fig. 7.7.

Compared to Legred et al. [70], our analysis favors a larger speed of sound around $2-4\rho_{\rm nuc}$ and a larger maximum speed of sound throughout. The 90% lower limit on the maximum speed of sound increases from ~ 0.51 in Ref. [70] to ~ 0.59 for our analysis. This higher maximum speed of sound is necessary to explain

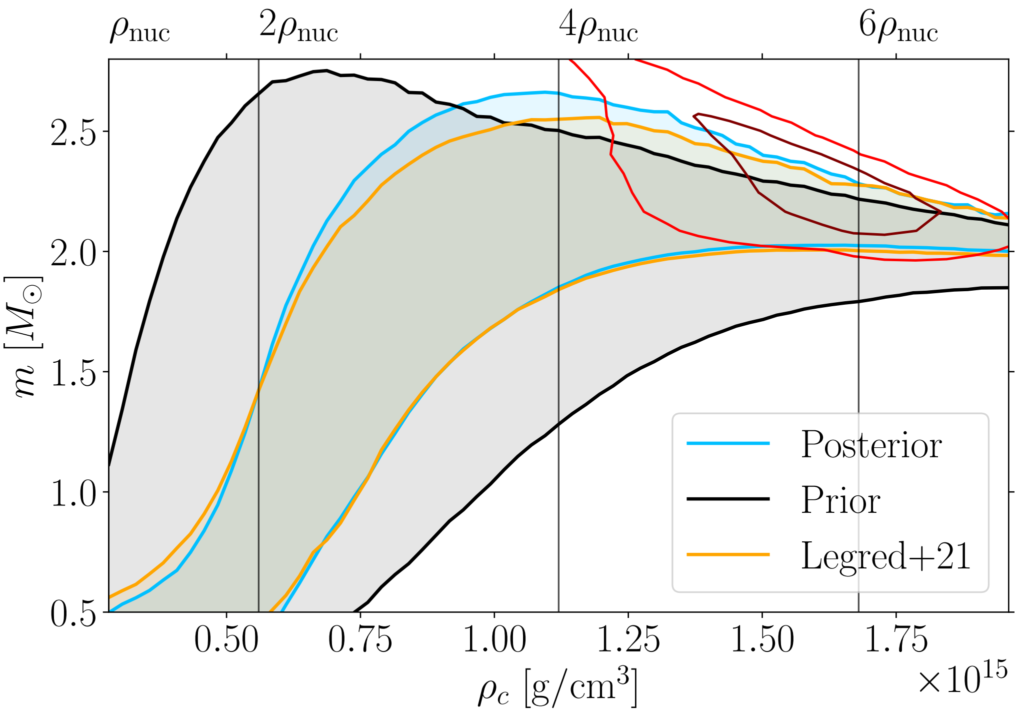

Figure 7.5: Mass-central density inference, we show the 90% symmetric credible region for the NS mass at each value of the central density ρ_c. We plot the prior (black), posterior from the main analysis that marginalizes over the mass distribution (blue), and posterior from Ref. [70] that fixes the mass distribution to flat and does not include J0437-4715. Vertical lines denote multiples of the nuclear saturation density. Maroon and red contours mark 1 and 2-σ credible regions, respectively, for the joint posterior on ρ_c-$M_{\rm TOV}$.

the high mass of certain galactic pulsars which, though poorly measured, can have exceptionally large median values, e.g., J01748-2021B with an estimated mass of $2.74^{+0.21}_{-0.21}\,M_\odot$ [56] at 68% credibility. The addition of the NICER radius measurement J0437-4715 also marginally impacts the inferred maximum sound speed; removing the radius measurement of J0437-4715 (Appendix 7.10) leads to a maximum c_s^2 value of $0.8^{+0.19}_{-0.31}$.

Joint constraints on the population and EoS

The joint EoS-mass inference allows us to separate the TOV mass, $M_{\rm TOV}$, from the maximum astrophysical mass in the two subpopulations, $M_{\rm pop,EM}$ and $M_{\rm pop,GW}$. Figure 7.8 shows the joint posterior for $M_{\rm TOV}$ and the two population maximum masses, denoted collectively as $M_{\rm pop}$. The limit $M_{\rm TOV} = M_{\rm pop}$ is marked with a dashed line; points near the line correspond to maximum population masses that are

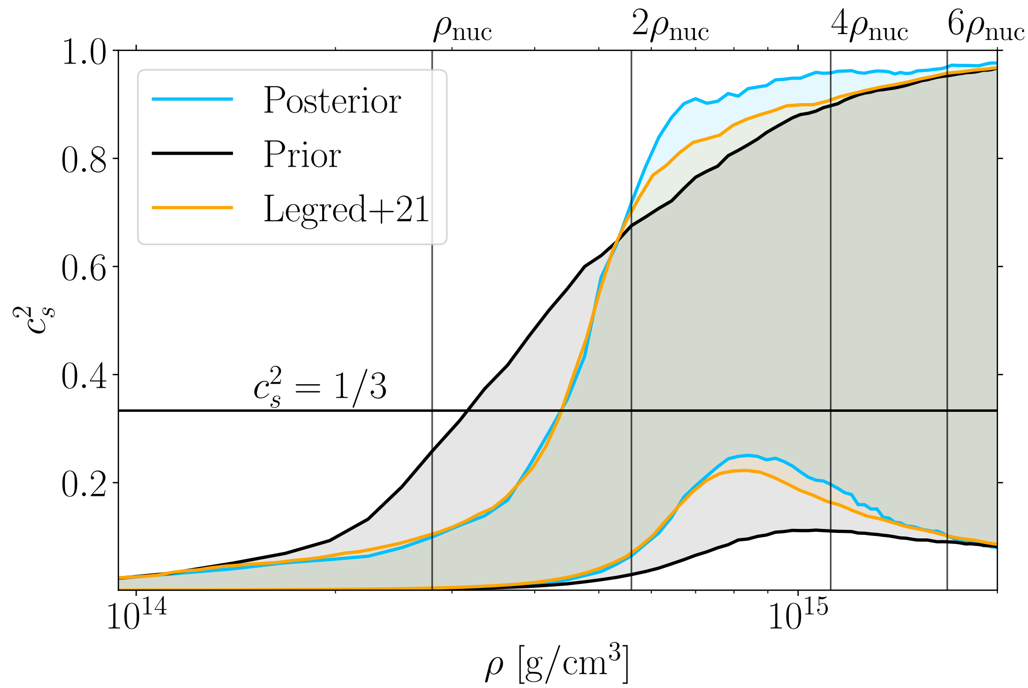

Figure 7.6: Speed of sound-density inference, we show the 90% symmetric credible region for the speed of sound squared, c_s^2 at each rest-mass density ρ. We plot the prior (black), posterior from the main analysis that marginalizes over the mass distribution (blue), and posterior from Ref. [70] that fixes the mass distribution to flat and does not include J0437-4715. Vertical lines denote multiples of the nuclear saturation density. The speed of sound increases by $\sim 5\%$ around densities $2-3$ times saturation density.

equal to the TOV mass. As also evident in Fig. 7.1, the two population maximum masses are consistent with each other within their statistical uncertainties. The difference between the maximum mass in the EM (GW) population and $M_{\rm TOV}$ is less than 0.53 $M_\odot$ (0.73 $M_\odot$) at 90% credibility.

We therefore have no evidence that the maximum mass of neutron stars formed astrophysically is different than the maximum mass possible from nuclear physics.

7.5 Conclusions

As a first step toward untangling the properties of NSs that depend on nuclear physics versus astrophysics, in this study we presented a joint inference of the dense matter EoS and the NS mass distribution. We considered two subpopulations of NSs corresponding to merging BNSs observed with GWs and galactic NSs observed with EM. All NSs share the same universal EoS modeled with a flexible GP mixture.

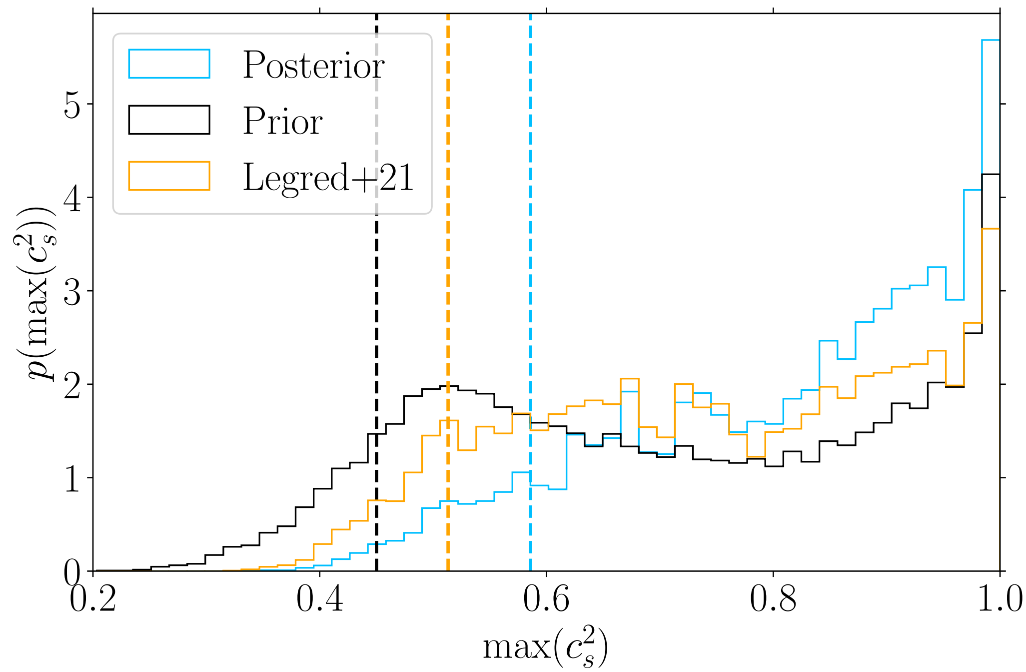

Figure 7.7: Marginalized posterior for the maximum speed of sound squared inside a stable NS. We plot the prior (black), posterior from the main analysis that marginalizes over the mass distribution (blue), and posterior from Ref. [70] that fixes the mass distribution to flat and does not include J0437-4715. The 90% lower limit on the maximum speed of sound, marked by dashed vertical lines, increases from ~0.51 to ~0.59.

Our results are consistent with existing EoS-only or mass-only inference where applicable [70, 50, 10]. However, the joint inference scheme allows us to begin addressing the interplay between nuclear physics and astrophysics in determining NS observational properties. Focusing on NS masses, we find no evidence that the maximum mass of NSs observed with either EM or GWs is different than the maximum mass allowed by nuclear physics. Moreover, we updated the estimates of the canonical NS radius and the TOV mass to $R_{1.4} = 12.2^{+0.8}_{-0.9}$ km and $M_{\rm TOV} = 2.28^{+0.41}_{-0.21} M_{\odot}$, respectively.

Past work

Our results are broadly consistent with comparable studies. Whereas we model the EoS phenomenologically as a GP, Rutherford et al. [95] used a piecewise-polytropic EoS model and the same data as Legred et al. [70] plus the radius measurement of J0437-4715; they found $R_{1.4} = 12.3^{+0.5}_{-0.8}$ km. Our result has a ~30% larger uncertainty likely due to the more flexible EoS model.

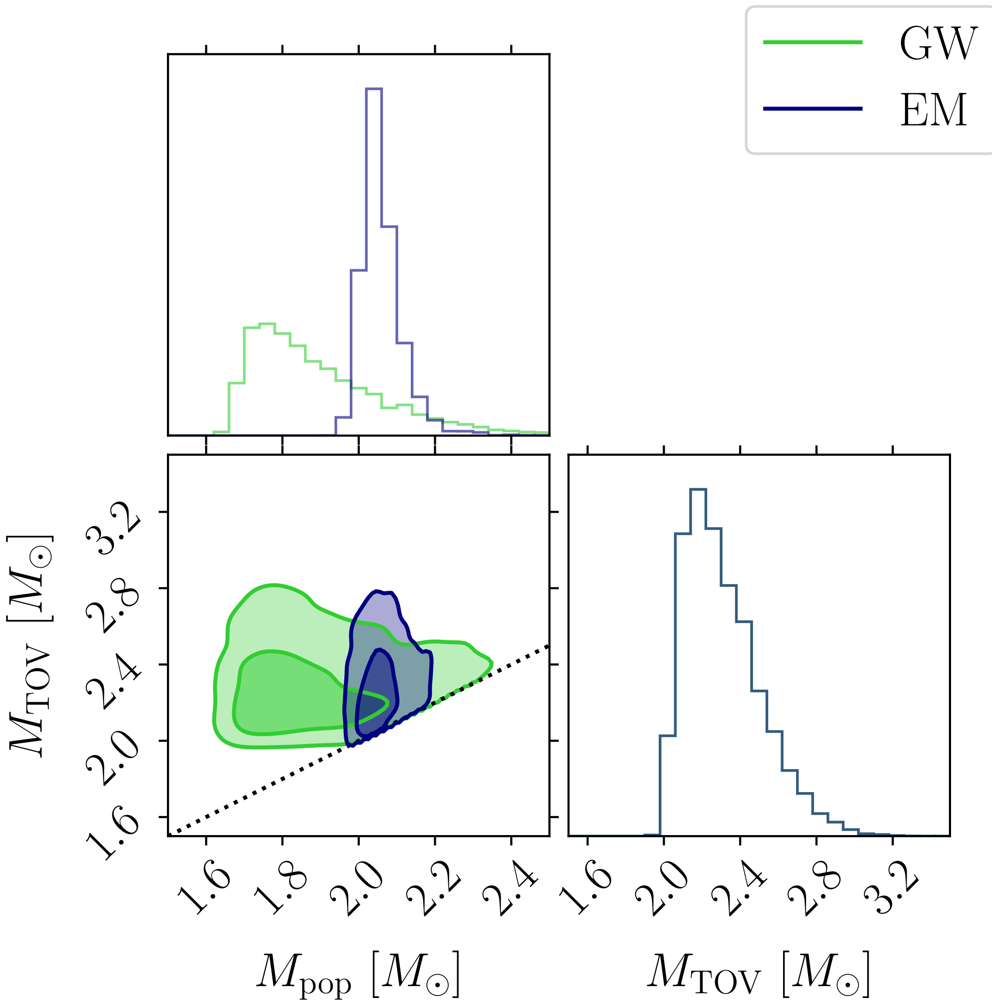

Figure 7.8: One-and two-dimensional posteriors for $M_{\rm TOV}$ and the maximum astrophysical mass $M_{\rm pop}$ for the galactic NSs (blue) and the merging BNSs (orange). The black dashed line represents $M_{\rm pop} = M_{\rm TOV}$, which is imposed in our analyses as we assume that all objects are NSs. The TOV mass is consistent with the astrophysical maximum mass for both populations. Contours are drawn at 50% and 90% levels.

Fan et al. [48] simultaneously inferred the mass distribution and the EoS, though they assumed the same mass distribution for all NSs, and that the upper truncation mass for the NS population is $M_{\rm TOV}$. They used the same data as our study except the radius measurement of J0437-4715, and included ~50 additional pulsar mass measurements. They used a variety of parameteric and nonparametric EoS models, but recovered similar values of $R_{1.4}$ and $M_{\rm TOV}$ for all models, indicating their non-parametric models may have limited flexibility (analogous to the "model-informed prior" of [65, 44]). They further incorporated information from perturbative quantum chromodynamics (pQCD) at high densities, and chiral perturbation theory at low densities, both of which strongly informed the estimate of $M_{\rm TOV}$ due to the choice of modeling of correlations. They found $M_{\rm TOV} = 2.25^{+0.08}_{-0.07}\, M_\odot$.

Biswas and Rosswog [24] also simultaneously inferred the population and the EoS, similarly requiring the NSs to form a single population which is truncated by $M_{\rm TOV}$. For the EoS they used a piecewise-polytropic parameterization, hybridized with a low-density prescription constrained by chiral effective field theory. They analyzed the same data as Fan et al. [48], and additionally the PREX-II [12] and CREX [13] measurements of the neutron skin thickness of ^{208}Pb and ^{48}Ca respectively.

They found $R_{1.4} = 12.5^{+0.3}_{-0.3}$ km, and $M_{\rm TOV} = 2.27^{+0.08}_{-0.09}\, M_\odot$. These uncertainties are substantially lower than our results. The radius constraint can at least in part be attributed to information from chiral perturbation theory, while the EoS parameterization also results in tighter inference throughout due to less modeling flexibility [45, 71]. Moreover, the use of a single mass distribution places a very strong prior on the masses of the GW events, with the mass of GW170817 for example likely tightly constrained to be within the primary peak of the bimodal mass distribution. Such improved mass measurement will translate to tighter tidal and hence EoS constraints. The impact of pQCD information [63] remains unclear [98, 64], though the prescription used in that analysis is likely informative of $M_{\rm TOV}$.

Other studies have obtained multimessenger constraints on the EOS by combining GW, gamma-ray burst, and kilonova observations surrounding GW170817 with fits to the EM emission from BNS simulations [87, 34, 35, 83]. While there are systematic and statistical uncertainties in the models and observations, these studies infer $R_{1.4}$ and $\Lambda_{1.4}$ broadly consistent with our results.

Caveats

Our findings depend on several analysis choices and assumptions. In the appendices, we examine their impact, and here we summarize our conclusions.

In our main analysis, we assume that selection biases in the radio and X-ray surveys are negligible. In Appendix 7.11 we consider the impact that modeling all galactic NSs with the same bimodal distribution without taking selection effects into account has. Compared to an analysis that fixes the pulsar mass distribution to uniform up to M_{TOV} [70], inference of the mass distribution leads to an EoS that is marginally softer at low densities and marginally stiffer at high densities. As a consequence, the evidence for a violation of the conformal limit $c_s^2 = 1/3$ increases and the lower limit on the maximum speed of sound increases by ~10%.

Data selection further influences our results. In particular, different interpretations of the NICER observations exist in the literature. Given systematic studies on the impact of analysis assumptions on NICER measurements [41, 105] we present results without J0030+0451 and/or J0437-4715 in Appendix 7.10. Excluding J0437-4715 leads to a stiffer inferred EoS with $R_{1.4} = 12.5^{+1.0}_{-0.9}$ km and consistent results with Ref. [70]. Excluding J0030+0451 results in a substantially reduced value of $R_{1.4} = 11.6^{+1.3}_{-0.9}$ km. However, all results are consistent with each other at 90% credibility; see Fig. 7.11 in Appendix 7.10.

Additionally, our main results assume a fixed spin distribution, extending in magnitude up to 0.05 for GW170817 and 0.4 for GW190425. Assumptions about the spin affect mass inference through the mass-spin correlation [38] and hence mass population inference. We explore the impact of restricting the spin of GW190425 further in Appendix 7.12. Imposing an upper limit of 0.05 results in a tighter constraint on its mass ratio and a lower primary mass, which correspondingly reduces the value of $M_{\mathrm{pop},GW}$. Consistency between $M_{\mathrm{pop,GW}}$ and M_{TOV} is reduced with their difference less than $0.77\,M_\odot$ at 90% credibility. Therefore we still find no strong evidence that the TOV and the maximum astrophysical mass are different. Simultaneous inference of the spin distribution [23], along with the EoS and mass distribution, is reserved for future work.

Finally, in this study, we restricted to two subpopulations of NSs: GW observations of BNSs and galactic NSs from radio or X-ray surveys. As a consequence, our mass distribution inference is only predictive below $2.5\,M_\odot$, which we took to be the (fixed) demarcation between NSs and BHs. Extending to higher masses would require simultaneously classifying GW events as BNSs, NSBHs, or BBHs within the analysis framework [43, 30], while introducing a third NS subpopulation associated with the NSBH mergers. This would allow us to treat other GW discoveries, such as GW230529_181500 [2] and GW190814 [7], whose nature is ambiguous. These and further extensions to the joint inference methodology presented here will become necessary to fully explore the interplay between nuclear physics and astrophysics on the properties of NSs as our catalog of informative NS observations increases in size.

7.6 Acknowledgements

We thank Will Farr for helpful discussions on hierarchical inference of subpopulations. We are also grateful to Reed Essick for useful discussions on population modeling with our dataset. We also thank Sylvia Biscoveanu for helpful comments on the manuscript. J.G. would like to gratefully acknowledge the support from the National Science Foundation through the Grant NSF PHY-2207758. I.L. and K.C. acknowledge support from the Department of Energy under award number DE-SC0023101, the Sloan Foundation, and by a grant from the Simons Foundation (MP-SCMPS-00001470). P.L. is supported by the Natural Sciences & Engineering Research Council of Canada (NSERC). Research at Perimeter Institute is supported in part by the Government of Canada through the Department of Innovation, Science and Economic Development and by the Province of Ontario through the Ministry of Colleges and Universities. The authors are grateful for computational resources provided by the LIGO Laboratory and supported by National Science Foundation Grants PHY-0757058 and PHY-0823459. This material is based upon work supported by NSF's LIGO Laboratory which is a major facility fully funded by the National Science Foundation. Software: `bilby` [18, 93], `dynesty` [99], `scipy` [106], `numpy` [80], `matplotlib` [61], `lwp` [46].

7.7 Reweighting scheme for the joint posterior

The joint posterior for the GP EoS ε and the population hyperparameters $\eta = \{\eta_{\mathrm{GW}}, \eta_{\mathrm{EM}}\}$ is [66, 29]

$$p(\varepsilon, \eta | d) = \frac{\mathcal{L}(d|\varepsilon, \eta)\pi(\varepsilon, \eta)}{p(d)}\,, \tag{7.9}$$

where d is the data, $\mathcal{L}(d|\varepsilon, \eta)$ is the likelihood, $\pi(\varepsilon, \eta)$ is the prior, and $p(d)$ is the evidence. We choose a prior of $\pi(\varepsilon, \eta) = \pi(\varepsilon)\pi(\eta)\Theta(M_{\mathrm{TOV}} - M_{\mathrm{pop,EM}})\Theta(M_{\mathrm{TOV}} - M_{\mathrm{pop,GW}})$, where $\pi(\epsilon)$, is the model agnostic prior defined in Refs. [65, 44] (uniform over GP draws), and $\pi(\eta)$ is the prior on the population hyperparameters, as described in the main text (uniform over all parameters). Since the GW and EM datasets are independent, the total likelihood factors into individual likelihoods

$$\mathcal{L}(d|\varepsilon,\eta) = \mathcal{L}_{\mathrm{GW}}(d|\varepsilon,\eta_{\mathrm{GW}})\mathcal{L}_{\mathrm{NICER}}(d|\varepsilon,\eta_{\mathrm{EM}})\mathcal{L}_{\mathrm{PSR}}(d|\varepsilon,\eta_{\mathrm{EM}})\,,$$

given in Eqs. (7.3), (7.6), and (7.8) respectively.

We evaluate the likelihood $\mathcal{L}(d|\varepsilon,\eta)$ with a reweighting scheme based on a simpler lower-dimensional EoS model ε_0, details about which are given in Appendix 7.8. We first obtain samples from the joint posterior for ε_0 and η using standard stochastic sampling [18].

$$p_0(\varepsilon_0,\eta|d) = \frac{\mathcal{L}_0(d|\varepsilon_0,\eta)\pi_0(\varepsilon_0,\eta)}{p_0(d)}\,. \tag{7.10}$$

We then use the marginal mass distribution posterior

$$p_0(\eta|d) = \int p_0(\varepsilon_0,\eta|d)d\varepsilon_0\,, \tag{7.11}$$

as a proposal distribution to rewrite Eq. (7.9) as

$$p(\varepsilon,\eta|d) \propto \mathcal{L}(d|\varepsilon,\eta)\frac{\pi(\eta)\Theta(M_{\mathrm{TOV}}-M_{\mathrm{pop}})}{p_0(\eta|d)}p_0(\eta|d)\pi(\varepsilon)\,, \tag{7.12}$$

where we have dropped the normalization $p(d)$ and defined $\Theta(M_{\mathrm{TOV}}-M_{\mathrm{pop}}) \equiv \Theta(M_{\mathrm{TOV}}-M_{\mathrm{pop,EM}})\Theta(M_{\mathrm{TOV}}-M_{\mathrm{pop,GW}})$. Reweighting includes

1. Compute a Kernel Density Estimate (KDE) of $p_0(\eta|d)$ so that we can directly evaluate the density for each value of η.

2. Draw samples $EoS \sim \pi(\varepsilon)$ and $\eta \sim p_0(\eta|d)$. If $M_{\mathrm{TOV}} < M_{\mathrm{pop,EM}}$ or $M_{\mathrm{TOV}} < M_{\mathrm{pop,GW}}$, reject the sample.

3. For accepted (ε,η) samples compute the weight

$$w = \mathcal{L}(d|\varepsilon,\eta)\frac{\pi(\eta)}{p_0(\eta|d)}\,. \tag{7.13}$$

   The term $p_0(\eta|d)$ is computed with the KDE from step #1 and the likelihood $\mathcal{L}(d|\varepsilon,\eta)$ is computed with a Monte Carlo sum over individual-event posterior samples.

4. Each sample (ε,η) is a weighted draw from the joint posterior $p(\varepsilon,\eta|d)$ with weight w.

In practice, we consider the EM likelihood for the two EM datasets

$$\mathcal{L}(d_{\mathrm{EM}}|\varepsilon, \eta_{\mathrm{EM}}) = \mathcal{L}(d_{\mathrm{NICER}}|\varepsilon, \eta_{\mathrm{EM}}) \times \mathcal{L}(d_{\mathrm{PSR}}|\varepsilon, \eta_{\mathrm{EM}}) \,, \tag{7.14}$$

and the combined likelihood

$$\mathcal{L}(d|\varepsilon, \eta) = \mathcal{L}(d_{\mathrm{EM}}|\varepsilon, \eta_{\mathrm{EM}}) \times \mathcal{L}(d_{\mathrm{GW}}|\varepsilon, \eta_{\mathrm{GW}}) \,, \tag{7.15}$$

from Eq. (7.12). In order to calculate the likelihood for the GW population parameters η_{GW}, we approximate

$$\begin{aligned}&\mathcal{L}(d|\eta_{\mathrm{GW}}) = \\ &\int \mathcal{L}(d_{\mathrm{EM}}|\eta_{\mathrm{EM}}, \varepsilon)\mathcal{L}(d_{\mathrm{GW}}|\eta_{\mathrm{GW}}, \varepsilon)\pi(\eta_{\mathrm{EM}}, \varepsilon) dEoS\, d\eta_{\mathrm{EM}}\end{aligned} \tag{7.16}$$

with the Monte Carlo sum:

$$\begin{aligned}\mathcal{L}(d|\eta_{\mathrm{GW}}) \approx \sum_{EoS\sim\pi(\varepsilon)} &\mathcal{L}(d_{\mathrm{GW}}|\eta_{\mathrm{GW}}, \varepsilon)\times \\ &\Big[\sum_{\eta_{\mathrm{EM}}\sim p_0(\eta_{\mathrm{EM}})} \frac{\mathcal{L}(d_{\mathrm{EM}}|\eta_{\mathrm{EM}}, \varepsilon)}{p_0(\eta_{\mathrm{EM}}|d)}\pi(\eta_{\mathrm{EM}}|\varepsilon)\Big] \,.\end{aligned} \tag{7.17}$$

The likelihood for the EM population parameters is obtained by by swapping GW $\leftrightarrow$ EM in Eq. (7.17).

Similarly, we compute the likelihood for the EoS ε as

$$\begin{aligned}\mathcal{L}(d|\varepsilon) \approx &\sum_{\eta_{\mathrm{GW}}\sim p_0(\eta_{\mathrm{GW}})} \frac{\mathcal{L}(d_{\mathrm{GW}}|\eta_{\mathrm{GW}}, \varepsilon)}{p_0(\eta_{\mathrm{GW}}|d)}\pi(\eta_{\mathrm{GW}}|\varepsilon)\times \\ &\sum_{\eta_{\mathrm{EM}}\sim p_0(\eta_{\mathrm{EM}})} \frac{\mathcal{L}(d_{\mathrm{EM}}|\eta_{\mathrm{EM}}, \varepsilon)}{p_0(\eta_{\mathrm{EM}}|d)}\pi(\eta_{\mathrm{EM}}|\varepsilon) \,.\end{aligned} \tag{7.18}$$

7.8 Approximate lower-dimensional EoS model

The reweighting scheme of Appendix 7.7 utilizes a lower-dimensional EoS model ε_0 that gets marginalized away in Eq. (7.11), solely for constructing an efficient proposal distribution for the hyperparameters η. The goal of including ε_0 in the first place is to avoid potential systematic biases in $p_0(\eta|d)$ if inferred without any reference to an EoS [57]. Such biases would make it an ineffective proposal distribution for the reweighting of Eq. (7.12). Our requirement for ε_0 is therefore that it can be evaluated efficiently and that it roughly captures typical EoS behaviors. Existing parametric models such as the piecewise-polytropic [88], spectral [73], or speed-of-sound [100, 58] models could play this role. However, we find that something even simpler suffices.

We take advantage of the simple relation between the NS moment-of-inertia I and mass m [111, 47] for hadronic EoSs. For EoSs without rapid changes in the speed of sound [47],

$$\frac{d\ln I}{d\ln m} \sim 1.6 \pm O(10^{-2})\,. \tag{7.19}$$

We therefore define ε_0 with a linear relationship between $\ln I$ and $\ln m$:

$$\ln I = a \ln m + b\,, \tag{7.20}$$

where the free parameters a and b define a specific EoS. From the $I(m)$ relation we can obtain $\Lambda(m)$ (used for analyzing GW data) and $R(m)$ (used for analyzing X-ray data) with the I-Love [110] and C-Love [109, 28] universal relations respectively. Since the model does not have a miscrophysics interpretation, it does not self-consistently lead to a maximum-mass solution. Instead we define its TOV mass as $\Lambda(M_{\text{TOV}}) = \Lambda_{\text{thresh}} = \exp(1.89)$ which empirically produces reasonable values for M_{TOV},

We find that this model is inexpensive to sample and accurate enough that that it leads to an improved reweighting efficiency. However, it would not be a reliable model for EoS inference due to its simplistic nature.

7.9 Method validation

We demonstrate the validity of the reweighting scheme described in Appendix 7.7 with simulated GW data. We simulate BNS observations from a uniform mass distribution with $\alpha = 0$ between $1\,M_\odot$ and $M_{\text{pop},GW} = 2.25\,M_\odot$, assigning positions and orientations isotropically, and distances according to a merger rate uniform in the frame of the source across redshifts. Spins are distributed isotropically with uniform magnitudes up to 0.05. Tidal deformabilities are simulated according to a pre-selected EoS from the GP prior with $M_{\text{TOV}} = 2.34\,M_\odot$ and $R_{1.4} = 12.5$ km. After filtering for events that pass a detectability threshold of signal-to-noise ratio above 8, we obtain posterior samples using `bilby` [18]. We then follow the procedure of Appendix 7.7 to compute the joint posterior for the mass distribution and the EoS.

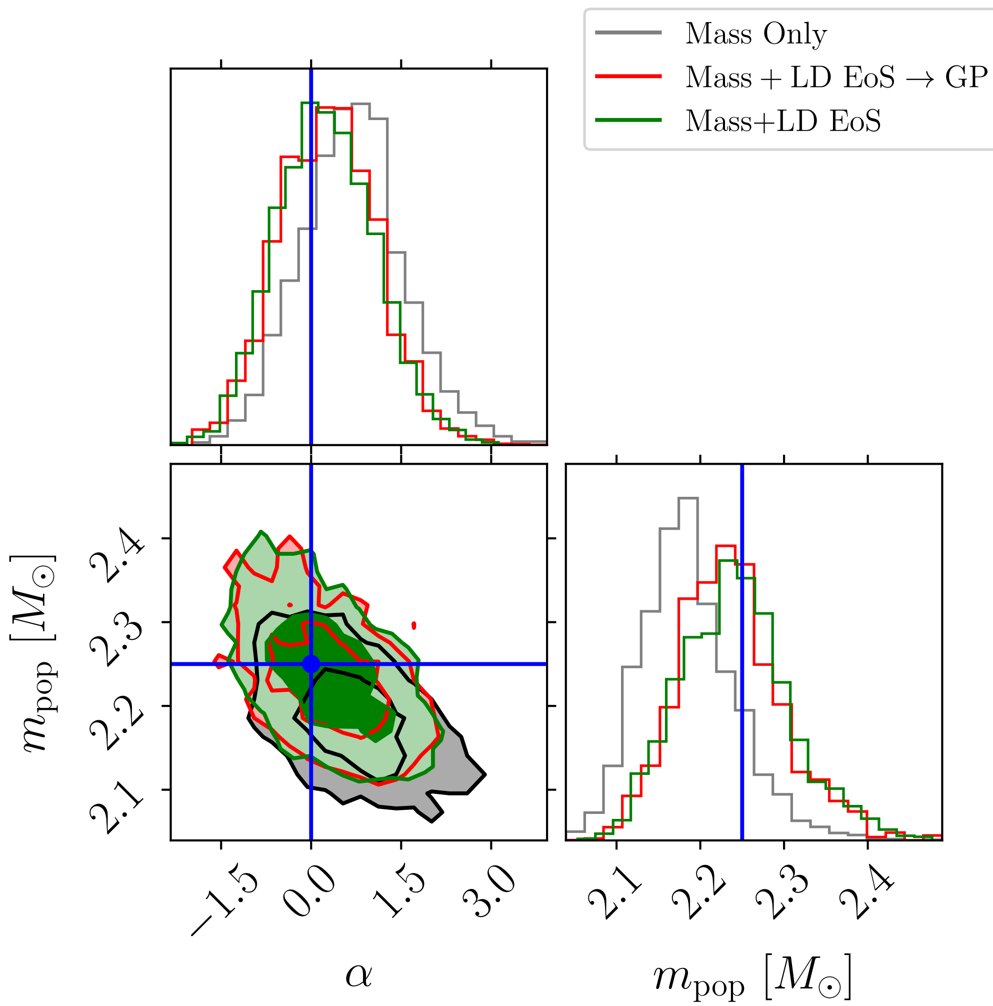

Figure 7.9: One- and two-dimensional posteriors for the mass distribution slope and maximum mass from 23 simulated BNSs. We plot mass-only population inference (grey) which defaults to the individual-event-inference prior on the tidal deformability, joint mass-EoS inference using the lower-dimensional EoS model (green) and the full mass-EoS joint inference with the GP EoS model (red). The reweighting scheme corrects the bias from inferring the mass distribution alone.

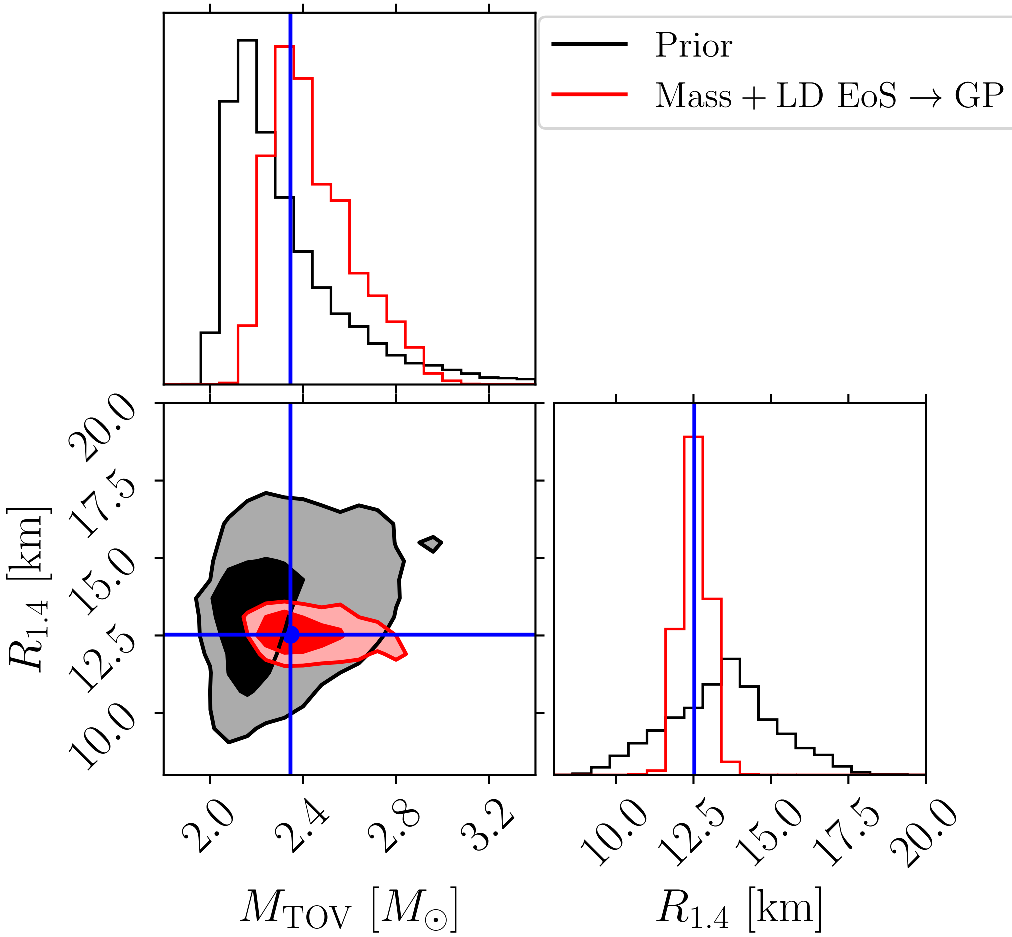

Figure 7.10: One- and two-dimensional posteriors for recovered EoS properties $M_{\rm TOV}$ and $R_{1.4}$ from 23 simulated BNSs. We plot the prior (black) and the result from reweighting to a full mass-EoS joint inference with the GP EoS model (red). The reweighting method is able to recover the true EoS (blue).

In Fig. 7.9 we show the inferred population hyperparameters under three analyses. The first (black) models only the mass distribution, which effectively means that the EoS model defaults to the tidal deformability prior used during sampling. This is selected to be uninformative to avoid restricting the posterior: flat between 0 and 1.5×10^3. Since this is not in reality how the tidal deformabilities of the analyzed objects are distributed, i.e., they follow a single EoS, mass inference is slightly biased [57]. The second analysis (green) corresponds to Eq. (7.11) that infers the mass distribution together with the lower-dimensional EoS model of Appendix 7.8. The inclusion of even this simple EoS model in the inference reduces the bias compared to the true parameters. This posterior is then used as a proposal to

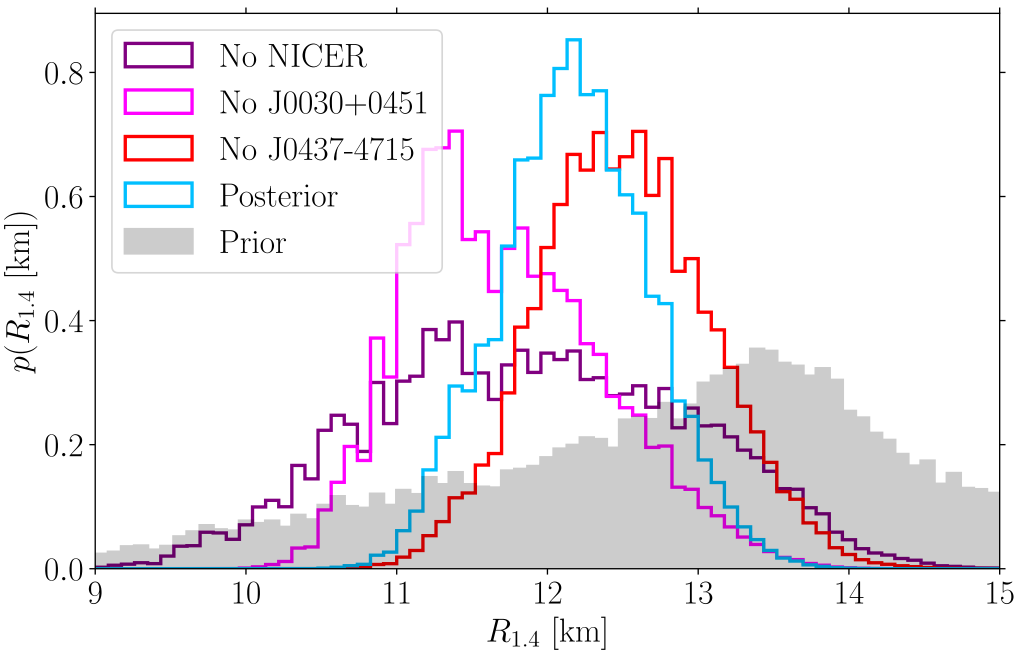

Figure 7.11: The effect of NICER constraints on EoS inference. We plot the prior (grey) and posterior for $R_{1.4}$, the radius of a $1.4\,M_\odot$ NS with different subsets of NICER data: all three pulsars (blue; main text analysis), excluding J0030+0451 (pink), excluding J0437-4715 (red), and excluding all NICER observations (purple).

reweight to the final mass-EoS inference with the GP EoS model (red), which again agrees with the injected values. Figure 7.10 further shows that this procedure can infer the EoS parameters.

7.10 Effect of NICER observations

In this appendix we quantify the impact of NICER observations on our inference. Specifically, we study the impact of J0030+0451 for which there is no concurrent radio-based mass measurement and the hotspot model has a large impact on inference [105] and J0437-4715 for which only one independent analysis is available [32]. We show results for $R_{1.4}$ in Fig. 7.11. Removing any NICER pulsars leads to an increased uncertainty and a shift to lower radii (when removing J0030+0451) or larger radii (when removing J0437-4715). However, all results are consistent with each other at the 90% credible level. Using no NICER data leads to $R_{1.4} = 11.9^{+1.7}_{-1.6}$ km, no J0030+0451 data to $R_{1.4} = 11.6^{+1.3}_{-0.9}$ km, and no J0437-4715 data to $R_{1.4} = 12.5^{+1.0}_{-0.9}$ km.

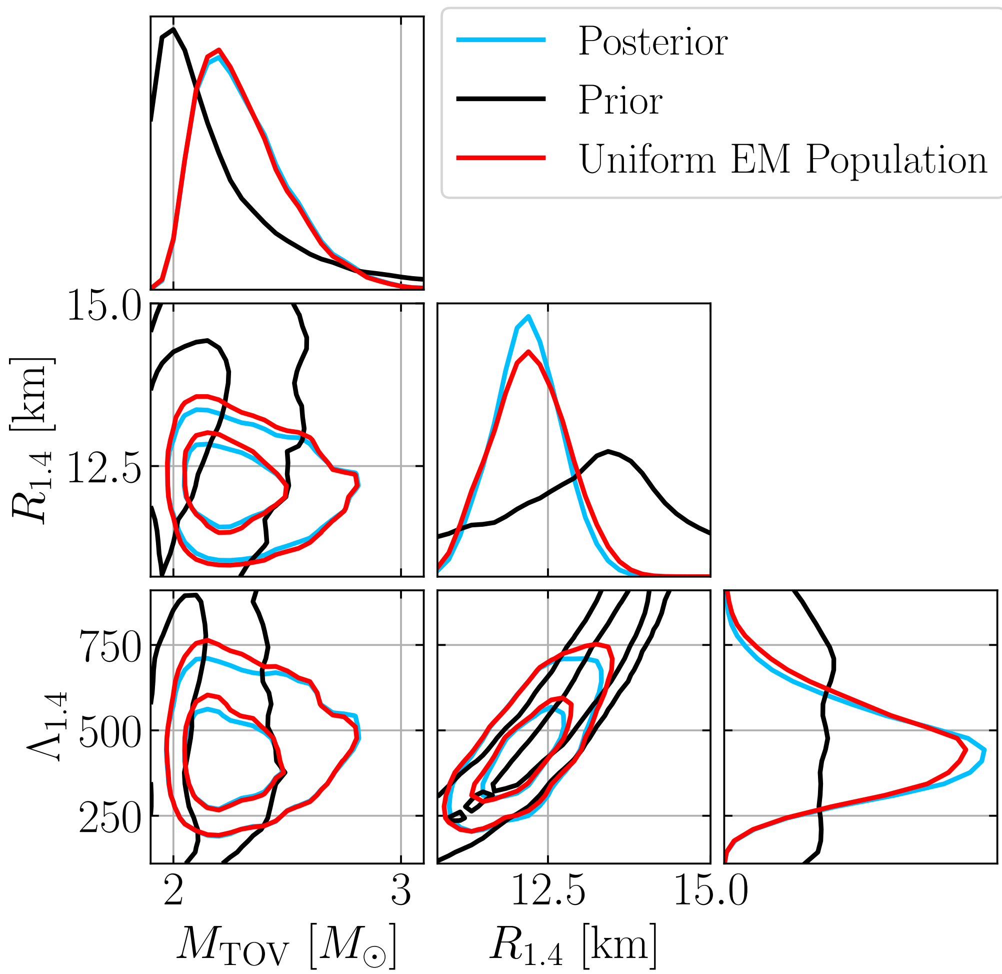

Figure 7.12: Impact of the EM population mass modeling on EoS inference. We plot the prior (black), the posterior from the full analysis (blue; same as Fig. 7.3), and the posterior when the EM mass distribution is uniform and independent of the EoS for J0030+0451 and J0437-4571 and uniform up to the TOV maximum mass of the EoS for J0740+6620 and J0348+0432. The posteriors are similar.

7.11 Uniform pulsar population

Since selection effects for pulsar radio surveys are not well quantified, it is not clear how the observed distribution of NS masses differs from the true distribution. To examine the impact of the observed EM population inference, we repeat the analysis using the approach of Ref. [70] for the EM population: it depends only on the EoS, and not on additional population hyperparameters. The GW population is still modeled with a truncated powerlaw per Sec. 7.2. We neglect all pulsars that do not contribute directly to the EoS (due to low mass) as well as spider pulsars for consistency with Ref. [70]. The EM data now include only J0030+0451 and J0437-4715 [76, 32] with a uniform mass distribution in $[1.0-1.9]\,M_\odot$, and J0740+6620 and J0438+0432 [77, 16] with a uniform mass distribution in $[1.0-M_{\rm TOV}]\,M_\odot$, with $M_{\rm TOV}$ given by the EoS model. This choice corresponds to a uniform distribution up to the maximum mass allowed by the EoS. Because of this choice, EoSs that predict a larger TOV mass are penalized by an *Occam* penalty for the two high-mass pulsars.

Results are shown in Fig. 7.12, where we find small changes to the inferred EoS quantities. In particular, $M_{\rm TOV}$ is relatively unchanged, $M_{\rm TOV} = 2.27^{+0.41}_{-0.20}\,M_\odot$ under the fixed population, which we attribute to the cancellation of two effects. One the one hand, the Occam penalty favors lower values of $M_{\rm TOV}$ under a fixed population. On the other hand, under the fixed-population scheme, the mass of the heaviest pulsars is not informed by lower-mass pulsars, and therefore ends up higher, which in turn results in a higher $M_{\rm TOV}$. The effect of the Occam penalty and the population-informed mass estimates in practice cancel out. The radius and tidal deformability change somewhat more, $R_{1.4} = 12.2^{+0.9}_{-1.0}$ km, with a $\sim$10% larger uncertainty than the inferred-population case, and $\Lambda_{1.4} = 450^{+247}_{-175}$ being slightly larger than the inferred-population case.

Overall, inferring the EM mass distribution leads to marginally higher $M_{\rm TOV}$ and lower $R_{1.4}$. Put differently, the high-density EoS is marginally stiffer and the low-density EoS is marginally softer. As a consequence, the maximum sound-speed is higher in order to connect the soft(er) low-density EoS to a stiff(er) high-density EoS. This leads to increased support for violation of the conformal limit, $c_s^2 > 1/3$. The natural logarithm of the Bayes factor in favor of conformal violation is $\ln \mathcal{B}^{c_s^2>1/3}_{c_s^2<1/3} = 5.85 \pm 0.30$ for the fixed population model, and $\ln \mathcal{B}^{c_s^2>1/3}_{c_s^2<1/3} = 7.39 \pm 0.52$ when the mass distribution of EM pulsars is inferred.

7.12 Low spin assumption for GW190425

Assumptions about the spin of GW190425 have an effect on the inferred component masses [6]. In the main text, we assume that the NSs in GW190425 can have dimensionless spin magnitudes up to 0.4. However, other studies assume NSs have spins 0.05, motivated by the spin distribution of pulsars in binary systems expected to merge within a Hubble time [112]. In Fig. 7.13, we present results with a low-spin assumption for GW190425, enforcing the same assumption in the sensitivity estimates as well. We find $M_{\mathrm{TOV}} = 2.26^{+0.39}_{-0.21}\,M_{\odot}$ and $M_{\mathrm{pop},GW} = 1.79^{+0.32}_{-0.1}\,M_{\odot}$. As GW190425 is not the main observation informing M_{TOV}, it values is consistent with the main analysis. However, as the low-spin restriction lowers the estimated masses of GW190425 due to the mass-spin correlation, we obtain a lower value for $M_{\mathrm{pop},GW}$, though still consistent with M_{TOV}.

References

[1] J. Aasi et al. "Advanced LIGO". In: *Class. Quant. Grav.* 32 (2015), p. 074001. DOI: 10.1088/0264-9381/32/7/074001. arXiv: 1411.4547 [gr-qc].

[2] A. G. Abac et al. "Observation of Gravitational Waves from the Coalescence of a 2.5 – 4.5 $M_{\odot}$ Compact Object and a Neutron Star". In: (Apr. 2024). arXiv: 2404.04248 [astro-ph.HE].

[3] B. P. Abbott et al. "GW170817: Measurements of neutron star radii and equation of state". In: *Phys. Rev. Lett.* 121.16 (2018), p. 161101. DOI: 10.1103/PhysRevLett.121.161101. arXiv: 1805.11581 [gr-qc].

[4] B. P. Abbott et al. "Properties of the binary neutron star merger GW170817". In: *Phys. Rev. X* 9.1 (2019), p. 011001. DOI: 10.1103/PhysRevX.9.011001. arXiv: 1805.11579 [gr-qc].

[5] B. P. Abbott, R. Abbott, and T. D. et al. Abbott. "GW170817: Observation of Gravitational Waves from a Binary Neutron Star Inspiral". In: *Phys. Rev. Lett.* 119.16, 161101 (Oct. 2017), p. 161101. DOI: 10.1103/PhysRevLett.119.161101. arXiv: 1710.05832 [gr-qc].

[6] B. P. Abbott, R. Abbott, and T. D. et al. Abbott. "GW190425: Observation of a Compact Binary Coalescence with Total Mass $\sim 3.4\ \mathrm{M}_{\odot}$". In: *The Astrophysical Journal Letters* 892.1, L3 (Mar. 2020), p. L3. DOI: 10.3847/2041-8213/ab75f5. arXiv: 2001.01761 [astro-ph.HE].

[7] R. Abbott et al. "GW190814: Gravitational Waves from the Coalescence of a 23 Solar Mass Black Hole with a 2.6 Solar Mass Compact Object". In: *Astrophys. J. Lett.* 896.2 (2020), p. L44. DOI: 10.3847/2041-8213/ab960f. arXiv: 2006.12611 [astro-ph.HE].

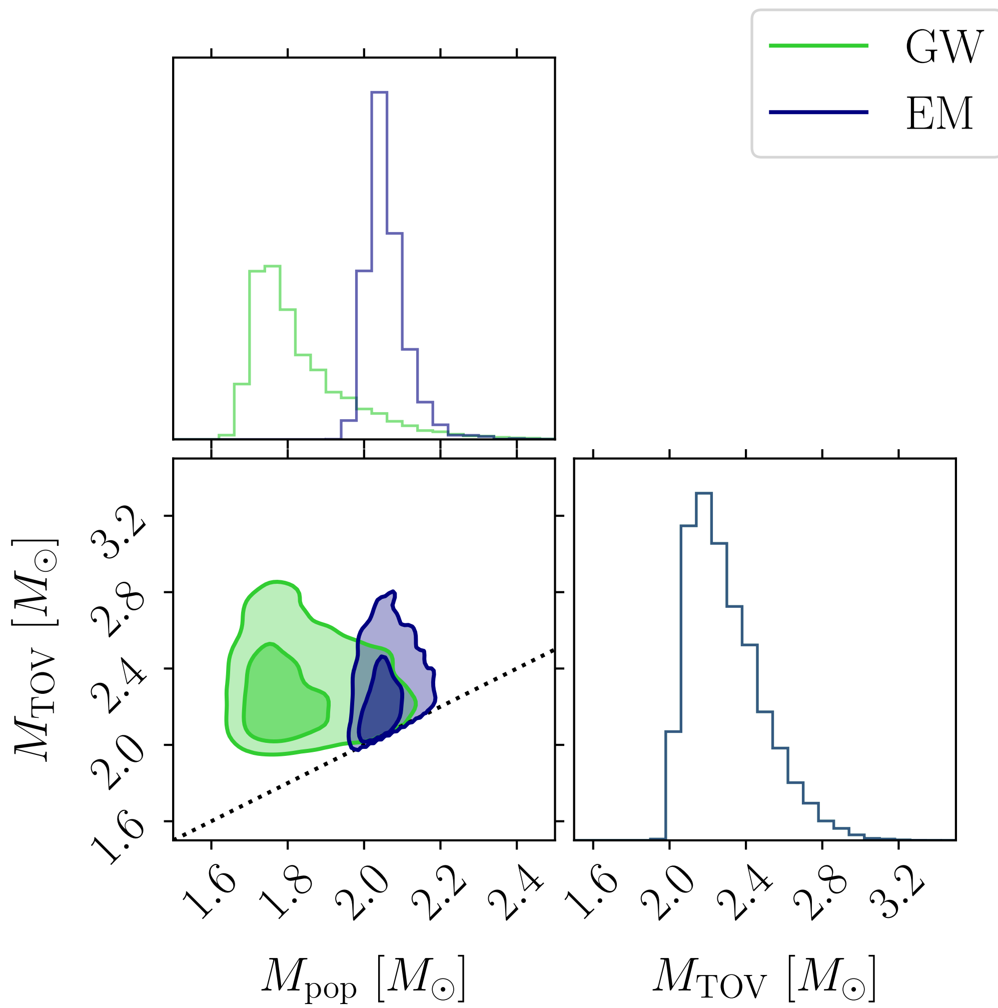

Figure 7.13: Similar to Fig. 7.8 but with a low-spin assumption for GW190425 of < 0.05.

[8] R. Abbott et al. "GWTC-3: Compact Binary Coalescences Observed by LIGO and Virgo during the Second Part of the Third Observing Run". In: *Phys. Rev. X* 13.4 (2023), p. 041039. DOI: 10.1103/PhysRevX.13.041039. arXiv: 2111.03606 [gr-qc].

[9] R. Abbott et al. "Observation of Gravitational Waves from Two Neutron Star–Black Hole Coalescences". In: *Astrophys. J. Lett.* 915.1 (2021), p. L5. DOI: 10.3847/2041-8213/ac082e. arXiv: 2106.15163 [astro-ph.HE].

[10] R. Abbott et al. "Population of Merging Compact Binaries Inferred Using Gravitational Waves through GWTC-3". In: *Phys. Rev. X* 13.1 (2023), p. 011048. DOI: 10.1103/PhysRevX.13.011048. arXiv: 2111.03634 [astro-ph.HE].

[11] F. Acernese et al. "Advanced Virgo: a second-generation interferometric gravitational wave detector". In: *Class. Quant. Grav.* 32.2 (2015), p. 024001. DOI: 10.1088/0264-9381/32/2/024001. arXiv: 1408.3978 [gr-qc].

[12] D. Adhikari et al. "Accurate Determination of the Neutron Skin Thickness of ^{208}Pb through Parity-Violation in Electron Scattering". In: *Phys. Rev. Lett.* 126.17 (2021), p. 172502. DOI: 10.1103/PhysRevLett.126.172502. arXiv: 2102.10767 [nucl-ex].

[13] D. Adhikari et al. "Precision Determination of the Neutral Weak Form Factor of ^{48}Ca". In: (May 2022). arXiv: 2205.11593 [nucl-ex].

[14] T. Akutsu et al. "Overview of KAGRA: Detector design and construction history". In: *PTEP* 2021.5 (2021), 05A101. DOI: 10.1093/ptep/ptaa125. arXiv: 2005.05574 [physics.ins-det].

[15] Justin Alsing, Hector O. Silva, and Emanuele Berti. "Evidence for a maximum mass cut-off in the neutron star mass distribution and constraints on the equation of state". In: *Mon. Not. Roy. Astron. Soc.* 478.1 (2018), pp. 1377–1391. DOI: 10.1093/mnras/sty1065. arXiv: 1709.07889 [astro-ph.HE].

[16] John Antoniadis et al. "A Massive Pulsar in a Compact Relativistic Binary". In: *Science* 340.6131 (2013), p. 1233232. DOI: 10.1126/science.1233232. arXiv: 1304.6875 [astro-ph.HE].

[17] John Antoniadis et al. "The millisecond pulsar mass distribution: Evidence for bimodality and constraints on the maximum neutron star mass". In: (2016). arXiv: 1605.01665 [astro-ph.HE].

[18] Gregory Ashton et al. "BILBY: A User-friendly Bayesian Inference Library for Gravitational-wave Astronomy". In: *The Astrophysical Journal Supplement Series* 241.2, 27 (Apr. 2019), p. 27. DOI: 10.3847/1538-4365/ab06fc. arXiv: 1811.02042 [astro-ph.IM].

[19] Kareem El-Badry et al. "A 1.9 solar-mass neutron star candidate in a 2-year orbit". In: *The Open Journal of Astrophysics* 7, 27 (Apr. 2024), p. 27. DOI: 10.33232/001c.116675. arXiv: 2402.06722 [astro-ph.SR].

[20] Kareem El-Badry et al. "A population of neutron star candidates in wide orbits from Gaia astrometry". In: (July 2024). DOI: 10.33232/001c.121261.

[21] Paulo Bedaque and Andrew W. Steiner. "Sound Velocity Bound and Neutron Stars". In: *PhRvL* 114.3, 031103 (Jan. 2015), p. 031103. DOI: 10.1103/PhysRevLett.114.031103. arXiv: 1408.5116 [nucl-th].

[22] Sylvia Biscoveanu, Philippe Landry, and Salvatore Vitale. "Population properties and multimessenger prospects of neutron star–black hole mergers following GWTC-3". In: *Mon. Not. Roy. Astron. Soc.* 518.4 (2022), pp. 5298–5312. DOI: 10.1093/mnras/stac3052. arXiv: 2207.01568 [astro-ph.HE].

[23] Sylvia Biscoveanu, Colm Talbot, and Salvatore Vitale. "The effect of spin mismodelling on gravitational-wave measurements of the binary neutron star mass distribution". In: *Mon. Not. Roy. Astron. Soc.* 511.3 (2022), pp. 4350–4359. DOI: 10.1093/mnras/stac347. arXiv: 2111.13619 [astro-ph.HE].

[24] Bhaskar Biswas and Stephan Rosswog. "Simultaneously Constraining the Neutron Star Equation of State and Mass Distribution through Multimessenger Observations and Nuclear Benchmarks". In: (Aug. 2024). arXiv: 2408.15192 [astro-ph.HE].

[25] R. Blandford and S. A. Teukolsky. "Arrival-time analysis for a pulsar in a binary system." In: *The Astrophysical Journal* 205 (Apr. 1976), pp. 580–591. DOI: 10.1086/154315.

[26] Slavko Bogdanov et al. "Constraining the Neutron Star Mass–Radius Relation and Dense Matter Equation of State with *NICER*. I. The Millisecond Pulsar X-Ray Data Set". In: *Astrophys. J. Lett.* 887.1 (2019), p. L25. DOI: 10.3847/2041-8213/ab53eb. arXiv: 1912.05706 [astro-ph.HE].

[27] Cosima Breu and Luciano Rezzolla. "Maximum mass, moment of inertia and compactness of relativistic stars". In: *Mon. Not. Roy. Astron. Soc.* 459.1 (2016), pp. 646–656. DOI: 10.1093/mnras/stw575. arXiv: 1601.06083 [gr-qc].

[28] Zack Carson, Andrew W. Steiner, and Kent Yagi. "Constraining nuclear matter parameters with GW170817". In: *Phys. Rev.* D99.4 (2019), p. 043010. DOI: 10.1103/PhysRevD.99.043010. arXiv: 1812.08910 [gr-qc].

[29] Katerina Chatziioannou. "Neutron star tidal deformability and equation of state constraints". In: *Gen. Rel. Grav.* 52.11 (2020), p. 109. DOI: 10.1007/s10714-020-02754-3. arXiv: 2006.03168 [gr-qc].

[30] Katerina Chatziioannou and Will M. Farr. "Inferring the maximum and minimum mass of merging neutron stars with gravitational waves". In: *Phys. Rev. D* 102.6 (2020), p. 064063. DOI: 10.1103/PhysRevD.102.064063. arXiv: 2005.00482 [astro-ph.HE].

[31] Katerina Chatziioannou et al. "Neutron stars and the dense matter equation of state: from microscopic theory to macroscopic observations". In: (July 2024). arXiv: 2407.11153 [nucl-th].

[32] Devarshi Choudhury et al. "A NICER View of the Nearest and Brightest Millisecond Pulsar: PSR J0437-4715". In: (July 2024). arXiv: 2407.06789 [astro-ph.HE].

[33] Sean M. Couch. "The mechanism(s) of core-collapse supernovae". In: *Philosophical Transactions of the Royal Society of London Series A* 375.2105, 20160271 (Sept. 2017), p. 20160271. DOI: 10.1098/rsta.2016.0271.

[34] Michael W. Coughlin et al. “Constraints on the neutron star equation of state from AT2017gfo using radiative transfer simulations”. In: *Mon. Not. Roy. Astron. Soc.* 480.3 (2018), pp. 3871–3878. DOI: 10.1093/mnras/sty2174. arXiv: 1805.09371 [astro-ph.HE].

[35] Michael W. Coughlin et al. “Multimessenger Bayesian parameter inference of a binary neutron star merger”. In: *Mon. Not. Roy. Astron. Soc.* 489.1 (2019), pp. L91–L96. DOI: 10.1093/mnrasl/slz133. arXiv: 1812.04803 [astro-ph.HE].

[36] H. Thankful Cromartie et al. “Relativistic Shapiro delay measurements of an extremely massive millisecond pulsar”. In: *Nature Astron.* 4.1 (2019), pp. 72–76. DOI: 10.1038/s41550-019-0880-2. arXiv: 1904.06759.

[37] Torrey Cullen et al. “Matter Effects on LIGO/Virgo Searches for Gravitational Waves from Merging Neutron Stars”. In: *Class. Quant. Grav.* 34.24 (2017), p. 245003. DOI: 10.1088/1361-6382/aa9424. arXiv: 1708.04359 [gr-qc].

[38] Curt Cutler and Eanna E. Flanagan. “Gravitational waves from merging compact binaries: How accurately can one extract the binary’s parameters from the inspiral wave form?” In: *Phys. Rev. D* 49 (1994), pp. 2658–2697. DOI: 10.1103/PhysRevD.49.2658. arXiv: gr-qc/9402014.

[39] Tim Dietrich et al. “Matter imprints in waveform models for neutron star binaries: Tidal and self-spin effects”. In: *Phys. Rev.* D99.2 (2019), p. 024029. DOI: 10.1103/PhysRevD.99.024029. arXiv: 1804.02235 [gr-qc].

[40] Tim Dietrich et al. “Multimessenger constraints on the neutron-star equation of state and the Hubble constant”. In: *Science* 370.6523 (2020), pp. 1450–1453. DOI: 10.1126/science.abb4317. arXiv: 2002.11355 [astro-ph.HE].

[41] Reed Essick. “Selection Effects in Periodic X-ray Data from Maximizing Detection Statistics”. In: (Nov. 2021). arXiv: 2111.04244 [astro-ph.HE].

[42] Reed Essick and Maya Fishbach. “Ensuring Consistency between Noise and Detection in Hierarchical Bayesian Inference”. In: *Astrophys. J.* 962.2 (2024), p. 169. DOI: 10.3847/1538-4357/ad1604. arXiv: 2310.02017 [gr-qc].

[43] Reed Essick and Philippe Landry. “Discriminating between Neutron Stars and Black Holes with Imperfect Knowledge of the Maximum Neutron Star Mass”. In: *Astrophys. J.* 904.1 (2020), p. 80. DOI: 10.3847/1538-4357/abbd3b. arXiv: 2007.01372 [astro-ph.HE].

[44] Reed Essick, Philippe Landry, and Daniel E. Holz. “Nonparametric Inference of Neutron Star Composition, Equation of State, and Maximum Mass with GW170817”. In: *Phys. Rev. D* 101.6 (2020), p. 063007. DOI: 10.1103/PhysRevD.101.063007. arXiv: 1910.09740 [astro-ph.HE].

[45] Reed Essick et al. “Direct Astrophysical Tests of Chiral Effective Field Theory at Supranuclear Densities”. In: *Phys. Rev. C* 102.5 (2020), p. 055803. DOI: 10.1103/PhysRevC.102.055803. arXiv: 2004.07744 [astro-ph.HE].

[46] Reed Essick et al. *lwp*. URL: https://git.ligo.org/reed.essick/lwp.

[47] Reed Essick et al. “Phase transition phenomenology with nonparametric representations of the neutron star equation of state”. In: *Phys. Rev. D* 108.4 (2023). I contributed substantially to this study which used nonparametric methods to constrain phase transitions in a nonparametric model of the equation of state. I performed the simulation analyses, developed several diagnostic statistics, and wrote large parts of the text., p. 043013. DOI: 10.1103/PhysRevD.108.043013. arXiv: 2305.07411 [astro-ph.HE].

[48] Yi-Zhong Fan et al. “Maximum gravitational mass MTOV=2.25-0.07+0.08M⊙ inferred at about 3% precision with multimessenger data of neutron stars”. In: *Phys. Rev. D* 109.4 (2024), p. 043052. DOI: 10.1103/PhysRevD.109.043052. arXiv: 2309.12644 [astro-ph.HE].

[49] Will M. Farr. “Accuracy Requirements for Empirically Measured Selection Functions”. In: *Research Notes of the AAS* 3.5 (May 2019), p. 66. ISSN: 2515-5172. DOI: 10.3847/2515-5172/ab1d5f. URL: http://dx.doi.org/10.3847/2515-5172/ab1d5f.

[50] Will M. Farr and Katerina Chatziioannou. “A Population-Informed Mass Estimate for Pulsar J0740+6620”. In: *Research Notes of the American Astronomical Society* 4.5, 65 (May 2020), p. 65. DOI: 10.3847/2515-5172/ab9088. arXiv: 2005.00032 [astro-ph.GA].

[51] Nicholas Farrow, Xing-Jiang Zhu, and Eric Thrane. “The mass distribution of Galactic double neutron stars”. In: *Astrophys. J.* 876.1 (2019), p. 18. DOI: 10.3847/1538-4357/ab12e3. arXiv: 1902.03300 [astro-ph.HE].

[52] Lee S. Finn. “Detection, measurement and gravitational radiation”. In: *Phys. Rev. D* 46 (1992), pp. 5236–5249. DOI: 10.1103/PhysRevD.46.5236. arXiv: gr-qc/9209010.

[53] Maya Fishbach, Daniel E. Holz, and Will M. Farr. “Does the Black Hole Merger Rate Evolve with Redshift?” In: *Astrophys. J. Lett.* 863.2 (2018), p. L41. DOI: 10.3847/2041-8213/aad800. arXiv: 1805.10270 [astro-ph.HE].

[54] Ryan J. Foley et al. “Updated Parameter Estimates for GW190425 Using Astrophysical Arguments and Implications for the Electromagnetic Counterpart”. In: *Mon. Not. Roy. Astron. Soc.* 494.1 (2020), pp. 190–198. DOI: 10.1093/mnras/staa725. arXiv: 2002.00956 [astro-ph.HE].

[55] E. Fonseca et al. “Refined Mass and Geometric Measurements of the High-mass PSR J0740+6620”. In: *Astrophys. J. Lett.* 915.1 (2021), p. L12. DOI: 10.3847/2041-8213/ac03b8. arXiv: 2104.00880 [astro-ph.HE].

[56] Paulo Cesar Carvalho Freire et al. "Eight New Millisecond Pulsars in NGC 6440 and NGC 6441". In: *Astrophys. J.* 675 (2008), p. 670. DOI: 10.1086/526338. arXiv: 0711.0925 [astro-ph].

[57] Jacob Golomb and Colm Talbot. "Hierarchical Inference of Binary Neutron Star Mass Distribution and Equation of State with Gravitational Waves". In: *Astrophys. J.* 926.1 (2022), p. 79. DOI: 10.3847/1538-4357/ac43bc. arXiv: 2106.15745 [astro-ph.HE].

[58] S. K. Greif et al. "Equation of state constraints from nuclear physics, neutron star masses, and future moment of inertia measurements". In: *Astrophys. J.* 901.2 (2020), p. 155. DOI: 10.3847/1538-4357/abaf55. arXiv: 2005.14164 [astro-ph.HE].

[59] Ming-Zhe Han et al. "Is GW190425 consistent with being a neutron star−black hole merger?" In: *Astrophys. J. Lett.* 891.1 (2020), p. L5. DOI: 10.3847/2041-8213/ab745a. arXiv: 2001.07882 [astro-ph.HE].

[60] Jason W. T. Hessels et al. "A Radio Pulsar Spinning at 716 Hz". In: *Science* 311.5769 (Mar. 2006), pp. 1901–1904. DOI: 10.1126/science.1123430. arXiv: astro-ph/0601337 [astro-ph].

[61] J. D. Hunter. "Matplotlib: A 2D graphics environment". In: *Computing in Science & Engineering* 9.3 (2007), pp. 90–95. DOI: 10.1109/MCSE.2007.55.

[62] Vassiliki Kalogera and Gordon Baym. "The maximum mass of a neutron star". In: *Astrophys. J. Lett.* 470 (1996), pp. L61–L64. DOI: 10.1086/310296. arXiv: astro-ph/9608059.

[63] Oleg Komoltsev and Aleksi Kurkela. "How Perturbative QCD Constrains the Equation of State at Neutron-Star Densities". In: *Phys. Rev. Lett.* 128.20 (2022), p. 202701. DOI: 10.1103/PhysRevLett.128.202701. arXiv: 2111.05350 [nucl-th].

[64] Oleg Komoltsev et al. "Equation of state at neutron-star densities and beyond from perturbative QCD". In: *Phys. Rev. D* 109.9 (2024), p. 094030. DOI: 10.1103/PhysRevD.109.094030. arXiv: 2312.14127 [nucl-th].

[65] Philippe Landry and Reed Essick. "Nonparametric inference of the neutron star equation of state from gravitational wave observations". In: *Phys. Rev. D* 99.8 (2019), p. 084049. DOI: 10.1103/PhysRevD.99.084049. arXiv: 1811.12529 [gr-qc].

[66] Philippe Landry, Reed Essick, and Katerina Chatziioannou. "Nonparametric constraints on neutron star matter with existing and upcoming gravitational wave and pulsar observations". In: *Phys. Rev. D* 101.12 (2020), p. 123007. DOI: 10.1103/PhysRevD.101.123007. arXiv: 2003.04880 [astro-ph.HE].

[67] Philippe Landry and Jocelyn S. Read. "The Mass Distribution of Neutron Stars in Gravitational-wave Binaries". In: *Astrophys. J. Lett.* 921.2 (2021), p. L25. DOI: 10.3847/2041-8213/ac2f3e. arXiv: 2107.04559 [astro-ph.HE].

[68] J. M. Lattimer and M. Prakash. "Neutron star structure and the equation of state". In: *Astrophys. J.* 550 (2001), p. 426. DOI: 10.1086/319702. arXiv: astro-ph/0002232.

[69] James M. Lattimer and Madappa Prakash. "The Equation of State of Hot, Dense Matter and Neutron Stars". In: *Phys. Rept.* 621 (2016), pp. 127–164. DOI: 10.1016/j.physrep.2015.12.005. arXiv: 1512.07820 [astro-ph.SR].

[70] Isaac Legred et al. "Impact of the PSR J0740 + 6620 radius constraint on the properties of high-density matter". In: *Phys. Rev. D* 104 (6 Sept. 2021). I led this study on the impact of the the NICER mass-radius constraint on the mllisecond x-ray pulsar J0740+6620 on nonparametric equation of state constraints. I developed software, some of which was contributed by other collaborators from previous projects, ran the analysis, and co-wrote the manuscript., p. 063003. DOI: 10.1103/PhysRevD.104.063003. URL: https://link.aps.org/doi/10.1103/PhysRevD.104.063003.

[71] Isaac Legred et al. "Implicit correlations within phenomenological parametric models of the neutron star equation of state". In: *Phys. Rev. D* 105.4 (2022). I led this study which compared parametric to nonparametric methods of inferring the equation of state. I developed a substantial amount of software, ran the analysis, and co-wrote the manuscript., p. 043016. DOI: 10.1103/PhysRevD.105.043016. arXiv: 2201.06791 [astro-ph.HE].

[72] LIGO Scientific Collaboration. "Parameter estimation sample release for GW190425". In: *https://dcc.ligo.org/LIGO-P2000026/public* (2020). URL: https://dcc.ligo.org/LIGO-P2000026/public.

[73] Lee Lindblom. "Spectral Representations of Neutron-Star Equations of State". In: *Phys. Rev. D* 82 (2010), p. 103011. DOI: 10.1103/PhysRevD.82.103011. arXiv: 1009.0738 [astro-ph.HE].

[74] R. N. Manchester. "Millisecond Pulsars, their Evolution and Applications". In: *J. Astrophys. Astron.* 38 (2017), p. 42. DOI: 10.1007/s12036-017-9469-2. arXiv: 1709.09434 [astro-ph.HE].

[75] Ilya Mandel, Will M. Farr, and Jonathan R. Gair. "Extracting distribution parameters from multiple uncertain observations with selection biases". In: *Mon. Not. Roy. Astron. Soc.* 486.1 (2019), pp. 1086–1093. DOI: 10.1093/mnras/stz896. arXiv: 1809.02063 [physics.data-an].

[76] M. C. Miller et al. "PSR J0030+0451 Mass and Radius from *NICER* Data and Implications for the Properties of Neutron Star Matter". In: *Astrophys.*

J. Lett. 887.1 (2019), p. L24. DOI: 10.3847/2041-8213/ab50c5. arXiv: 1912.05705 [astro-ph.HE].

[77] M. C. Miller et al. “The Radius of PSR J0740+6620 from NICER and XMM-Newton Data”. In: (May 2021). arXiv: 2105.06979 [astro-ph.HE].

[78] M. Coleman Miller, Cecilia Chirenti, and Frederick K. Lamb. “Constraining the equation of state of high-density cold matter using nuclear and astronomical measurements”. In: (2019). arXiv: 1904.08907 [astro-ph.HE].

[79] Elias R. Most et al. “A lower bound on the maximum mass if the secondary in GW190814 was once a rapidly spinning neutron star”. In: *Mon. Not. Roy. Astron. Soc.* 499.1 (2020), pp. L82–L86. DOI: 10.1093/mnrasl/slaa168. arXiv: 2006.14601 [astro-ph.HE].

[80] Travis Oliphant. *NumPy: A guide to NumPy*. USA: Trelgol Publishing. [Online; accessed <today>]. 2006–. URL: http://www.numpy.org/.

[81] J.R. Oppenheimer and G.M. Volkoff. “On Massive neutron cores”. In: *Phys. Rev.* 55 (1939), pp. 374–381. DOI: 10.1103/PhysRev.55.374.

[82] F. Özel and P. Freire. “Masses, Radii, and the Equation of State of Neutron Stars”. In: *Ann. Rev. Astron. Astrophys.* 54 (2016), pp. 401–440. DOI: 10.1146/annurev-astro-081915-023322. arXiv: 1603.02698 [astro-ph.HE].

[83] Peter T. H. Pang et al. “An updated nuclear-physics and multi-messenger astrophysics framework for binary neutron star mergers”. In: *Nature Commun.* 14.1 (2023), p. 8352. DOI: 10.1038/s41467-023-43932-6. arXiv: 2205.08513 [astro-ph.HE].

[84] Peter T. H. Pang et al. “Nuclear-Physics Multi-Messenger Astrophysics Constraints on the Neutron-Star Equation of State: Adding NICER’s PSR J0740+6620 Measurement”. In: (May 2021). arXiv: 2105.08688 [astro-ph.HE].

[85] G. Raaijmakers et al. “Constraining the dense matter equation of state with joint analysis of NICER and LIGO/Virgo measurements”. In: *Astrophys. J. Lett.* 893.1 (2020), p. L21. DOI: 10.3847/2041-8213/ab822f. arXiv: 1912.11031 [astro-ph.HE].

[86] G. Raaijmakers et al. “Constraints on the dense matter equation of state and neutron star properties from NICER’s mass-radius estimate of PSR J0740+6620 and multimessenger observations”. In: (May 2021). arXiv: 2105.06981 [astro-ph.HE].

[87] David Radice et al. “GW170817: Joint Constraint on the Neutron Star Equation of State from Multimessenger Observations”. In: *Astrophys. J.* 852.2 (2018), p. L29. DOI: 10.3847/2041-8213/aaa402. arXiv: 1711.03647 [astro-ph.HE].

[88] Jocelyn S. Read et al. “Constraints on a phenomenologically parameterized neutron-star equation of state”. In: *Phys. Rev. D* 79 (2009), p. 124032. doi: 10.1103/PhysRevD.79.124032. arXiv: 0812.2163 [astro-ph].

[89] Clifford E. Rhoades Jr. and Remo Ruffini. “Maximum mass of a neutron star”. In: *Phys. Rev. Lett.* 32 (1974), pp. 324–327. doi: 10.1103/PhysRevLett.32.324.

[90] Thomas E. Riley et al. “A *NICER* View of PSR J0030+0451: Millisecond Pulsar Parameter Estimation”. In: *Astrophys. J. Lett.* 887.1 (2019), p. L21. doi: 10.3847/2041-8213/ab481c. arXiv: 1912.05702 [astro-ph.HE].

[91] Thomas E. Riley et al. “A NICER View of the Massive Pulsar PSR J0740+6620 Informed by Radio Timing and XMM-Newton Spectroscopy”. In: (May 2021). arXiv: 2105.06980 [astro-ph.HE].

[92] Mallory S. E. Roberts. “Surrounded by spiders! New black widows and redbacks in the Galactic field”. In: *Neutron Stars and Pulsars: Challenges and Opportunities after 80 years*. Ed. by Joeri van Leeuwen. Vol. 291. Mar. 2013, pp. 127–132. doi: 10.1017/S174392131202337X. arXiv: 1210.6903 [astro-ph.HE].

[93] I. M. Romero-Shaw et al. “Bayesian inference for compact binary coalescences with bilby: validation and application to the first LIGO–Virgo gravitational-wave transient catalogue”. In: *Mon. Not. Roy. Astron. Soc.* 499.3 (2020), pp. 3295–3319. doi: 10.1093/mnras/staa2850. arXiv: 2006.00714 [astro-ph.IM].

[94] Isobel M. Romero-Shaw et al. “On the origin of GW190425”. In: *Mon. Not. Roy. Astron. Soc.* 496.1 (2020), pp. L64–L69. doi: 10.1093/mnrasl/slaa084. arXiv: 2001.06492 [astro-ph.HE].

[95] Nathan Rutherford et al. “Constraining the Dense Matter Equation of State with New NICER Mass–Radius Measurements and New Chiral Effective Field Theory Inputs”. In: *Astrophys. J. Lett.* 971.1 (2024), p. L19. doi: 10.3847/2041-8213/ad5f02. arXiv: 2407.06790 [astro-ph.HE].

[96] Jayana A. Saes, Raissa F. P. Mendes, and Nicolás Yunes. “Approximately universal I-Love-<cs2> relations for the average neutron star stiffness”. In: *Phys. Rev. D* 110.2 (2024), p. 024011. doi: 10.1103/PhysRevD.110.024011. arXiv: 2402.05997 [gr-qc].

[97] Mohammadtaher Safarzadeh, Enrico Ramirez-Ruiz, and Edo Berger. “Does GW190425 require an alternative formation pathway than a fast-merging channel?” In: *Astrophys. J.* 900.1 (2020), p. 13. doi: 10.3847/1538-4357/aba596. arXiv: 2001.04502 [astro-ph.HE].

[98] Rahul Somasundaram, Ingo Tews, and Jérôme Margueron. “Perturbative QCD and the Neutron Star Equation of State”. In: (Apr. 2022). arXiv: 2204.14039 [nucl-th].

[99] Joshua S. Speagle. "DYNESTY: a dynamic nested sampling package for estimating Bayesian posteriors and evidences". In: *Monthly Notices of the Royal Astronomical Society* 493.3 (Apr. 2020), pp. 3132–3158. DOI: 10.1093/mnras/staa278. arXiv: 1904.02180 [astro-ph.IM].

[100] Ingo Tews et al. "Constraining the speed of sound inside neutron stars with chiral effective field theory interactions and observations". In: *Astrophys. J.* 860.2 (2018), p. 149. DOI: 10.3847/1538-4357/aac267. arXiv: 1801.01923 [nucl-th].

[101] Eric Thrane and Colm Talbot. "An introduction to Bayesian inference in gravitational-wave astronomy: Parameter estimation, model selection, and hierarchical models". In: *Publications of the Astronomical Society of Australia* 36 (2019). ISSN: 1448-6083. DOI: 10.1017/pasa.2019.2. URL: http://dx.doi.org/10.1017/pasa.2019.2.

[102] Vaibhav Tiwari. "Estimation of the Sensitive Volume for Gravitational-wave Source Populations Using Weighted Monte Carlo Integration". In: *Class. Quant. Grav.* 35.14 (2018), p. 145009. DOI: 10.1088/1361-6382/aac89d. arXiv: 1712.00482 [astro-ph.HE].

[103] Richard C. Tolman. "Static solutions of Einstein's field equations for spheres of fluid". In: *Phys. Rev.* 55 (1939), pp. 364–373. DOI: 10.1103/PhysRev.55.364.

[104] J. Veitch et al. "Parameter estimation for compact binaries with ground-based gravitational-wave observations using the LALInference software library". In: *Phys. Rev. D* 91.4 (2015), p. 042003. DOI: 10.1103/PhysRevD.91.042003. arXiv: 1409.7215 [gr-qc].

[105] Serena Vinciguerra et al. "An Updated Mass–Radius Analysis of the 2017–2018 NICER Data Set of PSR J0030+0451". In: *Astrophys. J.* 961.1 (2024), p. 62. DOI: 10.3847/1538-4357/acfb83. arXiv: 2308.09469 [astro-ph.HE].

[106] Pauli Virtanen et al. "SciPy 1.0: Fundamental Algorithms for Scientific Computing in Python". In: *Nature Methods* 17 (2020), pp. 261–272. DOI: 10.1038/s41592-019-0686-2.

[107] Salvatore Vitale et al. "Inferring the Properties of a Population of Compact Binaries in Presence of Selection Effects". In: 45 (2022). Ed. by Cosimo Bambi, Stavros Katsanevas, and Konstantinos D. Kokkotas, p. 45. DOI: 10.1007/978-981-15-4702-7_45-1.

[108] Daniel Wysocki et al. "Inferring the neutron star equation of state simultaneously with the population of merging neutron stars". In: (2020). arXiv: 2001.01747 [gr-qc].

[109] Kent Yagi and Nicolas Yunes. "Approximate Universal Relations for Neutron Stars and Quark Stars". In: *Phys. Rept.* 681 (2017), pp. 1–72. DOI: 10.1016/j.physrep.2017.03.002. arXiv: 1608.02582 [gr-qc].

[110] Kent Yagi and Nicolas Yunes. "I-Love-Q". In: *Science* 341 (2013), pp. 365–368. DOI: 10.1126/science.1236462. arXiv: 1302.4499 [gr-qc].

[111] Kent Yagi and Nicolas Yunes. "I-Love-Q Relations in Neutron Stars and their Applications to Astrophysics, Gravitational Waves and Fundamental Physics". In: *Phys. Rev. D* 88.2 (2013), p. 023009. DOI: 10.1103/PhysRevD.88.023009. arXiv: 1303.1528 [gr-qc].

[112] Xingjiang Zhu et al. "Inferring the population properties of binary neutron stars with gravitational-wave measurements of spin". In: *Phys. Rev. D* 98 (2018), p. 043002. DOI: 10.1103/PhysRevD.98.043002. arXiv: 1711.09226 [astro-ph.HE].

Chapter 8

SEARCHING FOR BREAKDOWN OF A NUCLEAR THEORY USING NONPARAMETRIC METHODS

[1] Isaac Legred et al. "Nonparametric extensions of nuclear equations of state: probing the breakdown scale of relativistic mean-field theory". In: (May 2025). I led this study which examines how nonparametric models of the equation of state can be used to extend nuclear calculations. I developed the project idea, developed software, performed analyses, and wrote the bulk of the manuscript. arXiv: 2505.07677 [nucl-th].

Abstract

Phenomenological calculations of the properties of dense matter, such as relativistic mean-field theories, represent a pathway to predicting the microscopic and macroscopic properties of neutron stars. However, such theories do not generically have well-controlled uncertainties and may break down within neutron stars. To faithfully represent the uncertainty in this breakdown scale, we develop a hybrid representation of the dense-matter equation of state, which assumes the form of a relativistic mean-field theory at low densities, while remaining agnostic to any nuclear theory at high densities. To achieve this, we use a nonparametric equation of state model to incorporate the correlations of the underlying relativistic mean-field theory equation of state at low pressures and transition to more flexible correlations above some chosen pressure scale. We perform astrophysical inference under various choices of the transition pressure between the theory-informed and theory-agnostic models. We further study whether the chosen relativistic mean-field theory breaks down above some particular pressure and find no such evidence. Using simulated data for future astrophysical observations at about two-to-three times the precision of current constraints, we show that our method can identify the breakdown pressure associated with a potential strong phase transition.

8.1 Introduction

Uncovering the equation of state (EoS) of dense matter is central to understanding neutron stars, bridging nuclear physics and astrophysics [86, 93, 74, 79, 29]. While the EoS is in principle determined entirely by the standard model, in practice, there is currently no perturbative or exact approach to compute the properties of matter in the densest regions of neutron star cores. Therefore, for the purposes of interpreting macroscopic astronomical observables such as neutron star masses and radii, "model-agnostic" representations of the EoS minimize phenomenological model-dependence [72, 47, 78]. However, fully-agnostic approaches can overestimate uncertainties in regions where calculations from models of nuclear matter are reliable, for example, near nuclear saturation density (n_0), where a description of matter with nucleon degrees of freedom is applicable. In addition, extracting detailed microphysical information from model-agnostic approaches is not straightforward, because it is not usually clear what exact microscopic interaction is responsible for determining the EoS at different densities. Certain quantities are not accessible at all, such as the single-particle energies required to compute transport properties [97]. In contrast with model-agnostic strategies, a variety of approaches have been used to model dense matter up to very high densities, but these come with varying degrees of (often difficult to quantify) systematic uncertainty [35, 67, 24, 17, 43].

Chiral effective field theory [111] (χEFT) provides constraints on neutron-rich matter that are systematically improvable, but calculations cannot be extended to the cores of astrophysical neutron stars [104, 41, 106]. χEFT's nature as an effective theory allows us to systematically write down a series of interaction terms and compute an associated truncation uncertainty. However, its validity is limited to densities $\lesssim 2\,n_0$, which does not extend to neutron star cores. Relativistic mean-field theories (RMFTs), in contrast, are usable at densities and temperatures relevant in neutron stars and their mergers [109, 21, 99, 62, 43]. RMFTs are phenomenological, microphysical theories of dense matter based on meson-exchange Lagrangians. We refer to a specific Lagrangian function as a single RMFT. By specifying a set of interaction constants within the RMFT, we generate a particular RMFT model that can be used to compute the corresponding EoS.

Once the functional form of the Lagrangian and the nucleon-meson and meson-meson coupling constants are determined through fits to, e.g., properties of finite nuclei, nuclear matter, and astrophysical observations, e.g. Refs. [54, 103, 11], no further parameters are needed to obtain finite-temperature [12] or out-of-equilibrium [9, 10] properties. The EoS obtained from an RMFT model is also thermodynamically consistent and causal. An RMFT model thus allows us to relate the microscopic properties of dense matter to astrophysical observables of neutron stars such as their masses and radii.

Despite these major advantages, every RMFT also comes with limitations that could lead to a breakdown of the theory, i.e., where the RMFT is no longer a plausible description of nature. RMFTs are not obtained by a controlled expansion and thus do not have an intrinsic breakdown scale and a well-defined error. Furthermore, they rely on the mean-field approximation and describe nucleons as point-like interacting particles. Thus, while an RMFT can be used at arbitrary densities, it might not describe nature above a certain scale. Interpreting neutron star data assuming that the whole EoS (from the star surface to the core) is described by the RMFT model can lead to systematic biases both in macroscopic and microscopic quantities.

We employ the methodology introduced in Essick et al. [50, 49, 48] as a way to avoid such biases and infer the breakdown scale with astrophysical observations. Although we focus on a specific RMFT in this paper, this method is generic and can be applied to any nuclear framework that is expected to become less reliable with increasing density. The key element is the flexibility to choose how model information from the RMFT EoS is used in constructing an EoS prior with which to analyze the data. We achieve this by incorporating information from an RMFT EoS into an otherwise model-agnostic approach for representing the EoS based on Gaussian Processes (GPs). The means and covariances of the GP are modified such that they closely follow RMFT EoSs generated using different choices of model parameters up to some value for the pressure. That pressure corresponds to a choice of a scale up to which we trust the RMFT to describe the properties of dense matter. Beyond that pressure, the GP smoothly transitions from an RMFT-informed kernel to a model-agnostic one. We construct multiple GPs for different choices of this transition pressure. The specific RMFT EoSs we use are fit to χEFT calculations. Therefore, when we incorporate nuclear theory information, the assumptions we make are strictly stronger than those of Refs. [50, 49, 48].

If the true EoS can be described by an RMFT at certain densities but not up to arbitrarily high densities, then we expect this to be discernible using astrophysical observations of neutron stars. We consider gravitational-wave observations of masses and tidal deformabilities [3, 4], X-ray observations of masses and radii [84, 94, 83, 95, 30], and pulsar timing observations of heavy stars [14, 32, 56]. We use a hierarchical inference scheme to infer the EoS under a variety of hypotheses about the breakdown scale of the RMFT framework. We consider both simulated and real astrophysical data, and study the extent to which we can infer the breakdown scale from astrophysical data alone. We find that with current astrophysical constraints, there is no strong evidence in favor of a breakdown of the studied RMFT. Nonetheless, we also find that a breakdown can be approximately identified using observations at around three times the currently available measurement precision if such a breakdown is associated with, e.g., a strong, first-order phase transition.

Using an array of different astrophysical observables targeting different mass ranges is crucial. The primary difference between modeled and model-agnostic approaches is that the former imposes significantly stronger correlations between density scales, which might restrict its ability to fit observations [78]. For example, an RMFT EoS might not be capable to simultaneously explain observations of stars with a typical mass of ($\sim 1.4\,M_{\odot}$) and the highest mass ($\gtrsim 2\,M_{\odot}$) if a strong first-order phase transition causes massive stars to have large, exotic cores. On the other hand, the model-agnostic GP can produce EoSs with very short correlation lengths, able to model arbitrary causal and stable EoSs, including those with phase transitions [78, 51].

The rest of the paper is organized as follows. In Sec. 8.2, we discuss the RMFT EoSs we use in constructing a hybrid agnostic-informed analysis, the construction of model-agnostic and RMFT-informed GP priors, and the details of the hierarchical inference scheme. In Sec. 8.3, we demonstrate that the constructed EoS distributions allow us to identify a breakdown of the RMFT using sufficiently many simulated astrophysical observations. In Sec. 8.4, we discuss the current constraints. We do not find evidence against an RMFT description for the EoS because the uncertainties are substantial. We conclude in Sec. 9.5.

8.2 Methods

We now describe how we construct our hybrid RMFT-informed, model-agnostic GP prior, and infer the EoS using astrophysical data. In Sec. 8.2 we describe how the RMFT EoSs used in this study are generated. In Sec. 8.2 we review the GP EoS prior. In Sec. 8.2 we describe the process of building the hybrid RMFT-informed, model-agnostic GP kernel. Finally, in Sec. 8.2 we discuss intricacies of model selection relevant to the breakdown scale study.

The RMFT EoS set

Like any nuclear model, a specific RMFT depends on a number of ingredients. Firstly, if we choose a model with only nucleons and leptons as fundamental degrees of freedom, the RMFT will not show the appearance of or the transition to new degrees of freedom unless we explicitly construct a transition to a different theory or adjust the particle composition. For example, we can extend an existing theory with neutrons and protons to include strange baryons, delta resonances, or N(1535) resonances [61, 35, 69]. A transition to a completely different theory is also possible, for example, to model a phase of deconfined quark matter [23]. Secondly, the choice of the Lagrangian, including the meson fields that model the strong interaction, is somewhat arbitrary. In principle, there are an infinite number of meson interaction terms that can be included in an RMFT [98]. To avoid overfitting, we choose a widely used Lagrangian density with the least number of coupling constants (seven) that can make predictions consistent with low-energy nuclear physics and, in principle, with astrophysical observations of neutron star structure. We choose a Lagrangian with a functional form identical to the IU-FSU model with seven undetermined coupling constants [54].

Commonly, an RMFT is further constrained by astrophysical observables. However, we do not want to make such an assumption *a priori*, as we would potentially use observations of matter that might not be composed of nucleons at all. Thus, we do not require the RMFT EoSs to support $\sim 2\ M_\odot$ stars. Since in our hybrid approach the RMFT description only holds at low densities, the resulting hybrid EoSs might still be able to produce high mass NSs (see e.g. Ref. [23]).

Even in the absence of a phase transition, at densities a few times nuclear saturation density ($n_0 \approx 0.16\ \mathrm{fm}^{-3}$), a description of dense matter in terms of point-like nucleons is no longer plausible [110]. Since the RMFT does not include, e.g., short-range correlations between the nucleons, this effect can not be captured. Other potential breakdown scenarios of the RMFT include the appearance of inhomogeneous phases like chiral density waves, although this can be modeled with RMFTs [33, 88], or a breakdown of the mean-field approximation where approaches such as Ref. [57] may be needed. In this paper, we focus on nuclear matter consisting of neutrons, protons, and electrons. While muons could be added to the theory, they affect the total pressure at the one percent level [11].

We produce 1109 EoSs using the method described in Ref. [11]. All EoSs come from the same RMFT Lagrangian density with different nucleon-meson and meson-

meson coupling constants. The variation in these seven couplings is due to a fit to the χEFT energy per nucleon uncertainty band in neutron matter. All EoSs are causal, consistent with the saturation properties of isospin-symmetric nuclear matter, and consistent with χEFT at next-to-next-to leading order (N^{2}LO) up to $1.5\,n_0$ [106]. Of the 1109 EoSs, only 90 predict neutron stars with $M \geq 2$ M$_\odot$. This set serves as a fiducial representation of RMFT EoSs. We will occasionally refer to the RMFT EoS set as a "prior", by which we mean taking all EoSs from the set to be equally likely. More details are provided in Appendix 8.7.

The GP EoS prior

The GP EoS distribution is designed to be sufficiently flexible to incorporate information from the RMFT at low pressures while representing a fully model-agnostic EoS distribution at higher pressures. A GP achieves this flexibility by tuning correlations in the EoS between different scales, which are controlled directly by the covariance kernel. As in Refs. [72, 47, 50, 49, 48], we construct a prior which is a mixture of GPs on the variable

$$\phi(\log p) = \ln\left(\frac{1}{c_s^2} - 1\right), \tag{8.1}$$

where $\log p$ is the natural logarithm of the pressure and c_s is the zero-temperature, beta-equilibrated sound-speed (with $c = 1$). To generate an EoS, we sample a GP from the mixture model's mixing fractions and then draw ϕ from the corresponding GP (in practice, we use a finite number of pressure collocation points)

$$\phi(\log p_i) \sim \mathcal{N}(\mu_i, C_i), \tag{8.2}$$

where μ_i and C_i are the mean and covariance associated with the i-th component of the mixture model. For different choices of mean and covariance, each pair gives a prior $\pi(\epsilon|\mathcal{M})$, with ϵ the EoS and $\mathcal{M}$ the underlying choice of model, which corresponds to different assumptions about the EoS distribution. The base EoS prior is "agnostic" in the sense that we use a mixture of many different wide covariances with short correlation lengths. While these distributions are conditioned on nuclear models [72, 47], the choice of EoSs used in the conditioning does not strongly impact the EoS prior [78].

Constructing an RMFT-informed GP prior and hybridization with a model-agnostic GP

We construct EoS priors conditioned on the RMFT EoS distribution up to several maximum (or "transition") pressures as was done in Refs. [50, 49, 48] for χEFT.

However, unlike χEFT, the RMFT is not automatically equipped with theoretical uncertainty estimates. That is, the distribution of RMFT EoSs introduced in Sec. 8.2 does not include any estimate of systematic uncertainty from the fact that the RMFT Lagrangian includes a subset of all the possible terms. In contrast, χEFT systematic uncertainties are constructed from estimates of the truncation error introduced by only retaining terms up to a certain order in the EFT expansion. Therefore, at densities greater than saturation, the RMFT EoS distribution depends on the strategy we use to generate coupling constants from fitting inferred experimental results and *ab initio* calculations; see Sec. 8.2.

With these caveats in mind, we adopt the distribution of RMFT EoSs from Sec. 8.2 and extend them with flexible, model-agnostic EoS representations above the transition pressure. The marginal pressure distribution from the RMFT EoS is significantly skew-right and, therefore, is not well-modeled by a single GP. Instead we emulate the RMFT EoS set with a mixture of three GPs. Specifically, we separate the RMFT EoS set into three populations based on the marginal distribution of pressures at high densities; individual RMFT EoS tend to approach a constant c_s and therefore naturally separate into different populations at high densities and pressures. For each of these populations, we construct a separate GP using the sample mean and covariance of the RMFT EoSs. As a result, each GP contains strong intra-density correlations which are representative of the underlying subset of the RMFT EoS distribution it emulates; these correlations enforce smoothness in the resulting EoS realizations. A mixture over subpopulations is constructed by weighting each subpopulation's GP based on the number of RMFT EoS that belong to the corresponding subpopulation. Compared to Refs. [50, 49, 48], the distribution of RMFT EoS is more complicated and therefore requires a mixture of GPs instead of a single GP. Readers who are interested in other approaches to emulate EoS models with GPs may also be interested in Refs. [41, 42].

Equipped with a GP emulator for the RMFT EoS distribution, we then construct priors that closely follow the RMFT EoS distribution at low pressures but transition to more flexible model-agnostic priors above a transition pressure. References [50, 49, 48] achieved a similar effect by conditioning a model-agnostic prior on a χEFT emulator as if the emulator was an additional (noisy) observation. Nevertheless, we modify the approach here. Instead of conditioning an agnostic GP on the RMFT EoS emulator as if it was an additional observation, we instead construct a GP that exactly follows the RMFT EoS emulator at low pressures and then condition the

Table 8.1: Transition pressures for the hybrid RMFT-agnostic GPs in two different units.

p_t/c^2 [g/cm^3]	10^{11}	10^{12}	3×10^{12}	10^{13}	3×10^{13}	10^{14}
p_t/c^2[MeV/fm^3]	0.056	0.56	1.7	5.6	17	56

agnostic GP at higher pressures. The new procedure guarantees that the resulting GP will only support smooth functions at low densities if the RMFT EoS emulator only supports smooth functions at low densities. It can be shown that the two approaches are equivalent if the (co)variance in the RMFT EoS emulator is very small compared to the (co)variance in the agnostic GP. See Appendix 8.8 for details.

For emulators and agnostic priors that are mixture models of GPs (with N and M elements, respectively), we construct a new GP for each of the $N \times M$ pairs of GPs from the emulator and agnostic processes. We form a mixture model over all possible combinations with weights equal to the product of the individual weights within the emulator and agnostic mixtures. See Appendix 8.8 for more discussion. An implementation of this procedure is publicly available [44].

Using this procedure, we construct several priors that follow the RMFT EoS emulator up to different transition pressures, p_t. We consider six transition pressures at values given in Table 8.1. The two largest transition pressures correspond to approximately the central pressures of 0.6 and 1.4 $M_\odot$ stars respectively (see, e.g., Fig. 8.1's bottom two panels.). For each transition pressure, we generate 30,000 samples from the GP prior, composed of three sets of 10,000 EoS each drawn from GPs conditioned on hadronic, quarkyonic, and hyperonic EoSs [72, 47].

One advantage of using a low-density model which derives from microphysics is that it is possible to extract information about the underlying nuclear physics. We adopt the method of extracting the symmetry parameters of isospin-symmetric nuclear matter near saturation density from Refs. [49, 48]. We consider the symmetry energy at saturation $J = S(n_0)$, and the so-called slope of the symmetry energy $L = 3n_0 dS/dn|_{n_0}$. The nuclear energy per particle is expanded locally around nuclear saturation density in terms of proton-neutron asymmetry $(n_n - n_p)/(n_n + n_p) = (1 - 2Y_p)$ with Y_p the proton fraction[1] and the baryon number density n:

$$\frac{E_{\text{nuc}}}{A}(n, Y_p) = \frac{E_{\text{SNM}}(n)}{A} + S(n)(1 - 2Y_p)^2\,, \tag{8.3}$$

[1] The proton fraction is also (in our case) the charge fraction and the electron fraction as we assume the only charged leptons are electrons. We do not expect the addition of muons to substantially alter the recovered parameters [49, 48].

where E_{SNM} is the energy of symmetric nuclear matter, which we additionally expand as

$$E_{\mathrm{SNM}}(n) = E_{\mathrm{bind}} + K_0 \left(\frac{n - n_0}{3n_0} \right)^2 . \tag{8.4}$$

We sample E_{bind}, K_0, and n_0 from Gaussian distributions with mean and variance fit from the RMFT EoS set and given in Table 8.2. The nuclear energy per particle is equal to the total energy minus the contribution from electrons, which is known given the baryon number density and proton fraction

$$\frac{E_{\mathrm{nuc}}}{A}(n, Y_p) = \frac{\varepsilon(n, Y_p) - \varepsilon_e(n, Y_p)}{n} , \tag{8.5}$$

where ε and ε_e are the total and electron energy densities respectively. In particular, if Y_p is taken to be the beta-equilibrium charge fraction (Y_p^β), then $\varepsilon(n, Y_p^\beta)$ is precisely the beta-equilibrium energy density, which is computed for each GP draw. Therefore, if the beta-equilibrium charge fraction were known, then $E_{\mathrm{nuc}}(n, Y_p^\beta)$ would also be known, as would (rearranging Eq. (8.3))

$$S(n) = \left(\frac{E_{\mathrm{nuc}}}{A}(n, Y_p^\beta) - \frac{E_{\mathrm{SNM}}}{A}(n) \right) / (1 - 2Y_p^\beta)^2 . \tag{8.6}$$

The beta-equilibrium charge fraction can be found from setting $\mu_n = \mu_p + \mu_e$ (assuming a zero neutrino chemical potential); see Refs. [65, 49, 48] for details. From this we compute

$$J \equiv S(n_0) , \tag{8.7}$$

$$L \equiv 3n_0 \frac{dS(n)}{dn}\bigg|_{n=n_0} , \tag{8.8}$$

$$K_{\mathrm{sym}} \equiv 9n_0^2 \frac{d^2S(n)}{dn^2}\bigg|_{n=n_0} , \tag{8.9}$$

for each GP draw. We additionally verify that for our set of RMFT EoS draws, this procedure produces reasonable estimates for the (already known) symmetry parameters.

The Hierarchical Inference Scheme

Given an EoS prior and astrophysical data, we infer the EoS following Refs. [47, 73, 26]. In this subsection, we provide a brief overview and discuss considerations in interpreting Bayes factors. The key ingredients are

- $\pi(\epsilon|\mathcal{M})$: The prior on EoS ϵ, which depends upon the model $\mathcal{M}$.

Table 8.2: Mean and standard deviation of the parameters of symmetric matter used in computing the symmetry energy and its derivatives. These represent the mean and standard deviation of the corresponding parameters from our RMFT EoS distribution.

Parameter	μ	σ
n_0 [fm^{-3}]	0.1568	0.0017
E_{bind} [MeV]	-15.983	0.046
K_0 [MeV]	228	25

- $\mathcal{L}(d_i|\epsilon)$: The likelihood, which is the probability of receiving astrophysical data d_i given an EoS ϵ.

The posterior probability of a given EoS is

$$P(\epsilon|\{d_i\}, \mathcal{M}) = \frac{\prod_i \mathcal{L}(d_i|\epsilon)\pi(\epsilon|\mathcal{M})}{\mathcal{Z}(\{d_i\}|\mathcal{M})}\,, \tag{8.10}$$

where d_i represents the set of all observed data, and

$$Z(\{d_i\}_i|\mathcal{M}) = \int \pi(\epsilon|\mathcal{M}) \prod_i \mathcal{L}(d_i|\epsilon) d\epsilon\,, \tag{8.11}$$

is the evidence for model $\mathcal{M}$. In this work d_i could stand for data resulting from X-ray pulse profile measurements of neutron star mass-radii, pulsar timing observations of heavy neutron star masses, and gravitational-wave observations of neutron star masses and tidal deformabilities. Given two models $\mathcal{M}_1$ and $\mathcal{M}_2$, the Bayes factor compares their relative fit to the data

$$\mathcal{B}^{\mathcal{M}_1}_{\mathcal{M}_2} = \frac{\mathcal{Z}(\{d_i\}|\mathcal{M}_1)}{\mathcal{Z}(\{d_i\}|\mathcal{M}_2)}\,. \tag{8.12}$$

The Bayes factor is the average likelihood of one model relative to another, where the average is taken over the entire prior volume of each model. A model whose prior includes regions with a low likelihood will have a low Bayes factor relative to a model that excludes such regions. Nonparametric, model-agnostic models are explicitly designed to explore such regions in the name of flexibility. Indeed, most samples from a model-agnostic GP prior will have very low likelihood. To minimize this effect, we compute Bayes factors after conditioning the EoS prior distributions on heavy pulsar observations. This effectively removes EoSs that have too low a maximum mass, and provides a proxy for only including "astrophysically plausible" EoSs within the prior.

Table 8.3: The saturation and symmetry parameters of nuclear matter for the RMFT EoS we use to generate simulated data. E_B is the binding energy per nucleon in isospin-symmetric nuclear matter at saturation density, n_0; κ is the incompressibility of nuclear matter at n_0; J is the symmetry energy, the difference between the binding energy per nucleon of neutron matter and isospin-symmetric nuclear matter, evaluated at n_0; L characterizes how the symmetry energy varies with density; m^* is the Dirac in-medium nucleon mass at n_0.

n_0 [fm^{-3}]	E_B [MeV]	κ [MeV]	J [MeV]	L [MeV]	m^* [MeV]
0.158	-16	244	34	52.9	685

Excluding these EoSs prevents conclusions from being driven mainly by EoSs with masses much less than $2\,M_\odot$, instead targeting the likelihood of astrophysically plausible EoSs sampled from each model [50, 77, 51, 85].

8.3 Verification with simulated astrophysical observations

We demonstrate our methodology by using simulated astrophysical observations to infer the EoS, and in tandem, infer the breakdown scale of the underlying RMFT.

Simulated Data

We verify the hybrid RMFT-agnostic GPs with simulated data. To do this, we generate simulated observations using two EoSs. The first EoS is consistent with the distribution of RMFT EoSs at all density scales [11]; its saturation parameters are listed in Table 8.3. The second EoS is constructed to be inconsistent with the RMFT EoSs. At an energy density of $\varepsilon/c^2 = 1.7 m_N n_0 \approx 260\,\text{MeV}$, a strong phase transition with a latent heat of $\Delta\varepsilon/\varepsilon = 0.4$ is inserted, after which there is a constant speed of sound $c_s^2 = 0.8$. This transition happens at a baryon density of about $1.5\,n_0$, and a pressure of $\sim 12\,\text{MeV}/\text{fm}^3$.

We generate simulated data that represent potential observations via radio pulsar timing, x-ray pulse-profile modeling, and gravitational-wave observations. Starting with radio timing, we assume that pulsars are formed with masses up to the Tolman-Oppenheimer-Volkoff (TOV) maximum mass [86, 107], and the mass distribution is uniform. We simulate radio timing observations [100, 19], assuming a factor of ~ 2 reduction in uncertainty compared to current constraints [34, 14, 32]. See Table 8.4 for the masses and uncertainties for the RMFT EoS and Table 8.5 for the phase-transition case. In particular, we assume two heavy pulsars with well-measured masses.

For X-ray data, we simulate four sources. We assume that uncertainties are uncorrelated and Gaussian on the mass and radius, which is reasonable for sources with independently measured masses from radio timing, such as J0740+6620 [83, 95] and J0437-4715 [30]. This assumption further improves as more photon counts and better background estimates are included, [39, 96], indicating that for future observations nearly-Gaussian uncertainties are plausible. We sample the uncertainties on mass and radius from a uniform distribution. The uncertainties in the most optimistic cases are $\sim$ 2-3$\times$ smaller than current measurements. See Table 8.4 for the simulated X-ray sources for the EoS consistent with the RMFT and Table 8.5 for the EoS with a phase transition.

Table 8.4: Simulated neutron star observations for the RMFT EoS. Values given represent mean and 90% credible intervals.

Neutron Star	Mass ($M_\odot$)	Radius (km)
Radio 1	2.10 ± 0.03	NA
Radio 2	2.08 ± 0.13	NA
X-ray 0	1.20 ± 0.04	12.29 ± 1.25
X-ray 1	1.37 ± 0.11	12.26 ± 0.25
X-ray 2	1.45 ± 0.45	12.24 ± 0.69
X-ray 3	1.96 ± 0.43	11.77 ± 1.10

Table 8.5: Simulated neutron star observations for the phase-transition EoS; values given represent mean and 90% credible intervals.

Neutron Star	Mass ($M_\odot$)	Radius (km)
Radio 1	2.42 ± 0.06	NA
Radio 2	2.44 ± 0.07	NA
X-ray 0	1.20 ± 0.35	11.63 ± 1.08
X-ray 1	1.37 ± 0.02	11.70 ± 0.15
X-ray 2	1.45 ± 0.43	11.73 ± 0.94
X-ray 3	1.96 ± 0.00	11.93 ± 1.31

For gravitational waves, we perform full parameter estimation, because even at moderate signal-to-noise ratio (SNR) it is empirically not straightforward to construct an analytic expression for the posterior distribution on the relevant parameters (*e.g.* the distributions on the effective tidal deformability and mass ratio, $\tilde{\Lambda}$ and q are not approximately Gaussian [5, 6]). We recover posterior distributions on the quantities $m_1, m_2, \Lambda_1, \Lambda_2$, the primary and secondary masses, and primary and secondary tidal deformabilities, respectively. We then choose two sources sampled randomly from the set of recovered sources. We display these parameters for the RMFT EoS injection in Table 8.6. The second source is very similar to GW170817, both in terms of parameters and in terms of measurement precision. We display the corresponding parameters for the RMFT-PT EoS injections in Table 8.7. Further gravitational-wave injections are used in Appendix 8.9, which also includes a detailed description of simulation study.

Table 8.6: Simulated gravitational wave parameters including mass (m_1 and m_2), tidal deformability (Λ_1 and Λ_2), and SNR, for the RMFT EoS.

Binary	m_1 $[M_\odot]$	m_2 $[M_\odot]$	Λ_1	Λ_2	SNR
GW 0	1.5	1.18	266.6	1139.45	15.0
GW 1	1.49	1.17	273.1	1189.81	32.5

Table 8.7: Simulated gravitational wave parameters from the phase-transition EoS. Same as Table 8.6.

Binary	m_1 $[M_\odot]$	m_2 $[M_\odot]$	Λ_1	Λ_2	SNR
GW 0	1.26	1.09	473.89	1011.61	10.7
GW 1	1.23	1.2	542.88	613.32	26.5

Simulated inference results

Recovering an RMFT EoS

We begin with the case of an EoS that is consistent with the RMFT EoSs. We display the RMFT EoS used for the simulations and 200 fair draws from the posterior for prior distributions at four values of the transition pressures in Fig. 8.1. We additionally plot 1000 fair draws from each prior distribution. First, looking at the prior distributions, as more information from the underlying RMFT model is included, moving from lower to higher transition pressure (left to right and top to bottom panels), the EoS distribution is much smoother and narrower below the transition pressure. Conversely, above the transition, the prior is wider and less regular, with rapid changes to the radius with mass being much more common.

Moving on to the posteriors, for all transition pressures, the simulated EoS (light blue) is recovered correctly, with an uncertainty that increases for lower transition pressures. This is expected because priors with lower transition pressure incorporate less information from the underlying RMFT and its strong model constraints. This effect is most severe where the simulated astrophysical observations are least

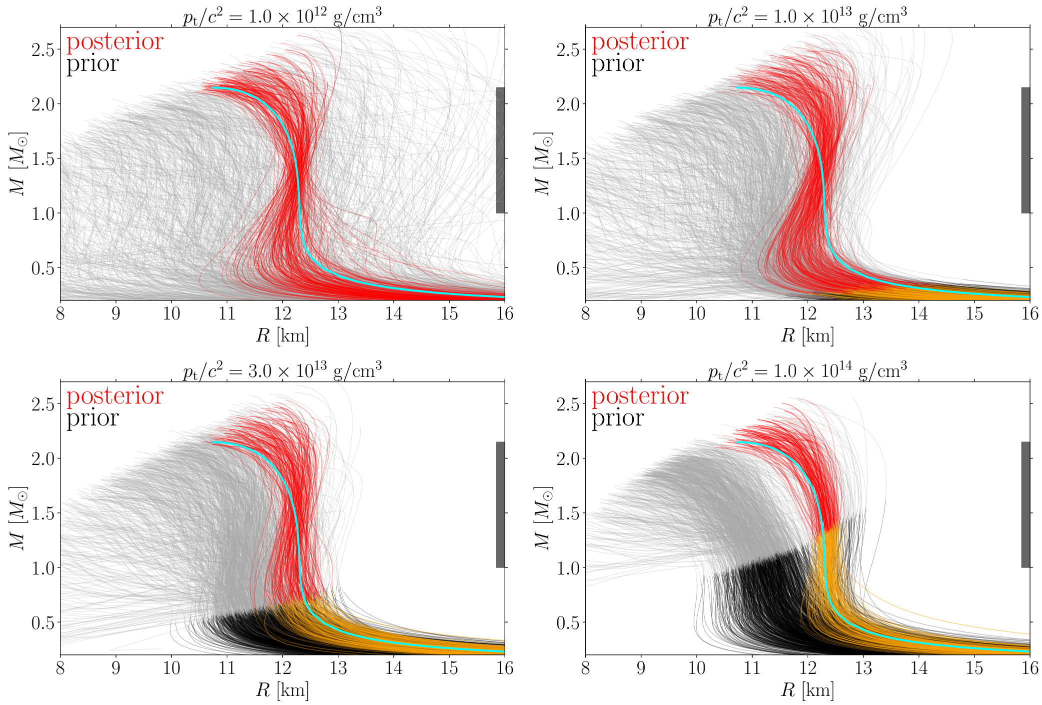

Figure 8.1: In gray/black, we show M-R curves of fair draw EoS from RMFT-agnostic hybrid distributions which transition at various densities, shown by subplot titles. Stars fully informed by the RMFT are shown in black, while stars with cores that have transitioned to the agnostic model are shown in gray. In cyan, we display the EoS used to generate simulated observations. In red/orange, we show samples from the posterior. In this case, points in orange are stars fully described by the RMFT, while points in red represent stars with cores that have transitioned to the agnostic model. On the right y-axis of each panel, we display a gray bar from $M \in (M_\odot, M_{\mathrm{TOV}})$ where M_{TOV} is the TOV maximum mass of the simulation EoS. This represents the approximate range of NS masses used in astrophysical inference.

informative, for example, at very high and low neutron star masses. The uncertainty in radius of a 2 $M_\odot$, for instance, is $\sim$ 1.25 km with the model agnostic prior at 90% credibility.

For comparison, we analyze the same data with the RMFT EoS prior set itself and display the results in Fig. 8.2. Comparing to Fig. 8.1, and in particular the bottom right panel which shows the distribution that carries the most RMFT information, we see that the overall structure of the RMFT EoS distribution is well captured by the GP emulator. This includes a "bimodality" in the mass-radius relation distribution for the RMFT EoS set. This bimodality arises because of the choice of initial fitting parameters, as multiple combinations of the RMFT parameters are able to effectively reproduce the properties of symmetric and pure neutron matter, which have very

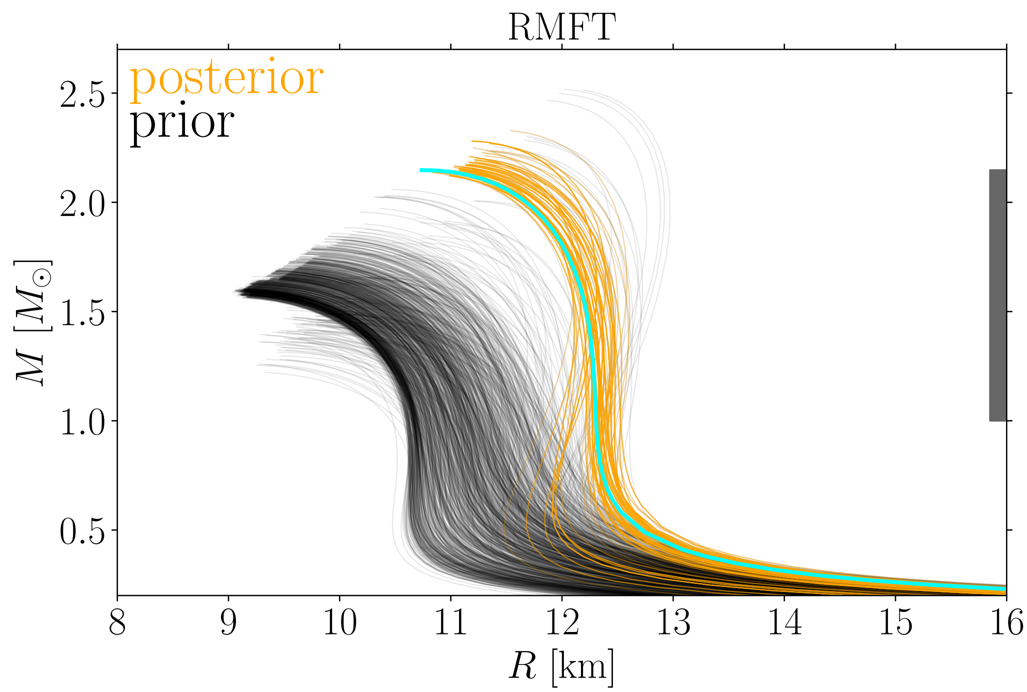

Figure 8.2: Inference with the RMFT prior itself. Same as Fig. 8.1, but with the set of RMFT EoS samples with uniform probability used as prior distribution. Since the RMFT EoSs are informed by the RMFT at all densities, we color the posterior orange and the prior black for all neutron stars, in analogy with Fig. 8.1.

different behavior at high density; see Appendix 8.7.

For each transition pressure, p_t, we compute the evidence $\mathcal{Z}(\{d_i\}|\mathcal{M} = p_t)$. This is to say, each GP conditioned at a different transition pressure forms a model $\mathcal{M}$, and we take a transition pressure of $p/c^2 = 10^{11}\mathrm{g/cm^3}$ as a fiducial "agnostic value" since this incorporates the least information from the underlying RMFT. We then compute each model's Bayes factor relative to the agnostic model and plot them in Fig. 8.3. There is a general preference for transitioning from RMFT to the more flexible GP at higher pressure, but it is weak with Bayes factors of 2-4. Under the RMFT EoS prior, the Bayes factor relative to the agnostic model is higher, ~ 11. This is a consequence of our choice to condition the Bayes factors on the existence of heavy pulsars. EoSs with $M_{tOV} \gtrsim 2.0$ effectively all appear in the posterior. Therefore, conditioned on the existence of heavy pulsars, the RMFT is more highly preferred than any agnostic model. In contrast, at $p_t/c^2 = 3 \times 10^{13}\ \mathrm{g/cm^3}$ there is a dip in the evidence. This is because at this transition pressure, EoSs with low values of $R_{1.4} \sim 11.5\,\mathrm{km}$, which are inconsistent with the radius of the injected EoS ($R_{1.4} \sim 12.5\,\mathrm{km}$) are able to stiffen to reach $M_{tOV} \gtrsim 2.1\,M_\odot$. Therefore low-radius

EoSs are common even after conditioning on the existence of massive pulsars in this case, and their marginal likelihood is lower. If we remove this conditioning, then the RMFT is no longer substantially preferred relative to the agnostic model, and conditioning at $p_t/c^2 = 10^{14}\,\mathrm{g/cm^3}$ is actually disfavored relative to the agnostic model despite the fact that the simulation EoS is itself an RMFT EoS.

The above discussion highlights the large dependence of Bayes Factors on relatively minor analysis choices, which is why we deem Bayes Factors of $O(10)$ as inconclusive. Nonetheless, the features of Fig. 8.3 are still meaningful; for example, the trend of increasing Bayes factor with transition pressure can be attributed to removing prior volume that is inconsistent with the RMFT, and will be assigned low-likelihood. If two models can describe the data equally well but one has less prior volume than the other (e.g., a model with a low transition pressure vs. a model whose prior is more tightly concentrated around the RMFT), the former is preferred. The Bayes factor for such a preference, though, is a fixed number, even in the limit of infinite measurement precision, since it is determined by the ratio of the probability density functions of each of the EoS priors at the simulation EoS. Therefore, depending on what this value is, we may or may not ever have decisive evidence in favor of the RMFT over the agnostic model.

Finally, we consider the symmetry energy parameters. We compute the posterior for J and L, the symmetry energy at saturation and the slope of the symmetry energy at saturation, respectively, and display the results in Fig. 8.4. The true symmetry parameters are comfortably recovered at 90% credibility regardless of the choice of transition pressure. As we increase the transition pressure, the prior and posterior become narrower and approach the result of using the RMFT EoS set itself. This is consistent with strengthening correlations between symmetry parameters and astrophysical observables as the RMFT is trusted to higher and higher pressures. These posteriors all incorporate the same data and have very similar marginal priors on the symmetry parameters. Therefore differences between them are driven solely by differences in the higher-dimensional EoS prior distributions, as also observed in Refs. [49, 48, 78].

Inferring a phase-transition EoS

We now switch to the case of a simulated EoS which is not derived from an RMFT model, and repeat the analysis of Sec. 8.3 using the phase-transition EoS described in Sec. 8.3. We display fair draws from the prior and posterior distributions on the

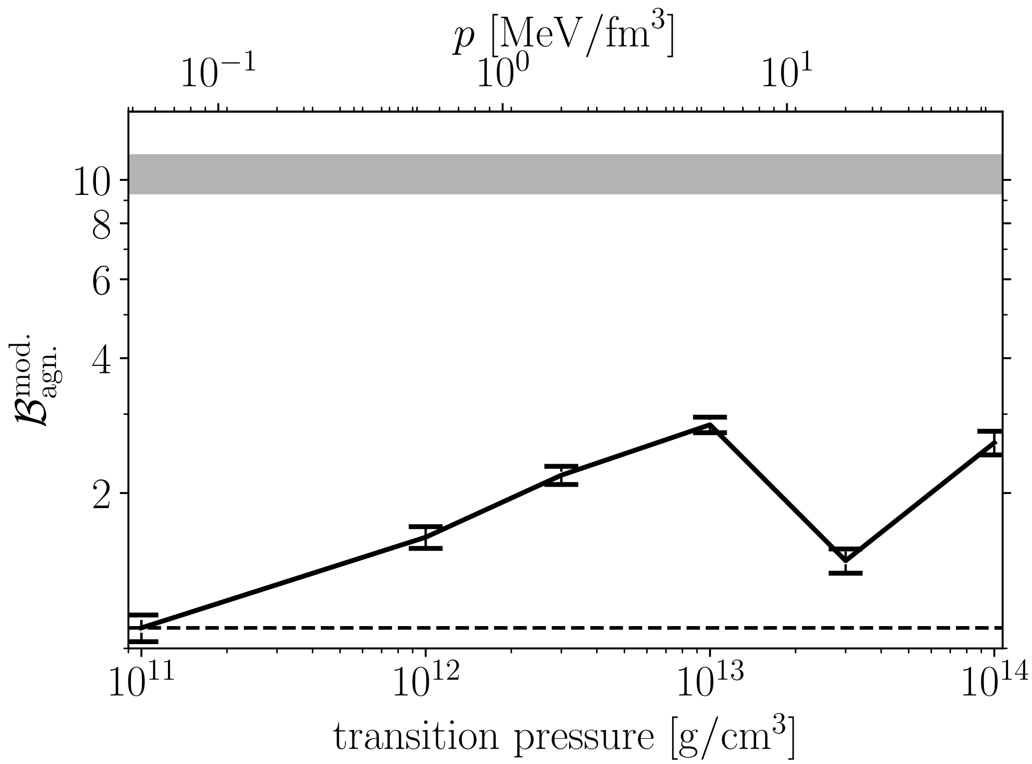

Figure 8.3: The Bayes factor of hybrid RMFT-agnostic GPs with various transition pressures compared to the "agnostic model" with a transition pressure of $10^{11}\,\mathrm{g/cm^3}$. Points show Monte-Carlo estimates, with error bars showing ± 1-σ error in the estimate from the limited sample size of the EoSs. The 1-σ region for the Bayes factor of the RMFT prior itself relative to the agnostic model is shown as a gray bar. There is an overall trend toward higher transition densities, but there is no conclusive preference for any transition pressure. The simulated data are consistent with all hybrid priors.

mass-radius relation in Fig. 8.5. The priors are the same as in Fig. 8.1. We find that as long as the transition pressure is sufficiently low, near or below the pressure at which the simulation EoS undergoes a phase transition ($p_{\rm t}/c^2 \sim 2.3 \times 10^{13}\,\mathrm{g/cm^3}$), the EoS is recovered effectively. By this, we mean that the mass-radius curves sampled from the posterior are reflective of the simulation EoS. For astrophysical neutron stars $M \in (\sim 1, M_{tOV})$, the radius is near the center of the distribution.

The phase-transition EoS represents a point of low prior probability in all EoS priors. This leads to poorer sampling resolution than in the case of recovering an EoS without a phase transition, particularly for the maximally agnostic cases.[2] For example, for the case of $p_{\rm t} = 10^{13}\,\mathrm{g/cm^3}$ and $3 \times 10^{13}\,\mathrm{g/cm^3}$ we have ~ 20 and

[2] See also Appendix C of Ref. [51].

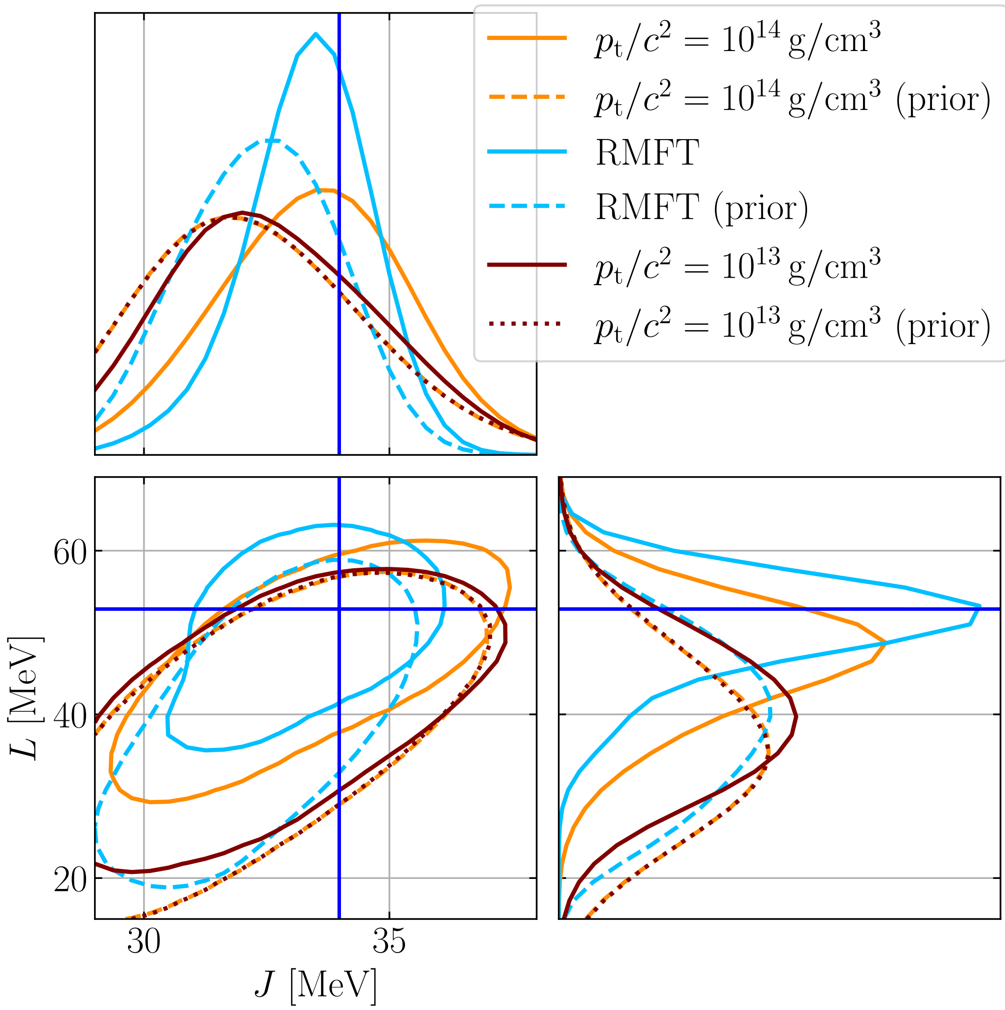

Figure 8.4: Prior (dashed) and posterior (solid) for the symmetry energy L and the slope of the symmetry energy J at saturation for various EoS priors. In light blue is the result from using the set of RMFT EoSs directly as a prior. In maroon and orange are results on the symmetry parameters (as estimated using Eq. 8.6) inferred using GP-priors which transitioned from RMFT-informed to model agnostic kernels at 10^{13} and $10^{14}\,\mathrm{g/cm^3}$ respectively. For the GP EoS distributions ($p_t/c^2 = 10^{13}$ and $p_t/c^2 = 10^{14}\,\mathrm{g/cm^3}$), the prior distributions are effectively identical, since both follow the same RMFT-informed GP at saturation density. Therefore, we mark the prior for the $p_t/c^2 = 10^{13}\,\mathrm{g/cm^3}$ with a dotted line to increase visibility.

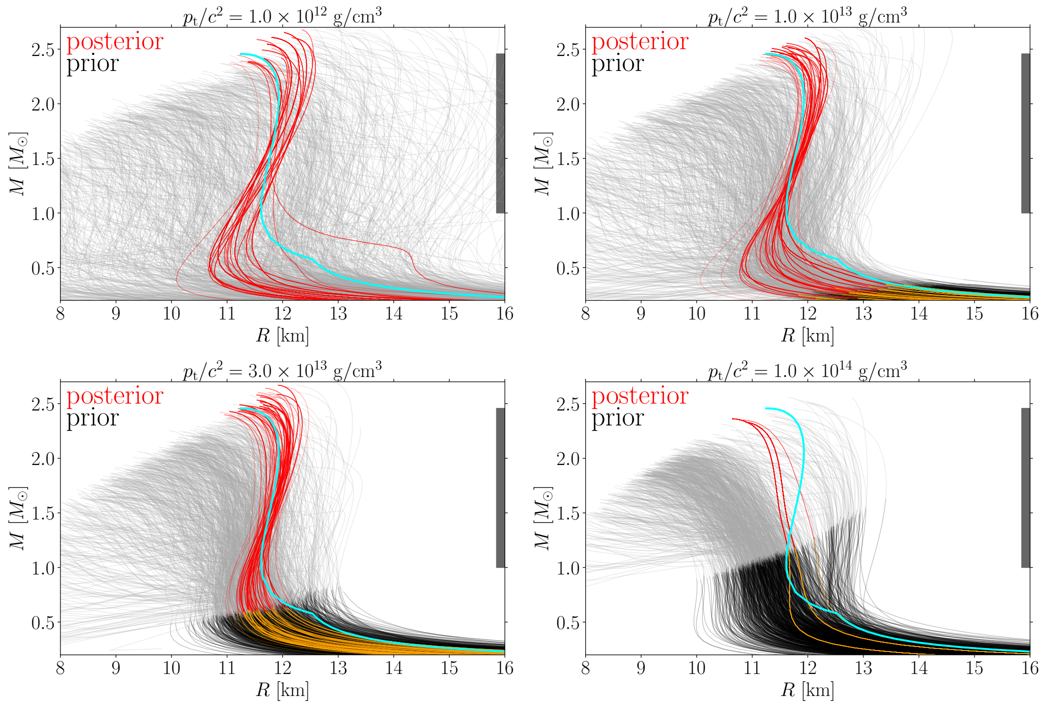

Figure 8.5: Same as Fig. 8.1, but for a simulated EoS that undergoes a phase transition from an RMFT EoS to a constant speed of sound model, shown in cyan. The RMFT description of the EoS holds only up to pressures slightly higher than the transition pressure ($\sim 1.8 \times 10^{13}$g/cm^3, which appears as a "kink" in the injected EoS). We plot 200 fair draws from the posterior and 1000 from the prior. We sample with replacement; if the same EoS from the posterior is sampled more than once (which happens generically if the posterior has few effective samples), the opacity of that EoS is proportional to the multiplicity of that sample. The gray bar has the same interpretation as in Fig. 8.1, except in this case the simulation EoS maximum mass is higher, so the bar extends to higher mass.

$\sim$ 46 effective samples,[3] respectively. Despite this, macroscopic observables are well recovered. In the cases above, $R_{1.4} = 11.76^{+0.09}_{-0.11}$ km, and $R_{1.4} = 11.73^{+0.12}_{-0.14}$ km for $p_t = 10^{13}$ g/cm^3 and 3×10^{13} g/cm^3, respectively (quoted at 90% credibility), consistent with the simulated value $R_{1.4} = 11.72$ km. For the case of a transition pressure $p/c^2 = 10^{14}$g/cm^3, however, the EoS is no longer recovered in that the posterior no longer reflects the simulation EoS within uncertainties. The maximum mass of all EoSs in the posterior is below the simulation EoS maximum mass. Furthermore, the posterior has only $\sim$ 2 effective samples.

For comparison, we display the result of the identical inference using the RMFT EoS

[3] We define the number of effective samples $n_{\rm eff} \equiv \exp(S)$, where S is the entropy of the underlying probability distribution $p(x)$, $S \equiv -\sum_i p(x_i) \ln p(x_i)$.

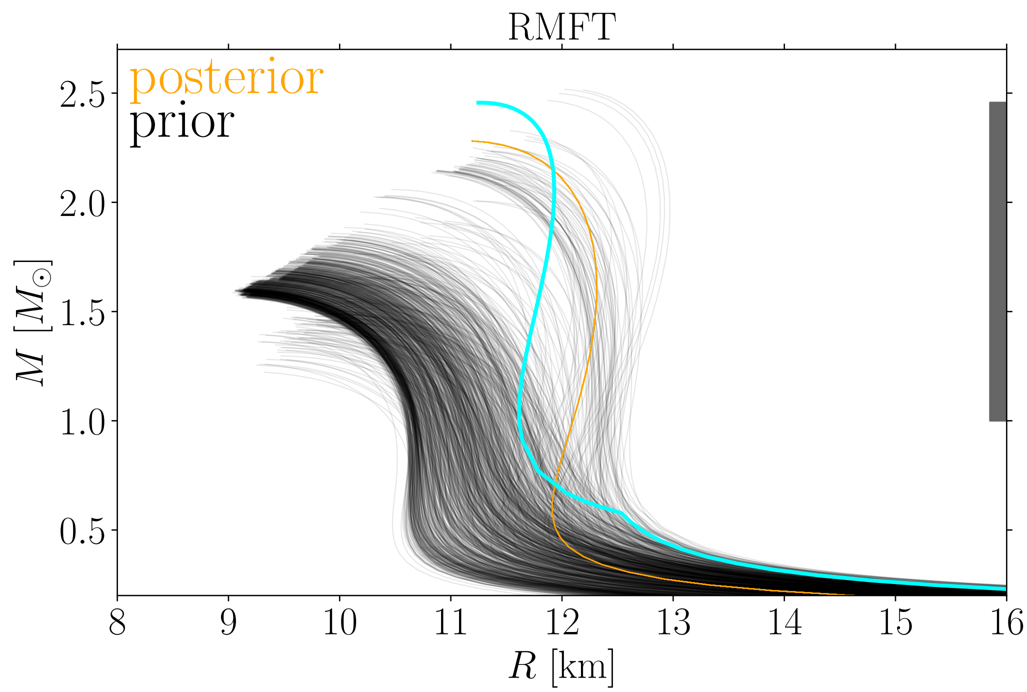

Figure 8.6: Same as Fig. 8.5, but for the RMFT prior distribution (same as Fig. 8.2). The RMFT is unable to recover the non-RMFT simulation EoS. There is only one posterior EoS displayed as the posterior contains only a single effective sample.

set as a prior in Fig. 8.6. The result is, in effect, the same as the result for the hybrid RMFT-informed model-agnostic posterior which transitions at $p/c^2 = 10^{14}\mathrm{g/cm^3}$, as there are too few effective samples from the analysis to even form a reasonable estimate for the posterior. We therefore conclude that the RMFT EoS prior, like the hybrid prior transitioning at $10^{14}\,\mathrm{g/cm^3}$, is effectively inconsistent with the simulated data.

Figure 8.7 shows the Bayes factor for each model with a different transition density. Most Bayes factors represent inconclusive evidence in favor of the RMFT description, with this evidence becoming stronger at higher transition pressures. This makes sense, as the low-density EoS is indeed well-described by the RMFT. For transition pressures that favor the RMFT-informed EoS over model-agnostic EoS, we find larger Bayes factors than the corresponding values in Fig. 8.3. This is due to two factors. First, one particular simulated x-ray measurement is highly informative (phase transition injection “X-ray 1”, in Tab. 8.5), and more precise than the most informative RMFT EoS injection by about a factor of 40%. This, however, is not sufficient to explain the very large difference in evidence. Removing this event leaves maximum Bayes factors of order ~ 10, still larger than those of Fig. 8.3.

The second cause of the large Bayes factors is the unusual location of the phase-transition EoS relative to all of the EoS priors used. Because the phase-transition EoS is "unusual" among both model-agnostic and RMFT EoSs, it lies at the margins of all of the prior distributions on the EoS. At these margins, small changes to the prior will lead to large changes in the (log) likelihood of the bulk of EoSs, analogous to how small changes in the z-score dramatically change the (log) probability of a Gaussian far from the mean. These large changes in evidence lead directly to large Bayes factors. These Bayes factors are indicative that the RMFT is the correct underlying description of the low-density EoS, but (comparing to Fig. 8.3), the size of the Bayes factors are due to the details of the prior construction and the location of simulation EoS.

For transition pressure $p_{\rm t}/c^2 = 10^{14}\,{\rm g/cm^3}$, we recover strong evidence against an RMFT description. While uncertainties are large, the Bayes factor for the $p_{\rm t}/c^2 = 10^{14}\,{\rm g/cm^3}$ model relative to the agnostic model is less than 10^{-4} at 90% credibility. This quantifies the statement that the RMFT-informed EoS prior is unable to produce candidate EoSs that closely mimic the simulation EoS, leading to few (or no) EoSs that are consistent with all astrophysical observations. Further, this confirms that if there is a strong phase transition, then we can identify the associated breakdown of the RMFT using our procedure given sufficient astrophysical data.

Finally, we show the inferred symmetry parameters in Fig. 8.8 for different transition pressures and when using the set of RMFT EoSs itself. Because we use the same RMFT parameters for the low-density EoS, the simulation EoS's symmetry parameters are the same as in Fig. 8.4. Moreover, since we use the same EoS priors, the marginal priors on J and L are consistent with the simulation EoS's values. Nonetheless, using the RMFT EoS set or the hybrid prior with $p_{\rm t}/c^2 \sim 10^{14}\,{\rm g/cm^3}$ does not recover the correct symmetry parameters. The correct symmetry parameters are recovered only for the GP EoS distribution that transitions at a lower pressure. This is because at low transition pressures, the marginal distribution on the symmetry parameters is effectively unchanged by the inclusion of astrophysical observations, indicating that astrophysical observations carry little information about the symmetry parameters under these models [49, 48]. When the RMFT description is trusted to higher pressures, however, the inclusion of astrophysical data renders the marginal distribution on the symmetry parameters inconsistent with the simulation EoS. This is reasonable, as the astrophysical properties of neutron stars with the simulation EoS are primarily determined by the "quark matter" (constant speed of sound EoS),

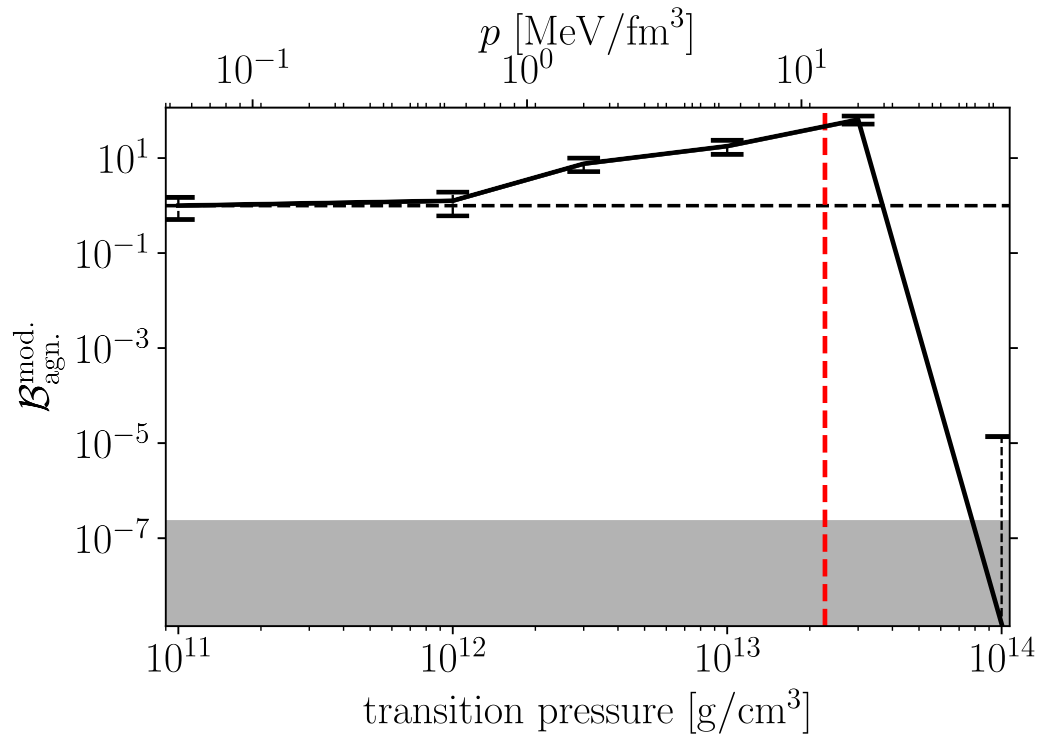

Figure 8.7: Same as Fig. 8.3, but for a simulated EoS with a strong phase transition to a constant speed-of-sound near 1.5 times saturation density (red vertical line).

not the low-density RMFT (hadronic) EoS. As such, inferring the properties of the hadronic EoS assuming it holds up to high pressures will lead to a bias.

8.4 Constraints on RMFT-breakdown with current astrophysical data

We finally turn to current astronomical data: radio timing observations of J0348+0432 [14], NICER x-ray pulse profile observations of J0030+0451 [82], J0740+6620 [83], and J0437-4715 [30], and gravitational-wave events GW170817 [5] and GW190425 [6]. We display fair draws from the prior and posterior for various choices of the transition pressure in Fig. 8.9. The posteriors are wider than in the simulation studies, since the current data are not as constraining. We find larger uncertainties at lower transition pressures, consistent with expectations that the RMFT-informed distribution imposes tighter constraints *a priori* than the model-agnostic GP. This, however, depends on mass, as $R_{1.4}$ is less variable between models than $R_{1.0}$, for example.

In Fig. 8.10 we show the prior and posterior distributions on various astrophysical quantities under different assumptions on the transition density. Trusting the RMFT to higher pressures favors a larger value of $R_{1.4}$ and $\Lambda_{1.4}$. For example,

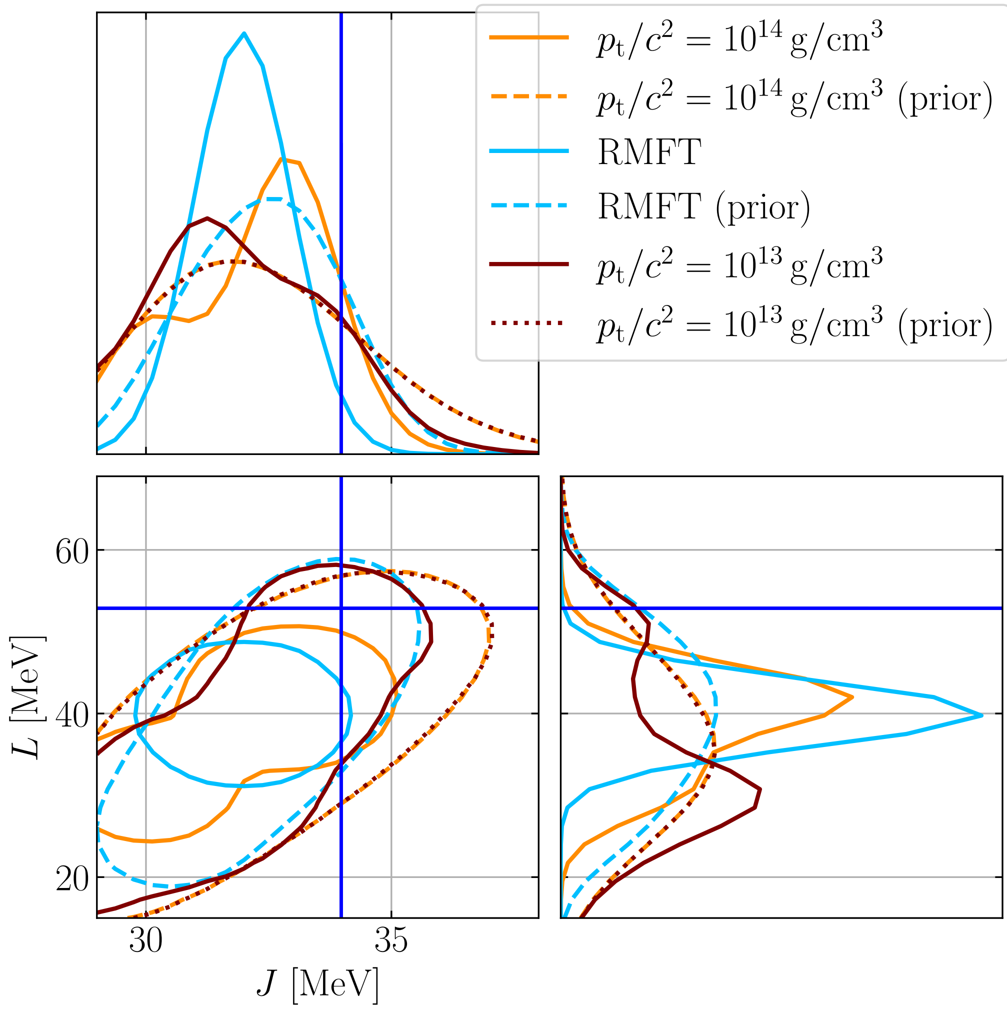

Figure 8.8: Same as Fig. 8.4 but with a simulation EoS which transitions to a constant speed of sound EoS.

$R_{1.4} = 11.80^{+0.92}_{-0.64}$ km for the model that transitions at $3 \times 10^{13}\,\mathrm{g/cm^3}$, whereas $R_{1.4} = 12.51^{+0.34}_{-1.21}$ km for the model transitioning at $10^{14}\,\mathrm{g/cm^3}$. This difference is a consequence of stronger correlations between lower and higher densities, which translates to stronger correlations between $R_{1.4}$ and M_{tOV} under the RMFT. Under the assumption of a transition density of $10^{14}\,\mathrm{g/cm^3}$, values of M_{tOV} greater than $\sim 2.2\,M_\odot$ are inconsistent with small neutron star radii (e.g. $R_{1.4} \lesssim 12$ km) *a priori*. This is not true for a lower transition pressure. Therefore, similar M_{TOV} posteriors result in different $R_{1.4}$ posteriors due to these correlations between high and low densities.

On the other hand, $\Lambda_{1.8}$ is inferred to be very similar between the two models. This

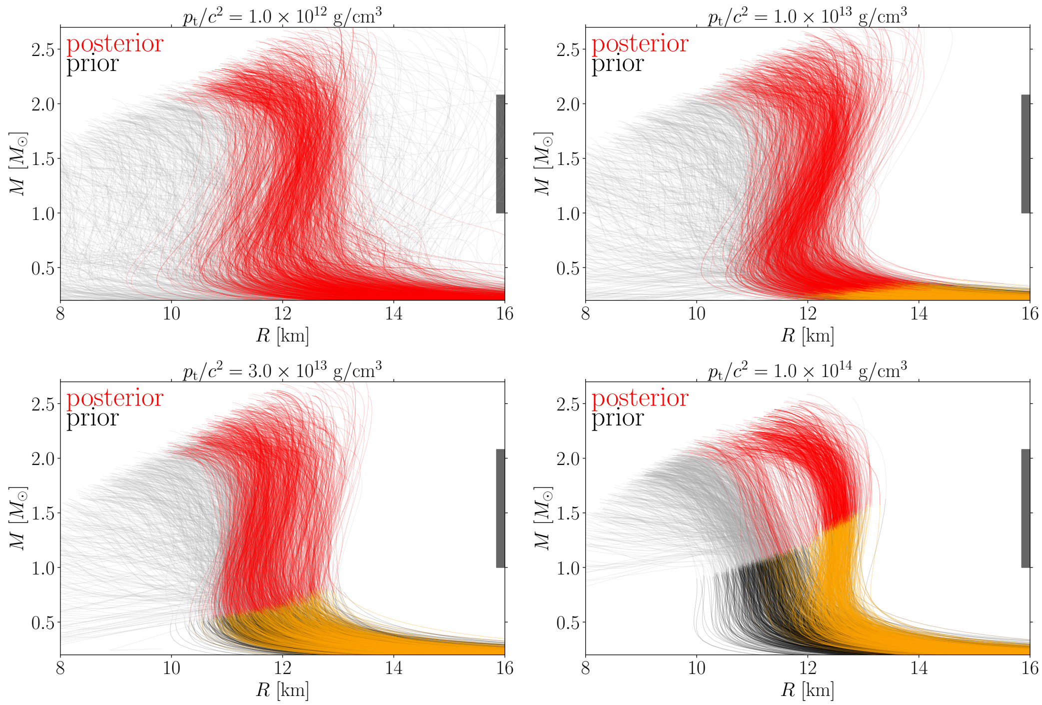

Figure 8.9: Same as Fig. 8.1, but with real astrophysical data instead of simulated data.

is because the tidal deformability is a strongly decreasing ($\Lambda \sim m^{-6}$ [66, 112]) function of the mass. Therefore, EoS differences are much suppressed in $\Lambda_{1.8}$. This convergence does not happen for $R_{1.8}$, however, which shows qualitatively the same picture as $R_{1.4}$. Therefore, even at constant fractional uncertainty in tidal parameters (which requires much louder gravitational wave signals), we expect neutron star mergers will be much better probes of RMFT breakdown at low masses than at high masses. Radius constraints, on the other hand, are similarly constraining at all masses.

In Fig. 8.11, we show the Bayes factors of each transition pressure compared to the lowest transition pressure. We generally find a preference for higher transition pressure with a mild decrease in evidence at the highest transition pressure, although the Bayes factors are all 2-3. Therefore, we do not find evidence against an RMFT description of the astrophysical EoS up to $p/c^2 \sim 10^{14}$ g/cm^3 using current astrophysical data. We additionally do not find strong evidence for the RMFT, though as discussed in Sec. 8.3, we do not necessarily expect such evidence if RMFT is the correct underlying model.

The symmetry energy and its slope at saturation are shown in Fig. 8.12 for the RMFT

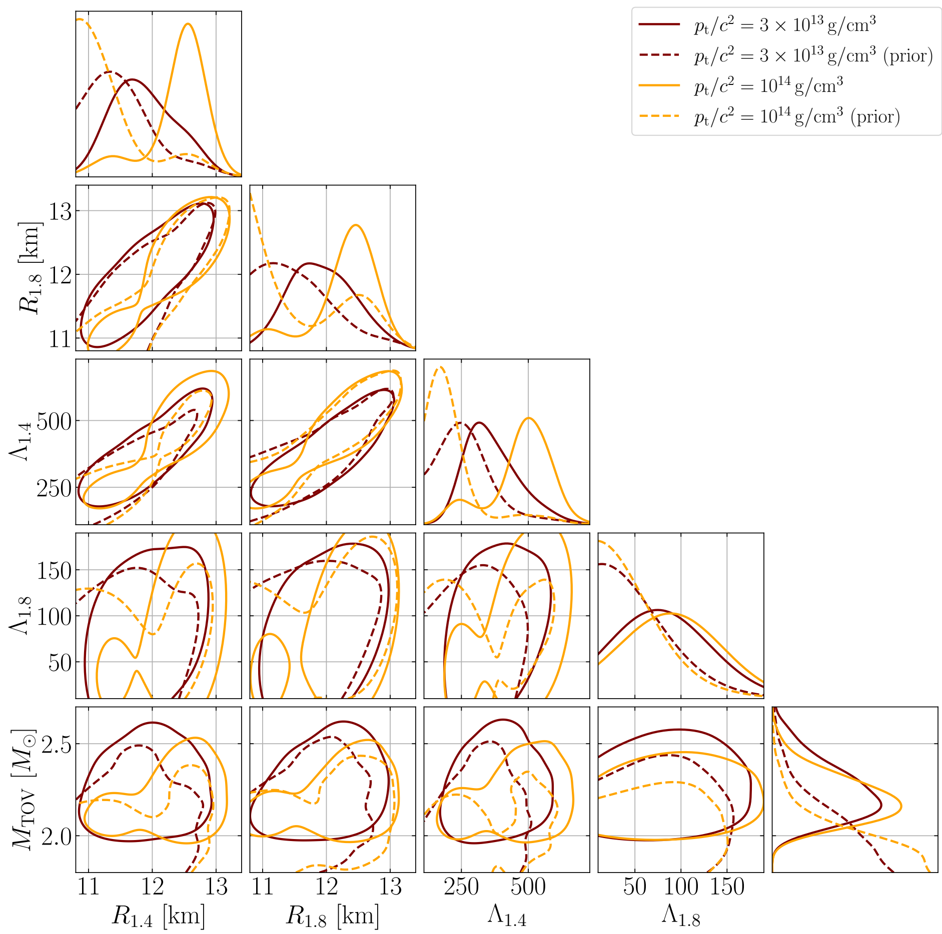

Figure 8.10: Prior (dashed) and posterior (solid) distributions for select parameters when transitioning from the RMFT-conditioned to the model-agnostic EoS prior at $3 \times 10^{13}\,\mathrm{g/cm^3}$ (maroon) and $10^{14}\,\mathrm{g/cm^3}$ (orange). Lines mark 90% credible regions. We show: the radius ($R_{1.4}$, $R_{1.8}$) and dimensionless tidal deformability ($\Lambda_{1.4}$, $\Lambda_{1.8}$) of 1.4 and 1.8 $M_\odot$ neutron stars respectively and the maximum TOV mass (M_{tOV}) of a neutron star.

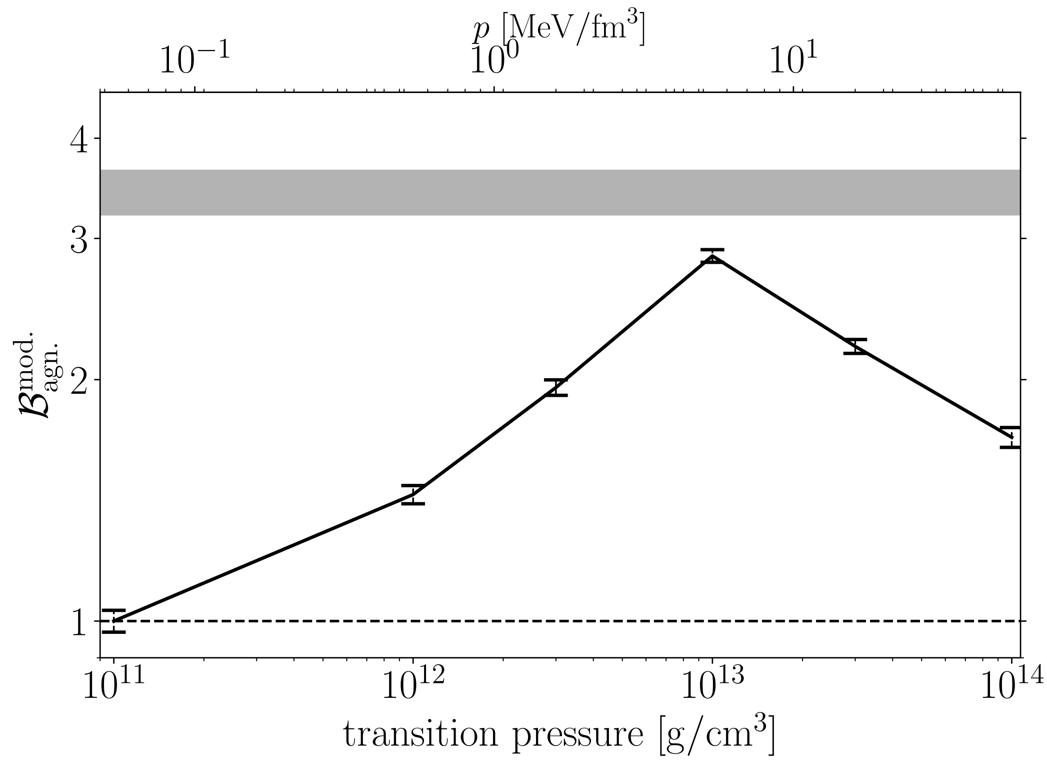

Figure 8.11: Same as Fig. 8.3, but using astrophysical observations rather than simulated data. We find no strong preference for any transition pressure.

EoS set and hybridized priors transitioning at $p_{\rm t}/c^2 = 10^{13}$ g/cm^3 and 10^{14} g/cm^3. The posteriors are largely consistent with each other, though for higher transition pressures, and for the RMFT EoS set itself, the values of both L and J are better constrained. We find, for example, that $L = 37.03^{+16.37}_{-14.42}$ MeV when we transition at 10^{13} g/cm^3, and $L = 47.87^{+11.15}_{-14.04}$ MeV when transitioning at 10^{14} g/cm^3. The recovered value of L is both larger and better constrained when we trust the RMFT up to higher densities, likely due to correlations between the large inferred maximum mass of neutron stars and the stiffness of matter near saturation under these models. Trusting the RMFT up to only $p_{\rm t}/c^2 = 10^{13}$ g/cm^3, which corresponds to a density $\sim 1.5\, n_0$, we find no meaningful constraints on the symmetry parameters relative to the priors. This is an indication that under the model-agnostic prior, the properties of matter near saturation are not strongly correlated with the matter in the cores of astrophysical neutron stars [49, 48].

The recovered values are consistent with existing results on the symmetry parameters, although they represent matter which is marginally softer near saturation than other studies. Reference [41], using constraints from χEFT at N^{3}LO, finds

$J = 31.7 \pm 1.1$ MeV and $L = 59.8 \pm 4.1$ MeV at 1σ uncertainty. Additionally, per Fig. 2 of Ref. [41] (based partly on Refs. [75, 76]) this range is also found to be largely consistent with a broad range of theoretical, experimental, and observational constraints of the nuclear symmetry energy. Our results are also consistent with values implied by PREX-II [8], though we do not consider that data here. For instance, Ref. [92] used PREX-II results to infer $L = 106 \pm 61$ MeV at 90% credibility. Combining PREX-II and low-density χEFT information in the GP framework yields $L = 53^{+14}_{-15}$ MeV [49, 48]. Using a less flexible EoS model, though with a wider range of astrophysical and nuclear data including PREX-II, Ref. [18] found $L = 54^{+10}_{-10}$ MeV at 90%.

Even though both the GPs which transition at $10^{13}\,\mathrm{g/cm^3}$ and $10^{14}\,\mathrm{g/cm^3}$ are described by the same RMFT framework near saturation density, we recover different posteriors on the EoS in this region. This is because correlations with the well-constrained high-density EoS are different under the two choices of model. To further show this, in Fig. 8.13 we display the inferred sound speed as a function of density under different choices of the transition pressure. The sound speed at saturation density is markedly different for the two posteriors, even though both of the distributions are closely emulating the underlying RMFT at that density and therefore have very similar prior distributions on c_s^2. This happens because higher-density observations can more strongly inform low-density physics when the RMFT description is trusted up to higher densities.

8.5 Discussion

We have constructed hybrid models of the dense-matter EoS informed by an RMFT at low pressures and model-agnostic above a certain transition pressure. We compare multiple models with different transition pressures to astrophysical data, and probe the scale up to which a specific RMFT EoS is able to describe the dense-matter EoS. We first explore how inference behaves under simulated data. If the true EoS is consistent with the RMFT description, evidence will remain inconclusive, unable to rule out the RMFT at any scale. This behavior is expected from prior volume arguments. If the true EoS is inconsistent with any RMFT EoS, for example due to a phase transition, we recover strong evidence (Bayes factors $\gtrsim 10^4$) against models that are informed by the RMFT beyond the pressure of the phase transition. We further demonstrate that a breakdown can be identified with sufficiently many gravitational-wave observations in App. 8.9, within expectations of upcoming observing campaigns.

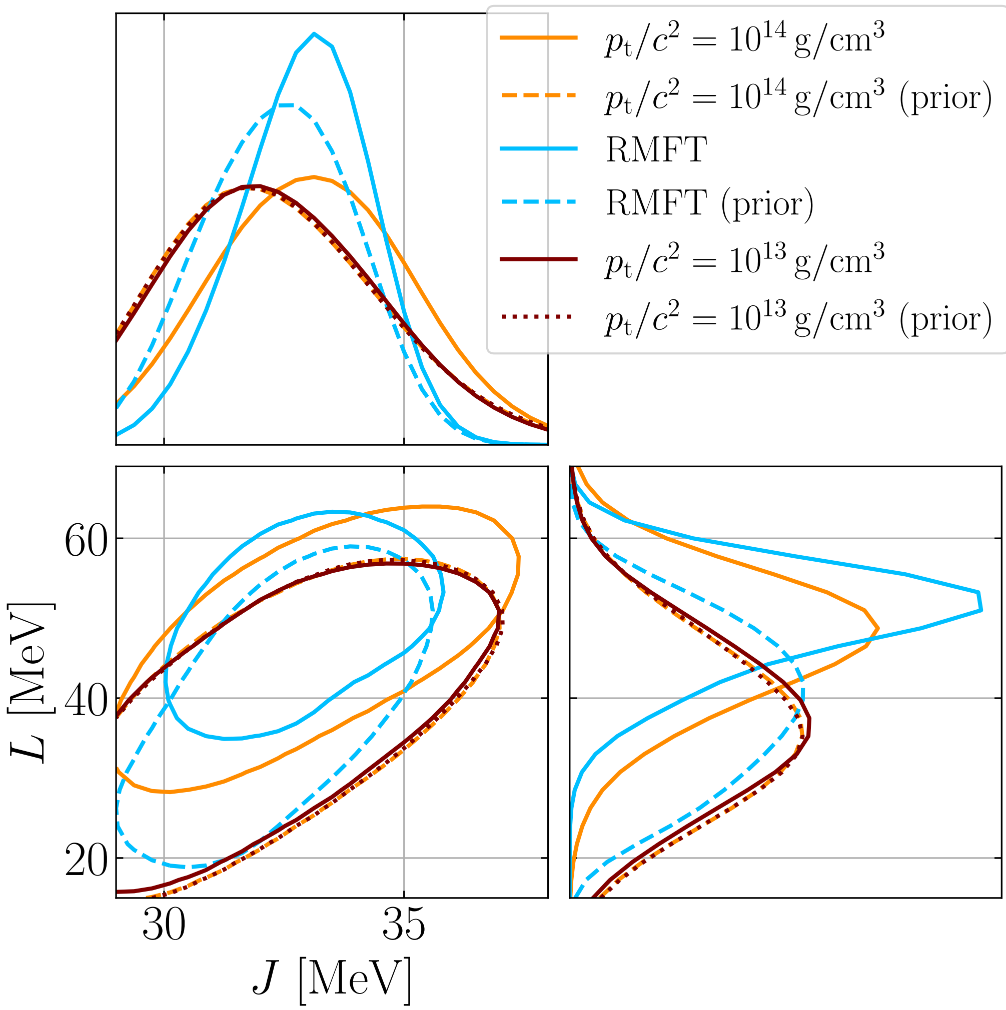

Figure 8.12: The inferred symmetry parameters using astrophysical observations, same as Fig. 8.4. The prior for the model which transitions at $10^{13}\,{\rm g/cm^3}$ (maroon dashed) is essentially the same as the posterior and the prior which transitions at $10^{14}\,{\rm g/cm^3}$ (same as in Fig. 8.4), and therefore we mark it with a dotted line to increase contrast.

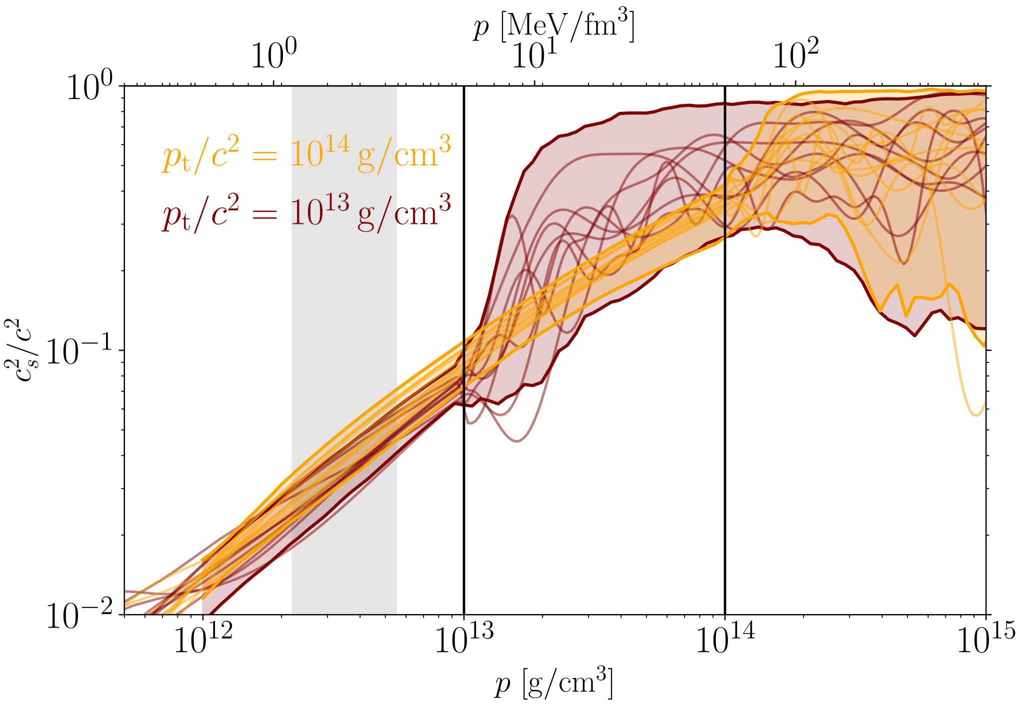

Figure 8.13: Speed-of-sound squared 90% credible intervals using current astrophysical data, along with fair draws for the prior transitioning to agnostic at 10^{13} g/cm^3 and 10^{14} g/cm^3. Transition pressures are marked by black vertical lines. A gray bar shows the approximate range of pressures at saturation density for the RMFT EoSs.

Applying our models to real astrophysical observations, we find no evidence against RMFT EoSs up to arbitrarily high densities. Nonetheless, the inferred macroscopic neutron star properties differ depending on the pressure up to which the RMFT is trusted. This behavior elucidates how the breakdown pressure can be constrained with future data. For example, the inferred radius of a 1.4 $M_\odot$ star depends on what pressure the RMFT is trusted up to. Conditioning up to a pressure of 1×10^{14} g/cm^3, we find $12 \lesssim R \lesssim 13$ km at $\sim$ 90% credibility, while conditioning up to only 3×10^{13} g/cm^3, yields $11-12.5$ km. This suggests that future constraints should be more informative about the breakdown scale if they reach $\sim$ 0.5 km precision and $R_{1.4} \sim 11.5$ km. Finally, as a note of caution, it is possible that biases emerge before evidence against a model appears. Therefore it is still important to consider other models of the EoS, including fully agnostic analyses.

If an RMFT-informed analysis is deemed inconsistent with astrophysical data, then the RMFT EoSs have broken down. Possible reasons and remedies are listed in the introduction. Our method not only yields evidence for the breakdown, but can also quantify the breakdown pressure. For example, if the breakdown occurs at $\sim 2-3\,n_0$, then it is possibly due to hyperon degrees of freedom [108]. Alternatively, if the breakdown happens at $\sim 4-6\,n_0$, then it is likely that the treatment of nucleons as point-like particles is insufficient as the average distance of the nucleons becomes smaller than their expected size [110]. More generally, understanding the regime where the RMFT has broken down can be challenging and comparing multiple models will likely be necessary.

Further observables, such as the post-merger gravitational wave signal [101, 89, 16, 22, 36], an electromagnetic counterpart [38, 113, 25, 31], or the lifetime of the remnant [81, 102], may also indicate that the breakdown is due to a strong phase transition. In that case, a range of approaches, both modeled and model-agnostic, can be used to constrain its properties [87, 28, 13, 51, 85]. We do not find evidence for a breakdown, and thus a strong phase transition, and therefore, our results are consistent with Refs. [87, 28, 13, 51, 85]. We do not explicitly use information from perturbative QCD [70, 71], unlike Ref. [13], which argues against EoSs that are hadronic up to very high densities. Our analysis is therefore broadly consistent with the existing literature, where such comparisons are possible.

Finally, we reiterate that our hybrid agnostic-informed formalism can be applied to any nuclear model that can make predictions about the EoS at supranuclear densities. However, the identification of a breakdown scale is only meaningful if the theory is somewhat trustworthy below some pressure/density scale. Therefore, constraints from experiments and *ab initio* calculations will be crucial to constrain and validate such theories near saturation density, while astrophysics will be essential for searching for their breakdown at the densities reached in neutron star cores.

8.6 Acknowledgments

L.B. and A.H. thank Mark Alford for useful conversations. I.L. thanks Philippe Landry for insightful discussions. I.L. and K.C. acknowledge support from the Department of Energy under award number DE-SC0023101, and by a grant from the Simons Foundation (MP-SCMPS-00001470). L.B. and A.H. are partly supported by the U.S. Department of Energy, Office of Science, Office of Nuclear Physics, under Award No. #DE-FG02-05ER41375. A.H. furthermore acknowledges financial support by the UKRI under the Horizon Europe Guarantee project EP/Z000939/1. R.E. is supported by the Natural Sciences & Engineering Research Council of Canada (NSERC) through a Discovery Grant (RGPIN-2023-03346).

The authors are grateful for computational resources provided by the LIGO Laboratory and supported by National Science Foundation Grants PHY-0757058 and PHY-0823459. This material is based upon work supported by NSF's LIGO Laboratory which is a major facility fully funded by the National Science Foundation.

8.7 Constructing the RMFT EoS distribution

In this appendix, we discuss how we construct the distribution of RMFT EoSs. More details are available in Ref. [11]. We construct a particular RMFT EoS by making a choice for the RMFT nucleon-meson and meson-meson coupling constants; we choose these constants (which we will here refer to as parameters) so that the resulting EoS is consistent with the properties of isospin-symmetric nuclear matter and neutron matter near saturation. Since there is uncertainty in the properties of neutron matter, we sample these properties according to *ab initio*, χEFT, predictions. We then fit the RMFT parameters using a nonlinear, least-squares procedure, which allows us to produce a set of RMFT parameters which are consistent with the empirical saturation properties of symmetric nuclear matter, and *ab initio* constraints of neutron matter near saturation ($0.5 - 1.5\, n_0$). Therefore, we produce a distribution on the EoS where the only explicit uncertainty comes from uncertainty in the properties of neutron-rich matter near saturation.

We first describe the phenomenological model for symmetric matter, and then the neutron matter constraints, but in practice, the fitting is performed simultaneously. We fit the binding energy of isospin-symmetric nuclear matter from baryon density $n_B = 0.8\, n_0$ to $n_B = 1.4\, n_0$. We evaluate the binding energy at 12 density points using the standard empirical power series,

$$\mathcal{E}(n_B) = (E_B + \frac{\kappa}{2!}\delta^2 + \cdots)\,, \tag{8.13}$$

where $\delta \equiv (n_B - n_0)/(3n_0)$. Here E_B is the binding energy at saturation density and κ is the incompressibility of nuclear matter. The parameter values for isospin-symmetric matter that we fit to are

$$E_B = -16\,\mathrm{MeV}\,, \tag{8.14}$$

$$n_0 = 0.16\,\mathrm{fm}^{-3}\,, \tag{8.15}$$

$$\kappa = 240\,\mathrm{MeV}\,. \tag{8.16}$$

In contrast with isospin-symmetric matter, neutron matter is not self-bound and therefore cannot be probed in a lab, so we do not have analogous empirical constraints. Therefore, instead, we fit to *ab initio* χEFT calculations of neutron matter [106]. The χEFT calculation we use is based on local χEFT interactions at N^{2}LO that were constructed in Refs. [60, 59, 105, 80]. We choose this χEFT calculation because, compared to χEFT calculations at higher order like Refs. [40, 68], Ref. [106] employs a more conservative estimate of the error band. The χEFT results are used over the density range $0.5\,n_0$ to $1.5\,n_0$, i.e., above the crust-core transition and where χEFT is reliable [106, 42].

We sample the χEFT uncertainty band by creating a set of representative χEFT neutron matter EoSs using the Gandolfi-Carlson-Reddy (GCR) parametrization [58], which expresses the binding energy per nucleon $\mathcal{E}$ of neutron matter in the form

$$\mathcal{E}_{\chi\mathrm{EFT}}(n_B) = a(n_B/n_0)^{\alpha} + b(n_B/n_0)^{\beta}\,. \tag{8.17}$$

We sample 200,000 EoSs generated from a wide range of GCR parameters (a, b, α, β), keeping the 1,109 EoSs that remain completely within the χEFT uncertainty band between $n_B = 0.5\,n_0$ and $n_B = 1.5\,n_0$. For each χEFT EoS, we fit the RMFT coupling constants, evaluating the χEFT EoS at 16 density points. A simultaneous fit to these points and the 12 density points of the phenomenological model for symmetric nuclear matter determines the RMFT coupling constants.

The mass-radius relation from the resulting RMFT EoSs is shown in Fig. 8.2; the multimodality in the RMFT EoSs is driven by a corresponding multimodality in the fit RMFT parameters. This multimodality is in turn driven by the existence of multiple regions of RMFT parameter space that fit the properties of symmetric and neutron-rich matter comparably well. For these EoSs we find that the choice of initial guess in the fitting procedure will impact the "optimal" value for the fit parameters. In particular, the choice of initial guess for the RMFT parameters we use in this work lead to some RMFT EoSs ($\sim 8\%$) with $M \geq 2\,M_{\odot}$. Using a different set of initial guesses, the multimodality vanishes, but we no longer generate RMFT EoSs with $M \geq 2\,M_{\odot}$. Since we are mainly interested in the range of models that the Lagrangian can produce, and since all RMFT models we generate are consistent with nuclear theory and experiment, we use the broader (*i.e.* multimodal) distribution.

Since the distribution of RMFT EoSs is influenced by the choice of initial guesses in the fitting procedure, the distribution we present here may not represent the full range of viable models consistent with low-energy nuclear physics for the chosen model Lagrangian. Nonetheless, the bulk of fit RMFT EoSs have maximum TOV masses below $2.0\,M_{\odot}$ regardless of the initial guess for the RMFT parameters.

Therefore, we do not expect the bulk features of the RMFT EoS distribution to change based on the choice of initial guess, though the distribution of EoSs which exceed $2.0\,M_\odot$ is likely much more sensitive to this choice. Strategies to achieve particular distributions of RMFT EoSs are left to future work.

8.8 Efficiently Conditioning high-density GPs on Low-Density Theory

The following is implemented within Ref. [44] and was first published there as a technical note alongside the source code. The description is technical, providing a complete record of the procedure of Sec. 8.2. In particular, we describe here the process necessary for modifying the model-agnostic GP so that at particular pressures it follows the distribution given by the RMFT EoSs. However, this procedure is generic, and therefore can be applied to modify any GP to strictly obey a particular covariance at particular entries.

Assume we have an existing GP that defines a measure for two vectors (f_a and f_b with N_a and N_b elements, respectively) and can be written as

$$p_{\mathrm{O}}(f_a, f_b) \sim \mathcal{N}\left([\mu_a, \mu_b], \begin{bmatrix} C_{aa} & C_{ab} \\ C_{ba} & C_{bb} \end{bmatrix}\right), \tag{8.18}$$

with mean vectors μ_a, μ_b and covariance matrix C decomposed into C_{aa} ($N_a \times N_a$ elements), C_{ab} ($N_a \times N_b$), C_{ba} ($N_b \times N_a$), and C_{bb} ($N_b \times N_b$). We note that

$$C_{aa} = C_{aa}^{\mathrm{T}}, \tag{8.19}$$

$$C_{ab} = C_{ba}^{\mathrm{T}}, \tag{8.20}$$

$$C_{bb} = C_{bb}^{\mathrm{T}}. \tag{8.21}$$

We wish to update this process so that the marginal distribution for f_b follows another process, namely

$$p_{\mathrm{E}}(f_b) = \mathcal{N}\left(y_b, \Sigma_{bb}\right), \tag{8.22}$$

while maintaining the rest of the covariance structure encoded in C. We do this by constructing a new process

$$p_{\mathrm{N}}(f_a, f_b) = p_{\mathrm{O}}(f_a|f_b)p_{\mathrm{E}}(f_b), \tag{8.23}$$

where $p_{\mathrm{O}}(f_a|f_b)$ can be derived from $p_{\mathrm{O}}(f_a, f_b)$ in the usual way [90] as

$$p_{\mathrm{O}}(f_a|f_b) = \mathcal{N}\left(\mu_a + C_{ab}C_{bb}^{-1}(f_b - \mu_b),\ C_{aa} - C_{ab}C_{bb}^{-1}C_{ba}\right). \tag{8.24}$$

Expanding the contractions, grouping like terms, and dropping those that do not depend on either f_a or f_b, we obtain a Gaussian in both f_a and f_b, and we obtain direct relations for the new mean vectors and (inverse) covariance defined by

$$p_{\mathrm{N}}(f_a, f_b) = \mathcal{N}\left([m_a, m_b], \begin{bmatrix} \Gamma_{aa} & \Gamma_{ab} \\ \Gamma_{ba} & \Gamma_{bb} \end{bmatrix}^{-1}\right), \tag{8.25}$$

as follows:

$$\Gamma_{aa} = \left(C_{aa} - C_{ab}C_{bb}^{-1}C_{ba}\right)^{-1}, \tag{8.26}$$

$$\Gamma_{ab} = -\left(C_{aa} - C_{ab}C_{bb}^{-1}C_{ba}\right)^{-1} C_{ab}C_{bb}^{-1}, \tag{8.27}$$

$$\Gamma_{bb} = C_{bb}^{-1}C_{ba}\left(C_{aa} - C_{ab}C_{bb}^{-1}C_{ba}\right)^{-1} C_{ab}C_{bb}^{-1} + \Sigma_{bb}^{-1}, \tag{8.28}$$

and

$$m_a = \mu_a + C_{ab}C_{bb}^{-1}\left(y_b - \mu_b\right), \tag{8.29}$$

$$m_b = y_b \,. \tag{8.30}$$

Finally, we can solve for

$$\gamma = \Gamma^{-1} = \begin{bmatrix} \gamma_{aa} & \gamma_{ab} \\ \gamma_{ba} & \gamma_{bb} \end{bmatrix}, \tag{8.31}$$

by recognizing that

$$\begin{bmatrix} \gamma_{aa} & \gamma_{ab} \\ \gamma_{ba} & \gamma_{bb} \end{bmatrix} \begin{bmatrix} \Gamma_{aa} & \Gamma_{ab} \\ \Gamma_{ba} & \Gamma_{bb} \end{bmatrix} = \mathbb{I}\,. \tag{8.32}$$

Further simplification yields

$$\gamma_{aa} = \left[\Gamma_{aa} - \Gamma_{ab}\Gamma_{bb}^{-1}\Gamma_{ba}\right]^{-1}, \tag{8.33}$$

$$\gamma_{ab} = C_{ab}C_{bb}^{-1}\Sigma_{bb}\,, \tag{8.34}$$

$$\gamma_{ba} = \Sigma_{bb}C_{bb}^{-1}C_{ba}\,, \tag{8.35}$$

$$\gamma_{bb} = \Sigma_{bb}\,, \tag{8.36}$$

where we have left γ_{aa} in terms of Γ because of the length of the expression but have substituted and simplified the rest of the terms. Note that the marginal distribution $p_{\mathrm{N}}(f_b) = \mathcal{N}(y_b, \Sigma_{bb}) = p_{\mathrm{E}}(f_b)$, as desired. On the other hand, the distribution of y_a is modified from its original form in Eq. (8.18). In our case, this is an indication that the conditioning process modifies the EoS distribution even at pressures which we did not explicitly require the distribution to follow RMFT.

Modifications for numerical stability

In general, m_a and γ_{aa} can suffer from issues associated with numerical stability. This is because they involve the inversion of (possibly) high-dimensional matrices that may be ill-conditioned. While the preceding is exact, we therefore implement two additional approximations to help better control the calculations.

Damping C_{ab}, C_{ba}, and C_{bb} to make them easier to invert

One issue we have found is that strong correlations in C_{bb} can make numerical inversion difficult. Given that we wish to replace C_{bb} with Σ_{bb} anyway, and really only wish there to be a relatively smooth transition between f_b and f_a, we modify C_{ab}, C_{ba}, and C_{bb} in order to damp the off-diagonal elements (and therefore make them easier to invert).

Specifically, we define a squared-exponential damping term

$$D(x_i, x_j) = \exp\left(-\frac{(x_i - x_j)^2}{l^2}\right), \tag{8.37}$$

and a white noise contribution that modify C so that

$$(C_{ab})_{ij} \to (C_{ab})_{ij} D(x_i, x_j), \tag{8.38}$$

$$(C_{bb})_{ij} \to (C_{bb})_{ij} D(x_i, x_j) + \sigma_{\mathrm{W}}^2 \delta_{ij}. \tag{8.39}$$

We then use these modified C_{ab} and C_{bb} within the expressions in the previous section.

This modifies the original process, but as long as l is relatively large and σ_{W} is relatively small, the modifications will be minor over the transition between f_b and f_a. Empirically, we find that $l = 5.0$ and $\sigma_{\mathrm{W}} = 0.01$ work well when updating our our model-agnostic priors.

Approximation for γ_{aa} when Σ_{bb} is small

Finally, it will often be the case that Σ_{bb} will be much smaller than C_{bb} (with respect to an appropriate matrix norm). That is, we wish to update a process to restrict the marginals of certain covariates to be more tightly constrained than they otherwise would be.

By repeated use of the approximation

$$(A + X)^{-1} \approx A^{-1} - A^{-1} X A^{-1}, \tag{8.40}$$

we can see that this limit corresponds to

$$\Gamma_{bb}^{-1} \approx \Sigma_{bb} - \Sigma_{bb} C_{bb}^{-1} C_{ba} \left(C_{aa} - C_{ab} C_{bb}^{-1} C_{ba} \right)^{-1} C_{ba} C_{bb}^{-1} \Sigma_{bb} \,, \tag{8.41}$$

and (retaining terms linear in Σ_{bb})

$$\begin{aligned}\gamma_{aa} &\approx C_{aa} - C_{ab} C_{bb}^{-1} C_{ba} + C_{ab} C_{bb}^{-1} \Gamma_{bb}^{-1} C_{bb}^{-1} C_{ba} \\ &\approx C_{aa} - C_{ab} C_{bb}^{-1} C_{ba} + C_{ab} C_{bb}^{-1} \Sigma_{bb} C_{bb}^{-1} C_{ba} \\ &\approx C_{aa} - C_{ab} C_{bb}^{-1} (C_{bb} - \Sigma_{bb}) C_{bb}^{-1} C_{ba} \,. \end{aligned} \tag{8.42}$$

This makes sense in two limiting cases

- $\Sigma_{bb} = 0$: we know f_b exactly and obtain the standard expression for the covariance for $f_a | f_b$,
- $\Sigma_{bb} = C_{bb}$: we do not update the original process, and as such we obtain $\gamma_{aa} = C_{aa}$.

Finally, we offer one more interpretation of this expression. If we considered the standard expression for $f_a | f_b$ with some covariance for f_b, say $\mathcal{C}_{bb}$, we would obtain

$$\gamma_{aa} = C_{aa} - C_{ab} \mathcal{C}_{bb}^{-1} C_{ba} \,, \tag{8.43}$$

and therefore, by matching this to our approximation, we see that

$$\begin{aligned}\mathcal{C}_{bb} &= C_{bb} \left(C_{bb} - \Sigma_{bb} \right)^{-1} C_{bb} \\ &\approx C_{bb} \left(C_{bb}^{-1} + C_{bb}^{-1} \Sigma_{bb} C_{bb}^{-1} \right) C_{bb} = C_{bb} + \Sigma_{bb} \,. \end{aligned} \tag{8.44}$$

In this limit, then, we can interpret updating the marginal distribution as equivalent to the standard procedure of conditioning the process for f_a on a noisy observation of f_b with observed values y_b and measurement uncertainty Σ_{bb}. Historically, this is what was actually done in Refs. [50, 49, 48], and we now see why it provided a decent approximation.

8.9 Inferring a breakdown with gravitational-wave signals and pulsar timing measurements alone

In this appendix, we consider the question of how many gravitational-wave observations (when paired with existing heavy pulsar mass measurements) will be required to determine the breakdown of an RMFT. We do this to explicitly evaluate the prospect of developments of future gravitational-wave detectors. With next generation detectors such as Cosmic Explorer [52, 64], or Einstein Telescope [2], in principle hundreds to thousands of informative binary neutron star mergers could be identified within a handful of years of operation [52, 2]. In contrast, there are a limited number of plausible x-ray timing targets with which to constrain the EoS [20].

We start with more details on the gravitational-wave injections. We use a binary population that is consistent with observations of merging neutron stars, sampling 50 sources from a representative population model which is uniform in component masses from 1.0 to 2.0 $M_\odot$.[4] We simulate signals corresponding to the sampled sources into Gaussian noise at the level of A+ detector sensitivity [1], placing the sources uniformly in comoving volume from 1 to 300 Mpc, which we expect to produce a substantial fraction of "informative" GW signals. Simulated neutron stars are spinning slowly, with dimensionless component spins isotropically distributed with magnitudes $|\vec{\chi}| < 0.05$. We analyze all sources that are recovered with optimal signal-to-noise ratio (SNR) > 10.0 using the `bilby` parameter estimation code [15] using the `IMRPhenomPV2_NRTidalv2` waveform [37].[5] We then downsample the total set of analyzed sources in order to produce variable catalog sizes.

In Fig. 8.14, we show the Bayes factor between models transitioning from RMFT-informed to model-agnostic priors at $p/c^2 = 10^{14}\,\mathrm{g/cm^3}$ and $3 \times 10^{13}\,\mathrm{g/cm^3}$, respectively. We consider two cases: inferring an RMFT EoS (top panel, see Sec. 8.3) and an RMFT EoS which has a phase transition to a constant speed of sound (bottom panel, see Sec. 8.3) at $p/c^2 = 2.3 \times 10^{13}\,\mathrm{g/cm^3}$. As in the main text, we find no strong evidence either for or against in the case of an RMFT injection. In this case, all models can describe the data, so the Bayes factors essentially reflect the priors. In the case of the phase transition, we find that meaningful evidence ($\mathcal{B} \lesssim 10^{-3}$) against an RMFT description up to high pressure after ~ 7 events,[6] with most of

[4] This is less than the TOV maximum mass for the EoSs we use for simulated data, assuming that the population of merging NSs is not limited by the TOV maximum mass; see e.g., Ref. [63] for a discussion. We assume this because high-mass neutron star mergers are essentially uninformative with respect to the EoS, and more importantly, high mass NSs are generally not distinguishable from black holes anyway in gravitational waves [53, 55, 46]

[5] In general, selecting events based on the optimal SNR can induce biases [45]. However, we do not change the population, and the EoS contributes negligibly to selection effects.

[6] This is a plausible estimate for the number of detections of neutron star binaries with LIGO A+ sensitivity given current rate estimates [7]. Future detectors will produce far more detections, which will lead to sampling challenges [51], and far louder detections [27], which will lead to systematic biases due to waveform mismodeling [91]. Collectively these considerations make projection with next-generation detectors using our methodology technically challenging, we therefore restrict to A+.

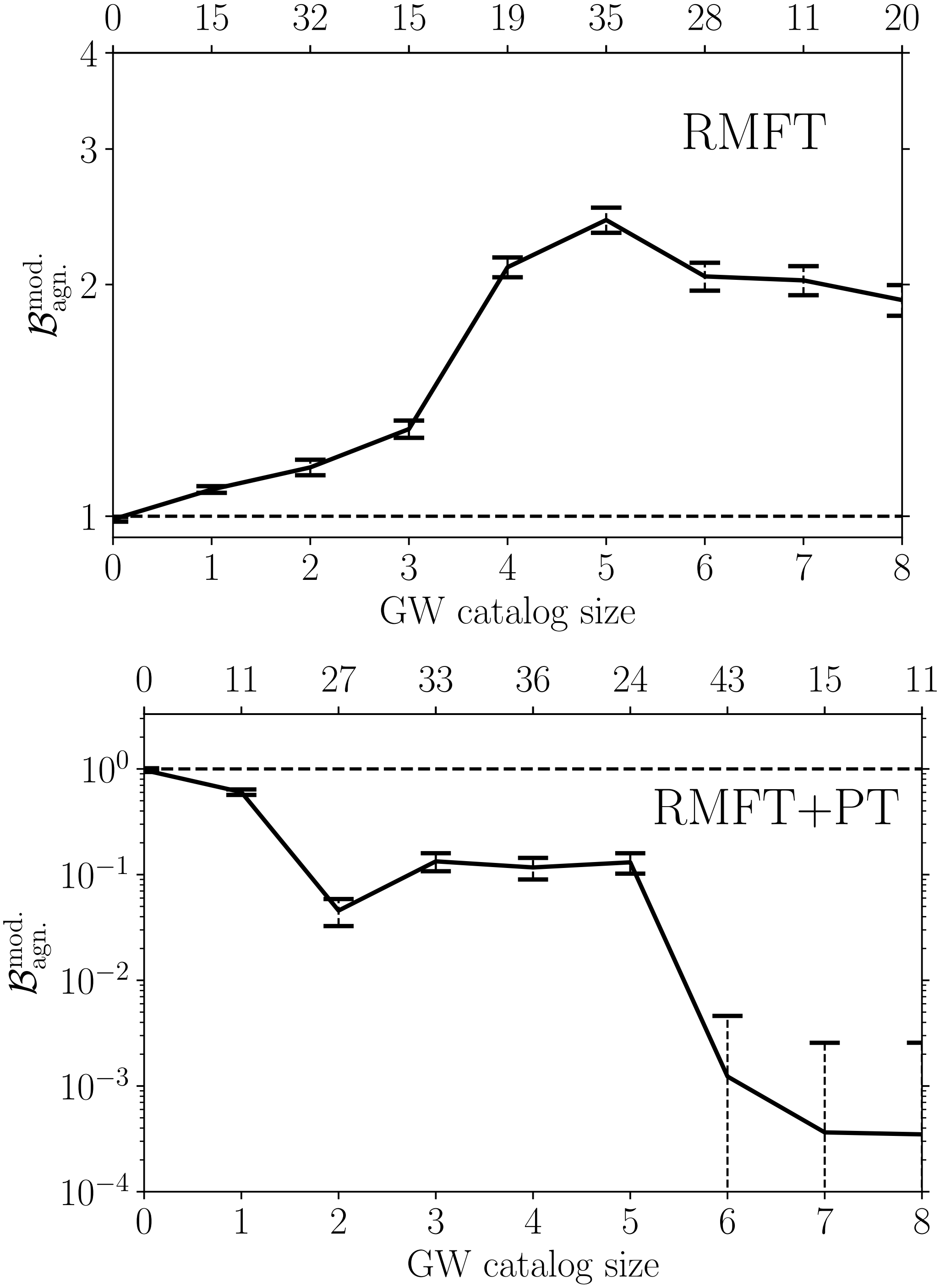

Figure 8.14: The ratio of evidences (i.e. Bayes factor), between models assuming a transition from an RMFT informed model at $p/c^2 = 10^{14}$ g/cm^3 and at $p/c^2 = 3 \times 10^{13}$ g/cm^3. The top panel is for the case of an RMFT injection, whereas the bottom panel is for the case of an RMFT that transitions to a constant speed-of-sound EoS. We plot the Bayes Factor as a function of the number of events analyzed. On the top x-axis of each figure, we include the SNR of the event added to the catalog.

the evidence accruing from a handful of informative events. For reference, the mass of the lowest mass neutron star with a core undergoing the phase transition (the "transition mass") is $\sim 0.6\,M_\odot$, well below any of the simulated neutron stars. Therefore all simulated neutron stars have substantial quark cores. The highest SNR event in the phase transition EoS case is also the most informative (SNR of 43, 6th event in the catalog). However, certain events even with large SNR ($\gtrsim 30$) are not necessarily informative, usually because their masses are too large and therefore lack a measurable tidal signature. Nonetheless, these results indicate that upcoming gravitational wave data could lead to stronger constraints on the RMFT breakdown scale.

References

[1] https://dcc.ligo.org/public/0149/T1800042/004/T1800042-v4.pdf.

[2] Adrian Abac et al. "The Science of the Einstein Telescope". In: (Mar. 2025). arXiv: 2503.12263 [gr-qc].

[3] B. P. Abbott et al. "GW170817: Measurements of neutron star radii and equation of state". In: *Phys. Rev. Lett.* 121.16 (2018), p. 161101. DOI: 10.1103/PhysRevLett.121.161101. arXiv: 1805.11581 [gr-qc].

[4] B. P. Abbott et al. "GW190425: Observation of a Compact Binary Coalescence with Total Mass $\sim 3.4 M_\odot$". In: *Astrophys. J. Lett.* 892.1 (2020), p. L3. DOI: 10.3847/2041-8213/ab75f5. arXiv: 2001.01761 [astro-ph.HE].

[5] B. P. Abbott, R. Abbott, and T. D. et al. Abbott. "GW170817: Observation of Gravitational Waves from a Binary Neutron Star Inspiral". In: *Phys. Rev. Lett.* 119.16, 161101 (Oct. 2017), p. 161101. DOI: 10.1103/PhysRevLett.119.161101. arXiv: 1710.05832 [gr-qc].

[6] B. P. Abbott, R. Abbott, and T. D. et al. Abbott. "GW190425: Observation of a Compact Binary Coalescence with Total Mass $\sim$ 3.4 $\mathrm{M}_\odot$". In: *The Astrophysical Journal Letters* 892.1, L3 (Mar. 2020), p. L3. DOI: 10.3847/2041-8213/ab75f5. arXiv: 2001.01761 [astro-ph.HE].

[7] R. Abbott et al. "Population of Merging Compact Binaries Inferred Using Gravitational Waves through GWTC-3". In: *Phys. Rev. X* 13.1 (2023), p. 011048. DOI: 10.1103/PhysRevX.13.011048. arXiv: 2111.03634 [astro-ph.HE].

[8] D. Adhikari et al. "Accurate Determination of the Neutron Skin Thickness of ^{208}Pb through Parity-Violation in Electron Scattering". In: *Phys. Rev. Lett.* 126.17 (2021), p. 172502. DOI: 10.1103/PhysRevLett.126.172502. arXiv: 2102.10767 [nucl-ex].

[9] Mark G. Alford, Alexander Haber, and Ziyuan Zhang. "Beyond modified Urca: The nucleon width approximation for flavor-changing processes in dense matter". In: *Phys. Rev. C* 110.5 (2024), p. L052801. DOI: 10.1103/PhysRevC.110.L052801. arXiv: 2406.13717 [nucl-th].

[10] Mark G. Alford, Alexander Haber, and Ziyuan Zhang. "Isospin equilibration in neutron star mergers". In: *Phys. Rev. C* 109.5 (2024), p. 055803. DOI: 10.1103/PhysRevC.109.055803. arXiv: 2306.06180 [nucl-th].

[11] Mark G. Alford et al. "Relativistic mean-field theories for neutron-star physics based on chiral effective field theory". In: *Phys. Rev. C* 106.5 (2022), p. 055804. DOI: 10.1103/PhysRevC.106.055804. arXiv: 2205.10283 [nucl-th].

[12] Mark G. Alford et al. "Tabulated equations of state from models informed by chiral effective field theory". In: *Phys. Scripta* 98.12 (2023), p. 125302. DOI: 10.1088/1402-4896/ad03c8. arXiv: 2304.07836 [nucl-th].

[13] Eemeli Annala et al. "Quark-matter cores in neutron stars". In: (2019). arXiv: 1903.09121 [astro-ph.HE].

[14] John Antoniadis et al. "A Massive Pulsar in a Compact Relativistic Binary". In: *Science* 340.6131 (2013), p. 1233232. DOI: 10.1126/science.1233232. arXiv: 1304.6875 [astro-ph.HE].

[15] Gregory Ashton et al. "BILBY: A User-friendly Bayesian Inference Library for Gravitational-wave Astronomy". In: *The Astrophysical Journal Supplement Series* 241.2, 27 (Apr. 2019), p. 27. DOI: 10.3847/1538-4365/ab06fc. arXiv: 1811.02042 [astro-ph.IM].

[16] A. Bauswein and N. Stergioulas. "Unified picture of the post-merger dynamics and gravitational wave emission in neutron star mergers". In: *Phys. Rev. D* 91 (12 June 2015), p. 124056. DOI: 10.1103/PhysRevD.91.124056. URL: http://link.aps.org/doi/10.1103/PhysRevD.91.124056.

[17] Michael Bender, Paul-Henri Heenen, and Paul-Gerhard Reinhard. "Self-consistent mean-field models for nuclear structure". In: *Rev. Mod. Phys.* 75 (1 Jan. 2003), pp. 121–180. DOI: 10.1103/RevModPhys.75.121. URL: https://link.aps.org/doi/10.1103/RevModPhys.75.121.

[18] Bhaskar Biswas and Stephan Rosswog. "Simultaneously Constraining the Neutron Star Equation of State and Mass Distribution through Multimessenger Observations and Nuclear Benchmarks". In: (Aug. 2024). arXiv: 2408.15192 [astro-ph.HE].

[19] R. Blandford and S. A. Teukolsky. "Arrival-time analysis for a pulsar in a binary system." In: *The Astrophysical Journal* 205 (Apr. 1976), pp. 580–591. DOI: 10.1086/154315.

[20] Slavko Bogdanov et al. "Constraining the Neutron Star Mass–Radius Relation and Dense Matter Equation of State with *NICER*. I. The Millisecond Pulsar X-Ray Data Set". In: *Astrophys. J. Lett.* 887.1 (2019), p. L25. DOI: 10.3847/2041-8213/ab53eb. arXiv: 1912.05706 [astro-ph.HE].

[21] J. Boguta and A. R. Bodmer. "Relativistic Calculation of Nuclear Matter and the Nuclear Surface". In: *Nucl. Phys. A* 292 (1977), pp. 413–428. DOI: 10.1016/0375-9474(77)90626-1.

[22] Matteo Breschi et al. "Kilohertz Gravitational Waves From Binary Neutron Star Mergers: Numerical-relativity Informed Postmerger Model". In: (May 2022). arXiv: 2205.09112 [gr-qc].

[23] Liam Brodie and Alexander Haber. "Nuclear and hybrid equations of state in light of the low-mass compact star in HESS J1731-347". In: *Phys. Rev. C* 108.2 (2023), p. 025806. DOI: 10.1103/PhysRevC.108.025806. arXiv: 2302.02989 [nucl-th].

[24] Michael Buballa. "NJL model analysis of quark matter at large density". In: *Phys. Rept.* 407 (2005), pp. 205–376. DOI: 10.1016/j.physrep.2004.11.004. arXiv: hep-ph/0402234.

[25] Collin D. Capano et al. "GW170817: Stringent constraints on neutron-star radii from multimessenger observations and nuclear theory". In: *arXiv e-prints*, arXiv:1908.10352 (Aug. 2019), arXiv:1908.10352. arXiv: 1908.10352 [astro-ph.HE].

[26] Katerina Chatziioannou. "Neutron star tidal deformability and equation of state constraints". In: *Gen. Rel. Grav.* 52.11 (2020), p. 109. DOI: 10.1007/s10714-020-02754-3. arXiv: 2006.03168 [gr-qc].

[27] Katerina Chatziioannou. "Uncertainty limits on neutron star radius measurements with gravitational waves". In: (Aug. 2021). arXiv: 2108.12368 [gr-qc].

[28] Katerina Chatziioannou and Sophia Han. "Studying strong phase transitions in neutron stars with gravitational waves". In: *Phys. Rev. D* 101.4 (2020), p. 044019. DOI: 10.1103/PhysRevD.101.044019. arXiv: 1911.07091 [gr-qc].

[29] Katerina Chatziioannou et al. "Neutron stars and the dense matter equation of state: from microscopic theory to macroscopic observations". In: (July 2024). arXiv: 2407.11153 [nucl-th].

[30] Devarshi Choudhury et al. "A NICER View of the Nearest and Brightest Millisecond Pulsar: PSR J0437-4715". In: (July 2024). arXiv: 2407.06789 [astro-ph.HE].

[31] Michael W. Coughlin et al. “Multimessenger Bayesian parameter inference of a binary neutron star merger”. In: *Mon. Not. Roy. Astron. Soc.* 489.1 (2019), pp. L91–L96. doi: 10.1093/mnrasl/slz133. arXiv: 1812.04803 [astro-ph.HE].

[32] H. Thankful Cromartie et al. “Relativistic Shapiro delay measurements of an extremely massive millisecond pulsar”. In: *Nature Astron.* 4.1 (2019), pp. 72–76. doi: 10.1038/s41550-019-0880-2. arXiv: 1904.06759.

[33] F. Dautry and E. M. Nyman. “PION CONDENSATION AND THE SIGMA MODEL IN LIQUID NEUTRON MATTER”. In: *Nucl. Phys. A* 319 (1979), pp. 323–348. doi: 10.1016/0375-9474(79)90518-9.

[34] Paul Demorest et al. “Shapiro Delay Measurement of A Two Solar Mass Neutron Star”. In: *Nature* 467 (2010), pp. 1081–1083. doi: 10.1038/nature09466. arXiv: 1010.5788 [astro-ph.HE].

[35] Carleton E. Detar and Teiji Kunihiro. “Linear σ Model With Parity Doubling”. In: *Phys. Rev. D* 39 (1989), p. 2805. doi: 10.1103/PhysRevD.39.2805.

[36] Tim Dietrich, Tanja Hinderer, and Anuradha Samajdar. “Interpreting Binary Neutron Star Mergers: Describing the Binary Neutron Star Dynamics, Modelling Gravitational Waveforms, and Analyzing Detections”. In: *Gen. Rel. Grav.* 53.3 (2021), p. 27. doi: 10.1007/s10714-020-02751-6. arXiv: 2004.02527 [gr-qc].

[37] Tim Dietrich et al. “Improving the NRTidal model for binary neutron star systems”. In: *Phys. Rev. D* 100.4 (2019), p. 044003. doi: 10.1103/PhysRevD.100.044003. arXiv: 1905.06011 [gr-qc].

[38] Tim Dietrich et al. “Multimessenger constraints on the neutron-star equation of state and the Hubble constant”. In: *Science* 370.6523 (2020), pp. 1450–1453. doi: 10.1126/science.abb4317. arXiv: 2002.11355 [astro-ph.HE].

[39] Alexander J. Dittmann et al. “A More Precise Measurement of the Radius of PSR J0740+6620 Using Updated NICER Data”. In: *Astrophys. J.* 974.2 (2024), p. 295. doi: 10.3847/1538-4357/ad5f1e. arXiv: 2406.14467 [astro-ph.HE].

[40] C. Drischler, K. Hebeler, and A. Schwenk. “Chiral interactions up to next-to-next-to-next-to-leading order and nuclear saturation”. In: *Phys. Rev. Lett.* 122.4 (2019), p. 042501. doi: 10.1103/PhysRevLett.122.042501. arXiv: 1710.08220 [nucl-th].

[41] C. Drischler et al. “How Well Do We Know the Neutron-Matter Equation of State at the Densities Inside Neutron Stars? A Bayesian Approach with Correlated Uncertainties”. In: *Phys. Rev. Lett.* 125.20 (2020), p. 202702. doi: 10.1103/PhysRevLett.125.202702. arXiv: 2004.07232 [nucl-th].

[42] C. Drischler et al. “Quantifying uncertainties and correlations in the nuclear-matter equation of state”. In: *Phys. Rev. C* 102.5 (2020), p. 054315. DOI: 10.1103/PhysRevC.102.054315. arXiv: 2004.07805 [nucl-th].

[43] M. Dutra et al. “Relativistic Mean-Field Hadronic Models under Nuclear Matter Constraints”. In: *Phys. Rev. C* 90.5 (2014), p. 055203. DOI: 10.1103/PhysRevC.90.055203. arXiv: 1405.3633 [nucl-th].

[44] Reed Essick. *Universality (2024-08-06)*. Aug. 2024. DOI: 10.5281/zenodo.13241272. URL: https://doi.org/10.5281/zenodo.13241272.

[45] Reed Essick and Maya Fishbach. “Ensuring Consistency between Noise and Detection in Hierarchical Bayesian Inference”. In: *Astrophys. J.* 962.2 (2024), p. 169. DOI: 10.3847/1538-4357/ad1604. arXiv: 2310.02017 [gr-qc].

[46] Reed Essick and Philippe Landry. “Discriminating between Neutron Stars and Black Holes with Imperfect Knowledge of the Maximum Neutron Star Mass”. In: *Astrophys. J.* 904.1 (2020), p. 80. DOI: 10.3847/1538-4357/abbd3b. arXiv: 2007.01372 [astro-ph.HE].

[47] Reed Essick, Philippe Landry, and Daniel E. Holz. “Nonparametric Inference of Neutron Star Composition, Equation of State, and Maximum Mass with GW170817”. In: *Phys. Rev. D* 101.6 (2020), p. 063007. DOI: 10.1103/PhysRevD.101.063007. arXiv: 1910.09740 [astro-ph.HE].

[48] Reed Essick et al. “A Detailed Examination of Astrophysical Constraints on the Symmetry Energy and the Neutron Skin of ^{208}Pb with Minimal Modeling Assumptions”. In: (July 2021). arXiv: 2107.05528 [nucl-th].

[49] Reed Essick et al. “Astrophysical Constraints on the Symmetry Energy and the Neutron Skin of ^{208}Pb with Minimal Modeling Assumptions”. In: (Feb. 2021). arXiv: 2102.10074 [nucl-th].

[50] Reed Essick et al. “Direct Astrophysical Tests of Chiral Effective Field Theory at Supranuclear Densities”. In: *Phys. Rev. C* 102.5 (2020), p. 055803. DOI: 10.1103/PhysRevC.102.055803. arXiv: 2004.07744 [astro-ph.HE].

[51] Reed Essick et al. “Phase transition phenomenology with nonparametric representations of the neutron star equation of state”. In: *Phys. Rev. D* 108.4 (2023). I contributed substantially to this study which used nonparametric methods to constrain phase transitions in a nonparametric model of the equation of state. I performed the simulation analyses, developed several diagnostic statistics, and wrote large parts of the text., p. 043013. DOI: 10.1103/PhysRevD.108.043013. arXiv: 2305.07411 [astro-ph.HE].

[52] Matthew Evans et al. “Cosmic Explorer: A Submission to the NSF MPSAC ngGW Subcommittee”. In: (June 2023). arXiv: 2306.13745 [astro-ph.IM].

[53] Amanda M. Farah et al. "Bridging the Gap: Categorizing Gravitational-Wave Events at the Transition Between Neutron Stars and Black Holes". In: (Nov. 2021). arXiv: 2111.03498 [astro-ph.HE].

[54] F. J. Fattoyev et al. "Relativistic effective interaction for nuclei, giant resonances, and neutron stars". In: *Phys. Rev. C* 82 (2010), p. 055803. DOI: 10.1103/PhysRevC.82.055803. arXiv: 1008.3030 [nucl-th].

[55] Maya Fishbach, Reed Essick, and Daniel E. Holz. "Does Matter Matter? Using the mass distribution to distinguish neutron stars and black holes". In: *Astrophys. J. Lett.* 899 (2020), p. L8. DOI: 10.3847/2041-8213/aba7b6. arXiv: 2006.13178 [astro-ph.HE].

[56] E. Fonseca et al. "Refined Mass and Geometric Measurements of the High-mass PSR J0740+6620". In: *Astrophys. J. Lett.* 915.1 (2021), p. L12. DOI: 10.3847/2041-8213/ac03b8. arXiv: 2104.00880 [astro-ph.HE].

[57] Bengt Friman and Wolfram Weise. "Neutron Star Matter as a Relativistic Fermi Liquid". In: *Phys. Rev. C* 100 (2019), p. 065807. DOI: 10.1103/PhysRevC.100.065807. arXiv: 1908.09722 [nucl-th].

[58] S. Gandolfi, J. Carlson, and Sanjay Reddy. "The maximum mass and radius of neutron stars and the nuclear symmetry energy". In: *Phys. Rev. C* 85 (2012), 032801(R). DOI: 10.1103/PhysRevC.85.032801. arXiv: 1101.1921.

[59] A. Gezerlis et al. "Local chiral effective field theory interactions and quantum Monte Carlo applications". In: *Phys. Rev. C* 90.5 (2014), p. 054323. DOI: 10.1103/PhysRevC.90.054323. arXiv: 1406.0454 [nucl-th].

[60] A. Gezerlis et al. "Quantum Monte Carlo Calculations with Chiral Effective Field Theory Interactions". In: *Phys. Rev. Lett.* 111.3 (2013), p. 032501. DOI: 10.1103/PhysRevLett.111.032501. arXiv: 1303.6243 [nucl-th].

[61] N. K. Glendenning. "THE HYPERON COMPOSITION OF NEUTRON STARS". In: *Phys. Lett. B* 114 (1982), pp. 392–396. DOI: 10.1016/0370-2693(82)90078-8.

[62] Norman K. Glendenning. *Compact Stars*. Springer, 1996.

[63] Jacob Golomb et al. "The interplay of astrophysics and nuclear physics in determining the properties of neutron stars". In: (Oct. 2024). I co-led this study with Jacob Golomb studying how astrophysical and dense-matter physics can be disentangled via hierarchical analysis. I performed equation of state analyses, and co-wrote the text of the manuscript. arXiv: 2410.14597 [astro-ph.HE].

[64] Ish Gupta et al. "Characterizing gravitational wave detector networks: from A$^\sharp$ to cosmic explorer". In: *Class. Quant. Grav.* 41.24 (2024), p. 245001. DOI: 10.1088/1361-6382/ad7b99. arXiv: 2307.10421 [gr-qc].

[65] K. Hebeler et al. “Equation of state and neutron star properties constrained by nuclear physics and observation”. In: *Astrophys. J.* 773 (2013), p. 11. DOI: 10.1088/0004-637X/773/1/11. arXiv: 1303.4662 [astro-ph.SR].

[66] Tanja Hinderer et al. “Tidal deformability of neutron stars with realistic equations of state and their gravitational wave signatures in binary inspiral”. In: *Phys. Rev. D* 81 (2010), p. 123016. DOI: 10.1103/PhysRevD.81.123016. arXiv: 0911.3535 [astro-ph.HE].

[67] Daisuke Jido, Makoto Oka, and Atsushi Hosaka. “Chiral symmetry of baryons”. In: *Prog. Theor. Phys.* 106 (2001), pp. 873–908. DOI: 10.1143/PTP.106.873. arXiv: hep-ph/0110005.

[68] J. Keller et al. “Neutron matter at finite temperature based on chiral effective field theory interactions”. In: *Phys. Rev. C* 103.5 (2021), p. 055806. DOI: 10.1103/PhysRevC.103.055806. arXiv: 2011.05855 [nucl-th].

[69] E. E. Kolomeitsev, K. A. Maslov, and D. N. Voskresensky. “Delta isobars in relativistic mean-field models with σ -scaled hadron masses and couplings”. In: *Nucl. Phys. A* 961 (2017), pp. 106–141. DOI: 10.1016/j.nuclphysa.2017.02.004. arXiv: 1610.09746 [nucl-th].

[70] Oleg Komoltsev and Aleksi Kurkela. “How Perturbative QCD Constrains the Equation of State at Neutron-Star Densities”. In: *Phys. Rev. Lett.* 128.20 (2022), p. 202701. DOI: 10.1103/PhysRevLett.128.202701. arXiv: 2111.05350 [nucl-th].

[71] Oleg Komoltsev et al. “Equation of state at neutron-star densities and beyond from perturbative QCD”. In: *Phys. Rev. D* 109.9 (2024), p. 094030. DOI: 10.1103/PhysRevD.109.094030. arXiv: 2312.14127 [nucl-th].

[72] Philippe Landry and Reed Essick. “Nonparametric inference of the neutron star equation of state from gravitational wave observations”. In: *Phys. Rev. D* 99.8 (2019), p. 084049. DOI: 10.1103/PhysRevD.99.084049. arXiv: 1811.12529 [gr-qc].

[73] Philippe Landry, Reed Essick, and Katerina Chatziioannou. “Nonparametric constraints on neutron star matter with existing and upcoming gravitational wave and pulsar observations”. In: *Phys. Rev. D* 101.12 (2020), p. 123007. DOI: 10.1103/PhysRevD.101.123007. arXiv: 2003.04880 [astro-ph.HE].

[74] J. M. Lattimer and M. Prakash. “Neutron star structure and the equation of state”. In: *Astrophys. J.* 550 (2001), p. 426. DOI: 10.1086/319702. arXiv: astro-ph/0002232.

[75] James M. Lattimer and Yeunhwan Lim. “Constraining the Symmetry Parameters of the Nuclear Interaction”. In: *Astrophys. J.* 771 (2013), p. 51. DOI: 10.1088/0004-637X/771/1/51. arXiv: 1203.4286 [nucl-th].

[76] James M. Lattimer and Andrew W. Steiner. "Constraints on the symmetry energy using the mass-radius relation of neutron stars". In: *Eur. Phys. J. A* 50 (2014), p. 40. DOI: 10.1140/epja/i2014-14040-y. arXiv: 1403.1186 [nucl-th].

[77] Isaac Legred et al. "Impact of the PSR J0740 + 6620 radius constraint on the properties of high-density matter". In: *Phys. Rev. D* 104 (6 Sept. 2021). I led this study on the impact of the the NICER mass-radius constraint on the mllisecond x-ray pulsar J0740+6620 on nonparametric equation of state constraints. I developed software, some of which was contributed by other collaborators from previous projects, ran the analysis, and co-wrote the manuscript., p. 063003. DOI: 10.1103/PhysRevD.104.063003. URL: https://link.aps.org/doi/10.1103/PhysRevD.104.063003.

[78] Isaac Legred et al. "Implicit correlations within phenomenological parametric models of the neutron star equation of state". In: *Phys. Rev. D* 105.4 (2022). I led this study which compared parametric to nonparametric methods of inferring the equation of state. I developed a substantial amount of software, ran the analysis, and co-wrote the manuscript., p. 043016. DOI: 10.1103/PhysRevD.105.043016. arXiv: 2201.06791 [astro-ph.HE].

[79] Alessandro Lovato et al. "Long Range Plan: Dense matter theory for heavy-ion collisions and neutron stars". In: (Nov. 2022). arXiv: 2211.02224 [nucl-th].

[80] J. E. Lynn et al. "Chiral Three-Nucleon Interactions in Light Nuclei, Neutron-α Scattering, and Neutron Matter". In: *Phys. Rev. Lett.* 116.6 (2016), p. 062501. DOI: 10.1103/PhysRevLett.116.062501. arXiv: 1509.03470 [nucl-th].

[81] Ben Margalit and Brian D. Metzger. "Constraining the Maximum Mass of Neutron Stars From Multi-Messenger Observations of GW170817". In: *Astrophys. J.* 850.2 (2017), p. L19. DOI: 10.3847/2041-8213/aa991c. arXiv: 1710.05938 [astro-ph.HE].

[82] M. C. Miller et al. "PSR J0030+0451 Mass and Radius from $NICER$ Data and Implications for the Properties of Neutron Star Matter". In: *Astrophys. J. Lett.* 887.1 (2019), p. L24. DOI: 10.3847/2041-8213/ab50c5. arXiv: 1912.05705 [astro-ph.HE].

[83] M. C. Miller et al. "The Radius of PSR J0740+6620 from NICER and XMM-Newton Data". In: (May 2021). arXiv: 2105.06979 [astro-ph.HE].

[84] M. Coleman Miller, Cecilia Chirenti, and Frederick K. Lamb. "Constraining the equation of state of high-density cold matter using nuclear and astronomical measurements". In: (2019). arXiv: 1904.08907 [astro-ph.HE].

[85] Debora Mroczek et al. "Nontrivial features in the speed of sound inside neutron stars". In: *Phys. Rev. D* 110.12 (2024), p. 123009. DOI: 10.1103/PhysRevD.110.123009. arXiv: 2309.02345 [astro-ph.HE].

[86] J.R. Oppenheimer and G.M. Volkoff. "On Massive neutron cores". In: *Phys. Rev.* 55 (1939), pp. 374–381. DOI: 10.1103/PhysRev.55.374.

[87] Peter T. H. Pang et al. "Parameter estimation for strong phase transitions in supranuclear matter using gravitational-wave astronomy". In: *Phys. Rev. Res.* 2.3 (2020), p. 033514. DOI: 10.1103/PhysRevResearch.2.033514. arXiv: 2006.14936 [astro-ph.HE].

[88] Orestis Papadopoulos and Andreas Schmitt. "How neutron star properties disfavor a nuclear chiral density wave". In: *Phys. Rev. D* 111.3 (2025), p. 034010. DOI: 10.1103/PhysRevD.111.034010. arXiv: 2411.08023 [nucl-th].

[89] David Radice, Luciano Rezzolla, and Filippo Galeazzi. "Beyond second-order convergence in simulations of binary neutron stars in full general-relativity". In: *Mon. Not. Roy. Astron. Soc.* 437 (2014), pp. L46–L50. DOI: 10.1093/mnrasl/slt137. arXiv: 1306.6052 [gr-qc].

[90] C.E. Rasmussen and C.K.I. Williams. *Gaussian Processes for Machine Learning*. Adaptive Computation and Machine Learning series. MIT Press, 2005. ISBN: 9780262182539. URL: https://books.google.ca/books?id=H3aMEAAAQBAJ.

[91] Jocelyn S. Read. "Waveform uncertainty quantification and interpretation for gravitational-wave astronomy". In: *Class. Quant. Grav.* 40.13 (2023), p. 135002. DOI: 10.1088/1361-6382/acd29b. arXiv: 2301.06630 [gr-qc].

[92] Brendan T. Reed et al. "Implications of PREX-2 on the Equation of State of Neutron-Rich Matter". In: *Phys. Rev. Lett.* 126.17 (2021), p. 172503. DOI: 10.1103/PhysRevLett.126.172503. arXiv: 2101.03193 [nucl-th].

[93] Clifford E. Rhoades Jr. and Remo Ruffini. "Maximum mass of a neutron star". In: *Phys. Rev. Lett.* 32 (1974), pp. 324–327. DOI: 10.1103/PhysRevLett.32.324.

[94] Thomas E. Riley et al. "A *NICER* View of PSR J0030+0451: Millisecond Pulsar Parameter Estimation". In: *Astrophys. J. Lett.* 887.1 (2019), p. L21. DOI: 10.3847/2041-8213/ab481c. arXiv: 1912.05702 [astro-ph.HE].

[95] Thomas E. Riley et al. "A NICER View of the Massive Pulsar PSR J0740+6620 Informed by Radio Timing and XMM-Newton Spectroscopy". In: (May 2021). arXiv: 2105.06980 [astro-ph.HE].

[96] Tuomo Salmi et al. "The Radius of the High-mass Pulsar PSR J0740+6620 with 3.6 yr of NICER Data". In: *Astrophys. J.* 974.2 (2024), p. 294. DOI: 10.3847/1538-4357/ad5f1f. arXiv: 2406.14466 [astro-ph.HE].

[97] Andreas Schmitt and Peter Shternin. "Reaction rates and transport in neutron stars". In: *Astrophys. Space Sci. Libr.* 457 (2018), pp. 455–574. DOI: 10.1007/978-3-319-97616-7_9. arXiv: 1711.06520 [astro-ph.HE].

[98] Brian D. Serot and John Dirk Walecka. “Recent progress in quantum hadrodynamics”. In: *Int. J. Mod. Phys. E* 6 (1997), pp. 515–631. DOI: 10.1142/S0218301397000299. arXiv: nucl-th/9701058.

[99] Brian D. Serot and John Dirk Walecka. “The Relativistic Nuclear Many Body Problem”. In: *Adv. Nucl. Phys.* 16 (1986), pp. 1–327.

[100] Irwin I. Shapiro. “Fourth Test of General Relativity”. In: *Phys. Rev. Lett.* 13 (1964), pp. 789–791. DOI: 10.1103/PhysRevLett.13.789.

[101] Masaru Shibata. “Constraining nuclear equations of state using gravitational waves from hypermassive neutron stars”. In: *Phys. Rev. Lett.* 94 (2005), p. 201101. DOI: 10.1103/PhysRevLett.94.201101. arXiv: gr-qc/0504082 [gr-qc].

[102] Masaru Shibata et al. “Constraint on the maximum mass of neutron stars using GW170817 event”. In: *Phys. Rev. D* 100.2 (2019), p. 023015. DOI: 10.1103/PhysRevD.100.023015. arXiv: 1905.03656 [astro-ph.HE].

[103] Andrew W. Steiner, Matthias Hempel, and Tobias Fischer. “Core-collapse supernova equations of state based on neutron star observations”. In: *Astrophys. J.* 774 (2013), p. 17. DOI: 10.1088/0004-637X/774/1/17. arXiv: 1207.2184 [astro-ph.SR].

[104] I. Tews et al. “Neutron matter at next-to-next-to-next-to-leading order in chiral effective field theory”. In: *Phys. Rev. Lett.* 110.3 (2013), p. 032504. DOI: 10.1103/PhysRevLett.110.032504. arXiv: 1206.0025 [nucl-th].

[105] I. Tews et al. “Quantum Monte Carlo calculations of neutron matter with chiral three-body forces”. In: *Phys. Rev. C* 93.2 (2016), p. 024305. DOI: 10.1103/PhysRevC.93.024305. arXiv: 1507.05561 [nucl-th].

[106] Ingo Tews et al. “Constraining the speed of sound inside neutron stars with chiral effective field theory interactions and observations”. In: *Astrophys. J.* 860.2 (2018), p. 149. DOI: 10.3847/1538-4357/aac267. arXiv: 1801.01923 [nucl-th].

[107] Richard C. Tolman. “Static solutions of Einstein’s field equations for spheres of fluid”. In: *Phys. Rev.* 55 (1939), pp. 364–373. DOI: 10.1103/PhysRev.55.364.

[108] Laura Tolos and Laura Fabbietti. “Strangeness in Nuclei and Neutron Stars”. In: *Prog. Part. Nucl. Phys.* 112 (2020), p. 103770. DOI: 10.1016/j.ppnp.2020.103770. arXiv: 2002.09223 [nucl-ex].

[109] J. D. Walecka. “A theory of highly condensed matter.” In: *Annals of Physics* 83 (Jan. 1974), pp. 491–529. DOI: 10.1016/0003-4916(74)90208-5. URL: https://www.sciencedirect.com/science/article/pii/0003491674902085.

[110] Fridolin Weber. “Strange quark matter and compact stars”. In: *Prog. Part. Nucl. Phys.* 54 (2005), pp. 193–288. DOI: 10.1016/j.ppnp.2004.07.001. arXiv: astro-ph/0407155.

[111] Steven Weinberg. “Nuclear forces from chiral Lagrangians”. In: *Phys. Lett. B* 251 (1990), pp. 288–292. DOI: 10.1016/0370-2693(90)90938-3.

[112] Tianqi Zhao and James M. Lattimer. “Tidal Deformabilities and Neutron Star Mergers”. In: *Phys. Rev. D* 98.6 (2018), p. 063020. DOI: 10.1103/PhysRevD.98.063020. arXiv: 1808.02858 [astro-ph.HE].

[113] Ying Zhou, Lie-Wen Chen, and Zhen Zhang. “Equation of state of dense matter in the multimessenger era”. In: *Phys.Rev.D* 99.12, 121301 (June 2019), p. 121301. DOI: 10.1103/PhysRevD.99.121301. arXiv: 1901.11364 [nucl-th].

Chapter 9

SIMULATIONS OF NEUTRON STARS WITH FLEXIBLE EQUATIONS OF STATE

[1] Isaac Legred et al. "Simulating neutron stars with a flexible enthalpy-based equation of state parametrization in spectre". In: *Phys. Rev. D* 107.12 (2023). I led this project building a flexible equation of state model, implementing it in the SpECTRE code, and running relativistic simulation of neutron stars. I developed the project idea, constructed the equation of state model, implemented it, and ran analyses. I also wrote the bulk of the text in the manuscript., p. 123017. DOI: 10.1103/PhysRevD.107.123017. arXiv: 2301.13818 [astro-ph.HE].

Abstract

Numerical simulations of neutron star mergers represent an essential step toward interpreting the full complexity of multimessenger observations and constraining the properties of supranuclear matter. Currently, simulations are limited by an array of factors, including computational performance and input physics uncertainties, such as the neutron star equation of state. In this work, we expand the range of nuclear phenomenology efficiently available to simulations by introducing a new analytic parametrization of cold, beta-equilibrated matter that is based on the relativistic enthalpy. We show that the new *enthalpy parametrization* can capture a range of nuclear behavior, including strong phase transitions. We implement the enthalpy parametrization in the SpECTRE code, simulate isolated neutron stars, and compare performance to the commonly used spectral and polytropic parametrizations. We find comparable computational performance for nuclear models that are well represented by either parametrization, such as simple hadronic EoSs. We show that the enthalpy parametrization further allows us to simulate more complicated hadronic models or models with phase transitions that are inaccessible to current parametrizations.

9.1 Introduction

Multimessenger observations of the gravitational wave event GW170817 [4, 3] have highlighted the role of neutron star binaries (BNS) in probing the physics of dense matter, e.g., [35, 23, 92]. In addition, further astronomical observations [4, 2, 27, 49, 82, 81, 106, 107, 12] and terrestrial nuclear experiments [5, 6] have facilitated new insights into the equation of state (EoS) of NS matter [1, 43, 90, 90, 95, 96, 71, 74, 82, 81]. Nonetheless significant uncertainty exists about the properties of dense matter above nuclear saturation density[1], $\rho_{\rm nuc} \equiv 2.8 \times 10^{14}\mathrm{g/cm}^3$, which translates to uncertainty in the properties of astrophysical NSs whose densities can reach $\sim 7\rho_{\rm nuc}$ [90, 74].

The merger phase of a BNS coalescence carries the largest imprint of nuclear matter and strong gravity and it can only be studied numerically. Numerical relativity (NR) simulations of BNS coalescences through merger require solving the equations of general relativistic magnetohydrodynamics (GRMHD) simultaneously with the Einstein field equations and, possibly, the Boltzmann equations for neutrino radiation transport [11, 50, 17]. The system of equations is closed with a nuclear EoS. See e.g. [15, 97, 52, 67, 104] for reviews of the field. Such simulations have been used to interpret existing signals, e.g. [79, 98, 111, 65, 10, 20], and targeted simulations will likely be an essential tool for understanding future observations.

The most generic strategy for representing the nuclear EoS numerically is piecewise, i.e., using independent expressions in different density or pressure intervals. For example, interpolated tables of thermodynamic quantities such as pressure and internal energy at every value of the density and composition offer access to the widest range of nuclear behavior. However, the temperature- and composition-dependent tables currently used, e.g. [117], have a significant memory footprint and evaluation requires computationally expensive operations such as constant access to the table and interpolation [112]. The latter may also be inaccurate (at low order) or prone to unphysical oscillations for EoSs with discontinuities or underresolved features (at high order). A related approach makes use of piecewise parametrizations such as a *piecewise-polytrope* [102], which is effectively a sparsely sampled table for the polytropic exponent. Though it can capture a range of high-density behavior, discontinuities in derivatives of thermodynamic quantities can degrade simulation accuracy [53, 101].

[1] The saturation density of atomic nuclei is determined via theory and experiments [38]; here we fix a value for convenience.

A different strategy is based on functional representations of the EoS that stay smooth across density scales, such as a *single-polytropic* or *spectral* parametrization [77, 55, 53, 101]. Such parametrizations typically cannot fully represent nuclear EoS models, as they are restricted to a finite number of parameters in the density range of interest [55, 53]. On top of this, smoothness across density scales fails to capture nuclear models that contain nuclear transitions to exotic degrees of freedom.

In this study, we propose a new parametrization of the nuclear EoS that bridges smooth and discontinuous models while balancing accuracy and computational efficiency.[2] We parametrize the relativistic enthalpy [76] via a combination of analytic polynomials and trigonometric functions. Unlike pressure, the difference in enthalpy at densities $[\rho_{\text{nuc}}, 3\rho_{\text{nuc}}]$ for two EoSs is typically small compared to the enthalpy of either. The enthalpy can thus be effectively written as a "baseline" part plus small corrections. We capitalize on this in order to write the enthalpy as a polynomial, typically capturing $\sim 99\%$ of the EoS, plus small trigonometric corrections, bringing the fit accuracy to 1 in 10^5. Such a decomposition can capture a wide range of phenomenology with modest changes to the relevant parameters. In addition, further thermodynamic quantities such as the pressure can be evaluated efficiently and analytically.

We implement this parametrization in SpECTRE [33, 63], a scalable next-generation multiphysics computational astrophysics code that uses task-based parallelism [60]. A primary science target for SpECTRE is fast and accurate GRMHD simulations of BNS coalescences. We use SpECTRE to test the *enthalpy parametrization* on isolated NSs in the Cowling approximation, i.e. we do not evolve the spacetime [26], while evolving the ideal GRMHD equations [17] with a discontinuous Galerkin-finite difference (DG-FD) hybrid scheme [31, 30]. Though these simulations assume a static spacetime, they still allow us to evaluate the role of the enthalpy parametrization in questions of convergence, efficiency, and resolvability of nuclear physics in simulations.

We show that the enthalpy parametrization is able to effectively represent a wide range of nuclear behavior, while incurring small additional computational costs relative to simpler parametrizations. After reviewing the general requirements a parametrization must meet in Sec. 9.2, we introduce the enthalpy parametrization in Sec. 9.3. We demonstrate that it can faithfully fit various nuclear models rang-

[2] We use the term "model" to refer to a nuclear-theoretic prediction and "parametrization" for a functional form for the EoS.

ing from smooth EoSs to phase transitions in Sec. 9.4. We perform numerical simulations with SpECTRE and find that for resolutions of at least 130 m, the EoS evaluation cost is subdominant to other simulation components. We also simulate hybrid stars with quark cores and find that such simulations can be carried out stably with better-than-expected runtime scaling properties under increasing resolution. We conclude with discussions in Sec. 9.5.

9.2 EoS Parametrizations for Relativistic Simulations

General requirements

We begin with a general discussion of the requirements phenomenological parametrizations of the nuclear EoS must meet for efficient use in numerical simulations. These include (i) faithful representation of target nuclear models, (ii) parametric extensibility, and (iii) computational performance related to smoothness (to the extent allowed by the underlying nuclear physics) and/or a fully analytic formalism.

The first requirement is that the parametrization is generic enough that it can faithfully represent the target nuclear physics. While no standard faithfulness metrics exist, a common test is the L^2 difference of quantities of interest [77, 102]. Nonetheless it is unclear how different metrics relate, for example the L^2 difference of the local polytropic indices and that of the mass-radius curve [78, 53]. One particular challenge to smooth parametrizations is modeling strong phase transitions [57, 91]. In general we would like a parametrization where, whatever the metric, we can improve the fit via iterative approximation. In principle this is available to any parametrization by adding more parameters and smoothly changing parameter values. In practice, however, the functional form of the parametrization may limit the accessible parameter space, as shown in [124] for the spectral parametrization.

The second requirement is that the parametrization allows us to parametrically explore a wide range of possible high-density behavior. This entails continuously, and without significant fine-tuning, extending the parametrization to produce EoSs that might differ from existing nuclear models. An example of such an extension would be a parameter which controls the pressure at a particular density and thus allows us to isolate the effect of this density scale on macroscopic observables. Another benefit of such continuous extensibility is that it allows us to construct a map from the EoS to observables, e.g. [89]. This approach has already been successfully used in the case of binary black hole mergers to produce accurate *surrogates* of the map of binary configurations to gravitational waves [18, 120].

A similar methodology could be used to construct a surrogate for the post-merger gravitational-wave signature of BNS mergers, whose EoS dependence is not well captured by a small number of parameters [122, 19].

At the same time, we consider practical requirements in terms of computational performance: speed and accuracy of the relevant evaluations, and smoothness of the thermodynamic quantities where possible. A fully analytic form for the EoS and all the relevant thermodynamic quantities is a sufficient (but perhaps not necessary) condition. Tabulated EoSs, while guaranteeing maximal flexibility, fail in this regard. Consider, for example, primitive variable recovery. Numerical simulations evolve the components of the stress-energy tensor which are nonlinear functions of primitive variables such the rest-mass baryon density ρ, pressure p, and specific internal energy ϵ. This process involves inverting the relation between the stress-energy tensor and the primitive variables with root-finding routines during which the EoS, for example $p(\epsilon)$, is evaluated repeatedly. For tabulated EoSs this includes computing the temperature T from ϵ via another root-find and then computing $p(T)$ via a table lookup and interpolation. The EoS tables are typically too large to store in the CPU caches and so the nested root-finding routines require repeated loading of data from main memory, causing significant overhead that dominates simulation cost [112].

Another advantage of fully analytical parametrizations is that they enable efficient computation of all necessary thermodynamic quantities in a consistent way. Besides tabulated EoSs, this also applies to certain parametrizations that require interpolation or numerical integration. For example, the spectral parametrization allows for analytic evaluation but not integration of $d\epsilon/d\rho$. Then, $\epsilon(\rho)$ is computed via a computationally expensive numerical integral as high accuracy is required to avoid thermodynamic inconsistency during primitive variable recovery. Even if tables are used in simulations, ensuring smoothness and consistency requires building higher-order interpolants (or sampling very densely). This effectively amounts to constructing local parametrizations of the EoS which satisfy some stitching constraints. Therefore, even the use of tables in NR simulations stands to gain from understanding fully analytic representations of the nuclear EoS.

Existing parametrizations of the EoS

The simplest parametrization of cold, beta-equilibrated, dense matter is a single polytrope that prescribes a relationship between the rest-mass baryon density ρ and the pressure p

$$p(\rho) = K\rho^{\Gamma}, \tag{9.1}$$

where Γ is the the polytropic exponent and K is the polytropic constant; both are independent of ρ. For example, a degenerate neutron gas would obey a polytropic relation with $\Gamma = 5/3$. Polytropes have a long history in NS simulations, e.g., [110, 48, 14, 40], and more recent code tests, e.g., [99, 28, 30], due to their simplicity, low computational cost, and the fact that they allow for analytic evaluation of pressure, internal energy, specific enthalpy, and rest-mass density. Nonetheless, their simplicity makes polytropes incompatible with realistic EoS nuclear models, either hadronic (for example, polytropes do not satisfy the same universal relations as hadronic models [125]) or hybrid ones that include multiple degrees of freedom.

Piecewise-polytropes [103] extend single-polytropes to multiple polytropic segments at different densities, thereby decoupling low- and high-density behavior. With enough piecewise segments, piecewise-polytropes can also fit EoSs with strong phase transitions [118]. While piecewise-polytropes retain some of the computational simplicity of the single-polytrope and have been employed in BNS mergers [58, 69, 36, 34], the lack of smoothness across stitching boundaries tends to increase the computational cost and decrease the accuracy [53, 101]. Extensions to continuous polytropic indices [86, 101] guarantee differentiability of the pressure; however, it is unclear how to extend the parametrization to guarantee further derivatives of the pressure exist at the stitching point. Generically stitching two C^n functions to form a globally C^n function requires matching $n + 1$ derivatives, which may require the introduction of functions to the parametrization of $p(\rho)$ for example, which make it difficult to solve for $e(\rho)$ analytically.

Finally, the spectral parametrization [77] accurately reflects a broad range of nuclear models while maintaining smoothness across density scales. The parametrization has a similar form to a polytrope

$$p(\rho) = K\rho^{\Gamma(\rho)}, \tag{9.2}$$

but now $\Gamma(\rho)$ is expanded in a basis of smooth functions, typically a polynomial. The spectral parametrization can successfully reproduce hadronic nuclear models with a comparable number of parameters as polytropes, though it cannot capture sharp changes in the speed of sound that are associated with phase transitions [77, 53]. Compared to piecewise polytropes and other EoS with discontinuities, the spectral parametrization can lead to reduced computational cost in simulations [53] for a given accuracy requirement, while remaining more computationally intensive than pure polytropes. Our current implementation of the spectral EoS balances faithfulness to nuclear models and computational efficiency by expressing $\Gamma(\rho)$ as a a polynomial in $\log \rho$ [53]. More complex basis functions could improve faithfulness, but they would come at the cost of computational efficiency since computation of the internal energy requires a numeric integral whose accuracy depends on how rapidly $\Gamma(\rho)$ varies.

The above discussion highlights the role of balancing faithfulness and computational efficiency in selecting EoS parametrizations for numerical simulations. While the single-polytrope is computationally efficient, it is too restrictive in terms of nuclear physics. Piecewise-polytropes expand the range of nuclear models accessible, but at the cost of longer runtimes and loss of accuracy due to non-smoothness at the stitching boundaries. The spectral parametrization strikes some balance, but performs optimally when few parameters are used; it is therefore restricted to simple nuclear models. Ultimately, we would prefer an EoS parametrization which is able to fit to a problem-specific precision, matching the level of other errors in simulations at the lowest possible cost. This motivates the introduction of a new parametrization with increased flexibility to model a wider range of nuclear EoSs without considerable performance losses.

9.3 enthalpy parametrization of the EoS

In this section we introduce a new *enthalpy parametrization* with a flexible number of degrees of freedom that expands the range of microscopic physics we are able to represent in numerical simulations. In the following, we work in geometric units: $c = 1, G = 1$.

Parametrizing the enthalpy

The specific enthalpy of a system h is defined as the enthalpy per unit mass. In relativistic contexts it represents the energy required to inject a unit of rest mass into the system while remaining in thermodynamic equilibrium. The first law of thermodynamics requires that at zero temperature T and in $\beta-$equilibrium,

$$h(\rho) \equiv \left(\frac{\partial e}{\partial \rho}\right)_{T,\beta} = \frac{de}{d\rho} = \frac{p(\rho) + e(\rho)}{\rho}\,, \tag{9.3}$$

where e and p are the energy density and pressure, while ρ is the rest-mass energy density of baryons.

We choose to directly parameterize the enthalpy for three primary reasons. First, the enthalpy is a monotonically-increasing and slowly-varying function of the baryon density, which is numerically beneficial. Second, the enthalpy can be intuitively interpreted as a measure of the stiffness of the EoS: a larger enthalpy corresponds to higher pressure and energy density. Third, and importantly for hydrodynamic simulations, the enthalpy in cold, beta-equibrilated matter is related to other thermodynamic quantities by linear operations, which facilitates analytic calculations and avoids interpolation or numerical integration.

From the first law, we have

$$\frac{dh}{d\log\rho} = \frac{de}{d\rho} + \frac{dp}{d\rho} - h \tag{9.4}$$

$$= \frac{dp}{d\rho} = \frac{dp}{de}\frac{de}{d\rho} \tag{9.5}$$

$$= hc_s^2\,, \tag{9.6}$$

Equation (9.5) suggests that $dp/d\rho$ is zero if and only if $dh/d\rho$ is zero. Equation (9.6) provides the motivation for our parametrization choices. Consider, for example, a constant speed of sound $c_s = c_{s,0}$. Then

$$c_{s,0}^2 = c_s^2 = \frac{dp}{de} \implies p = p_0 + c_{s,0}^2\Delta e\,, \tag{9.7}$$

with $p_0 = p(e_0)$ and $\Delta e \equiv e - e_0$. In this special case Eq. (9.6) becomes

$$\begin{aligned} h(\log\rho) &\propto \exp\left(c_{s,0}^2\log\rho\right) \\ &\approx \rho_0\left[1 + c_{s,0}^2\log\left(\rho/\rho_0\right) + \ldots\right]\,, \end{aligned} \tag{9.8}$$

where ρ_0 is some fiducial density. Equation (9.8) suggests that if c_s^2 is slowly varying,[3] the enthalpy can be approximated as exponential in $\log\rho$. Moreover, a smaller c_s^2 accelerates the convergence of the series of Eq. (9.8), though this also depends on the choice of density scale ρ_0. We therefore choose the Taylor expansion in Eq. (9.8) as the starting point of the enthalpy parametrization.

We further select $\log\rho/\rho_0$, as the independent variable of the parametrization. This choice enables us to better resolve the low-density EoS. Equation (9.8) further suggests that $h(\log\rho) \propto \exp(c_{s,0}^2\log\rho)$ is analytically and computationally simpler than $h(\rho) \propto \rho^{c_{s,0}^2}$ as the Taylor expansion of $\rho^{c_{s,0}^2}$ converges more slowly than the expansion of $\exp(c_{s,0}^2\log\rho)$ for non-integer $c_{s,0}$.

[3]In general, causality and stability bound $0 \leq c_s^2 \leq 1$.

Lastly, a desirable property of the specific enthalpy is that it is continuous across first-order phase transitions. This can be seen from Eq. (9.5) where maintaining a constant pressure across the transition guarantees that the enthalpy will be constant as well. This indicates that across certain weak transitions the enthalpy can be expanded in a basis of continuous functions, unlike, for example, a local polytropic exponent.

Decomposition

Motivated by Eq. (9.8), we introduce a parametrization of $h(\log \rho)$. Given an EoS in some density region $\rho_{\min} \le \rho \le \rho_{\max}$ we select a density scaling parameter $\rho_0 \le \rho_{\min}$ such that $z \equiv \log(\rho/\rho_0)$ is positive in the relevant density range. Importantly, ρ_0 is not necessarily equal to $\rho_{\min}$, thus introducing an additional parameter. We then write

$$h(z) \approx h_p(z) \equiv \sum_{i=0}^{i_{\max}} \gamma_i z^i \,, \tag{9.9}$$

where $h(z)$ is the target enthalpy and $h_p(z)$ is its approximation. This polynomial decomposition is motivated by the previous observation that $h(z)$ is approximately exponential in z for nearly constant speeds of sound, corresponding to $\gamma_i \sim c_{s,0}^{2i}/i!$. The rapid convergence of the γ_i sequence indicates that the $i > i_{\max}$ terms will be small provided that the speed of sound is slowly varying.

Given that $h(z)$ is positive and increasing and $z_i > 0$, catastrophic floating point cancellation in numerical calculations can be avoided by restricting to $\gamma_i \ge 0$. This guarantees that each term $\gamma_i z^i$ is a small and positive correction to previous terms. Furthermore, the polynomial expansion of Eq. (9.9) can be efficiently and stably evaluated with Horner's method [94]. Allowing for more general γ_i is possible, but this comes at a risk of oscillatory behavior and cancellation of large terms which make convergence predictions difficult. The implications and rationale behind the choice to set $\gamma_i \ge 0$ are further discussed in App. 9.9.

A consequence of setting $\gamma_i \ge 0$ is that Eq. (9.9) is unable to model certain EoSs, for example the case where $dh/dz = hc_s^2$ is not strictly increasing, even with $i_{\max} \to \infty$. Such a non-monotonic speed of sound could be encountered for complicated hadronic models or more generically if non-hadronic degrees of freedom are introduced [80, 116, 61, 57]. We therefore augment Eq. (9.9) by decomposing

$h_t(z) \approx h(z) - h_p(z)$ as a Fourier series

$$h_t(z) \equiv \sum_{j=1}^{j_{\max}} a_j \sin(jkz) + b_j \cos(jkz)\,, \tag{9.10}$$

where k sets the "wavelength scale" of the fit. In a Fourier series k is typically fixed to

$$k = k_F \equiv \frac{2\pi}{z_{\max} - z_{\min}} = \frac{2\pi}{\log(\rho_{\max}/\rho_{\min})}\,, \tag{9.11}$$

but here we vary it and find that $k \gtrapprox k_F$ leads to good fits. The effect of perturbing k around k_F is small, as we explore in App. 9.7. The trigonometric expansion of Eq. (9.10) can also serve as a low-pass filter to remove high-frequency oscillations from the tabulated EoS data that may not be physical or computationally resolvable. In summary, the enthalpy parametrization is

$$h_*(z) \equiv h_t(z) + h_p(z) \approx h(z)\,. \tag{9.12}$$

In Fig. 9.1 we demonstrate the enthalpy parametrization fit of Eq. (9.12) and its polynomial, Eq. (9.9), and trigonometric, Eq. (9.10), components for a phenomenological EoS drawn from a Gaussian process prior [72, 44]. The polynomial fit alone is accurate to about $O(1\%)$, while the total fit is good to about one part in 10^5. For reference, we also plot $c_s^2 = (1/h)dh/dz$, as a measure of the complexity of the EoS. Even though c_s^2 is not globally nearly constant, it is slowly varying and nearly monotonic.

Given the generic form of the enthalpy parametrization, there is no guarantee that a particular fit will satisfy stability $c_s^2 \geq 0$ and causality $c_s^2 \leq 1$. If $h_t(z) = 0$, the fit is guaranteed to be stable, and a sufficient but not necessary condition for causality is $\gamma_i \leq \gamma_{i-1}/i$, which becomes necessary and sufficient in the case of a constant sound speed. If $h_t(z)$ is nonzero, then $h_*(z)$ can oscillate, changing on scales of order the most quickly varying Fourier mode. Therefore, both conditions must be checked on a grid of spacing

$$\delta z \lesssim \frac{1}{j_{\max} k}\,, \tag{9.13}$$

where, as above, $j_{\max}$ is the index of the fastest varying "Fourier" mode.

While an unstable fit to the EoS cannot be tolerated in a numerical simulation, an acausal fit may be used if it is very nearly causal (i.e. if $\sqrt{c_s^2 - 1}$ is small compared to the velocity resolution of the simulation). In practice, however, fits typically are

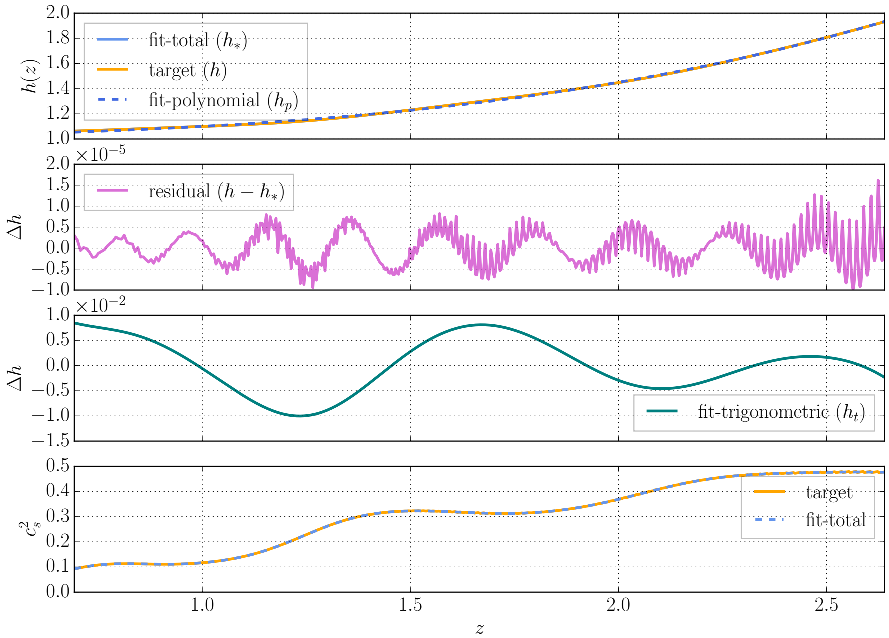

Figure 9.1: Results of a fit to an EoS drawn from a Gaussian process with the enthalpy parametrization. We plot various thermodynamic quantities as a function of z. The fit parameters are $\rho_{\min} = \rho_{\text{nuc}}$, $\rho_{\max} = 7\rho_{\text{nuc}}$, $\rho_0 = 0.5\rho_{\text{nuc}}$, $k = \pi/(\log(7))$, and $i_{\max} = j_{\max} = 10$. *Top Panel:* The tabulated EoS h (solid, orange) and the total fit h_* (solid, light blue). We also plot the polynomial fit to the EoS h_p (dashed, indigo). Both the total and the polynomial fit are indistinguishable from the tabulated EoS by eye. *Second Panel:* The residuals of the total fit $h - h_*$. In this metric, the fit demonstrates excellent agreement relative to $h-1 = p/\rho+\epsilon \gtrsim 1\times 10^{-2}$ *Third Panel:* The trigonometric fit $h_r = h - h_p$. *Fourth Panel:* $(1/h)dh/dz = c_s^2$, for both the tabulated EoS and the total fit. Heuristically, the speed of sound has a comparable number of plateaus to the number of obvious peaks in h_t.

neither acausal nor unstable; if they are it is often a sign that the fit to the EoS is poor and more parameters should be used.

Computing thermodynamic quantities

Given the expansion of Eq. (9.12), we can analytically compute the thermodynamic quantities needed for GRMHD evolution as formulated in `SpECTRE` [33, 30], or similar codes [83]. For example, the energy density is

$$\frac{de}{dz} = \rho \frac{de}{d\rho} = \rho_0 \exp(z)\, h(z) \Rightarrow$$
$$e(z) = \rho_0 \int_{z_0}^{z} \exp(z')\, h(z') dz' + e(z_0)\,. \tag{9.14}$$

Since $h(z)$ is expressed in terms of sines, cosines, and polynomials, the integral of Eq. (9.14) can be computed using the following identities

$$\int \exp(z) \sin(nkz) dz$$
$$= \exp(z) \frac{\sin(nkz) - nk\cos(nkz)}{1 + n^2k^2} + C\,, \tag{9.15}$$
$$\int \exp(z) \frac{z^n}{n!} dz$$
$$= \exp(z) \frac{z^n}{n!} - \int \frac{z^{n-1}}{(n-1)!} \exp(z)\, dz = \dots\,, \tag{9.16}$$

where the ellipses indicate that integration by parts can be repeated until the integral becomes trivial. Equation (9.16) is also a gamma function, but it is typically incomplete. Nonetheless, all integrals can be evaluated analytically and $e(z)$ has an expansion of the form

$$e(z) = \exp(z) \times$$
$$\left(\sum_i \gamma'_i z^i + \sum_j a'_j \sin(kjz) + b'_j \cos(kjz) \right)$$
$$+ e_*\,, \tag{9.17}$$

where the constant e_* is determined by setting $e(z_{\min}) = e_{\min}$ and the coefficients satisfy

$$\gamma'_i = \frac{1}{i!} \sum_{i_{\max} \geq \ell \geq i} (-1)^{i_{\max} - \ell} \ell! \gamma_\ell\,, \tag{9.18}$$
$$a'_j = \frac{a_j}{1 + j^2k^2} + \frac{b_j jk}{1 + j^2k^2}\,, \tag{9.19}$$
$$b'_j = \frac{b_j}{1 + j^2k^2} - \frac{a_j jk}{1 + j^2k^2}\,. \tag{9.20}$$

The pressure $p(z)$ can also be evaluated analytically with a similar expansion given that

$$p(z) = \rho_0 h(z) \exp(z) - e(z) = h\rho - e\,. \tag{9.21}$$

This equation showcases the benefits of setting $\gamma_i \geq 0$ in Eq. (9.9) to avoid cancellations in the enthalpy expansion. The pressure is computed as the difference of two relatively large quantities, each typically 1–3 orders of magnitude larger than the pressure itself in the relevant density interval. If the expansion of $h(z)$ additionally had large coefficients (i.e. much larger than the enthalpy) terms of $e(z)$ will be computed by sums of alternating large numbers, which is numerically undesirable. However, because $\gamma_\ell \sim 1/\ell!$ for EoSs with slowly varying speed of sound, the terms in Eq. (9.18) are of comparable size, and about the same size as corresponding terms of $h(z)$. Thus the terms of $p(z)$ are computed to comparable precision as the terms of $e(z)$ and $h(z)$. We find this holds more broadly, even when the speed of sound is not slowly varying, as γ_ℓ is typically decreasing even if it is not decreasing exponentially as in the constant-c_s^2 case.

Lastly, we can also analytically compute

$$\frac{dp}{d\rho} = \frac{dh}{dz}, \tag{9.22}$$

through

$$\begin{aligned} \frac{dh}{dz} = &\sum_i i\gamma_i z^{i-1} \\ &+ \sum_j jk\left[a_j \cos(jkz) - b_j \sin(jkz)\right] . \end{aligned} \tag{9.23}$$

As can be seen from Eqs. (9.17) and (9.23), parameters that enter linearly in the original expansion of $h(z)$ also appear linearly in all relevant thermodynamic quantities.

Low-Density Stitching

The enthalpy parametrization is best suited for high-density regions where pressure and energy density are comparable. Low-density regions with $p \ll h\rho \sim e$ might be better fit by direct parametrizations of the pressure. We therefore combine the enthalpy parametrization with a simpler low-density parametrization below $\rho_{\rm min}$. Incidentally, this density region coincides with the region of validity of nuclear theory calculations [115, 39, 47] and terrestrial experiments [5, 6, 108, 45, 46]. The low-density EoS is therefore better constrained and thus there is reduced need for flexibility in the EoS parametrization. Moreover, the low-density EoS has a reduced impact on NS observables, especially if the simulation resolution is low, such that $(dp/dr)\Delta r > \delta p$, where Δr is the grid spacing and δp is the difference induced by EoS mismodeling.

A number of options exist for the low-density EoS, including direct parametrizations of nuclear models [115] or chiral effective field theory(χ-EFT) results [114, 90]. Here we select the existing spectral parametrization implementation [53], as it is more flexible than single-polytropes, but smoother than piecewise-polytropes and tabulated EoSs. In certain cases, we explore extending the spectral parametrization up to relatively high densities $\sim 2\rho_{\rm nuc}$ if it can fit the target EoS well-enough in this density regime. Due to the low number of parameters in the spectral parametrization, all degrees of freedom are determined by requiring differentiability of the pressure and continuity of the internal energy at the stitching points. We verify this stitching maintains C^1 smoothness; see App. 9.7.

Free parameters and fitting

The number of free parameters needed to achieve good fits of arbitrary EoSs will impact the simulation cost. Indeed, the cost of evaluating any EoS-dependent quantity is proportional to the number of coefficients used for the enthalpy parametrization. Therefore it is prudent to use only as many terms as necessary to achieve an accurate fit; accuracy in the context of numerical simulations is measured relative to other simulation errors. There is no definitive metric for EoS mismodeling error, as the relevant error will depend on the application. For example, in applications to BNS inspirals, the relevant errors are in GW phase, matter hydrodynamic variables, and magnetic field variables. When considering the fitness of an EoS parametrization for use in simulations, all these factors should be taken into consideration.

Nonetheless, it is pragmatically necessary to define surrogate goodness-of-fit statistics in order to both fit the enthalpy parametrization to data and determine approximately if such a fit is good. We describe the fitting procedure of the parametrization to a tabulated model that we employ in App. 9.7. Briefly, we fit the specific enthalpy $h(z)$ on a linear grid in z but with variable precision, requiring higher precision at lower densities to achieve equal cost across density scales. However, fitting is not the only way to extract coefficients for use in the enthalpy parametrization; for example, coefficients to approximate a polytropic EoS are derived in App. 9.8 using a Taylor expansion of the specific enthalpy. Nonetheless, for realistic nuclear models, fitting the specific enthalpy is usually necessary.

One convenient benchmark is to examine the error in radius of a typical neutron star induced by using a enthalpy parametrization fit as compared to a tabulated model. In order to demonstrate the general requirements for fitting, we fit a collection of realistic nuclear theoretic EoSs, compute the error in the radius of a $1.4 M_\odot$ NS (ΔR_{typ}) and display the results in Table 9.1. These fits are all carried out with $i_{\max} = 12$, and $j_{\max} \leq 5$, and have typical NS radius error of less than 70 m. EoS modelling error would therefore likely not be limiting in simulations with $\sim$ 70 meter resolution; this is a conservative choice of error measure as realistic simulation errors will likely dominate static errors. Additionally, we fit phenomenolgical EoSs drawn from a Gaussian process-mixture model priors [70, 44]. We examine two cases: the first is draws from a model-agnostic prior, which are only loosely informed by nuclear theory calculations, the second class is Gaussian process draws conditioned on χ-EFT up to $1.5\rho_{\mathrm{nuc}}$ [43, 46]. Both nuclear-theoretic and phenomenological EoSs show comparable fit quality, indicating that the enthalpy parametrization is able to reproduce a wide range of EoS models.

We list $j_{\max}$ in Table 9.1 as we expect that the number of trigonometric terms is the leading-order driver of cost to evaluate the parametrization. We quantify this further in Sec. 9.4. Contrarily we expect little dependence of evaluation cost of $i_{\max}$ because evaluation of polynomials using Horner's method is extremely efficient. For realistic EoSs, fine-tuning of low-density stitching and nonlinear parameters can reduce the number of trigonometric correction terms that are required to achieve a good fit. Even when no fine-tuning is required, typically good fits are achieved with $j_{\max} \sim 4$. We quantify this in Fig. 9.2 by showing the error in the radius of a typical star for six different χ-EFT informed Gaussian process draws, when no fine tuning of nonlinear or low-density parameters is performed. The fits are better when more trigonometric correction terms are included, all falling below 100 m error by $j_{\max} = 4$. These errors are often due to the EoS at low-densities, and so typically fine-tuning of certain parameters, such as the low density polytropic index, or the energy density of EoS at the stitching density, must be carried out to achieve $\sim$ 10-meter-error fits. In practice, though, this may not be necessary as quantities such as the tidal deformability are determined by the bulk of the matter, interior to the crust, therefore crust modeling errors may be less significant then predicted by using the radius as a metric. These considerations will be especially important for BNS simulations where GW emission is predominately determined by tidal deformability, and other sources of error may overshadow EoS modeling error.

Use cases

The primary function of the enthalpy parametrization is to represent EoS models

Table 9.1: A list of EoS fits with the enthalpy parametrization to nuclear theoretic and phenomenological EoS. Theoretic EoSs are listed according to the conventions of [102]. Phenemenological EoSs are drawn from Gaussian process priors. The EoSs gp1 and gp2 are drawn from a model agnostic Gaussian process prior [70, 44]. EoSs gpχeft1, gpχeft3, and gpχeft5 are drawn from Gaussian process priors conditioned on χ-EFT predictions at low densities. These three EoSs represent draws from hadronic, hyperonic, and quarkyonic conditioned GPs, respectively.

EoS	$R_{\rm typ}$ [km]	$\Delta R_{\rm typ}$ [km]	$\Delta M_{\rm max}$ [$M_\odot$]	$j_{\rm max}$	Ref.
alf2	12.968	-0.028	-0.003	3	[8]
bsk19	10.763	-0.006	-0.001	5	[93]
ap4	10.595	-0.02	0.001	3	[7]
H4	12.931	0.01	0.001	3	[68]
bbb2	11.442	-0.05	-0.008	5	[16]
eng	12.306	-0.071	-0.009	2	[41]
mpa1	11.696	-0.062	-0.003	5	[85]
ms1	14.223	-0.015	-0.007	5	[84]
qmc700	11.942	-0.008	-0.002	5	[105]
sly	11.873	-0.053	-0.003	5	[37]
wff2	10.373	-0.049	-0.002	5	[123]
gp1	12.302	-0.02	-0.007	4	[70]
gp2	12.345	-0.024	0.001	4	[70]
gpχeft1	10.496	-0.052	0.001	5	[43]
gpχeft3	10.509	-0.049	0.001	5	[43]
gpχeft5	10.789	-0.057	-0.002	5	[43]

for use in numerical simulations containing dense matter. Given the wide range of models of nuclear matter, the enthalpy parametrization is intentionally very flexible. Existing parametrizations of the nuclear EoS typically have a handful of parameters, and extending them might be nontrivial. In contrast, well-interpolated tables have many "parameters", or tabulation points, some of which we would prefer not to resolve in simulations (such as artificially rapid changes in some pressure derivative). The enthalpy balances these requirements in such a way that the maximal level of flexibility can be found without introducing extraneous parameters. This allows us to resolve EoSs from nuclear theory (Sec. 9.4) as well as EoSs which extend or modify nuclear models (Sec. 9.4). Such flexibility is crucial for determining the observational implications of new degrees of freedom at arbitrary density scales.

Furthermore, the requirements laid out in Sec. 9.2 are tailored for a specific application of EoS parametrizations, namely numerical simulations involving NSs. These requirements are domain specific and need not necessarily lead to efficient parametrizations for different applications, for example EoS inference using as-

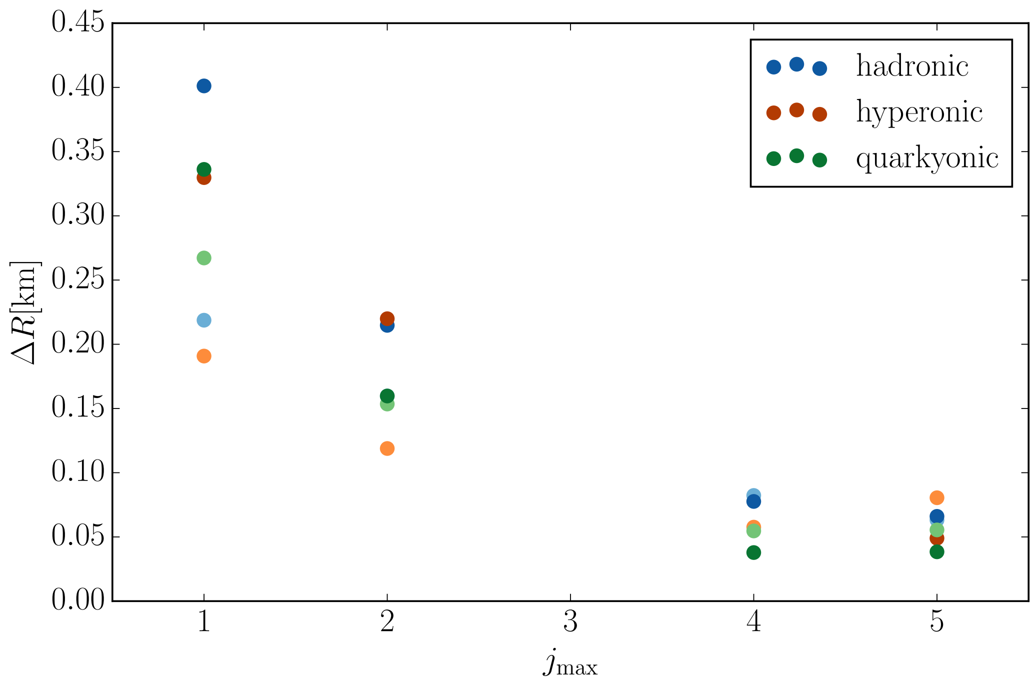

Figure 9.2: Radius error in fitting Gaussian Process-generate EoSs conditioned on χ-EFT [43, 46] with the enthalpy parametriation. We plot two hadronic-conditioned draws, two quark-conditioned draws, and two hyperonic draws. This indicates the draws are from processes conditioned on EoS models of the given type, so that e.g. the hadronic process is consistent with known hadronic EoSs. Nonetheless the processes use "agnsotic" kernels which lead to very compatible distributions on EoSs for each of the three cases [70, 44]. A problem with stitching stability affected multiple of the fits at $j_{\max} = 3$, so we exclude these.

trophysical data. Besides the general faithfulness and computational efficiency considerations, EoS parametrizations employed in inference need to satisfy an additional requirement: they must provide a reliable path from the observed data to the EoS constraints. Specifically, the data must be the primary driver of inference while the impact of the EoS parametrization itself must be either minimal or driven by first principles and nuclear theory. Parametrizations that impose a functional form for the EoS in terms of a finite number of parameters may fail this requirement [55, 22]. Specifically, the spectral, piecewise-polytropic, and speed-of-sound parametrizations impose additional phenomenological correlations between different densities that are not guided by nuclear theory but instead by the arbitrary functional form of the parametrization itself [75]. Though we have not repeated the analysis of [75], we expect that the enthalpy parametrization has the same pitfall as it possesses many nearly-irrelevant degrees of freedom that are not constrained by current observations and will generically impart correlations between density scales. We therefore caution against using it for inference purposes.

9.4 Parametrization Verification and simulations

In this section, we look in depth at fitting nuclear and phenomenological models with the enthalpy parametrization and perform numerical simulations. First, we use SLy1.35 [53], a spectral fit to the SLy EoS [37, 102] with a low-density polytropic exponent of 1.35962. This represents a nuclear EoS which has been effectively simplified by being fit with a spectral EoS. Therefore, this test allows us to analyze the performance of the enthalpy parametrization on a problem where lower dimensional parametrizations are applicable, in terms of both accuracy and computational performance. We next consider a tabulated DBHF [56] EoS, derived from relativistic, *ab initio* calculations of protons and neutrons *dressed* via interactions with one-boson exchange potentials.[4] It is relatively stiff, with a typical NS radius of ~ 13.5km. This allows us to assess the accuracy with which we can fit realistic nuclear models. We then modify the DBHF EoS using a constant-speed-of-sound parametrization [9] to construct a model with a strong phase transition, DBHF_2507. With this we assess the ability of the enthalpy parametrization to augment realistic low-density models with phenomenological extensions inspired by nuclear theory.

Using the three models presented above, we study the evolution of isolated NSs by numerical simulation. As in Ref. [30], we work with `SpECTRE` within the Cowling approximation and examine NS modes that are sourced by density perturbations due to numerical noise. We neglect spacetime dynamics and magnetic fields, which will likely be most relevant in crust physics where magnetic and matter pressure are comparable. We run each simulation for 40,000 CFL-limited time steps [25]. For the DG-FD hybrid solver of `SpECTRE` we use a sixth-order (P_5) discontinuous Galerkin scheme where each element uses 6^3 Gauss-Lobatto points on the mesh. If an element switches its mesh from discontinuous Galerkin to finite difference, we use 11^3 uniformly spaced grid points for finite difference cells. The finite difference solver needs to compute the solution (in our case ρ, p, and Wv^i, where W is the Lorentz factor and v^i the spatial velocity) at cell interfaces (halfway between grid points). We compute these using two different reconstruction schemes: the widely employed monotonized central [119] and a positivity-preserving adaptive order scheme which was recently implemented in `SpECTRE` [29]. In the n-th order adaptive scheme, we first try reconstructing the finite-difference interface values with

[4] The EoS we use has employed the Bonn A potential defined in Ref. [56].

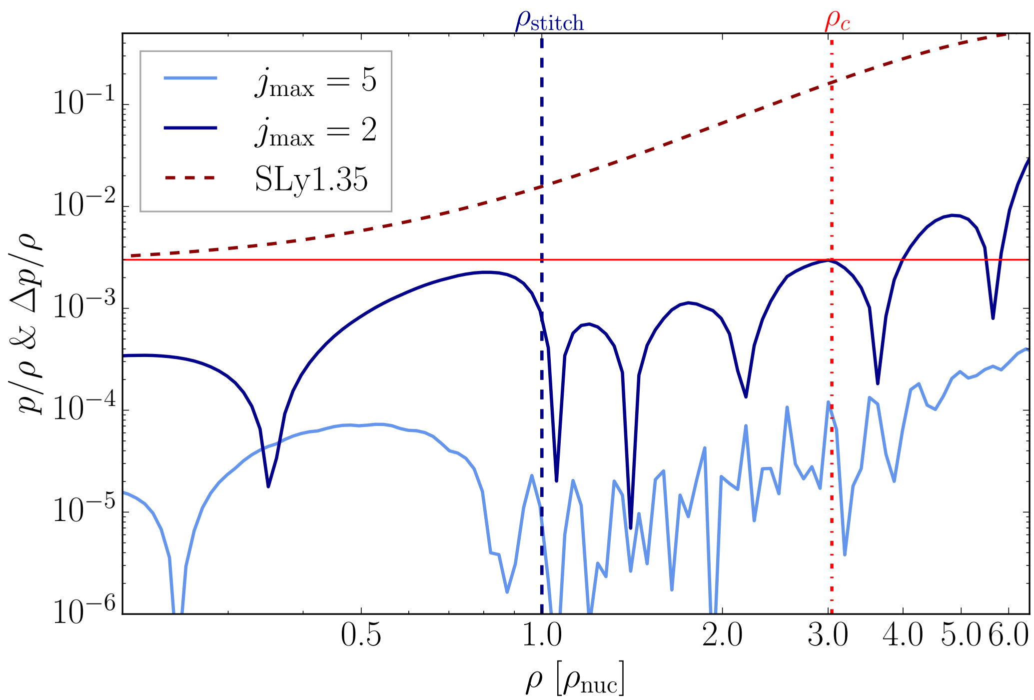

Figure 9.3: Fitting SLy1.35 (a spectral model of SLy) with the enthalpy parametrization, expressed through the difference in pressure divided by the density. The SLy1.35 EoS value for $p(\rho)/\rho$ is marked by a maroon dashed line for comparison to the residuals. The $j_{\rm max} = 5$ and $j_{\rm max} = 2$ fit residuals are marked in light blue and indigo. The vertical blue dashed line marks the stitching density between the enthalpy and the spectral parametrizations, while the vertical red dot-dashed line marks the central density of the NS we simulate in Sec. 9.4. The solid red horizontal line marks an error level of 3×10^{-3} for comparison with fits in Sec. 9.4; errors below 3×10^{-3} at $(1, 3)\rho_{\rm nuc}$ serve as a heuristic for a good fit.

a degree $n-1$ polynomial without any limiting procedure. If the reconstructed values are (i) not positive or (ii) trigger a certain oscillation-detecting criterion, we repeat the reconstruction with progressively lower-order methods. In this work we use the fifth-order adaptive scheme which first tries reconstruction with a quartic polynomial and switches to monotonized central if the reconstructed values fail to satisfy the conditions described above. Finally, if the monotonized central reconstruction did not produce positive values at the interface, first-order reconstruction is used.

Table 9.2: Analysis settings for the SpECTRE simulations with fits to the SLy1.35, DBHF, DBHF_2507 EoSs, and a polytropic EoS. *Labels* are chosen to serve as unique identifiers for the runs. The integer suffix represents the approximate grid spacing of the run in meters. *Elts* describes the number of computational elements used in the (three-dimensional) domain. *FD* Δx represents the finite-difference grid spacing, in meters, of the finite-difference cells in each element when using finite-difference instead of discontinuous-Galerkin methods; this is the primary measure of resolution of the run and allows for easy comparison to other codes. ρ_c represents the initial central (rest-mass) density of the NS being simulated. *Cost*, in cpu-minutes per CFL-limited timestep, is the approximate cost of computing one time step in this simulation. While runtime depends on an array of factors and may not always be indicative of EoS evaluation speed, differences of $\gtrsim 20\%$ represent on otherwise identical runs likely represent EoS-induced slowdown. *Figs* represents which figures contain plots pertaining to this run. *Info* represents the section in which more information about the EoS can be found. *Radius* represents the TOV radius of the NS being simulated. *Elts/D* represents the approximate number of computational elements across the diameter of the star.

Label	Elts	FD Δx (m)[a]	$\rho_c (1/M_\odot^2)$	Cost(cpum/st)	Figs	Info	Radius (km)	Elts/D
spectral-sly-mc-220	$(24)^3$	224	0.00138	3.5	9.5	9.4	11.5	9
enthalpy-sly-mc-220	$(24)^3$	224	0.00138	4.1	9.5	9.4	11.5	9
spectral-dbhf-mc-130	$(24)^3$	134	0.001	4.1	9.8	9.4	13.4	18
enthalpy-dbhf-mc-130	$(24)^3$	134	0.001	3.7	9.8	9.4	13.5	18
enthalpy-pt-mc-130	$(24)^3$	134	0.0021	5.1	N/A	9.4	11.8	16
enthalpy-pt-ppao-70	$(48)^3$	67	0.0021	24.6	9.10	9.4	11.8	32
enthalpy-pt-mc-70	$(48)^3$	67	0.0021	20.7	9.10	9.4	11.8	32
enthalpy-polytrope-mc-130	$(24)^3$	134	0.00128	2.07	9.16	9.8	14.1	19
polytropic-polytrope-mc-130	$(24)^3$	134	0.00128	2.1	9.16	9.8	14.1	19
enthalpy-smoothpt-170	$(24)^3$	168	0.0021	3.5	NA	9.4	11.9	12

[a] We express resolution in finite difference grid spacing for easy comparison to finite difference codes.

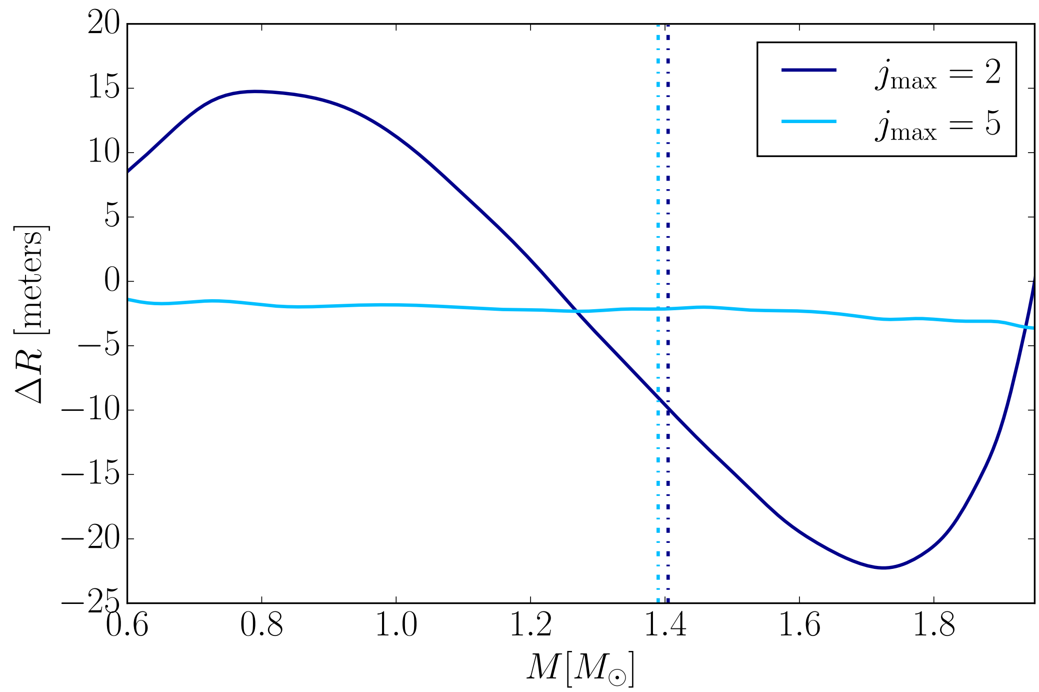

Figure 9.4: Radius error ΔR as a function of mass for the SLy1.35 EoS and the $j_{\max} = 10$ and $j_{\max} = 5$ enthalpy parametrization fits. We mark the mass of the stars with central density $\rho_c \sim 3.04\rho_{\rm nuc}$, (simulated in Sec. 9.4), with dashed-dot lines. Consistently with the microscopic comparison of Fig. 9.3, the enthalpy fit can reproduce macroscopic quantities with excellent agreement. The error decreases with more trigonometric terms, but always remains small compared to 200 m grid resolution.

SLy1.35

SLy1.35: fit results

We fit SLy1.35 with the enthalpy parametrization and show the error in pressure divided by density as a function of density in Fig. 9.3. We vary the number of trigonometric terms in Eq. (9.10) and show results with $j_{\max} = 2$ and $j_{\max} = 5$. The $j_{\max} = 5$ fit shows exceptional agreement; the error measure, $\Delta p/\rho$, is near or below 1×10^{-4} over essentially the entire domain. The $j_{\max} = 5$ fit shows increased error, though $\Delta(p/\rho)$ remains near or below 3×10^{-3} above $\rho_{\rm nuc}$. We stitch to a spectral parametrization below $\rho_{\rm nuc}$, marked in the Fig. 9.3 as a vertical dashed blue line. Even though the low-density behavior of the EoS is a spectral EoS fitting a spectral EoS, it is not guaranteed the low-density fit is good, because we prioritize smooth stitching to the enthalpy solution above accurate low-density EoS modeling; see App. 9.7. In line with this, we see a significantly better low-density fit for $j_{\max} = 5$.

Parametrization \ Evaluation Cost (ns)	$p(\rho)$	$\epsilon(\rho)$
enthalpy, $j_{\max} = 5$	224	225
enthalpy, $j_{\max} = 2$	120	120
spectral	62	315

Table 9.3: Evaluation cost in nanoseconds for the spectral and two different enthalpy fits to SLy1.35 for the pressure and internal energy evaluated at $\rho = 5 \times 10^{-4} M_{\odot}^{2}$. The spectral parametrization has a shorter (longer) pressure (internal energy) evaluation time. The enthalpy evaluation cost further increases with the number of trigonometric terms employed.

SLy1.35: Relativistic simulations

We carry out simulations directly with SLy1.35 using the defining spectral expansion [53] as well as the $j_{\max} = 5$ enthalpy parametrization fit; details are given in Table 9.2. We evolve a NS with an initial central density of $\sim 3.04\rho_{\rm nuc}$ which has a Tolman-Oppenheimer-Volkoff (TOV) [88] mass of about $1.4M_{\odot}$ and a radius of about 11.5 km; see Figs. 9.3 and 9.4. The simulation resolution corresponds approximately to a 220 m finite difference grid spacing. We plot the central density as a function of time and its spectrum

$$\hat{\rho_{\rm c}}(\omega) = \int_0^T \rho_{\rm c}(t) e^{-i\omega t} dt\,, \tag{9.24}$$

in Fig. 9.5 and find essentially identical evolution between the spectral and enthalpy fits, in line with expectations from the static tests of Sec. 9.4. This demonstrates that the enthalpy parametrization is able to faithfully reproduce results from lower-dimensional parametrizations.

With regards to computational cost, the enthalpy parametrization results in an overall 15% increase in total runtime compared to the spectral parametrization on similar hardware. To isolate the EoS evaluation cost, we benchmark the $p(\rho)$ and $\epsilon(\rho)$ evaluation in Table 9.3. The two parametrizations have comparable evaluation times though exact numbers are sensitive to the number of trigonometric terms in the enthalpy case. While $p(\rho)$ evaluation is in general faster with the spectral parametrization, the opposite is true for $\epsilon(\rho)$. This is because the spectral parametrization needs to perform a quadrature to calculate $\epsilon(\rho)$; see Sec. 9.2. In the enthalpy parametrization, trigonometric terms cause slowdowns, although even with $2 \times j_{\max} = 10$ terms the $p(\rho)$ cost does not exceed a factor of 4. Further studies with

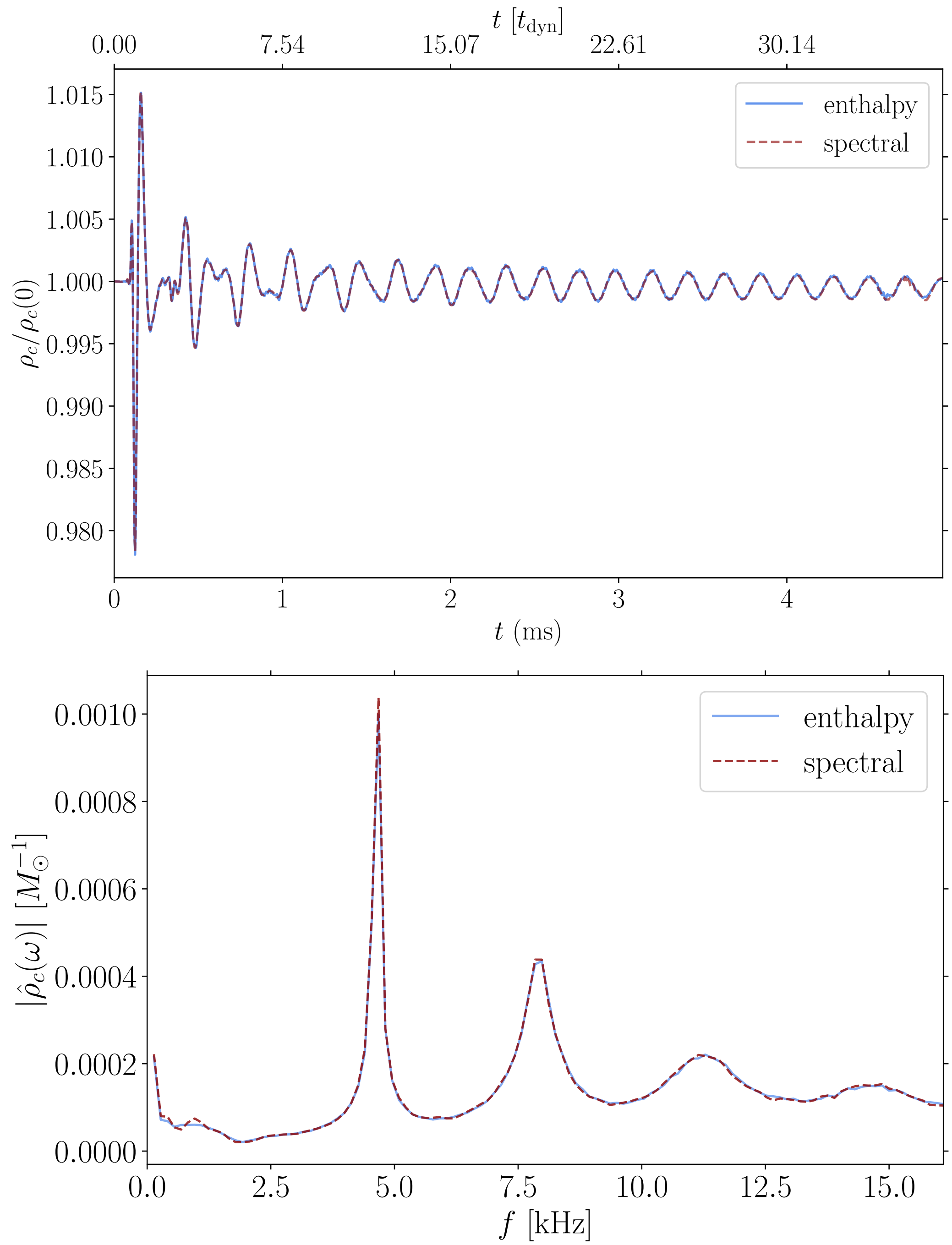

Figure 9.5: NS central density as a function of time (top panel) and its spectrum (bottom panel) for SpECTRE simulations with SLy1.35 (red dashed) and its $j_{\rm max} = 10$ enthalpy fit (blue solid). These runs are labeled spectral-sly-mc-220 and enthalpy-sly-mc-220 in Table 9.2. In both plots the curves are nearly indistinguishable. We plot times in both milliseconds (ms), and dynamical times ($t_{\rm dyn} \equiv 1/\sqrt{\rho_{\rm c}}$)

single-polytropic nuclear EoSs suggest that this disadvantage effectively disappears if $j_{\max} = 0$; see App. 9.8.

DBHF

DBHF: Fitting a tabulated nuclear model

We fit the tabulated DBHF EoS with the enthalpy parametrization and further explore the effect of low-density stitching to the spectral parametrization by probing two different stitch densities: $\rho_{\rm nuc}$ and $2.5\rho_{\rm nuc}$; these fits are referred to as "low-stitch" and "high-stitch" in what follows. In the high-stitch case we use $j_{\max} = 10$ trigonometric terms, while we find that $j_{\max} = 5$ is enough for the low-stitch one. See App. 9.7 for more details. We examine the microscopic and macroscopic performance of both fits in Figs. 9.6 and 9.7. On the microscopic side, the low-stitch fit achieves higher accuracy above $1.1\rho_{\rm nuc}$, but worse accuracy below.

The macroscopic side presents a clearer picture. When we use the enthalpy parametrization to describe the EoS down to a density of $\rho_{\rm nuc}$, we obtain excellent agreement with the tabulated EoS, with radius differences $O(1)$ m for astrophysically relevant NS masses. However, when we stitch to the spectral parametrization at $2.5\rho_{\rm nuc}$ the radius error increases to $O(100)$ m at $1.4M_{\odot}$. The improved agreement between the $2.5\rho_{\rm nuc}$ and the $\rho_{\rm nuc}$ stitching fits can be attributed to the high accuracy of the enthalpy parametrization in the range $\rho_{\rm nuc}$ to $2.5\rho_{\rm nuc}$, as seen in Fig. 9.6. The difference in the two errors is particularly pronounced near $2\rho_{\rm nuc}$, consistent with the observed strong correlation between the pressure at twice saturation density and radius of a $1.4M_{\odot}$ star [73]. This further establishes the importance of the enthalpy parametrization as a flexible EoS parametrization at nuclear saturation and above, in this case it appears errors in p/ρ must be at most 3×10^{-3} to achieve high-precision reproduction of astrophysical observables. However, this is not an indication that the spectral parametrization *cannot* fit DBHF well, it just cannot fit DBHF well while maintaining C^1 pressure smoothness at the high-density transition to the enthalpy parametrization and the low density transition to the crust; see App. 9.7.

DBHF: Relativistic simulations

We next turn to `SpECTRE` simulations using the DBHF fits from the previous section. Since the low- and high-stitch fits predict $O(100)$ m differences for $R_{1.4}$, we target a resolution at that level in order to resolve their effect. We select a NS central density of $2.21\rho_{\rm nuc}$ that lies between the two stitching densities of $\rho_{\rm nuc}$ and $2.5\rho_{\rm nuc}$; see

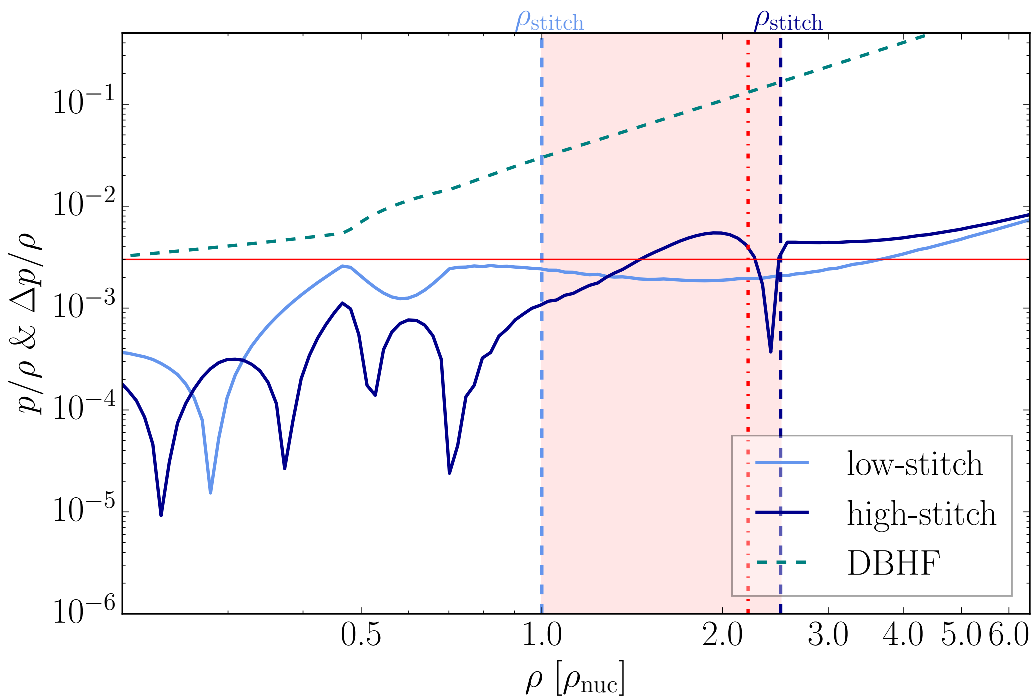

Figure 9.6: Same as Fig. 9.3 but for the DBHF nuclear EoS model and two enthalpy fits that are stitched to a spectral parametrization at $\rho_{\rm nuc}$ (low-stitch, light blue) and $2.5\rho_{\rm nuc}$ (high-stitch, indigo). We also plot the tabulated DBHF model $p(\rho)/\rho$ in dashed-teal for reference. The vertical dashed lines denote the stitching densities. We also mark the value $\Delta p/\rho = 3\times 10^{-3}$ as a solid red horizontal line for reference. We mark the central density of the star we simulate in Sec. 9.4 with a vertical red, dot-dash line.

Figs. 9.6 and 9.7. Run details and settings are given in Table 9.2. As a consequence, the NS resulting from the high-stitch EoS is fully described by the spectral part of the EoS. In the low-stitch EoS, the NS is described with the enthalpy parametrization out to $r/R \approx 7/8$, about two-thirds of the coordinate volume of the star.

While the high-stitch EoS does represent a spectral fit to the DBHF EoS, the spectral parameters are selected by the requirement that the spectral parametrization reproduces the correct low-density behavior of DBHF and is smoothly stitched to the enthalpy parametrization. It is important to note that a better spectral fit to any particular astrophysical quantity, such as $R_{1.4}$ may be possible, but the fit accuracy is typically lower than in the enthalpy parametrization case. Even if the few degrees of freedom in the spectral model are fit to minimize errors in astrophysical observables, fixing the low-density behavior of the EoS often results in $R(M)$ deviations of 50 m or more [53]. In what follows, we leverage the mismatch of Fig. 9.7 to examine

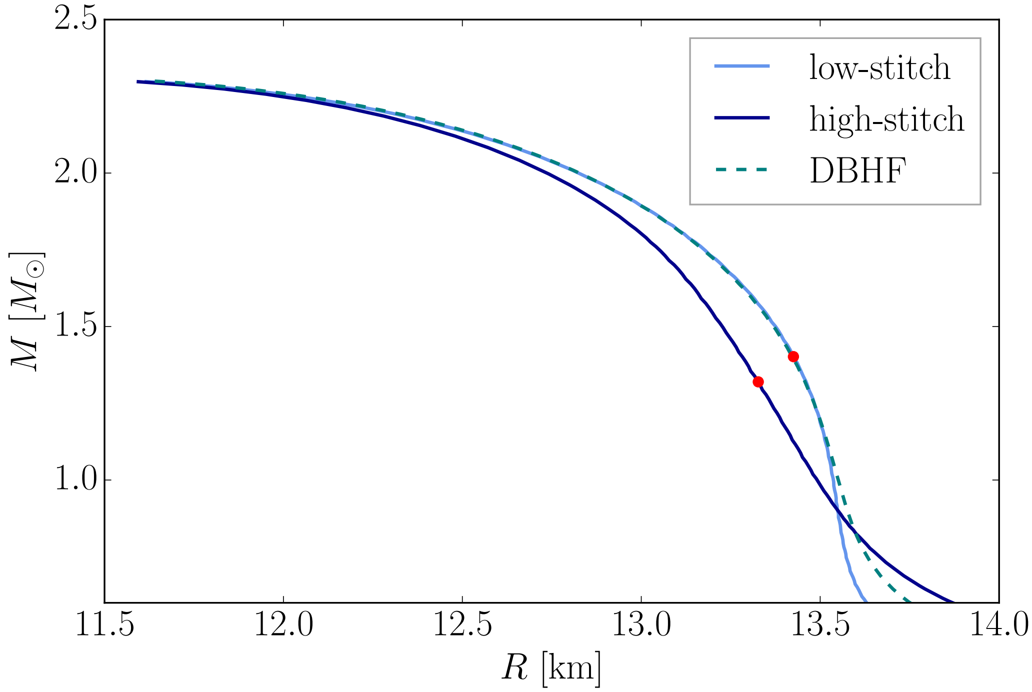

Figure 9.7: The NS mass-radius relation but for the DBHF nuclear model and two enthalpy fits that are stitched to a spectral parametrization at $\rho_{\rm nuc}$ (low-stitch, light blue) and $2.5\rho_{\rm nuc}$ (high-stitch, indigo). We find visibly improved fits to the M–R relation when the enthalpy parametrization extends down to lower densities. Red dots mark the NSs we evolve in Sec. 9.4.

how well we can resolve EoSs with $\sim$ 100 m radius differences in simulations with similar resolution. Since the high-stitch NS is fully described by the spectral parametrization, this test also serves as a comparison of runtimes between the spectral and enthalpy parametrizations. We do not utilize the tabulated version of DBHF because SpECTRE currently cannot perform GRMHD simulations using tables.

We carry out simulations as detailed in Table 9.2 and plot the spectrum of the central density of each star in Fig. 9.8. The two spectra disagree both in the location of the NS modes and their strength, a consequence of the EoS mismodeling shown in Figs. 9.6 and 9.7. In particular, the fundamental radial modes disagree by nearly 3.5%, a difference of $\sim$ 130 Hz in this case. Table 9.2 further shows the simulation runtime which is comparable in the 130 m resolution case; each run took about a day on $\sim$ 70 processing elements. Based on the benchmarking results of Sec. 9.4, total EoS evaluation time should be comparable for the two runs, as the spectral parametrization evalautes the pressure about twice as quickly as the

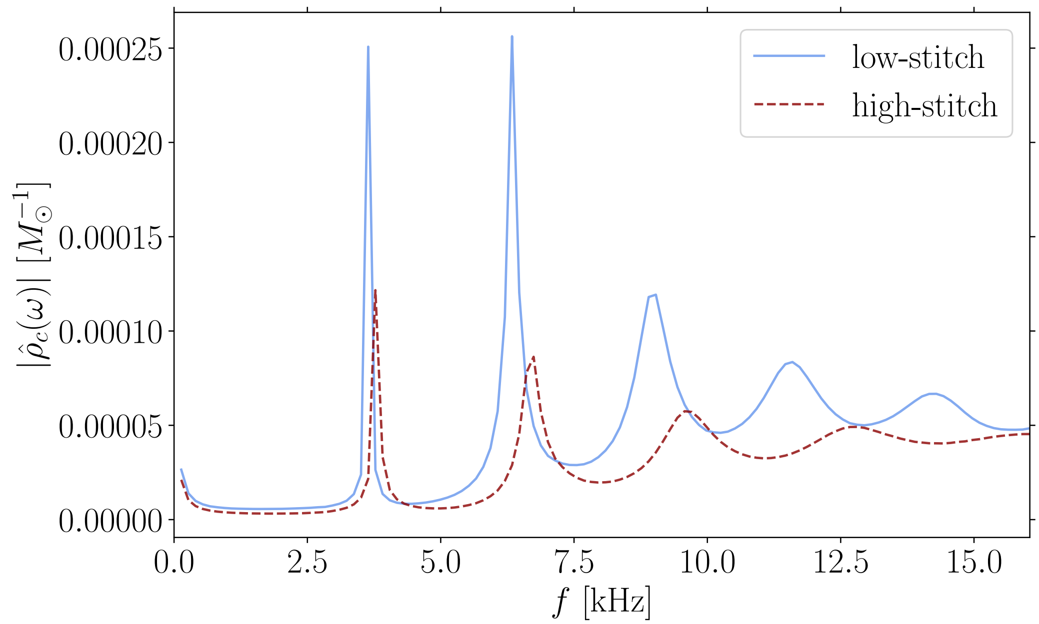

Figure 9.8: NS central density spectrum for SpECTRE simulations with enthalpy fits to the DBHF nuclear EoS that are stitched to the spectral parametrization at ρ_{nuc} (low-stitch, blue solid) and $2.5\rho_{\text{nuc}}$ (high-stitch, red dashed). These runs are labeled enthalpy-dbhf-mc-130 and spectral-dbhf-mc-130 respectively in Table 9.2. The simulated star has a central density of $\approx 2.2\rho_{\text{nuc}}$; it is marked in Figs. 9.6 and 9.7. In the red case, the NS is completely described by the spectral EoS as its central density is below $2.5\rho_{\text{nuc}}$.

enthalpy parametrization, but evaluates the internal energy about three times slower. Since the number of pressure and internal energy evaluations throughout the entire simulation is not known *a priori*, we cannot preemptively conclude which should run faster, though it is likely the difference would be small. This is reflected in the runtime; differences of 10% are found, with the enthalpy parametrization running slightly faster. Nonetheless, this could be due to an array of confounding factors such as task allocation efficiency, and hardware differences. We therefore conclude that the enthalpy parametrization, despite having more flexibility, is not slower than lower dimensional parametrizations at these resolutions for practical problems.

DBHF_2507: Phase transitions

We now turn our attention to EoS with strong phase transitions and study both smooth and non-smooth (i.e., piecewise) EoSs. We base our studies on DBHF_2507 which is constructed by combining DBHF with the constant-speed-of-sound phenomenological parametrization for strong phase transitions [9]. We select a transition density of $\rho_t = 2.5\rho_{\rm nuc}$ and latent heat ratio $\Delta e/e = 0.7$ [57, 24]. The pressure remains constant during the phase transition, while above that it has a constant speed of sound with $c_s^2 = 1$. The induced phase transition causes a second stable branch to appear in the M–R relation above masses $\sim 1.6 M_\odot$.

DBHF_2507: piecewise parametrization

In its original form described above, DBHF_2507 is piecewise smooth, and it can be represented effectively by a piecewise version of the enthalpy parametrization. Below the phase transition we use either the low- or high-stitch fits from Sec. 9.4, and transition to a new enthalpy segment after the transition. In the high-stitch case, the hadronic part of the EoS is completely described with the spectral parametrization. During the transition, DBHF_2507 possesses a formally constant pressure as a function of density; however, constructing TOV solutions using the method of Lindblom [76]—the TOV method implemented in SpECTRE—requires $dh/dz = dp/d\rho$ to be strictly positive. Therefore, in the transition region we modify the EoS to exhibit $dh/dz = \delta$, where δ is some quantity large enough to guarantee that $h(z)$ is numerically invertible, but still small enough to have a small impact on the TOV solution relative to the target resolution.[5] After the end of the phase transition, $h(z)$ is given by a constant speed of sound form, (see Eq. (9.8)); this is similar to the procedure demonstrated in [54].

The advantage of the enthalpy parametrization in this problem is that it is able to model constant-speed-of-sound matter (see App. 9.8 for the polytropic case) efficiently and with no fine-tuning. Compare this to polytropic (or spectral) models, which can only model constant-speed-of-sound matter well when

$$\Gamma \equiv \frac{\rho}{p}\frac{dp}{d\rho} = \frac{\rho}{p} h c_s^2 = \frac{p+e}{p} c_s^2 \tag{9.25}$$

is slowly varying. This is typically not true until some density greater than the phase transition, where $p = p_0 + c_s^2 \Delta e \approx c_s^2 \Delta e$, especially if c_s^2 is small compared to 1, such as models where $c_s^2 = 1/3$ in the core [66, 116]. In contrast, the enthalpy parametrization can model constant-speed-of-sound matter to arbitrary precision, and benchmarking results demonstrate that in such cases it can even outperform polytropic EoSs by up to 25%.

[5] At a central density of $5.07\rho_{\rm nuc}$, the difference in radius induced by using $\delta = 1\times10^{-4}$ instead of $\delta = 1\times10^{-3}$ is less than 5 m.

We plot the M–R curve in Fig. 9.9, using the low-stitch and high-stitch fits for the hadronic part of the EoS as discussed in Sec. 9.4. The low-stitch EoS shows better agreement with DBHF_2507, consistent with previous results; see Fig. 9.7. The transition mass and radius for the low-stitched model are functionally identical to the tabulated values with errors of $\lesssim 0.01\,M_\odot$ and $\lesssim 1$ m. In the high-stitch case the errors increase to $0.05\,M_\odot$ and ~ 100 m. Nonetheless, errors decrease with increasing central density and the maximum mass $M_{\rm max}$ is consistent to $\sim 0.01\,M_\odot$ for both fits. This indicates that the enthalpy parametrization can produce effective EoS fits at high densities even when extending a (relatively) poor low-density fit.[6]

DBHF_2507: Relativistic simulations

We perform SpECTRE simulations with both the high- and low-stitch EoSs and NSs with central density of $\rho_c = 4.67\rho_{\rm nuc}$, above the transition density from nuclear to quark matter; see the red dots in Fig. 9.9. Preliminary results with low spatial resolutions demonstrated that for such $\rho_c > \rho_{\rm t}$, the NS undergoes strong density oscillations that are quickly damped. Given that the fundamental mode is long-lived [64], this short damping timescale is probably related to numerical dissipation. Therefore we perform and compare simulations at various grid resolutions to ensure convergence, increasing the number of computational elements while the number of grid points inside each element is fixed. The main results presented below correspond to a ~ 70 m resolution. We also restrict to the low-stitch fit since the differences between the low- and high-stitch fits are likely resolvable for < 130 m resolution; see Fig. 9.9.

We plot the central density and the spectrum in the top and bottom panels of Fig. 9.10 for both reconstruction schemes. We find good agreement in the frequency and damping time of the density modes, though the monotonized central scheme predicts more than double the power of the adaptive order method below ~ 80 kHz. Interestingly, we find that the presence of a quark core in the NS changes the spectrum qualitatively, c.f., Fig. 9.8. The spectrum is now dominated by modes in the $O(10)$ kHz range, an order of magnitude higher than the hadronic NS case

[6] Such comparisons to tabulated models might be difficult to interpret, as a 1% interpolation inconsistency in $\rho(p)$ can lead to differences of $O(100\text{ m})$ on the second stable branch. This problem is more pronounced here as the DBHF_2507 construction requires computing $\rho(e) = 2.5\rho_{\rm nuc}$ via table-based root finding, a procedure that depends on the interpolation strategy and, in turn, affects the transition mass and radius. For hadronic EoSs this issue is suppressed, as differences in interpolation are smoothed over by the integration of the TOV equations. The enthalpy parametrization, having an analytic expression for $e(\rho)$, does not face this issue.

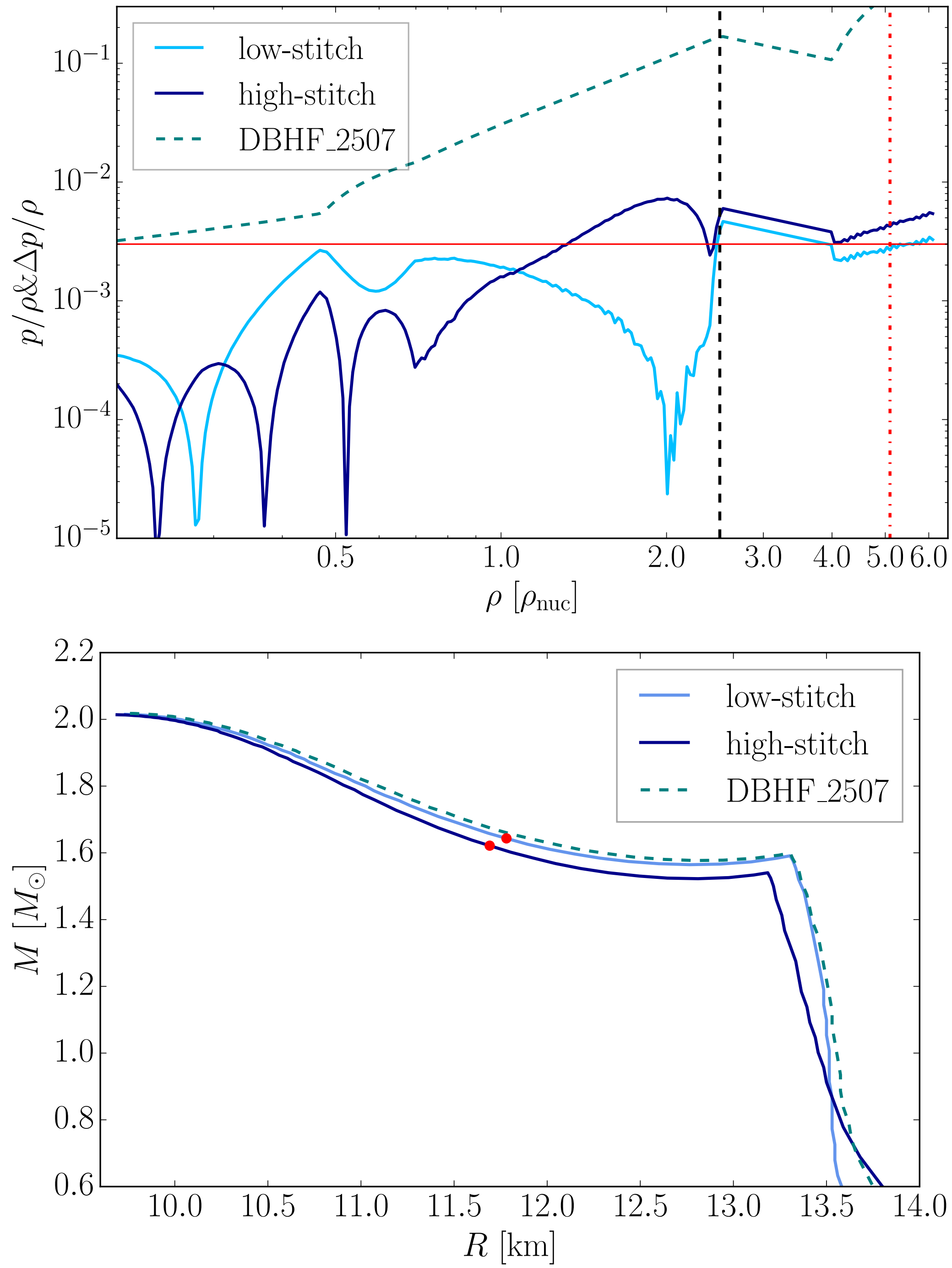

Figure 9.9: Same as Figs. 9.6 & 9.7 but for the DBHF_2507 EoS. The procedure by which the low- and high-stitch EoSs of Sec. 9.4 are extended through the phase transition is described in Sec. 9.4. Consistent with Fig. 9.7, the low-stitch case can more accurately reproduce the parameters of the phase transition, though caution must be exercised when comparing to tabulated models as differences in interpolation in this case can be substantial. See the text of Sec. 9.4. In the top panel, the black vertical dashed line marks the onset of the phase transition. The red dot-dashed line in the top panel and the red dots in the bottom panel mark the NSs we use in subsequent simulations, analogous to Figs. 9.6 & 9.7 respectively.

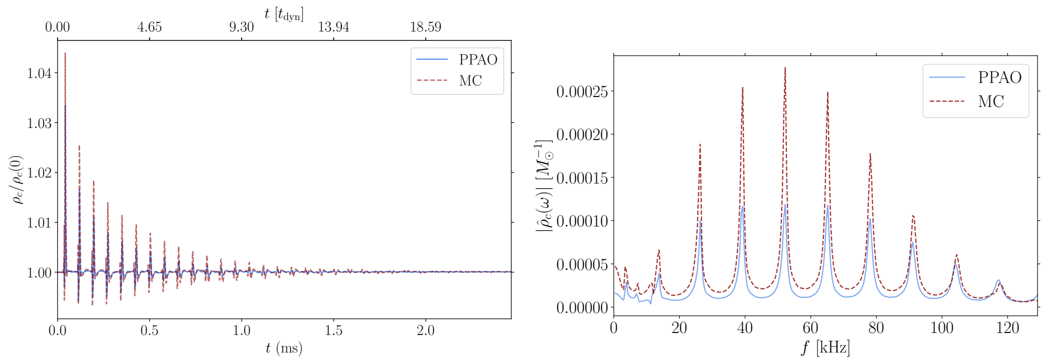

Figure 9.10: Normalized NS central density as a function of time (top panel) and its spectrum (bottom panel) for `SpECTRE` simulations with enthalpy fits to the DBHF_2507 nuclear EoS that are stitched to the spectral parametrization at $\rho_{\rm nuc}$ for two different choices of finite-difference reconstruction schemes. The adapative order reconstructor is marked in blue and the monotonized central reconstructor is marked in red. Run details are listed as enthalpy-pt-ppao-70 and enthalpy-pt-mc-70 respectively in Table 9.2. The simulated star has a central density of $\sim 4.67\rho_{\rm nuc}$; it is marked in Fig. 9.9. We find excellent agreement on mode frequencies but slight differences in power distribution.

of Fig. 9.8. The spacing of the modes, about 16 kHz, is of order $c/2R_{\rm core}$, where $R_{\rm core} \sim 6$ km is the radius of the quark core. We attribute this to density perturbations that are confined to the quark core and are only weakly coupled to the bulk behavior of the star across the transition. In order to confirm this, we plot the density profile of the star extracted from the run enthalpy-pt-ppao-70 as a function of radius in Fig. 9.11 at different times. Most of the oscillation power sourced in the quark core is reflected back into the core at the quark-hadronic boundary, with only a small fraction getting transmitted into the hadronic region. The reflected pulse gets inverted (fixed-end reflection); this is consistent with theoretical expectations since the sound speed changes from $c_s^2 = 1$ in the quark core to $c_s^2 \sim 0.3$ in the hadronic region at the boundary.

The initial perturbation needed to drive these modes is provided by numerical noise near the transition, with $O(50 - 100\text{kHz})$ being the scale of the sound crossing frequency of a computational element of our domain. High frequency modes, in particular p-modes being primarily confined to the core of the star is in line with expectations for radial modes [109].

Simulation runtimes are provided in Table 9.2. We find that the adaptive-order simulation (enthalpy-pt-ppao-70) has a $\sim 20\%$ longer runtime than the monotonized

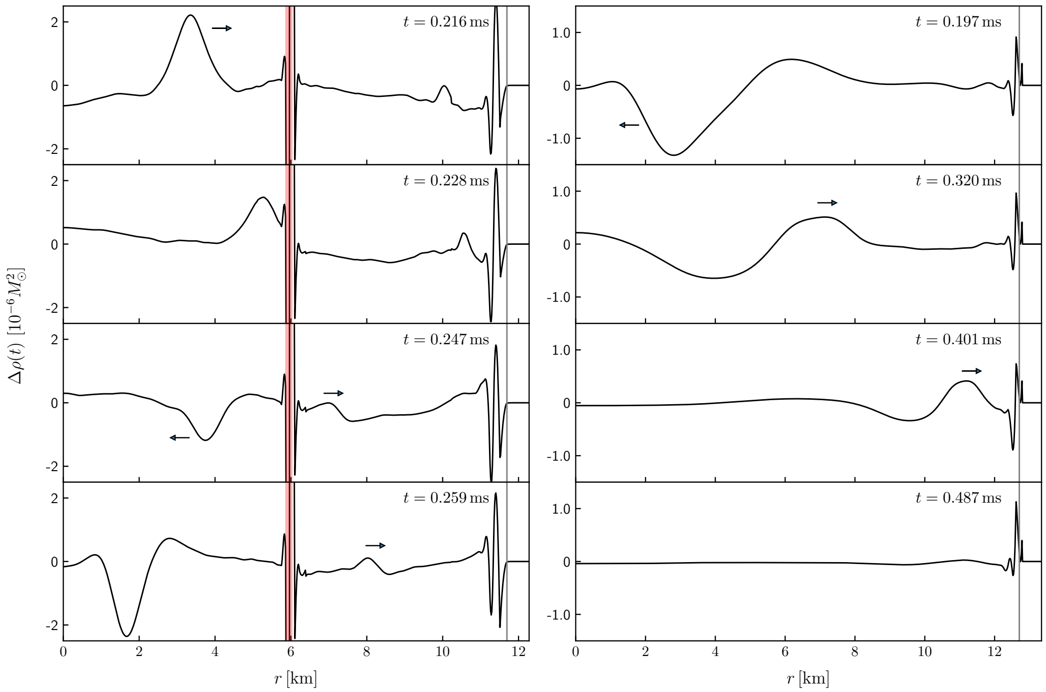

Figure 9.11: Rest-mass density profile relative to the initial profile $\Delta\rho \equiv \rho(r,t) - \rho(r,0)$ as a function of radius for a hybrid star described with DBHF_2507 (left panel; details in Sec. 9.4) and a simple polytrope with $\Gamma = 2$ (right panel; details in App. 9.8) for different times (top to bottom). We denote the NS surface with a vertical solid gray line in each panel and the quark-hadronic boundary with a vertical red line in the left panel. We show snapshots of the density at four different times in order to examine the dynamical behavior of the density oscillations. For the hybrid star (left) density perturbations are partially transmitted and reflected at the quark-hadronic boundary, while for the polytrope (right) the wave smoothly propagates back and forth within the NS interior. Small black arrows highlight the wave packet and its traveling direction. The hybrid star snapshots are from the run enthalpy-pt-ppao-70 and the polytrope snapshots are from a simulation with identical domain, finite-difference reconstruction scheme, and central density, but a polytropic EoS (9.33) in place of DBHF_2507. See polytropic-polytrope-mc-130 for details of a lower-resolution polytropic simulation.

central (enthalpy-pt-mc-70) simulation, which is expected. Turning to the EoS and comparing enthalpy-pt-mc-130 and enthalpy-dbhf-mc-130 at identical resolutions, number of CPUs, and reconstruction schemes, we find a $O(40\%)$ increase in runtime for DBHF_2507 as compared to DBHF. We do not attribute this runtime slowdown to increased EoS evaluation time, as the enthalpy EoS employed beyond the phase transition uses no trigonometric correction terms, and thus is nearly computationally identical to the polytrope profiled in Table 9.4. This indicates that individual EoS evaluations (above the transition) are actually somewhat cheaper than in either of the fits to DBHF, discussed in Sec. 9.4 (below the transition they are identical). Instead, we attribute the slowdown to the non-smoothness of this EoS; $p(\rho)$ is not analytically C^1 across the phase transition, and $\rho(p)$ is an incredibly sensitive function near the transition. Since our default primitive recovery scheme requires root-finding to determine $\rho(p)$ [62], this can result in significant slowdowns.

Comparing the simulations enthalpy-pt-mc-130 and enthalpy-pt-mc-70, we also find that refining the grid resolution from 134 m to 67 m results in only a 4-fold increase in runtime, compared to the expected $(134/67)^3 = 8$.[7] We attribute this lower-than-expected increase to the DG-FD hybrid scheme [31]. At higher resolutions each cell is smaller, therefore finite-difference cells are more tightly concentrated in regions with discontinuities. This results in a lower fraction of the NS reverting to the slower finite-difference scheme from the faster discontinuous Galerkin scheme. We display a slice of the NS for enthalpy-pt-ppao-70 in Fig. 9.12, and mark the cells which have reverted to finite-difference in red. The majority of the NS interior is indeed using the discontinuous Galerkin method, with finite difference being used only at the phase-transition and surface interfaces.

Smooth transitions

Due to its flexibility, the enthalpy parametrization can also be used to model smoother transitions in the EoS, such as those that may arise from a crossover transition. To demonstrate this, we begin with DBHF_2507 and average the speed of sound at nearby points over the entire EoS. This is distinct from the small perturbation added to the EoS in in Sec. 9.4, as in this case we expect the resulting EoS to be well described by a smooth interpolant. To demonstrate this, we fit this new smoothed EoS with $j_{\max} = 4$ trigonometric terms and display the fit in Fig. 9.13. We find sub-1% agreement in the $1 - 2\rho_{\rm nuc}$ density region which most directly affects macroscopic observables. Relative errors are typically higher below the enthalpy-spectral transition point (set to $\rho_{\rm nuc}$ here). This is because smoothing the EoS is done by locally averaging the speed of sound, so that after averaging the speed of sound is locally close to being constant. For polytropic and nearly polytropic EoSs the speed of sound is not nearly constant at low densities, so a spectral parametrization cannot effectively fit the smooth c_s^2 EoS.

We expect simulating NSs with EoSs displaying smooth but rapidly varying speeds

[7] Since we run simulations with the fixed number of time steps, refining the grid does not lead to any major slowdown from time stepping. This would not be the case if we ran to a fixed final time.

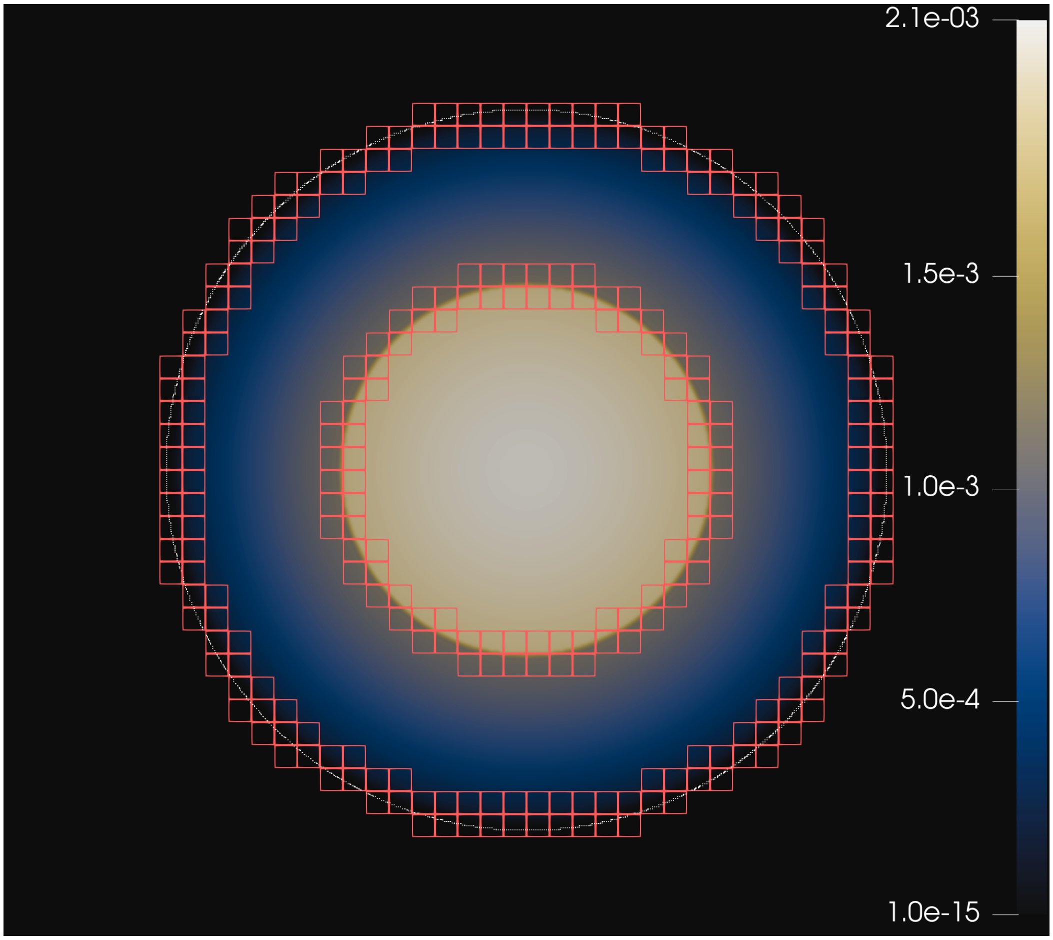

Figure 9.12: NS rest mass density (colorbar, units of $M_{\odot}^{-2}$) on the $y-z$ plane at $t = 100M_{\odot}$ for the run enthalpy-pt-ppao-70. Red marks subdomain elements where finite-difference is used. The finite-difference cells are confined near the NS surface (outer circle, white solid line) and the phase transition layer (inner circle) where discontinuities are expected. The majority of the star is still evolved with the more computationally efficient discontinuous-Galerkin method.

of sound to be slower. This is for two primary reasons. First, fitting EoSs to some fixed degree of precision for more complicated EoSs typically requires adding more parameters, increasing evaluation time. Second, EoSs with rapid changes in $dp/d\rho$ tend to slow down primitive recovery, as the function $\rho(p)$ must be evaluated by root-finding. Even though the EoS in this case is analytically smooth, root-finding algorithms require more evaluations if the function is quickly varying.

We perform a run with identical central density, $\rho \sim 4.67\rho_{\mathrm{nuc}}$ for 10,000 CFL limited time steps, in order to bound performance decreases. We display the results in Table 9.2 as enthalpy-smoothpt-170 . We find that the EoS presented in Fig. 9.13

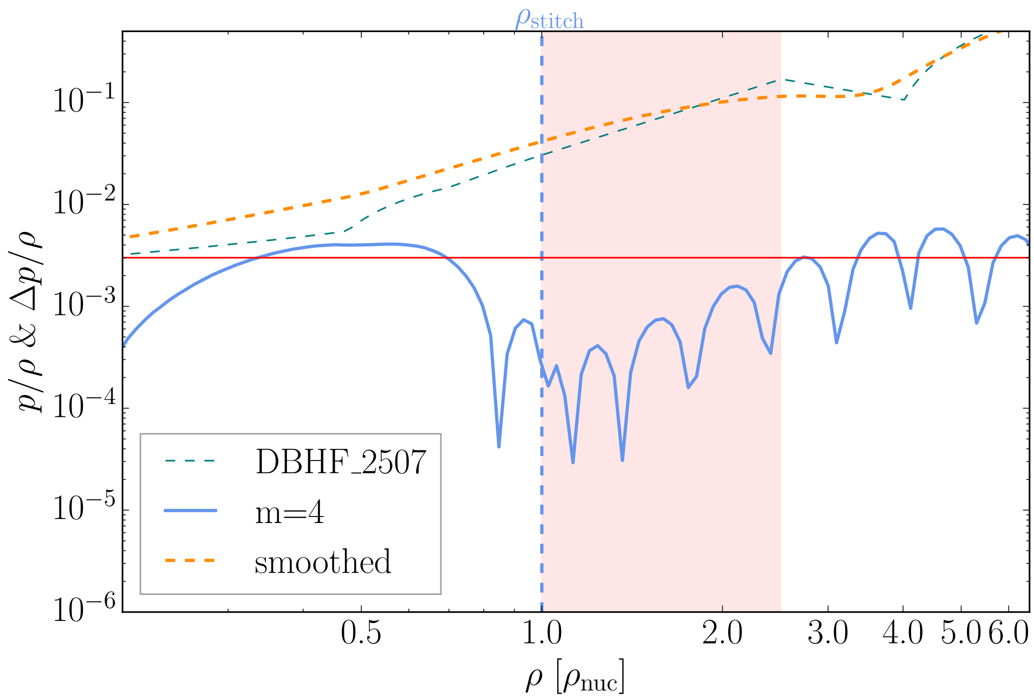

Figure 9.13: Same as Fig. 9.6 but for the smoothed version of DBHF_2507 constructed in Sec. 9.4. The enthalpy parametrization achieves sub-1% errors in the most relevant region, $1-2\rho_{\rm nuc}$.

requires a comparable time per evolution step to enthalpy-dbhf-mc-130 indicating the EoS is sufficiently smooth to not induce a large slowdown at this resolution. We further plot the oscillations of the central density of both the smooth-transition DBHF_2507 model (smooth) and enthalpy-pt-mc-130 (sharp) in Fig. 9.14. We find that the smoothed fit does not lead to the characteristic decoupling of core modes, meaning that such a model would be a poor representation of the true DBHF_2507 EoS, even if it is able to reproduce other characteristics of DBHF_2507, such as a small radius near $M_{\rm max}$.

In general, we expect smooth EoSs to be most effectively represented by globally smooth parametrizations, while EoSs with discontinuities will be better modeled by piecewise parametrizations. In addition, nonsmoothness can lead to a loss of accuracy in simulations [53], so an additional trade-off may exist between accuracy and performance in the choice to use a smooth versus a piecewise representation. The enthalpy parameterization is flexible enough to be effective in both the piecewise EoS and the smooth EoS cases.

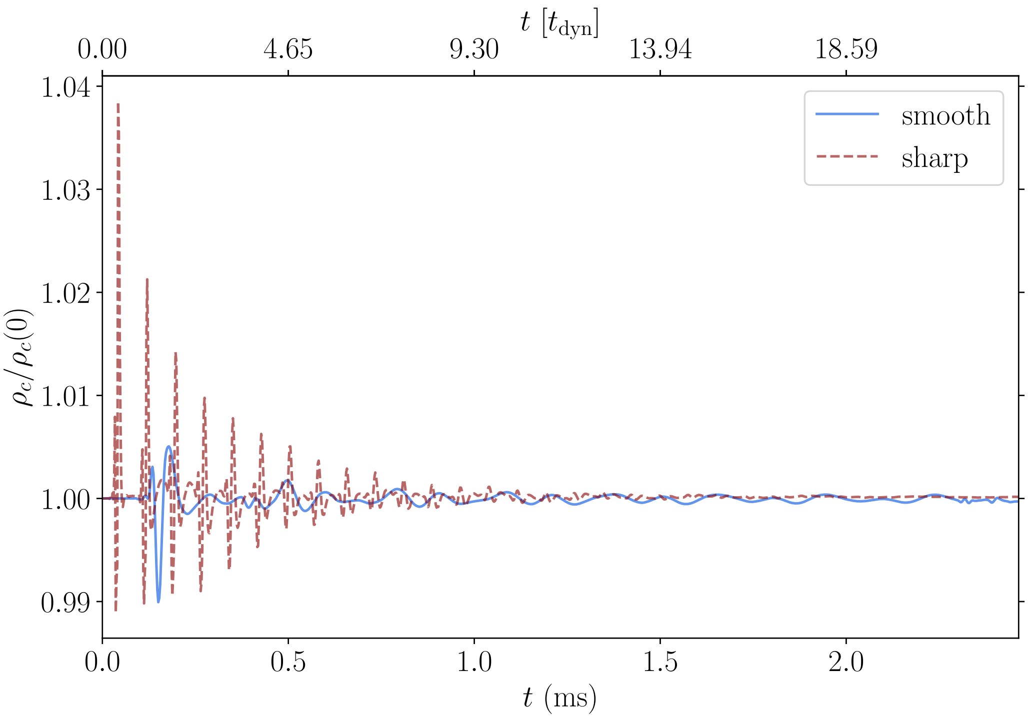

Figure 9.14: NS central density as a function of time for the run enthalpy-smoothpt-170 (blue, solid) and enthalpy-pt-mc-130 (red, dashed). The smooth fit poorly reflects the mode structure of the true DBHF_2507 EoS, even though the behavior of the microscopic EoS is qualitatively similar.

9.5 Discussion

We introduced a new enthalpy-based parametrization for the cold nuclear EoS that can capture a wide range nuclear models and their phenomenological extensions using polynomials and trigonometric terms. The *enthalpy parametrization* emphasizes *flexibility*, as it is able to effectively model both smooth and non-smooth nuclear models, and *computational performance* as its evaluation cost scales with the number of parameters used. For example, it displays comparable performance to single-polytrope parametrizations for the case of polytropic EoSs, while the computational cost scales with the number of fit parameters for more complex (such as non-smooth) models. This trade-off between computational performance and flexibility allows us to tune EoS fits to the resolution requirements of the problem at hand.

Computational performance is achieved by inexpensive evaluation of the various thermodynamic quantities. The $p(\rho)$ evaluation cost does not exceed $O(4)$ times that of a polytropic EoS for any case we investigated, even when many trigonometric terms are used. In cases where this slowdown is significant, the enthalpy parametrization may be sped up significantly by using Clenshaw's method [94]. We obtain faster evaluation of $\epsilon(\rho)$ than the existing spectral parametrization in all cases, as the latter evaluates ϵ numerically, while the enthalpy parametrization computes all thermodynamic quantities analytically. Overall, the additional computational cost of the enthalpy parametrization on top of other existing parametrizations is always smaller than the cost of other simulation components.

With the caveat that quantifying EoS fitting accuracy is subtle and depends on the parameters one compares, we overall find that the enthalpy parametrization is able to successfully fit nuclear models. In principle and in the context of numerical simulations, EoS parametrizations need only fit the nuclear EoS as well as the simulation resolution. Nonetheless, even subpercent errors in the pressure near $\rho_{\rm nuc} - 2\rho_{\rm nuc}$ can lead to ~ 100 m differences in NS radii. In contrast to lower-dimensional or less flexible parametrizations, we show that the enthalpy parametrization is able to fit tabulated and phenomenological nuclear models to effectively arbitrary precision by using additional parameters. The optimal number of parameters is then determined by balancing accuracy and computational cost for a given numerical resolution.

The enthalpy parametrization's flexibility allows us to efficiently and with little fine tuning represent both smooth and non-smooth nuclear models. The latter may correspond to models with strong phase transitions that we can fit and numerically evolve using SpECTRE. Our simulations demonstrate that we can stably evolve such stars in the Cowling approximation. However, studying the evolution of hybrid hadronic-quark NSs away from an unstable EoS branch that falls between the hadronic and the quark branches [42] hinges on full metric evolution coupled to GRMHD. SpECTRE's hybrid DG-FD scheme is crucial for the computational performance of these simulations. The DG-FD scheme allows phase transitions to be modeled with lower-order finite-difference methods while continuing to use higher-order discontinuous-Galerkin methods throughout the individual hadronic and quark regions. This leads to better computational scaling than might be expected upon mesh refinement, as better resolution of boundaries (such as the quark-hadronic matter boundary) within the star reduces the amount of the domain which uses the slower finite-difference approach.

The enthalpy parametrization is a step toward ensuring that numerical simulations can efficiently represent a wide range of nuclear phenomenology. Accurate simulations of NSs will continue being crucial for the interpretation of new astrophysical and experimental data. Even with current EoS constraints, the space of potential BNS phenomenology is large, and many questions remain regarding the impact of magnetic fields, instabilities, temperature effects [21, 100], and transport physics. Future steps include extending the applicability of the enthalpy parametrization beyond cold, beta-equilibrated nuclear matter, and incorporating more physical effects in SpECTRE simulations.

The simulations presented here were performed with SpECTRE commit hash 2df19579a84385b3d5ab4663e3da7e33012e0355. The earliest release of SpECTRE with this commit is version 2023.01.13 [32]. Input files for the runs performed, including enthalpy fit parameters for each EoS studied, are available on Github [113].

9.6 Acknowledgements

I.L. thanks Tianqi Zhao for helpful conversations in preparing this manuscript. The authors thank Reed Essick, Ingo Tews, Phil Landry, and Achim Schwink for access to χ-EFT conditioned Gaussian process draws. Charm++/Converse [60] was developed by the Parallel Programming Laboratory in the Department of Computer Science at the University of Illinois at Urbana-Champaign. This project made use of python libraries including `scipy` and `numpy` [121, 87]. Figures were produced using `matplotlib` [59] and `ParaView` [13]. Computations were performed with the Wheeler cluster at Caltech, which is supported by a grant from the Sherman Fairchild Foundation and Caltech. This work was supported in part by the Sherman Fairchild Foundation at Caltech and Cornell, as well as by NSF Grants No. PHY-2011961, No. PHY-2011968, and No. OAC-1931266 at Caltech and by NSF Grants No. PHY-1912081 and No. OAC-1931280 at Cornell. IL and KC acknowledge support from the Department of Energy under award number DE-SC0023101. FF gratefully acknowledges support from the Department of Energy, Office of Science, Office of Nuclear Physics, under contract number DE-AC02-05CH11231, from NASA through grant 80NSSC22K0719, and from the NSF through grant AST-2107932. The authors are grateful for computational resources provided by the LIGO Laboratory and supported by National Science Foundation Grants PHY-0757058 and PHY-0823459.

9.7 Fitting the enthalpy parametrization

In this appendix we provide details about the procedure with which we fit some tabulated EoS data with the enthalpy parametrization which includes the following parameters:

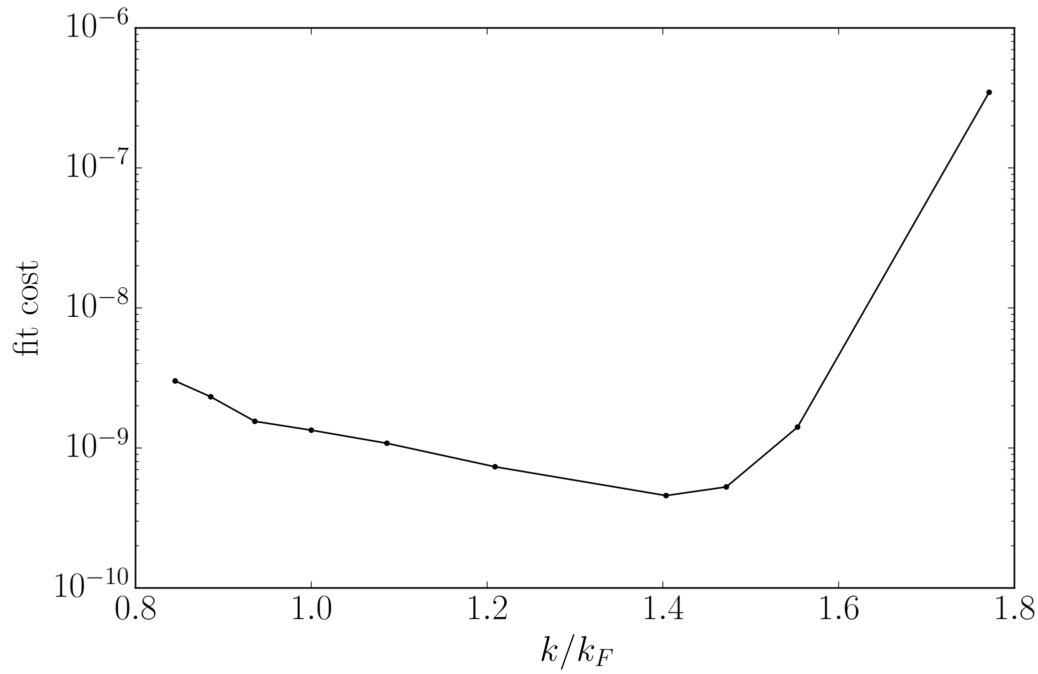

Figure 9.15: Cost, Eq 9.26, in arbitrary units, of the fit to the phenomenological EoS of Fig. 9.1 as a function of k. The minimum occurs at k slightly larger than k_F, in this case near $k = 1.4k_F$.

- The upper ρ_{max} and lower ρ_{min} density limits are chosen based on the densities of interest. For NS simulations, reasonable values are $\rho_{\text{min}} = \rho_{\text{nuc}}$, $\rho_{\text{max}} = 7\rho_{\text{nuc}}$, but the upper limit depends on the maximum density expected in the simulation.

- The scaling parameters ρ_0 and the wavenumber of the trigonometric correction terms k are not fit, but rather fixed. When we extend a model via a constant speed of sound (Sec. 9.4) the choice of ρ_0 is determined by the modeling problem. When the EoS is fit, ρ_0 is chosen $\rho_0 \in (0, \rho_{\text{min}}]$, so that $z_{\text{max}} = \log(\rho_{\text{max}}/\rho_0) \lesssim i_{\text{max}}$; see Sec. 9.9. We find $\rho_0 = \rho_{\text{min}}/2$ is generally a robust choice. Analogous to how ρ_0 controls the scale of polynomial terms, k controls the scale of trigonometric oscillations. As described in Sec. 9.3, typically $k \approx k_F$ is a good choice, but small perturbations $k \in [k_F/2, 2k_F]$ may improve the fit quality for certain problems, depending on the details of the EoS. Figure 9.15 shows that the effect of varying k is small for the particular test problem displayed in Fig. 9.1.

- The parameters i_{max} and j_{max} determine the number of polynomials and trigonometric terms respectively; see Eq. (9.9) and Eq. (9.10). The quality of the fit is a strong function of i_{max} and j_{max}, but increasing j_{max} above ~ 10 comes at a considerable computational cost even at low resolutions. On the other hand the cost of increasing i_{max} is small, typically of order 2% or less of the total cost of the $p(\rho)$ evaluation per additional polynomial term.

- The coefficients of the polynomial γ_i, Eq. (9.9), and the trigonometric a_j, b_j, Eq. (9.10), expansion are fit through a linear least-squares approach.

- The energy density of the EoS at the stitching point, $e_{\mathrm{min}} = e(z_{\mathrm{min}})$. This is the integration constant associated with solving $de/dz = \rho h$. This parameter is constrained by $\rho_{\mathrm{min}} h_{\mathrm{min}} - e_{\mathrm{min}} = p_{\mathrm{min}} \geq 0$. In principle $e(z_{\mathrm{min}})$ can be computed from EoS tables, but in practice EoS tables may be too coarsely tabulated, or may contain violations of the first law of thermodynamics at levels which significantly affect the computed value of ϵ. For example, a fractional error of 1×10^{-3} in e_{min} will often translate to a fractional error of $\sim 1 \times 10^{-1}$ in ϵ, which therefore shifts the value of $p(z)$ by 10%, as $h\rho = p + \epsilon$ is fixed by the parametrization. Therefore in certain cases it is more effective to treat e_{min} as a free parameter, and further use it to optimize the values of $p(\rho)$. In practice e_{min} is set by the low-density EoS parametrization to guarantee thermodynamic consistency.

Given a target EoS with enthalpy $h(z_i)$ at discrete densities z_i, the linear fit is based on minimizing the cost function

$$C(a_j, b_j, c_i) = \sum_k \left(\frac{h_*(z_k; a_j, b_j, c_i) - h(z_k)}{\sigma(z)} \right)^2 , \tag{9.26}$$

where h_* is given in Eq. (9.12). The factor $\sigma(z)$ is the fit tolerance which can be chosen such that the fit is optimal at different density regions. We choose to target similar relative uncertainty on the non-rest-mass component of the enthalpy density $(h-1)\rho = p + \epsilon\rho$ across density scales: $\sigma(z) \propto \rho(z) \propto \exp(z)$. Overall, the tolerance scales as $1/\rho$, so the fit is relatively better (with respect to h) at low densities. The energy density at the stitching point is then selected; if the tabulated EoS is sufficiently high-resolution, it can be computed by, e.g., the trapezoidal rule. Otherwise, there is no canonical choice for this value, we choose it to maximize agreement with tabulated $p(\rho)$ at high densities.

Finally, the EoS fit is completed by stitching to some other EoS parametrizaton at $\rho_{\mathrm{stitch}} = \rho_{\mathrm{min}}$. In the majority of cases this is the spectral parametrization, though we also explore another enthalpy segment in Sec. 9.4 and a polytrope in App. 9.8. The low-density spectral EoS itself transitions to a lower-density polytrope at some fixed reference density ρ_r. Following Ref. [53], we define $x \equiv \log(\rho/\rho_r)$ and write the spectral pressure as

$$p_s(x) = \begin{cases} p_0 \exp\left[\Gamma_0 x\right] & x \leq 0\,, \\ p_0 \exp\left[\sum_{i=0}^{3} \frac{1}{i+1} \Gamma_i x^{i+1}\right] & x > 0\,, \end{cases} \tag{9.27}$$

where p_0 controls the overall pressure, and Γ_0, Γ_i are the spectral coefficients. The low-density behavior fixes Γ_0, while requiring a C^1 transition to the enthalpy parametrization, i.e., continuity in pressure, energy density, and pressure derivative fixes three more parameters. In practice because $e_{\rm min} = e_{\rm stitch}$ is an integration constant in the enthalpy parametrization, we can freely set it to the value computed for $e_{\rm stitch}$ from the low-density parametrization, guaranteeing exact consistency.

The remaining 1 degree of freedom is selected by either maximizing smoothness across the lower-density transition to the polytrope or maximizing accuracy of the low-density EoS. Smoothness is prioritized when the stitching density is below the core density of typical NS. Then, we set $\Gamma_1 = 0.0$ [53], guaranteeing that Eq. (9.27) is C^2 across the transition ρ_r. This typically produces good fits to the overall M–R curve for the entire EoS. If the spectral parametrization is stitched to the enthalpy parametrization at a higher density (near the core density of astrophysical NSs as is the case in the high-stitch fit of Sec.9.4) we instead allow Γ_1 to vary, choosing it to maximize the agreement of the total parametrized EoS with the target. Both strategies typically result in machine-precision level C^1-stitching to the enthalpy parametrization, with residuals much smaller than mismodeling in the low-density regime.

9.8 Approximating a single polytrope

As an example of the strategy for fitting a target EoS with the enthalpy parametrization, we consider a single-polytrope. In this case, the enthalpy coefficients can be computed analytically. The general goal is to express the EoS in the form of Eq. (9.8), i.e., compute the enthalpy as a function of log-density.

The polytropic exponent is defined as

$$\Gamma(z) \equiv \frac{d \log p}{d \log \rho} = \frac{\rho}{p}\frac{dh}{dz} = \frac{\rho}{p}\frac{d\left(\frac{1}{\rho}\frac{de}{dz}\right)}{dz}\,. \tag{9.28}$$

For a constant polytropic exponent $\Gamma(z) = \Gamma_0$ and using the identity

$$p(z) = h(z)\rho(z) - e(z) = \frac{de}{dz} - e(z)\,, \tag{9.29}$$

Eq. (9.28) becomes

$$\frac{d^2e}{dz^2} - (\Gamma_0 + 1)\frac{de}{dz} + \Gamma_0 e = 0\,. \tag{9.30}$$

The solution to this differential equation is

$$e(z) = (e_0 - \rho_0)\exp(\Gamma_0 z) + \rho_0 \exp(z)\,, \tag{9.31}$$

where we have enforced $e(z = 0) = e_0$ and $e(z \to -\infty) \to \rho(z)$[8] and the enthalpy is

$$h(z) = \frac{1}{\rho}\frac{de}{dz} = \frac{e_0 - \rho_0}{\rho_0}\Gamma_0 \exp\left[(\Gamma_0 - 1)z\right] + 1\,. \tag{9.32}$$

Comparing with Eq. (9.9) the polynomial coefficients of the enthalpy expansion are $\gamma_i = h_0\,(\Gamma_0 - 1)^i\,/i!$, with $h_0 = \Gamma_0\,(e_0 - \rho_0)\,/\rho_0$, if $i \neq 0$, and $\gamma_0 = h_0\,(\Gamma_0 - 1) + 1$. In practice, evaluating the polynomial expansion of Eq. (9.9) requires many floating point operations. Nonetheless, this computation is not necessarily slower than evaluating a simple polytrope if Γ_0 is not an integer, because floating-point exponentiation typically at least an order of magnitude slower than multiplication and addition.

We use this enthalpy parametrization of the polytrope model to compare against the direct single-polytrope SpECTRE implementation and verify the predicted Cowling-approximation NS modes [51, 30]. The low-density EoS in the enthalpy parametrization case is stitched to the exact polytropic expression

$$P(\rho) = \frac{100}{M_\odot^{-2.0}}\rho^{2.0}\,. \tag{9.33}$$

We evolve a NS with central density $1.28 \times 10^{-3} M_\odot^{-2} \approx 2.84\rho_{\rm nuc}$, which is the same as the stars evolved in Refs. [51, 30]. The number of terms necessary in the polynomial expansion depends on the desired accuracy. For a resolution of 130 m we find that $i_{\rm max} = 8$ is more than sufficient. This is consistent with theoretical expectations, as the first neglected term, is of order $1/9! \approx 2 \times 10^{-6}$, indicating errors should be of this scale or smaller. Results are shown in Fig. 9.16 where

[8] This is equivalent to assuming the specific internal energy ϵ is 0 in ordinary, low-density cold matter. This can be done by defining the baryon “rest” mass to be the average mass of a baryon in the outer crust of a NS (despite the fact these baryons may be bound in, e.g. iron and therefore differ from the mass of a free neutron/proton by up to 1%).

Parametrization \ Evaluation Cost (ns)	$p(\rho)$	$\epsilon(\rho)$
enthalpy	43	44
polytrope	57	58

Table 9.4: Performance (in nanoseconds) of the enthalpy and single-polytropic fits to a single polytrope in evaluating the pressure and internal energy at $\rho = 5.0{\times}10^{-4} M_\odot^2$. The enthalpy parametrization outperforms then polytrope in both cases.

the enthalpy fit to the polytrope and the direct single-polytropic parametrization return essentially identical results. We display the run details in Table 9.2, as enthalpy-polytrope-mc-130 and polytropic-polytrope-mc-130.

We find effectively no difference in the runtime for the simulations using each of the polytropic and enthalpy parametrizations. Examining the cost of individual EoS calls in Table 9.4, we find the enthalpy parametrization is somewhat faster in both $p(\rho)$ and $\epsilon(\rho)$ evaluation, indicating that in this case, EoS evaluation time is not a significant contribution to runtime. This speedup is also expected to extend to constant-speed-of-sound matter, which has an identical functional form to a polytropic EoS when expanded in the enthalpy / parametrization, the only difference being the values of the coefficients.

The reason the polytropic EoS evaluation is not faster despite having a very simple analytic expression is the inefficiency of floating-point exponentiation. In the case of our test problem the floating point exponent `2.0` is only known during runtime, and so the compiler cannot optimize EoS calls. If the exponent is known to be an integer at compile time, the calls can be evaluated using repeated multiplication. We implement this improvement for this particular test problem, and find the cost of polytropic $p(\rho)$ evaluations to be 10 ns on identical hardware, indicating a 5-fold improvement. Nonetheless, this speedup is not reflected in the total evolution runtime for resolutions of at least $\sim$ 120 m as the EoS evaluation cost is subdominant to other simulation components.

9.9 Numerical considerations for enthalpy coefficients

Here we expand upon numerical considerations for choices of polynomial, coefficients γ_i. The choice, $\gamma_i \geq 0$ in Eq. (9.9) effectively bounds the number of terms in the polynomial expansion which can be practically used. To see this, consider $z_{\max} \equiv \log\left(\rho_{\max}/\rho_0\right)$. Coefficients γ_i must satisfy $\gamma_i z_{\max}^i \lesssim O(\gamma_0) \sim 1$, otherwise they would be larger than the total enthalpy in this region, which is typically also of

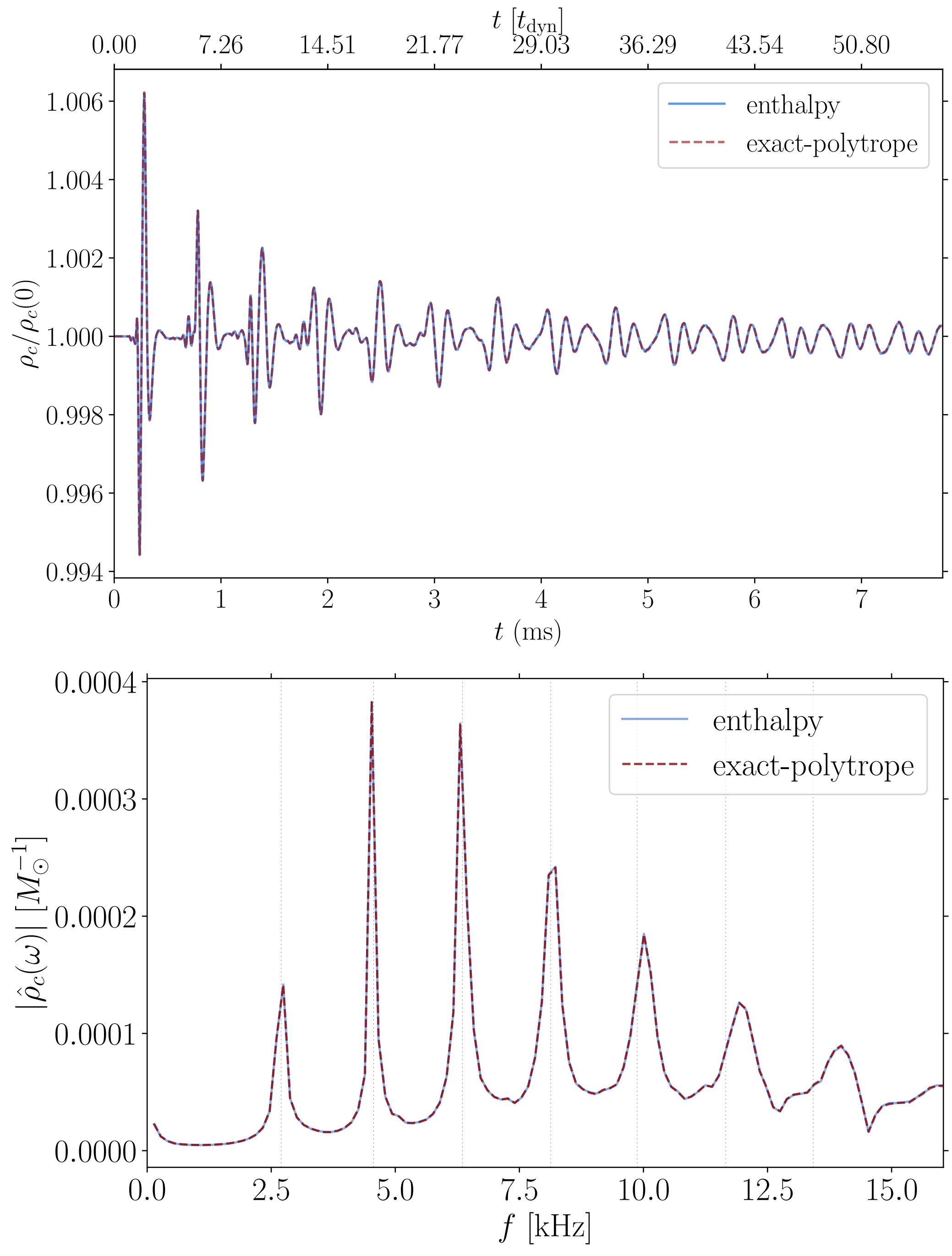

Figure 9.16: NS central density as a function of time (top panel) and its spectrum (bottom panel) for SpECTRE simulations with an enthalpy fit to a single polytrope with $\Gamma_0 = 2.0$ (blue) and a direct single-polytropic parametrization (red, dashed). Known Cowling frequencies [51] are marked as dashed vertical lines. The spectra are identical by eye.

this scale. With this in mind, we consider i as "too large" if $i \gg z_{\max}$, as any term which satisfies $\gamma_i z_{\max}^i \lesssim \gamma_0$ has

$$\frac{\gamma_i z^i}{\gamma_i z_{\max}^i} = \left(\frac{z}{z_{\max}}\right)^i, \tag{9.34}$$

small except when z is nearly $z_{\max}$. That is, the degree of freedom is only relevant at the highest densities, and this density region shrinks as i gets larger. For typical scales, such as $\rho_0 = 0.5\rho_{\rm nuc}$, $\rho_{\min} = \rho_{\rm nuc}$, and $\rho_{\max} = 7\rho_{\rm nuc}$, then $z_{\max} \sim \log(14) \approx 2.6$.

One can decrease ρ_0 to increase the relevant value of $z_{\max}$, but this requires adding more parameters, which may not be desirable, since many of them may be irrelevant, or degenerate. One way to view this, is that in the Taylor expansion of the exponential function (equivalently the expansion of $h(z)$ in a constant speed of sound case), the term $z^i/i!$ is the largest term on $z \in (i-1, i)$, and is generally decreasing in relevance away from this region relative to other terms. Therefore the $i^{\rm th}$ term of this expansion is most relevant near $z \lesssim i$, and is unimportant far from this region. This implies that flexibility is essentially equidistributed in $\log(\rho)$ for this approximation (the same argument applies to the spectral parametrization), and that higher polynomial terms cannot resolve features at low densities. Instead, we choose to switch to a new function basis at this point, optimized to capture the largest scale features at lowest order of approximation.

References

[1] B. P. Abbott et al. "GW170817: Measurements of neutron star radii and equation of state". In: *Phys. Rev. Lett.* 121.16 (2018), p. 161101. DOI: 10.1103/PhysRevLett.121.161101. arXiv: 1805.11581 [gr-qc].

[2] B. P. Abbott et al. "GW190425: Observation of a Compact Binary Coalescence with Total Mass $\sim 3.4 M_\odot$". In: *Astrophys. J. Lett.* 892.1 (2020), p. L3. DOI: 10.3847/2041-8213/ab75f5. arXiv: 2001.01761 [astro-ph.HE].

[3] B. P. Abbott et al. "Multi-messenger Observations of a Binary Neutron Star Merger". In: *Astrophys. J. Lett.* 848.2 (2017), p. L12. DOI: 10.3847/2041-8213/aa91c9. arXiv: 1710.05833 [astro-ph.HE].

[4] Benjamin P. Abbott et al. "GW170817: Observation of Gravitational Waves from a Binary Neutron Star Inspiral". In: *Phys. Rev. Lett.* 119.16 (2017), p. 161101. DOI: 10.1103/PhysRevLett.119.161101. arXiv: 1710.05832 [gr-qc].

[5] D. Adhikari et al. "Accurate Determination of the Neutron Skin Thickness of ^{208}Pb through Parity-Violation in Electron Scattering". In: *Phys. Rev. Lett.* 126.17 (2021), p. 172502. DOI: 10.1103/PhysRevLett.126.172502. arXiv: 2102.10767 [nucl-ex].

[6] D. Adhikari et al. "Precision Determination of the Neutral Weak Form Factor of ^{48}Ca". In: (May 2022). arXiv: 2205.11593 [nucl-ex].

[7] A. Akmal, V. R. Pandharipande, and D. G. Ravenhall. "The Equation of state of nucleon matter and neutron star structure". In: *Phys. Rev. C* 58 (1998), pp. 1804–1828. DOI: 10.1103/PhysRevC.58.1804. arXiv: nucl-th/9804027.

[8] Mark Alford et al. "Hybrid stars that masquerade as neutron stars". In: *Astrophys. J.* 629 (2005), pp. 969–978. DOI: 10.1086/430902. arXiv: nucl-th/0411016.

[9] Mark G. Alford et al. "Constraining and applying a generic high-density equation of state". In: *Phys. Rev. D* 92.8 (2015), p. 083002. DOI: 10.1103/PhysRevD.92.083002. arXiv: 1501.07902 [nucl-th].

[10] Eemeli Annala et al. "Multimessenger Constraints for Ultradense Matter". In: *Phys. Rev. X* 12.1 (2022), p. 011058. DOI: 10.1103/PhysRevX.12.011058. arXiv: 2105.05132 [astro-ph.HE].

[11] Luis Antón et al. "Numerical 3+1 general relativistic magnetohydrodynamics: a local characteristic approach". In: *The Astrophysical Journal* 637 (Jan. 2006), pp. 296–312. DOI: 10.1086/498238.

[12] John Antoniadis et al. "A Massive Pulsar in a Compact Relativistic Binary". In: *Science* 340.6131 (2013), p. 1233232. DOI: 10.1126/science.1233232. arXiv: 1304.6875 [astro-ph.HE].

[13] Utkarsh Ayachit. *The ParaView Guide: A Parallel Visualization Application*. Clifton Park, NY, USA: Kitware, Inc., 2015. ISBN: 1930934300.

[14] Luca Baiotti, Bruno Giacomazzo, and Luciano Rezzolla. "Accurate evolutions of inspiralling neutron-star binaries: prompt and delayed collapse to black hole". In: *Phys. Rev. D* 78 (2008), p. 084033. DOI: 10.1103/PhysRevD.78.084033. arXiv: 0804.0594 [gr-qc].

[15] Luca Baiotti and Luciano Rezzolla. "Binary neutron star mergers: a review of Einstein?s richest laboratory". In: *Rept. Prog. Phys.* 80.9 (2017), p. 096901. DOI: 10.1088/1361-6633/aa67bb. arXiv: 1607.03540 [gr-qc].

[16] M. Baldo, I. Bombaci, and G. F. Burgio. "Microscopic nuclear equation of state with three-body forces and neutron star structure". In: *Astron. Astrophys.* 328 (1997), pp. 274–282. arXiv: astro-ph/9707277.

[17] Thomas W. Baumgarte and Stuart L. Shapiro. *Numerical Relativity: Solving Einstein's Equations on the Computer*. Cambridge University Press, 2010. DOI: 10.1017/CBO9781139193344.

[18] Jonathan Blackman et al. “Fast and Accurate Prediction of Numerical Relativity Waveforms from Binary Black Hole Coalescences Using Surrogate Models”. In: *Phys. Rev. Lett.* 115.12 (2015), p. 121102. DOI: 10.1103/PhysRevLett.115.121102. arXiv: 1502.07758 [gr-qc].

[19] Matteo Breschi et al. “Kilohertz Gravitational Waves From Binary Neutron Star Mergers: Numerical-relativity Informed Postmerger Model”. In: (May 2022). arXiv: 2205.09112 [gr-qc].

[20] A. Camilletti et al. “Numerical relativity simulations of the neutron star merger GW190425: microphysics and mass ratio effects”. In: (Apr. 2022). DOI: 10.1093/mnras/stac2333. arXiv: 2204.05336 [astro-ph.HE].

[21] Arianna Carbone and Achim Schwenk. “Ab initio constraints on thermal effects of the nuclear equation of state”. In: *Phys. Rev. C* 100.2 (2019), p. 025805. DOI: 10.1103/PhysRevC.100.025805. arXiv: 1904.00924 [nucl-th].

[22] Matthew F. Carney, Leslie E. Wade, and Burke S. Irwin. “Comparing two models for measuring the neutron star equation of state from gravitational-wave signals”. In: *Phys. Rev.* D98.6 (2018), p. 063004. DOI: 10.1103/PhysRevD.98.063004. arXiv: 1805.11217 [gr-qc].

[23] Katerina Chatziioannou. “Neutron star tidal deformability and equation of state constraints”. In: *Gen. Rel. Grav.* 52.11 (2020), p. 109. DOI: 10.1007/s10714-020-02754-3. arXiv: 2006.03168 [gr-qc].

[24] Katerina Chatziioannou and Sophia Han. “Studying strong phase transitions in neutron stars with gravitational waves”. In: *Phys. Rev. D* 101.4 (2020), p. 044019. DOI: 10.1103/PhysRevD.101.044019. arXiv: 1911.07091 [gr-qc].

[25] R. Courant, K. Friedrichs, and H. Lewy. “On the Partial Difference Equations of Mathematical Physics”. In: *IBM Journal of Research and Development* 11.2 (1967), pp. 215–234. DOI: 10.1147/rd.112.0215.

[26] T. G. Cowling. “The non-radial oscillations of polytropic stars”. In: *mnras* 101 (Jan. 1941), p. 367. DOI: 10.1093/mnras/101.8.367.

[27] H. Thankful Cromartie et al. “Relativistic Shapiro delay measurements of an extremely massive millisecond pulsar”. In: *Nature Astron.* 4.1 (2019), pp. 72–76. DOI: 10.1038/s41550-019-0880-2. arXiv: 1904.06759.

[28] Jackson DeBuhr et al. “Relativistic Hydrodynamics with Wavelets”. In: *Astrophys. J.* 867.2 (2018), p. 112. DOI: 10.3847/1538-4357/aae5f9. arXiv: 1512.00386 [astro-ph.IM].

[29] Nils Deppe et al. “"A positivity-preserving adaptive-order finite-difference for GRMHD"”. In: (in preparation).

[30] Nils Deppe et al. “Simulating magnetized neutron stars with discontinuous Galerkin methods”. In: *Phys. Rev. D* 105.12 (2022), p. 123031. DOI: 10.1103/PhysRevD.105.123031. arXiv: 2109.12033 [gr-qc].

[31] Nils Deppe et al. “A high-order shock capturing discontinuous Galerkin–finite difference hybrid method for GRMHD”. In: *Classical and Quantum Gravity* 39.19 (Aug. 2022), p. 195001. DOI: 10.1088/1361-6382/ac8864. URL: https://dx.doi.org/10.1088/1361-6382/ac8864.

[32] Nils Deppe et al. *SpECTRE*. Version 2023.01.13. Jan. 2023. DOI: 10.5281/zenodo.7535144. URL: https://doi.org/10.5281/zenodo.7535144.

[33] Nils Deppe et al. *SpECTRE v2022.08.01*. 10.5281/zenodo.6949324. Version 2022.08.01. Aug. 2022. DOI: 10.5281/zenodo.6949324. URL: https://spectre-code.org.

[34] Tim Dietrich, Sebastiano Bernuzzi, and Wolfgang Tichy. “Closed-form tidal approximants for binary neutron star gravitational waveforms constructed from high-resolution numerical relativity simulations”. In: *Phys. Rev.* D96.12 (2017), p. 121501. DOI: 10.1103/PhysRevD.96.121501. arXiv: 1706.02969 [gr-qc].

[35] Tim Dietrich, Tanja Hinderer, and Anuradha Samajdar. “Interpreting Binary Neutron Star Mergers: Describing the Binary Neutron Star Dynamics, Modelling Gravitational Waveforms, and Analyzing Detections”. In: *Gen. Rel. Grav.* 53.3 (2021), p. 27. DOI: 10.1007/s10714-020-02751-6. arXiv: 2004.02527 [gr-qc].

[36] Tim Dietrich et al. “High-resolution numerical relativity simulations of spinning binary neutron star mergers”. In: *26th Euromicro International Conference on Parallel, Distributed and Network-based Processing*. 2018, pp. 682–689. DOI: 10.1109/PDP2018.2018.00113. arXiv: 1803.07965 [gr-qc].

[37] F. Douchin and P. Haensel. “A unified equation of state of dense matter and neutron star structure”. In: *Astron. Astrophys.* 380 (2001), p. 151. DOI: 10.1051/0004-6361:20011402. arXiv: astro-ph/0111092.

[38] C. Drischler et al. “Neutron matter from chiral two- and three-nucleon calculations up to N^3LO”. In: *Phys. Rev. C.* 94.5, 054307 (Nov. 2016), p. 054307. DOI: 10.1103/PhysRevC.94.054307. arXiv: 1608.05615 [nucl-th].

[39] C. Drischler et al. “Neutron matter from chiral two- and three-nucleon calculations up to N^3LO”. In: *Phys. Rev. C* 94.5 (2016), p. 054307. DOI: 10.1103/PhysRevC.94.054307. arXiv: 1608.05615 [nucl-th].

[40] Matthew D. Duez et al. “Evolving black hole-neutron star binaries in general relativity using pseudospectral and finite difference methods”. In: *Phys. Rev. D* 78 (2008), p. 104015. DOI: 10.1103/PhysRevD.78.104015. arXiv: 0809.0002 [gr-qc].

[41] L. Engvik et al. “Asymmetric nuclear matter and neutron star properties”. In: *Astrophys. J.* 469 (1996), p. 794. DOI: 10.1086/177827. arXiv: nucl-th/9509016.

[42] Pedro L. Espino and Vasileios Paschalidis. “Fate of twin stars on the unstable branch: Implications for the formation of twin stars”. In: *Phys. Rev. D* 105.4 (2022), p. 043014. DOI: 10.1103/PhysRevD.105.043014. arXiv: 2105.05269 [astro-ph.HE].

[43] Reed Essick. “Selection Effects in Periodic X-ray Data from Maximizing Detection Statistics”. In: (Nov. 2021). arXiv: 2111.04244 [astro-ph.HE].

[44] Reed Essick, Philippe Landry, and Daniel E. Holz. “Nonparametric Inference of Neutron Star Composition, Equation of State, and Maximum Mass with GW170817”. In: *Phys. Rev. D* 101.6 (2020), p. 063007. DOI: 10.1103/PhysRevD.101.063007. arXiv: 1910.09740 [astro-ph.HE].

[45] Reed Essick et al. “A Detailed Examination of Astrophysical Constraints on the Symmetry Energy and the Neutron Skin of ^{208}Pb with Minimal Modeling Assumptions”. In: (July 2021). arXiv: 2107.05528 [nucl-th].

[46] Reed Essick et al. “Astrophysical Constraints on the Symmetry Energy and the Neutron Skin of ^{208}Pb with Minimal Modeling Assumptions”. In: (Feb. 2021). arXiv: 2102.10074 [nucl-th].

[47] Reed Essick et al. “Direct Astrophysical Tests of Chiral Effective Field Theory at Supranuclear Densities”. In: *Phys. Rev. C* 102.5 (2020), p. 055803. DOI: 10.1103/PhysRevC.102.055803. arXiv: 2004.07744 [astro-ph.HE].

[48] Zachariah B. Etienne et al. “Fully General Relativistic Simulations of Black Hole-Neutron Star Mergers”. In: *Phys. Rev. D* 77 (2008), p. 084002. DOI: 10.1103/PhysRevD.77.084002. arXiv: 0712.2460 [astro-ph].

[49] E. Fonseca et al. “Refined Mass and Geometric Measurements of the High-mass PSR J0740+6620”. In: *Astrophys. J. Lett.* 915.1 (2021), p. L12. DOI: 10.3847/2041-8213/ac03b8. arXiv: 2104.00880 [astro-ph.HE].

[50] Jose A. Font. “Numerical hydrodynamics and magnetohydrodynamics in general relativity”. In: *Living Rev. Rel.* 11 (2008), p. 7. DOI: 10.12942/lrr-2008-7.

[51] Jose A. Font et al. “Three-dimensional general relativistic hydrodynamics. 2. Long term dynamics of single relativistic stars”. In: *Phys. Rev. D* 65 (2002), p. 084024. DOI: 10.1103/PhysRevD.65.084024. arXiv: gr-qc/0110047.

[52] Francois Foucart. “A brief overview of black hole-neutron star mergers”. In: *Front. Astron. Space Sci.* 7 (2020), p. 46. DOI: 10.3389/fspas.2020.00046. arXiv: 2006.10570 [astro-ph.HE].

[53] Francois Foucart et al. “Smooth Equations of State for High-Accuracy Simulations of Neutron Star Binaries”. In: *Phys. Rev. D* 100.10 (2019), p. 104048. DOI: 10.1103/PhysRevD.100.104048. arXiv: 1908.05277 [gr-qc].

[54] Henrique Gieg, Tim Dietrich, and Maximiliano Ujevic. “Simulating Binary Neutron Stars with Hybrid Equation of States: Gravitational Waves, Electromagnetic Signatures, and Challenges for Numerical Relativity”. In: *Particles* 2.3 (2019), pp. 365–384. DOI: 10.3390/particles2030023. arXiv: 1908.03135 [gr-qc].

[55] S. K. Greif et al. “Equation of state sensitivities when inferring neutron star and dense matter properties”. In: *Mon. Not. Roy. Astron. Soc.* 485.4 (2019), pp. 5363–5376. DOI: 10.1093/mnras/stz654. arXiv: 1812.08188 [astro-ph.HE].

[56] T. Gross-Boelting, C. Fuchs, and Amand Faessler. “Covariant representations of the relativistic Bruckner T matrix and the nuclear matter problem”. In: *Nucl. Phys. A* 648 (1999), pp. 105–137. DOI: 10.1016/S0375-9474(99)00022-6. arXiv: nucl-th/9810071.

[57] Sophia Han and Andrew W. Steiner. “Tidal deformability with sharp phase transitions in (binary) neutron stars”. In: *Phys. Rev. D* 99.8 (2019), p. 083014. DOI: 10.1103/PhysRevD.99.083014. arXiv: 1810.10967 [nucl-th].

[58] Kenta Hotokezaka et al. “Binary Neutron Star Mergers: Dependence on the Nuclear Equation of State”. In: *Phys. Rev. D* 83 (2011), p. 124008. DOI: 10.1103/PhysRevD.83.124008. arXiv: 1105.4370 [astro-ph.HE].

[59] J. D. Hunter. “Matplotlib: A 2D graphics environment”. In: *Computing in Science & Engineering* 9.3 (2007), pp. 90–95. DOI: 10.1109/MCSE.2007.55.

[60] Laxmikant Kale et al. *UIUC-PPL/charm: Charm++ version 6.10.2*. Version v6.10.2. Aug. 2020. DOI: 10.5281/zenodo.3972617. URL: https://doi.org/10.5281/zenodo.3972617.

[61] J. I. Kapusta and T. Welle. “Neutron stars with a crossover equation of state”. In: *Phys. Rev. C* 104.1 (2021), p. L012801. DOI: 10.1103/PhysRevC.104.L012801. arXiv: 2103.16633 [nucl-th].

[62] Wolfgang Kastaun, Jay Vijay Kalinani, and Riccardo Ciolfi. “Robust Recovery of Primitive Variables in Relativistic Ideal Magnetohydrodynamics”. In: *Phys. Rev. D* 103.2 (2021), p. 023018. DOI: 10.1103/PhysRevD.103.023018. arXiv: 2005.01821 [gr-qc].

[63] Lawrence E. Kidder et al. “SpECTRE: a task-based discontinuous Galerkin code for relativistic astrophysics”. In: *J. Comput. Phys.* 335 (2017), pp. 84–114. DOI: 10.1016/j.jcp.2016.12.059. arXiv: 1609.00098 [astro-ph.HE].

[64] Kostas. D. Kokkotas and Johannes Ruoff. “Radial oscillations of relativistic stars”. In: *Astron. Astrophys.* 366 (2001), p. 565. DOI: 10.1051/0004-6361:20000216. arXiv: gr-qc/0011093.

[65] Sven Köppel, Luke Bovard, and Luciano Rezzolla. “A General-relativistic Determination of the Threshold Mass to Prompt Collapse in Binary Neutron Star Mergers”. In: *Astrophys. J. Lett.* 872.1 (2019), p. L16. DOI: 10.3847/2041-8213/ab0210. arXiv: 1901.09977 [gr-qc].

[66] Aleksi Kurkela, Paul Romatschke, and Aleksi Vuorinen. “Cold Quark Matter”. In: *Phys. Rev. D* 81 (2010), p. 105021. DOI: 10.1103/PhysRevD.81.105021. arXiv: 0912.1856 [hep-ph].

[67] Koutarou Kyutoku, Masaru Shibata, and Keisuke Taniguchi. “Coalescence of black hole–neutron star binaries”. In: *Living Rev. Rel.* 24.1 (2021), p. 5. DOI: 10.1007/s41114-021-00033-4. arXiv: 2110.06218 [astro-ph.HE].

[68] Benjamin D. Lackey, Mohit Nayyar, and Benjamin J. Owen. “Observational constraints on hyperons in neutron stars”. In: *Phys. Rev. D* 73 (2006), p. 024021. DOI: 10.1103/PhysRevD.73.024021. arXiv: astro-ph/0507312 [astro-ph].

[69] Benjamin D. Lackey et al. “Extracting equation of state parameters from black hole-neutron star mergers: aligned-spin black holes and a preliminary waveform model”. In: *Phys. Rev. D* 89.4 (2014), p. 043009. DOI: 10.1103/PhysRevD.89.043009. arXiv: 1303.6298 [gr-qc].

[70] Philippe Landry and Reed Essick. “Nonparametric inference of the neutron star equation of state from gravitational wave observations”. In: *Phys. Rev. D* 99.8 (2019), p. 084049. DOI: 10.1103/PhysRevD.99.084049. arXiv: 1811.12529 [gr-qc].

[71] Philippe Landry, Reed Essick, and Katerina Chatziioannou. “Nonparametric constraints on neutron star matter with existing and upcoming gravitational wave and pulsar observations”. In: *Phys. Rev. D* 101.12 (2020), p. 123007. DOI: 10.1103/PhysRevD.101.123007. arXiv: 2003.04880 [astro-ph.HE].

[72] Philippe Landry and Bharat Kumar. “Constraints on the moment of inertia of PSR J0737-3039A from GW170817”. In: *Astrophys. J.* 868.2 (2018), p. L22. DOI: 10.3847/2041-8213/aaee76. arXiv: 1807.04727 [gr-qc].

[73] J. M. Lattimer and M. Prakash. “Neutron star structure and the equation of state”. In: *Astrophys. J.* 550 (2001), p. 426. DOI: 10.1086/319702. arXiv: astro-ph/0002232.

[74] Isaac Legred et al. “Impact of the PSR J0740 + 6620 radius constraint on the properties of high-density matter”. In: *Phys. Rev. D* 104 (6 Sept. 2021). I led this study on the impact of the the NICER mass-radius constraint

on the mllisecond x-ray pulsar J0740+6620 on nonparametric equation of state constraints. I developed software, some of which was contributed by other collaborators from previous projects, ran the analysis, and co-wrote the manuscript., p. 063003. DOI: 10.1103/PhysRevD.104.063003. URL: https://link.aps.org/doi/10.1103/PhysRevD.104.063003.

[75] Isaac Legred et al. "Implicit correlations within phenomenological parametric models of the neutron star equation of state". In: *Phys. Rev. D* 105.4 (2022). I led this study which compared parametric to nonparametric methods of inferring the equation of state. I developed a substantial amount of software, ran the analysis, and co-wrote the manuscript., p. 043016. DOI: 10.1103/PhysRevD.105.043016. arXiv: 2201.06791 [astro-ph.HE].

[76] Lee Lindblom. "Determining the Nuclear Equation of State from Neutron-Star Masses and Radii". In: *The Astrophysical Journal* 398 (Oct. 1992), p. 569. DOI: 10.1086/171882.

[77] Lee Lindblom. "Spectral Representations of Neutron-Star Equations of State". In: *Phys. Rev. D* 82 (2010), p. 103011. DOI: 10.1103/PhysRevD.82.103011. arXiv: 1009.0738 [astro-ph.HE].

[78] Lee Lindblom and Nathaniel M. Indik. "Spectral Approach to the Relativistic Inverse Stellar Structure Problem II". In: *Phys. Rev.* D89.6 (2014). [Erratum: Phys. Rev.D93,no.12,129903(2016)], p. 064003. DOI: 10.1103/PhysRevD.89.064003, 10.1103/PhysRevD.93.129903. arXiv: 1310.0803 [astro-ph.HE].

[79] Ben Margalit and Brian D. Metzger. "Constraining the Maximum Mass of Neutron Stars From Multi-Messenger Observations of GW170817". In: *Astrophys. J.* 850.2 (2017), p. L19. DOI: 10.3847/2041-8213/aa991c. arXiv: 1710.05938 [astro-ph.HE].

[80] Larry McLerran and Sanjay Reddy. "Quarkyonic Matter and Neutron Stars". In: *Phys. Rev. Lett.* 122.12 (2019), p. 122701. DOI: 10.1103/PhysRevLett.122.122701. arXiv: 1811.12503 [nucl-th].

[81] M. C. Miller et al. "The Radius of PSR J0740+6620 from NICER and XMM-Newton Data". In: (May 2021). arXiv: 2105.06979 [astro-ph.HE].

[82] M. Coleman Miller, Cecilia Chirenti, and Frederick K. Lamb. "Constraining the equation of state of high-density cold matter using nuclear and astronomical measurements". In: (2019). arXiv: 1904.08907 [astro-ph.HE].

[83] Philipp Mösta et al. "GRHydro: A new open source general-relativistic magnetohydrodynamics code for the Einstein Toolkit". In: *Class. Quant. Grav.* 31 (2014), p. 015005. DOI: 10.1088/0264-9381/31/1/015005. arXiv: 1304.5544 [gr-qc].

[84] H. Müller and B. D. Serot. "Relativistic mean field theory and the high density nuclear equation of state". In: *Nucl. Phys.* A606 (1996), pp. 508–537. DOI: 10.1016/0375-9474(96)00187-X. arXiv: nucl-th/9603037 [nucl-th].

[85] H. Müther, M. Prakash, and T. L. Ainsworth. "The nuclear symmetry energy in relativistic Brueckner-Hartree-Fock calculations". In: *Phys. Lett. B* 199 (1987), pp. 469–474. DOI: 10.1016/0370-2693(87)91611-X.

[86] Michael F. O'Boyle et al. "Parametrized equation of state for neutron star matter with continuous sound speed". In: *Phys. Rev. D* 102.8 (2020), p. 083027. DOI: 10.1103/PhysRevD.102.083027. arXiv: 2008.03342 [astro-ph.HE].

[87] Travis Oliphant. *NumPy: A guide to NumPy*. USA: Trelgol Publishing. [Online; accessed <today>]. 2006–. URL: http://www.numpy.org/.

[88] J.R. Oppenheimer and G.M. Volkoff. "On Massive neutron cores". In: *Phys. Rev.* 55 (1939), pp. 374–381. DOI: 10.1103/PhysRev.55.374.

[89] Feryal Özel and Dimitrios Psaltis. "Reconstructing the neutron-star equation of state from astrophysical measurements". In: *Phys.Rev.D* 80.10, 103003 (Nov. 2009), p. 103003. DOI: 10.1103/PhysRevD.80.103003. arXiv: 0905.1959 [astro-ph.HE].

[90] Peter T. H. Pang et al. "Nuclear-Physics Multi-Messenger Astrophysics Constraints on the Neutron-Star Equation of State: Adding NICER's PSR J0740+6620 Measurement". In: (May 2021). arXiv: 2105.08688 [astro-ph.HE].

[91] Peter T. H. Pang et al. "Parameter estimation for strong phase transitions in supranuclear matter using gravitational-wave astronomy". In: *Phys. Rev. Res.* 2.3 (2020), p. 033514. DOI: 10.1103/PhysRevResearch.2.033514. arXiv: 2006.14936 [astro-ph.HE].

[92] J. Piekarewicz. "The Nuclear Physics of Neutron Stars". In: (Sept. 2022). arXiv: 2209.14877 [nucl-th].

[93] A. Y. Potekhin et al. "Analytical representations of unified equations of state for neutron-star matter". In: *Astron. Astrophys.* 560 (2013), A48. DOI: 10.1051/0004-6361/201321697. arXiv: 1310.0049 [astro-ph.SR].

[94] William H. Press et al. *Numerical Recipes 3rd Edition: The Art of Scientific Computing*. 3rd ed. USA: Cambridge University Press, 2007. ISBN: 0521880688.

[95] G. Raaijmakers et al. "Constraining the dense matter equation of state with joint analysis of NICER and LIGO/Virgo measurements". In: *Astrophys. J. Lett.* 893.1 (2020), p. L21. DOI: 10.3847/2041-8213/ab822f. arXiv: 1912.11031 [astro-ph.HE].

[96] G. Raaijmakers et al. "Constraints on the dense matter equation of state and neutron star properties from NICER's mass-radius estimate of PSR J0740+6620 and multimessenger observations". In: (May 2021). arXiv: 2105.06981 [astro-ph.HE].

[97] David Radice, Sebastiano Bernuzzi, and Albino Perego. "The Dynamics of Binary Neutron Star Mergers and GW170817". In: *Ann. Rev. Nucl. Part. Sci.* 70 (2020), pp. 95–119. DOI: 10.1146/annurev-nucl-013120-114541. arXiv: 2002.03863 [astro-ph.HE].

[98] David Radice and Liang Dai. "Multimessenger Parameter Estimation of GW170817". In: *Eur. Phys. J. A* 55.4 (2019), p. 50. DOI: 10.1140/epja/i2019-12716-4. arXiv: 1810.12917 [astro-ph.HE].

[99] David Radice, Luciano Rezzolla, and Filippo Galeazzi. "Beyond second-order convergence in simulations of binary neutron stars in full general-relativity". In: *Mon. Not. Roy. Astron. Soc.* 437 (2014), pp. L46–L50. DOI: 10.1093/mnrasl/slt137. arXiv: 1306.6052 [gr-qc].

[100] Carolyn A. Raithel, Feryal Ozel, and Dimitrios Psaltis. "Finite-temperature extension for cold neutron star equations of state". In: *Astrophys. J.* 875.1 (2019), p. 12. DOI: 10.3847/1538-4357/ab08ea. arXiv: 1902.10735 [astro-ph.HE].

[101] Carolyn A. Raithel and Vasileios Paschalidis. "Improving the convergence order of binary neutron star merger simulations in the Baumgarte- Shapiro-Shibata-Nakamura formulation". In: *Phys. Rev. D* 106.2 (2022), p. 023015. DOI: 10.1103/PhysRevD.106.023015. arXiv: 2204.00698 [gr-qc].

[102] Jocelyn S. Read et al. "Constraints on a phenomenologically parameterized neutron-star equation of state". In: *Phys. Rev. D* 79 (2009), p. 124032. DOI: 10.1103/PhysRevD.79.124032. arXiv: 0812.2163 [astro-ph].

[103] Jocelyn S. Read et al. "Measuring the neutron star equation of state with gravitational wave observations". In: *Phys. Rev. D* 79 (2009), p. 124033. DOI: 10.1103/PhysRevD.79.124033. arXiv: 0901.3258 [gr-qc].

[104] L. Rezzolla and O. Zanotti. *Relativistic Hydrodynamics*. Oxford University Press, Sept. 2013.

[105] J. Rikovska-Stone et al. "Cold uniform matter and neutron stars in the quark-mesons-coupling model". In: *Nucl. Phys. A* 792 (2007), pp. 341–369. DOI: 10.1016/j.nuclphysa.2007.05.011. arXiv: nucl-th/0611030.

[106] Thomas E. Riley et al. "A *NICER* View of PSR J0030+0451: Millisecond Pulsar Parameter Estimation". In: *Astrophys. J. Lett.* 887.1 (2019), p. L21. DOI: 10.3847/2041-8213/ab481c. arXiv: 1912.05702 [astro-ph.HE].

[107] Thomas E. Riley et al. "A NICER View of the Massive Pulsar PSR J0740+6620 Informed by Radio Timing and XMM-Newton Spectroscopy". In: (May 2021). arXiv: 2105.06980 [astro-ph.HE].

[108] X. Roca-Maza et al. "The neutron skin thickness from the measured electric dipole polarizability in ^{68}Ni, ^{120}Sn, and ^{208}Pb". In: *Phys. Rev. C* 92 (2015), p. 064304. DOI: 10.1103/PhysRevC.92.064304. arXiv: 1510.01874 [nucl-th].

[109] Souhardya Sen et al. "Radial oscillations in neutron stars from unified hadronic and quarkyonic equation of states". In: (May 2022). arXiv: 2205.02076 [nucl-th].

[110] Masaru Shibata and Koji Uryu. "Simulation of merging binary neutron stars in full general relativity: Gamma = two case". In: *Phys. Rev. D* 61 (2000), p. 064001. DOI: 10.1103/PhysRevD.61.064001. arXiv: gr-qc/9911058.

[111] Masaru Shibata et al. "Constraint on the maximum mass of neutron stars using GW170817 event". In: *Phys. Rev. D* 100.2 (2019), p. 023015. DOI: 10.1103/PhysRevD.100.023015. arXiv: 1905.03656 [astro-ph.HE].

[112] Daniel M. Siegel et al. "Recovery schemes for primitive variables in general-relativistic magnetohydrodynamics". In: *Astrophys. J.* 859.1 (2018), p. 71. DOI: 10.3847/1538-4357/aabcc5. arXiv: 1712.07538 [astro-ph.HE].

[113] SXS. *paper-2023-spectre-enthalpy-eos*. https://github.com/sxs-collaboration/paper-2023-spectre-enthalpy-eos. 2023.

[114] I. Tews, J. Margueron, and S. Reddy. "Critical examination of constraints on the equation of state of dense matter obtained from GW170817". In: *Phys. Rev. C* 98.4 (2018), p. 045804. DOI: 10.1103/PhysRevC.98.045804. arXiv: 1804.02783 [nucl-th].

[115] Ingo Tews. "Quantum Monte Carlo Methods for Astrophysical Applications". In: *Frontiers in Physics* 8 (2020). ISSN: 2296-424X. DOI: 10.3389/fphy.2020.00153. URL: https://www.frontiersin.org/articles/10.3389/fphy.2020.00153.

[116] Ingo Tews et al. "Constraining the speed of sound inside neutron stars with chiral effective field theory interactions and observations". In: *Astrophys. J.* 860.2 (2018), p. 149. DOI: 10.3847/1538-4357/aac267. arXiv: 1801.01923 [nucl-th].

[117] S. Typel et al. "CompOSE Reference Manual". In: (Mar. 2022). arXiv: 2203.03209 [astro-ph.HE].

[118] Maximiliano Ujevic et al. "Back and Forth: Reverse Phase Transitions in Numerical Relativity Simulations". In: (Nov. 2022). arXiv: 2211.04662 [gr-qc].

[119] Bram Van Leer. "Towards the ultimate conservative difference scheme. IV. A new approach to numerical convection". In: *Journal of Computational Physics* 23.3 (1977), pp. 276–299. ISSN: 0021-9991. DOI: 10.1016/0021-9991(77)90095-X. URL: https://www.sciencedirect.com/science/article/pii/002199917790095X.

[120] Vijay Varma et al. "Surrogate model of hybridized numerical relativity binary black hole waveforms". In: *Phys. Rev. D* 99.6 (2019), p. 064045. DOI: 10.1103/PhysRevD.99.064045. arXiv: 1812.07865 [gr-qc].

[121] Pauli Virtanen et al. "SciPy 1.0: Fundamental Algorithms for Scientific Computing in Python". In: *Nature Methods* 17 (2020), pp. 261–272. DOI: 10.1038/s41592-019-0686-2.

[122] Marcella Wijngaarden et al. "Probing neutron stars with the full premerger and postmerger gravitational wave signal from binary coalescences". In: *Phys. Rev. D* 105.10 (2022), p. 104019. DOI: 10.1103/PhysRevD.105.104019. arXiv: 2202.09382 [gr-qc].

[123] Robert B. Wiringa, V. Fiks, and A. Fabrocini. "Equation of state for dense nucleon matter". In: *Phys. Rev. C* 38 (1988), pp. 1010–1037. DOI: 10.1103/PhysRevC.38.1010.

[124] Daniel Wysocki et al. "Inferring the neutron star equation of state simultaneously with the population of merging neutron stars". In: (2020). arXiv: 2001.01747 [gr-qc].

[125] Kent Yagi and Nicolas Yunes. "I-Love-Q Relations in Neutron Stars and their Applications to Astrophysics, Gravitational Waves and Fundamental Physics". In: *Phys. Rev. D* 88.2 (2013), p. 023009. DOI: 10.1103/PhysRevD.88.023009. arXiv: 1303.1528 [gr-qc].

Chapter 10

INITIAL DATA FOR BINARY NEUTRON STAR MERGERS IN SPECTRE

10.1 Intro

This is a technical discussion of the solver for binary neutron star initial data as implemented in SpECTRE. In particular, I discuss the solver for hydrostatic equilibrium which is based on the method proposed in Baumgarte and Shapiro [1], and implemented in SpECTRE using the DG elliptic solver described in Ref. [2]. The principle goal of this solver is to produce a self-consistent distribution of matter, given by it's density and velocity, which is locally unchanging when viewed in a corotating reference frame. In practice, this situation is complicated by the fact that the system is relativistic, so rather than a "corotating refernece frame", a (timelike) killing vector is identified, which is called the "rotational killing vector". The requirement that the system be (1) mass conserving, (2) momentum conserving, and (3) constant under the action of this timelike killing vector, when coupled with a barotropic equation of state, leave a system which is surprisingly simple for the velocity distribution of the matter.

10.2 Conventions

h is the specific enthalpy.
ρ is the rest mass density.
e is the energy density.
p is the pressure.
The EoS is barotropic, so knowing any of the above quantities is equivalent to knowing all of them.
u^a is the four velocity.
$P^a_b = \delta^a_b - n^a n_b$ is the spatial projection operator. u^i is the spatial four velocity, i.e. $u^i = P^i_a u^a$.

The problem consists of solving for the initial distribution of enthalpy h and four velocity of the fluid u_a (although it suffices to know the spatial part $u_i = P^a_i u_a$). There are two special cases Corotational Stars and Irrotational Stars. In both cases we decompose the four-velocity as

$$u^a = u^t \left(\xi_h^a + V^a\right), \tag{10.1}$$

Where ξ_h is a (timelike) helical killing vector that represents the approximate rotational symmetry of the initial data. I.e. $\mathcal{L}_{\xi_h} u^a = 0$, $\mathcal{L}_{\xi_h} \rho = 0$, and V^a is spatial. Therefore $\xi_h^0 = 1$. We also define

$$\hat{u}^i \equiv \gamma^i_a h u^a. \tag{10.2}$$

10.3 Equations

With these variables, the conservation of momentum and rest mass density become ([1] 15.42, 15.43)

$$D_i \left(\frac{h}{u^t} + \hat{u}_j V^j\right) + V^j \left(D_j \hat{u}_i - D_i \hat{u}_j\right) = 0, \tag{10.3}$$

and

$$D_i(\alpha u^t \rho_0 V^i) = 0. \tag{10.4}$$

10.4 Corotational Stars

This is the easy but astrophysically less interesting case of stars which are tidally locked. We take $V^i = 0$. Now rest-mass conservation is satisfied identically, and the momentum equation can be integrated to

$$\frac{h}{u^t} = C; \tag{10.5}$$

with C a constant. Therefore the only problem that remains is finding a killing vector ξ_h^a. The spatial velocity is given by [1] (15.13).

$$k^i = \Omega_j x_k \epsilon^{ijk} \tag{10.6}$$

in Cartesian coordinates. There's an exercise that has the reader express u^t in terms of the rotation parameters, coordinates, metric variables, and enthalpy,

$$h \left\{\alpha^2 - \psi^4 \left((\Omega y - \beta^x)^2 + (\Omega x + \beta^y)^2 + (\beta^z)\right)^2\right\}^{1/2} = C. \tag{10.7}$$

This completely determines the matter distribution.

$$v^i := \langle \Omega y, -\Omega x, 0\rangle \tag{10.8}$$

$$h := C \left\{\alpha^2 - \psi^4 \left((\Omega y - \beta^x)^2 + (\Omega x + \beta^y)^2 + (\beta^z)\right)^2\right\}^{-1/2} \tag{10.9}$$

Rotational velocity is set by Ω, and the central density of the star is set by C. There are no PDEs to be solved, but it may still be useful to have a corotational binary XTCS initial data somehow.

10.5 Irrotational Stars

In this case, the total velocity field (rather, the enthalpy four-current) is given as the gradient of a scalar potential.

$$hu_a = \nabla_a \Phi. \tag{10.10}$$

This makes the second term in Eq. (10.3) vanish (as $\hat{u}_i = D_i \Phi$), so the momentum equation becomes

$$D_i \left(\frac{h}{u^t} + V^j D_j \Phi \right) = 0, \tag{10.11}$$

which can be integrated to

$$\frac{h}{u^t} + V^j D_j \Phi = C. \tag{10.12}$$

The rest-mass continuity equation gives

$$\nabla_a \left(\rho / h \nabla^a \Phi \right) = 0 \tag{10.13}$$

Defining all the relevant variables[1].

$$t_a \equiv \nabla_a t \tag{10.14}$$

$$k^a \equiv \xi_h^a - t^a \tag{10.15}$$

$$B^a \equiv k^a + \beta^a \tag{10.16}$$

$$B^a \underset{t=\alpha n+\beta}{=} \xi_h^a - \alpha n^a \tag{10.17}$$

$$V^i \underset{\text{shuffle defs}}{=} \frac{1}{u^t h} D^i \Phi - B^i \tag{10.18}$$

$$\alpha u^t \underset{\text{norm}}{=} \left(1 + h^{-2} D_i \Phi D^i \Phi \right)^{1/2} \tag{10.19}$$

$$\alpha u^t \underset{(10.12)\text{+above}}{=} \frac{1}{\alpha h} \left(C + B^i D_i \Phi \right). \tag{10.20}$$

The big point is that we need an equation for the velocity potential (which will be furnished by the continuity equation), and one for the enthalpy (which will come from the integrated momentum equation). The equation for enthalpy involves manipulating the above equations

$$h^2 = \frac{1}{\alpha^2} \left(C + B^i D_i \Phi \right)^2 - D_i \Phi D^i \Phi. \tag{10.21}$$

This equation depends on the integration constant (which will again determine (or be determined by) the central density), B^i which depends on the shift and the initial spatial velocity of the stars, and $D_i \Phi$ which we can now write down an equation for. First, we expand the continuity equation:

$$D_i \left(\alpha \rho / h D^i \Phi \right) - D_i \left(\alpha u^t \rho B^i \right) = 0. \tag{10.22}$$

The first term represents the "dynamical" divergence which will become the principle part of the PDE, while the second term represents the "background" flow.

$$D_i D^i \Phi - D_i \left(\frac{C + B^j D_j \Phi}{\alpha^2} B^i \right) = \left(\frac{C + B^j D_j \Phi}{\alpha^2} B^i - D^i \Phi \right) D_i \ln \frac{\alpha \rho}{h}. \tag{10.23}$$

We'll return to the discussion of the boundary conditions needed at the stellar surface. Some manipulations need to be done to put this into the form we need it, i.e. [2] Eq. (1),

$$\hat{u}^i \equiv D^i \Phi = h u^i. \tag{10.24}$$

We define the flux $\mathcal{F}^i$

$$\mathcal{F}^i = \hat{u}^i - \frac{B^j \hat{u}_j}{\alpha^2} B^i. \tag{10.25}$$

The continuity equation is now

$$D_i \mathcal{F}^i = -\mathcal{F}^i D_i \ln \frac{\alpha \rho}{h} + D_i \frac{C}{\alpha^2} B^i + \frac{C}{\alpha^2} B^i D_i \ln \frac{\alpha \rho}{h}, \tag{10.26}$$

which must be supplemented with the boundary condition

$$\mathcal{F}^i D_i \rho |_{\text{stellar surface}} = \frac{C}{\alpha^2} B^i D_i \rho |_{\text{stellar surface}}. \tag{10.27}$$

Note that because the EoS is barotropic, if we define the stellar surface via an isodensity contour than $D_i \rho \propto n_i$ at the surface, so we can replace $D_i \rho \to n_i$ in Eq. (10.28). Which gives

$$\mathcal{F}^i n_i |_{\text{stellar surface}} = \frac{C}{\alpha^2} B^i n_i |_{\text{stellar surface}}, \tag{10.28}$$

which is a Neumann boundary condition.

So fluxes + field-containing sources for the primal variable is

$$\mathcal{F}^i_\Phi = \mathcal{F}^i \tag{10.29}$$

$$\mathcal{S}_\Phi = -\mathcal{F}^i D_i \ln \frac{\alpha \rho}{h} - \Gamma^i_{ij} \mathcal{F}^j \tag{10.30}$$

$$\mathcal{S}^{\text{fixed}}_\Phi = -D_i \frac{C}{\alpha^2} B^i - \frac{C}{\alpha^2} B^i D_i \ln \frac{\alpha \rho}{h}. \tag{10.31}$$

In the fixed sources, we note that

$$D_i \frac{C}{\alpha^2} B^i = -2 \frac{C}{\alpha^3} B^i D_i \alpha + \frac{C}{\alpha^2} D_i \beta^i. \tag{10.32}$$

I guess this form shoves under the rug the fact that h is a nonlinear function of U_i, but to zeroth order this decomposition is correct. This is maybe fine if we have a loop structure

1. $k_i := \ldots, C = \ldots$
2. a) compute h, compute the domain maps needed for the PDE solve
   b) i. Solve the linear PDEs (10.41)
      ii. return to 2.

I would expect this to work because we can get good guess for $h(r)$ and $D_i\Phi$ from the TOV equations + boosts.

Limiting properties of the equations.

We can, as an example, compute the quantities above in the trivial case of a NS in a binary with an infinitely long period (e.g. $\Omega = 0$). In this case the bulk of terms are trivial, for example, assuming $\beta^i = 0$, then $B^i = 0$, $u^i = 0$, although certain equations, such as $h^2 = C^2/\alpha^2$ are not completely trivial. Moving on to the case of very small rotation $\Omega \ll \sqrt{M_{\rm NS}/R_{\rm NS}^3}$, the equations are linear and homogeneous in the small rotation, we thus analyze the system solely in terms of the "background" terms acting as coefficients. Because B^i and $D_i\Phi$ both receive corrections at order Ω, however, terms such as $B^iD_i\Phi$ vanish to leading order, and $\mathcal{F}^i = \hat{u}^i$. The term $D_i \ln(\alpha\rho/h)$ can be split into $D_i \ln(\alpha/h) + D_i \ln\rho$, which is useful because in a TOV star $D_i \ln(\alpha) = -2D_i \ln(h)$, though $D_i \ln\rho$ is still cannot be explicitly expressed as a derivative of $\ln\alpha$ generically without knowledge of the equation of state. Therefore

$$D_i \ln h \overset{\text{1-D eos}}{=} c_s^2 D_i \ln\rho \overset{\text{in TOV}}{\Longrightarrow} D_i \ln\rho = -\frac{1}{2}\frac{1}{c_s^2} D_i \ln\alpha \tag{10.33}$$

Where c_s^2 is the speed of sound squared in the fluid, which is determined by the equation of state. Therefore, in a TOV star

$$D_i \ln\left(\frac{\alpha\rho}{h}\right) = D_i \ln\alpha \left(3 - \frac{1}{2c_s^2}\right). \tag{10.34}$$

Finally, in a polytropic fluid, $c_s^2 \to \ln(h)/n$ at low values of the enthalpy, and the TOV equations prescribe that near the surface (since $P \ll M/R^3$)

$$\frac{d\ln h}{dr} = -\frac{M}{r^2}\left(1 - \frac{2M}{r}\right)^{-1/2}. \tag{10.35}$$

Taking $r = R - \delta r$

$$\ln h \approx \frac{M}{R^2}\left(1 - \frac{2M}{R}\right)^{-1/2} \delta r. \tag{10.36}$$

Therefore the enthalpy approaches zero linearly as one approaches the surface of a TOV star from the inside. However, on the outside of the star the enthalpy is identically zero, so the solution is not analytic at the boundary. This appears to be a numerical challenge more broadly, as in the generic case of a deformed star we do not know where the boundary is. Therefore, caution has to be exercised to only solve the equations inside the star, as the use of any spectral method across the surface of the star immediately leads to very large errors.

10.6 Rotating Case

Note: This is not yet implemented in SpECTRE*, however because of the ultimate form of the equations, it could be implemented merely as an additional initial data for the BNS initial data system.* The easiest way to get rotating NSs is just to add some rotational component to the velocity which is solved for, which is in principle like perturbing the case of an irrotational star,

$$\hat{u}^i = D_i\Phi + W^i. \tag{10.37}$$

W^i is something like

$$W^i = h\epsilon^{ijk}\omega_j(x - x_{\mathrm{NS}})_k. \tag{10.38}$$

Exactly what metric should be used for ϵ^{ijk} seems to be unclear, with Ref. [3] suggesting using the conformal metric. In general it seems like an arbitrary rotation profile could be used, and will likely work as long as the rotation is sufficiently small.

The energy equation changes quite predictably

$$h^2 = \frac{1}{\alpha^2}\left(C + B^i(D_i\Phi + W_i)\right)^2 - (D_i\Phi + W_i)(D^i\Phi + W^i). \tag{10.39}$$

Because the continuity equation is linear in the velocity potential, all of additional terms involving to W^i appear as fixed sources proportional to W^i, therefore the overall structure of the system is little changed by the inclusion of the additional rotational velocity.

$$D_i(D^i\Phi + W^i) - D_i\left(\frac{C + B^j(D_j\Phi + W_j)}{\alpha^2}B^i\right) = \left(\frac{C + B^j(D_j\Phi + W_j)}{\alpha^2}B^i - (D^i\Phi - W^i)\right)D_i \ln\frac{\alpha\rho}{h}. \quad (10.40)$$

Therefore, the modified fluxes and sources are

$$\mathcal{F}^i_\Phi = \mathcal{F}^i \quad (10.41)$$

$$\mathcal{S}_\Phi = -\mathcal{F}^i D_i \ln\frac{\alpha\rho}{h} - \Gamma^i_{ij}\mathcal{F}^j \quad (10.42)$$

$$\mathcal{S}^{\text{fixed}}_\Phi = -D_i\frac{C}{\alpha^2}B^i - \frac{C}{\alpha^2}B^i D_i \ln\frac{\alpha\rho}{h} + D_i\left(W^i - \frac{B^j W_j B^i}{\alpha^2}\right) - \left(W^i - \frac{B^j W_j B^i}{\alpha^2}\right)D_i \ln\frac{\alpha\rho}{h}. \quad (10.43)$$

References

[1] Thomas W. Baumgarte and Stuart L. Shapiro. *Numerical Relativity: Solving Einstein's Equations on the Computer*. Cambridge University Press, 2010. DOI: 10.1017/CBO9781139193344.

[2] Nils L. Fischer and Harald P. Pfeiffer. "Unified discontinuous Galerkin scheme for a large class of elliptic equations". In: *Phys. Rev. D* 105.2 (2022), p. 024034. DOI: 10.1103/PhysRevD.105.024034. arXiv: 2108.05826 [math.NA].

[3] Nick Tacik et al. "Binary Neutron Stars with Arbitrary Spins in Numerical Relativity". In: *Phys. Rev. D* 92.12 (2015). [Erratum: Phys.Rev.D 94, 049903 (2016)], p. 124012. DOI: 10.1103/PhysRevD.92.124012. arXiv: 1508.06986 [gr-qc].

Chapter 11

CONCLUSIONS AND FUTURE DIRECTIONS

Neutron star physics currently faces two primary challenges: first, insufficient data, and second, insufficient theory. I have attempted in this thesis to outline some of the ways that considering careful estimates of both observational and theoretical uncertainty can serve to clarify these challenges. Nonetheless, neutron stars have a number of properties that make projections difficult.

Arguably the most troublesome of these features is just that neutron stars are very small. The incredible compactness of neutron stars makes them nearly indistinguishable from black holes (or in some cases white dwarfs, e.g. [11]) in many observational scenarios. It also leads to many science objectives being particularly challenging. For example the tidal deformability of compact objects scaling with radius to the 5th power means that the tidal properties of merging neutron stars are barely detectable in gravitational-wave observations [47, 29]. Similarly, the relatively small size of the neutron star moment of inertia (which scales like the radius to the second power), makes relativistic measurements challenging [54, 48][1]. Neutron star luminosity in thermal emission is generally also small because of their small size (since the surface are also scales like R^2). In some cases though, young or accreting neutron stars can be quite visible though because of their high temperatures [52, 65].

On the other hand, the incredible compactness of neutron stars also in some cases allows remarkable physics to be possible which give new windows to understanding. A prototypical example of this is the possibility of constraining the neutron star mass and radius by using the gravitational lensing of thermal x-rays [15]. Pulsars, and in particular pulsar timing represent a tremendous source of data about neutron stars [14, 73]. Pulsars are only possible because of the extreme astrophysical environment provided by neutron stars [68] (in particular such a strong magnetic field as is found in pulsars must be anchored to incredibly dense matter). Finally, neutron stars high density is the only reason they merge at frequencies visible to ground based gravitational-wave detectors [40, 5].

[1] For example, moment of inertia such measurements are now possible for at least one white dwarf in a white dwarf-neutron star binary [48], though constraints on neutron star moments of inertia will likely not be possible until the 2030's.

In my work, I have developed robust requirements for equation of state constraints given the substantial systematic uncertainty in equation of state models. While we face challenges due to the tiny target that is the neutron star, we have demonstrated that we can rule out particular microphysics with sufficient observations [56, 37]. Related to this, but from another point of view, I have worked to determine exactly how sensitive relativistic simulations are to the details of dense matter [57]. A question for the future remains "can we afford to fully distinguish microphysical scenarios in relativistic simulations?". One way to address the huge diversity of possible merger scenarios is to constrain the equation of state. Simply, fewer possible equations of state means more complete parameter space coverage with fewer expensive simulations. Nonetheless, thermal and out-of-equilibrium effects are relevant in neutron star mergers and supernova, and likely these targets will be substantially more difficult to constrain because they leave weaker impacts on observables.

I have also not discussed, to any satisfactory degree, many aspects of neutron star physics which are to varying degrees well-understood (or at least partially well-understood). These include things such as the extreme electrodynamics of neutron star magnetospheres [43], including the remarkable physics of radio pulsars [68]. I have also not discussed the exceptional state of the inner neutron star crust, including the delightfully-named "pasta" phases of dense matter [22]. Importantly, I have also neglected to discuss superfluidity and superconductivity [27], and the related studies of neutron star cooling [64]. Further, I have also not discussed the details of highly impressive observational strategies used to infer neutron star properties [16]. Nonetheless, it would be an understatement to say that new observational techniques lie at the heart of future neutron star science. Such approaches themselves represent very diverse and interesting physics. For example pulsar timing [14], which has been used to precisely measure the masses of neutron stars(e.g. [32]), has also been used recently to observe a nanohertz gravitational wave background [6]. Nevertheless, the abundance of interesting physics in neutron stars is also challenging, as often poorly understood aspects of one domain can limit precision in another. For example, in NICER's observations of neutron stars, poorly understood aspects of the neutron star magnetosphere and atmosphere directly lead to increased uncertainty in the equation of state [80, 72]. Finally, the extreme nature of neutron stars means that many even speculative factors may be relevant, such as deviations from general relativity, or the existence of dark matter halos or cores in neutron stars. Many of these questions will be addressed by future instruments; here I point to next-generation gravitational-wave detectors Cosmic Explorer, and Einstein Telescope as observatories which could substantially increase our understanding of neutron star physics [38, 1].

Therefore, the path to the future of neutron star science is promising, but also formidable. Constraints on dense matter coming from nuclear theory, experiment, and astrophysical observations will lay the groundwork for better models of neutron stars, which more nearly reflect the true astrophysical neutron stars we encounter in nature. Finally, I would expect that a healthy dose of humility will be required in the coming years; it remains a distinct possibility that the correct understanding of the matter in neutron star cores has not yet been developed. Whatever future experiments and observations show, it seems likely that neutron stars will continue to drive nuclear, gravitational, and extreme electromagnetic physics in the years to come.

BIBLIOGRAPHY

[1] Adrian Abac et al. “The Science of the Einstein Telescope”. In: (Mar. 2025). arXiv: 2503.12263 [gr-qc].

[2] B. P. Abbott et al. “GW170817: Measurements of neutron star radii and equation of state”. In: *Phys. Rev. Lett.* 121.16 (2018), p. 161101. DOI: 10.1103/PhysRevLett.121.161101. arXiv: 1805.11581 [gr-qc].

[3] B. P. Abbott et al. “GW190425: Observation of a Compact Binary Coalescence with Total Mass $\sim 3.4 M_\odot$”. In: *Astrophys. J. Lett.* 892.1 (2020), p. L3. DOI: 10.3847/2041-8213/ab75f5. arXiv: 2001.01761 [astro-ph.HE].

[4] B. P. Abbott et al. “Multi-messenger Observations of a Binary Neutron Star Merger”. In: *Astrophys. J. Lett.* 848.2 (2017), p. L12. DOI: 10.3847/2041-8213/aa91c9. arXiv: 1710.05833 [astro-ph.HE].

[5] B. P. Abbott, R. Abbott, and T. D. et al. Abbott. “GW170817: Observation of Gravitational Waves from a Binary Neutron Star Inspiral”. In: *Phys. Rev. Lett.* 119.16, 161101 (Oct. 2017), p. 161101. DOI: 10.1103/PhysRevLett.119.161101. arXiv: 1710.05832 [gr-qc].

[6] Gabriella Agazie et al. “The NANOGrav 15 yr Data Set: Evidence for a Gravitational-wave Background”. In: *Astrophys. J. Lett.* 951.1 (2023), p. L8. DOI: 10.3847/2041-8213/acdac6. arXiv: 2306.16213 [astro-ph.HE].

[7] Mark G. Alford et al. “Relativistic mean-field theories for neutron-star physics based on chiral effective field theory”. In: *Phys. Rev. C* 106.5 (2022), p. 055804. DOI: 10.1103/PhysRevC.106.055804. arXiv: 2205.10283 [nucl-th].

[8] Justin Alsing, Hector O. Silva, and Emanuele Berti. “Evidence for a maximum mass cut-off in the neutron star mass distribution and constraints on the equation of state”. In: *Mon. Not. Roy. Astron. Soc.* 478.1 (2018), pp. 1377–1391. DOI: 10.1093/mnras/sty1065. arXiv: 1709.07889 [astro-ph.HE].

[9] W. Baade and F. Zwicky. “On Super-novae”. In: *Proceedings of the National Academy of Science* 20.5 (May 1934), pp. 254–259. DOI: 10.1073/pnas.20.5.254.

[10] Kareem El-Badry et al. “A 1.9 solar-mass neutron star candidate in a 2-year orbit”. In: *The Open Journal of Astrophysics* 7, 27 (Apr. 2024), p. 27. DOI: 10.33232/001c.116675. arXiv: 2402.06722 [astro-ph.SR].

[11] Kareem El-Badry et al. “A population of neutron star candidates in wide orbits from Gaia astrometry”. In: (July 2024). DOI: 10.33232/001c.121261.

[12] Thomas W. Baumgarte and Stuart L. Shapiro. *Numerical Relativity: Solving Einstein's Equations on the Computer*. Cambridge University Press, 2010. DOI: 10.1017/CBO9781139193344.

[13] Gordon Baym, Christopher Pethick, and Peter Sutherland. "The Ground State of Matter at High Densities: Equation of State and Stellar Models". In: *The Astrophysical Journal* 170 (Dec. 1971), p. 299. DOI: 10.1086/151216.

[14] R. Blandford and S. A. Teukolsky. "Arrival-time analysis for a pulsar in a binary system." In: *The Astrophysical Journal* 205 (Apr. 1976), pp. 580–591. DOI: 10.1086/154315.

[15] Slavko Bogdanov et al. "Constraining the Neutron Star Mass–Radius Relation and Dense Matter Equation of State with *NICER*. I. The Millisecond Pulsar X-Ray Data Set". In: *Astrophys. J. Lett.* 887.1 (2019), p. L25. DOI: 10.3847/2041-8213/ab53eb. arXiv: 1912.05706 [astro-ph.HE].

[16] Alice Borghese. "Exploring the neutron star zoo: An observational review". In: *IAU Symp.* 363 (2020), pp. 51–60. DOI: 10.1017/S1743921322000357. arXiv: 2405.02368 [astro-ph.HE].

[17] R. Brockmann and R. Machleidt. "Relativistic nuclear structure. I. Nuclear matter". In: *Phys. Rev. C* 42 (5 Nov. 1990), pp. 1965–1980. DOI: 10.1103/PhysRevC.42.1965. URL: https://link.aps.org/doi/10.1103/PhysRevC.42.1965.

[18] Rolf Bühler and Roger Blandford. "The surprising Crab pulsar and its nebula: A review". In: *Rept. Prog. Phys.* 77 (2014), p. 066901. DOI: 10.1088/0034-4885/77/6/066901. arXiv: 1309.7046 [astro-ph.HE].

[19] Adam Burrows and David Vartanyan. "Core-Collapse Supernova Explosion Theory". In: *Nature* 589.7840 (2021), pp. 29–39. DOI: 10.1038/s41586-020-03059-w. arXiv: 2009.14157 [astro-ph.SR].

[20] Adam Burrows, Tianshu Wang, and David Vartanyan. "Physical Correlations and Predictions Emerging from Modern Core-collapse Supernova Theory". In: *Astrophys. J. Lett.* 964.1 (2024), p. L16. DOI: 10.3847/2041-8213/ad319e. arXiv: 2401.06840 [astro-ph.HE].

[21] Wit Busza, Krishna Rajagopal, and Wilke van der Schee. "Heavy Ion Collisions: The Big Picture, and the Big Questions". In: *Ann. Rev. Nucl. Part. Sci.* 68 (2018), pp. 339–376. DOI: 10.1146/annurev-nucl-101917-020852. arXiv: 1802.04801 [hep-ph].

[22] M. E. Caplan and C. J. Horowitz. "Colloquium : Astromaterial science and nuclear pasta". In: *Rev. Mod. Phys.* 89.4 (2017), p. 041002. DOI: 10.1103/RevModPhys.89.041002. arXiv: 1606.03646 [astro-ph.HE].

[23] E. Caurier et al. "The Shell Model as Unified View of Nuclear Structure". In: *Rev. Mod. Phys.* 77 (2005), pp. 427–488. DOI: 10.1103/RevModPhys.77.427. arXiv: nucl-th/0402046.

[24] E. Chabanat et al. “A Skyrme parametrization from subnuclear to neutron star densities. 2. Nuclei far from stablities”. In: *Nucl. Phys. A* 635 (1998). [Erratum: Nucl.Phys.A 643, 441–441 (1998)], pp. 231–256. DOI: 10.1016/S0375-9474(98)00180-8.

[25] J. Chadwick. “Possible Existence of a Neutron”. In: *Nature* 129.3252 (Feb. 1932), p. 312. DOI: 10.1038/129312a0.

[26] N. Chamel. “Neutron star crust beyond the Wigner-Seitz approximation”. In: (Sept. 2007). DOI: 10.1142/9789812797049_0014. arXiv: 0709.3798 [astro-ph].

[27] N. Chamel. “Superfluidity and Superconductivity in Neutron Stars”. In: *J. Astrophys. Astron.* 38 (2017), p. 43. DOI: 10.1007/s12036-017-9470-9. arXiv: 1709.07288 [astro-ph.HE].

[28] Katerina Chatziioannou. “Neutron star tidal deformability and equation of state constraints”. In: *Gen. Rel. Grav.* 52.11 (2020), p. 109. DOI: 10.1007/s10714-020-02754-3. arXiv: 2006.03168 [gr-qc].

[29] Katerina Chatziioannou. “Neutron-star tidal deformability and equation-of-state constraints”. In: *General Relativity and Gravitation* 52.11 (Nov. 2020). ISSN: 1572-9532. DOI: 10.1007/s10714-020-02754-3. URL: http://dx.doi.org/10.1007/s10714-020-02754-3.

[30] Katerina Chatziioannou et al. “Neutron stars and the dense matter equation of state: from microscopic theory to macroscopic observations”. In: (July 2024). arXiv: 2407.11153 [nucl-th].

[31] Gregory B. Cook, Stuart L. Shapiro, and Saul A. Teukolsky. “Rapidly rotating polytropes in general relativity”. In: *Astrophys. J.* 422 (1994), pp. 227–242.

[32] H. Thankful Cromartie et al. “Relativistic Shapiro delay measurements of an extremely massive millisecond pulsar”. In: *Nature Astron.* 4.1 (2019), pp. 72–76. DOI: 10.1038/s41550-019-0880-2. arXiv: 1904.06759.

[33] Arnab Dhani et al. “Prospects for direct detection of black hole formation in neutron star mergers with next-generation gravitational-wave detectors”. In: *Phys. Rev. D* 109.4 (2024), p. 044071. DOI: 10.1103/PhysRevD.109.044071. arXiv: 2306.06177 [gr-qc].

[34] Tim Dietrich, Sebastiano Bernuzzi, and Wolfgang Tichy. “Closed-form tidal approximants for binary neutron star gravitational waveforms constructed from high-resolution numerical relativity simulations”. In: *Phys. Rev.* D96.12 (2017), p. 121501. DOI: 10.1103/PhysRevD.96.121501. arXiv: 1706.02969 [gr-qc].

[35] C. Drischler, J. W. Holt, and C. Wellenhofer. "Chiral Effective Field Theory and the High-Density Nuclear Equation of State". In: *Ann. Rev. Nucl. Part. Sci.* 71 (2021), pp. 403–432. DOI: 10.1146/annurev-nucl-102419-041903. arXiv: 2101.01709 [nucl-th].

[36] C. Drischler et al. "How Well Do We Know the Neutron-Matter Equation of State at the Densities Inside Neutron Stars? A Bayesian Approach with Correlated Uncertainties". In: *Phys. Rev. Lett.* 125.20 (2020), p. 202702. DOI: 10.1103/PhysRevLett.125.202702. arXiv: 2004.07232 [nucl-th].

[37] Reed Essick et al. "Phase transition phenomenology with nonparametric representations of the neutron star equation of state". In: *Phys. Rev. D* 108.4 (2023). I contributed substantially to this study which used nonparametric methods to constrain phase transitions in a nonparametric model of the equation of state. I performed the simulation analyses, developed several diagnostic statistics, and wrote large parts of the text., p. 043013. DOI: 10.1103/PhysRevD.108.043013. arXiv: 2305.07411 [astro-ph.HE].

[38] Matthew Evans et al. "Cosmic Explorer: A Submission to the NSF MPSAC ngGW Subcommittee". In: (June 2023). arXiv: 2306.13745 [astro-ph.IM].

[39] G. Gamow. "Mass Defect Curve and Nuclear Constitution". In: *Proceedings of the Royal Society of London Series A* 126.803 (Mar. 1930), pp. 632–644. DOI: 10.1098/rspa.1930.0032.

[40] Jacob Golomb et al. "Using equation of state constraints to classify low-mass compact binary mergers". In: *Phys. Rev. D* 110.6 (2024). I co-led this study with Jacob Golomb examining whether subsolar mass neutron stars could be reliably distinguished from subsolar mass black holes with current LIGO detectors. I performed the equation of state inference step, and co-wrote the manuscript, p. 063014. DOI: 10.1103/PhysRevD.110.063014. arXiv: 2403.07697 [astro-ph.HE].

[41] S. Goriely, N. Chamel, and J. M. Pearson. "Further explorations of Skyrme-Hartree-Fock-Bogoliubov mass formulas. XII: Stiffness and stability of neutron-star matter". In: *Phys. Rev. C* 82 (2010), p. 035804. DOI: 10.1103/PhysRevC.82.035804. arXiv: 1009.3840 [nucl-th].

[42] Sophia Han et al. "Treating quarks within neutron stars". In: *Phys. Rev. D* 100 (10 Nov. 2019), p. 103022. DOI: 10.1103/PhysRevD.100.103022. URL: https://link.aps.org/doi/10.1103/PhysRevD.100.103022.

[43] Alice K. Harding and Dong Lai. "Physics of Strongly Magnetized Neutron Stars". In: *Rept. Prog. Phys.* 69 (2006), p. 2631. DOI: 10.1088/0034-4885/69/9/R03. arXiv: astro-ph/0606674.

[44] James B. Hartle. "Slowly Rotating Relativistic Stars. I. Equations of Structure". In: *The Astrophysical Journal* 150 (Dec. 1967), p. 1005. DOI: 10.1086/149400.

[45] K. Hebeler et al. “Equation of state and neutron star properties constrained by nuclear physics and observation”. In: *Astrophys. J.* 773 (2013), p. 11. DOI: 10.1088/0004-637X/773/1/11. arXiv: 1303.4662 [astro-ph.SR].

[46] Matthias Hempel et al. “New Equations of State in Simulations of Core-Collapse Supernovae”. In: *Astrophys. J.* 748 (2012), p. 70. DOI: 10.1088/0004-637X/748/1/70. arXiv: 1108.0848 [astro-ph.HE].

[47] Tanja Hinderer. “Tidal Love numbers of neutron stars”. In: *Astrophys. J.* 677 (2008), pp. 1216–1220. DOI: 10.1086/533487. arXiv: 0711.2420 [astro-ph].

[48] Huanchen Hu and Paulo C. C. Freire. “Measuring the Lense–Thirring Orbital Precession and the Neutron Star Moment of Inertia with Pulsars”. In: *Universe* 10.4 (2024), p. 160. DOI: 10.3390/universe10040160. arXiv: 2403.18785 [gr-qc].

[49] R. A. Hulse and J. H. Taylor. “Discovery of a pulsar in a binary system.” In: *The Astrophysical Journal Letters* 195 (Jan. 1975), pp. L51–L53. DOI: 10.1086/181708.

[50] Yoonsoo Kim et al. “Black Hole Pulsars and Monster Shocks as Outcomes of Black Hole–Neutron Star Mergers”. In: *Astrophys. J. Lett.* 982.2 (2025), p. L54. DOI: 10.3847/2041-8213/adbff9. arXiv: 2412.05760 [astro-ph.HE].

[51] Oleg Komoltsev et al. “Equation of state at neutron-star densities and beyond from perturbative QCD”. In: *Phys. Rev. D* 109.9 (2024), p. 094030. DOI: 10.1103/PhysRevD.109.094030. arXiv: 2312.14127 [nucl-th].

[52] Michael Kramer. “Observational manifestations of young neutron stars: spin-powered pulsars”. In: *IAU Symp.* 218 (2004), p. 13. arXiv: astro-ph/0310451.

[53] Philippe Landry and Eric Poisson. “Tidal deformation of a slowly rotating material body. External metric”. In: *Phys. Rev.* D91 (2015), p. 104018. DOI: 10.1103/PhysRevD.91.104018. arXiv: 1503.07366 [gr-qc].

[54] James M. Lattimer and Bernard F. Schutz. “Constraining the Equation of State with Moment of Inertia Measurements”. In: *The Astrophysical Journal* 629.2 (Aug. 2005), pp. 979–984. DOI: 10.1086/431543. URL: https://doi.org/10.1086%2F431543.

[55] Isaac Legred et al. “Impact of the PSR J0740 + 6620 radius constraint on the properties of high-density matter”. In: *Phys. Rev. D* 104 (6 Sept. 2021), p. 063003. DOI: 10.1103/PhysRevD.104.063003. URL: https://link.aps.org/doi/10.1103/PhysRevD.104.063003.

[56] Isaac Legred et al. "Impact of the PSR J0740 + 6620 radius constraint on the properties of high-density matter". In: *Phys. Rev. D* 104 (6 Sept. 2021). I led this study on the impact of the the NICER mass-radius constraint on the mllisecond x-ray pulsar J0740+6620 on nonparametric equation of state constraints. I developed software, some of which was contributed by other collaborators from previous projects, ran the analysis, and co-wrote the manuscript., p. 063003. DOI: 10.1103/PhysRevD.104.063003. URL: https://link.aps.org/doi/10.1103/PhysRevD.104.063003.

[57] Isaac Legred et al. "Simulating neutron stars with a flexible enthalpy-based equation of state parametrization in spectre". In: *Phys. Rev. D* 107.12 (2023). I led this project building a flexible equation of state model, implementing it in the SpECTRE code, and running relativistic simulation of neutron stars. I developed the project idea, constructed the equation of state model, implemented it, and ran analyses. I also wrote the bulk of the text in the manuscript., p. 123017. DOI: 10.1103/PhysRevD.107.123017. arXiv: 2301.13818 [astro-ph.HE].

[58] Lee Lindblom. "Phase transitions and the mass radius curves of relativistic stars". In: *Phys. Rev. D* 58 (1998), p. 024008. DOI: 10.1103/PhysRevD.58.024008. arXiv: gr-qc/9802072.

[59] P. N. McDermott et al. "The nonradial oscillation spectra of neutron stars." In: *The Astrophysical Journal Letters* 297 (Oct. 1985), pp. L37–L40. DOI: 10.1086/184553.

[60] Elias R. Most, Andrei M. Beloborodov, and Bart Ripperda. "Monster Shocks, Gamma-Ray Bursts, and Black Hole Quasi-normal Modes from Neutron-star Collapse". In: *Astrophys. J. Lett.* 974.1 (2024), p. L12. DOI: 10.3847/2041-8213/ad7e1f. arXiv: 2404.01456 [astro-ph.HE].

[61] J. R. Oppenheimer and G. M. Volkoff. "On Massive Neutron Cores". In: *Phys. Rev.* 55 (4 Feb. 1939), pp. 374–381. DOI: 10.1103/PhysRev.55.374. URL: https://link.aps.org/doi/10.1103/PhysRev.55.374.

[62] J. R. Oppenheimer and G. M. Volkoff. "On Massive Neutron Cores". In: *Phys. Rev.* 55 (4 Feb. 1939), pp. 374–381. DOI: 10.1103/PhysRev.55.374. URL: https://link.aps.org/doi/10.1103/PhysRev.55.374.

[63] Lidia M. Oskinova et al. "X-rays observations of a super-Chandrasekhar object reveal an ONe and a CO white dwarf merger product embedded in a putative SN Iax remnant". In: *Astronomy and Astrophysics* 644, L8 (Dec. 2020), p. L8. DOI: 10.1051/0004-6361/202039232. arXiv: 2008.10612 [astro-ph.SR].

[64] Dany Page et al. "Minimal cooling of neutron stars: A New paradigm". In: *Astrophys. J. Suppl.* 155 (2004), pp. 623–650. DOI: 10.1086/424844. arXiv: astro-ph/0403657.

[65] Alessandro Patruno and Anna L. Watts. "Accreting Millisecond X-ray Pulsars". In: *Timing Neutron Stars: Pulsations, Oscillations and Explosions*. Ed. by Tomaso M. Belloni, Mariano Méndez, and Chengmin Zhang. Vol. 461. Astrophysics and Space Science Library. Jan. 2021, pp. 143–208. DOI: 10.1007/978-3-662-62110-3_4. arXiv: 1206.2727 [astro-ph.HE].

[66] J. M. Pearson and S. Goriely. "Nuclear mass formulas for astrophysics". In: *Nucl. Phys. A* 777 (2006), pp. 623–644. DOI: 10.1016/j.nuclphysa.2004.06.005.

[67] Philip Carl Peters. "Gravitational radiation and the motion of two point masses". PhD thesis. California Institute of Technology, Jan. 1964.

[68] Alexander Philippov, Andrey Timokhin, and Anatoly Spitkovsky. "Origin of Pulsar Radio Emission". In: *Phys. Rev. Lett.* 124.24 (2020), p. 245101. DOI: 10.1103/PhysRevLett.124.245101. arXiv: 2001.02236 [astro-ph.HE].

[69] J. Piekarewicz. "The Nuclear Physics of Neutron Stars". In: (Sept. 2022). arXiv: 2209.14877 [nucl-th].

[70] David Radice, Sebastiano Bernuzzi, and Albino Perego. "The Dynamics of Binary Neutron Star Mergers and GW170817". In: *Ann. Rev. Nucl. Part. Sci.* 70 (2020), pp. 95–119. DOI: 10.1146/annurev-nucl-013120-114541. arXiv: 2002.03863 [astro-ph.HE].

[71] P. G. Reinhard. "The Relativistic Mean Field Description of Nuclei and Nuclear Dynamics". In: *Rept. Prog. Phys.* 52 (1989), p. 439. DOI: 10.1088/0034-4885/52/4/002.

[72] Tuomo Salmi et al. "Atmospheric Effects on Neutron Star Parameter Constraints with NICER". In: *Astrophys. J.* 956.2 (2023), p. 138. DOI: 10.3847/1538-4357/acf49d. arXiv: 2308.09319 [astro-ph.HE].

[73] Irwin I. Shapiro. "Fourth Test of General Relativity". In: *Phys. Rev. Lett.* 13 (1964), pp. 789–791. DOI: 10.1103/PhysRevLett.13.789.

[74] S. L. Shapiro and S. A. Teukolsky. *Black holes, white dwarfs, and neutron stars: The physics of compact objects*. 1983. ISBN: 978-0-471-87316-7, 978-3-527-61766-1. DOI: 10.1002/9783527617661.

[75] Peter Skands. "Introduction to QCD". In: *Theoretical Advanced Study Institute in Elementary Particle Physics: Searching for New Physics at Small and Large Scales*. 2013, pp. 341–420. DOI: 10.1142/9789814525220_0008. arXiv: 1207.2389 [hep-ph].

[76] T. H. R. Skyrme. "CVII. The nuclear surface". In: *Phil. Mag.* 1 (1956), pp. 1043–1054. DOI: 10.1080/14786435608238186.

[77] Agnieszka Sorensen et al. "Dense nuclear matter equation of state from heavy-ion collisions". In: *Prog. Part. Nucl. Phys.* 134 (2024), p. 104080. DOI: 10.1016/j.ppnp.2023.104080. arXiv: 2301.13253 [nucl-th].

[78] Theodoros Soultanis, Andreas Bauswein, and Nikolaos Stergioulas. "Analytic models of the spectral properties of gravitational waves from neutron star merger remnants". In: *Phys. Rev. D* 105.4 (2022), p. 043020. DOI: 10.1103/PhysRevD.105.043020. arXiv: 2111.08353 [astro-ph.HE].

[79] Richard C. Tolman. "Static Solutions of Einstein's Field Equations for Spheres of Fluid". In: *Phys. Rev.* 55 (4 Feb. 1939), pp. 364–373. DOI: 10.1103/PhysRev.55.364. URL: https://link.aps.org/doi/10.1103/PhysRev.55.364.

[80] Serena Vinciguerra et al. "X-PSI Parameter Recovery for Temperature Map Configurations Inspired by PSR J0030+0451". In: *Astrophys. J.* 959.1 (2023), p. 55. DOI: 10.3847/1538-4357/acf9a0. arXiv: 2308.08409 [astro-ph.HE].

[81] Steven Weinberg. "Nuclear forces from chiral Lagrangians". In: *Phys. Lett. B* 251 (1990), pp. 288–292. DOI: 10.1016/0370-2693(90)90938-3.

[82] Clifford M. Will. "Equations of motion for compact binary systems in general relativity: Do they depend on the bodies' internal structure at the third post-Newtonian order?" In: (Mar. 2025). arXiv: 2503.03189 [gr-qc].

[83] Clifford M. Will. "On the unreasonable effectiveness of the post-Newtonian approximation in gravitational physics". In: *Proc. Nat. Acad. Sci.* 108 (2011), p. 5938. DOI: 10.1073/pnas.1103127108. arXiv: 1102.5192 [gr-qc].

[84] Kent Yagi and Nicolas Yunes. "I-Love-Q Relations in Neutron Stars and their Applications to Astrophysics, Gravitational Waves and Fundamental Physics". In: *Phys. Rev. D* 88.2 (2013), p. 023009. DOI: 10.1103/PhysRevD.88.023009. arXiv: 1303.1528 [gr-qc].

[85] Hang Yu, Phil Arras, and Nevin N. Weinberg. "Dynamical tides during the inspiral of rapidly spinning neutron stars: Solutions beyond mode resonance". In: *Phys. Rev. D* 110.2 (2024), p. 024039. DOI: 10.1103/PhysRevD.110.024039. arXiv: 2404.00147 [gr-qc].

[86] Xingjiang Zhu et al. "Inferring the population properties of binary neutron stars with gravitational-wave measurements of spin". In: *Phys. Rev. D* 98 (2018), p. 043002. DOI: 10.1103/PhysRevD.98.043002. arXiv: 1711.09226 [astro-ph.HE].